UiT The Arctic University of Norway

Faculty of Science and Technology, Department of Chemistry

New Building Blocks for Cancer Phototherapeutics: 5d Metallocorroles

Rune Finsås Einrem

A dissertation for the degree of Philosophiae Doctor October 2022

Acknowledgement

I would like to thank my supervisors – Prof. Abhik Ghosh for the many opportunities that made this work possible and Prof. Odrun A. Gederaas for introducing me to a new area of research. I appreciate them both for believing in me and supporting me academically as well as professionally.

My gratitude goes to all members of our research group at UiT including Dr. Ivar Thomassen, Hans-Kristian Norheim, Dr. Simon Larsen, Dr. Sumit Ganguly, Dr. Hugo Vazques-Lima, Dr. Kolle E. Thomas, Einar Jonsson, Gulbrand Nilsen and most notably Dr. Abraham Alemayehu for day-to-day supervision, collaboration, and never-failing humour!

It has also been a great honour to collaborate with, and learn from, many leading international scientists including Prof. Roger Alberto and Dr. Henrik Braband of the University of Zurich, Dr. Sergey Borisov of the Graz University of Technology, Dr. Laura McCormick of the Advanced Light Source, Berkeley, Prof. Penelope Brothers of The University of Auckland and Prof. Jeanet Conradie of the University of Free State, South Africa.

I also thank our departmental administration, including Annette Bayer, Ronny Helland, Renate Lie Larsen, and Stig Eide, and engineers Jostein Johansen, Fredrick Leeson, Arnfinn Kvarsnes, and Truls Ingebrigtsen for their advice and assistance on practical matters.

I would like to thank my fellow students and colleagues in the Chemical Synthesis and Analysis group, especially Prof. Tore Lejon, for making a good learning environment and pleasant social atmosphere.

Finally, I thank my family and friends for believing in me and always being supportive. Above all, I am grateful to Ane Kongsro Finstad, the rock of my life, for allowing the necessarily self-centred life as a PhD required. My immense gratitude also goes to Susi and Bark.

Rune F. Einrem

Abstract

Corroles are triprotic aromatic molecule with a slightly contracted cavity compared with its diprotic counterpart, porphyrin. Both porphyrins and corroles give rise to highly distinctive coordination chemistry. Although corrole was first synthesized in 1965, their chemistry lay largely dormant until the very end of the twentieth century, when the Gross and Paolesse groups independently reported one-pot synthetic methods for corrole. The early years of the twenty-first century witnessed the rapid exploration of many aspects of corrole chemistry. An interesting decade started in 2008 with the synthesis of iridium corroles and a quest for the entire 5d metallocorrole series.

Porphyrins and corroles light absorption abilities makes them interesting compounds for sensitisers in different applications. Investigations have shown that gold corroles could serve as multifunctional materials. Preliminary experiments had shown that Au corroles and ReO corroles shared several similar properties. This made ReO corroles an interesting starting point for further application studies.

From photophysical investigations it became apparent that ReO corroles exhibit the highest phosphorescence quantum yields (1-1.5%) among all metallocorroles. It also became clear that ReO corroles also sensitize singlet oxygen formation with high quantum yields (0.72±0.02) and serve as oxygen sensors and as triplet-triplet annihilation upconverters. An investigation of their potential as photosensitizers in *in vitro* photodynamic therapy experiments was the natural next step. Accordingly amphiphilic *meta*/*para*-carboxyl-appended ReO triphenylcorroles were synthesised and found that they exhibit high photocytotoxicity against two different cancer cell lines, AY27 and WiDr.

Further it was found that amphiphilic meta/para-carboxyl-appended Au, ReO and OsN metallocorroles also exhibit photovoltaic activity in dye-sensitized solar cells. Time-resolved spectroscopic studies indicated that the photovoltaic activity results from singlet-state, rather than triplet-state reactivity.

To enhance the photophysical properties of the ReO corroles electrophilic chlorination and bromination was studied. X-ray structures of ReO octachloro- and octabromocorroles yielded showed similar conformation as unsubstituted ReO corroles. Another synthetic study afforded an innovative approach to water-soluble iridium corroles, involving the use of water-soluble axial ligands. These were found to be unstable or not phosphorescence.

With the goal to enhance the binding abilities to surface materials like TiO and graphene, formylation of ReO and Au triarylcorroles were studied. Using Vilsmeier-Haack conditions it became clear that the two metallocorroles favoured regioselectivity affording 3-monoformyl products for the ReO corrole, while the Au corrole yielded the 3,17-diformyl products. Presumably reflecting the higher nucleophilicity of the Au complexes. The formylcorrole products could be postfunctionalized, via the Knoevenagel reaction. Such post-functionalization protocols should allow the installation of different anchoring groups, setting the stage for bio- and nanoconjugated 5d metallocorroles for advanced materials, and targeted cancer therapies.

List of publications and contributions

Paper A: “Ambient-temperature near-IR phosphorescence and potential applications of rhenium-oxo corroles” Borisov, S. M.; Einrem, R. F.; Alemayehu, A. B.; Ghosh, A. *Photochem. Photobiol. Sci.* **2019**, 18, 1166-1170.

I synthesised all the corrole complexes and characterised them prior to photophysical measurement. I was also involved in the selection of compounds which should further be investigated by photophysical methods. The photophysical measurements were caried out by Dr. Sergey Borisov of the Graz University of Technology. I also contributed, to a smaller extent, to the writing of the publication.

Paper B: “Amphiphilic Rhenium-Oxo Corroles as a New Class of Sensitizers for Photodynamic Therapy.” Einrem, R. F.; Ghosh, A.; Alemayehu, A. B.; Borisov, S. M.; Gederaas, O. A. *ACS Omega*. **2020,** 5, 10596 – 10601.

I synthesised four new rhenium-oxo corroles, and characterised them using 1H NMR, UV-vis, IR, ESI-MS and x-ray crystallography. I also conducted a full cell viability study using the MTT assay. The cell viability study was performed at NTNU in collaboration with supervisor Dr. Odrun A. Gederaas. I had the major responsibility of coordinating the project and the writing.

Paper C: “Synthesis and Molecular Structure of Perhalogenated Rhenium-Oxo Corroles” Alemayehu, A. B.; Einrem, R.F.; McCormick, L. J.; Settineri, N. S.; Ghosh, A. *Sci. Rep.* **2020**, 10, 19727.

I was heavily involved in the planning of the experiments and the optimization leading to the octabrominated rhenium corrole complexes. The chlorination and the analyses were primarily performed by the first author.

Paper D: “Heavy Metal Effects on the Photovoltaic Properties of Metallocorroles in Dye-Sensitized Solar Cells” Higashino, T.; Kurumisawa, Yuma, Alemayehu, A. B.; Einrem, R. F.; Sahu, D.; Packwood, D. M; Kato, K.; Yamakata, A.; Ghosh, A.; Imahori, H. *ACS Appl. Energy Mater.* **2020**, 3, 12, 12460-12467.

I synthesised and analysed the rhenium corroles studied in this paper. The photovoltaic measurements were performed by our partners. I was to a lesser extent involved in the writing of the paper, and in the interpretation of the results.

Paper E: “Regioselective formylation of rhenium-oxo and gold corroles substituent effects on optical spectra and redox potentials” Einrem, R.F.; Jonsson, E.T.; Teat, S.J.; Settineri, S. S.; Alemayehu, A.B.; Ghosh, A. *RSC Adv*. **2021**, *11*, 34086.

I was primarily responsible for the conception of the project and contributed approximately ¾ of the synthetic work, as well as most of the analyses. I also supervised several undergraduates who performed preliminary experiments in this project.

Paper F: “A Simple, Axial Ligand-Mediated Route to Water-Soluble Iridium Corroles”, Thomassen, I. K.; Rasmussen, D.; Einrem, R. F.; Ghosh, A. *ACS Omega*. **2021**, 6, 25, 16683-16687.

I did about 40% of the synthetic and analytical work and writing. I also initially supervised the undergraduate involved in the project.

Appendix 1: “The Story of 5d Metallocorroles: From Metal–Ligand Misfits to New Building Blocks for Cancer Phototherapeutics.” Alemayehu, A. B.; Thomas, K. E.; Einrem, R. F.; Ghosh, A. *Acc. Chem. Res*. **2021**, *54*, 3095– 3107.

Contributed to a general understanding of the field of which the scope of the publication embraced. Contributed to smaller amounts of text, tables, data, schematics, and illustrations.

Table of Contents

List of abbreviations

Acac	acetylacetone
COD	1,5-cyclooctadiene
DCM	dichloromethane
DDQ	2,3-dichloro-5,6-dicyano-1,4-benzoquinone
DMF	dimethylformamide
NBS	*N*-bromosuccinimide
NCS	*N*-chlorosuccinimide
NFP	*N*-fused porphyrin
NIS	*N*-iodosuccinimide
NIR	near-infrared
NMR	nuclear magnetic resonance
PDT	photodynamic therapy
TFA	trifluoroacetic acid
THF	tetrahydrofuran
TPP	tetraphenylporphyrin
TPC	triphenylcorrole
TPFPP	tetrakis(pentafluorophenyl)porphyrin
TPFPC	tris(pentafluorophenyl)corrole
UV-vis	ultraviolet-visible
XAS	X-ray absorption spectroscopy

Chapter 1: Synthesis of porphyrins and porphyrin analogues

1.1 Introductory comments

Throughout history, humans have wondered “why is the grass green and blood red?” [1] Today we know that the green pigment of grass, and the red blood are porphyrinoids, a diverse class of macrocyclic tetrapyrroles. This class of molecules can be found throughout Nature, in *Archaea*, *Bacteria* and *Eukarya*, including our own bodies where the porphyrin cofactor heme b, is involved in oxygen transport as part of hemoglobin and myoglobin. Other related biological molecules include the heme protins cytochrome P450 and cytochrome *b* and *c*. The cobalt-containing porphyrinoid B_{12} is an essential nutrient for humans and acts as a cofactor in many biological reactions, whereas F_{430}, a nickel-containing porphyrinoid, is the cofactor of methylcoenzyme M reductase, the enzyme that catalyses the last step of biological methane production. [2] Figure 1 depicts some naturally occurring porphyrin derivatives.

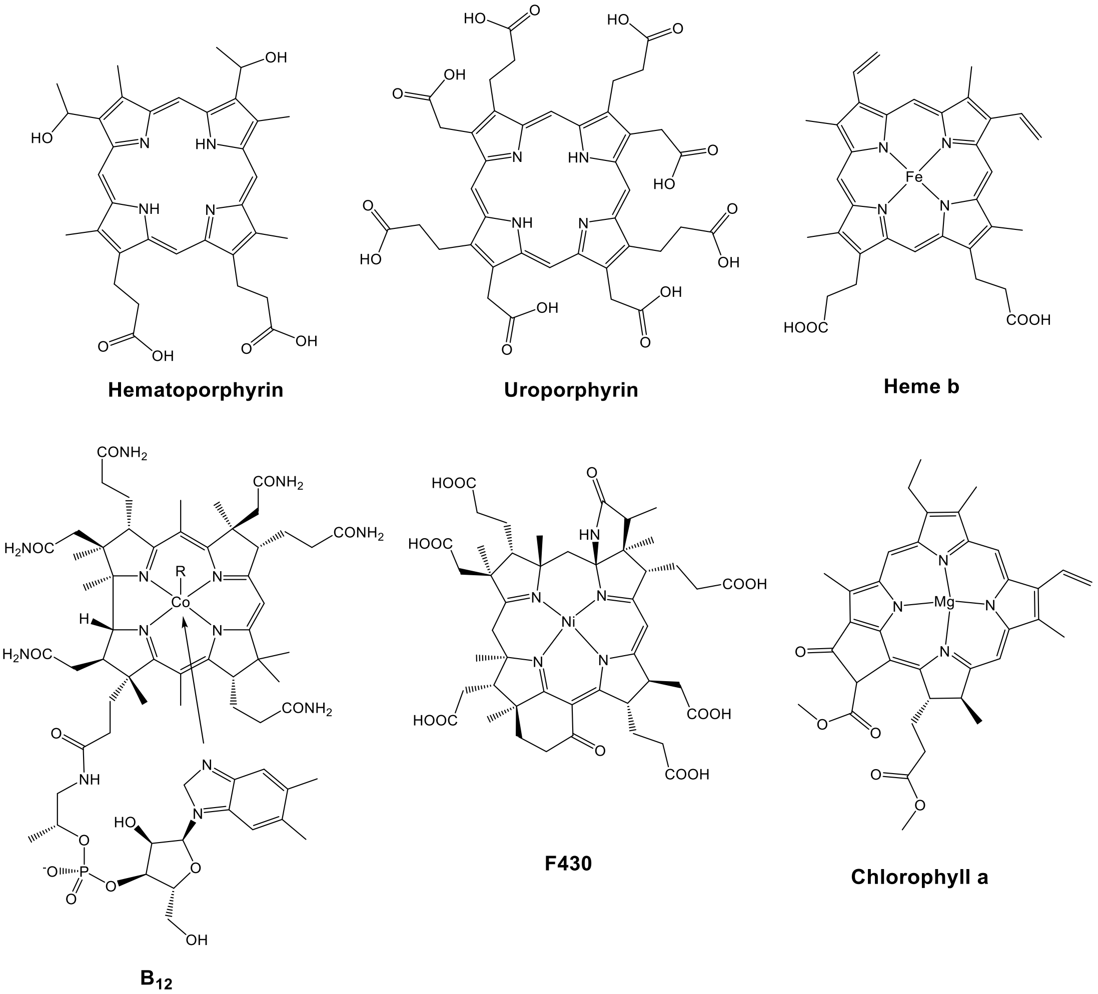

Hematoporphyrin **Uroporphyrin** **Heme b**

B_{12} **F430** **Chlorophyll a**

Figure 1. Six naturally occurring porphyrinoids.

A classic porphyrin is built from four pyrrole rings joined by methine bridges resulting in an 18π-electron aromatic macrocycle. The carbon atoms within the pyrrole rings are called α and β carbons and the bridging methine carbons are called *meso* carbons. Figure 2 depicts the IUPAC numbering for the porphyrin ring. Note that the stable form of metal-free porphyrin, so-called free-base porphyrin, has the two central hydrogens on opposite nitrogens. The alternative *cis* tautomer is several kcal/mol higher in energy and is only implicated as a short-lived intermediate in the interconversion of two trans tautomers. [3] Very recently, the *cis* tautomer has been stabilized as a termolecular hydrogen bonded complex, which has been structurally characterized by one of my co-workers. [4]

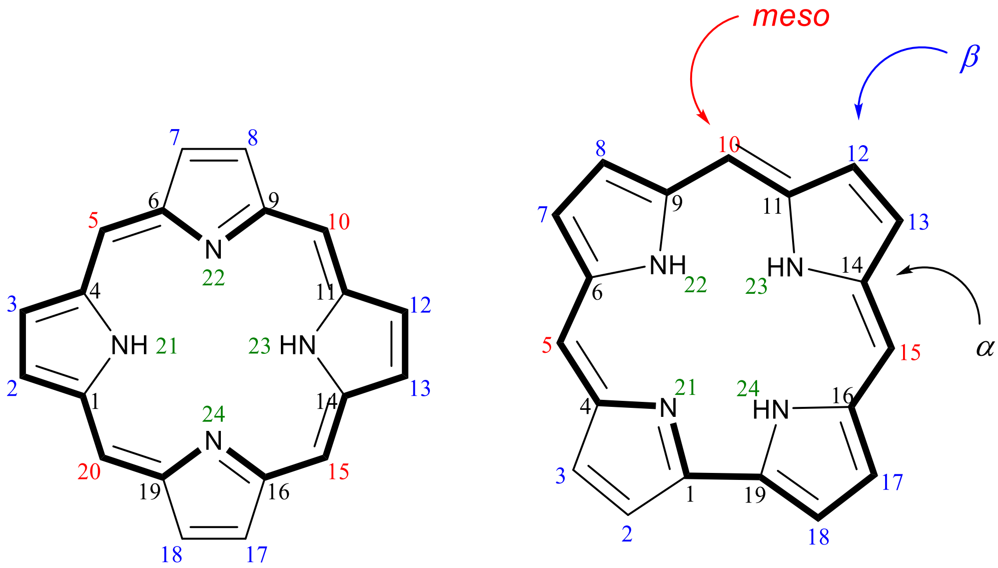

Figure 2. Molecular structure of unsubstituted porphyrin (left) and corrole (right), including IUPAC numbering of skeletal atoms and definition of α, β, and *meso* positions. Formal 18-electron aromatic pathways are indicated in bold.

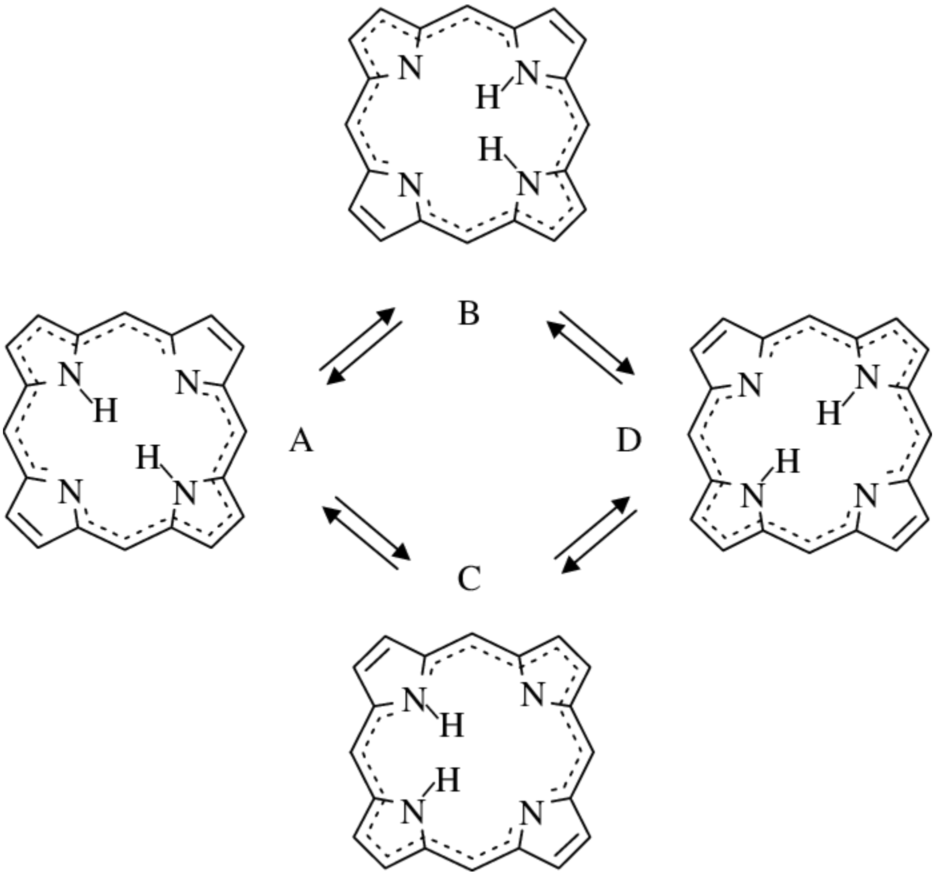

Figure 3. Tautomerism in free-base porphyrins, with *cis* porphyrin intermediates. Reused with permission from ref 3. *Copyright © 1996 American Chemical Society*.

Over the last half-century, the chemistry of porphyrins has undergone an incredible expansion. The field, summarized in a single volume by Falk in 1964[5] and in seven volumes in *The Porphyrins* edited by David Dolphin, is now covered by an ongoing *Handbook of Porphyrin Science* that currently stands at 46 volumes. A 2017 special issue of *Chemical Reviews* ran to over 1600 pages, the largest single issue of the journal to date.[6] Understandably, then, the introductory parts of this thesis will address key topics only very briefly. The present Chapter focuses on the organic chemistry of porphyrinoid synthesis. Chapter 2 presents aspects on coordination chemistry, with emphasis on corroles. Chapter 3 focuses on functionalization of the porphyrinoid (corrole) peripheries. Chapter 4 focuses on applications of porphyrinoids, again with emphasis on corroles. Finally, Chapter 5 presents a personal perspective of my published papers.

1.2 Some classical porphyrin syntheses

The first artificial porphyrin was reported by Hans Fischer in 1929, a major achievement underlying his Nobel Prize in 1930. He heated dipyrromethene salts in different organic acids, as illustrated in Figure 4. Careful attention to symmetry considerations is required when using this approach and the syntheses result in poor yields of only a few percent. Although a large variety of porphyrins were prepared with this method, it is now largely of historical interest. [7]

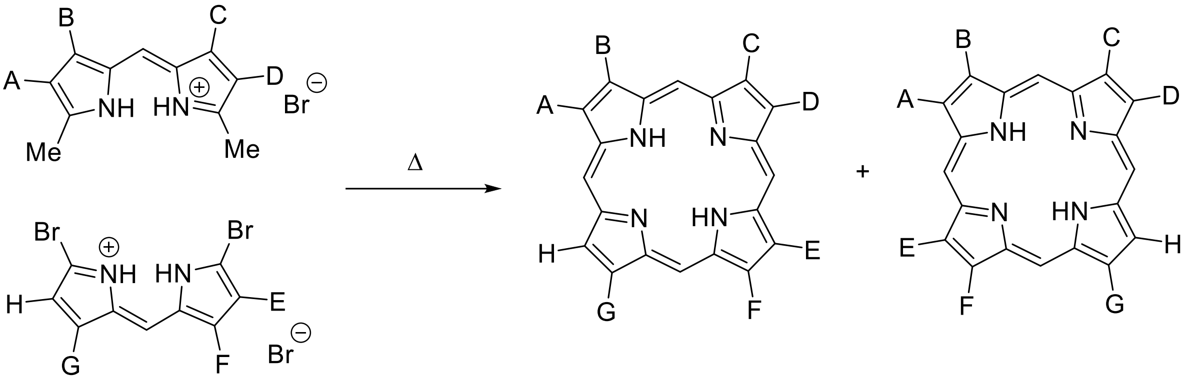

Figure 4. Symmetry problems in Fischer-type synthesis of porphyrins via [2 + 2] addition of dipyrromethene salts.

A paradigm shift in porphyrin synthesis came in 1960 through the MacDonald method. [8] Due to dipyrromethanes' sensitivity to acids, most of the early work was done on dipyrromethenes. MacDonald however, used dipyrromethane, as shown in Figure 5. He showed that 1,9-diformyldipyrromethane could be condensed with either a 1,9-di-unsubstituted dipyrromethane or its 1,9-dicarboxylic acid in the presence of an acid. The biggest advantage using MacDonald's synthesis was that it yields up to 60%. During Woodward's investigation in the total synthesis of chlorophyll a, he solved a crucial step using a variety of the MacDonald approach. [8, 9] Robert B. Woodward was awarded the Nobel Prize in chemistry in 1965, largely thanks to his chlorophyll synthesis.

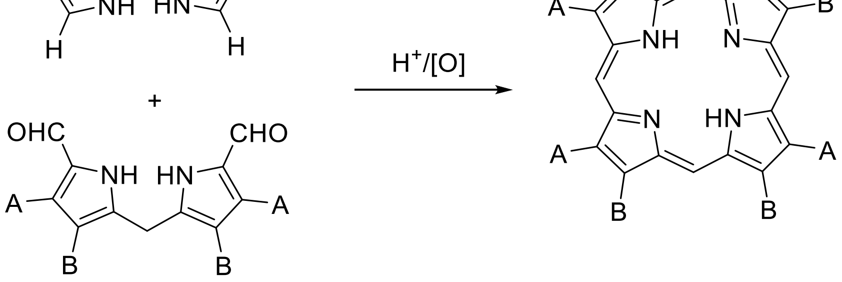

Figure 5. MacDonald's [2 + 2] porphyrin synthesis.

Through condensation of pyrrole and aldehydes in a sealed tube and heating at high temperature, Rothemund was the first, in 1935, to report a one-pot approach for free-base porphyrins. However, this procedure newer caught particular attention. A modification of Rothemund synthesis by mixing equimolar amounts of pyrrole and benzaldehyde in propionic acid resulting in the corresponding tetraphenylporphyrine marked the beginning of a new chapter in porphyrin synthesis. [10]

In 1987 Lindsey and co-workers reported a mild synthetic approach for free-base porphyrins. By mixing equimolar amounts of aldehyde and pyrrole in dichloromethane, in the presence of trifluoroacetic acid or boron trifluoride-etherate under inert atmosphere, followed by oxidation by DDQ or *p*-chloranil (Figure 6), a wide variety of *meso*-arylporphyrins could be obtained. [11]

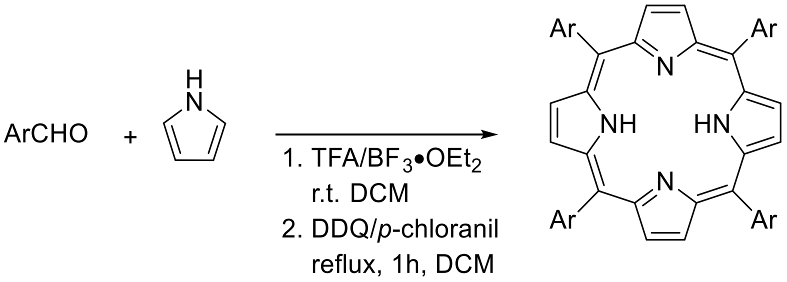

Figure 6. Quasi-one-pot synthesis of porphyrin through condensation of pyrrole and an aromatic aldehyde followed by oxidation.

Since the 1990s, it has emerged that pyrrole-aldehyde condensations may provide a variety of porphyrin analogues, in addition to true porphyrins. Obviously, the process is sensitive to the exact reaction conditions and substituents and is not method of choice for all the macrocycles shown in Figure 7. However, the method works well for corroles and *N*-confused tetraarylporphyrins. Synthetic methods for several of these macrocycles are discussed in the following sections.

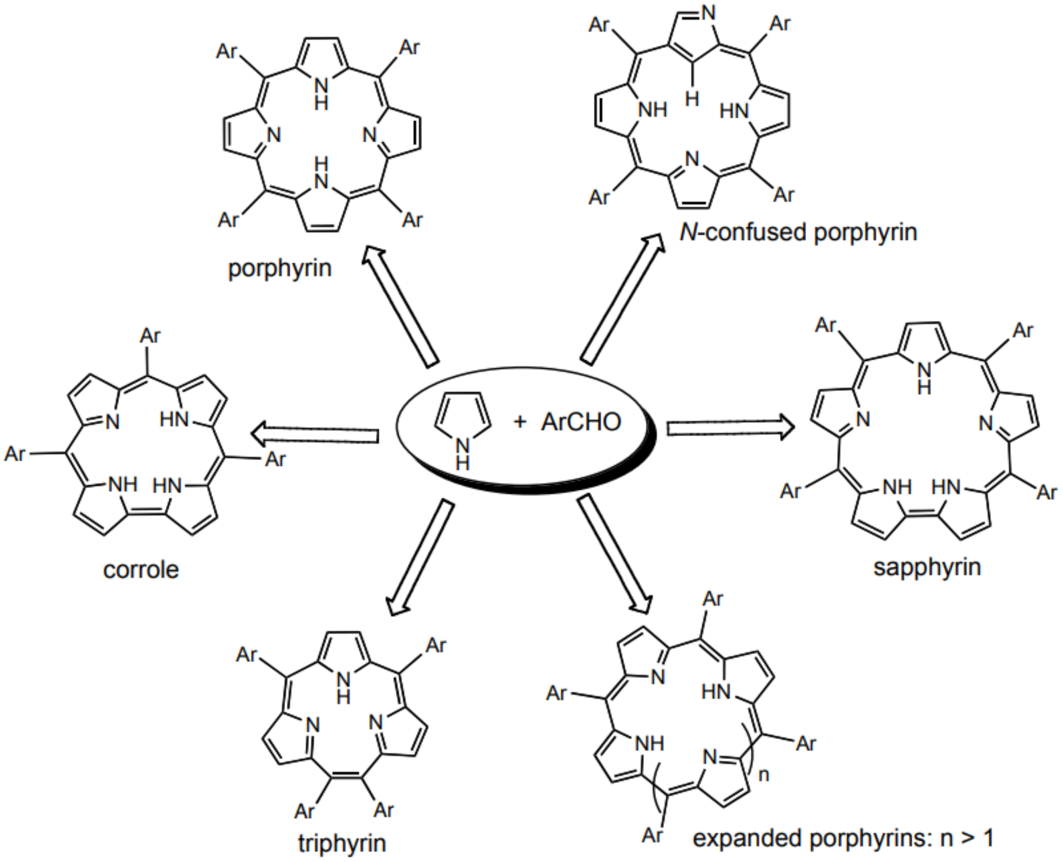

Figure 7. Porphyrinoid macrocycles obtained via pyrrole-aldehyde condensations. Reused with permission from “Letters to a Young Chemist”, *Copyright © 2011, John Wiley & Sons*.

1.3 Porphyrazines and phtalocyanines

Porphyrazines and phthalocyanines (Figure 8) are generally synthesized via the templated condensation of the corresponding maleonitrile and phthalonitrile, respectively. Although the metal complexes thus obtained are less readily demetallated than porphyrins, both macrocycles exhibit a vast coordination geometry and wide-ranging applications.[12]

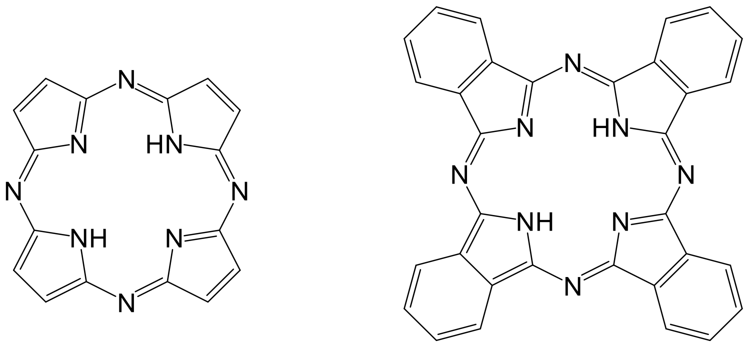

Figure 8. Free-base porphyrazine (left) and phthalocyanine (right).

1.4 Porphyrin isomers

Figure 9 depicts several constitutional isomers of porphyrin that have been synthesized to date. Of these, porphycenes are the best known and are most conveniently accessed via McMurry coupling of bipyrrole-dialdehyde precursor (whose synthesis is not shown), as illustrated in Figure 10.[13] Likewise, intramolecular McMurry coupling of an open-chain tetrapyrrole-dialdehyde has led to corrphycene, another porphyrin isomer, as shown in Figure 11.[14]

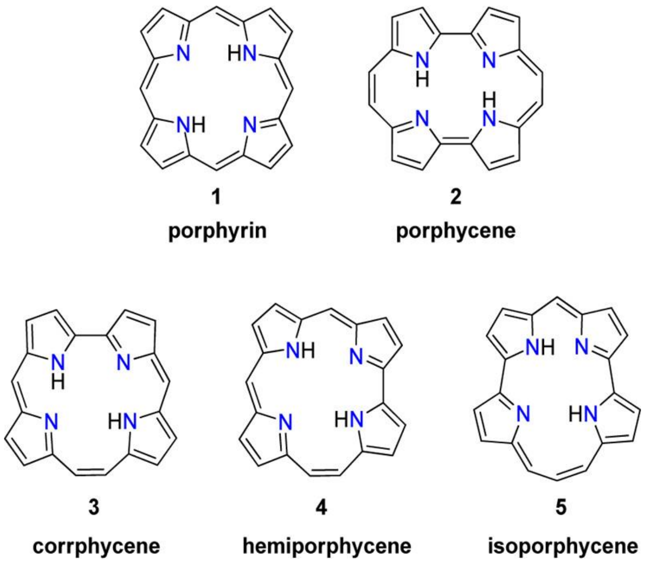
1 **porphyrin**; **2** **porphycene**; **3** **corrphycene**; **4** **hemiporphycene**; **5** **isoporphycene**

Figure 9. Porphyrin and selected constitutional isomers. Reused with permission from ref 13. *Copyright © 2016 American Chemical Society*.

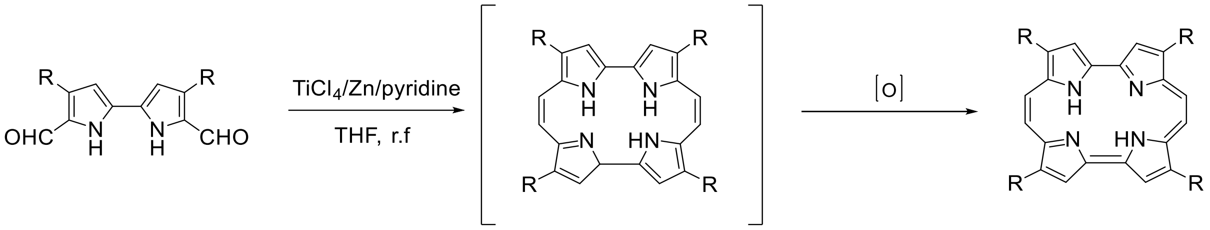

Figure 10. McMurry coupling-mediated rout to porphycene. Redrawn from ref [13].

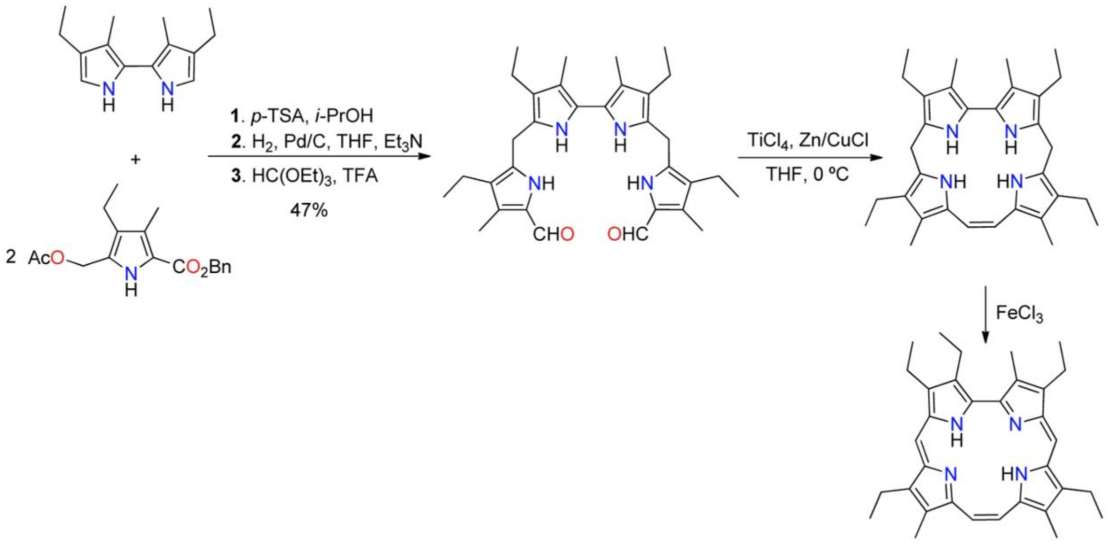

Figure 11. Synthesis of corrphycene. Reproduced with permission from ref 14. *Copyright © 1994 by VCH Verlagsgesellschaft mbH, Germany*

1.5 Heteroporphyrins, Carbaporphyrins and *N*-confused porphyrins

Although porphyrazines and phthalocyanines might be viewed as heteroatom-substituted porphyrins or heteroporphyrins, the latter term often refers to porphyrin derivatives where one or more of the pyrrole nitrogen's have been replaced by another element, as exemplified in Figure 12.

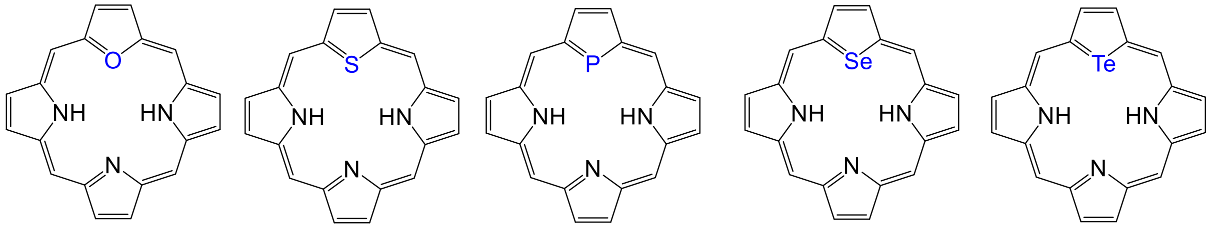

Figure 12. Examples of heteroporphyrins.

A typical synthesis involves a quasi-one-pot oxidative condensation of a pyrrole-dicarbinol, an aromatic aldehyde, and pyrrole, as shown in Figure 13.[15]

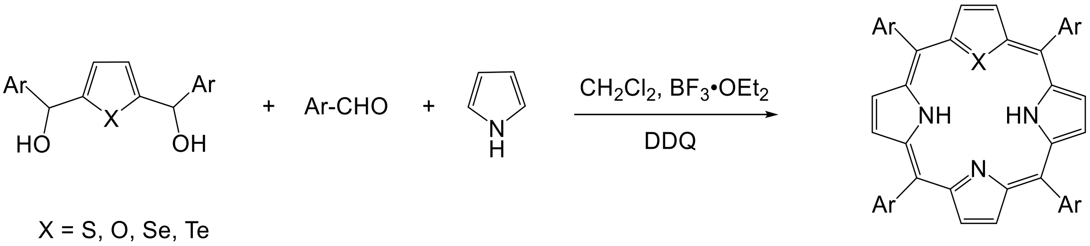

Figure 13. Synthesis of symmetrical 21-monoheteroatom-substituted porphyrins with X = O, S, Se, Te. Redrawn from ref 15.

Carbaporphyrins are a variant of heteroporphyrins in which one or more of the four central nitrogens of porphyrin have been replaced by carbon. Figure 14 depicts selected monocarbaporphyrins that have been synthesized to date. [16]

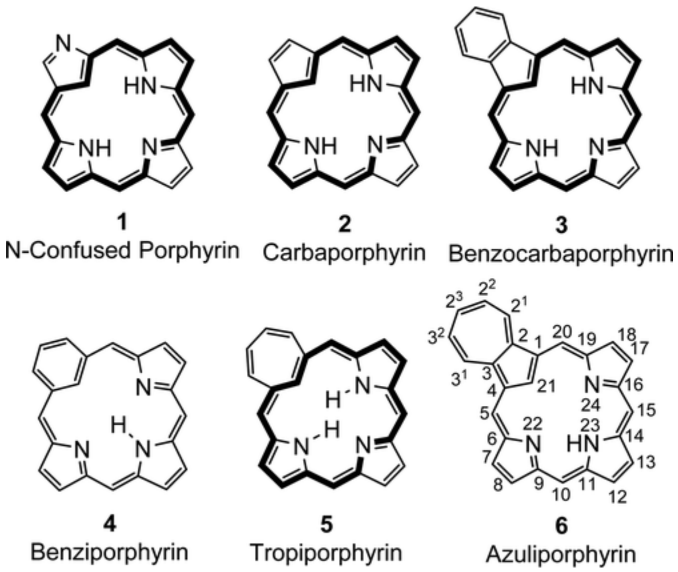
1 N-Confused Porphyrin
2 Carbaporphyrin
3 Benzocarbaporphyrin
4 Benziporphyrin
5 Tropiporphyrin
6 Azuliporphyrin

Figure 14. Examples of carbaporphyrinoids. Reused with permission from ref 16. *Copyright © 2016, American Chemical Society.*

Of the above, the *N*-confused porphyrins were the first to be discovered - serendipitously and independently - by Latos-Grazynski *et al*. [17] and Furuta *et al*. [18] as by-products of standard one-pot porphyrin syntheses. Azuliporphyrin too can be synthesized via a one-pot condensation of pyrrole, an aromatic aldehyde, and azulene, as illustrated in Figure 15.[19] Fascinatingly, azuliporphyrin, a diprotic ligand, undergoes oxidative ring contraction to benzocarbaporphyrin, a triprotic base. *N*-Confused porphyrin, azuliporphyrin, and benzocarbaporphyrin all exhibit rich coordination chemistries.[16]

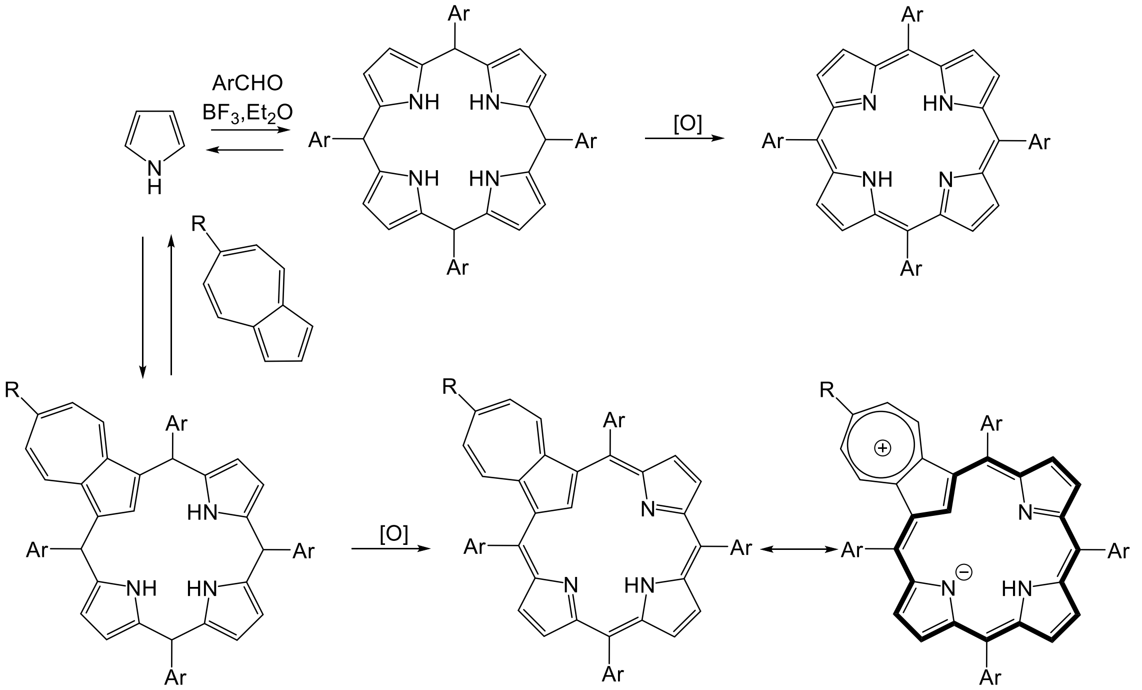

Figure 15. Lindsey-Rothemund synthesis of *meso*-tetraarylazuliporphyrins. Redrawn from ref 16.

Interestingly, *N*-confused porphyrin can exist as one of two different tautomeric forms, depending on the solvent, as shown in Figure 16. Unsurprisingly, it can act as both dianionic and trianionic ligands toward transition metal ions.[20]

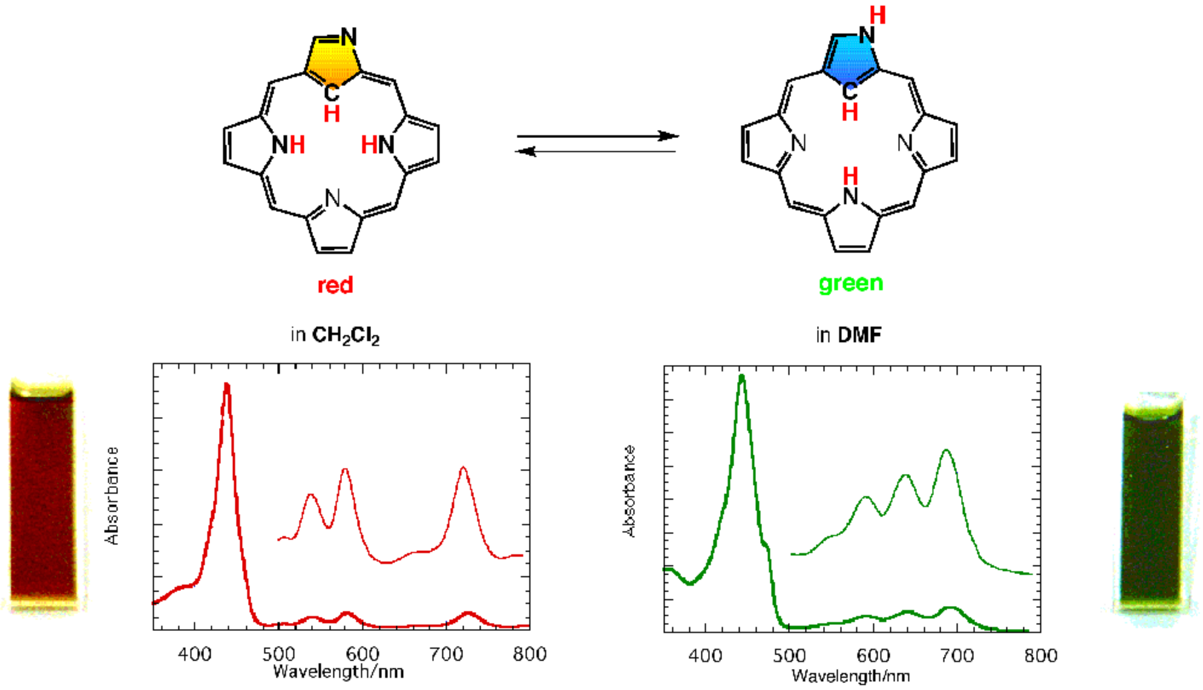

Figure 16. Solvent-dependent tautomerism of *N*-confused porphyrin:absorption spectra and colour change. Reused with permission from ref 20. *Copyright © 2020, American Chemical Society.*

N-confused porphyrins can also be obtained via a more rational route, notably a modified MacDonald synthesis, involving a [3 + 1] addition of a dialdehyde and a tripyrrane. [18, 21] In the same spirit, the first doubly *N*-confused porphyrin was synthesized via a Lewis-acid-catalysed [2 + 2] coupling of an *N*-confused dipyrromethane, as illustrated in Figure 17.[22]

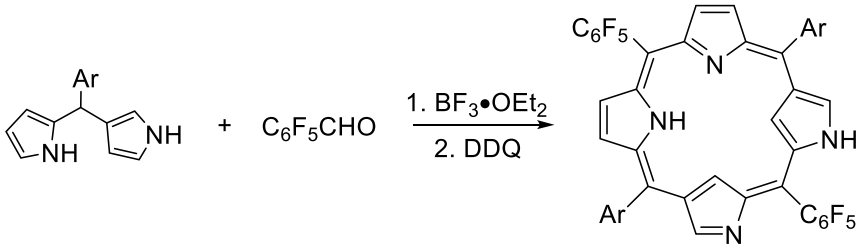

Figure 17. Synthesis of a doubly *N*-confused porphyrin starting from *N*-confused dipyrromethane. Adapted from ref 22.

A handful of *N*-confused porphyrin metal complexes are known, such as the group 10 (Ni, Pd, Pt), [23] group 11 (Cu, Ag, Au) as well as Co and Rh. Osuka *et al*. did managed to synthesis both Cu and Ag doubly *N*-confused porphyrins through acid-catalysed condensation of perfluoro benzaldehyde with *N*-confused dipyrrometane, oxidation with DDQ and then reacting the molecule with M(I) acetate (M = Cu, Ag), as illustrated in Figure 18.[24, 25]

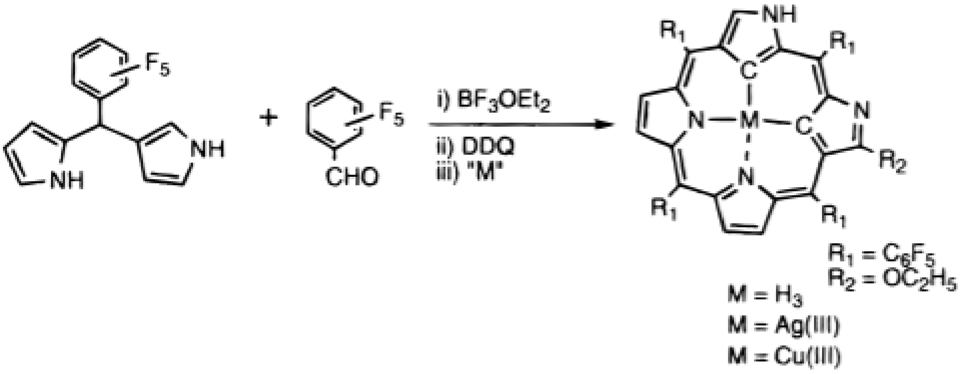

Figure 18. Synthetic pathway to Cu(III) and Ag(III) doubly *N*-confused porphyrin. Reused with permission from ref 24. *Copyright © 2000, American Chemical Society*.

In 2002, Lash and co-workers reported a silver complex of benzocarbaporphyrin. The compound could be synthesised by mixing the free-base benzocarbaporphyrinoid with silver(I) acetate in methanol:dichloromethane at room temperature.[26] Several additional metallobenzacarbaporphyrins have been synthesised including rhenium-oxo derivatives by UiT colleague Dr. Abraham Alemayehu.[27]

N-confused porphyrins undergo selective monobromination on the internal carbon (Figure 19). The product on activation by a base, such as pyridine, leads to the novel macrocycle *N*-fused porphyrin (NFP). The same process can be repeated to produce a doubly *N*-fused porphyrin (Figure 19).[28]

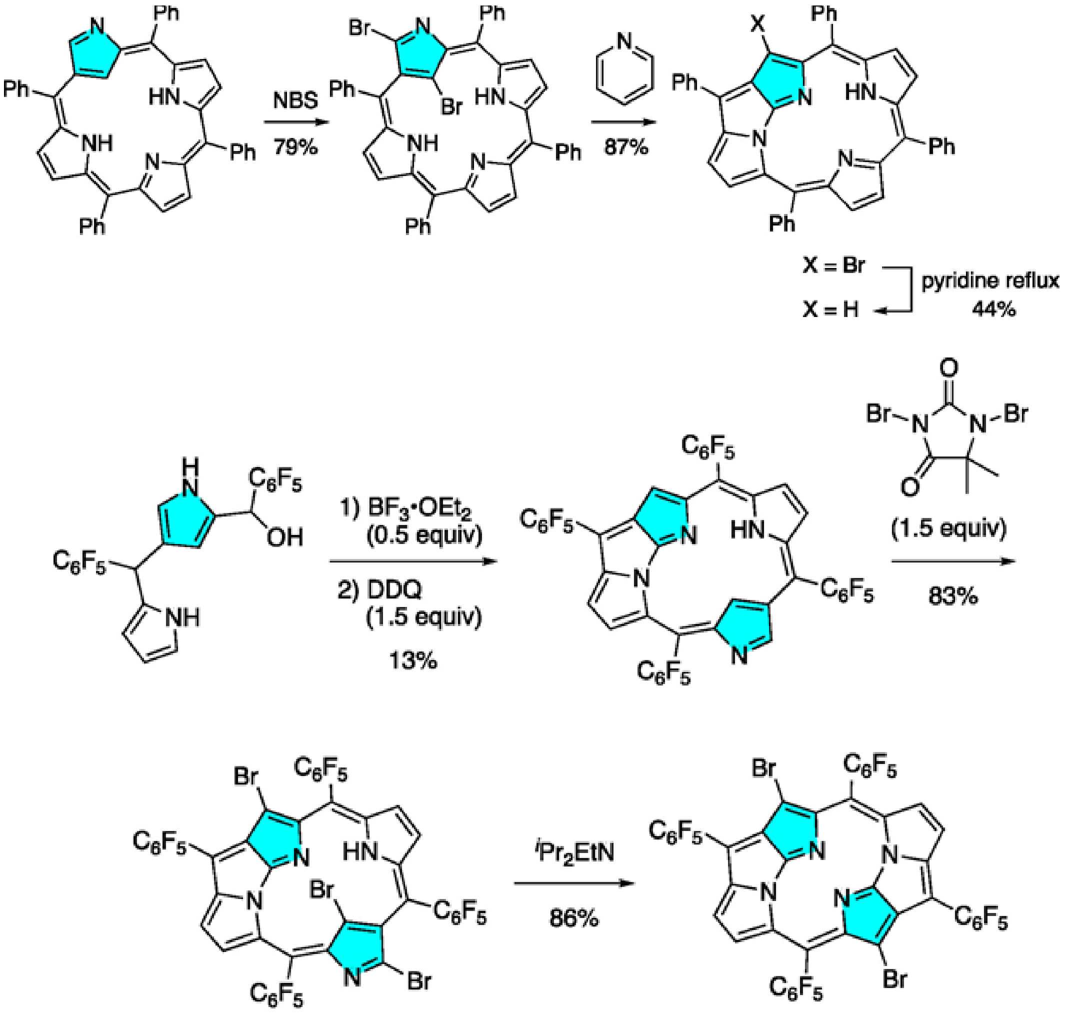

Figure 19. Synthetic approaches for *N*-fused porphyrin (top) and doubly n-fused porphyrin (bottom). Reused with permission from ref 28. *Copyright © 2022, American Chemical Society*

Finally, oxaporphyrin[29] and thiaporphyrin[30] are monoanionic porphyrin analogues, which are of interest as models for the nickel(I) cofactor F_{430} (see Figure 1 for structure) of the enzyme methylcoenzyme M reductase, which is the key enzyme responsible for biological methane production.

1.6 Expanded porphyrins

Sapphyrin, the first expanded porphyrin to be described, was prepared by R. B. Woodward and co-workers over a half-century ago.[31] Today the field has been enormously expanded (Figure 20), most notably through the efforts of the Vogel[32], Sessler[33], and Osuka[34] groups.

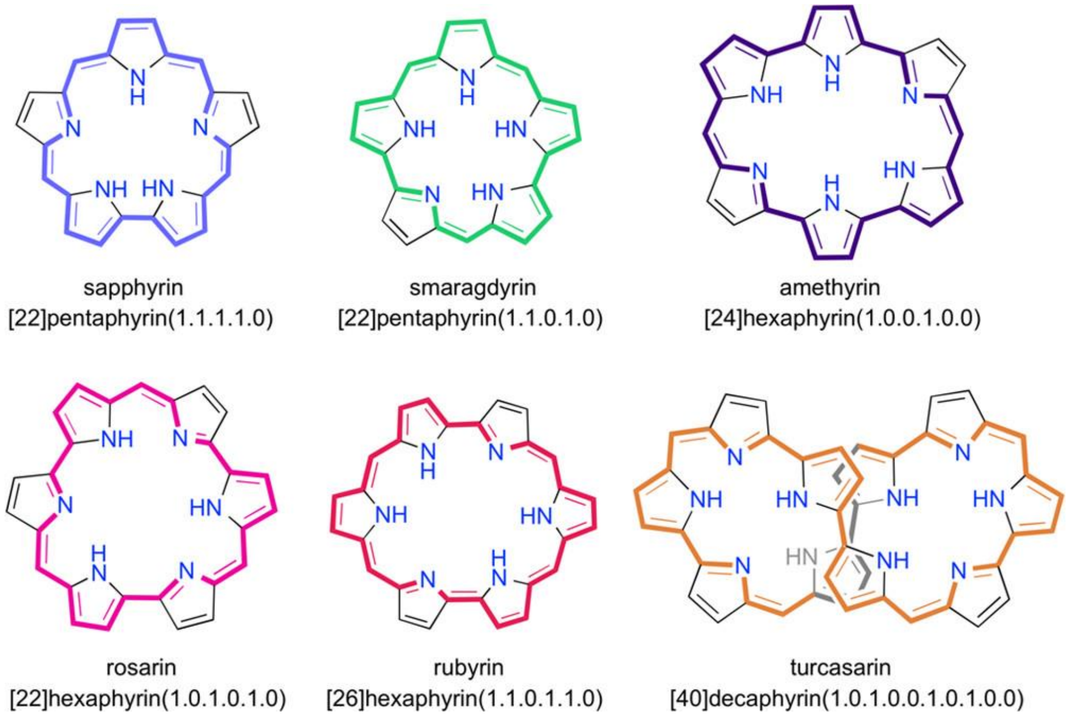

sapphyrin
[22]pentaphyrin(1.1.1.1.0)

smaragdyrin
[22]pentaphyrin(1.1.0.1.0)

amethyrin
[24]hexaphyrin(1.0.0.1.0.0)

rosarin
[22]hexaphyrin(1.0.1.0.1.0)

rubyrin
[26]hexaphyrin(1.1.0.1.1.0)

turcasarin
[40]decaphyrin(1.0.1.0.0.1.0.1.0.0)

Figure 20. Structures and common names of some expanded porphyrins. Reused with permission from ref 34. *Copyright © 2016 American Chemical Society*.

Osuka and co-workers demonstrated that many *meso*-aryl expanded porphyrins are simply accessible via quasi-one-pot pyrrole aldehyde condensations (Figure 21). The larger ring systems variously exhibit aromatic-antiaromatic redox equilibria and Möbius aromaticity.[34]

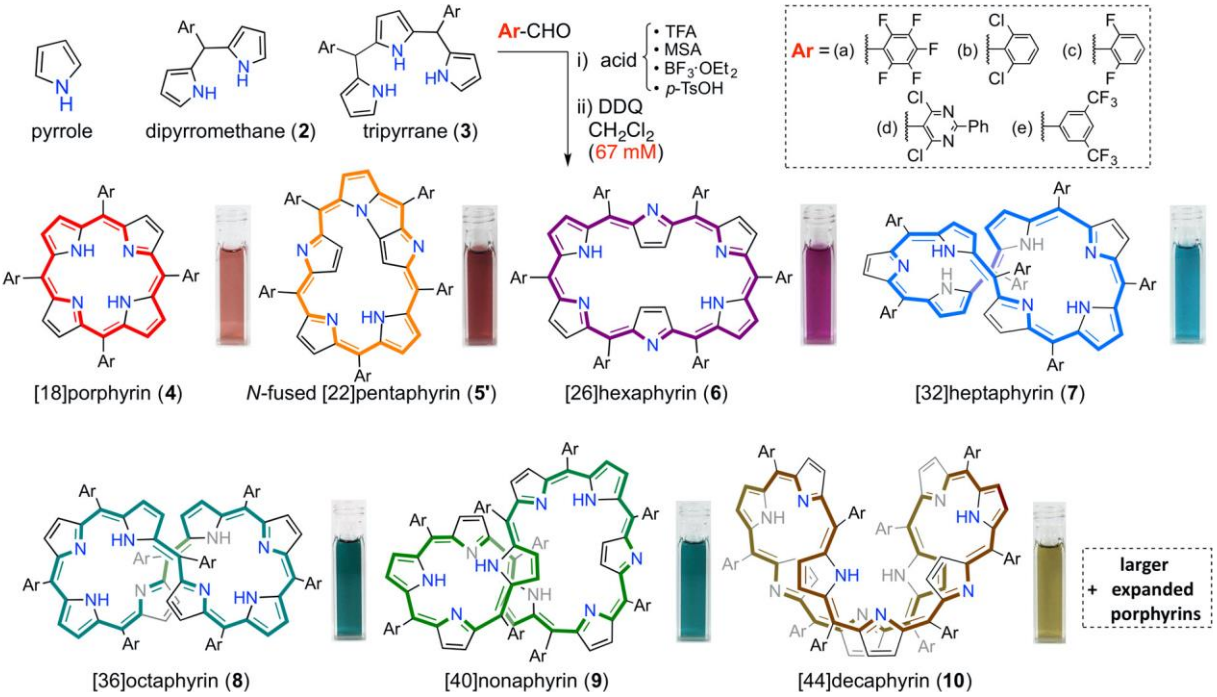

Figure 21. One-pot synthetic approach to expanded porphyrins. Reused with permission from ref 34. *Copyright © 2017, American Chemical Society.*

The smaller expanded porphyrins (with 5 and 6 central nitrogen's) also exhibit a rich coordination chemistry involving actinides (Figure 22).[35]

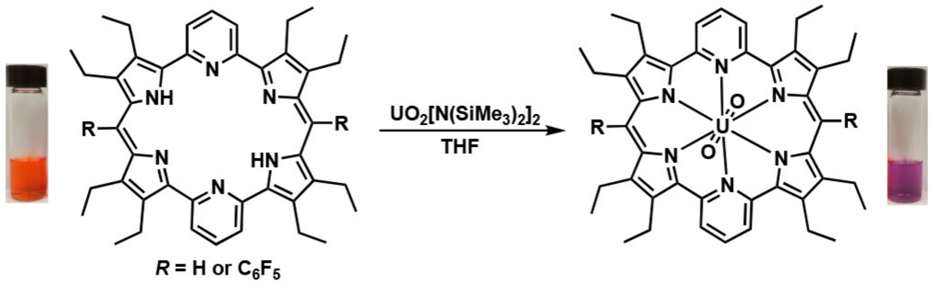

47 **48**

Figure 22. Synthesis of a uranyl-dipyriamethyrin- complex. Reused with permission from ref 30. *Copyright © 2017, American Chemical Society.*

1.7 Contracted porphyrins

Subporphyrinoids are a newer but increasingly important class of contracted porphyrins. True subporphyrins are invariably accessed via boron-templated condensations (Figure 23) and, as of today, are only available as their boron derivatives.[36]

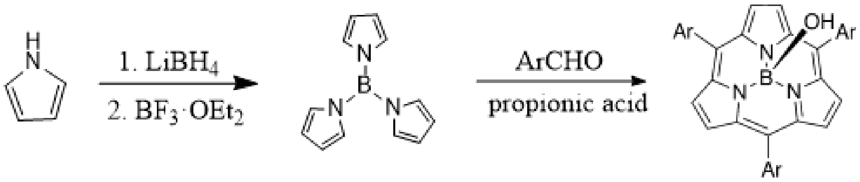

Figure 23. Synthesis of boron-subporphyrin. Adapted from ref 36.

Two improved variations of the method are presented in Figure 24.

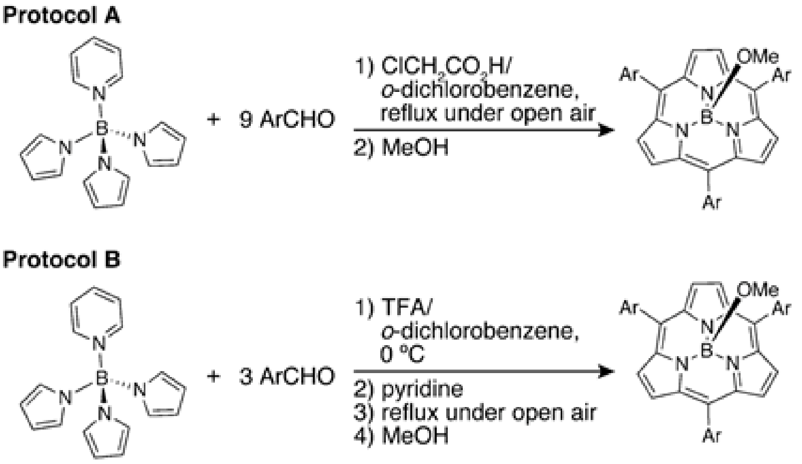

Figure 24. Improved synthetic methods of A_3-type meso-aryl-substituted subporphyrins. Reused with permission from ref 36. *Copyright © 2016 American Chemical Society.*

In contrast, topologically similar [14]triphyrin(2.1.1) has been synthesized in free-base form by a variety of routes; a McMurry coupling-based route is illustrated in Figure 25.[37]

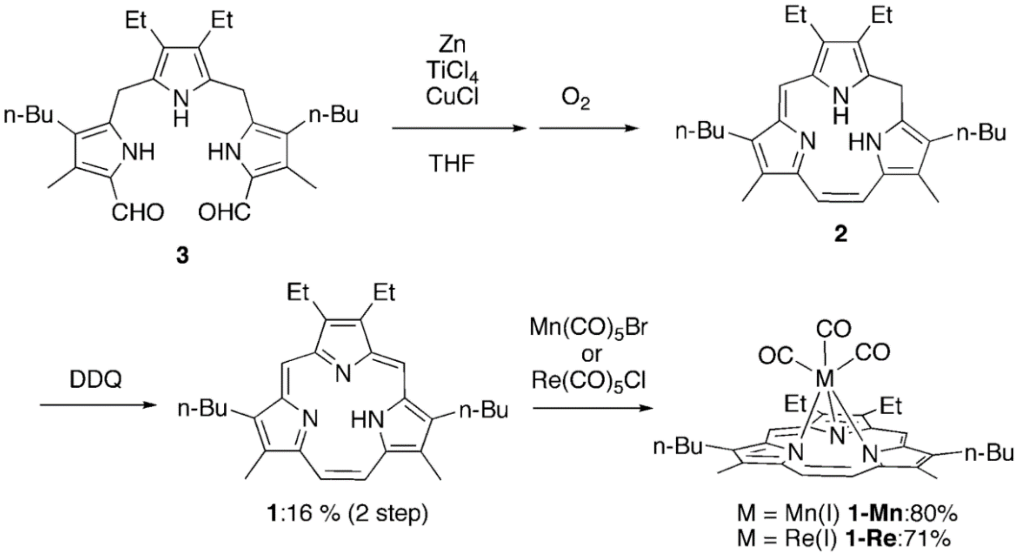

Figure 25. Synthetic approaches for manganese and rhenium triphyrins. Reused from ref 37, with permission from the Royal Society of Chemistry.

1.8 Corroles

Like porphyrins, corroles are aromatic molecules with rich spectroscopic properties. Free-base and nontransition metal corroles are generally fluorescent. [38] First-row transition metal corroles, like their porphyrin analogue, are generally nonluminescent. On the other hand, many 5d metallocorroles, including Re^VO corroles reported in this thesis, exhibit near-IR phosphorescence. [39] Corrole derivatives, however, have only been applied to a limited extent in photodynamic therapy – a state of affairs that the present work will hopefully change in the near future. [40, 41]

Corrole was first reported by Johnson and Kay in 1964 in the course of their unsuccessful attempt to synthesize corrin, the ring system of Vitamin B_{12}. [42] Progress from that point on was slow, until two groups led by Gross[43] and Paolesse[44] in 1999 independently reported one-pot syntheses of *meso*-triarylcorroles. In Gross's approach, pyrrole and pentafluorobenzaldehyde were reacted at 100˚C for 4 hours in the presence of a solid support (silica or alumina) but no solvent, followed by DDQ oxidation (Figure 26).

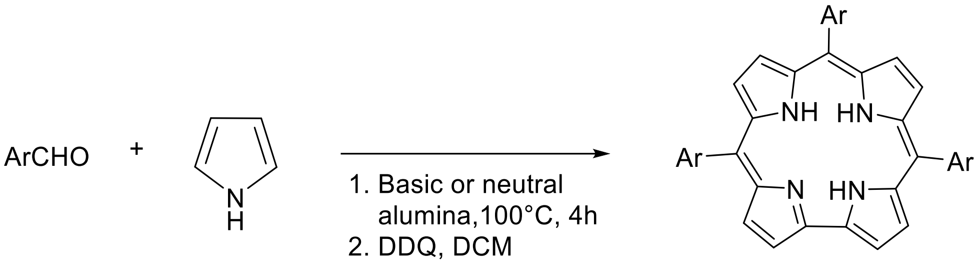

Figure 26. Gross and co-workers' solvent-free corrole synthesis on a solid support.

Paolesse's conditions were similar to a Rothemund porphyrin synthesis, using a 3:1 mixture of pyrrole and benzaldehyde in refluxing acetic acid (Figure 27).[44]

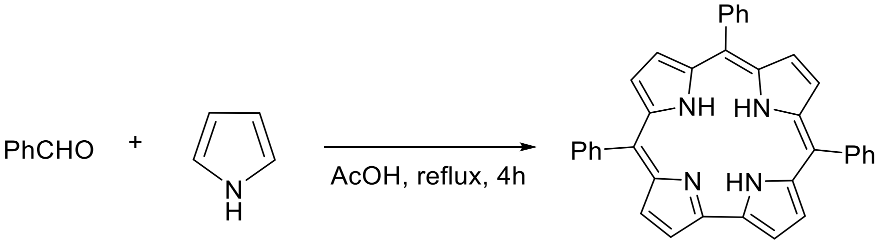

Figure 27. Paolesse and co-workers' synthesis of *meso*-triphenylcorrole.

Ghosh and co-workers[45] extended the method of the Gross group to aromatic aldehydes other than benzaldehyde as well as 3,4-difluoropyrrole (Figure 28).

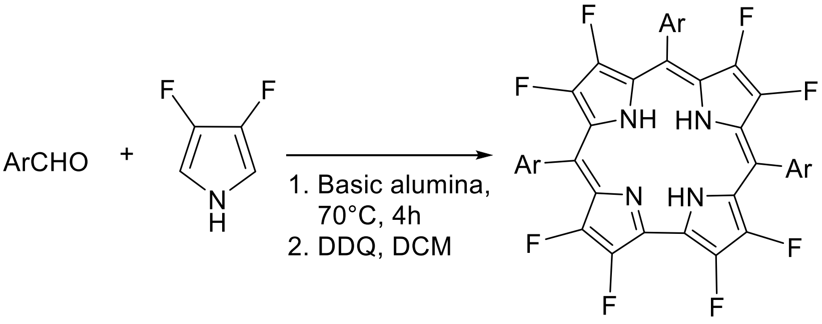

Figure 28. Ghosh and co-workers' synthesis of free-base octafluorocorroles.

The above syntheses all proceeded with poor yields, ranging from 5-20%. They nonetheless enjoyed a certain popularity because of the simple, one-pot procedures involved.

In 2006, Koszarna and Gryko reported a major improvement in corrole synthesis.[46] Their protocol involved two steps: the reaction of an aldehyde and pyrrole (2:1 molar ratio) in an acidified 1:1 water-methanol solution, followed by extraction of the resulting bilane and its oxidation to corrole with *p*-chloranil or DDQ (Figure 29). The method routinely led to yields above 20%.

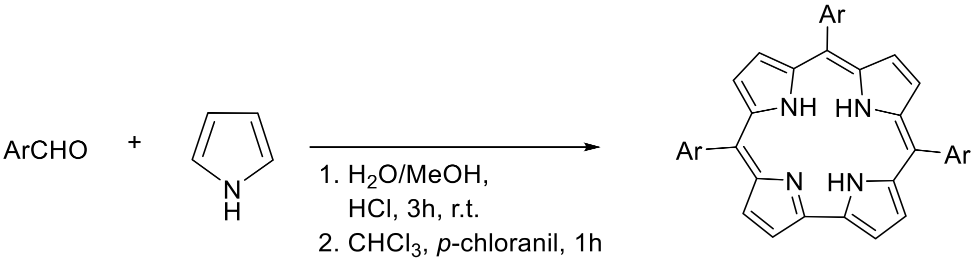

Figure 29. One-pot synthesis of corrole via Koszarna and Gryko's water-methanol method.

In the same paper,[46] the authors also reported a preparative route to *trans*-A_2B triarlycorroles. The synthesis required an additional step, namely the synthesis of an arlydipyrromethane (Figure 30).

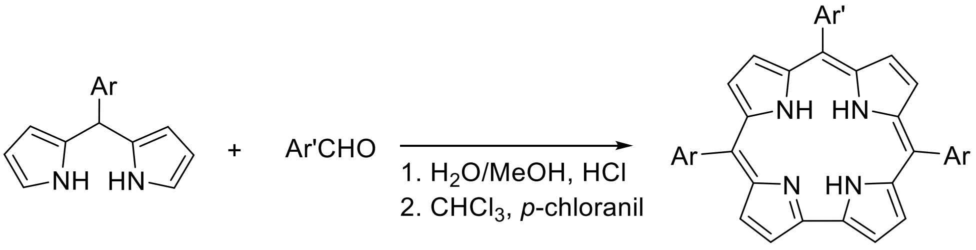

Figure 30. Synthesis of A_2B corroles.

Soon afterward, Gryko and co-workers reported an improved synthesis of 5-aryldipyrromethanes (Figure 31).[47] The method consists of the interaction of an aromatic aldehyde and pyrrole (1:3) in water acidified with HCl and yields a dipyrromethane in excellent yields (80-97%).

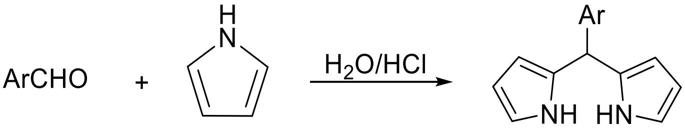

Figure 31. Gryko's synthesis of 5-aryldipyrromethanes.

1.9 Isocorroles and heteroisocorroles

Isocorroles are corrole tautomers with a saturated *meso* carbon. Accordingly, isocorroles are isosteric with corroles but act as di-anionic ligands like porphyrins. The steric and electronic relationship among the three ligands is schematically illustrated in Figure 32.[48]

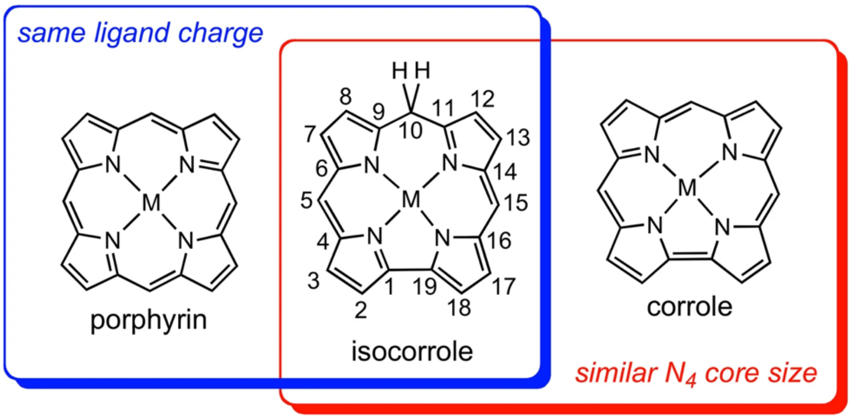

Figure 32. Skeletal comparison of porphyrin, isocorrole and corrole. Reused with permission of the author of ref 48.

Isocorroles have been traditionally synthesized via the addition of a nucleophile such as Grignard reagent to a corrole. An exceptionally facile synthesis was developed by my colleague Dr. Simon Larsen who found that corroles undergo oxidative coupling with pyrrole to yield pyrrole-appended isocorroles (Figure 33).[49] Isocorroles are of great interest as NIR-absorbing homoaromatic species. However, the coordination chemistry of isocorroles remains underdeveloped.

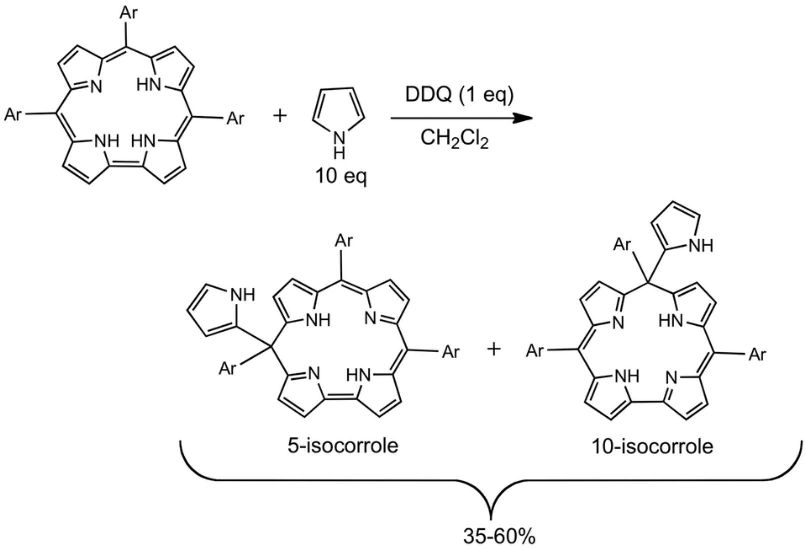

Figure 33. Synthesis of pyrrole-appended isocorroles. Reused with permission from ref 49 with permission from the Royal Society of Chemistry.

Bröring and co-workers have reported 10-heteroisocorroles (often referred to simply as heterocorroles) via a [2 + 2] coupling procedure, as depicted below.[50]

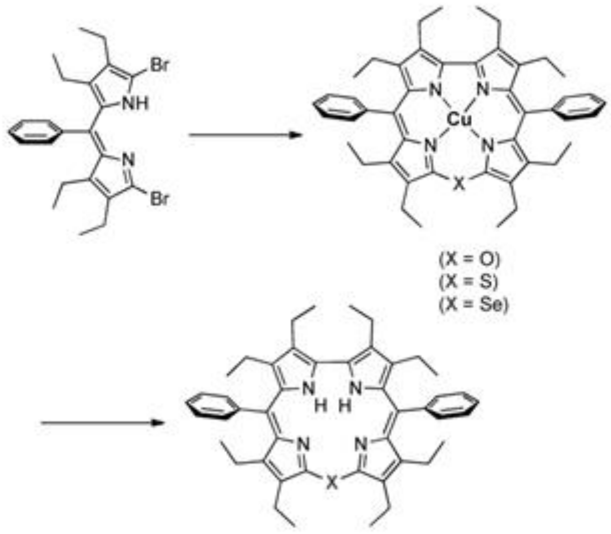

Figure 34 Synthesis of 10-heteroisocorrole via the copper complex followed by reduction. Reused from ref 50. *Copyright © 2013 WILEY-VCH Verlag GmbH & Co. KGaA, Weinheim*

Both isocorroles and heteroisocorroles are of interest as hybrid ligands with the 2- charge of porphyrins, but with the contracted core size of corroles. These properties may lead to the stabilization of unusual spin states, such intermediate-spin $Fe^{III}Cl$ derivatives.[50]

1.10 Norcorroles

Norcorroles were first proposed theoretically as the smallest possible tetrapyrrole macrocycles. Bröring *et al*. reported the first (rather cumbersome) synthesis of the macrocycle in metal-complexed form, as illustrated in Figure 35.[51]

Figure 35. Synthesis of iron norcorrole derivatives. Reused from ref 51. *Copyright © 2008 WILEY-VCH Verlag GmbH & Co. KGaA, Weinheim*

Subsequently, Shinokubo *et al*. reported a gram-scale synthesis of nickel(II)-norcorrole through a reductive coupling, as depicted in Figure 36.[52] They later generalized their original synthesis to also synthesize Zn, Co, and Cu norcorrole derivatives.[53]

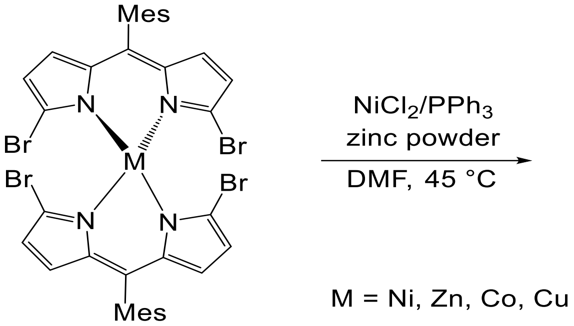

Figure 36. Synthesis of different metallonorcorroles. Redrawn from ref 53. *Copyright © 2017 Wiley-VCH Verlag GmbH & Co. KGaA, Weinheim*

Starting from copper norcorrole, Shinokubo *et al*. obtained free-base norcorrole in good yields. Form the free-base, they also obtained the Pd norcorrole complex, as illustrated in Figure 37.

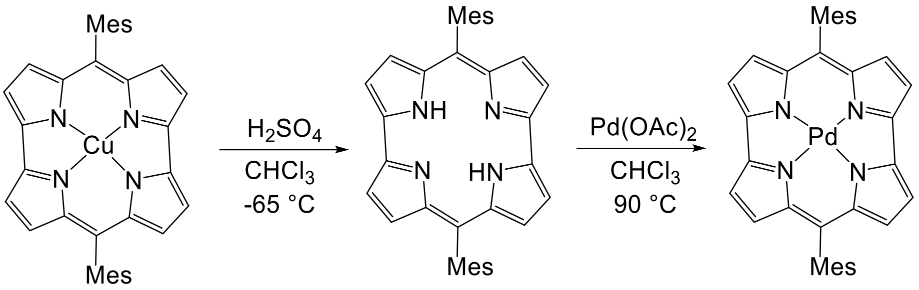

Figure 37. Demetallation of copper norcorrole and synthesis of palladium norcorrole. Reused from ref 53. *Copyright © 2017 Wiley-VCH Verlag GmbH & Co. KGaA, Weinheim*

Norcorroles embody a fascinating tussle between aromaticity/delocalized bonding and antiaromaticity. Structurally, each dipyrrin half is delocalized, as expected for a vinylogous amidinate, but the macrocycle has a whole exhibit magnetic antiaromaticity.[54]

1.11 Hydroporphyrins

Hydroporphyrins are best known as the parent ring systems of chlorophyll and bacteriochlorophyll (Figure 38).[55] A distinctive feature of hydroporphyrins is their strong absorption in the red or near-infrared; their Q bands are essentially as strong as their Soret bands, a property with major implications for their deployment as photosensitizers in photodynamic therapy.[56]

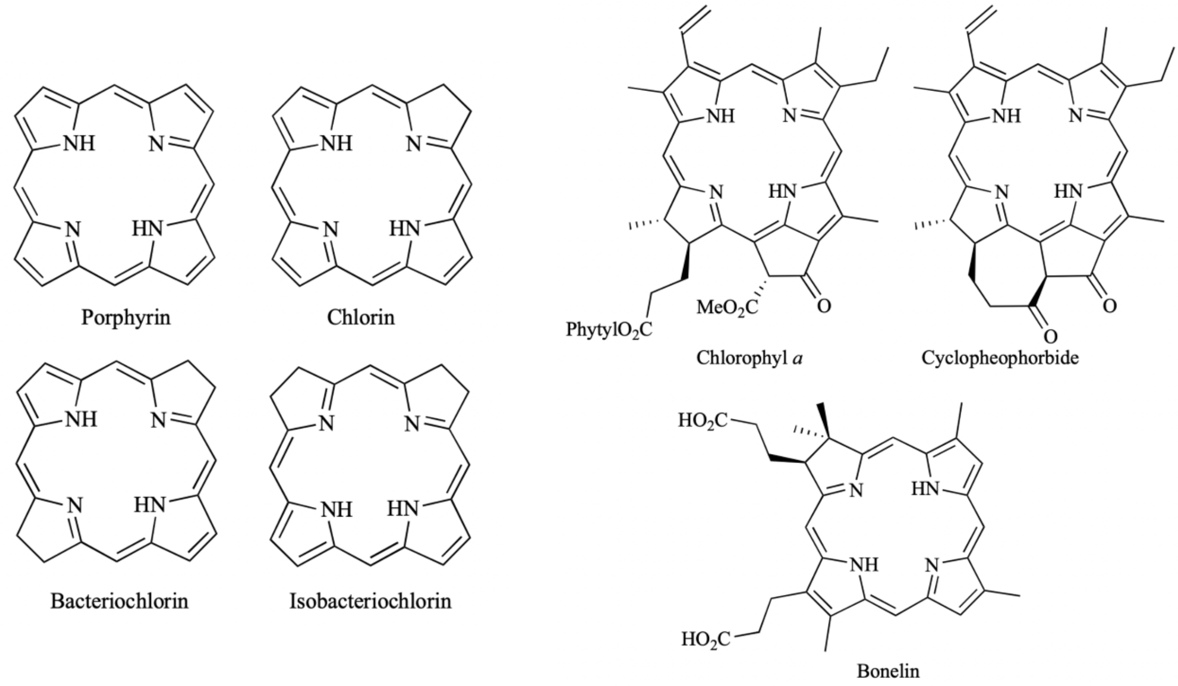

Figure 38. Structure of parent porphyrin and hydroporphyrins (left) and of some naturally occurring chlorins (right). Adapted with permission from ref 55. *Copyright © 2008 WILEY-VCH Verlag GmbH & Co. KGaA, Weinheim.*

Some of the most convenient syntheses understandably involve addition to the β-β double bonds of porphyrins. A well-known example is the addition of two hydroxy groups by the use of OsO_4 in pyridine followed by addition of H_2S as illustrated in Figure 39.[57]

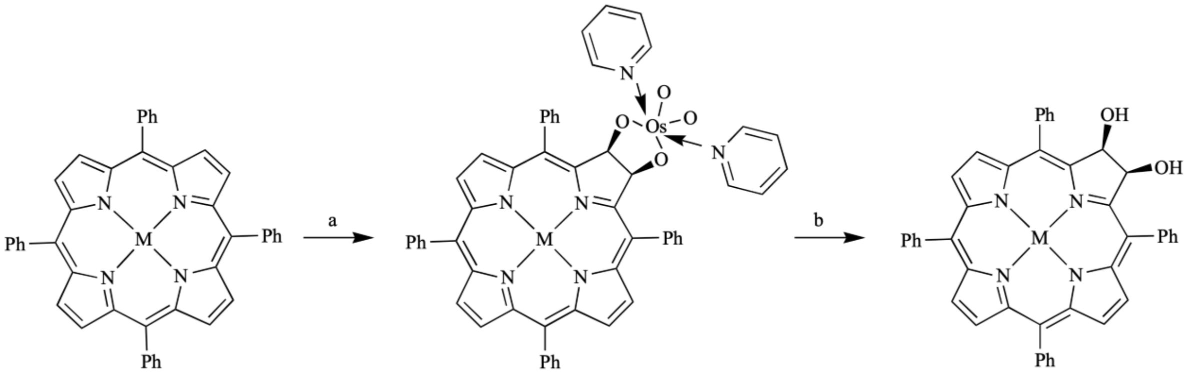

Figure 39. β-Dihydroxylation of porphyrins with osmium tetroxide. M = 2H, Zn; (a) OsO_4, pyridine, (b) H_2S. Adapted with permission from ref 55. *Copyright © 2008 WILEY-VCH Verlag GmbH & Co. KGaA, Weinheim*

Alternatively, β-vinylporphyrins can be used as the diene component in a Diels-Alder approach to chlorins, as shown in below.[58]

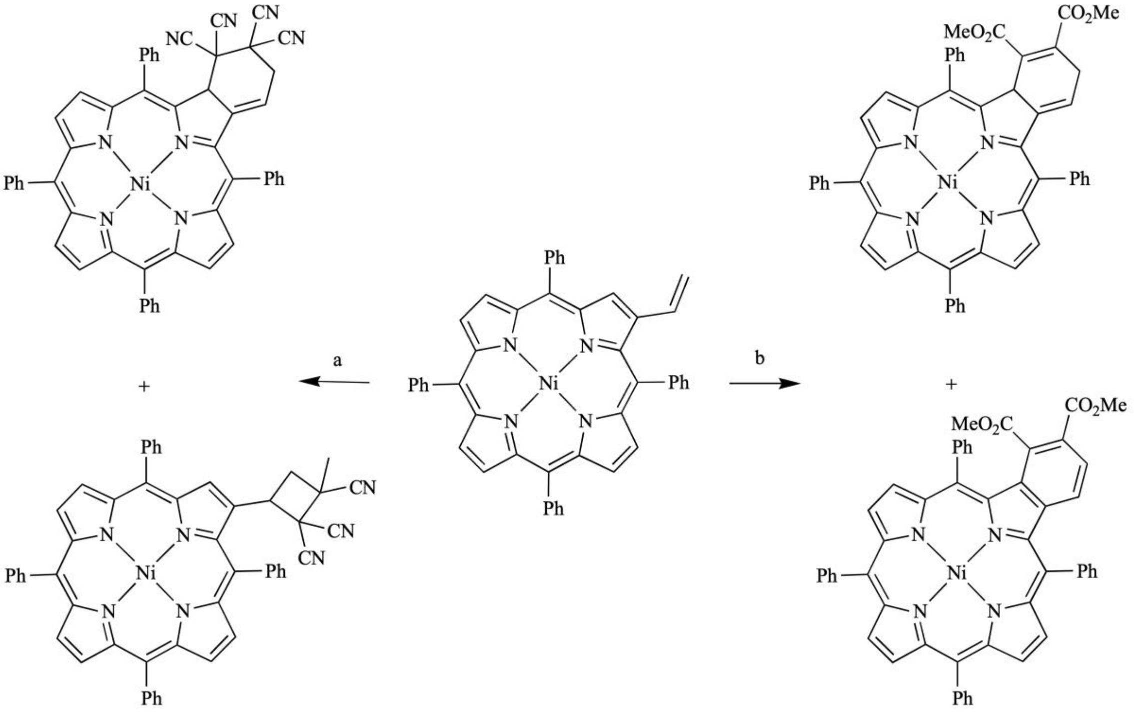

Figure 40. Diels-Alder-based functionalization of (β-vinyl)-NiTPP; (a) TCNE, (b) DMAD. *Copyright © 2008 WILEY-VCH Verlag GmbH & Co. KGaA, Weinheim.*

1.12 Metalloporphyrins

Methods for metal insertion into porphyrins have been well-established for decades and porphyrin derivatives are known for the vast majority of metals in the periodic table. Accordingly, only a few brief comments are made here as a prelude to a much longer discussion on metal insertion into corroles.

The most common method for metal insertion into porphyrins is refluxing with a metal halide or carboxylate in a high boiling basic solvent such as pyridine or DMF (the basic solvent neutralises the acid produced upon ionization of the porphyrin's central hydrogens). [59] Another popular method involves boiling a porphyrin with a metal carbonyl or another low-valent organometallic compound. I adopted this approach to synthesize ^{99}Tc^{V}O and Re^{V}O. Somewhat surprisingly, the analogous ^{99}Tc porphyrins are still unknown, but a 2:1 ^{99}Tc-porphyrin complex is well-known.[60]

Yet a third method involves preforming lithium salt of a porphyrin analogue and metalating it using a metal chloride.[61] This method has been commonly used for early 4d and 5d metals as well as f-elements.[62]

Besides these general approaches, metal insertion nowadays is facilitated by a variety of approaches such as microwave heating and mechanochemistry (ball-milling).[63]

1.13 Nonplanarity in porphyrins and corroles

Although many simple porphyrins and metalloporphyrins are planar, as expected for aromatic compounds, they do undergo nonplanar deformations in response to steric and electronic stimuli. [64] There are four, classic named deformation of the porphyrin macrocycle – ruffled, saddled, domed, and waved (Figure 41) – and many porphyrins are known to exhibit varying degrees of mixtures among these deformations.[65] Of these, ruffling and saddling are very common, doming distinctly less so, and waving is restricted to a few special substitution patterns.

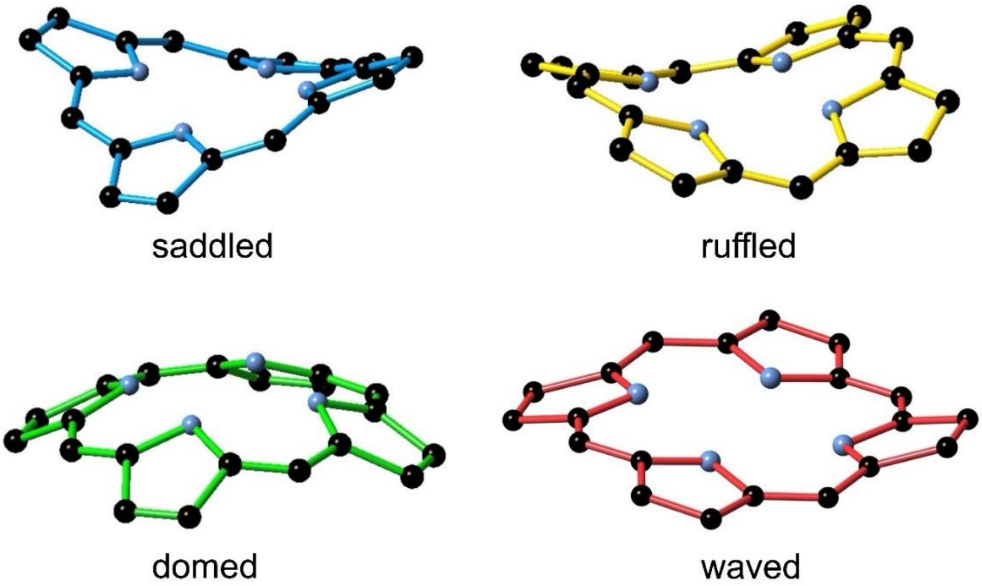

Figure 41. Graphical depiction of the four classic nonplanar distortions of porphyrins.

Saddling, in which the pyrrole rings alternately tilted up and down, most commonly relieves steric repulsions among peripheral substituents. It is typically observed among dodecasubstituted porphyrin derivatives.[64, 66]

Ruffling, in which the *meso* positions are displaced alternately above and below the mean porphyrin plane, is most commonly driven by a small metal ion such as low-spin Ni(II) but may be accentuated by bulky *meso*-substituents.

Doming typically occurs for compounds where the metal ion is too large for the inner N4 core of the corrole, such as Pb(II) or Bi(III).

The common occurrence of saddling and ruffling in porphyrins may be contrasted with the much greater resistance of corroles toward nonplanar deformations. The direct pyrrole-pyrrole linkage of corroles neither twists nor pyramidalizes easily. Mild doming on the other hand is common for corroles.

Chapter 2: Corrole coordination chemistry

The coordination chemistry of corroles has developed by leaps and bounds over the last 20-25 years and, as of today, corroles have been coordinated to the majority of stable (nonradioactive) metallic elements of the periodic table as well as to a substantial number of nonmetals (Figure 42).[67] In many ways, this chemistry differs profoundly from that of porphyrins – a difference that ultimately boils down to two factors. First, corroles coordinate as formally trianionic ligands, unlike dianionic porphyrins. Second, the central N_4 core of corroles is contracted relative to that of porphyrins. These two factors join together to stabilize formally high-valent metal complexes, although on closer inspection, some of the complexes are better viewed as noninnocent, i.e., involving a lower-valent metal and a corrole$^{\bullet 2-}$ radical. Compared with porphyrins, corroles also exhibit significant differences with regard to coordination geometry. Because of the contracted N_4 core, five-coordinate, mildly domed geometries are common, while six-coordinate states are less common. Ruffled and saddled conformations are also rare for corrole derivatives because the direct pyrrole-pyrrole linkage resists both pyramidalization and twisting.[67, 68]

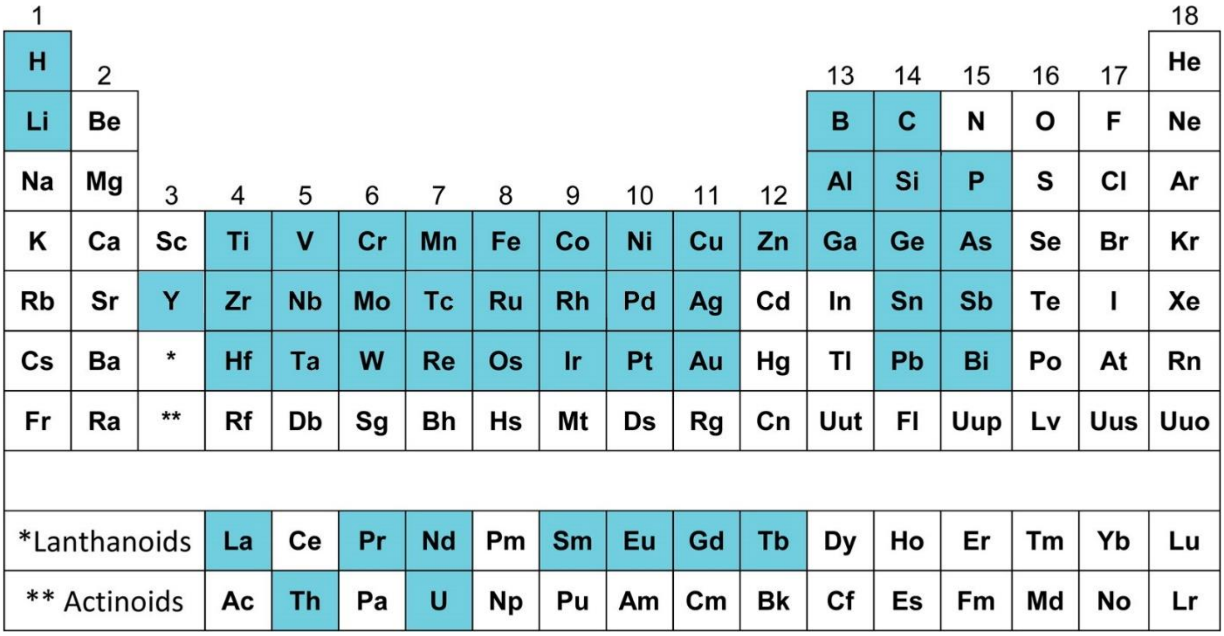

1	2	3	4	5	6	7	8	9	10	11	12	13	14	15	16	17	18
H																	He
Li	Be											B	C	N	O	F	Ne
Na	Mg											Al	Si	P	S	Cl	Ar
K	Ca	Sc	Ti	V	Cr	Mn	Fe	Co	Ni	Cu	Zn	Ga	Ge	As	Se	Br	Kr
Rb	Sr	Y	Zr	Nb	Mo	Tc	Ru	Rh	Pd	Ag	Cd	In	Sn	Sb	Te	I	Xe
Cs	Ba	*	Hf	Ta	W	Re	Os	Ir	Pt	Au	Hg	Tl	Pb	Bi	Po	At	Rn
Fr	Ra	**	Rf	Db	Sg	Bh	Hs	Mt	Ds	Rg	Cn	Uut	Fl	Uup	Lv	Uus	Uuo
*Lanthanoids			La	Ce	Pr	Nd	Pm	Sm	Eu	Gd	Tb	Dy	Ho	Er	Tm	Yb	Lu
** Actinoids			Ac	Th	Pa	U	Np	Pu	Am	Cm	Bk	Cf	Es	Fm	Md	No	Lr

Figure 42. The periodic table of corroles. The blue shaded elements are those known to be coordinated to a corrole.

2.1 Main-group (s- and p-block) element complexes

As far as the s-block is concerned, lithium is the only element that has been coordinated to corrole. A lithium corrole was first made by Buckly *et al*. in 2012 via the reaction of free-base 10-(4-methoxyphenyl)-5,15-dimesitylcorrole with three equivalents of $LiN(SiMe_3)_2$ in THF at -40°C.[69] An immediate colour change occurred from purple to deep green. The product Li_3[Mes$_2$*p*OMePhC]·6THF could be isolated through filtration in good yields, ~76%. X-ray analysis of the related salt Li_3[Mes$_2$*p*OMePhC]·4DME revealed a corrole with two lithium ions above and below the macrocycle plane (Figure 43). Key geometry parameters include an average Li-N distance of 2.141 Å, an Li-N_4 displacement of 1.03 ± 0.01 Å, and an Li-Li distance of 2.066 Å. The structure differs from that of lithium porphyrins, in which a lithium ion sits at the centre of the porphyrin, with a second one coordinated by solvent.

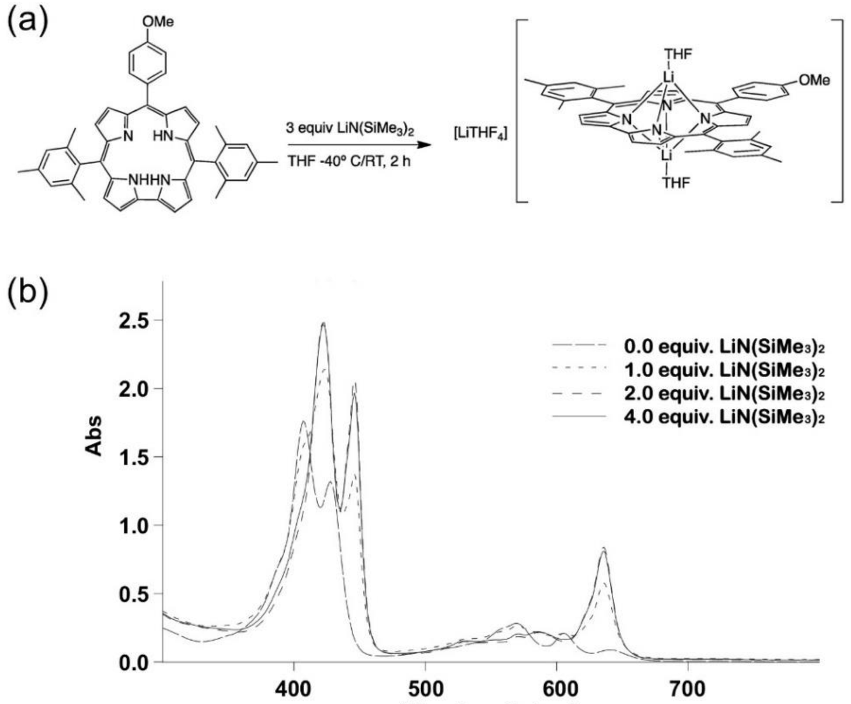

Figure 43. Interaction of H_3[Mes$_2$*p*OMePhC] and $LiN(SiMe_3)_2$ in THF: (a) schematic of the synthetic protocol and (b) the UV-vis spectrum as a function of added $LiN(SiMe_3)_2$. Reproduced from ref 69 with permission from the Royal Society of Chemistry.

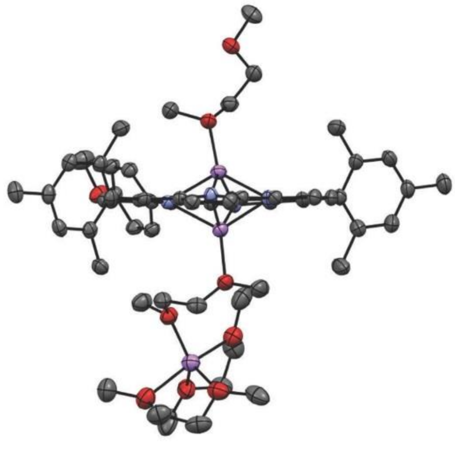

Figure 44. X-ray structure of $Li_3[Mes_2pOMePhC]\cdot 4DME$. Reproduced with permission from ref 69.

As far as the p-block is concerned, several Group 13, 14, and 15 elements have been coordinated to corrole, as shown in Figure 45. Chloride starting materials have been most used. However, acetate, acac, and nitrate derivatives have also been used for the more electropositive metalloidal elements. Only in the case of aluminium has a metal-alkyl, Al_2Me_6, proved essential.[70] The significance of p-block element corrole complexes derives primarily from their strong fluorescence and hence applications in bioimaging. For these applications, the most promising complexes seem to be those of B[71-73], Al[70, 74], Ga[75], P[76] and Si[77, 38]

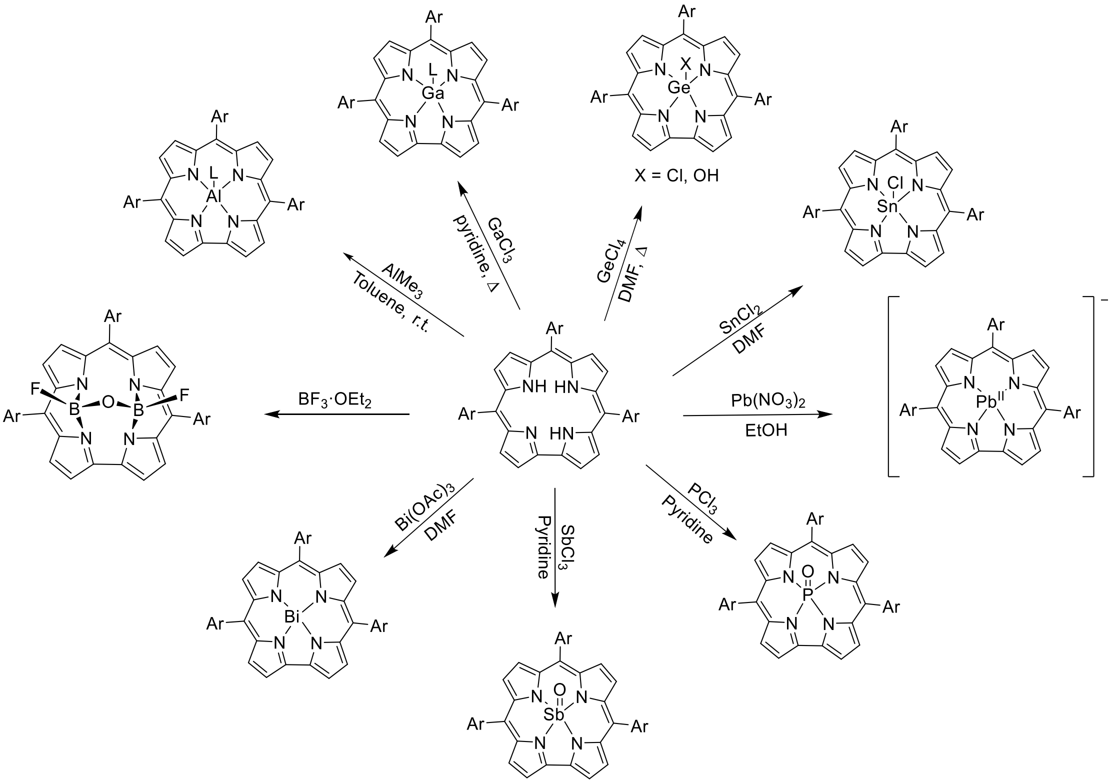

Figure 45. Synthetic approaches for some main-group p-block triarylcorroles.

The chemistry of boron porphyrins and corroles have been developed most notably by Prof. Penny Brothers at the University of Auckland, partly in collaboration with the Ghosh group. [71] These complexes are unique in that the porphyrin and the corrole act as binucleating ligands, binding two boron's in a variety of coordination geometries, as summarized in
Figure 46.

There are two major routs of obtaining boron corroles. One is by the use of *meso*-triarylkorrole and BF_3-OEt_2 in the presence of ethyldiisopropylamine. [78] The second approach is by the use of *meso*-triarylcorrole reacted with $PhBCl_2$ in the presence of $NEtiPr_2$. [71] The boron-corrole complexes showed a variety of conformation, none of which included a single boron in the inner N4 core of the corrole.[72, 73]

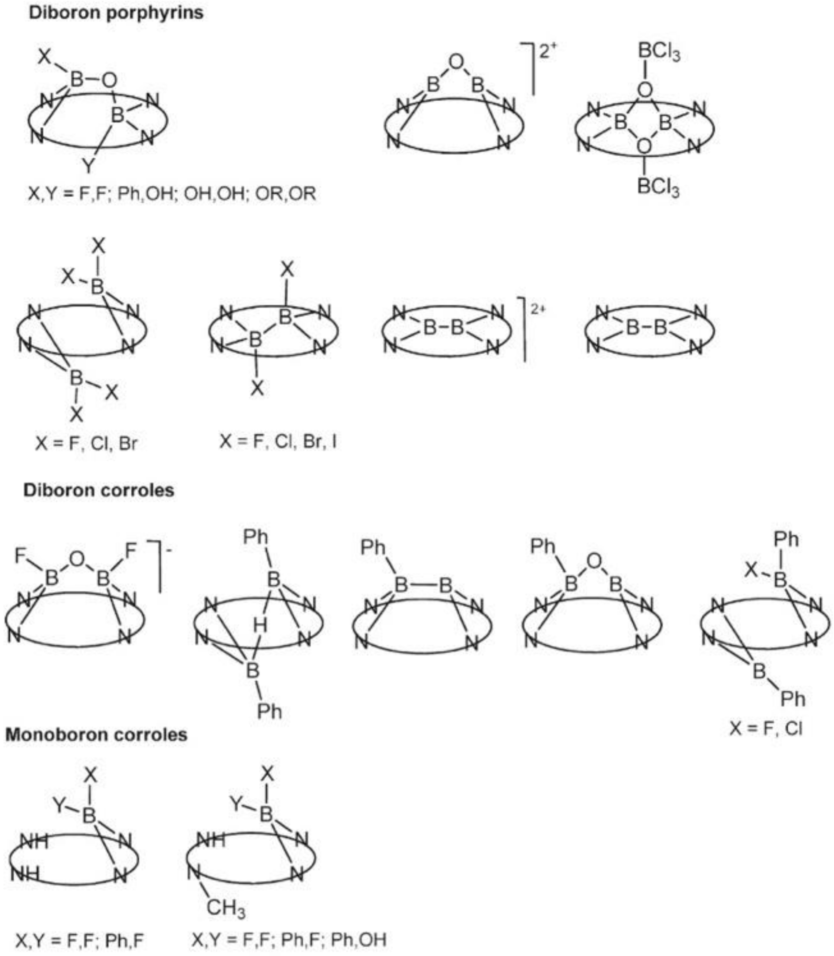

Figure 46. Summary of structural types observed for boron porphyrins and corroles. Reproduced with permission from ref 73. *Copyright © 2011 American Chemical Society*.

Phosphorus corroles invariably involve pentavalent phosphorus. Phosphorus is typically inserted with either PCl_3 or $POCl_3$ in pyridine. The resulting P(V)-oxy/hydroxy products have been derivatized to a variety of complexes with different axial ligands, as shown in Figure 47.[76]

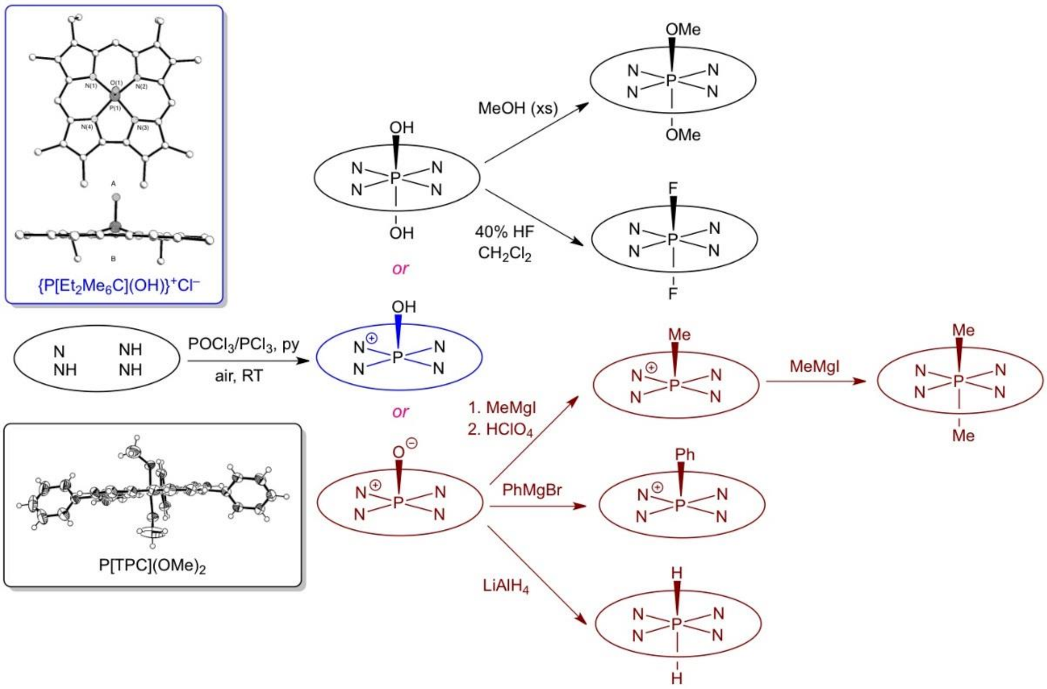

Figure 47. Schematic summary of the chemistry of phosphorus corroles, with insets showing side views of representative five- and six-coordinate X-ray structures. The crystal structures have been adapted with permission from refs 79. *Copyright © 2000 American Chemical Society*

In 2018, two groups reported synthesizing silicon corroles using free-base corroles and a silicon chloride as starting materials. Both obtained the square-pyramidal silicon complexes with an axial OH ligand. The group of Osuka used a variety of A_3 and A_2B triarylcorroles and an excess of $SiCl_4$ and *N*,*N*-diisopropylethylamine dissolved in dichloromethane under prolonged heating (Figure 48), which gave excellent yields of up to 93%. Interaction of the SiOH corrole with methanesulfonyl chloride in pyridine at 100 °C then led to the μ-oxo dimer.[77]

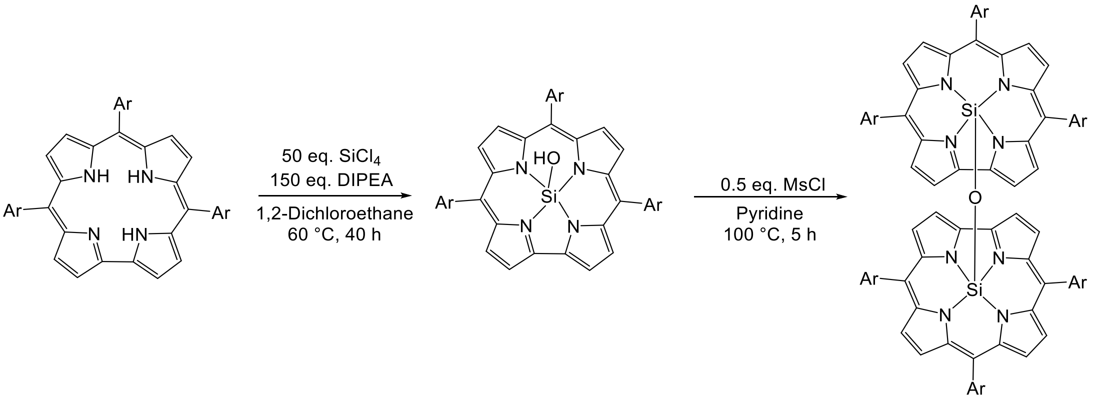

Figure 48. Synthesis of silicon corroles.

The group of Paolesse used Si_2Cl_6 as the silicon source in refluxing pyridine for 1 hour, obtaining both the SiOH monomer and the μ-oxo dimer as products. However, the ratio of monomer to dimer was found to be influenced by peripheral substituents. Electron-withdrawing peripheral substituents appeared to favour the SiOH monomer, while electron-donating substituents led preferentially to the μ-oxo dimer.[80]

As shown in Figure 45, germanium and tin can be inserted into corroles using $GeCl_4$ and $SnCl_2$ as the metal sources, respectively. A key distinction from Si is the extensive subvalent chemistry of Ge and Sn corroles. In the case of Ge, a Ge[Cor](H) species provides the key entry point to Ge(II)-corrole anions, which in turn reacts with a variety of carbon electrophiles, yielding organometallic derivatives, as illustrated in Figure 49. Qualitatively similar behaviour is also observed for Sn(II)-corroles (Figure 50).[74, 75, 81]

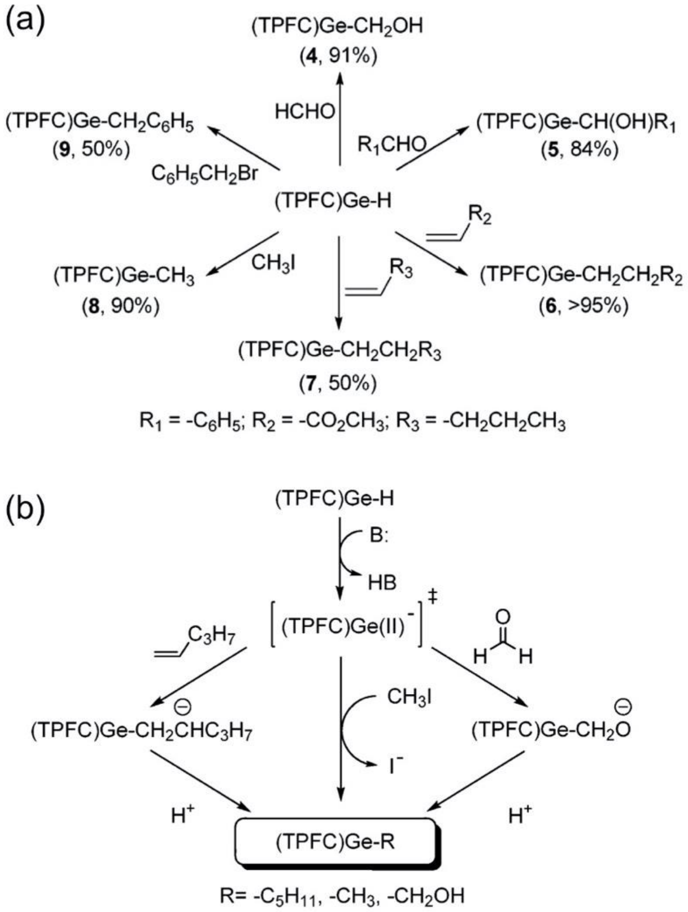

Figure 49. Chemical reactivity of (a) Ge[TPFPC](H) and (b) the $(Ge[TPFPC])^-$ anion. Adapted from ref 82 with permission from the Royal Society of Chemistry.

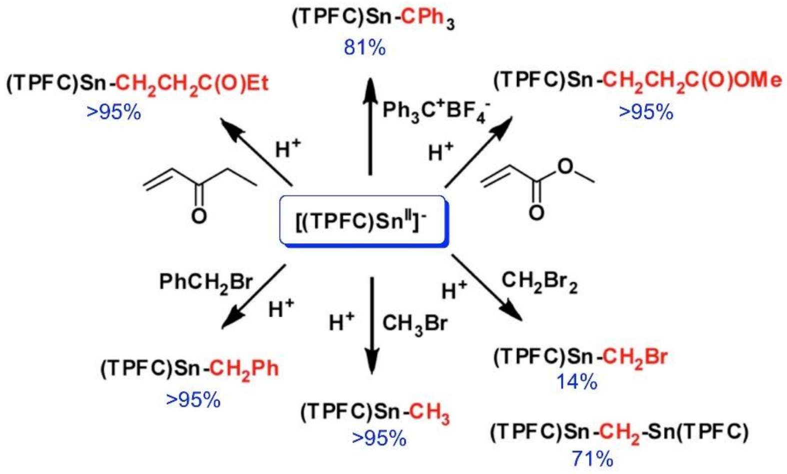

Figure 50. Chemical reactivity of the (Sn^{II}[TPFPC])$^{–}$ anion. Modified with permission from ref 83. *Copyright © 2014, American Chemical Society*.

2.2 Early d-block element corroles

The chemistry of Group 4 and 5 metallocorroles was largely developed by the group of Arnold and co-workers and has been reviewed by these authors.[84] Many of the syntheses relied on the lithium corrole reagent Li$_3$[Mes$_2$*p*OMePhC], as shown in Figure 51. The halido and imido products generally proved exceptionally sensitive to hydrolysis, consistent with highly electropositive and oxophilic nature of these elements.

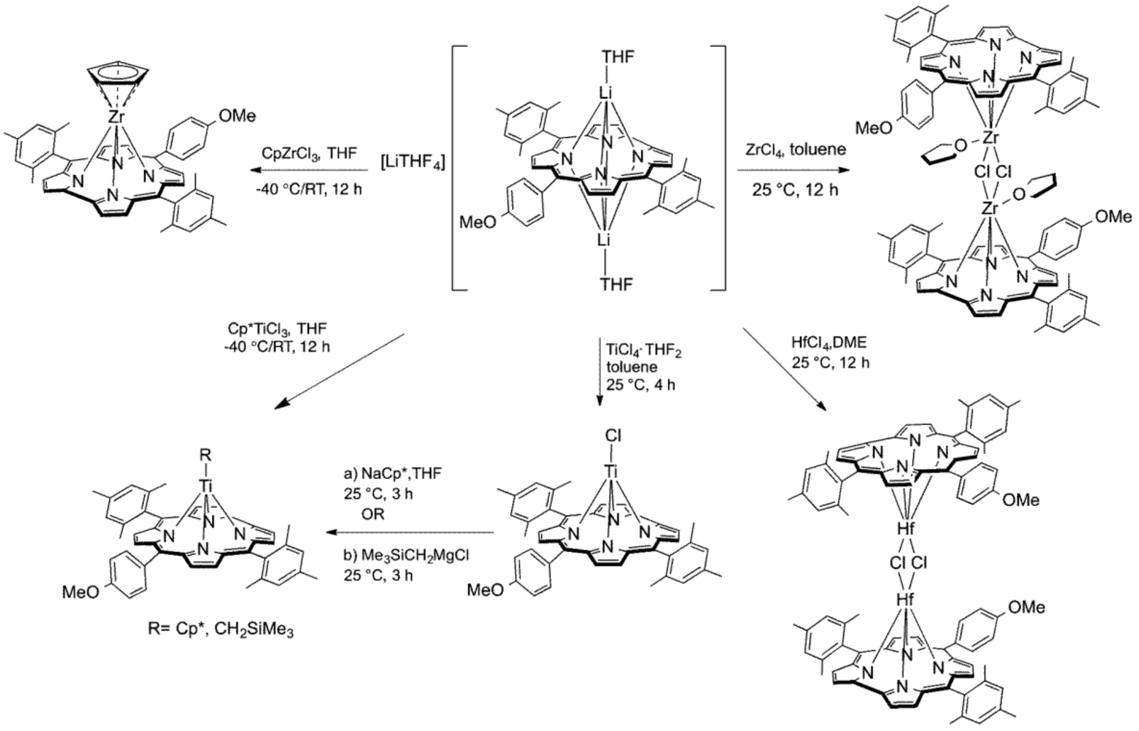

Figure 51. Preparation of Group 4 corrole complexes from lithium corrole. Reused from ref 85 with permission from the Royal Society of Chemistry.

2.3 Middle and late d-block element corroles

In the following section the coordination chemistry of the late d-block element corroles, will be presented. We proceed group by group, from Group 6 through 11. For many of the middle 4d and 5d metals, the preferred precursors were carbonyls or other low-valent organometallic compounds. For the 3d metals and group 11 metals, the acetates were generally the most suitable starting materials. The synthesis of the late d-block metallocorroles have provided key background for my own work on the coordination chemistry of corroles.

2.3.1 Group 6

Chromium and molybdenum are most conveniently inserted into corroles by heating with $M(CO)_6$ in an aprotic solvent such as toluene, DMF or decalin.[86, 87] In the case of Cr and Mo, the standard products are $Cr^{V}O$ and $Mo^{V}O$ corroles.[88] Interestingly, the analogous $W^{V}O$ corroles are yet unknown. However, interaction of the above-mentioned lithium corrole (section 2.1) with WCl_6 in toluene at -40˚C leads to $W^{V}Cl_2$ corrole.[89] Fascinatingly, under strictly anaerobic conditions in a high-boiling solvent, free-base corroles react with $Mo(CO)_6$ and $W(CO)_6$ to yield metal biscorrole derivatives. These eight-coordinate complexes exhibit eight-coordinate geometries and are inherently chiral and have been resolved into enantiomers.[88, 90]

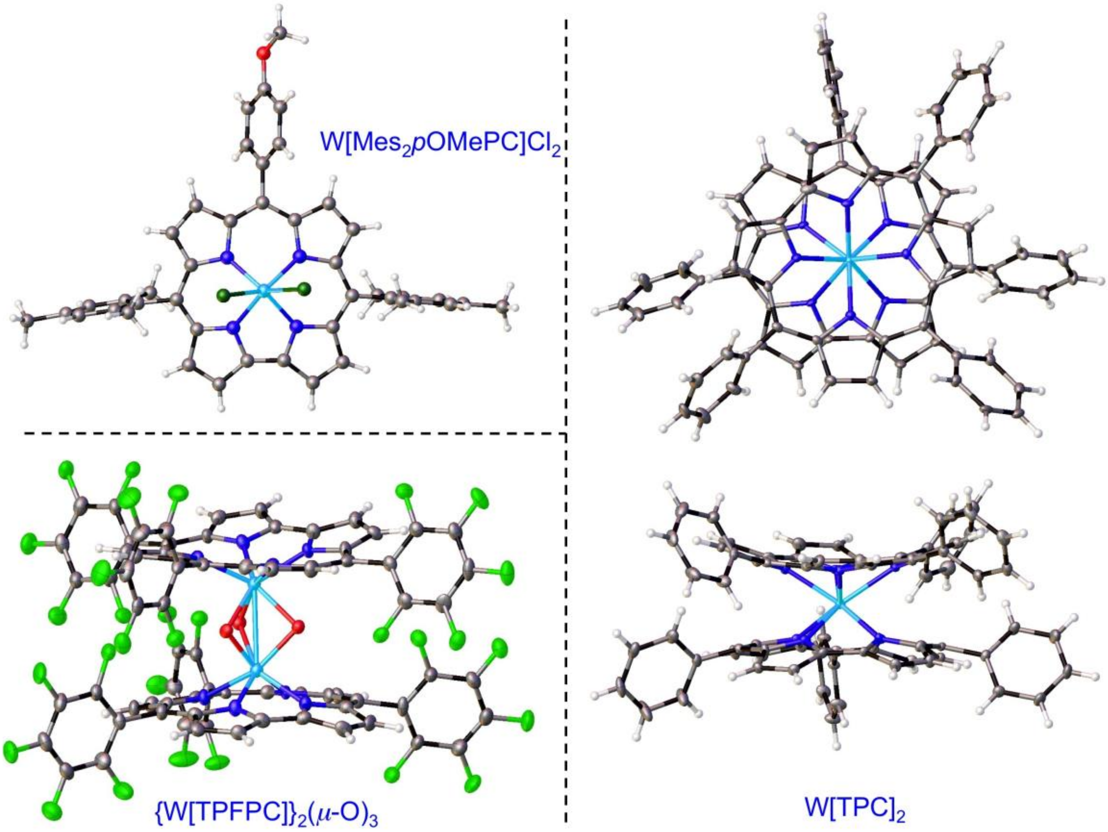

Figure 52. Three x-ray structures of tungsten corroles. Reused with permission from the authors from ref 91.

2.3.2 Group 7

Manganese is readily inserted into corroles with $Mn(OAc)_3$ in refluxing DMF or with $Mn_2(CO)_{10}$ in refluxing MeOH or pyridine. [92, 93] Manganese(III) corroles can even be used starting materials for Mn(IV) and even Mn(V) corroles, as shown in Figure 53.[94] Interestingly, $S = 3/2$ MnCl corroles are best viewed as Mn(III) corrole$^{\bullet 2-}$ radicals, whereas MnPh corroles (also $S = 3/2$) are essentially nonradical Mn(IV) species. Much more reactive are $S = 0$ Mn^VO species, which have been investigated as possible electron-, oxygen-, and hydrogen atom transfer agents. [95] The isoelectronic Mn^VO species are distinctly more stable and can even be chromatographed on a column. [96, 97]

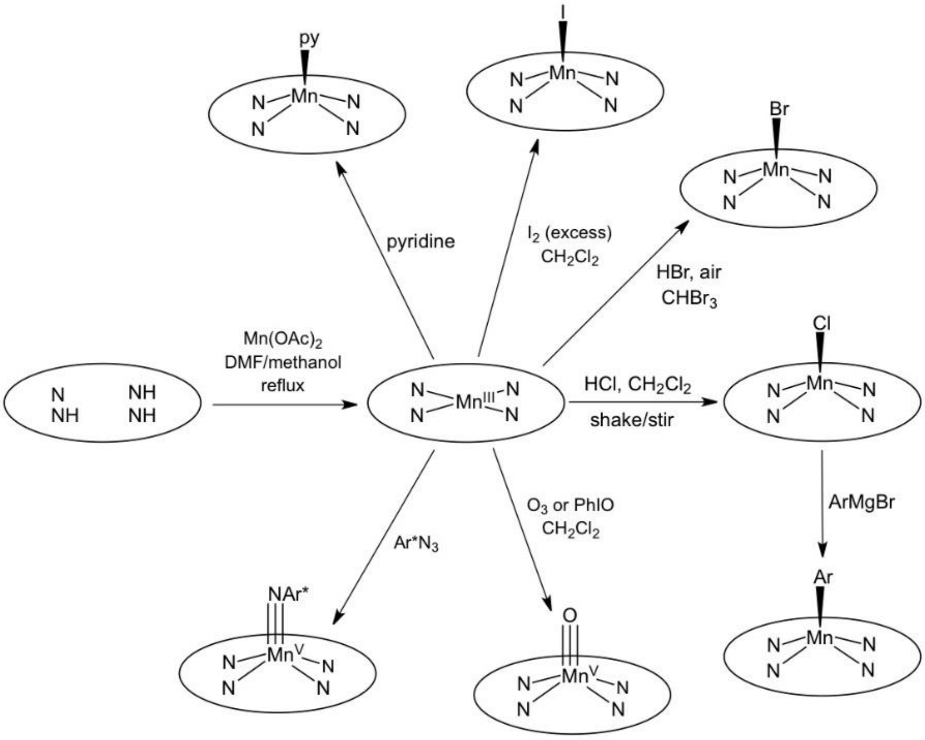

Figure 53. Synthesis and common transformation of Mn corroles.

As part of my master's studies, the chemistry of ^{99}Tc and Re corroles were developed during guest visits and in great collaboration with the group of Prof. Roger Alberto at his laboratory at the University of Zürich. Technetium could be coordinated to a corrole using $(Et_4N)_2[^{99}Tc^{I}(CO)_3Cl_3]$ in decalin as solvent with potassium carbonate as an added base. Heating the mixture at ~180°C for a few hours led to relatively good yields of Tc^VO corroles (IR ν_{TcO}: 973 ± 5 cm^{-1}). A single-crystal X-ray structure could be obtained for ^{99}Tc[T*p*OCH$_3$PC](O) which revealed an ^{99}Tc-N distances of 1.9 Å and an M-N$_4$ displacement of 0.68 Å. As of today, these $^{99}Tc^{V}O$ corroles are the only reported examples true Tc tetrapyrrole complexes where the tetrapyrrole acts as a normal square-planar tetradentate ligand. The only other report of a $^{99(m)}Tc$ porphyrinoid is that of mesoporphyrin IX dimethyl ester coordinated to one or two $\{^{99}Tc(CO)_3\}^+$ units, with each unit facially coordinated by three porphyrin nitrogen atoms.[60]

A rhenium(V)-oxo corrole was the first 5d element corrole to be synthesized – in a serendipitous discovery almost a quarter-century ago.[98] When *meso*-tetrakis(trifluoromethyl)porphyrin was reacted with dirhenium decacarbonyl in refluxing benzonitrile, the porphyrin underwent ring contraction, affording a 9% yield of the ReO *meso*-tetrakis(trifluoromethyl)corrole (Figure 54).

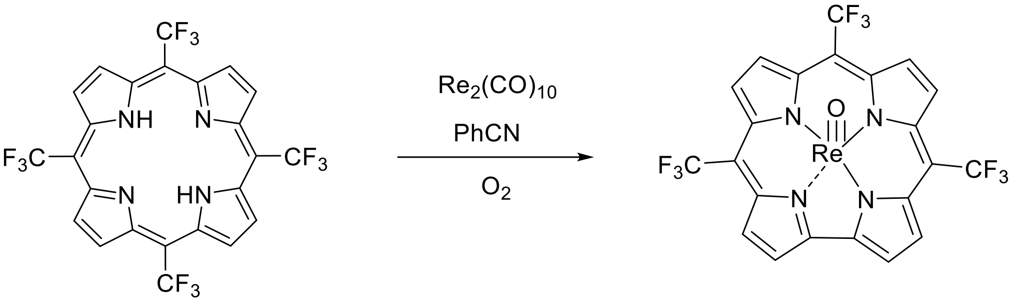

Figure 54. First, accidental synthesis of a rhenium corrole via ring contraction of a porphyrin.

Almost two decades after that initial report, a general protocol for the preparation of ReO corroles was developed.[99] The procedure involved heating a *meso*-triarylcorrole with $Re_2(CO)_{10}$ and potassium carbonate in decalin at 180°C generally overnight. The synthesis proved robust for a variety of substituted corroles and the desired ReO corroles (IR ν_{ReO}: 984±6 cm^{-1}) were isolated in excellent yields, making these complexes the most readily accessible among all 5d metallocorroles. Figure 55 depicts the preferred reaction conditions for the synthesis of key ^{99}Tc and Re corroles.

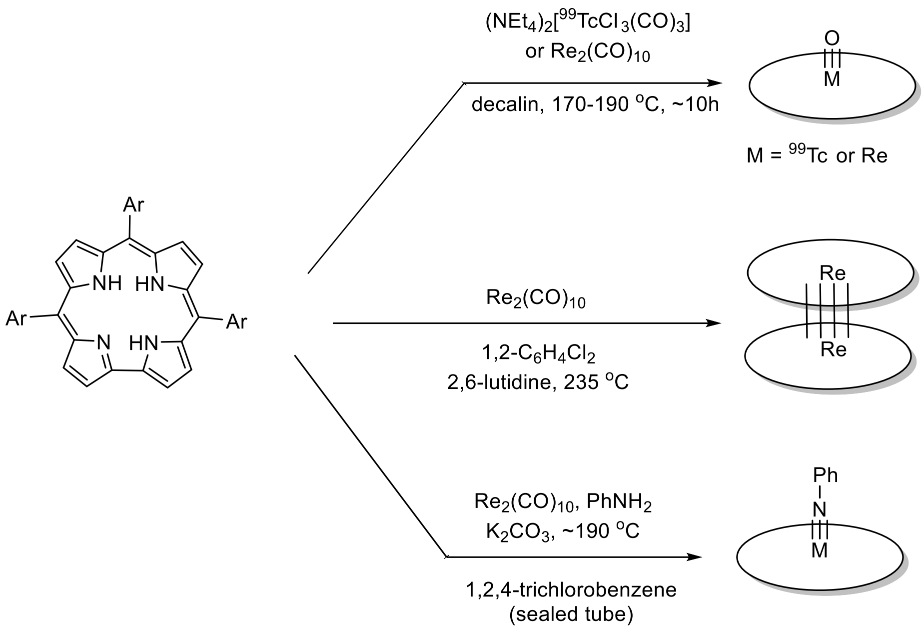

Figure 55. Synthetic approaches for different technetium and rhenium corroles.

Like their Mn^VO counterparts, $^{99}Tc^VO$ and Re^VO corroles are diamagnetic compounds with d_{xy2} ground states, thanks to metal-oxo π-bonding which engages the d_{xz} and d_{yz} orbitals. The latter complexes, however, are vastly more stable. Numerous crystal structures of ReO corroles have been obtained, the bond distances to Re being almost identical to those involving ^{99}Tc. The ReO corroles are the most strongly phosphorescent among the 5d metallocorroles and are also excellent singlet oxygen sensitizers, as described in Chapter 4.

Despite their stability, the group of Bröring managed to activate Re^VO corroles with $SiCl_4$ to generate Re^VCl_2 with a Viking-helmet-like *cis*-$ReCl_2$ unit. [100] My colleague Dr. Abraham Alemayehu also managed to synthesize Re-imido corroles via a simple modification of the ReO corrole synthesis. The method involved heating a free-base corrole in 1,2,4-trichlorobenzene in a sealed tube with $Re_2(CO)_{10}$ and potassium carbonate under anaerobic conditions. [101]

2.3.3 Group 8

Iron is commonly inserted into corroles with $FeCl_2$ in DMF under anaerobic conditions. The product is commonly isolated as an S = 3/2 Fe(III) bis(ether) complex, which serves as a versatile starting material for further derivatization (Figure 42). [92] In an exact parallel with Mn corroles, $S = 1$ FeCl corroles are best viewed as involving intermediate-spin S = 3/2 Fe(III) centers coupled to $\text{corrole}^{\bullet 2-}$ radicals, whereas $S = 1$ FePh corroles are closer to true S =1 Fe(IV) species. Interestingly, $S = 0$ FeNO corroles, long thought of as isoelectronic to $Fe^{II}CO$ hemes, are actually best viewed as $S = ½$ $Fe^{II}NO$ centers coupled to corrole$^{•2–}$ radicals. Evidence for such noninnocent electronic structures derives from a variety of sources, including substituent-senstive Soret bands (signifying charge-transfer character), skeletal bond length alternations, X-ray absorption spectroscopy, electrochemistry, and quantum chemical calulations, among others. [68, 102]

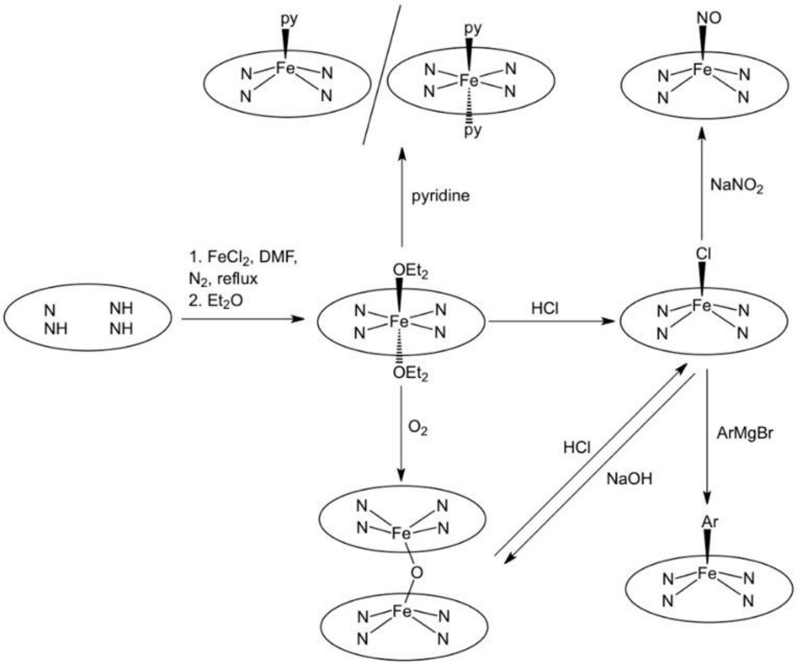

Figure 56. Schematic diagram of the major synthetic transformations involving Fe corroles. Recycled with permission from ref 103. *Copyright © 2017, American Chemical Society*

Early attempts at synthesizing ruthenium corroles via the reaction of a free-base octamethylcorrole with $Ru_3(CO)_{12}$ or $RuCl_3$ failed and led instead to the corresponding porphyrin (Figure 57).[92]

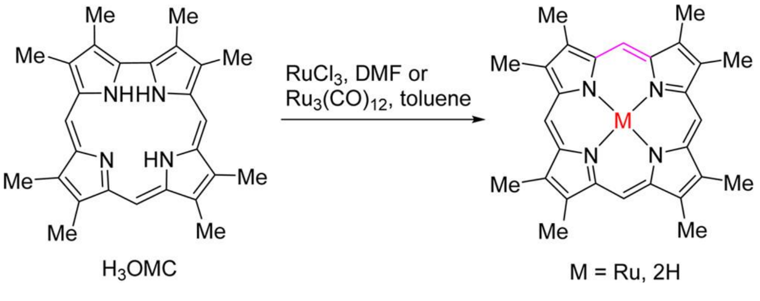

Figure 57. Attempted synthesis of a ruthenium corrole resulting in a ruthenium porphyrin via ring expansion. Adapted from ref 92, with permission from the Royal Society of Chemistry

Subsequently Ru corroles have been prepared by several groups, generally using a free-base corrole and $[Ru(cod)Cl_2]_2$ in refluxing 2-methoxyethanol in the presence of trimethylamine. [104] In the absence of other additives, the product is a chemically inert metal-metal triple-bonded Ru corrole dimer. Subsequently, it was found that the initially formed mononuclear Ru-corrole intermediates could be trapped by $NaNO_2$, affording RuNO corroles. Prolonged heating resulted in deoxygenation of the RuNO corrole, leading to ruthenium(VI)-nitrido corroles, which have been structurally characterized (Figure 58).[103]

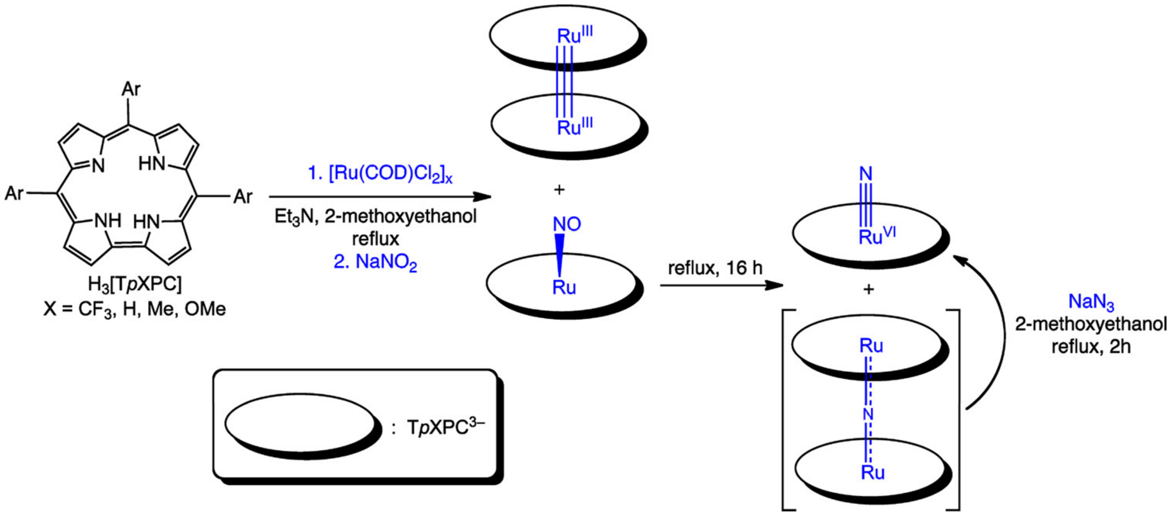

Figure 58. Synthetic routes to ruthenium *meso*-triarylcorroles. Recycled with permission from ref 103. *Copyright © 2017, American Chemical Society*.

Osmium has also been inserted into corroles as depicted in Figure 59. The $Os^{VI}N$ corroles thus obtained are isoelectronic with $Re^{V}O$ corroles and do also exhibit room-temperature NIR phosphorescence and singlet oxygen sensitization. [105]

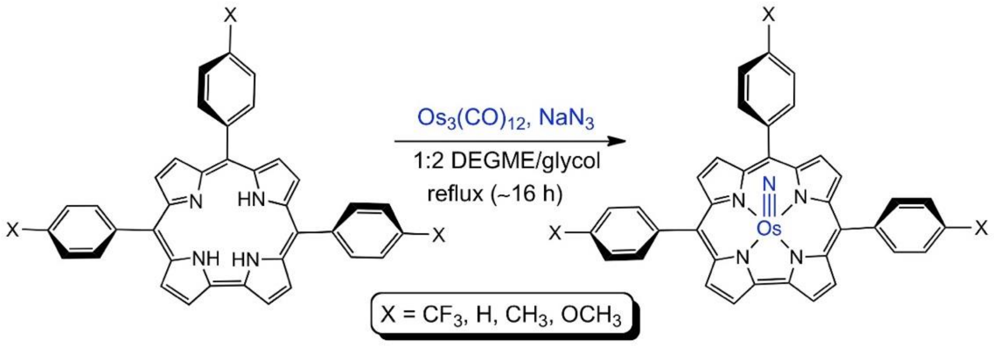

Figure 59. Synthetic route to OsN corroles. Reproduced with permission from ref 105. © *Wiley-VCH Verlag GmbH & Co. KGaA, Weinheim.*

2.3.4 Group 9

Cobalt corroles are readily synthesized by reacting a free-base corrole with $Co^{II}(OAc)_2$ in either refluxing pyridine or in MeOH in the presence of PPh_3, [87, 106] conditions that yield Co^{III}-corrole with either two axial pyridines or one axial PPh_3 ligand. Rhodium is inserted via the interaction of free-base corroles with $[Rh(CO)_2Cl]_2$ in the presence of PPh_3 and K_2CO_3 in an aprotic solvent, which results in affords rhodium(III) corroles axially coordinated to a PPh_3 ligand. [107]

In 2008, Gray and co-workers reported the first syntheses of iridium corroles, using $[Ir(cod)Cl]_2$ and K_2CO_3 in THF under argon. The initially formed iridium(I)-cod-corrole intermediate was converted to iridium(III) corroles upon exposure to air or to another oxidant. In the presence of a ligand such as ammonia or pyridine, the product is obtained in axially bis-ligated form. [108, 109] Additional examples were reported by my colleague Dr. Ivar Thomassen (Figure 60). Their studies showed that although Ir(III) corroles are only weakly phosphorescent, they are still exceedingly effective singlet oxygen sensitizers. This behaviour contrasts with that of Ir(III) porphyrins, which are strongly phosphorescent. The reasons for the difference remain to be elucidated. [110]

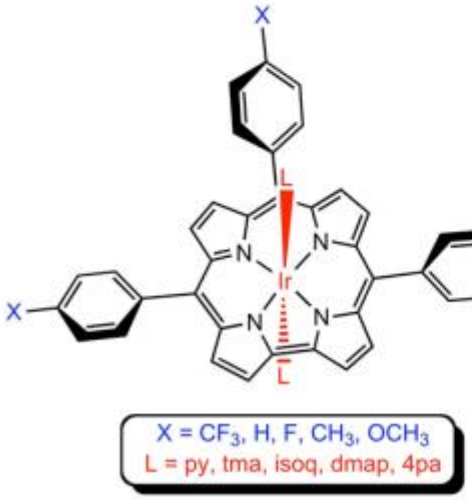

Figure 60. Structural drawing of some recent iridium corrole complexes. Recycled from ref 110 with permission from the authors.

2.3.5 Group 10

The chemistry Group 10 corroles is somewhat underdeveloped. Nickel corroles, known from the earliest days of corrole chemistry, are known to be Ni(II) corrole$^{\bullet 2-}$ radicals. [111] Palladium(II) corrole anions are of more recent provenance and Pd(IV) corroles are as yet unknown. Platinum was first inserted into corroles by my colleague Dr. Abraham Alemayehu, after a great deal of trial and error. The procedure that finally worked involved heating a free-base corrole with tetranuclear $[Pt(OAc)_2]_4 \bullet 2AcOH$ in benzonitrile under aerobic conditions and microwave irradiation at 140-150˚C. [112] Remarkably, platinum insertion was accompanied by C-H activation of benzonitrile so the initial product was a Pt^{IV}-aryl complex, with the aryl ligand derived from benzonitrile. This product proved unstable but could be readily converted to other stable Pt(IV) corroles, as shown in Figure 61. Interestingly, the Pt^{IV}[Corrole](Ar)(py) complexes were found to exhibit NIR phosphorescence. [113]

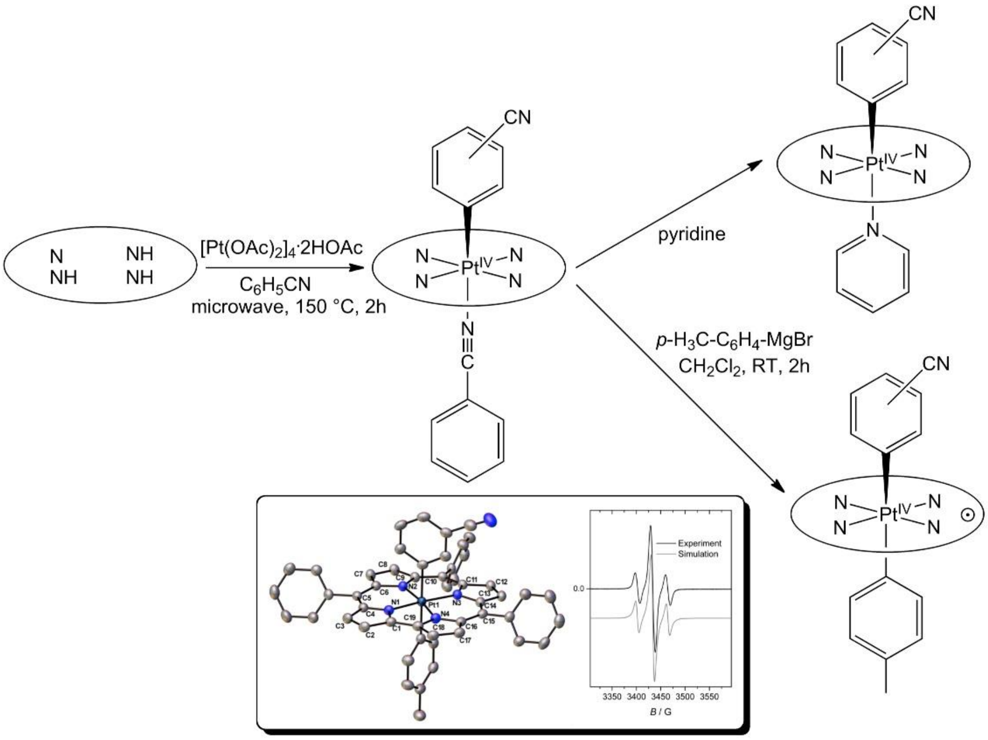

Figure 61. Synthesis and transformation of platinum corroles, with inset showing X-ray structure and EPR spectrum. Reused with permission of author from ref 112.

2.3.6 Group 11

Formally trivalent copper and silver corroles are readily synthesized from the corresponding free bases using Cu(II) and Ag(I) acetate, respectively, with pyridine as solvent. [42, 45, 114] Gold corroles are much trickier to synthesize. Although gold was first inserted with $HAuCl_4$. [115] However, my colleague Dr. Kolle E. Thomas showed that $Au(OAc)_3$ was a much superior reagent and is now the current reagent of choice, as shown in Figure 62 below. [116]

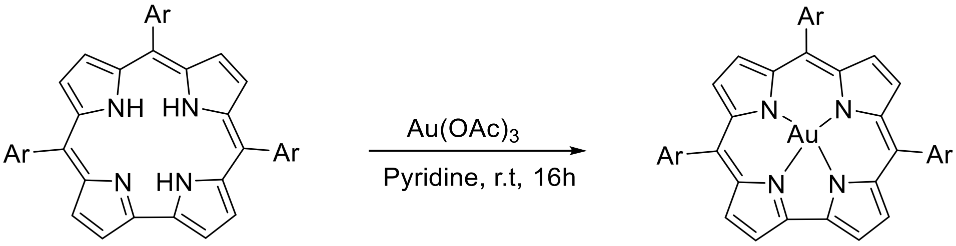

Figure 62. Preferred synthetic rout to Au(III) corroles.

The group 11 metallocorroles illustrate a great deal comparative coordination chemistry. Copper corroles are unique among metallocorroles in being inherently saddled. Thus, even sterically unhindered Cu triarylcorroles are distinctly saddled and the degree of saddling increases with increasing levels of steric hindrance on the corrole periphery. A great deal of physical evidence (UV-vis, NMR, and XAS, among others) points to a noninnocent Cu^{II}-corrole$^{\bullet 2-}$ electronic configuration for Cu corroles, in which spin coupling between the Cu(d_{x2-y2}) electron and the corrole π-radical leads to significant saddling of the corrole macrocycle. In contrast, Au corroles are generally planar, with no indication corrole radical character. Silver corroles appear to straddle a knife-edge between the innocent and noninnocent regimes. [117] Simple Ag corroles are thought to be relatively planar and innocent, but sterically hindered silver corroles, such as Ag β-octabromo-*meso*-triarylcorroles, are strongly saddled (Figure 63) and are believed to be noninnocent. Table 1 provides a comparison of experimentally observed saddling dihedrals for different copper, silver and gold corroles. [42, 45, 118]

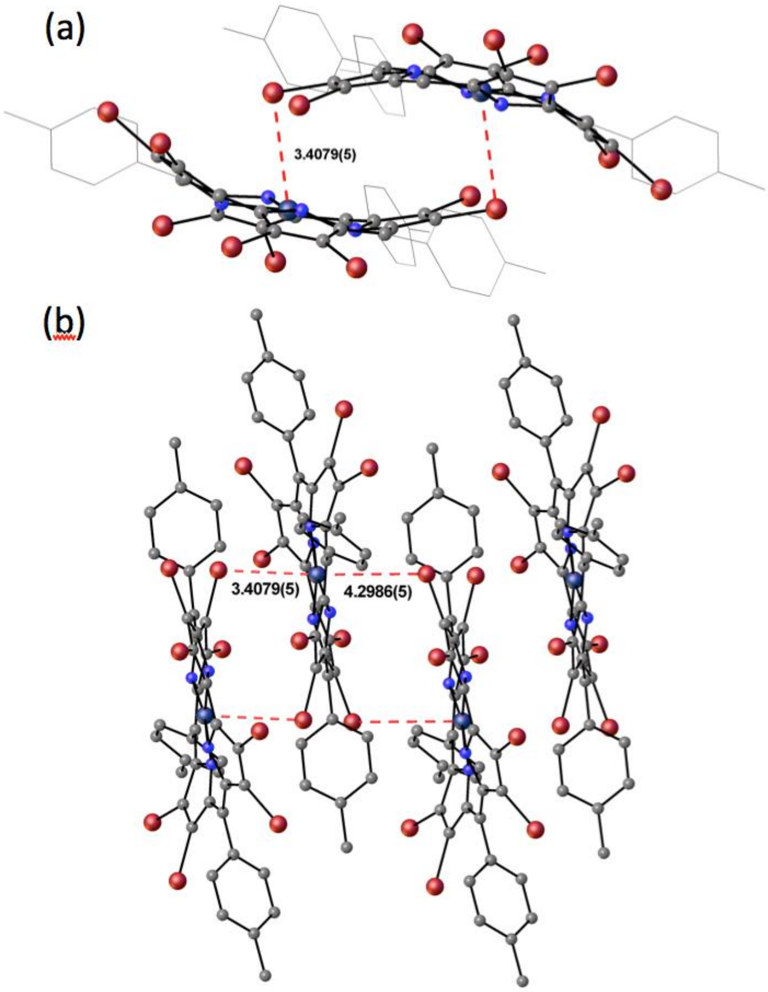

Figure 63. Two views of the crystal structure of Ag[Br$_8$T*p*MePC]. Reused with permission from ref 117. *© 2015 WILEY-VCH Verlag GmbH & Co.*

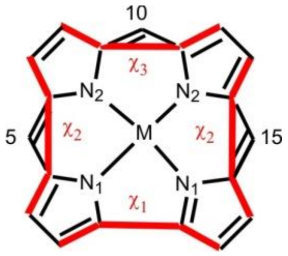

Table 1. Selected distances [Å] based on crystal structure. Data from ref [91].

Complex	M-N$_1$[a]	M-N$_2$[a]	χ_1	χ_2[a]	χ_3
Cu[TPC]	1.891(4)	1.891(4)	27.5	53.4	48.7
Cu[Br$_8$T*p*MePC]	1.916(2)	1.916(2)	44.7	65.9	57.3
Ag[T*p*FPC]	1.943(3)	1.964(3)	19.9	38.8	38.8
Ag[Br$_8$T*p*MePC]	1.983(3)	1.983(3)	45.0	68.5	63.5
Au[T*p*FPC]	1.939(2)	1.956(2)	13.8	23.1	24.5
Au[Br$_8$TPFPC]	1.938(19)	1.970(19)	1.6	7.2	7.9

[a] Average of two values for each experimental structure.

A most useful property of Cu corroles is that they undergo reductive demetallation with concentrated sulfuric acid and 5-200 eq. of FeCl$_2$ or SnCl$_2$. Since Cu corroles are also readily derivatized with various electrophilic aromatic substitutions, demetallation also provides a route to a wide range of functionalized free-base corroles, which can now be coordinated to other metals. As discussed further in Chapter 3, such a strategy, for example, provided the first reliable syntheses of free-base *β*-octabromo-*meso*-triarylcorroles. [111, 118]

2.3.7 Group 12 (Zn, Cd, Hg)

The chemistry of Group 12 metallocorroles is rather underdeveloped. One of the few notable papers is one by Bröring, reporting the synthesis and X-ray structure of the Zn[TMC$^\bullet$] radical, where TMP refers to *meso*-trimesitylcorrole. [119]

2.4 f-Block element corroles

Like early d-block elements, f-block elements are electropositive, strongly oxophilic, and hydrolysis-prone. The group of Arnold and co-workers successfully used their lithium corrole reagent Li$_3$[Mes$_2p$OMePhC] to develop the coordination chemistry of f-block element corroles (Figure 64). An alternative strategy, in which a free-base corrole is treated with lanthanide amide, has also worked for two lanthanide corroles (Figure 64).[120]

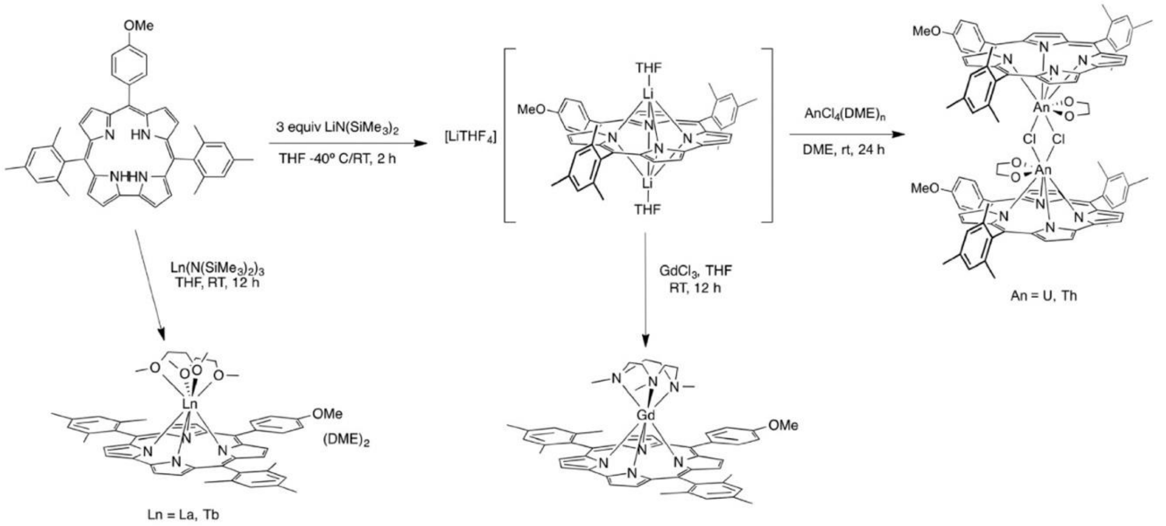

Figure 64. Synthetic approaches to f-block metallocorroles. Adapted from ref 120 with permission from the Royal Society of Chemistry.

Lanthanide corroles (involving trivalent La, Gd, and Tb) generally exhibit strongly domed, 7- or 8-coordinate geometries, with amines or ethers as neutral capping ligands (Figure 65). In general, the M-N distances are 2.65 ± 0.1 Å, and the M-N$_4$ displacements are 1.26-1.27 Å for

Gd and Tb and slightly longer, 1.47 Å, for La (Figure 66) (which has a longer ionic radius). Finally, cerium(III) corroles with cyclopentadienyl and hydrotris(pyrazolyl)borate capping ligands have also been reported. [120]

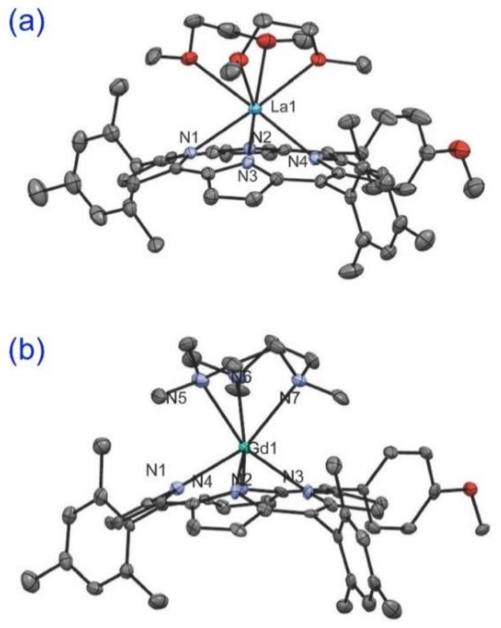

Figure 65. X-ray structures of (a) La[Mes$_2$*p*OMePhC]·4.5DME and (b) Gd[Mes$_2$*p*OMePhC](Me3TACN). Reproduced from ref 120 with permission from the Royal Society of Chemistry.

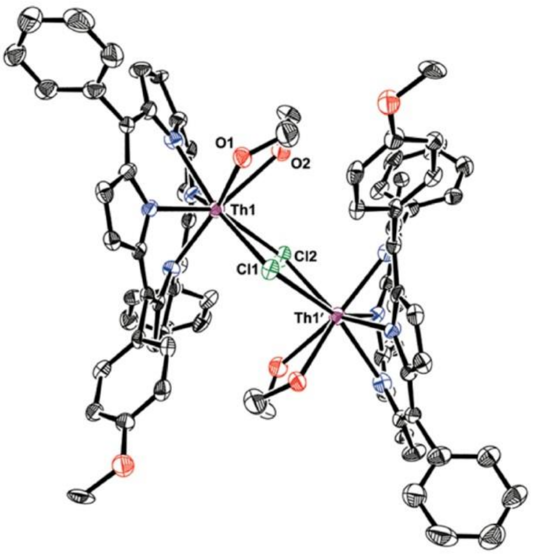

Figure 66. X-ray structure of (Th^{IV}[Mes$_2$*p*OMePhC](μ-Cl)(DME))2. Reproduced with permission from ref 121. *Copyright 2013 American Chemical Society*.

The Arnold group has also reported two isostructural actinide corroles, (M^{IV}[Mes$_2$*p*OMePhC](μ-Cl)(DME))$_2$ (M = Th, U), with unique binuclear M$^{IV}_2$(μ-Cl)$_2$ diamond cores (Figure 66).[121] The metallocorrole units in the two complexes are also structurally very similar, with M-N distances within 2.29-2.41 Å and M-N$_4$ out-of-plane displacements of ~1.40 Å. Detailed NMR studies on the Th(IV) complex, however, indicate fluxional behaviour in solution, involving pseudo rotation about the Th-Th axis, as schematically illustrated in Figure 65.[122]

2.5 Innocence and noninnocence in corroles

Many corroles exhibit a phenomenon called ligand noninnocence. The term was introduced well over half a century ago, by the Danish chemist C. K. Jørgensen, to denote ligands that do not allow unambiguous assignment to the oxidation state of a coordinated metal atom. That scenario is very common among first row metallocorroles, much more so that first row metalloporphyrins. Thus, many metallocorroles $M^{x}[Cor^{3-}]$ (L), where x is the formal metal oxidation state, are better described as $M^{x-1}[Cor^{\bullet 2-}]$(L) the corrole in these complexes are partially oxidised and may be described as partial dianion-radical. Examples include Mn[Cor]Cl, Fe[Cor]Cl, Fe[Cor](NO), Co[Cor](L) and Cu[Cor], which are best described as $Mn^{III}[Cor^{\bullet 2-}]Cl$, $Fe^{III}[Cor^{\bullet 2-}]Cl$, $Fe^{II}[Cor^{\bullet 2-}](NO)$, $Co^{II}[Cor^{\bullet 2-}](L)$ and $Cu^{II}[Cor^{\bullet 2-}]$. In contrast, Mn[Cor]Ph, Fe[Cor]Ph, $Co[Cor](Py)_2$ are innocent and are best described as Mn(IV), Fe(IV) and Co(III), respectively. The 4d and 5d metallocorroles of key interest to this thesis are generally innocent and noninnocent examples are rare.

The presence of ligand noninnocence can be indicated through a variety of probes, such as skeletal bond distance alternations, characteristic spin density plots, substituent-sensitive Soret maxima, and characteristic signatures in metal K-edge X-ray absorption spectra. These have been summarized in depth by Ganguly and Ghosh in a recent review article. [123]

Chapter 3: Functionalization of corroles

As aromatic compounds, porphyrins undergo a variety of electrophilic aromatic substitutions including chlorination, bromination, iodination, nitration, formylation, sulfonation, chlorosulfonylation, and acylation, among others. Some of the more notable transformations include one-pot *β*-octachlorination and *β*-octabromination. Polynitration up to heptanitration has been accomplished with fuming nitric acid. Brominated porphyrins undergo a variety of palladium-catalysed reactions, notably Suzuki coupling, and *β*-octabromo-*meso*-tetraarylporphyrin derivatives have been converted to dodecaarylporphyrins via eightfold Suzuki couplings. *β*-Formyl porphyrins likewise serve as a gateway to other functionalized porphyrins, for example via the Knoevenagel reaction. Unsurprisingly, many of the same reactions also apply to corroles and other porphyrinoids, as described below.

3.1 Chlorination

Except for fluorine, the larger halogens can be directly attached to the corrole periphery using elemental Cl_2, Br_2, or I_2. The first report of an octachlorinated corrole was accomplished on a copper *meso*-pyrimidinyl corrole, which was treated with *N*-chlorosuccinimide (NCS) in a high boiling solvent. The corresponding octachlorinated free-base corrole could then be obtained via reductive demetalation. [124] In a much improved protocol for *β*-octachlorination resulting in yields up to 90%, the group of Gross exposed a Co[TPFPC] with an excess of Cl_2 in benzene, followed by quenching with pyridine and $NaBH_4$. [125] Presumably in an attempt of synthesising tungsten corroles the Bröring group obtained selective dichlorination resulting in the formation of 3,17-dichloro-5,10,15trimitylcorrole. In their work they used 5,10,15-mesitylcorrole which they reacted with WCl_6/$W(CO)_6$ in benzonitrile and heated at 200 °C for 8 hours. [126]

Using Palau'chlor, and their "*meso*-free corroles", the Osuka group made 5-and 10-chloro-corroles, as shown in Figure 67. They found that the selectivity towards the 10-isomer was strongly favoured, resulting in 80% yield, while the 5-chloro was only obtained in trace amounts. [127]

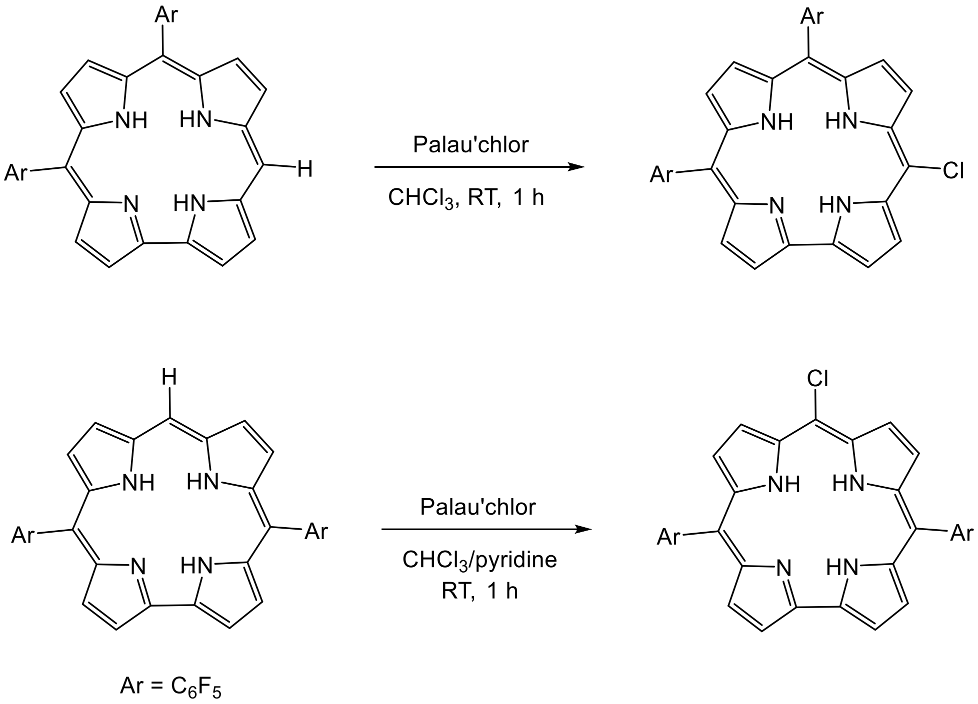

Figure 67. *Meso*-chlorination of corroles with Palau'chlor.

3.2 Bromination

Early brominations were done using chloroform as solvent and NBS as bromination reagent. The Paolesse group was the first to report complete bromination of the *β*-positions on the corroles when they reacted TPC and 5,10,15-tris(4-nitrophenyl)corrole with NBS, Figure 68. However, they discovered that this resulted in the corresponding isocorrole analogue. When they reacted the *β*-octabromo isocorrole further with Co(OAc)$_2$ they isolated the Co(III)-*β*-octabromo corrole in good yields. [128]

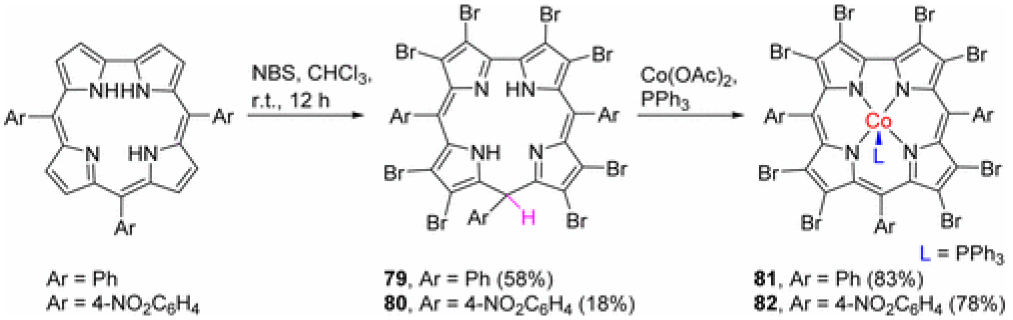

Figure 68. Bromination of free-base corrole resulting in *β*-octabromoisocorrole, back to corrole upon metalcoordination. Adapted from ref 67. *Copyright © 2016 American Chemical Society*

Through careful control of the equivalents of NBS in a CH_2Cl_2/MeCN mixture at room temperature, Du *et al*. reported a procedure of selective bromination of the 2,3,17 and/or 18 position of the corrole. By using 1.1 equivalent of NBS they obtained the mono brominated compound. However, they did not manage to isolate the 2- and 3- isomer. Increasing the NBS up to 4.4 equivalents, they isolated the di-, tri, or tetrabrominated derivatives. [129] The group of Paolesse has studied selectivity and reaction behind bromination of corroles. By reacting the free-base 5-hydoxyisocorrole or the silver complex of 3-NO_2-T*p*MePC with NBS in $CHCl_3$, the monobrominated 2- or 3- isomer could be obtained, as illustrated in Figure 69.[130]

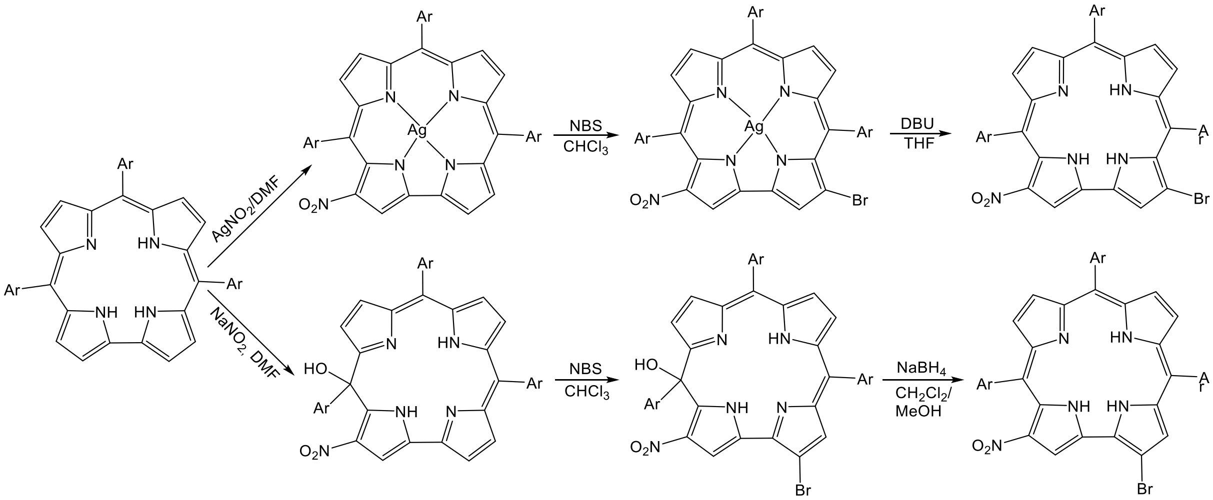

Figure 69. Selective bromination depending through corrole/isocorrole intermediate. Adapted from ref 130.

3.3 Iodination

Iodination of the corroles β-position has proven far more cumbersome than bromination. The Gross group have isolated partially iodinated Al, Ga and group 11 metals. By treating a solution of M[TPFC](py)2 (M = Al, Ga) in methanol or acetonitrile with NIS, the corresponding 2,3,17,18-tetraiodinated derivatives could be isolated. [131]

In another iodination protocol, the group of Gross showed that tetraiodinated corrole complexes could be isolated by refluxing M[TPFC]$(py)_2$ (M = Al, Ga) in a mixture of toluene and pyridine with an excess of I_2. [132]

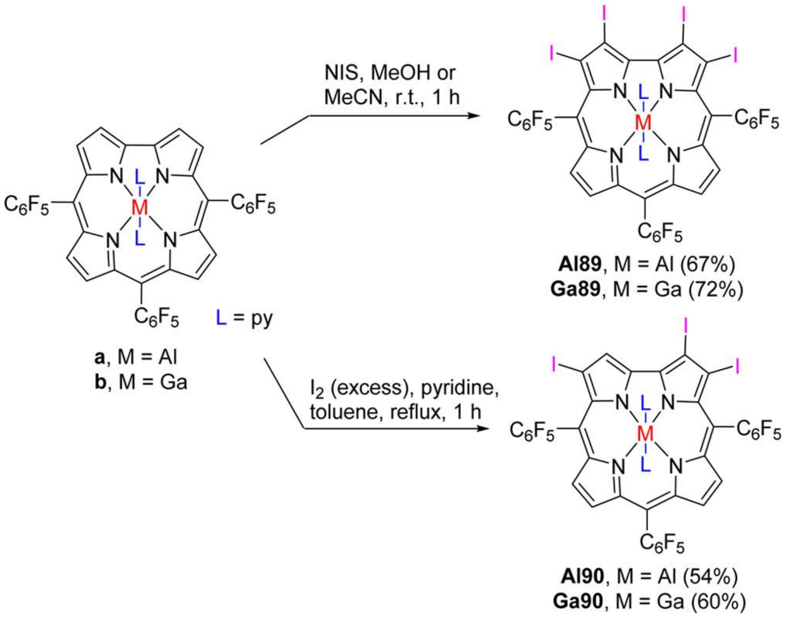

Figure 70. Iodination of Al(III) and Ga(III) corroles. Adapted from ref 67. *Copyright © 2016 American Chemical Society*.

For group 11, metal insertion and tetraiodination could be carried out via a facile one-pot protocol involving the room-temperature interaction of H_3[TPFC], NIS and a metal acetate in pyridine (Figure 71).[133]

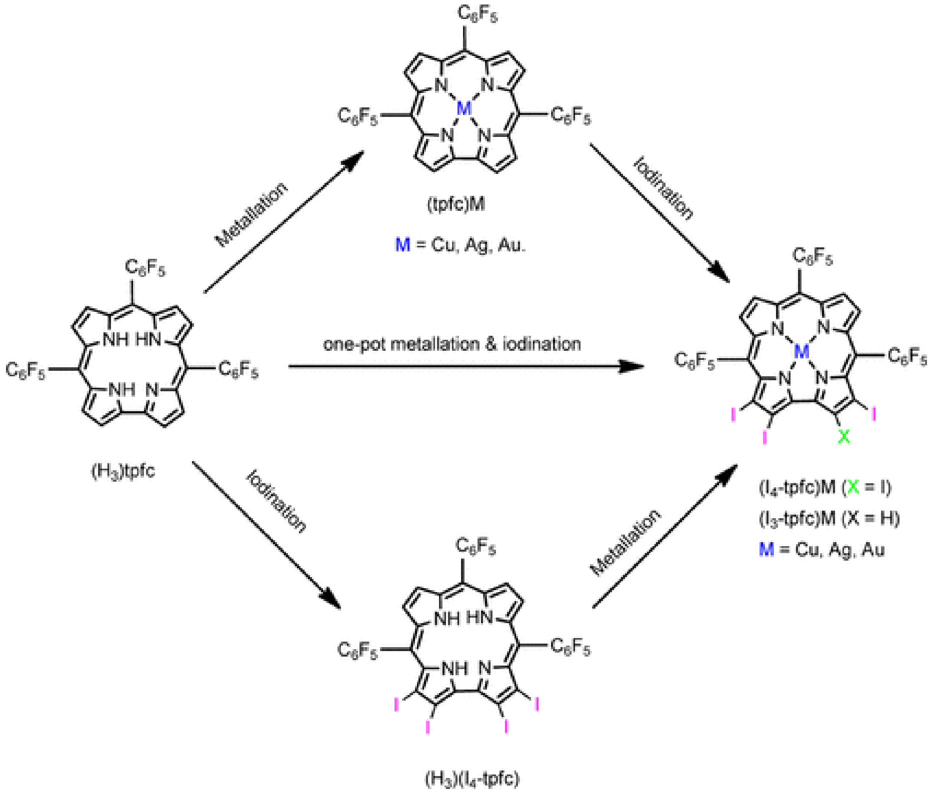

Figure 71. Three approaches for the synthesis of group 11 metal complexes of β-pyrrole iodinated corroles. Reproduced with permission from ref 133. *Copyright © 2016 American Chemical Society*.

After the successfully synthesis of β-octaiodoporphyrins by Ivar K. Thomassen, he chanced his focus on the synthesising β-octaiodocorroles (Figure 72). After a significant amount of trial and error, he had a breakthrough using the electron-deficient Cu[T*p*CNPC] and NIS in TFA. The single-crystal X-ray structure of the product, illustrated in Figure 73, showed one of the most strongly saddled corrole macrocycles observed to date. [66, 134]

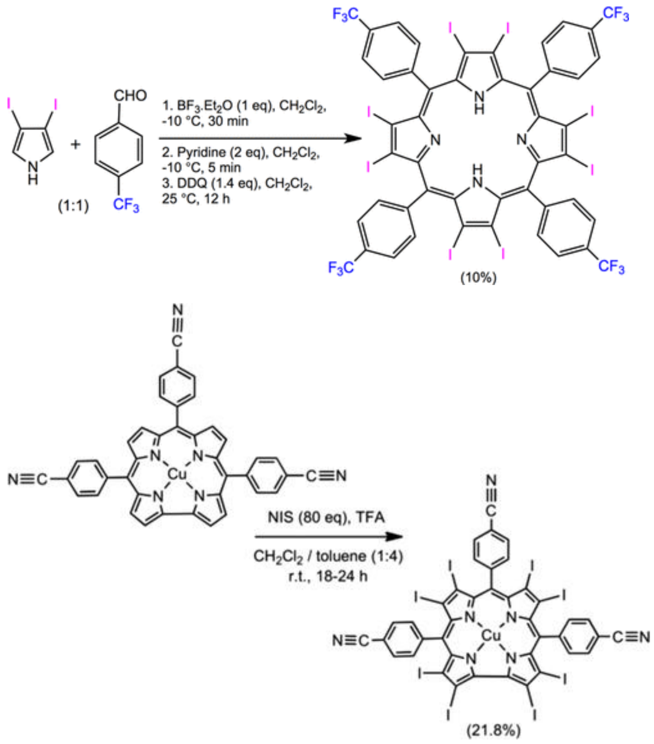

Figure 72. (Top) synthesis of octaiodoporphyrin, (bottom) synthesis of Cu[T*p*CNPC]. Reused with permission from ref 66. *Copyright © 2015 American Chamical Society.*

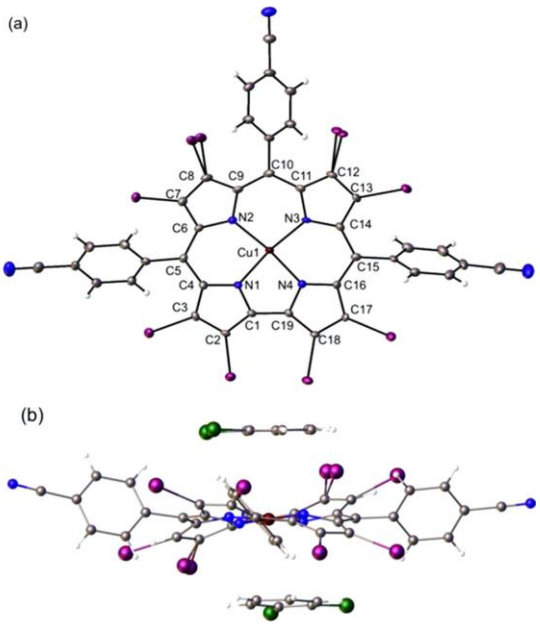

Figure 73. (a) Top and (b) side views of the x-ray structure of Cu[I$_8$T*p*CNPC]. Reused with permission from ref 134. *Copyright © 2018 American Chemical Society*.

3.4 β-Fluorinated corroles

To our knowledge, electrophilic fluorination of corroles has not been reported. Nevertheless, β-octafluorocorrole derivatives are well-known. The reported procedures use 3,4-difluoropyrrole as the key fluorinated starting material. With pentafluorobenzaldehyde and Gross's solvent-free protocol, Chang and co-workers obtained the fully fluorinated 2,3,7,8,12,13,17,18-octafluoro-5,10,15-tris(pentafluorophenyl)corrole.[96] Ghosh and co-workers applied the same approach to a larger selection of aromatic aldehydes.[45] Unfortunately, the labour involved in the synthesis of 3,4-difluorocorrole has discouraged widespread applications of β-octafluorocorrole derivatives. A couple of crystal structures, however, have been reported by the Ghosh group at UiT (Figure 74).[135]

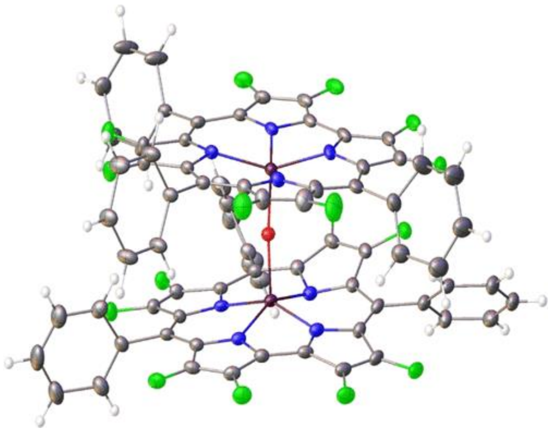

Figure 74. X-ray structure of $\{Fe[F_8TPC]\}_2O$. Reused with permission from ref 135. *Copyright © 2020 American Chemical Society*.

3.5 Formylation

As early as 1997, by reacting *meso*-unsubstituted H_3[OMC] with $POCl_3$/DMF (Vilsmeier conditions), Paolesse *et al*. obtained the corresponding 10-dimethylaminomethene derivative. Likewise, by using the 10-phenylcorrole under the same conditions, they obtained the 5-dimethylaminomethene compound. Cobalt insertion into the products with $Co(OAc)_2$ and PPh_3 in refluxing methanol then afforded the corresponding formyl derivatives. [136] Starting from Co(OMC)(PPh_3) and reacting it with Vilsmeier reagents exclusively resulted in the *meso*-formyl complex. Later they turned their attention to formylation *meso*-triarylcorroles. With H_3[TPC], they isolated the corresponding 3-formyl derivative as the major product. By increasing the amount of DMF, they obtained the 2-formyl derivative as the major product. [137] Starting with Ga[TPFC](py), Gross *et al*. isolated the 3-formyl and 2,17-diformyl derivatives as the major products. [138]

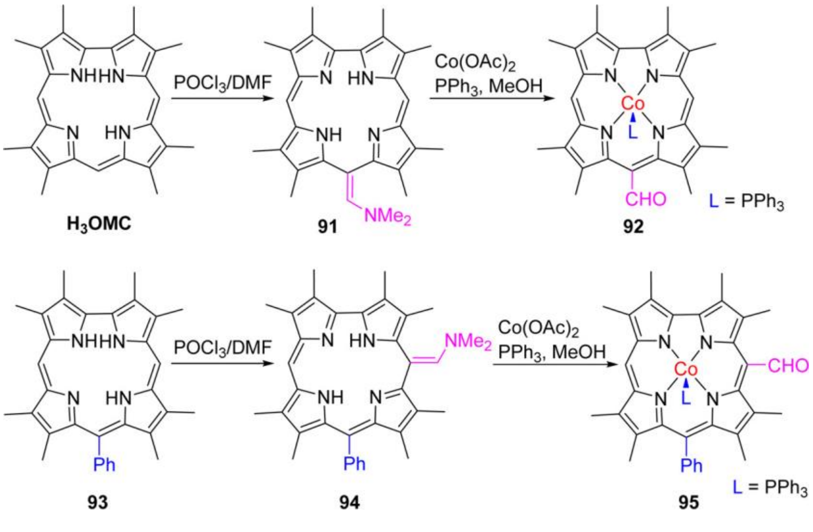

Figure 75. Formylation of free-base corrole. Reused with permission from ref 67. *Copyright © 2016 American Chemical Society.*

3.6 Carboxylation

The only report of a caboxylated free-base corrole is one by the group of Giribaby, in which they oxidised a *β*-formyl corrole under mild conditions to obtain the *β*-carboxy free-base corrole. They also made the corresponding copper corrole complex (Figure 76).[139]

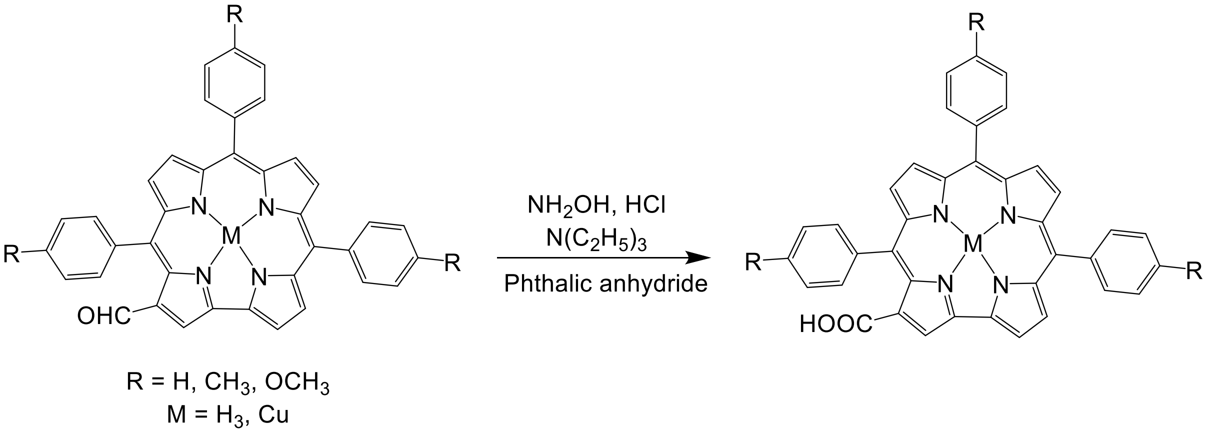

Figure 76. Synthesis of *β*-carboxy corrole through oxidation of an aldehyde.

Attaching a carboxylic acid directly to a corrole has only been done by Gross *et al.* on gallium tris(pentafluorophenyl)corrole via the use of phosgene in pyridine.[140]

3.7 Chlorosulfonation

Gross and co-workers were the first to report peripheral chlorosulfonation of corroles when they added chlorosulfonic acid to free-base *meso*-tris(pentafluorophenyl)corrole at room temperature. This led to an almost quantitative yield of the corresponding 2,17-bis(chlorosulfonyl)corrole (Figure 77).[141]

The same group also reported another synthesis to obtain the sulfonic acid analogue. By treating free-base *meso*-tris(pentafluorophenyl)corrole with concentrated sulphuric acid at room temperature the 2,17-bis-sulfuric acid corrole could be isolated in very good yield. The authors reported that this approach preferred the 2,17-isomer over the 3,17-isomer by a factor of 9:1. Using two different phosphorus triarylcorroles, Gross *et al.* found that the isomer selectivity depends strongly on the corroles *meso*-substituents.[142] Furthermore, they concluded, based on the experimental results and DFT calculations, that while the first chlorosulfonation is under kinetic control, the second is under thermodynamic control.[143]

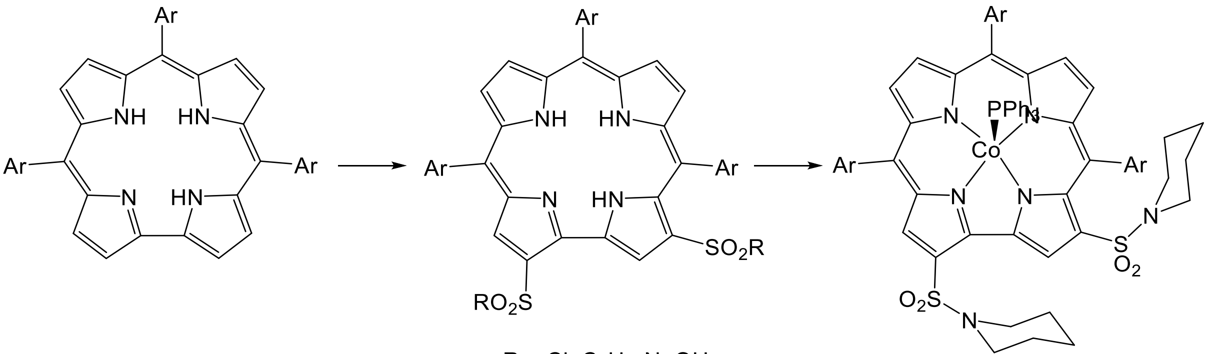

R = Cl, $C_5H_{10}N$, OH

Figure 77. Selective chlorosulfonation of H_3[TPFPC] and further transformations.

3.8 Nitration

Attaching nitro groups to the *β*-position of corroles can be achieved through several protocols, readily leading up to *β*-tetanitro products. Gross *et al.* showed Ga-corroles could be selectively nitrated using $NaNO_2$ and tris(4-bromophenyl)aminium hexachloroantimonate in dry acetonitrile (Figure 78). By increasing the amount of tris(4-bromophenyl)aminium hexachloroantimonate to 200 mol % they obtained the 3,17-dinitro compound in 94% yield, while increasing to 300 mol % resulted in the 3,17,18-trinitro compound in 27 % yield. [138]

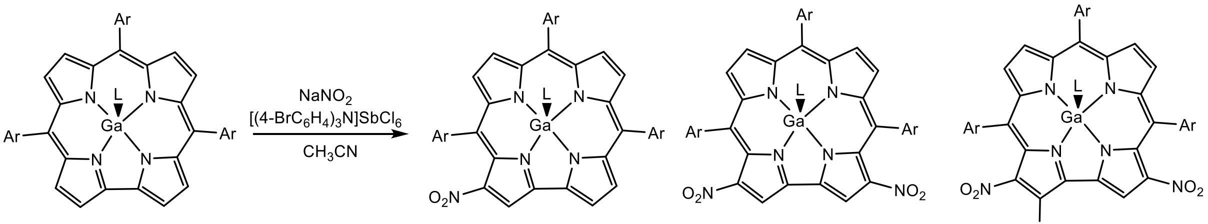

Ar = C_6F_5, L = pyridine

Figure 78. Selective nitration of Ga-corrole. Based on ref 138.

Synthesizing free-base nitrocorroles has proven somewhat more troublesome since the conditions used for nitration of gallium complexes led to decomposition of free-base substrate. The Paolesse group addressed this problem by attempting to nitrate free-base corroles using $AgNO_2$ in a solution of acetonitrile. However, instead of obtaining the desired free-base nitrocorrole, they isolated the corresponding silver 3-nitro-corrole. [144]

The Paolesse group later published a procedure for the preparation of free-base nitrocorroles. By adding $AgNO_2/NaNO_2$ into a refluxing solution of triarylcorrole in DMF, the corresponding 3-nitrocorrole could be isolated as the major product with a smaller quantity of the 2-nitro derivative. Changing the molar concentrations of corrole and $AgNO_2/NaNO_2$ resulted in a variety of nitrocorroles products, as depicted in Figure 79.[145]

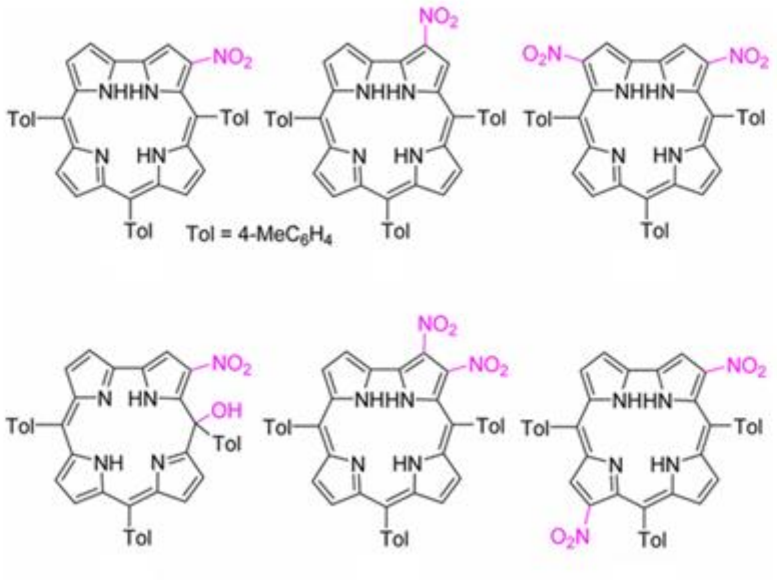

Figure 79. Diverse nitrocorrole products obtained via the AgNO2/NaNO2 method. Reused with permission from ref 67. *Copyright © 2016, American Chemical Society*.

3.9 Borylation

A regioselective and high-yielding protocol for corrole borylation has been reported by Osuka and co-workers. The method involves heating a dioxane solution of H_3[TPFPC], bis(pinacolato)diborane (1.1 eq), catalytic amounts of $[Ir(cod)OMe]_2$ (1.5 mol %) and 4,4′-di-*t*-butyl-2,2′-bipyridyl (dtbpy; 3.0 mol %), at 100 °C for 24 h, as shown in Figure 80 below. [146]

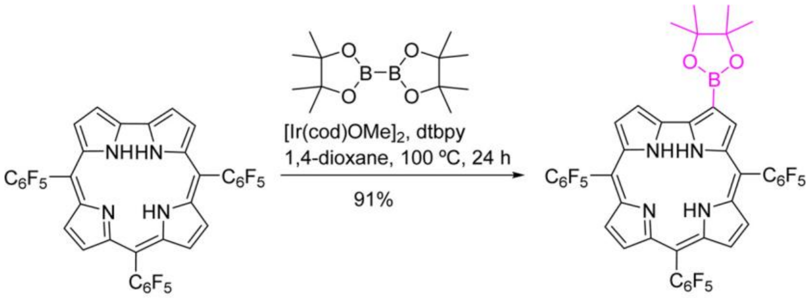

Figure 80. Borylation of H_3[TPFPC]. Reused with permission from ref 67. *Copyright © 2017 American Chemical Society*.

3.10 Diels-Alder reaction

Cavaleiro and co-workers showed that H_3[TPFPC] can act as a Diels-Alder dienophile toward pentacene in 1,2,4-trichlorobenzene at 110 °C, affording the dehydrogenated cycloadducts shown in Figure 81. Also *β*-Vinylcorroles can act as Diels-Alder dienes, as discussed in section 1.11[147]

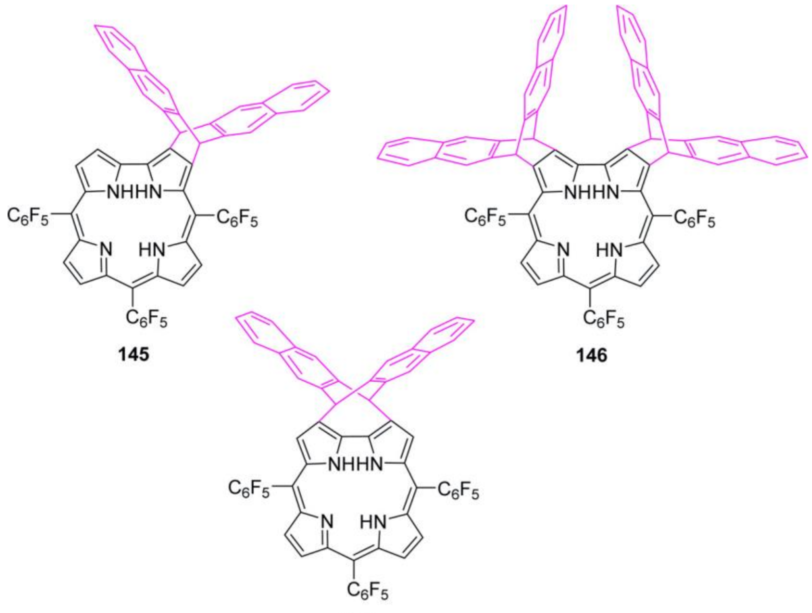

145

146

147

Figure 81. Cycloaddition-dehydrogenation products from the reaction of H_3[TPFPC] with pentacene. Reused with permission from ref 67. *Copyright © 2017 American Chemical Society*.

3.11 Oxidation and oxidative coupling

With strongly nonplanar geometries and reduced aromaticity relative to porphyrins, free-base corroles are readily photooxidized to the corresponding hydroxyisocorroles and biliverdins, [148] as shown in Figure 82 for two free-base *meso*-aryl-*β*-octaethylcorroles. [149]

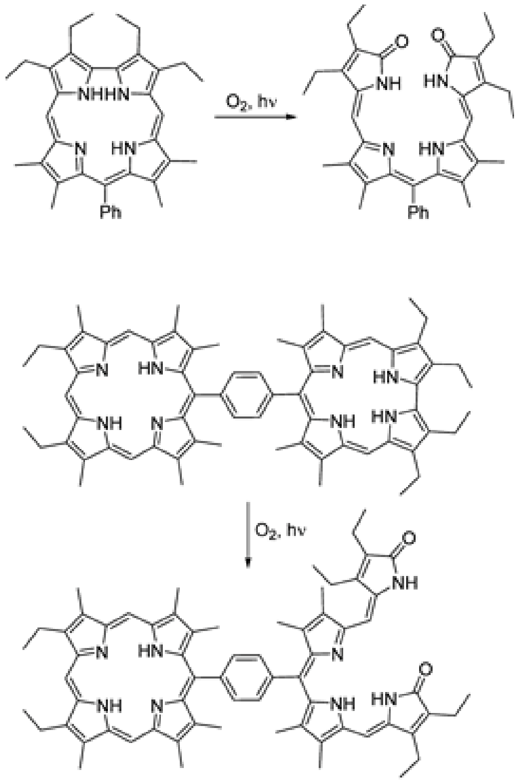

Figure 82. Photodegradation of two free-base *meso*-aryl-*β*-octaethylcorroles. Reused with permission from ref 67. *Copyright © 2017, American Chemical Society*.

For *meso*-triarylcorroles, the products are typically a mixture of *meso*-hydroxyisocorroles and biliverdins (Figure 83).

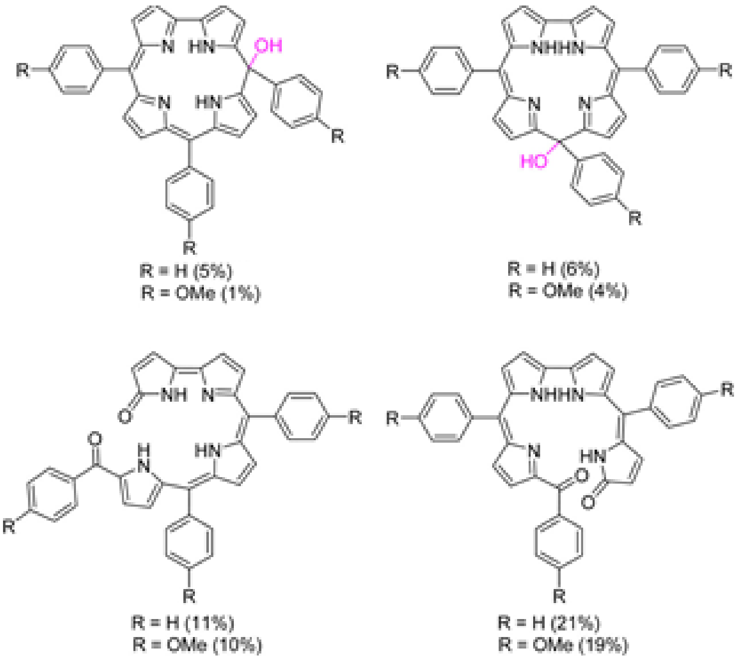

Figure 83. Isocorrole and ring-opened compounds obtained from the photooxidation of unhindered A_3-type corroles. Adapted from ref 67. *Copyright © 2017, American Chemical Society*

Corroles are also readily oxidized by purely chemical (nonphotochemical) means. Thus, simple heating of H_3[TPFPC] in 1,2,4-trichlorobenzene at 200 °C leads to a variety of dimeric, trimeric, and tetrameric β,β'-linked products (Figure 84).[150] A milder and more selective method involves heating the corrole with *p*-chloranil in refluxing chloroform, which affords the 3,3'-linked dimer as the major product in 62% yield.[151]

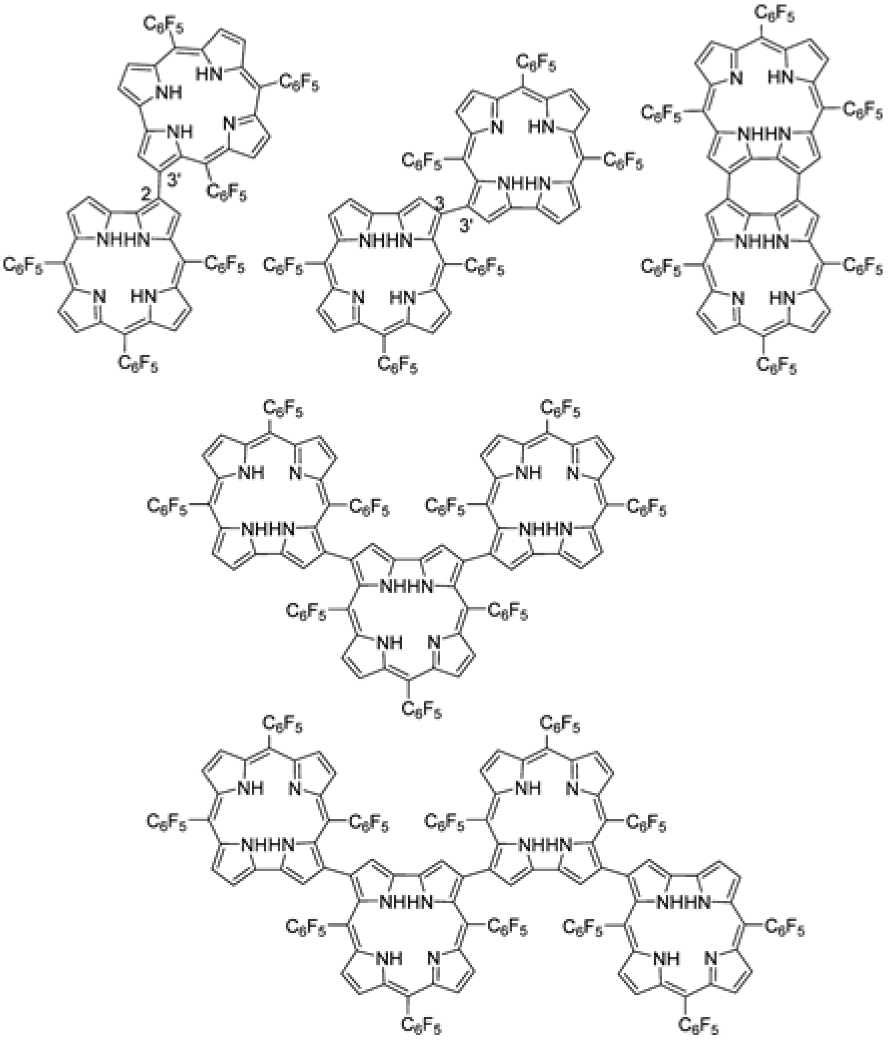

Figure 84. Corrole oligomers obtained by oxidation of H_3[TPFC]**.** Adapted with permission from ref 67. *Copyright © 2017, American Chemical Society*

3.12 Ring expansions

Corroles readily undergo ring expansion on exposure to carbenes, nitrenes, and related species as illustrated in Figure 85. Thus, with Ru reagents and a source of C1-species, octamethylcorrole ring-expands to octamethylporphyrin: [152]

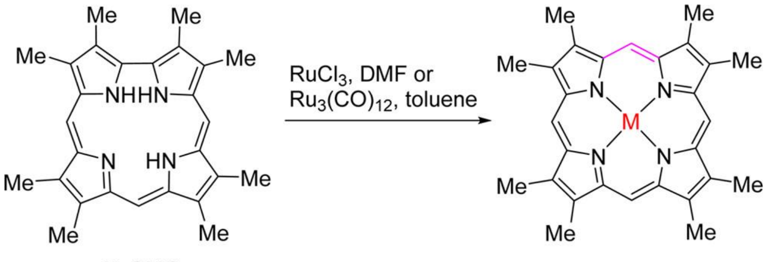

H_3OMC

M = Ru, 2H

Figure 85. Ring expansion of corrole to a porphyrin. Adapted from ref 67. *Copyright © 2016 American Chemical Society*

With analogous nitrogen species such as unsubstituted nitrene, corroles yield 2-azahemiporphycenes, as illustrated by the experimental conditions in Figure 86.

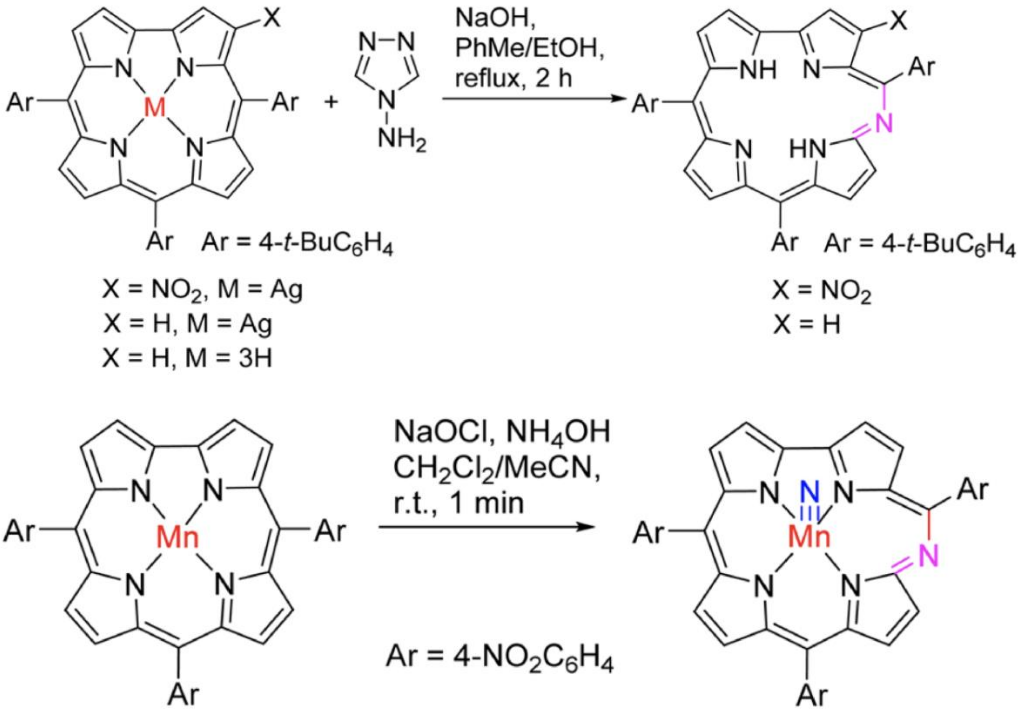

Figure 86. Formation of azahemiporphycene. Adapted from ref 67. *Copyright © 2016 American Chemical Society*

3.13 Postfunctionalization

As for other aromatic compounds, substituents and functional groups appended to corroles can be further derivatized in a variety of ways. While a fuller discussion is outside the scope of this thesis, the point will illustrate here with applications of β-octabrominated corroles.

Early work from the Ghosh group provided facile access to Cu β-octabromo-*meso*-triarylcorroles via the reaction of simple Cu corroles with a large excess of Br_2 in $CHCl_3$.[45] In another major breakthrough, the group accomplished reductive demetallation by treatment with $Fe^{2+}/H_2SO_{4.}$[118] The procedure provided access to free-base β-octabromo-*meso*-triarylcorroles for a variety of other applications Figure 87.

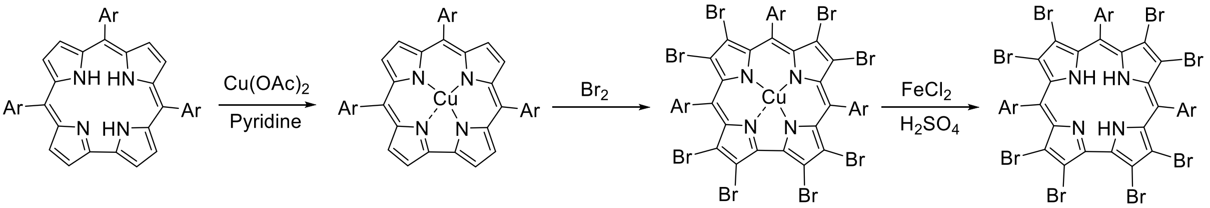

Figure 87. Synthesis of free-base β-octabromocorrole through reductive demetallation of the copper complex.

β-Octabromo-*meso*-triarylcorrole derivatives serve as substrates for a variety of palladium-catalysed cross-coupling reactions, such as Suzuki-Miyaura couplings. Figure 88 illustrates the concerted use of bromination, reductive demetallation, and Suzuki-Miyaura coupling in two alternative paths to gold undecaarylcorroles.

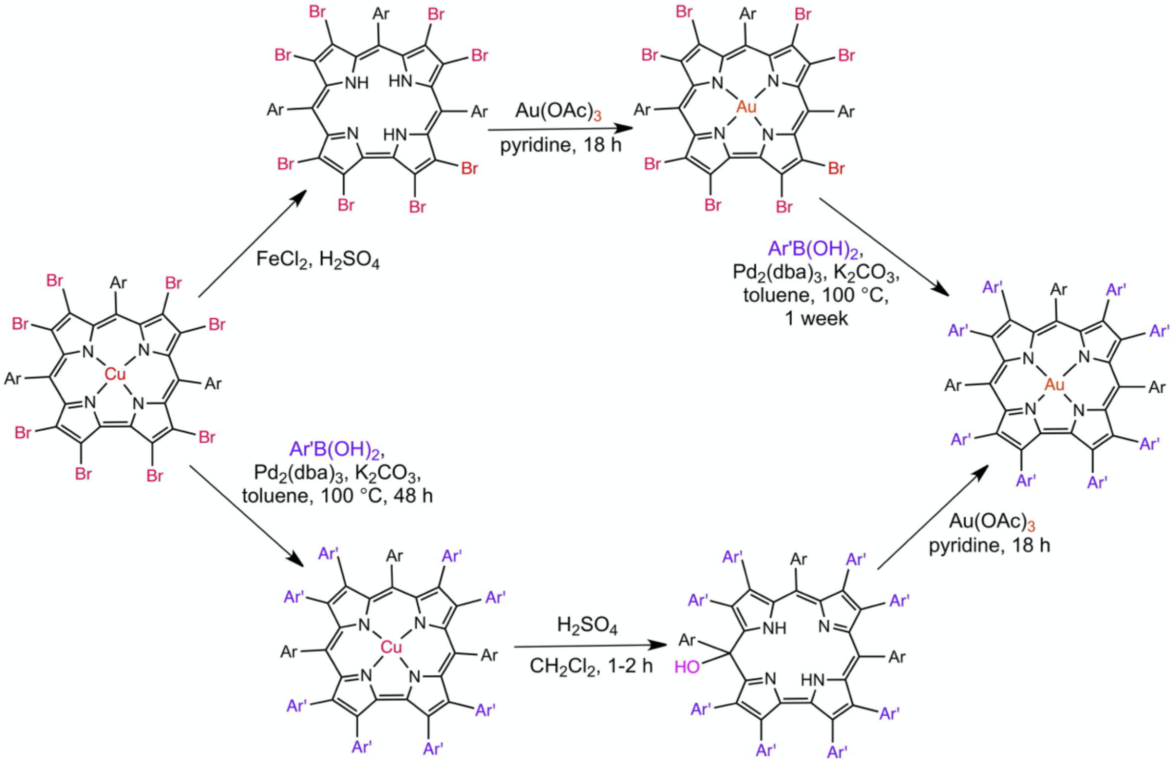

Figure 88. Cross-coupling reactions and transformation on Cu[Br_8T*p*XPC].

UiT researcher Dr. Kolle E. Thomas reacted a series of copper *β*-octabromo-*meso*-triarylcorrole derivatives with methyl 2,2-difluoro-2-(fluorosulfonyl)acetate ($FO_2SCF_2CO_2Me$) to generate the corresponding *β*-octakis(trifluoromethyl)-*meso*-triarylcorrole complexes in moderate yields (14–40%) (Figure 89). The reaction was performed in DMF at 100°C in the presence of $Pd_2(dba)_3{\cdot}CHCl_3$ (5 mol %), $AsPh_3$ (40 mol %), and CuI (42 equiv). [116]

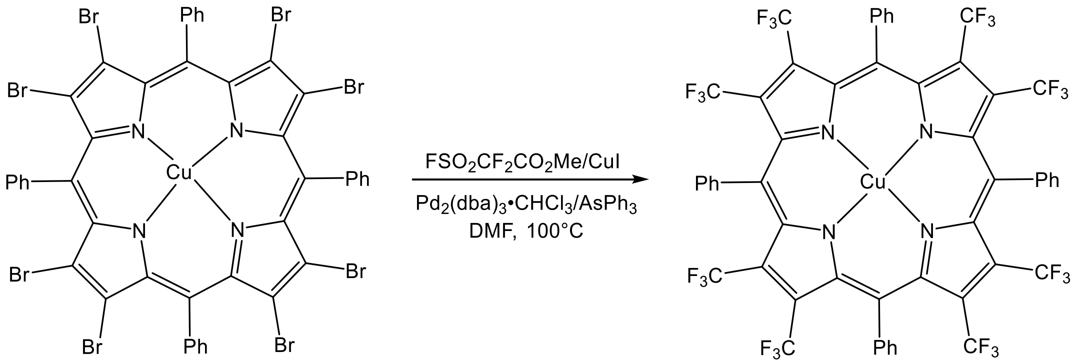

Figure 89. Cu[Br_8T*p*XPC] to Cu[$(CF_3)_8$T*p*XPC] using the following conditions.

In the same vein, Stille coupling of *β*-brominated corroles with *n*-tributylphenylethynylstannane in 1,4-dioxane at 75 °C with $Pd(PPh_3)_4$ as a catalyst has led to the corresponding *β*-phenylethynylcorroles (Figure 90).[153, 154]

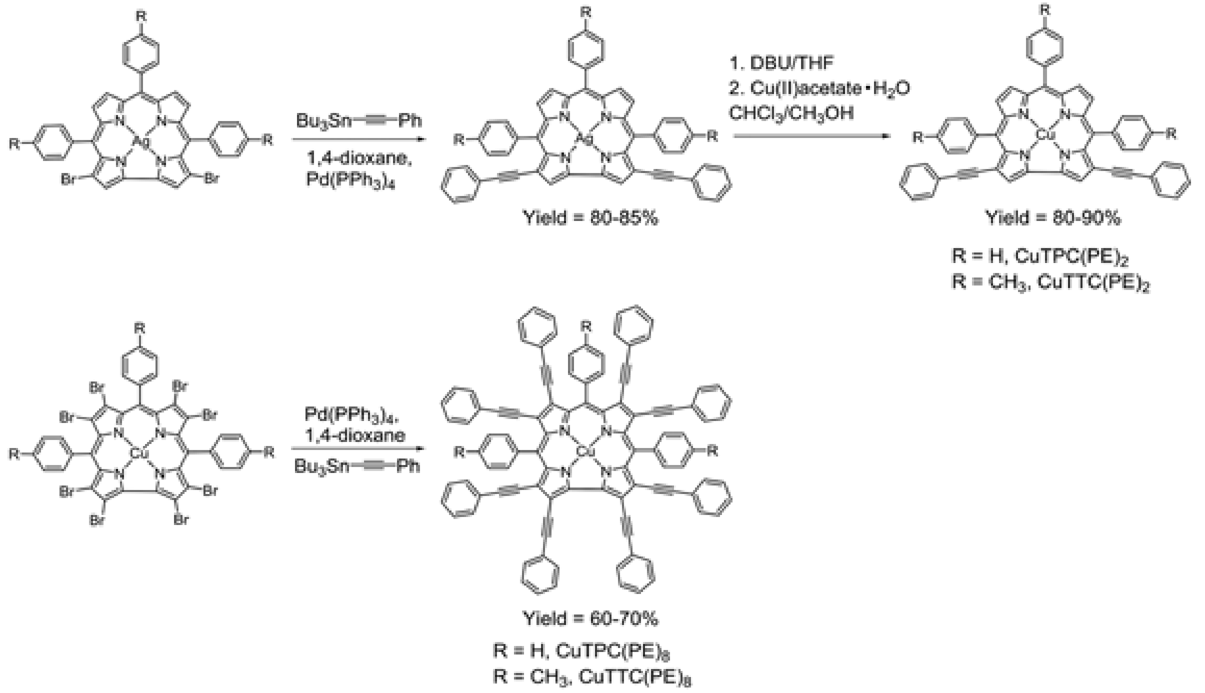

Figure 90. Synthetic route for phenylethynyl-substituted copper corrole. Reused from ref 153 with permission from the Royal Society of Chemistry.

In yet another example of corrole postfunctionalization, Cu *β*-octabromo-*meso*-triarylcorroles were successfully elaborated through an eightfold Heck coupling with methyl acrylate leading to ester-appended tetrabenzocorroles(Figure 91).[155]

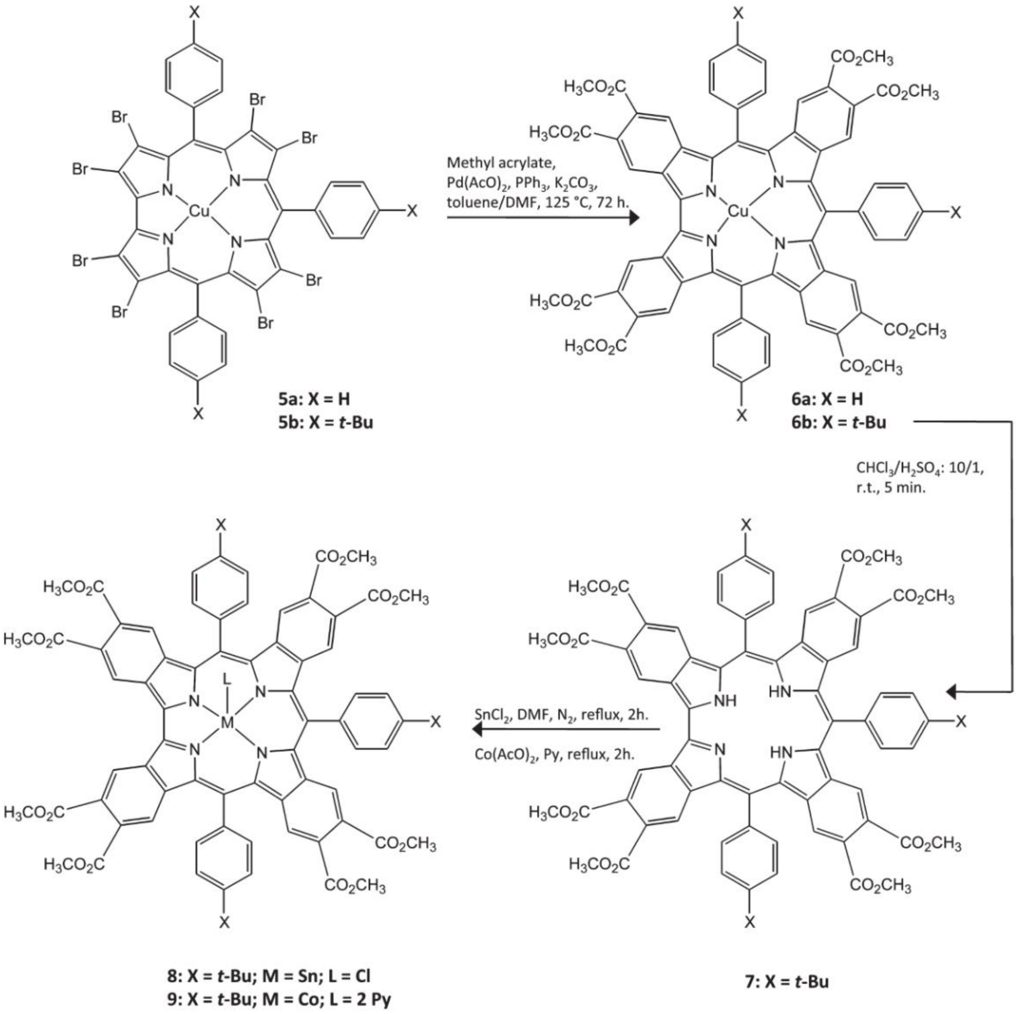

Figure 91. Synthesis of benzocorroles via Heck cross-coupling. Reused with permission from ref 155. *Copyright © 2020 American Chemical Society*.

Chapter 4: Photophysics, photochemistry and photodynamic therapy

4.1 Electronic absorption spectra of porphyrins and corroles

The colours of porphyrin-type molecules result from their conjugated π-systems, which absorb strongly in the near-UV and visible regions and in some cases also in the near-IR. Both porphyrins and corroles exhibit a strong near-ultraviolet absorption around 400 nm (called the Soret or B band) and two to four weaker absorptions in the 500-700 nm region (Q bands). [1, 156] Figure 92 depicts the absorption of a typical free-base corrole and its ReO complex. Metal chelation usually results in an increase in effective symmetry of the π-system and hence a decrease in the number of Q bands. In addition, both metal chelation and peripheral substituents may engender red- (bathochromic) and blue- (hypsochromic) shifts of the Soret and Q bands.

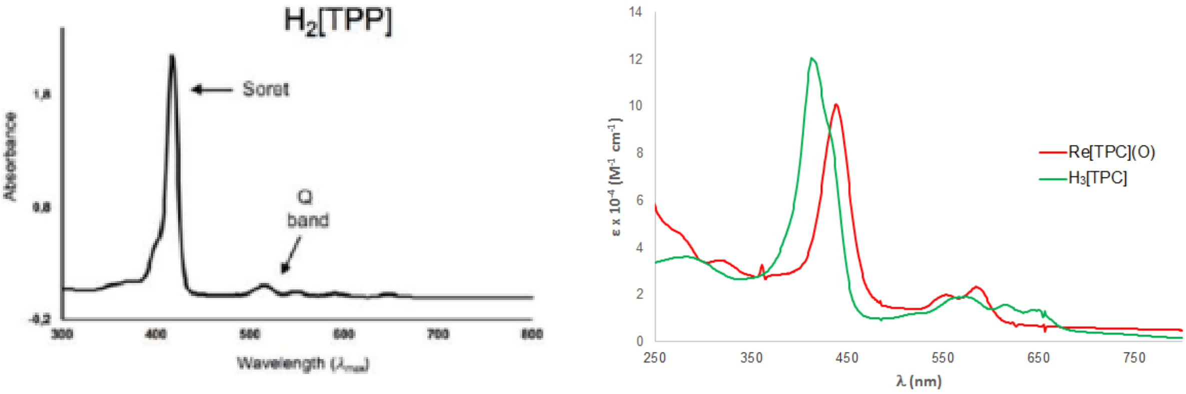

Figure 92. UV-visible spectra of free-base tetraphenylporphyrin (left) and merged spectra with free-base triphenylcorrole and rhenium-oxo-triphenylcorrole (right), green and red curve respectively.

Martin Gouterman explained the electronic absorption spectra of simple porphyrins in terms of a "four-orbital model". According to the model, the absorption spectra reflect transitions between two near-degenerate HOMOs and two degenerate LUMOs. Under D_{4h} symmetry, the two HOMOs transform as a_{1u} and a_{2u}, while the two LUMOs transform as e_g. [157] Figure 93 schematically illustrates the relative contributions from individual atomic orbitals together making up these molecular orbital. The shapes of these MOs allow us to make qualitative arguments regarding the effects of metal chelation and peripheral substituents.

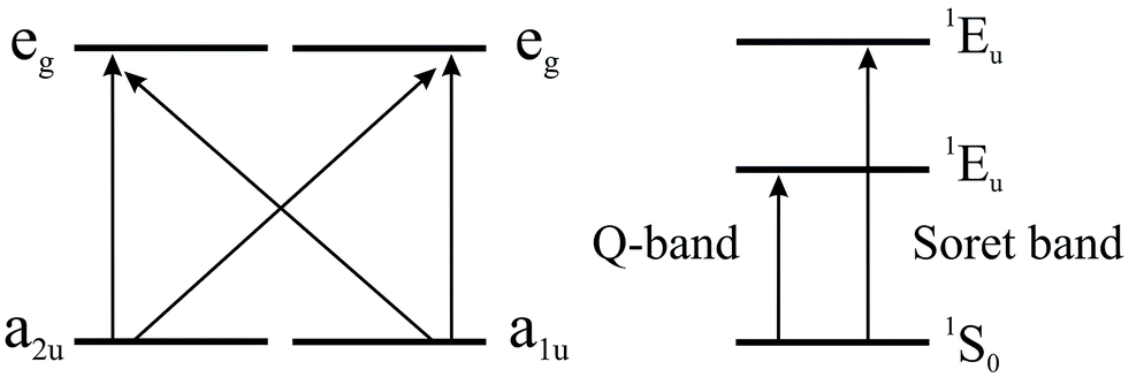

Figure 93. Possible transitions between the HOMOs and LUMOs (left) of a D_{4h} porphyrin, leading to the two degenerate Soret and Q bands.

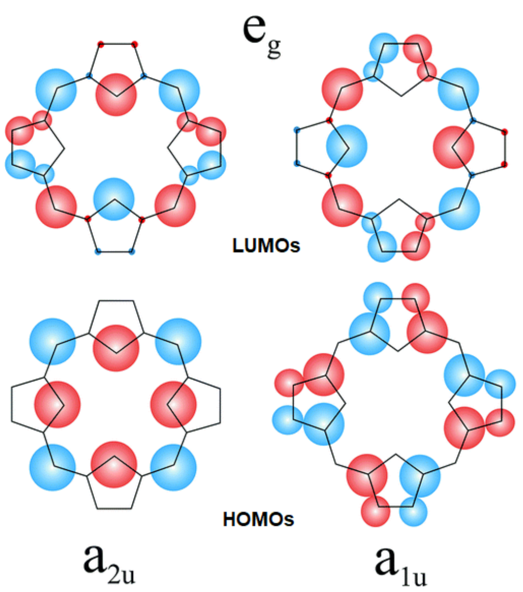

Figure 94. The four frontier orbitals of porphyrins.

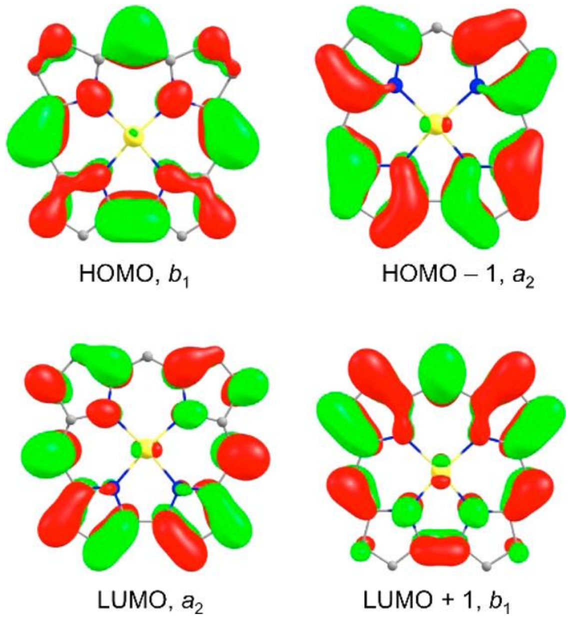

Figure 95. Frontier MOs of gold corrole. Reused with permission from ref 68. *Copyright © 2017, American Chemical Society.*

Quantum chemical studies by Ghosh *et al*. proved that Gouterman's four-orbital model also applies for corroles. Despite the lower symmetry for corroles (C_{2v}) than porphyrins (D_{4h}), the calculations showed that the shapes and symmetry properties of the frontier MOs of corroles are similar to those of porphyrins. [158]

4.2 Fluorescence and phosphorescence in porphyrins and corroles

The processes taking place in a photosensitizer are probably most conveniently explained via a Jablonski diagram, such as the one shown in Figure 96. We assume a singlet ground state, (S_0), a typical scenario for most stable organic compounds and many inorganic complexes. Upon absorption of a photon, the photosensitizer is excited to a higher singlet state, S_n, where n > 0. The higher singlet states quickly decay in a nonradiative manner to S_1, the lowest excited singlet state, a process known as internal conversion (IC). For purely organic porphyrin-type molecules and many of their p-block derivatives, the S_1 state is the key emissive state and decay to the S_0 state is accompanied by radiation known as fluorescence. For heavy element derivatives of porphyrin-type molecules, S1 may undergo a spin flip to yield the lowest triplet state, T_1, a process known as intersystem crossing (ISC). For many heavy element compounds, T1 is a key emissive state and emitted radiation accompanying decay to the S_0 state is called phosphorescence. Thus, both intersystem crossing and phosphorescence entail a spin state change (and are sometimes referred to as spin-forbidden), which are by a phenomenon called spin-orbit coupling, which is prevalent in heavy element compounds. These two processes are generally significantly slower than the spin-allowed processes – internal conversion and fluorescence. Another key generalization is embodied in Kasha's rule, according to which radiative decay is almost invariably effective only from the lowest excited state of each multiplicity, i.e., S_1 and T_1 in our case.

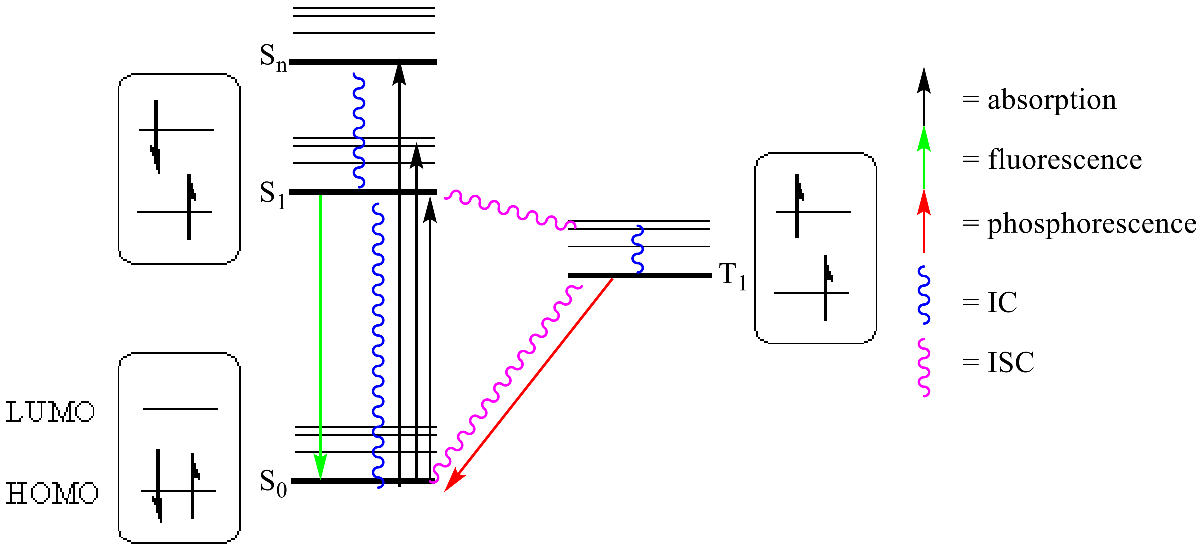

Figure 96. Jablonski diagram illustrating the different excited states and the various radiative (arrows) and nonradiative decay paths (wavy lines).

For porphyrins and corroles, fluorescence is most commonly observed for free-base and lighter p-block element derivatives. Free-base *meso*-triarylcorroles have been shown to exhibit stronger fluorescence than corresponding porphyrins. [68] The most strongly fluorescent corroles, as of today, are Ga(III) and Al(III) corroles. [159]

Many 4d and 5d metalloporphyrins are moderately to strongly phosphorescent. Their long-lived triplet states have been exploited for oxygen sensing and photodynamic therapy. Gouterman and co-workers famously exploited platinum(II) porphyrins to devise pressure-sensitive paints for airplane wings. More recently, 5d metallocorroles including ReO[160] OsN[161], Ir, [109] Pt(IV) and Au[162] corroles, have been found to exhibit NIR phosphorescence under ambient conditions. Figure 97 below depicts the excitation and phosphorescence emission spectra of a rhenium-oxo corrole.

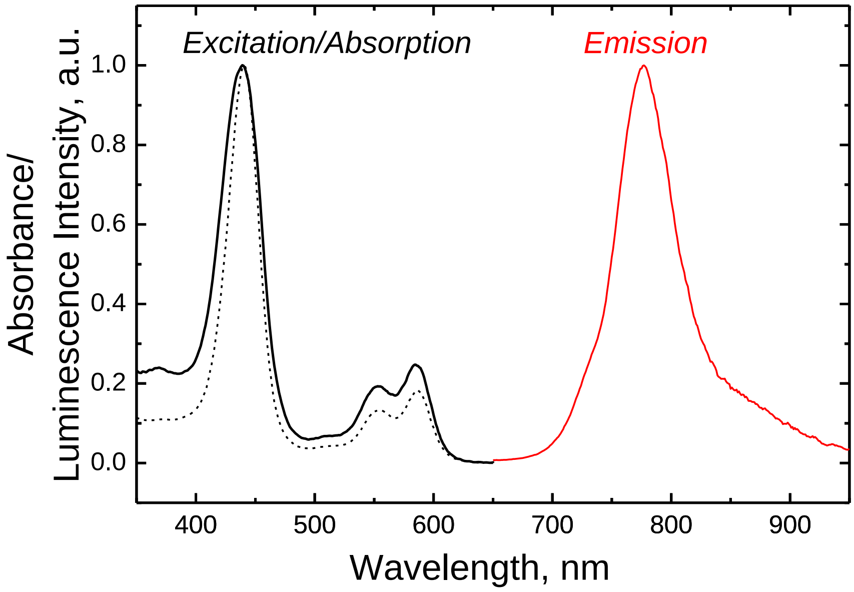

Figure 97. Absorption (black dashed line), phosphorescence excitation (black solid line; λ_{em} 775 nm) and emission (red line; λ_{exc} 590 nm) spectra of Re[T*p*CF_3PC](O) in toluene. Phosphorescence spectra were measured in anoxic conditions. Reused from ref 163 with permission from The Royal Society of Chemistry.

4.3 Photodynamic therapy

In photodynamic therapy, three fundamental ingredients necessary: light, molecular oxygen and a photosensitizer. In a typical scenario, light excites the photosensitizer to an excited singlet state, which in a matter of ns decays to a longer-lived triplet state. The triplet photosensitizer then transfers its extra energy to molecular oxygen, a ground-state triplet, to generate singlet oxygen, an excited state of molecular oxygen, and ground-state photosensitizer, a process known as triplet-triplet annihilation. Singlet oxygen is highly reactive, reacting with virtually all forms of organic matter, and is a member of the Reactive Oxygen Species (ROS) family. In biological systems, ROS derive primarily from atmospheric oxygen and to a lesser extent from water. They commonly arise via "leakage" from oxygenated forms of heme proteins and other metalloproteins, including globins, peroxidases, and superoxide dismutases. Common ROS includes hydrogen peroxide (H_2O_2), the superoxide radical anion ($O_2^{\bullet-}$), hydroxyl radicals ($OH^{\bullet}$), ozone (O_3), and singlet oxygen ($^1O_2$). Schematic MO diagrams for a few of these species are depicted in Figure 98.

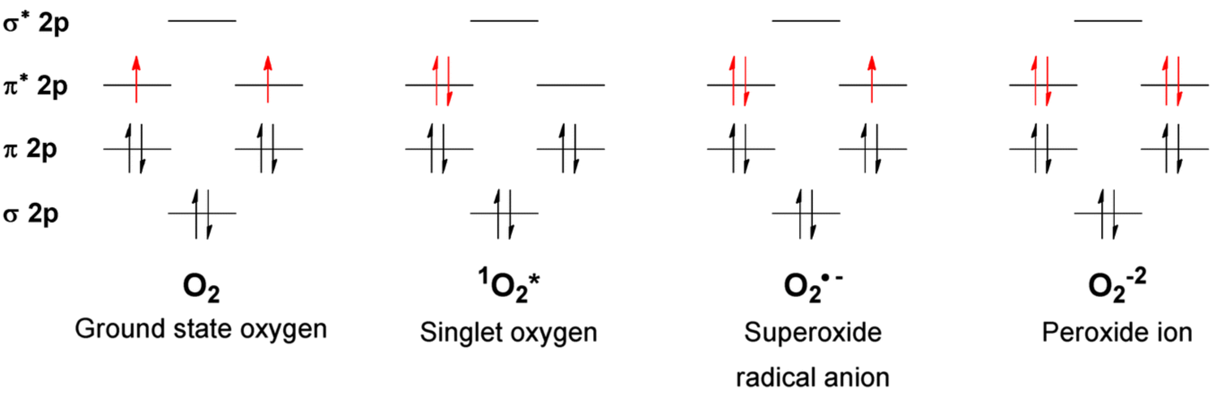

Figure 98. Molecular orbital diagrams for various O_2 species.

Less common ROS include alkoxy ($RO^{\bullet}$) and peroxy ($ROO^{\bullet}$) radicals. ROS are of great biological importance in that they can inflict damage to DNA, proteins, and other cellular components. Aerobic organisms have evolved a variety of defensive mechanisms to deal with ROS that arise naturally in their bodies. A number of reactive nitrogen species (RNS), including nitrogen dioxide radicals ($NO_2^{\bullet}$), and peroxynitrite ($ONOO^-$) play similar role as ROS.

Photodynamic therapy results in the localized production of ROS in the neighbourhood of the photosensitizer. As alluded to above, by far the greatest proportion of these ROS is singlet oxygen. Figure 99 presents a more complete picture of photosensitizer-oxygen reactions in which they are divided into two different categories, Type I and Type II reactions. Type I is sometimes further subdivided into two different categories, depending on whether the photosensitizer is reduced or oxidised. Reaction Type II is the above-mentioned triplet-triplet annihilation process that affords singlet oxygen.

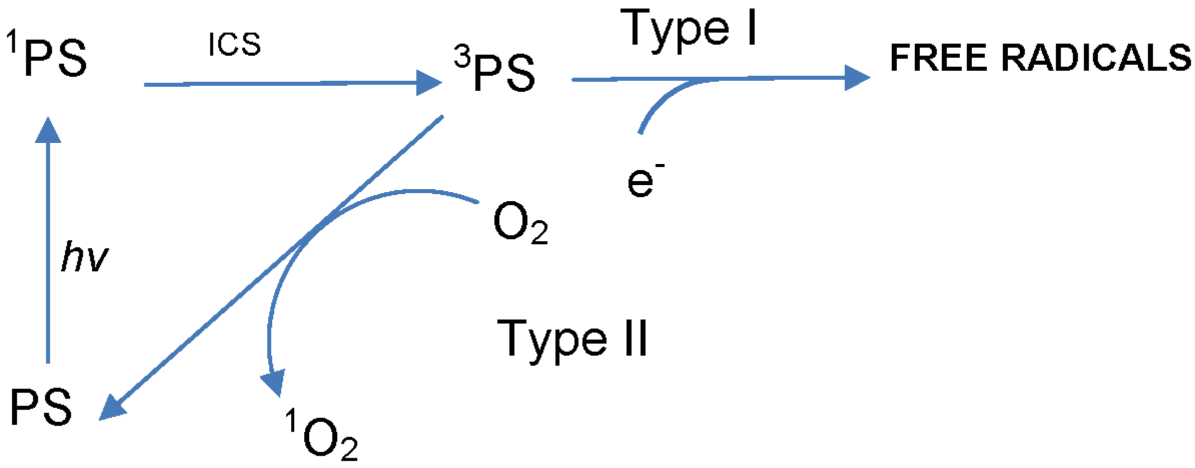

Figure 99. Schematic illustration of Type I and Type II reactions of photosensitizer and oxygen.

The biological window for which electromagnetic radiation has the greatest depth of penetration into tissues is roughly 600 – 1200 nm. For photodynamic therapy, wavelengths of 600 – 800 nm are standard, as higher wavelengths are generally not energetic enough to generate singlet oxygen. For wavelengths in the 600-800 nm range, light penetrates only a few millimetres to about 1 cm in soft tissue, with higher wavelengths (700 – 800 nm) preferred where deeper penetration is necessary. A key consideration is the short lifetime of singlet oxygen, < 50 ns. The photosensitizer accordingly has to be within the immediate vicinity of the intended site of cell damage, essentially within an approximately 20-nm radius. [164]

An effective photosensitizer should satisfy the following criteria:

(i) Strong absorption with a high extinction coefficient in the red/NIR-region.
(ii) Long triplet state lifetimes and high singlet oxygen yields (as measured by the quantum yield for singlet oxygen production).
(iii) Solubility in biological media, especially water.
(iv) Negligible dark toxicity.
(v) Rapid clearance from blood.
(vi) Chemically well-characterised.
(vii) Biocompatible (bioorthogonal).
(viii) High tumour specificity and selectivity.

Two examples of molecules which meet most of the requirements are aluminium phthalocyanine and fimaporfin.

The great advantage of photodynamic therapy is that, unlike chemotherapy, it provides highly localized treatment that spares healthy cells. It is already FDA-approved for treatment of age-related macular degeneration, actinic keratosis, esophageal cancers, and non-small cell lung cancer. Preclinical studies and clinical trials have been reported for a much wider variety of cancers, including skin, bladder, prostate, brain, and head and neck cancers, and malignant mesothelioma. Photodynamic therapy also holds great promise for antimicrobial treatment.

4.4 Corroles as photosensitizers for singlet oxygen

The photophysical data for different groups of corroles are presented below. Selected free-base corroles in Table 2, main group corroles (Table 3) and transition metallocorroles (Table 4). The tables list triplet state lifetimes (τ), phosphorescence quantum yields (ϕ_P), and quantum yields for singlet oxygen generation (ϕ_Δ). The tables are adapted from a recent review by Lemon, which provides more extensive tabulations of similar data. The data collectively lead to the intriguing conclusion that certain fluorinated corroles lead to longer triplet lifetimes and higher quantum yields for both phosphorescence and singlet oxygen generation. [41]

Table 2. Photophysical properties, including excited triplet state lifetimes (τ) and the quantum yield for singlet oxygen, $^1O_2$, (ϕ_Δ), of some free-base corroles.

Compound	τ (μs)	ϕ_Δ	Ref
H_3[TPFPC]	150	0.71	[165]
H_3[TPC]	55	0.51	[165]
H_3[TP-(3,5-CF_3)-PC]	65	0.64	[165]
H_3[5,15-PF-10-Ph-PC]	91	0.70	[166]
H_3[5,15-PF-10-CH_3-Ph-PC]	136	0.77	[165]
H_3[5,15-PF-10-(2-OH-Ph)-PC]	130	0.60	[167]

Table 3 lists key photophysical properties of some main group corroles. Several of these are strongly fluorescent while a handful display weak phosphorescence. A striking observation is that P[TPFPC]$(F)_2$ exhibits a longer triplet lifetime than Ga[TPFPC]$(pyr)_2$ but a smaller singlet oxygen quantum yield (ϕ_Δ), contrary to what is normally observed. In general, the singlet oxygen quantum yield increases with increasing atomic weight of the central atom, as expected.

Table 3. Photophysical properties, excited triplet state lifetime (τ) and the quantum yield for singlet oxygen, $^1O_2$, (ϕ_Δ), of some main group metallocorroles.

Compound	τ (μs)	ϕ_Δ	Ref
P[TPFPC](F)$_2$	312	0.49	[168]
P[TPF-I$_4$-PC](F)$_2$	179	0.67	[168]
P[TPF-8-SO$_3$-PC](OH)$_2$	-	0.58	[169]
P[*p*pyridyl-PC](OH)$_2$	-	0.51	[170]
P[T*p*(2,6-F)-PC](F)$_2$	192	0.46	[168]
P[T*p*(2,6-F)P-I$_4$-C](F)$_2$	181	0.71	[168]
Ga[TPFPC](pyr)$_2$	67	0.52	[166]
Sn[TPC](Cl)	-	0.54	[171]
Sn[T*p*SCH$_3$PC](Cl)	231	0.60	[172]
Sb[TPF-SO$_3$-PC](O)		0.66	[169]

The 5d metallocorroles exhibit fascinating variations in their photophysical properties. In general, ReO triarylcorroles exhibit the highest phosphorescence quantum yields, while those for Ir corroles are surprisingly low. The latter are surprising, in view of the high phosphorescence quantum yields of Ir porphyrins. [173] In general, and somewhat disappointingly, the phosphorescence quantum yields (on the order of 1 %) of 5d metallocorroles are approximately an order of magnitude smaller than those of Pd, Pt, and Ir porphyrins. [174] Fortunately, these results do not impact the use of 5d metallocorroles as oxygen sensors or as dyes in photodynamic therapy, since they all appear to exhibit high quantum yields for singlet oxygen generation.

Table 4. Photophysical properties, including excited triplet state lifetimes (τ_T), phosphorescence quantum yields (ϕ_P), and quantum yields for singlet oxygen generation (ϕ_Δ), for 5d transition metallocorroles.

Compound	τ (μs)	ϕ_P (%)	ϕ_Δ	Ref
Re[T*p*MePC](O)	64	1.07	–	163
Re[TPC](O)	60	1.15	–	163
Re[T*p*CF_3PC](O)	74	1.52	–	163
Re[T*p*FPC](O)	70	1.19	–	163
Re[T*p*OMePC](O)	56	1.07	–	163
Re[T*p*CO_2CH_3PC](O)	66	0.012	0.72	175
Re[T*m*CO_2CH_3PC](O)	57	0.011	0.72	175
Re[*p*TCPC](O)	38	–	–	175
Re[*m*TCPC](O)	59	–	–	175
Os[TPC](N)	128	0.013	0.88	176
Os[T*p*CF_3PC](N)	150	0.013	0.76	176
Os[T*p*OCH_3PC](N)	110	0.009	0.95	176
Ir[T*p*CF_3PC]$(pyr)_2$	–	0.0004	0.71	110
Ir[T*p*CF_3PC]$(pyr)_2$	–	0.0002	0.38	110
Ir[*p*CN-P)$_2$(3,4,5-MeO-P)C]$(pyr)_2$	–	<0.0001	0.14	177
Ir[*p*CN-P)$_2$(3,4,5-MeO-P)C]$(bpy)_2$	–	<0.0001	0.15	177
Ir[T*p*CNPC]$(pyr)_2$	–	<0.0001	0.09	177
Au[TPFPC]	–	–	0.25	133
Au[I_4TPFPC]	–	–	0.94	133

4.5 Corroles as medicine

Modern photodynamic therapy started in earnest during the last quarter of the twentieth century, with focus on heme synthesis and accumulation of porphyrins.

Some flagship first- and second- generation photodrugs were Photophrin, a hematoporphyrin derivative, and Verteporfin, a benzoporphyrin derivative, respectively. This period also coincided with the deployment of platinum anticancer drugs, initially cisplatin, and subsequently carboplatin and oxaliplatin. Porphyrin chemists jumped into the drug development effort and identified numerous porphyrin derivatives as promising non-photochemical anticancer compounds. Cationic gold porphyrins are emerging as particularly promising in this regard. [178]

The first report of a corrole deployed as an anticancer drug came in 2000 in the form of a water-soluble compound P1021 (Figure 100). Comparing its cytotoxicity with related porphyrins, the authors, Gross *et al*., found it to be significantly better at inhibiting the lung metastasis in a mouse model, as illustrated in Figure 101.[179] Further work on P1021, however, was abandoned, since the synthesis was thought to be too onerous for upscaling to industrial production.

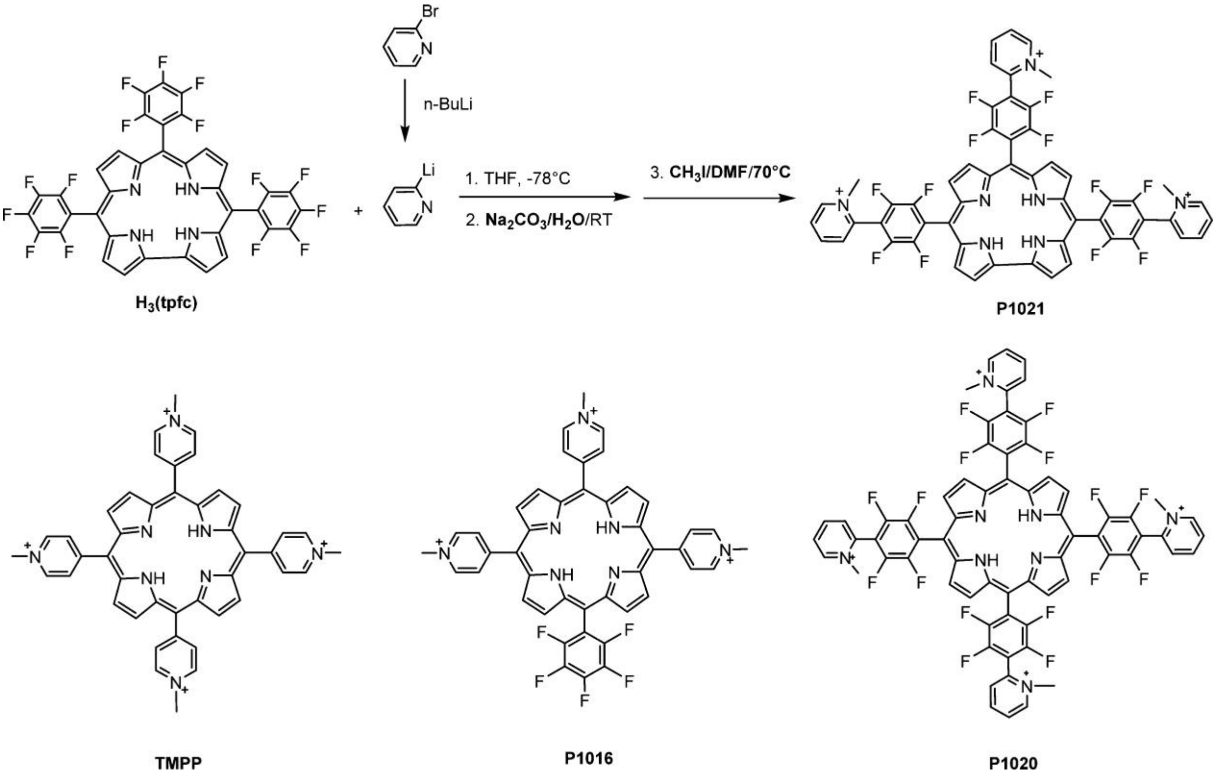

Figure 100. First synthesis of a water-soluble corrole (P1021), the first corrole employed in cancer cell studies. Bottom: porphyrin derivatives included in the same study. Reused with permission from ref 40. *Copyright © 2017, American Chemical Society.*

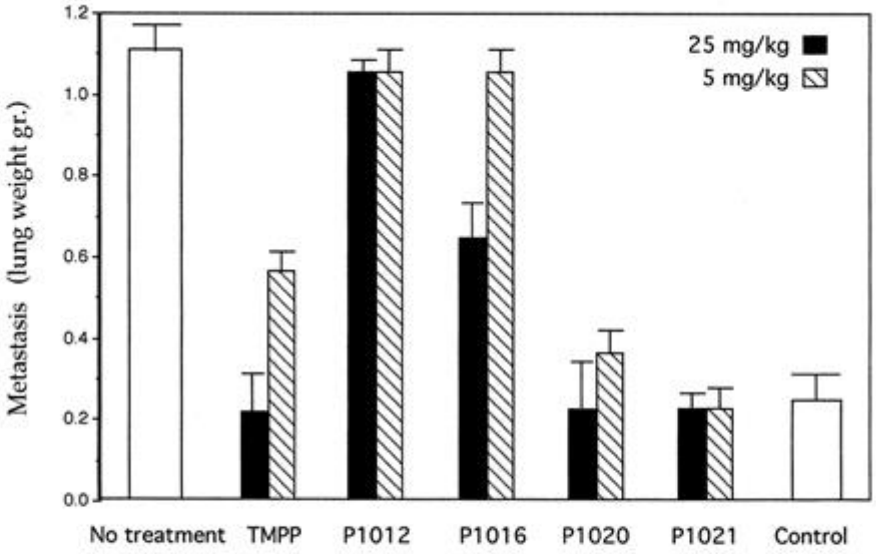

Figure 101. Cell survivor dependent on concentration of different corrole and porphyrinsoids, P1021 is the corroles. Reused with permission from ref 179. *Copyright © 2000, American Association for Cancer Research*.

A variety of free-base and Mn(III) corroles were then examined, appended with cationic substituents (Figure 102). The free-base corroles are thought in ionize under physiological conditions to yield planar $[(Cor)H_2]^-$ species while Mn(III) corroles are also planar species with only a weak affinity for axial ligands. These compounds were found to intercalate into DNA, specifically telomeres, and several were found to exhibit anticancer activity, presumably via inhibiting the enzyme telomerase. In particular, MnT[N-methyl-3-pyridyl]corrole was found to be cytostatic and cytotoxic against ovarian, breast, and melanoma cell lines, while Mn[5,15-N-methyl-4-pyridyl-10-anisyl]corrole (two lowest structures in Figure 102, respectively) was found to be ineffective up to the concentrations studied (30 μM). [180] The inactivity of the latter was thought to be due to the ortho methyl groups interfering with DNA intercalation. Fascinatingly, GaT[N-methyl-4-pyridyl]corrole (top right Figure 102) under photochemical conditions was found to be 3 orders of magnitude more effective against HepG2 cells (as measured by IC50 values) relative to its dark activity. [181]

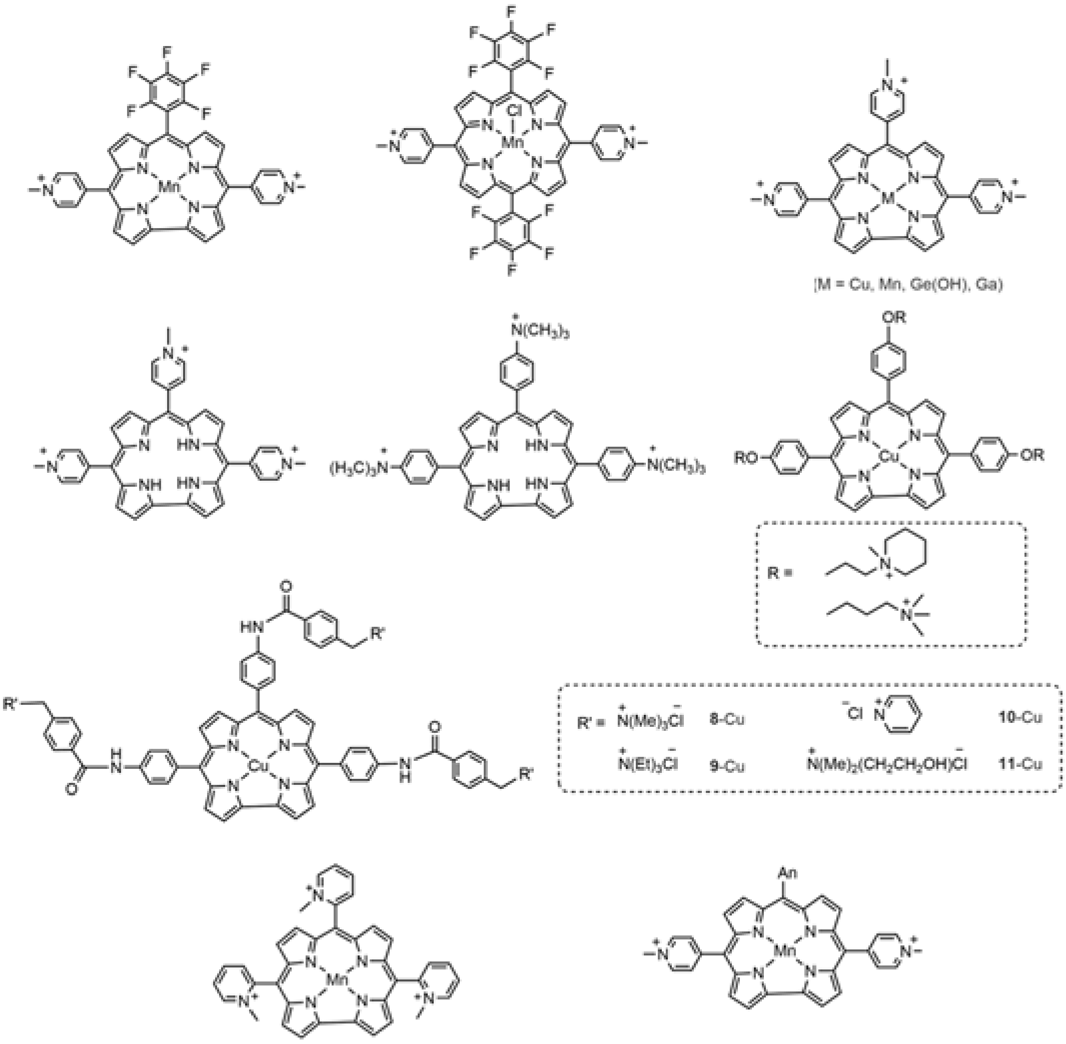

Figure 102. Corroles with positively charged substituents. Reused from ref 40. *Copyright © 2016 American Chemical Society*

Another class of corroles that have been studied in detail as anticancer compounds are anionic, amphipolar systems based on 2,17-bis(sulfonato)-5,10,15-tris(pentafluorophenyl)corrole (Figure 103).[141] Interestingly, despite their anionic character, their uptake into cells does not appear to be inhibited, potentially indicating the importance of the nonpolar corrole moiety. These corroles also undergo spontaneous association with albumin, a process that has also been modeled with molecular docking calculations. It appears likely that this corrole undergoes endocytosis assisted by albumin and other serum proteins(Figure 104).[182]

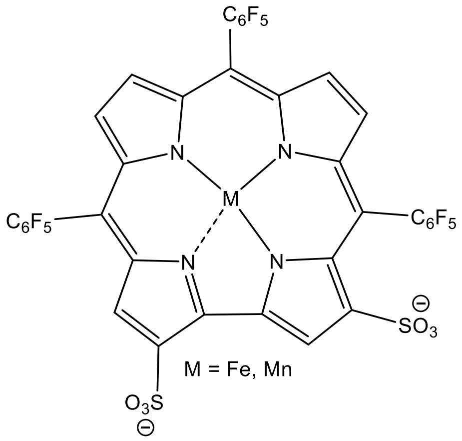

Figure 103. Structural illustration of β-di-sulfonated tris(pentafluorophenyl)corrole.

To minimize adverse off-target effects, modern approaches to cancer treatment seek to achieve targeted delivery of chemo- and phototherapeutics. Thus, the Ga complex of the above anionic corrole was found to form a very tight bioconjugate with an adenovirus protein, HerPBK10, which in turn was known to bind to ErbB receptors that are prevalent on the cell surface of ErbB2$^+$ human breast cancer cells. [183] Experiments using *in vivo* imaging indicated that the bioconjugate indeed retained the expected breast cancer selectivity and intracellular transport properties of the adenovirus protein. [184] A variety of targeted therapeutics based partly on porphyrins and corroles are currently under development, and from a national point of view it can refers to companies as Photocure ASA and PCI Biotech AS. Some brief remarks on derivatizing my own compounds for biotargeting are presented in Chapter 5.

Metalloporphyrins and metallocorroles are also of great interest as therapeutics for several noncancer diseases, such as Parkinson's disease, ALS, Alzheimer's disease, and Huntington's disease, where treatment consists catalytic decomposition of excessive quantities of reactive oxygen and nitrogen species. [185] Once again, the most extensively investigated corrole is the above-mentioned disulfonated tris(pentafluorophenyl)corrole and its manganese and iron derivatives, as illustrated in Figure 103. Kupersmidt *et al.* investigated the cytoprotective abilities of these compounds against oxidative and nitrative stress, which have been implicated as causative factors in carcinogenesis, with the Mn corrole emerging as highly cytoprotective. [186]

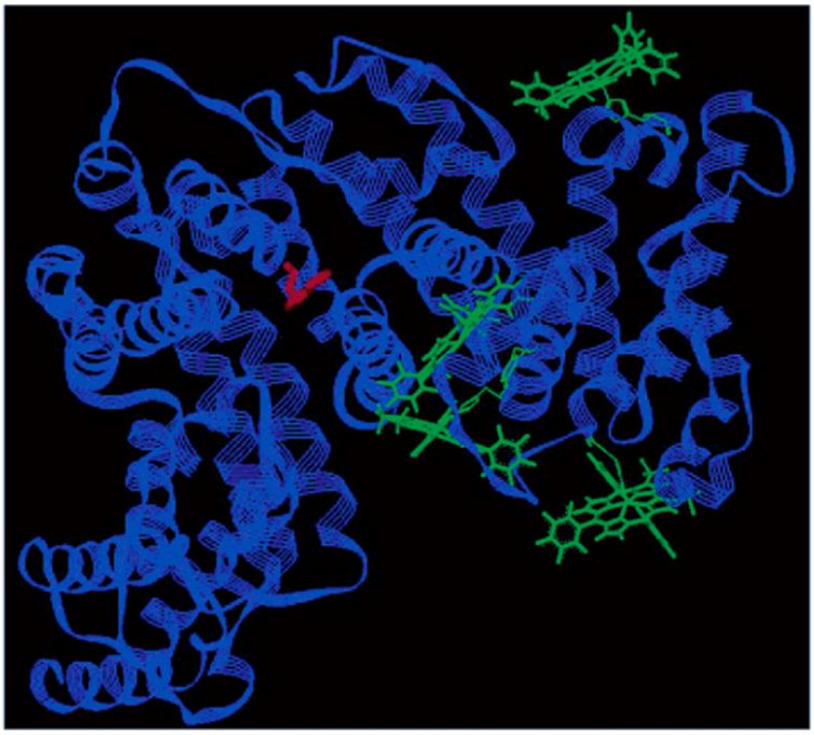

Figure 104. Four potential binding sites for a gallium corrole in human serum albumin. Reused with permission from ref 182. *Copyright © 2004, American Chemical Society*.

While most of the complexes listed in Table 5 are fluorescent free-base and Group 13 derivatives (primarily Ga), this thesis focuses particularly on triplet photosensitizers in the form of 5d metallocorroles, especially amphiphilic ReO corroles. The results clearly show that these novel compounds are highly active and ripe for further development for targeted biodelivery and other advanced approaches such as combination therapies (such as combined photodynamic and photothermal therapies). Some other corroles which are promising as sensitisers in PDT are structurally illustrated in Figure 105.

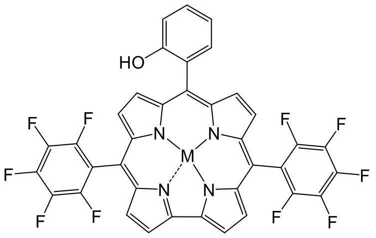

M[5,15-TPF-10-(2-OH-P)C]

M = H_3, Ga

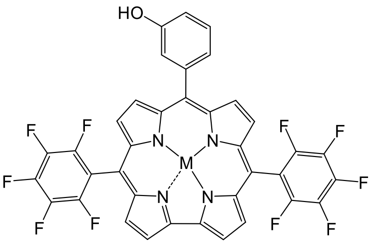

M[5,15-TPF-10-(3-OH-P)C]

M = H_3, Ga

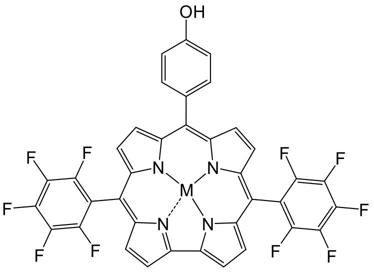

M[5,15-TPF-10-(4-OH-P)C]

M = H_3, P, Ga

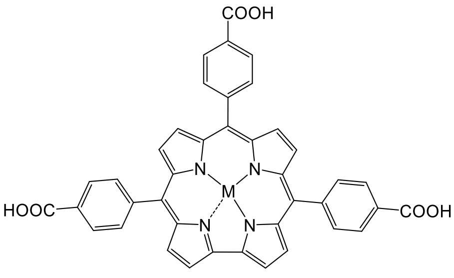

M = H_3, Re, Au

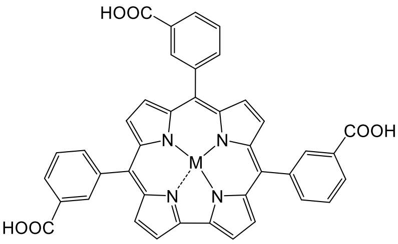

M = H_3, Re, Au

Figure 105. Structural formulas of key compounds included in Table 5, including some of the most promising corroles used as photosensitizers in PDT.

Table 5. Corrole derivatives that have been used as photosensitizers in *in vitro* photodynamic therapy experiments, cell line, description of cell line, inhibitory concentration in dark and inhibitory concentration in light (μM).

Compound	Cell line	Description	IC$_{50}$ dark (μM)	IC$_{50}$ light (μM)	Ref
H_3[5,15-TPF-10-(2-OH-P)C]	MDA-MB-231	Breast cancer	50.84± 9.16	5.81 ±0.37	187
	4T1	Mouse breast cancer	>100	0.46±0.04	187
Ga[5,15-TPF-10-(2-OH-P)C]	MDA-MB-231	Breast cancer	>100	23.16±1.83	187
	4T1	Mouse breast cancer	>100	1.36±0.12	187
H_3[5,15-TPF-10-(3-OH-P)C]	MDA-MB-231	Breast cancer	>100	1.64±0.33	187
	4T1	Mouse breast cancer	>100	0.57±0.07	187
Ga[5,15-TPF-10-(3-OH-P)C]	MDA-MB-231	Breast cancer	41.59±2.40	0.15±0.05	187
	4T1	Mouse breast cancer	>100	2.67±0.60	187
H_3[5,15-TPF-10-(4-OH-P)C]	MDA-MB-231	Breast cancer	>100	0.42±0.03	187
	4T1	Mouse breast cancer	>100	0.30±0.02	187
	BEL-7402	Liver carcinoma	29.1±2.3	1.1±0.4	188
	A549	Lung carcinoma	>100	0.7±0.1	188
	SiHa	Cervical cancer	>100	3.5±0.8	188
P[5,15-TPF-10-OH-PhPC](OH)	H460	Liver carcinoma	>80	1.2	189
	A549	Liver carcinoma	>80	1.7	189
Ga[5,15-TPF-10-(4-OH-P)C]	MDA-MB-231	Breast cancer	47.50±2.63	0.06±0.03	188
	4T1	Mouse breast cancer	>100	0.30±0.02	188
	BEL-7402	Liver carcinoma	8.3±1.1	0.2±0.01	188
	A549	Lung carcinoma	1.6±0.1	0.2±0.04	188
	SiHa	Cervical cancer	11.4±0.1	0.1±0.01	188
H_3[*p*TCPC]	AY27	Rat bladder cancer	~300	-	190
Re[*p*TCPC](O)	AY27	Rat bladder cancer	-	7 min	175
	WiDr	Colon carcionoma	-	12 min	175
Au[*p*TCPC]	AY27	Rat bladder cancer	~100	17 min	190
H_3[*m*TCPC]	AY27	Rat bladder cancer	~300	-	190
Re[*m*TCPC](O)	AY27	Rat bladder cancer	-	5 min	175
	WiDr	Colon carcionoma	-	8 min	175
Au[*m*TCPC]	AY27	Rat bladder cancer	~100	2.5 min	190

Chapter 5: Summary of original contributions

The road leading to this work started to a large extent by the developing of facile syntheses of rhenium(V)-oxo corroles[99] and ^{99}Tc-oxo corroles.[191] The work presented herein has been dedicated to further elaboration of ReO corroles and their evaluation as photosensitizers in *in vitro* photodynamic therapy experiments. Expanding the chemistry of 5d metallocorroles toward applications in nanomaterials and within medicinal applications has been the driving force in this work.

5.1 Photophysical and photocytotoxicity studies

Based on resent results showing that both Au[190] and OsN[176] exhibit near-IR phosphorescence and efficiently sensitize the formation of singlet oxygen. It was of interest to investigat whether ReO corroles had the same photophysical properties as their counterparts, making them equally interesting for further investigation. The results showed that ReO corroles exhibit a phosphorescence quantum between 1.07 – 1.52 %. As of today, these are the highest phosphorescence quantum yields among all classes of metallocorroles. As listed in Table 4 (Chapter 4), the phosphorescence quantum yields increase slightly with electron-withdrawing para substituents on the *meso*-phenyl groups.[163] The ReO corroles were also found to sensitize singlet oxygen formation with quantum yields of > 70%.

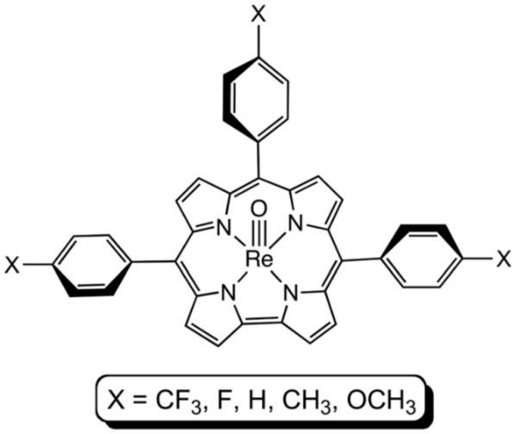

Figure 106. ReO corroles examined in an early photophysical study.

It was accordingly of great interest to synthesise and test water soluble ReO corroles as sensitizers in photodynamic therapy experiments. Two amphiphilic ReO complexes were synthesised based on *meso*-tris(*meta*/*para*-carboxyphenyl)corrole ligands, hereafter denoted as Re[*m*TCPC](O) and Re[*p*TCPC](O). The photocytotoxicity of the complexes was tested in *in* *vitro* experiments against two cancer cell lines (AY27 and WiDr). The results are illustrated in Figure 108 in terms of cell viability against time of light irradiation.[175] For the AY27 cells, dark toxicity measurements indicated around ~90% cell survival for both the Re[*m*TCPC](O) and Re[*p*TCPC](O) after incubation for 24 hours. For photocytotoxicity, both isomers were found to be essentially equivalent, as shown by LD$_{50}$ at ~5 min and nearly complete cell death after 10-20 minutes of illumination. For the WiDr cell line, dark toxicity measurements indicated around ~80% cell survival over 24 hours for the Re[*m*TCPC](O) and ~70% for the Re[*p*TCPC](O), i.e., a slightly higher cell survival for the Re[*m*TCPC](O) prior to illumination. For the WiDr cells, Figure 108 shows a higher photocytotoxicity for Re[*m*TCPC](O) with LD$_{50}$ at around ~10 minutes of light exposure, compared to ~15 minutes for Re[*p*TCPC](O). However, both isomers result in complete cell death after by ~20 minutes of illumination.

Table 6 below compares cell viability data for the two cell lines compared for free-base ligands H$_3$[*m/p*TCPC] and the ReO and Au complexes. The results show that the ReO corroles are just as potent as the Au corroles. Given that ReO corroles are more easily accessible, in terms of ease of synthesis, yield (60-80% compared to 30% for Au corroles),[133, 163, 175, 190] and use of cheaper starting materials, makes the compound of great interest for further cytotoxicity experiments.they are great interest for additional cytotoxicity and in vivo testing.

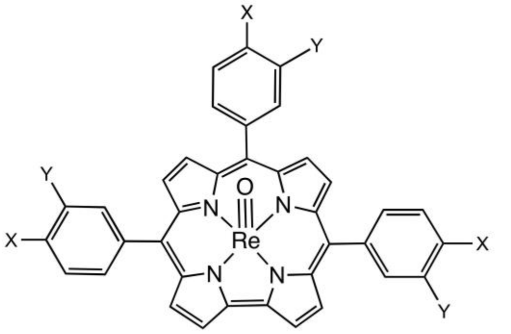

	X	Y
Re[T*p*CO$_2$CH$_3$PC](O)	CO$_2$CH$_3$	H
Re[T*m*CO$_2$CH$_3$PC](O)	H	CO$_2$CH$_3$
Re[*p*TCPC](O)	CO$_2$H	H
Re[*m*TCPC](O)	H	CO$_2$H

Figure 107. Carboxyl and ester-appended ReO corroles.

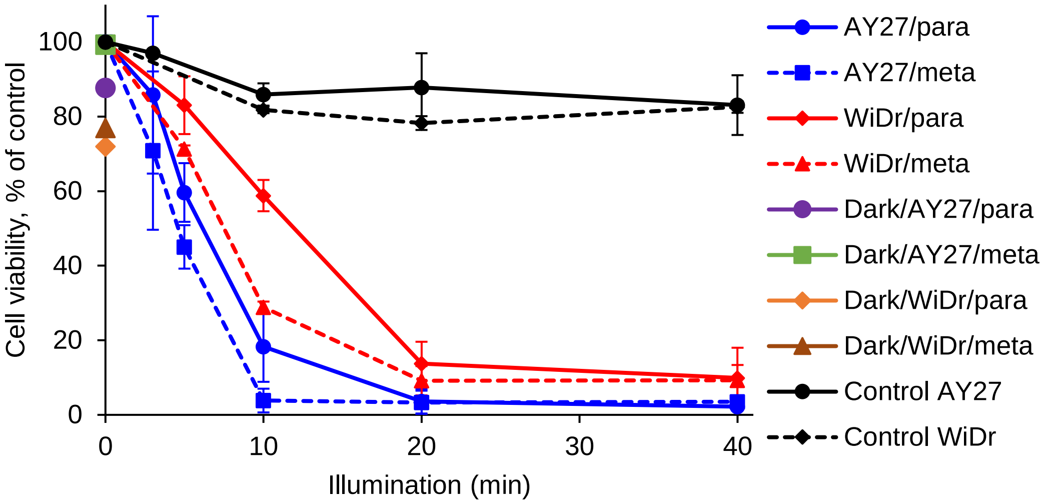

Figure 108. Cell viability studies of Re[*p*TCPC](O) and Re[*m*TCPC](O) on AY27 rat bladder cancer cells and WiDr human colon cancer cell lines, as a function of light exposure of blue light (435 nm,0-40 min), after incubation of corrole (10 μM, 24h) The black lines represent cells exposed only to light. The black curves represent cells exposed only to light, while the red and blue curves correspond to WiDr and AY27, respectively. A continuous line represents the *meta*-carboxy complex, while a dotted line corresponds to the *para*-carboxy complex. Error bars are ± SD of two parallels. Dots in black, green or pink colours along the y-axis correspond to dark toxicity (0 min light). Reused with permission from ref 175. *Copyright © 2020 American Chemical Society*

Table 6. Free-base, gold- and rhenium- corrole derivatives that have been used as photosensitizers in in vitro photodynamic therapy experiments.

Compound	Cell line	LD$_{50}$ dark (µM)	LD$_{50}$ light (µM)	Ref
H_3[*p*TCPC]	AY27	~300	-	190
Re[*p*TCPC](O)	AY27	-	7 min	175
	WiDr	-	12 min	175
Au[*p*TCPC]	AY27	~100	17 min	190
H_3[*m*TCPC]	AY27	~300	-	190
Re[*m*TCPC](O)	AY27	-	5 min	175
	WiDr	-	8 min	175
Au[*m*TCPC]	AY27	~100	2.5 min	190

Given that Au-TCPC derivatives are known to be active in both photodynamic therapy and dye-sensitized solar cells (DSSCs),[190] the efficacy of Re[*m*TCPC](O) and Re[*p*TCPC](O) were also examined in DSSCs experiments.[192] Time-resolved spectroscopic studies led to the surprising conclusion that the activity of 5d metallocorroles in DSSCs reflects singlet-state activity, rather than the T_1 state, which is thought to account for the photocytotoxicity of the compounds. The results indicate that the T_1 state is not energetic enough to inject an electron into the semiconductor titania.

5.2 Functionalization of 5d corroles

A second aspect of this thesis was to develop functionalization schemes for ReO corroles, with a view to developing advanced intermediates for new photosensitizers, bioconjugates, and nanoconjugates. Three significant achievements were made in this line of work.

(a) *β*-Octahalogenation. *β*-Octahalogeno derivatives were of interest not only as a probe of the heavy atom effect on photophysical properties, but also as advanced intermediates for further peripheral functionalization, such as via palladium-catalysed coupling reactions. As sections 3.2 and 3.13 address, there are generally two approaches to obtaining octabrominated corroles either through direct bromination or by pre-formed *β*-octabromocorroles ligands. Synthesising fully *β*-octabrominated ReO corroles proved challenging. Free-base octabromocorroles[118] did not survive the harsh high-temperature conditions of rhenium insertion. Bromination with elemental bromine in chloroform also tended to yield incompletely brominated products. In addition, the different partly brominated compounds were impossible to separate, which made ESI-MS analyses the only way of monitoring the course of the reaction. Through careful optimization of the direct bromination approach, including repeated addition of a large excess of bromine over several days, ultimately led to the isolation of fully *β*-brominated ReO corroles. In contrast, *β*-octachlorination of ReO corroles proceeded quickly, reaching completion within a few minutes.[193]

Single-crystal X-ray structures obtained (Figure 109) showed that the halogenated ReO corroles had essentially the same Re-O and Re-N bond distance as the unsubstituted complexes. Redshifts were observed for the Soret band upon halogenation from the general 438 nm for Re[TPC](O) to 448 nm for Re[Cl_8TPC](O) to 456 nm for Re[Br_8TPC](O).

As of yet,the *β*-octachlorination or *β*-octabrominated ReO corroles have been further functionalised nor photochemically analysed.

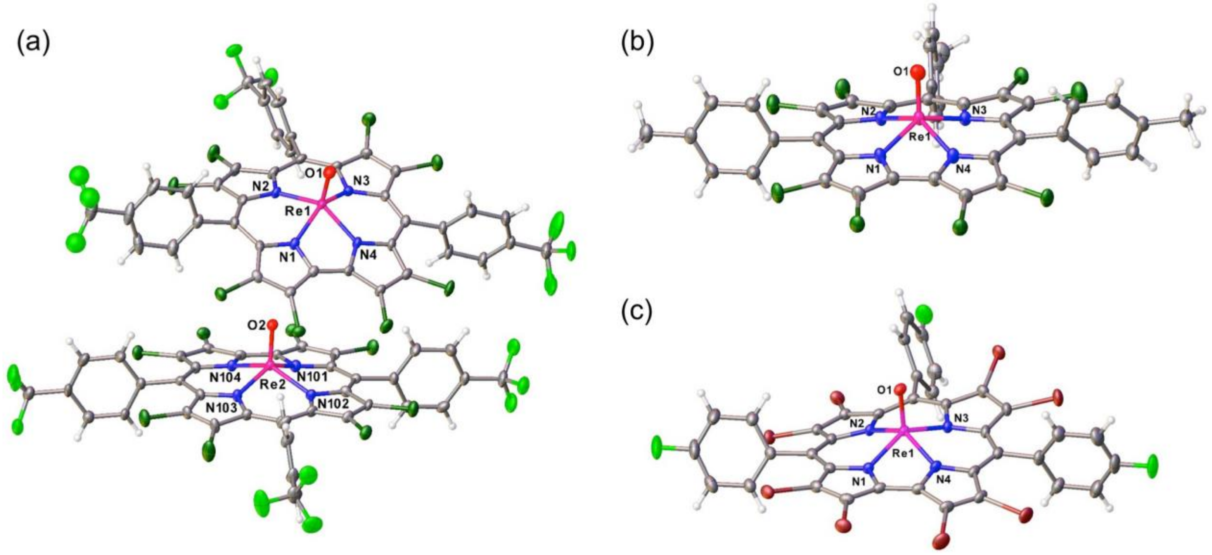

Figure 109. X-ray structures of selected β-octahalogenated ReO corroles. (Color code: Re purple, nitrogen blue, oxygen red, bromine dark red, fluorine light green, and chlorine dark green.). Reused from ref 193.

(b) Formylation. Formylation was another reaction of great interest, since formylcorroles in principle can serve as a gateway to a variety of polar anchoring groups that lend themselves to bio-[195] and nano-conjugation.[196] Although formylation of porphyrin-type macrocycles has been accomplished prior to this work (section 3.5),[194] this work showed that the ReO and Au metallocorrole families react in a regioselective manner. Thus, while Au triarylcorroles yield 3,17-diformyl derivatives as the major product, ReO corroles yield 3-monoformyl derivatives as the major product. This generalization appears to hold true for a variety of *meso*-aryl groups. The regioselectivity appears to correlate with their oxidation potentials Au and ReO corroles, with the former some 200 mV easier to oxidize for a given substitution pattern. Postfunctionalisation of the formylcorrole products was demonstrated in a preliminary way via the Knoevenagel reaction.

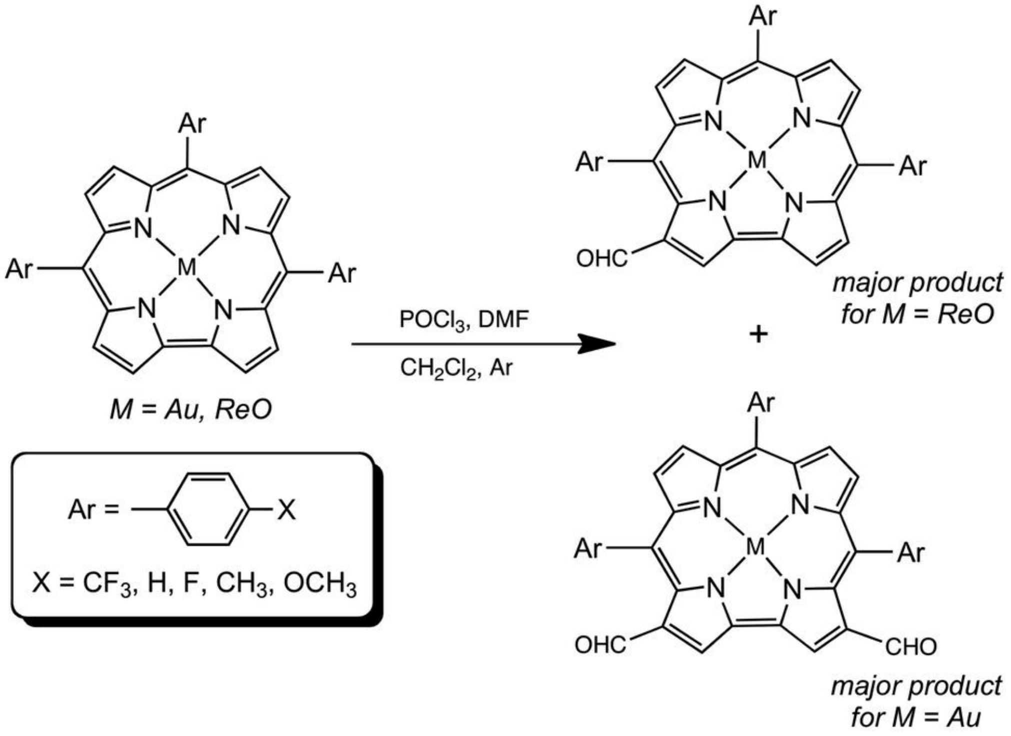

Figure 110. Regioselective Vilsmeier-Haack formylation of ReO and Au corroles. Reused from ref 194 with permission from The Royal Society.

The formyl and Knoevenagel derivatives were found to redshift the Soret maximum of the parent complex Re[T*p*CH3PC](O) at 440 nm to ~450 nm for the mono-formylated compound Re[T*p*CH3PC-3-CHO](O) and to ~480 nm for the cyanoacetic acid condensate Re[T*p*CH3PC-CH(CN)(COOH)](O), as shown in Figure 111. Similar spectral redshits are also observed for Au corroles, as also shown in Figure 111. The redshifted absorption spectra also exhibit a weakening in the Soret band, potentially indicating a weakening of the macrocyclic aromaticity, while the stronger intensity in the Q-band might be due to charge transfer to the formyl group.

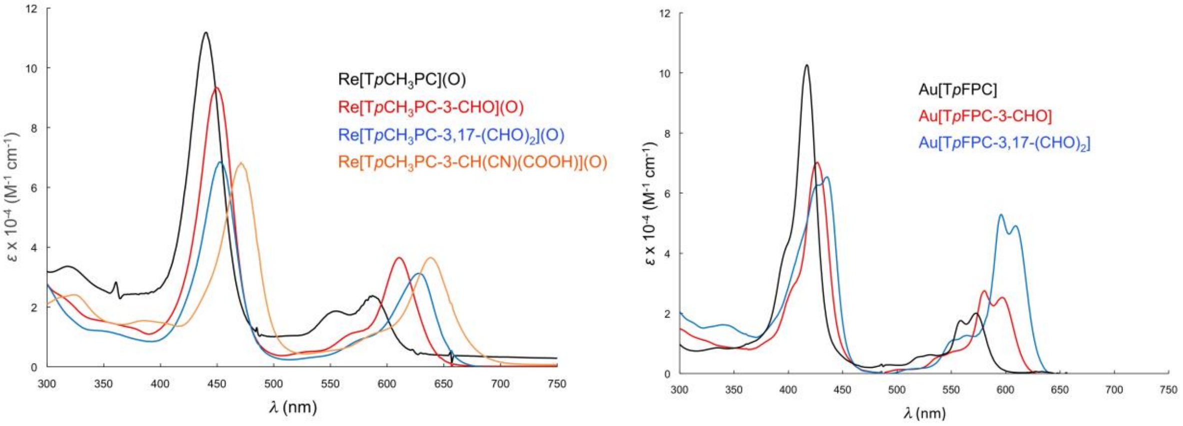

Figure 111. Absorption spectra of a series of conjugated ReO corroles (left); comparison of mono- and diformylated Au[T*p*FPC] (right). Reused from ref 194 with permission from The Royal Society.

(c) Water-soluble iridium corroles. As described in section 2.3.4, iridium corroles are known to coordinate to a variety of axial ligands. Accordingly, a potentially efficient route to water-soluble iridium corroles was investigated involving the use of water-soluble axial ligands. This simple idea proved surprisingly challenging to implement. Although water-soluble amines readily yielded six-coordinate complexes, they turned out to be relatively unstable, decomposing upon storage or upon column chromatography. However, we identified water-soluble phosphines that yielded highly stable, water-soluble five-coordinate complexes that exhibited long-term stability both as solids and in aqueous solution.[197] Photophysical and photocytotoxicity studies of these complexes, however, have not been completed.

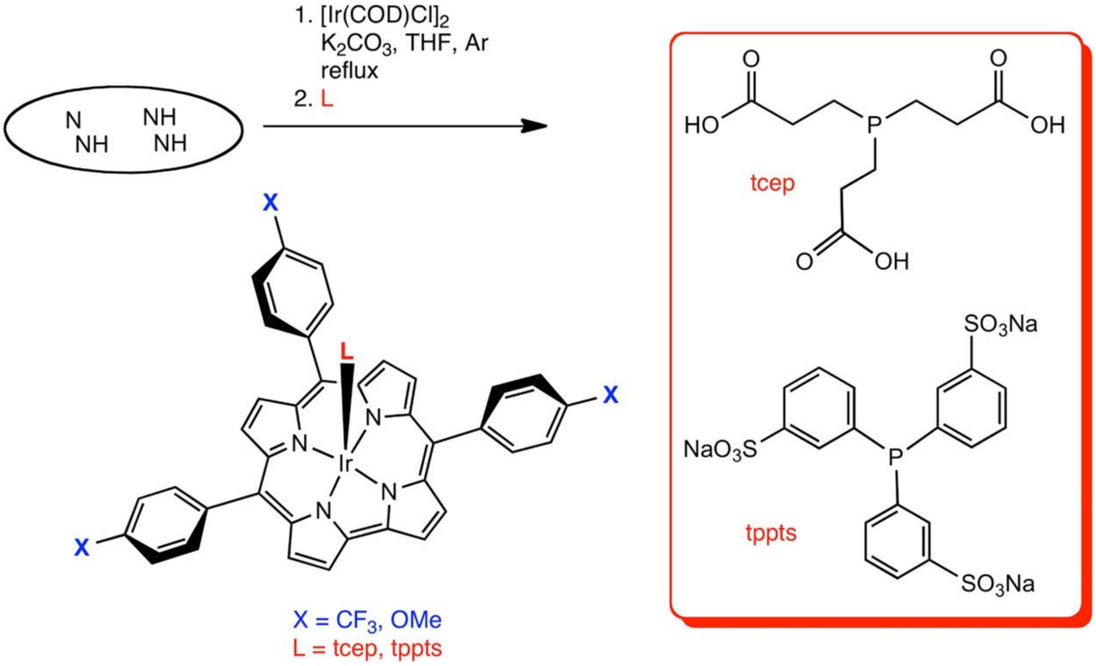

Figure 112. Synthesis of water-soluble five-coordinate Ir corroles. Reused from ref 197.

5.3 Conclusion and future directions

In summary, several new 5d metallocorrole complexes have been synthesised in the course of this research. Rhenium-oxo corroles have been found to exhibit near-IR phosphorescence with quantum yields of 1-1.5%, the highest among all metallocorroles, and high singlet oxygen sensitization quantum yields of over 70%. Two of the complexes, Re[*m*TCPC](O) and Re[*p*TCPC](O), have been found to exhibit considerable promise in *in vitro* photodynamic therapy experiments against two different cancer cell lines (WiDr and AY27).

Several synthetic routes have been worked out for a variety of functionalized 5d metallocorroles. General protocols have been worked out for *β*-octabrominated and octachlorinated ReO corroles. Water-soluble axial ligands, especially phosphines, have been exploited to develop a simple route to water-soluble iridium corroles. Finally, Vilsmeier-Haack formylation of ReO and Au corroles has been found to proceed with remarkable selectivity: ReO triarylcorroles were found to selectively yield 3-formyl derivatives while their Au counterparts yielded 3,17-diformyl derivatives. The formyl derivatives could be further postfunctionalized via Knoevenagel condensation with cyanoacetic acid.

Thanks to the versatility of the formyl group, facile access to 5d metal formylcorroles promises a variety of bio- and nanoconjugation studies. Peptides, sugars, aptamers, and antibodies on the one hand and nanoparticles and 2D materials (such as graphene and metal dichalcogenides) on the other hand are all attractive conjugants. The conjugates thus obtained should facilitate improved biotargeting in photodynamic therapy and multimodal cancer therapy.[195] It would be of great interest to study uptake mechanism of promising corrole derivative with a panel of human cell lines. Thereafter the study could go further with animal cancer models with the most promising compounds.

The photothermal effects of 5d metallocorroles remain to be explored. Such measurements promise new reagents for photothermal therapy and combined photodynamic and photothermal therapy.[196] In the same vein, the synthesis of ^{99m}Tc corroles can open the door towards new diagnostic and theranostic agents.

Cationic 5d metallocorroles are another class of attractive targets, which may prove effective in antimicrobial photodynamic therapy against Gram-positive bacteria.[198]

References

(1) With, T. K. A short history of porphyrins and the porphyrias. *Int. J. Biochem.* **1980**, *11* (3), 189-200. DOI: 10.1016/0020-711X(80)90219-0.

(2) Milgrom, L. R. *The colours of life : an introduction to the chemistry of porphyrins and related compounds*; Oxford University Press, 1997.

(3) Braun, J.; Schwesinger, R.; Williams, P. G.; Morimoto, H.; Wemmer, D. E.; Limbach, H.-H. Kinetic H/D/T Isotope and Solid State Effects on the Tautomerism of the Conjugate Porphyrin Monoanion. *J. Am. Chem. Soc.* **1996**, *118* (45), 11101-11110. DOI: 10.1021/ja961313q.

(4) Thomas, K. E.; McCormick, L. J.; Vazquez-Lima, H.; Ghosh, A. Stabilization and Structure of the *cis* Tautomer of a Free-Base Porphyrin. *Angew. Chem. Int. Ed.* **2017**, *56* (34), 10088-10092. DOI: 10.1002/anie.201701965.

(5) Falk, J. E. Porphyrins and metalloporphyrins: Their General, Physical and Coordination Chemistry, and Laboratory Methods. Elsevier, 1964.

(6) Sessler, J. L.; Gross, Z.; Furuta, H. Introduction: Expanded, Contracted, and Isomeric Porphyrins. *Chem. Rev* **2017**, *117* (4), 2201-2202. DOI: 10.1021/acs.chemrev.7b00036.

(7) Kitaoka, S.; Nobuoka, K.; Ishikawa, Y. Ionic liquids for tetraarylporphyrin preparation. *Tetrahedron* **2005**, *61* (32), 7678-7685. DOI: 10.1016/j.tet.2005.05.097.

(8) Arsenault, G. P.; Bullock, E.; MacDonald, S. F. Pyrromethanes and Porphyrins Therefrom. *J. Am. Chem. Soc.* **1960**, *82* (16), 4384-4389. DOI: 10.1021/ja01501a066.

(9) Woodward, R. B.; Ayer, W. A.; Beaton, J. M.; Bickelhaupt, F.; Bonnett, R.; Buchschacher, P.; Closs, G. L.; Dutler, H.; Hannah, J.; Hauck, F. P.; et al. The total synthesis of chlorophyll. *J. Am. Chem. Soc.* **1960**, *82* (14), 3800-3802. DOI: 10.1021/ja01499a093.

(10) Rothemund, P. Formation of porphyrins from pyrrole and aldehydes [4]. *J. Am. Chem. Soc.* **1935**, *57* (10), 2010-2011. DOI: 10.1021/ja01313a510. Adler, A. D.; Longo, F. R.; Finarelli, J. D.; Goldmacher, J.; Assour, J.; Korsakoff, L. A simplified synthesis for meso-tetraphenylporphine. *J. Org. Chem.* **1967**, *32* (2), 476-476. DOI: 10.1021/jo01288a053.

(11) Lindsey, J. S.; Schreiman, I. C.; Hsu, H. C.; Kearney, P. C.; Marguerettaz, A. M. Rothemund and Adler-Longo Reactions Revisited: Synthesis of Tetraphenylporphyrins under Equilibrium Conditions. *J. Org. Chem.* **1987**, *52* (5), 827-836. DOI: 10.1021/jo00381a022.

(12) Araujo, A. R. L.; Tome, A. C.; Santos, C. I. M.; Faustino, M. A. F.; Neves, M. G. P. M. S.; Simoes, M. M. Q.; Moura, N. M. M.; Abu-Orabi, S. T.; Cavaleiro, J. A. S. Azides and Porphyrinoids: Synthetic Approaches and Applications. Part 2-Azides, Phthalocyanines, Subphthalocyanines and Porphyrazines. *Molecules* **2020**, *25* (7), 1745. DOI: 10.3390/molecules25071745.

(13) Anguera, G.; Sánchez-García, D. Porphycenes and Related Isomers: Synthetic Aspects. *Chem. Rev.* **2017**, *117* (4), 2481-2516. DOI: 10.1021/acs.chemrev.6b00345.

(14) Sessler, J. L.; Brucker, E. A.; Weghorn, S. J.; Kisters, M.; Schäfer, M.; Lex, J.; Vogel, E. Corrphycene: A New Porphyrin Isomer. *Angew. Chem. Int. Ed.* **1994**, *33* (22), 2308-2312. DOI: 10.1002/anie.199423081.

(15) Chatterjee, T.; Shetti, V. S.; Sharma, R.; Ravikanth, M. Heteroatom-Containing Porphyrin Analogues. *Chem. Rev.* **2017**, *117* (4), 3254-3328. DOI: 10.1021/acs.chemrev.6b00496.

(16) Lash, T. D. Carbaporphyrinoid Systems. *Chem. Rev* **2017**, *117* (4), 2313-2446. DOI: 10.1021/acs.chemrev.6b00326.

(17) Chmielewski, P. J.; Latos-Grażyński, L.; Rachlewicz, K.; Glowiak, T. Tetra-*p*-tolylporphyrin with an Inverted Pyrrole Ring: A Novel Isomer of Porphyrin. *Angew. Chem. Int. Ed.* **1994**, *33* (7), 779-781. DOI: 10.1002/anie.199407791.

(18) Furuta, H.; Asano, T.; Ogawa, T. N-confused porphyrins – a new isomer of tetraphenylporphyrins. *J. Am. Chem. Soc.* **1994**, *116* (2), 767-768.

(19) Lash, T. D.; Chaney, S. T. Azuliporphyrin: A Case of Borderline Porphyrinoid Aromaticity. *Angew. Chem. Int. Ed.* **1997**, *36* (8), 839-840. DOI: 10.1002/anie.199708391.

(20) Ishizuka, T.; Sakashita, R.; Iwanaga, O.; Morimoto, T.; Mori, S.; Ishida, M.; Toganoh, M.; Takegoshi, K.; Osuka, A.; Furuta, H. NH Tautomerism of N-Confused Porphyrin: Solvent/Substituent Effects and Isomerization Mechanism. *J. Phys. Chem. A* **2020**, *124* (28), 5756-5769. DOI: 10.1021/acs.jpca.0c04779.

(21) Lash, T. D.; Richter, D. T.; Shiner, C. M. Conjugated macrocycles related to the porphyrins. Part 16. Synthesis of hexa- and heptaalkyl-substituted inverted or *N*-confused porphyrins by the '3 + 1' methodology. *J. Org. Chem.* **1999**, *64* (21), 7973-7982. DOI: 10.1021/jo991019r.

(22) Furuta, H.; Maeda, H.; Osuka, A. Theoretical study of stability, structures, and aromaticity of multiply *N*-confused porphyrins. *J. Org. Chem.* **2001**, *66* (25), 8563-8572. DOI: 10.1021/jo016051b.

(23) Chmielewski, P. J.; Latos-Grażyński, L.; Głowiak, T. Reactions of Nickel(II) 2-Aza-5,10,15,20-tetraphenyl-21- carbaporphyrin with Methyl Iodide. The First Structural Characterization of a Paramagnetic Organometallic Nickel(II) Complex. *J. Am. Chem. Soc.* **1996**, *118* (24), 5690-5701. DOI: 10.1021/ja9527028.

(24) Furuta, H.; Maeda, H.; Osuka, A. Doubly N-Confused Porphyrin: A New Complexing Agent Capable of Stabilizing Higher Oxidation States. *J. Am. Chem. Soc.* **2000**, *122* (5), 803-807. DOI: 10.1021/ja992679g.

(25) Maeda, H.; Furuta, H. A dozen years of N-confusion: From synthesis to supramolecular chemistry. *Pure Appl. Chem.* **2006**, *78* (1), 29-44. DOI: 10.1351/pac200678010029.

(26) Muckey, M. A.; Szczepura, L. F.; Ferrence, G. M.; Lash, T. D. Silver(III) Carbaporphyrins: The First Organometallic Complexes of True Carbaporphyrins. *Inorg. Chem* **2002**, *41* (19), 4840-4842. DOI: 10.1021/ic020285b.

(27) Alemayehu, A. B.; Vazquez-Lima, H.; Teat, S. J.; Ghosh, A. Unexpected Molecular Structure of a Putative Rhenium-Dioxo-Benzocarbaporphyrin Complex. Implications for the Highest Transition Metal Valence in a Porphyrin-Type Ligand Environment. *Chemistry Open (Weinheim)* **2019**, *8* (10), 1298-1302. DOI: 10.1002/open.201900271.

(28) Toganoh, M.; Furuta, H. Creation from Confusion and Fusion in the Porphyrin World - The Last Three Decades of *N*-Confused Porphyrinoid Chemistry. *Chem. Rev.* **2022**, *122* (9), 8313-8437. DOI: 10.1021/acs.chemrev.1c00065.

(29) Ryeng, H.; Gonzalez, E.; Ghosh, A. DFT at Its Best: Metal- versus Ligand-Centered Reduction in Nickel Hydroporphyrins. *J. Phys. Chem. B* **2008**, *112* (47), 15158-15173. DOI: 10.1021/jp805486b.

(30) Latos-Grazynski, L.; Olmstead, M. M.; Balch, A. L. The first structural characterization of a nickel(I) macrocyclic system: structure of nickel(I) diphenyldi-p-toyl-21-thiaporphyrin. *Inorg. Chem* **1989**, *28* (22), 4065-4066. DOI: 10.1021/ic00321a005.

(31) Bauer, V. J.; Clive, D. L. J.; Dolphin, D.; Paine, J. B.; Harris, F. L.; King, M. M.; Loder, J.; Wang, S. W. C.; Woodward, R. B. Sapphyrins: novel aromatic pentapyrrolic macrocycles. *J. Am. Chem. Soc.* **1983**, *105* (21), 6429-6436. DOI: 10.1021/ja00359a012.

(32) Vogel, E. Porphyrinoid macrocycles: A cornucopia of novel chromophores. *Pure Appl. Chem.* **1996**, *68* (7), 1355-1360. DOI: 10.1351/pac199668071355.

(33) Sessler, J. L.; Seidel, D. Synthetic Expanded Porphyrin Chemistry. *Angew. Chem. Int. Ed.* **2003**, *42* (42), 5134-5175. DOI: 10.1002/anie.200200561.

(34) Tanaka, T.; Osuka, A. Chemistry of meso-Aryl-Substituted Expanded Porphyrins: Aromaticity and Molecular Twist. *Chem. Rev.* **2017**, *117* (4), 2584-2640. DOI: 10.1021/acs.chemrev.6b00371.

(35) Brewster, J. T.; Zafar, H.; Root, H. D.; Thiabaud, G. D.; Sessler, J. L. Porphyrinoid f-Element Complexes. *Inorg. Chem.* **2020**, *59* (1), 32-47. DOI: 10.1021/acs.inorgchem.9b00884.

(36) Shimizu, S. Recent Advances in Subporphyrins and Triphyrin Analogues: Contracted Porphyrins Comprising Three Pyrrole Rings. *Chem. Rev.* **2017**, *117* (4), 2730-2784. DOI: 10.1021/acs.chemrev.6b00403.

(37) Kuzuhara, D.; Yamada, H.; Xue, Z.; Okujima, T.; Mori, S.; Shen, Z.; Uno, H. New synthesis of meso -free-[14]triphyrin(2.1.1) by McMurry coupling and its derivatization to Mn(I) and Re(I) complexes. *Chem. Commun.* **2010**, *47* (2), 722-724. DOI: 10.1039/c0cc04286b.

(38) Lee, W.; Zhan, X.; Palma, J.; Vestfrid, J.; Gross, Z.; Churchill, D. G. Minding our P-block and Q-bands: paving inroads into main group corrole research to help instil broader potential. *Chem. Commun. (Camb)* **2021**, *57* (38), 465-4641. DOI: 10.1039/d1cc00105a.

(39) Ricchelli, F. Photophysical properties of porphyrins in biological membranes. *J. Photochem. Photobiol. B* **1995**, *29* (2), 109-118. DOI: 10.1016/1011-1344(95)07155-U.

(40) Teo, R. D.; Hwang, J. Y.; Termini, J.; Gross, Z.; Gray, H. B. Fighting Cancer with Corroles. *Chem. Rev.* **2016**. DOI: 10.1021/acs.chemrev.6b00400.

(41) Lemon, C. M. Corrole photochemistry. *Pure Appl. Chem.* **2020**, *92* (12), 1901-1919. DOI: 10.1515/pac-2020-0703.

(42) Johnson, A. W.; Kay, I. T. 306. Corroles. Part I. Synthesis. *J. Chem. Soc. (Resumed)* **1965**, 1620-1629. DOI: 10.1039/JR9650001620.

(43) Gross, Z.; Galili, N.; Saltsman, I. The First Direct Synthesis of Corroles from Pyrrole. *Angew. Chem. Int. Ed.* **1999**, *38* (10), 1427-1429. DOI: 10.1002/(SICI)1521-3773(19990517)38:10<1427::AID-ANIE1427>3.0.CO;2-1.

(44) Paolesse, R.; Jaquinod, L.; Nurco, D.; Mini, S.; Sagone, F.; Boschi, T.; Smith, K. 5,10,15-Triphenylcorrole: a product from a modified Rothemund reaction. *Chem. Commun.* **1999**, (14), 1307-1308.

(45) Wasbotten, I.; Wondimagegn, T.; Ghosh, A. Electronic absorption, resonance Raman, and electrochemical studies of planar and saddled copper(III) *meso*-triarylcorroles. Highly substituent-sensitive soret bands as a distinctive feature of high-valent transition metal corroles. *J. Am. Chem. Soc.* **2002**, *124* (27), 8104-8116. DOI: 10.1021/ja0113697.

(46) Koszarna, B.; Gryko, D. T. Efficient synthesis of *meso*-substituted corroles in a H_2O-MeOH mixture. *J. Org. Chem.* **2006**, *71* (10), 3707-3717. DOI: 10.1021/jo060007k.

(47) Rohand, T.; Dolusic, E.; Ngo, T. H.; Maes, W.; Dehaen, W. Efficient synthesis of aryldipyrromethanes in water and their application in the synthesis of corroles and dipyrromethenes. *Arkivoc* **2007**, *2007* (10), 307-324. DOI: 10.3998/ark.5550190.0008.a20.

(48) Foroutan-Nejad, C.; Larsen, S.; Conradie, J.; Ghosh, A. Isocorroles as Homoaromatic NIR-Absorbing Chromophores: A First Quantum Chemical Study. *Sci. Rep.* **2018**, *8* (1), 11952-11910. DOI: 10.1038/s41598-018-29819-3.

(49) Larsen, S.; McCormick, L. J.; Ghosh, A. Rapid one-pot synthesis of pyrrole-appended isocorroles. *Org. Biomol. Chem.* **2019**, *17* (12), 3159-3166. DOI: 10.1039/c9ob00168a.

(50) Sakow, D.; Böker, B.; Brandhorst, K.; Burghaus, O.; Bröring, M. 10-Heterocorroles: Ring-Contracted Porphyrinoids with Fine-Tuned Aromatic and Metal-Binding Properties. *Angew. Chem. Int. Ed.* **2013**, *52* (18), 4912-4915. DOI: 10.1002/anie.201300757.

(51) Bröring, M.; Köhler, S.; Kleeberg, C. Norcorrole: Observation of the Smallest Porphyrin Variant with a N4 Core. *Angew. Chem. Int. Ed.* **2008**, *47* (30), 5658-5660. DOI: 10.1002/anie.200801196.

(52) Ito, T.; Hayashi, Y.; Shimizu, S.; Shin, J.-Y.; Kobayashi, N.; Shinokubo, H. Gram-Scale Synthesis of Nickel(II) Norcorrole: The Smallest Antiaromatic Porphyrinoid. *Angew. Chem. Int. Ed.* **2012**, *51* (34), 8542-8545. DOI: 10.1002/anie.201204395.

(53) Yonezawa, T.; Shafie, S. A.; Hiroto, S.; Shinokubo, H. Shaping Antiaromatic π-Systems by Metalation: Synthesis of a Bowl-Shaped Antiaromatic Palladium Norcorrole. *Angew. Chem. Int. Ed.* **2017**, *56* (39), 11822-11825. DOI: 10.1002/anie.201706134.
(54) Karadakov, P. B. Norcorrole: Aromaticity and Antiaromaticity in Contest. *Org. Lett* **2020**, *22* (21), 8676-8680. DOI: 10.1021/acs.orglett.0c03254.
(55) Galezowski, M.; Gryko, D. Recent Advances in the Synthesis of Hydroporphyrins. *Curr. Org. Chem.* **2007**, (11), 1310-1338.
(56) Ptaszek, M. Hydroporphyrins in Fluorescence In Vivo Imaging. Reviews in Fluorescence, Cham: Springer International Publishing, 2019; pp 21-51.
(57) Brückner, C.; Dolphin, D. 2,3- vic-Dihydroxy- *meso*-tetraphenylchlorins from the osmium tetroxide oxidation of *meso*-tetraphenylporphyrin. *Tetrahedron Lett.* **1995**, *36* (19), 3295-3298. DOI: 10.1016/0040-4039(95)00524-G.
(58) Faustino, M. A. F.; Neves, M. G. P. M. S.; Vicente, M. G. H.; Silva, A. M. S.; Cavaleiro, J. S. Diels-Alder reactions of Ni(II) *β*-vinyl- meso-tetraarylporphyrins. *Tetrahedron Lett.* **1996**, *37* (20), 3569-3570. DOI: 10.1016/0040-4039(96)00623-5.
(59) Adler, A. D.; Longo, F. R.; Kampas, F.; Kim, J. On the preparation of metalloporphyrins. *J. inorg. Nuc. Chem.* **1970**, *32* (7), 2443-2445. DOI: 10.1016/0022-1902(70)80535-8.
(60) Zanelli, G. D.; Bjarnason, I.; Smith, T.; Crawley, J. C. W.; Levi, A. J.; Copeland, R. I. Technetium-99m labelled porphyrin as an imaging agent for occult infections and inflammation. *Nucl. Med. Comm.* **1986**, *7* (1), 17-24.
(61) Arnold, J.; Dawson, D. Y.; Hoffman, C. G. Synthesis and characterization of lithium, sodium, and potassium porphyrin complexes. X-ray crystal structures of $Li_2(C_6H_{12}O_2)_2$TMPP, $Na_2(THF)_4$OEP, and $K_2(pyridine)_4$OEP. *J. Am. Chem. Soc.* **1993**, *115* (7), 2707-2713. DOI: 10.1021/ja00060a020.
(62) Pushkarev, V. E.; Tomilova, L. G.; Tomilov, Y. V. Synthetic approaches to lanthanide complexes with tetrapyrrole type ligands. *Russ. Chem. Rev.* **2008**, *77* (10), 875-907. DOI: 10.1070/RC2008v077n10ABEH003879.
(63) (a) Dean, M. L.; Schmink, J. R.; Leadbeater, N. E.; Bruckner, C. Microwave-promoted insertion of Group 10 metals into free base porphyrins and chlorins: scope and limitations. *Dalton. Trans.* **2008**, (10), 1341-1345. DOI: 10.1039/b716181f.
(b) Henriques, C. A.; Pinto, S. M. A.; Pineiro, M.; Canotilho, J.; Eusebio, M. E. S.; Pereira, M. M.; Calvete, M. J. F. Solventless metallation of low melting porphyrins synthesized by the water/microwave method. *RSC Adv.* **2015**, *5* (80), 64916-64924. DOI: 10.1039/c5ra11820d.
(c) Ralphs, K.; Zhang, C.; James, S. L. Solventless mechanochemical metallation of porphyrins. *Green Chem.* **2017**, *19* (1), 102-105. DOI: 10.1039/c6gc02420c.
(64) Conradie, J.; Ghosh, A. Energetics of Saddling versus Ruffling in Metalloporphyrins: Unusual Ruffled Dodecasubstituted Porphyrins. *ACS Omega* **2017**, *2* (10), 6708-6714. DOI: 10.1021/acsomega.7b01004.
(65) Kingsbury, C. J.; Senge, M. O. The shape of porphyrins. *Coord. Chem. Rev.* **2021**, *431*, 213760. DOI: 10.1016/j.ccr.2020.213760.
(66) Thomassen, I. K.; Vazquez-Lima, H.; Gagnon, K. J.; Ghosh, A. Octaiodoporphyrin. *Inorg. Chem.* **2015**, *54* (23), 11493-11497. DOI: 10.1021/acs.inorgchem.5b02127.
(67) Barata, J. F. B.; Neves, M. G. P. M. S.; Faustino, M. A. F.; Tomé, A. C.; Cavaleiro, J. A. S. Strategies for Corrole Functionalization. *Chem. Rev.* **2016**. DOI: 10.1021/acs.chemrev.6b00476.
(68) Ghosh, A. Electronic Structure of Corrole Derivatives: Insights from Molecular Structures, Spectroscopy, Electrochemistry, and Quantum Chemical Calculations. *Chem. Rev.* **2017**, *117* (4), 3798-3881. DOI: 10.1021/acs.chemrev.6b00590.
(69) Buckley, H. L.; Chomitz, W. A.; Koszarna, B.; Tasior, M.; Gryko, D. T.; Brothers, P. J.; Arnold, J. Synthesis of lithium corrole and its use as a reagent for the preparation of

cyclopentadienyl zirconium and titanium corrole complexes. *Chem. Commun.* **2012**, *48* (87), 10766-10768. DOI: 10.1039/c2cc35984g.

(70) Mahammed, A.; Gross, Z. Aluminum corrolin, a novel chlorophyll analogue. *Inorg. Biochem.* **2002**, *88* (3-4), 305-309. DOI: 10.1016/S0162-0134(01)00373-7.

(71) Albrett, A. M.; Boyd, P. D. W.; Clark, G. R.; Brothers, P. J.; Gonzalez, E.; Ghosh, A. Reductive coupling and protonation leading to diboron corroles with a B-H-B bridge. *Dalton Trans.* **2010**, *39* (17), 4032-4034. DOI: 10.1039/c002885c.

(72) Albrett, A. M.; Conradie, J.; Ghosh, A.; Brothers, P. J. DFT survey of monoboron and diboron corroles: regio- and stereochemical preferences for a constrained, low-symmetry macrocycle. *Dalton Trans.* **2008**, (33), 4464-4473. DOI: 10.1039/b718755f.

(73) Brothers, P. J. Boron complexes of porphyrins and related polypyrrole ligands: unexpected chemistry for both boron and the porphyrin. *Chem. Commun.* **2008**, (18), 2090-2102. DOI: 10.1039/b714894a.

(74) Blumenfeld, C. M.; Grubbs, R. H.; Moats, R. A.; Gray, H. B.; Sorasaenee, K. Decorating metal oxide surfaces with fluorescent chlorosulfonated corroles. *Inorg. Chem.* **2013**, *52* (9), 4774. DOI: 10.1021/ic400410k.

(75) Pomarico, G.; Nardis, S.; Naitana, M. L.; Vicente, M. G. a. H.; Kadish, K. M.; Chen, P.; Prodi, L.; Genovese, D.; Paolesse, R. Aluminum, Gallium, Germanium, Copper, and Phosphorus Complexes of *meso*-Triaryltetrabenzocorrole. *Inorg. Chem.* **2013**, *52* (7), 4061-4070. DOI: 10.1021/ic400162y.

(76) (a) Simkhovich, L.; Mahammed, A.; Goldberg, I.; Gross, Z. Synthesis and Characterization of Germanium, Tin, Phosphorus, Iron, and Rhodium Complexes of Tris(pentafluorophenyl)corrole, and the Utilization of the Iron and Rhodium Corroles as Cyclopropanation Catalysts. *Chem. Eur. J.* **2001**, *7* (5), 1041-1055. DOI: 10.1002/1521-3765(20010302)7:5<1041::AID-CHEM1041>3.0.CO;2-8.

(b) Liang, X.; Mack, J.; Zheng, L.-M.; Shen, Z.; Kobayashi, N. Phosphorus(V)-corrole: synthesis, spectroscopic properties, theoretical calculations, and potential utility for in vivo applications in living cells. *Inorg. Chem.* **2014**, *53* (6), 2797. DOI: 10.1021/ic402347w.

(c) Ghosh, A.; Ravikanth, M. Synthesis, Structure, Spectroscopic, and Electrochemical Properties of Highly Fluorescent Phosphorus(V)– meso -Triarylcorroles. *Chem. Eur. J.* **2012**, *18* (20), 6386-6396. DOI: 10.1002/chem.201103226.

(77) Ueta, K.; Fukuda, M.; Kim, G.; Shimizu, S.; Tanaka, T.; Kim, D.; Osuka, A. The First Silicon(IV) Corrole Complexes: Synthesis, Structures, Properties, and Formation of a μ-Oxo Dimer. *Chem. Eur J.* **2018**, *24* (30), 7637-7646. DOI: 10.1002/chem.201800165.

(78) Albrett, A. M.; Conradie, J.; Boyd, P. D. W.; Clark, G. R.; Ghosh, A.; Brothers, P. J. Corrole as a binucleating ligand: preparation, molecular structure and density functional theory study of diboron corroles. *J. Am. Chem. Soc.* **2008**, *130* (10), 2888. DOI: 10.1021/ja077785u.

(79) Kadish, K. M.; Erben, C.; Ou, Z.; Adamian, V. A.; Will, S.; Vogel, E. Corroles with group 15 metal ions. Synthesis and characterization of octaethylcorroles containing As, Sb, and Bi ions in +3, +4, and oxidation states. *Inorg. Chem.* **2000**, *39* (15), 3312. DOI: 10.1021/ic991361m.

(80) Pomarico, G.; Monti, D.; Bischetti, M.; Savoldelli, A.; Fronczek, F. R.; Smith, K. M.; Genovese, D.; Prodi, L.; Paolesse, R. Silicon(IV) Corroles. *Chem. Eur. J.* **2018**, *24* (33), 8438-8446. DOI: 10.1002/chem.201801246.

(81) Bendix, J.; Dmochowski, I. J.; Gray, H. B.; Mahammed, A.; Simkhovich, L.; Gross, Z. Structural, Electrochemical, and Photophysical Properties of Gallium(III) 5,10,15-Tris(pentafluorophenyl)corrole. *Angew. Chem. Int. Ed.* **2000**, *39* (22), 4048-4051. DOI: 10.1002/1521-3773(20001117)39:22<4048::AID-ANIE4048>3.0.CO;2-7.

(82) Fang, H.; Ling, Z.; Brothers, P. J.; Fu, X. Reactivity studies of a corrole germanium hydride complex with aldehydes, olefins and alkyl halides. *Chem. Commun. (Camb)* **2011**, *47* (42), 11677-11679. DOI: 10.1039/c1cc15076f.

(83) Yun, L.; Vazquez-Lima, H.; Fang, H.; Yao, Z.; Geisberger, G.; Dietl, C.; Ghosh, A.; Brothers, P. J.; Fu, X. Synthesis and Reactivity Studies of a Tin(II) Corrole Complex. *Inorg. Chem* **2014**, *53* (13), 7047-7054. DOI: 10.1021/ic501103c.

(84) Padilla, R.; Buckley, H. L.; Ward, A. L.; Arnold, J. Synthesis, structure and reactivity of group 4 corrole complexes. *Chem. Commun.* **2014**, *50* (22), 2922-2924. DOI: 10.1039/c4cc00037d.

(85) Buckley, H. L.; Arnold, J. Recent developments in out-of-plane metallocorrole chemistry across the periodic table. *Dalton Trans.* **2014**, *44* (1), 30-36. DOI: 10.1039/c4dt02277g.

(86) Murakami, Y.; Matsuda, Y.; Yamada, S. Transition-metal complexes of pyrrole pigments. Part 20. Redox behaviour of chromium complexes with macrocyclic tetrapyrroles. *J. Chem. Soc., Dalton Trans.* **1981**, (3), 855. DOI: 10.1039/dt9810000855.

(87) Meier-Callahan, A. E.; Di Bilio, A.; Simkhovich, L.; Mahammed, A.; Goldberg, I.; Gray, H.; Gross, Z. Chromium corroles in four oxidation states. *Inorg. Chem.* **2001**, *40* (26), 6788-6793. DOI: 10.1021/ic010723z.

(88) Luobeznova, I.; Raizman, M.; Goldberg, I.; Gross, Z. Synthesis and full characterization of molybdenum and antimony corroles and utilization of the latter complexes as very efficient catalysts for highly selective aerobic oxygenation reactions. *Inorg. Chem.* **2006**, *45* (1), 386-394. DOI: 10.1021/ic051483g.

(89) Padilla, R. Preparation and characterization of a tungsten(V) corrole dichloride complex. *J. Porphy. Phthalocyanines* **2015**, *150* (19). DOI: 10.1142/S1088424614500990.

(90) Alemayehu, A. B.; Vazquez-Lima, H.; Gagnon, K. J.; Ghosh, A. Tungsten Biscorroles: New Chiral Sandwich Compounds. *Chem. Eur. J.* **2016**, *22* (20), 6914-6920. DOI: 10.1002/chem.201504848.

(91) Alemayehu, A. B.; Thomas, K. E.; Einrem, R. F.; Ghosh, A. The Story of 5d Metallocorroles: From Metal–Ligand Misfits to New Building Blocks for Cancer Phototherapeutics. *Acc. Chem. Res.* **2021**, *54* (15), 3095-3107. DOI: 10.1021/acs.accounts.1c00290.

(92) Boschi, T.; Licoccia, S.; Paolesse, R.; Tagliatesta, P.; Tehran, M. A. Synthesis and characterization of novel metal(III) complexes of corrole – crystal and molecular structure of (2,3,7,8,12,13,17,18-octamethylcorrolato)(triphenylarsine)rhodium(III). *J. Chem. Soc. Dalton Trans.* **1990**, (2), 463-468.

(93) Kadish, K. M.; Adamian, V. A.; Van Caemelbecke, E.; Gueletii, E.; Will, S.; Erben, C.; Vogel, E. Electrogeneration of oxidized corrole dimers. Electrochemistry of (OEC)M where M = Mn, Co, Ni, or Cu and OEC is the trianion of 2,3,7,8,12,13,17,18- octaethylcorrole. *J. Am. Chem. Soc.* **1998**, *120* (46), 11986-11993. DOI: 10.1021/ja9814570.

(94) Singh, P.; Dutta, G.; Goldberg, I.; Mahammed, A.; Gross, Z. Expected and unexpected transformations of manganese(III) tris(4-nitrophenyl)corrole. *Inorg. Chem.* **2013**, *52* (16), 9349. DOI: 10.1021/ic400918d.

(95) (a)Gross, Z.; Golubkov, G.; Simkhovich, L. Epoxidation Catalysis by a Manganese Corrole and Isolation of an Oxomanganese(V) Corrole. *Angew. Chem. Int. Ed.* **2000**, *39* (22), 4045-4047.

(b) Gershman, Z.; Goldberg, I.; Gross, Z. DNA Binding and Catalytic Properties of Positively Charged Corroles. *Angew. Chem. Int. Ed.* **2007**, *46* (23), 4320-4324. DOI: 10.1002/anie.200700757.

(c) Liu, H.; Mahmood, M.; Qiu, S.; Chang, C. Recent developments in manganese corrole chemistry. *Coord. Chem. Rev.*, 2013; Vol. 257, 1306-1333.

(96) Liu, H. Y.; Lai, T. S.; Yeung, L. L.; Chang, C. K. First synthesis of perfluorinated corrole and its Mn=O complex. *Org. Lett.* **2003**, *5* (5), 617-620. DOI: 10.1021/ol027111i.

(97) Bougher, C. J.; Liu, S.; Hicks, S. D.; Abu-Omar, M. M. Valence Tautomerization of High-Valent Manganese(V)-Oxo Corrole Induced by Protonation of the Oxo Ligand. *J. Am. Chem. Soc.* **2015**, *137* (45), 14481. DOI: 10.1021/jacs.5b09759.

(98) Tse, M.; Zhang, Z.; Mak, T.; Chan, K. S. Synthesis of an oxorhenium(v) corrolate from porphyrin with detrifluoromethylation and ring contraction. *Chem. Commun.* **1998**, (11), 1199-1200.

(99) Einrem, R. F.; Gagnon, K. J.; Alemayehu, A. B.; Ghosh, A. Metal-Ligand Misfits: Facile Access to Rhenium-Oxo Corroles by Oxidative Metalation. *Chem. Eur. J.* **2016**, *22* (2), 517-520. DOI: 10.1002/chem.201504307.

(100) Schweyen, P.; Brandhorst, K.; Hoffmann, M.; Wolfram, B.; Zaretzke, M. K.; Bröring, M. Viking Helmet Corroles: Activating Inert Oxidometal Corroles. *Chem. Eur. J.* **2017**, *23* (56), 13897-13900. DOI: 10.1002/chem.201703721.

(101) Alemayehu, A. B.; Teat, S. J.; Borisov, S. M.; Ghosh, A. Rhenium-Imido Corroles. *Inorg. Chem* **2020**, *59* (9), 6382-6389. DOI: 10.1021/acs.inorgchem.0c00477.

(102) (a) Vazquez-Lima, H.; Norheim, H. K.; Einrem, R. F.; Ghosh, A. Cryptic noninnocence: FeNO corroles in a new light. *Dalton Trans.* **2015**, *44* (22), 10146-10151. DOI: 10.1039/c5dt01495f.

(b) Norheim, H. K.; Capar, J.; Einrem, R. F.; Gagnon, K. J.; Beavers, C. M.; Vazquez-Lima, H.; Ghosh, A. Ligand noninnocence in FeNO corroles: insights from beta-octabromocorrole complexes. *Dalton Trans* **2016**, *45* (2), 681-689. DOI: 10.1039/c5dt03947a.

(c) Ganguly, S.; Vazquez-Lima, H.; Ghosh, A. Wolves in Sheep's Clothing: μ-Oxo-Diiron Corroles Revisited. *Chem. Eur. J.* **2016**, *22* (30), 10336-10340. DOI: 10.1002/chem.201601062.

(d) Steene, E.; Wondimagegn, T.; Ghosh, A. Electrochemical and Electronic Absorption Spectroscopic Studies of Substituent Effects in Iron(IV) and Manganese(IV) Corroles. Do the Compounds Feature High-Valent Metal Centers or Noninnocent Corrole Ligands? Implications for Peroxidase Compound I and II Intermediates. *J. Phys. Chem. B* **2001**, *105* (46), 11406-11413. DOI: 10.1021/jp012037r.

(103) Alemayehu, A. B.; Vazquez-Lima, H.; Gagnon, K. J.; Ghosh, A. Stepwise Deoxygenation of Nitrite as a Route to Two Families of Ruthenium Corroles: Group 8 Periodic Trends and Relativistic Effects. *Inorg. Chem.* **2017**, *56* (9), 5285-5294. DOI: 10.1021/acs.inorgchem.7b00377.

(104) (a) Jérôme, F.; Billier, B.; Barbe, J. M.; Espinosa, E.; Dahaoui, S.; Lecomte, C.; Guilard, R. Evidence for the Formation of a Ru III −Ru III Bond in a Ruthenium Corrole Homodimer. *Angew. Chem. Int. Ed.* **2000**, *39* (22), 4051-4053. (b) A. Simkhovich, L.; Luobeznova, I.; Goldberg, I.; Gross, Z. Mono- and Binuclear Ruthenium Corroles: Synthesis, Spectroscopy, Electrochemistry, and Structural Characterization. *Chem. Eur. J.* **2003**, *9* (1), 201-208. DOI: 10.1002/chem.200390013.

(105) Alemayehu, A. B.; Gagnon, K. J.; Terner, J.; Ghosh, A. Oxidative Metalation as a Route to Size-Mismatched Macrocyclic Complexes: Osmium Corroles. *Angew. Chem. Int. Ed.* **2014**, *53* (52), 14411-14414. DOI: 10.1002/anie.201405890.

(106) Conlon, M.; Johnson, A. W.; Overend, W. R.; Rajapaksa, D.; Elson, C. M. Structure and reactions of cobalt corroles. *J. Chem. Soc., Perkin Trans. 1* **1973**, 2281. DOI: 10.1039/p19730002281.

(107) Simkhovich, L.; Galili, N.; Saltsman, I.; Gross, Z.; Goldberg, I. Coordination chemistry of the novel 5,10,15-tris(pentafluorophenyl)corrole: Synthesis, spectroscopy, and structural characterization of its cobalt(III), rhodium(III), and iron(IV) complexes. *Inorg. Chem.* **2000**, *39* (13), 2704-2705. DOI: 10.1021/ic991342c.

(108) Palmer, J. H.; Mahammed, A.; Lancaster, K. M.; Gross, Z.; Gray, H. B. Structures and Reactivity Patterns of Group 9 Metallocorroles. *Inorg. Chem.* **2009**, *48* (19), 9308-9315. DOI: 10.1021/ic901164r. Palmer, J. H.; Lancaster, K. M. Molecular Redox: Revisiting the Electronic Structures of the Group 9 Metallocorroles. *Inorg. Chem.* **2012**, *51* (22), 12473-12482. DOI: 10.1021/ic3018826.

(109) Palmer, J. H.; Day, M. W.; Wilson, A. D.; Henling, L. M.; Gross, Z.; Gray, H. B. Iridium Corroles. *J. Am. Chem. Soc.* **2008**, *130* (25), 7786-7787. DOI: 10.1021/ja801049t.

(110) Thomassen, I. K.; McCormick-McPherson, L. J.; Borisov, S. M.; Ghosh, A. Iridium Corroles Exhibit Weak Near-Infrared Phosphorescence but Efficiently Sensitize Singlet Oxygen Formation. *Sci. Rep.* **2020**, *10* (1), 7551-7551. DOI: 10.1038/s41598-020-64389-3.

(111) Will, S.; Lex, J.; Vogel, E.; Schmickler, H.; Gisselbrecht, J.-P.; Haubtmann, C.; Bernard, M.; Gross, M. Nickel and Copper Corroles: Well-Known Complexes in a New Light. *Angew. Chem. Int. Ed.* **1997**, *36* (4), 357-361. DOI: 10.1002/anie.199703571.

(112) Alemayehu, A. B.; Vazquez-Lima, H.; Beavers, C. M.; Gagnon, K. J.; Bendix, J.; Ghosh, A. Platinum corroles. *Chem. Commun.* **2014**, *50* (76), 11093-11096. DOI: 10.1039/c4cc02548b.

(113) Alemayehu, A. B.; M, L. J.; Gagnon, K. J.; Borisov, S. M.; Ghosh, A. Stable Platinum(IV) Corroles: Synthesis, Molecular Structure, and Room-Temperature Near-IR Phosphorescence. *ACS Omega* **2018**, *3* (8), 9360-9368. DOI: 10.1021/acsomega.8b01149.

(114) Brückner, C.; Barta, C. A.; Briñas, R. P.; Bauer, J. A. K. Synthesis and structure of [*meso*-triarylcorrolato]silver(III). *Inorg. Chem.* **2003**, *42* (5), 1673-1680. DOI: 10.1021/ic0261171.

(115) Thomas, K. E.; Alemayehu, A. B.; Conradie, J.; Beavers, C.; Ghosh, A. Synthesis and molecular structure of gold triarylcorroles. *Inorg. Chem.* **2011**, *50* (24), 12844. DOI: 10.1021/ic202023r.

(116) Thomas, K. E.; Beavers, C. M.; Ghosh, A. Molecular Structure of a Gold *β*-Octakis(trifluoromethyl)- *meso* -triarylcorrole: An 85° Difference in Saddling Dihedral Relative to Copper. *Mol. Phys.* **2012**. DOI: 10.1080/00268976.2012.695031.

(117) Thomas, K. E.; Vazquez-Lima, H.; Fang, Y.; Song, Y.; Gagnon, K. J.; Beavers, C. M.; Kadish, K. M.; Ghosh, A. Ligand Noninnocence in Coinage Metal Corroles: A Silver Knife-Edge. *Chem. Eur. J.* **2015**, *21* (47), 16705-16705. DOI: 10.1002/chem.201503939.

(118) Capar, C.; Thomas, K. E.; Ghosh, A. Reductive demetallation of copper corroles: first simple route to free-base octabromocorroles. *J. Porphyr. Phthalocyanines* **2008**, (12), 964-967.

(119) Schweyen, P.; Brandhorst, K.; Wicht, R.; Wolfram, B.; Bröring, M. The Corrole Radical. *Angew. Chem. Int. Ed.***2015**, *54* (28), 8213-8216. DOI: 10.1002/anie.201503624.

(120) Buckley, H. L.; Anstey, M. R.; Gryko, D. T.; Arnold, J. Lanthanide corroles: a new class of macrocyclic lanthanide complexes. *Chem. Commun. (Cambridge, England)* **2013**, *49* (30), 3104. DOI: 10.1039/c3cc38806a.

(121) Ward, A. L.; Buckley, H. L.; Lukens, W. W.; Arnold, J. Synthesis and characterization of thorium(IV) and uranium(IV) corrole complexes. *J. Am. Chem. Soc.* **2013**, *135* (37), 13965. DOI: 10.1021/ja407203s.

(122) Lu, G.; Li, J.; Yan, S.; He, C.; Shi, M.; Zhu, W.; Ou, Z.; Kadish, K. M. Self-assembled organic nanostructures and nonlinear optical properties of heteroleptic corrole–phthalocyanine europium triple-decker complexes. *Dyes Pigm.* **2015**, *121*, 38-45. DOI: 10.1016/j.dyepig.2015.05.008.

(123) Ganguly, S.; Ghosh, A. Seven Clues to Ligand Noninnocence: The Metallocorrole Paradigm. *Acc. Chem. Res* **2019**, *52* (7), 2003-2014. DOI: 10.1021/acs.accounts.9b00115.

(124) Ngo, T. H.; Van Rossom, W.; Dehaen, W.; Maes, W. Reductive demetallation of Cu-corroles - a new protective strategy towards functional free-base corroles. *Org. Biomol. Chem.* **2009**, *7* (3), 439-443. DOI: 10.1039/b819185a.

(125) Mahammed, A.; Botoshansky, M.; Gross, Z. Chlorinated corroles. *Dalton Trans.* **2012**, *41* (36), 10938-10940. DOI: 10.1039/c2dt31261a.

(126) Schweyen, P.; Brandhorst, K.; Wicht, R.; Wolfram, B.; Bröring, M. The Corrole Radical. *Angew. Chem. Int. Ed.* **2015**, *54* (28), 8213-8216. DOI: 10.1002/anie.201503624.

(127) Ooi, S.; Yoneda, T.; Tanaka, T.; Osuka, A. meso-Free Corroles: Syntheses, Structures, Properties, and Chemical Reactivities. *Chem. Eur. J.* **2015**, *21* (21), 7772-7779. DOI: 10.1002/chem.201500894.

(128) Paolesse, R.; Nardis, S.; Sagone, F.; Khoury, R. G. Synthesis and Functionalization of m eso -Aryl-Substituted Corroles. *J. Org. Chem.* **2001**, *66* (2), 550-556. DOI: 10.1021/jo005661t.

(129) Du, R.-B.; Liu, C.; Shen, D.-M.; Chen, Q.-Y. Partial Bromination and Fluoroalkylation of 5,10,15-Tris(pentafluorophenyl)corrole. *Synlett* **2009**, *2009* (16), 2701-2705. DOI: 10.1055/s-0029-1217955. Lemon, C. M.; Huynh, M.; Maher, A. G.; Anderson, B. L.; Bloch, E. D.; Powers, D. C.; Nocera, D. G. Electronic Structure of Copper Corroles. *Angew. Chem. Int. Ed.* **2016**, *55* (6), 2176-2180. DOI: 10.1002/anie.201509099.

(130) Tortora, L.; Nardis, S.; Fronczek, F. R.; Smith, K. M.; Paolesse, R. Functionalization of the corrole ring: the role of isocorrole intermediates. *Chem. Commun. (Camb)* **2011**, *47* (14), 4243-4245. DOI: 10.1039/c0cc05837h.

(131) Vestfrid, J.; Botoshansky, M.; Palmer, J. H.; Durrell, A. C.; Gray, H. B.; Gross, Z. Iodinated aluminum(III) corroles with long-lived triplet excited states. *J. Am. Chem. Soc.* **2011**, *133* (33), 12899. DOI: 10.1021/ja202692b.

(132) Vestfrid, J.; Goldberg, I.; Gross, Z. Tuning the Photophysical and Redox Properties of Metallocorroles by Iodination. *Inorg. Chem.* **2014**, *53* (19), 10536-10542. DOI: 10.1021/ic501585a.

(133) Soll, M.; Sudhakar, K.; Fridman, N.; Müller, A.; Röder, B.; Gross, Z. One-Pot Conversion of Fluorophores to Phosphorophores. *Org. Lett.* **2016**, *18* (22), 5840-5843. DOI: 10.1021/acs.orglett.6b02877.

(134) Thomassen, I. K.; M, L. J.; Ghosh, A. Synthesis and Molecular Structure of a Copper Octaiodocorrole. *ACS Omega* **2018**, *3* (5), 5106-5110. DOI: 10.1021/acsomega.8b00616.

(135) Thomas, K. E.; Settineri, N. S.; Teat, S. J.; Steene, E.; Ghosh, A. Molecular Structure of Copper and μ-Oxodiiron Octafluorocorrole Derivatives: Insights into Ligand Noninnocence. *ACS Omega* **2020**, *5* (17), 10176-10182. DOI: 10.1021/acsomega.0c01035.

(136) Paolesse, R.; Jaquinod, L.; Senge, M. O.; Smith, K. M. Functionalization of Corroles: Formylcorroles. *J. Org. Chem.* **1997**, *62* (18), 6193-6198. DOI: 10.1021/jo9706739.

(137) Paolesse, R.; Nardis, S.; Venanzi, M.; Mastroianni, M.; Russo, M.; Fronczek, F. R.; Vicente, M. G. H. Vilsmeier Formylation of 5,10,15-Triphenylcorrole: Expected and Unusual Products. *Chem. Eur. J.* **2003**, *9* (5), 1192-1197. DOI: 10.1002/chem.200390136.

(138) Saltsman, I.; Mahammed, A.; Goldberg, I.; Tkachenko, E.; Botoshansky, M.; Gross, Z. Selective Substitution of Corroles: Nitration, Hydroformylation, and Chlorosulfonation. *J. Am. Chem. Soc.* **2002**, *124* (25), 7411-7420. DOI: 10.1021/ja025851g.

(139) Sudhakar, K.; Velkannan, V.; Giribabu, L. Synthesis, electrochemical and photophysical properties of β-carboxy triaryl corroles. *Tetrahedron. Lett.* **2012**, *53* (8), 991-993. DOI: 10.1016/j.tetlet.2011.12.068. Sudhakar, K.; Giribabu, L.; Salvatori, P.; Angelis, F. D. Triphenylamine-functionalized corrole sensitizers for solar-cell applications. *Phys. Status Solidi A* **2015**, *212* (1), 194-202. DOI: 10.1002/pssa.201431169.

(140) Saltsman, I.; Goldberg, I.; Gross, Z. One-step conversions of a simple corrole into chiral and amphiphilic derivatives. *Tetrahedron. Lett.* **2003**, *44* (30), 5669-5673. DOI: 10.1016/S0040-4039(03)01356-X.

(141) Mahammed, A.; Gross, Z.; Goldberg, I. Highly selective chlorosulfonation of tris(pentafluorophenyl)corrole as a synthetic tool for the preparation of amphiphilic corroles and metal complexes of planar chirality. *Org. Lett.* **2001**, *3* (22), 3443-3446. DOI: 10.1021/ol0163878.

(142) Gross, Z.; Mahammed, A. Selective sulfonation and deuteration of free-base corrole. *J. Porpyr. Phthalocyanines* **2002**, *06* (09), 553-555.

(143) Mahammed, A.; Gross, Z. Chlorosulfonated Corrole: A Versatile Synthon for Advanced Materials. *J. Porphyr. Phthalocyanines* **2010**, *14*, 911-923.

(144) Stefanelli, M.; Mastroianni, M.; Nardis, S.; Licoccia, S.; Fronczek, F. R.; Smith, K. M.; Zhu, W.; Ou, Z.; Kadish, K. M.; Paolesse, R. Functionalization of Corroles: The Nitration Reaction. *Inorg. Chem.* **2007**, *46* (25), 10791-10799. DOI: 10.1021/ic7014572.

(145) Stefanelli, M.; Pomarico, G.; Tortora, L.; Nardis, S.; Fronczek, F. R.; McCandless, G. T.; Smith, K. M.; Manowong, M.; Fang, Y.; Chen, P.; et al. β-Nitro-5,10,15-tritolylcorroles. *Inorg. Chem.* **2012**, *51* (12), 6928-6942. DOI: 10.1021/ic3007926.

(146) Hiroto, S.; Hisaki, I.; Shinokubo, H.; Osuka, A. Synthesis of Corrole Derivatives through Regioselective Ir-Catalyzed Direct Borylation. *Angew. Chem. Int. Ed.* **2005**, *44* (41), 6763-6766. DOI: 10.1002/anie.200502335.

(147) Barata, J. F.; Silva, A. M.; Faustino, M. A.; Neves, M. G.; Tomé, A. C.; Silva, A. M.; Cavaleiro, J. A. Novel Diels-Alder and Thermal [4+4] Cycloadditions of Corroles. *Synlett* **2004**, *2004* (7), 1291-1293. DOI: 10.1055/s-2004-822916.

(148) Tardieux, C.; Gros, C. P.; Guilard, R. On corrole chemistry. An isomerization study and oxidative cleavage of the corrole macroring to a biliverdin structure. *J. Heterocycl. Chem.* **1998**, *35* (4), 965-970. DOI: 10.1002/jhet.5570350430.

(149) Paolesse, R.; Sagone, F.; Macagnano, A.; Boschi, T.; Prodi, L.; Montalti, M.; Zaccheroni, N.; Bolletta, F.; Smith, K. M. Photophysical Behaviour of Corrole and its Symmetrical and Unsymmetrical Dyads. *J. Porphyr. Phthalocyanines* **1999**, *03* (05), 364-370.

(150) Barata, J. F. B.; Silva, A. M. G.; Neves, M. G. P. M. S.; Tomé, A. C.; Silva, A. M. S.; Cavaleiro, J. A. S. β,β′–Corrole dimers. *Tetrahedron. Lett.* **2006**, *47* (46), 8171-8174. DOI: 10.1016/j.tetlet.2006.09.026.

(151) Hirabayashi, S.; Omote, M.; Aratani, N.; Osuka, A. Directly Linked Corrole Oligomers via Facile Oxidative 3-3' Coupling Reaction. *Bull. Chem. Soc. Jpn.* **2012**, *85* (5), 558-562.

(152) Boschi, T.; Licoccia, S.; Paolesse, R.; Tagliatesta, P.; Tehran, M. A.; Pelizzi, G.; Vitali, F. Synthesis and characterization of novel metal(III) complexes of corrole. Crystal and molecular structure of (2,3,7,8,12,13,17,18-octamethylcorrolato)(triphenylarsine) rhodium(III). *Dalton Trans.* **1990**. DOI: https://doi.org/10.1039/DT9900000463.

(153) Yadav, P.; Sankar, M.; Ke, X.; Cong, L.; Kadish, K. M. Highly reducible pi-extended copper corroles. *Dalton Trans.* **2017**, *46* (30), 10014-10022. DOI: 10.1039/c7dt01814b.

(154) Stefanelli, M.; Ricci, A.; Chiarini, M.; Lo Sterzo, C.; Berionni Berna, B.; Pomarico, G.; Sabuzi, F.; Galloni, P.; Fronczek, F. R.; Smith, K. M.; et al. β-Arylethynyl substituted silver corrole complexes. *Dalton Trans.* **2019**, *48* (36), 13589-13598. DOI: 10.1039/c9dt03166a.

(155) Pomarico, G.; Nardis, S.; Paolesse, R.; Ongayi, O. C.; Courtney, B. H.; Fronczek, F. R.; Vicente, M. G. a. H. Synthetic Routes to 5,10,15-Triaryl-tetrabenzocorroles. *J. Org. Chem.* **2011**, *76* (10), 3765-3773. DOI: 10.1021/jo200026u.

(156) Soret, J. L. Sur la température du Soleil (extrait d'une lettre de M. J.-L. Soret à M. H. Sainte-Claire Deville). *Annales scientifiques de l'École normale supérieure* **1874**, *3*, 435-439. DOI: 10.24033/asens.120.

(157) Gouterman, M. Spectra of porphyrins. *J. Mol. Spec.* **1961**, *6* (C), 138-163. DOI: 10.1016/0022-2852(61)90236-3. Gouterman, M.; Wagnière, G. H.; Snyder, L. C. Spectra of porphyrins: Part II. Four orbital model. *J. Mol. Spec.* **1963**, *11* (1), 108-127. DOI: 10.1016/0022-2852(63)90011-0.

(158) Ghosh, A.; Wondimagegn, T.; Parusel, A. B. J. Electronic Structure of Gallium, Copper, and Nickel Complexes of Corrole. High-Valent Transition Metal Centers versus Noninnocent Ligands. *J. Am. Chem. Soc.* **2000**, *122* (21), 5100-5104. DOI: 10.1021/ja9943243.

(159) Liu, X.; Mahammed, A.; Tripathy, U.; Gross, Z.; Steer, R. P. Photophysics of Soret-excited tetrapyrroles in solution. III. Porphyrin analogues: Aluminum and gallium corroles. *Chem. Phys. Lett.* **2008**, *459* (1), 113-118. DOI: 10.1016/j.cplett.2008.05.038. Kowalska, D.; Liu, X.; Tripathy, U.; Mahammed, A.; Gross, Z.; Hirayama, S.; Steer, R. P. Ground- and Excited-State Dynamics of Aluminum and Gallium Corroles. *Inorg. Chem.* **2009**, *48* (6), 2670-2676. DOI: 10.1021/ic900056n.

(160) Borisov, S. M.; Einrem, R. F.; Alemayehu, A. B.; Ghosh, A. Ambient-temperature near-IR phosphorescence and potential applications of rhenium-oxo corroles. *Photochem. Photobiol. Sci.* **2019**, *18* (5), 1166-1170. DOI: 10.1039/c8pp00473k.

(161) Borisov, S. M.; Alemayehu, A.; Ghosh, A. Osmium-nitrido corroles as NIR indicators for oxygen sensors and triplet sensitizers for organic upconversion and singlet oxygen generation. *J. Mater. Chem. C* **2016**, *4* (24), 5822-5828. DOI: 10.1039/c6tc01126h.

(162) Alemayehu, A. B.; Day, N. U.; Mani, T.; Rudine, A. B.; Thomas, K. E.; Gederaas, O. A.; Vinogradov, S. A.; Wamser, C. C.; Ghosh, A. Gold Tris(carboxyphenyl)corroles as Multifunctional Materials: Room Temperature Near-IR Phosphorescence and Applications to Photodynamic Therapy and Dye-Sensitized Solar Cells. *ACS Appl. Mater. Interfaces* **2016**, *8* (29), 18935-18942. DOI: 10.1021/acsami.6b04269.

(163) Borisov, S. M.; Einrem, R. F.; Alemayehu, A. B.; Ghosh, A. Ambient-temperature near-IR phosphorescence and potential applications of rhenium-oxo corroles. *Photochem. Photobiol. Sci.* **2019**, *18* (5), 1166-1117. DOI: 10.1039/c8pp00473k.

(164) Hemmer, E.; Benayas, A.; Légaré, F.; Vetrone, F. Exploiting the biological windows: current perspectives on fluorescent bioprobes emitting above 1000 nm. *Nanoscale Horiz.* **2016**, *1* (3), 168-184. DOI: 10.1039/c5nh00073d.

(165) Ventura, B.; Esposti, A.; Koszarna, B.; Gryko, D.; Flamigni, L. Photophysical characterization of free-base corroles, promising chromophores for light energy conversion and singlet oxygen generation. *New J. Chem.* **2005**, *29*, 1559-1566.

(166) Shao, W.; Wang, H.; He, S.; Shi, L.; Peng, K.; Lin, Y.; Zhang, L.; Ji, L.; Liu, H. Photophysical Properties and Singlet Oxygen Generation of Three Sets of Halogenated Corroles. *J. Phys. Chem. B* **2012**, *116* (49), 14228-14234. DOI: 10.1021/jp306826p.

(167) Zhao, F.; Zhan, X.; Lai, S.-H.; Zhang, L.; Liu, H.-Y. Photophysical properties and singlet oxygen generation of meso-iodinated free-base corroles. *RSC Adv* **2019**, *9* (22), 12626-12634. DOI: 10.1039/c9ra00928k.

(168) Mahammed, A.; Chen, K.; Vestfrid, J.; Zhao, J.; Gross, Z. Phosphorus corrole complexes: from property tuning to applications in photocatalysis and triplet-triplet annihilation upconversion. *Chem. Sci. (Cambridge)* **2019**, *1* (29), 791-713. DOI: 10.1039/c9sc01463b.

(169) Preuss, A.; Saltsman, I.; Mahammed, A.; Pfitzner, M.; Goldberg, I.; Gross, Z.; Roeder, B. Photodynamic inactivation of mold fungi spores by newly developed charged corroles. *J Photochem Photobiol B* **2014**, *133*, 39-46. DOI: 10.1016/j.jphotobiol.2014.02.013.

(170) Lai, S.-H.; Wang, L.-L.; Wan, B.; Lu, A.-W.; Wang, H.; Liu, H.-Y. Photophysical properties, singlet oxygen generation and DNA binding affinity of Tris(4-pyridyl)corrole and its phosphorous, gallium and tin complexes. *J. Photochem. Photobiol. A.* **2020**, *390*, 112283. DOI: 10.1016/j.jphotochem.2019.112283.

(171) Babu, B.; Prinsloo, E.; Mack, J.; Nyokong, T. Synthesis, characterization and photodynamic activity of Sn() triarylcorroles with red-shifted Q bands. *New J. Chem.* **2019**, *43* (47), 1885-18812. DOI: 10.1039/c9nj03391b.

(172) Dingiswayo, S.; Babu, B.; Prinsloo, E.; Mack, J.; Nyokong, T. A comparative study of the photophysicochemical and photodynamic activity properties of *meso*-4-methylthiophenyl functionalized Sn (IV) tetraarylporphyrins and triarylcorroles. *J. Porphyr. Phthalocyanines* **2020**. DOI: 10.1142/S1088424620500273".

(173) Castro, M. C. R.; Sedrine, N. B.; Monteiro, T.; Machado, A. V. Iridium(III)porphyrin arrays with tuneable photophysical properties. *Spectrochim. Acta. A,* **2020**, *235*, 118309. DOI: 10.1016/j.saa.2020.118309.

(174) Jana, A.; McKenzie, L.; Wragg, A. B.; Ishida, M.; Hill, J. P.; Weinstein, J. A.; Baggaley, E.; Ward, M. D. Porphyrin/Platinum(II) C^N^N Acetylide Complexes: Synthesis, Photophysical Properties, and Singlet Oxygen Generation. *Chem. Eur. J.* **2016**, *22* (12), 4164-4174. DOI: 10.1002/chem.201504509.

(175) Einrem, R. F.; Alemayehu, A. B.; Borisov, S. M.; Ghosh, A.; Gederaas, O. A. Amphiphilic Rhenium-Oxo Corroles as a New Class of Sensitizers for Photodynamic Therapy. *ACS Omega* **2020**, *5* (18), 10596-10601. DOI: 10.1021/acsomega.0c01090.

(176) Borisov, S. M.; Alemayehu, A.; Ghosh, A. Osmium-nitrido corroles as NIR indicators for oxygen sensors and triplet sensitizers for organic upconversion and singlet oxygen generation. *J. Mater. Chem. C.* **2016**, *4* (24), 5822-5828. DOI: 10.1039/c6tc01126h.

(177) Sinha, W.; Ravotto, L.; Ceroni, P.; Kar, S. NIR-emissive iridium(III) corrole complexes as efficient singlet oxygen sensitizers. *Dalton Trans.* **2015**, *44* (40), 17767-17773. DOI: 10.1039/c5dt03041b.

(178) Tong, K.-C.; Hu, D.; Wan, P.-K.; Lok, C.-N.; Che, C.-M. Anticancer Gold(III) Compounds With Porphyrin or *N*-heterocyclic Carbene Ligands. *Frontiers Chem.* **2020**, *8*, 587207-587207. DOI: 10.3389/fchem.2020.587207.

(179) Aviezer, D.; Cotton, S.; David, M.; Segev, A.; Khaselev, N.; Galili, N.; Gross, Z.; Yayon, A. Porphyrin analogues as novel antagonists of fibroblast growth factor and vascular endothelial growth factor receptor binding that inhibit endothelial cell proliferation, tumor progression, and metastasis. *Cancer Res.* **2000**, *60* (11), 2973.

(180) Lim, P.; Mahammed, A.; Okun, Z.; Saltsman, I.; Gross, Z.; Gray, H. B.; Termini, J. Differential Cytostatic and Cytotoxic Action of Metallocorroles against Human Cancer Cells: Potential Platforms for Anticancer Drug Development. *Chem. Res. Toxicol.* **2012**, *25* (2), 400-409. DOI: 10.1021/tx200452w.

(181) Zhang, Z.; Wen, J. Y.; Lv, B. B.; Li, X.; Ying, X.; Wang, Y. J.; Zhang, H. T.; Wang, H.; Liu, H. Y.; Chang, C. K. Photocytotoxicity and G-quadruplex DNA interaction of water-soluble gallium(III) tris(N-methyl-4-pyridyl)corrole complex. *Appl. Org. Chem.* **2016**, *30* (3), 132-139. DOI: 10.1002/aoc.3408.

(182) Mahammed, A.; Gray, H. B.; Weaver, J. J.; Sorasaenee, K.; Gross, Z. Amphiphilic Corroles Bind Tightly to Human Serum Albumin. *Bioconjugate Chem.* **2004**, *15* (4), 738-746. DOI: 10.1021/bc034179p.

(183) Agadjanian, H.; Weaver, J. J.; Mahammed, A.; Rentsendorj, A.; Bass, S.; Kim, J.; Dmochowski, I. J.; Margalit, R.; Gray, H. B.; Gross, Z.; et al. Specific delivery of corroles to cells via noncovalent conjugates with viral proteins. *Pharm. Res.* **2006**, *23* (2), 367-377. DOI: 10.1007/s11095-005-9225-1.

(184) Sun, S.; Han, Y.; Liu, J.; Fang, Y.; Tian, Y.; Zhou, J.; Ma, D.; Wu, P. Trichostatin A Targets the Mitochondrial Respiratory Chain, Increasing Mitochondrial Reactive Oxygen Species Production to Trigger Apoptosis in Human Breast Cancer Cells. *PLoS One.* **2014**, *9* (3), e91610-e91610. DOI: 10.1371/journal.pone.0091610.

(185) Gorman, A. M.; McGowan, A.; O'Neill, C.; Cotter, T. Oxidative stress and apoptosis in neurodegeneration. *J. Neurol. Sci.* **1996**, *139* (suppl), 45-52. DOI: 10.1016/0022-510X(96)00097-4.

(186) Kupershmidt, L.; Okun, Z.; Amit, T.; Mandel, S.; Saltsman, I.; Mahammed, A.; Bar-Am, O.; Gross, Z.; Youdim, M. B. H. Metallocorroles as cytoprotective agents against oxidative and nitrative stress in cellular models of neurodegeneration. *J. Neurochem.* **2010**, *113* (2), 363-373. DOI: 10.1111/j.1471-4159.2010.06619.x.

(187) Sun, Y.-M.; Jiang, X.; Liu, Z.-Y.; Liu, L.-G.; Liao, Y.-H.; Zeng, L.; Ye, Y.; Liu, H.-Y. Hydroxy-corrole and its gallium(III) complex as new photosensitizer for photodynamic therapy against breast carcinoma. *Eur. J. Med. Chem.* **2020**, *208*, 112794-112794. DOI: 10.1016/j.ejmech.2020.112794.

(188) Fan, C.; Wang, H.-H.; Ali, A.; Kandhadi, J.; Wang, H.; Wang, X.-L.; Liu, H.-Y. Photophysical properties and photodynamic anti-tumor activity of corrole-coumarin dyads. *J. Porphyr. phthalocyanines* **2018**, *22* (10), 886-898. DOI: https://doi.org/10.1142/S1088424618500724.

(189) Wang, Y.-G.; Zhang, Z.; Wang, H.; Liu, H.-Y. Phosphorus(V) corrole: DNA binding, photonuclease activity and cytotoxicity toward tumor cells. *Bioorg. Chem.* **2016**, *67*, 57-63. DOI: 10.1016/j.bioorg.2016.05.007.

(190) Alemayehu, A. B.; Day, N. U.; Mani, T.; Rudine, A. B.; Thomas, K. E.; Gederaas, O. A.; Vinogradov, S. A.; Wamser, C. C.; Ghosh, A. Gold Tris(carboxyphenyl)corroles as Multifunctional Materials: Room Temperature Near-IR Phosphorescence and Applications to Photodynamic Therapy and Dye-Sensitized Solar Cells. *ACS Appl. Mater. Interfaces* **2016**, *8* (29), 18935-18942. DOI: 10.1021/acsami.6b04269.

(191) Einrem, R. F.; Braband, H.; Fox, T.; Vazquez-Lima, H.; Alberto, R.; Ghosh, A. Synthesis and Molecular Structure of ^{99}Tc Corroles. *Chem Eur. J.* **2016**. DOI: 10.1002/chem.201605015.

(192) Higashino, T.; Kurumisawa, Y.; Alemayehu, A. B.; Einrem, R. F.; Sahu, D.; Packwood, D.; Kato, K.; Yamakata, A.; Ghosh, A.; Imahori, H. Heavy Metal Effects on the Photovoltaic Properties of Metallocorroles in Dye-Sensitized Solar Cells. *ACS Appl. Energy Mater.* **2020**, *3* (12), 12460-12467. DOI: 10.1021/acsaem.0c02427.

(193) Alemayehu, A. B.; Einrem, R. F.; McCormick-McPherson, L. J.; Settineri, N. S.; Ghosh, A. Synthesis and molecular structure of perhalogenated rhenium-oxo corroles. *Sci. Rep.* **2020**, *10* (1), 19727-19727. DOI: 10.1038/s41598-020-76308-7.

(194) Einrem, R. F.; Jonsson, E. T.; Teat, S. J.; Settineri, N. S.; Alemayehu, A. B.; Ghosh, A. Regioselective formylation of rhenium-oxo and gold corroles: substituent effects on optical spectra and redox potentials. *RSC Adv.* **2021**, *11* (54), 3486-3494. DOI: 10.1039/d1ra05525a.

(195) Monteiro, A. R.; Neves, M. G. P. M. S.; Trindade, T. Functionalization of Graphene Oxide with Porphyrins: Synthetic Routes and Biological Applications. *ChemPlusChem* **2020**, *85* (8), 1857-1880. DOI: 10.1002/cplu.202000455.

(196) Montaseri, H.; Kruger, C. A.; Abrahamse, H. Recent Advances in Porphyrin-Based Inorganic Nanoparticles for Cancer Treatment. *Int. J. Mol. Sci.* **2020**, *21* (9), 3358. DOI: 10.3390/ijms21093358.

(197) Thomassen, I. K.; Rasmussen, D.; Einrem, R. F.; Ghosh, A. Simple, Axial Ligand-Mediated Route to Water-Soluble Iridium Corroles. *ACS Omega* **2021**, *6* (25), 16683-16687. DOI: 10.1021/acsomega.1c02399.

(198) Merchat, M.; Bertolini, G.; Giacomini, P.; Villaneuva, A.; Jori, G. Meso-substituted cationic porphyrins as efficient photosensitizers of gram-positive and gram-negative bacteria. *J Photochem. Photobiol. B.* **1996**, *32* (3), 153-157. DOI: 10.1016/1011-1344(95)07147-4.

Paper A

Photochemical & Photobiological Sciences

PAPER

Cite this: *Photochem. Photobiol. Sci.*, 2019, **18**, 1166

Ambient-temperature near-IR phosphorescence and potential applications of rhenium-oxo corroles†

Sergey M. Borisov, *[a] Rune F. Einrem,[b] Abraham B. Alemayehu[b] and Abhik Ghosh *[b]

Received 22nd October 2018,
Accepted 18th February 2019
DOI: 10.1039/c8pp00473k
rsc.li/pps

Presented herein is a first photophysical investigation of a series of rhenium(v)-oxo tris(*p*-X-phenyl)corroles, Re[T*p*XPC](O), where X = CF_3, F, H, CH_3, and OCH_3. The complexes all exhibit near-IR phosphorescence in anoxic toluene at room temperature, with emission maxima at 780 ± 10 nm, phosphorescence decay times of 56–74 μs and quantum yields of 1.07–1.52%, the highest reported to date for phosphorescent corrole derivatives. We have also demonstrated that the dyes may serve as indicators in optical oxygen sensors and as sensitizers in triplet–triplet-annihilation-based upconversion. Although the ReO corroles are not superior to benchmark benzoporphyrin complexes that are currently used in these applications, they may prove useful in certain areas such as optical multianalyte sensing owing to improved flexibility in the available spectral properties of the dyes. The high thermal and photochemical stability of the complexes also bodes well for their deployment as new, phosphorescent sensitizers in photodynamic therapy.

Introduction

Dyes exhibiting room temperature phosphorescence enjoy a wide range of applications – as emitters in OLEDs,[1] as probes for sensing and imaging,[2,3] and as sensitizers for triplet–triplet annihilation upconversion (TTAU).[4,5] Particularly attractive is a combination of near-infrared (NIR) emission and absorption in the red, which allows for *in vivo* sensing of oxygen and glucose as well as for photon upconversion systems capable of harvesting red light.[6] The various classes of 5d metallocorroles recently synthesized in our laboratory[7–11] and elsewhere[12,13] are of considerable interest in this regard.[14] In spite of the steric mismatch between the large 5d transition metal ion and the sterically constrained N_4 cavity of the corrole, the great majority of these complexes exhibit impressive thermal and photochemical stability. To date, room-temperature near-IR phosphorescence has been documented for OsN,[15] Ir,[16,17] Pt,[18] and Au[19,20] corroles. Of these, OsN corroles have been investigated as oxygen sensors and as sensitizers for TTAU,[15] while Au corroles have also been studied as photosensitizers for photodynamic therapy and dye-sensitized solar cells.[19] Herein we document room temperature near-IR phosphorescence for a series of rhenium(v)-oxo tris(*p*-X-phenyl)corroles, Re[T*p*XPC](O) (Chart 1) as well as an evaluation of one of the complexes (X = CF_3) *vis-à-vis* oxygen sensing and TTAU.

Results and discussion

Photophysical properties

The photophysical properties were investigated with toluene as solvent (Table 1). As is typical of electronically "innocent"

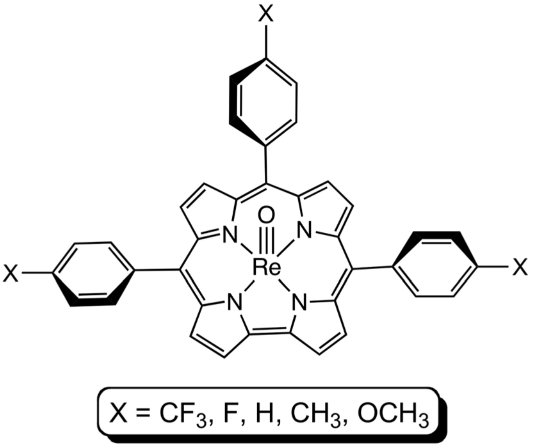

Chart 1 Molecules studied in this work.

---

[a] *Institute of Analytical Chemistry and Food Chemistry, Graz University of Technology, Stremayrgasse 9, 8010 Graz, Austria. E-mail: sergey.borisov@tugraz.at*
[b] *Department of Chemistry, UiT, The Arctic University of Norway, N-9037 Tromsø, Norway. E-mail: abhik.ghosh@uit.no, rune.einrem@uit.no, abraham.alemayehu@uit.no*

† Electronic supplementary information (ESI) available. See DOI: 10.1039/c8pp00473k

Table 1 Photophysical properties of ReO corroles in anoxic toluene at 23 °C

Compound	Absorbance maxima (nm)			Emission maximum[a] (nm)	Lifetime (μs)	Rel. quantum yield (%)
	Soret	Q	Q			
Re[T*p*MePC](O)	442	556	588	782	64	1.07
Re[TPC](O)	440	554	586	770	60	1.15
Re[T*p*CF$_3$PC](O)	440	553	586	777	74	1.52
Re[T*p*FPC](O)	440	554	586	775	70	1.19
Re[T*p*OMePC](O)	443	557	590	788	56	1.07
Pt[TPTBP][b]	430	564	614	770	48	21
Os[T*p*CF$_3$PC](N)[c]	444	553	593	771	183	0.39
Pt^{IV}[T*p*CF$_3$PC](*m*-C$_6$H$_4$CN)(py)[d]	430	569	595	813	23	0.27

[a] λ_{ex} 590 nm. [b] Pt[TPTBP] was used as the reference for quantum yield measurements.[21] [c] Ref. 15. [d] Ref. 18.

metallotriarylcorroles, the UV-vis spectra of the complexes are relatively invariant with respect to the *meso*-aryl *para* substituent (Table 1 and Fig. S1–S12†).[14] They exhibit moderate NIR phosphorescence (Fig. 1 and Fig. S9–S12†), which is only slightly affected by the *meso* substituent (Table 1). As for Au[19] and OsN[15] triarylcorroles, electron-donating *para* substituents result in a small bathochromic shift of the emission spectra. The excitation spectra (Fig. 1 and Fig. S5–S8†) are identical to the absorption spectra (Fig. 1 and Fig. S1–S4†). Notably, only phosphorescence but no fluorescence has been detected. Considering that metal-free corroles are fluorescent, this fact indicates highly efficient inter-system crossing in ReO corroles.

The phosphorescence lifetimes (obtained with a pulsed LED in time domain mode, Fig. S13 and S14†) vary from 56 to 74 μs (Table 1). The luminescence quantum yields, determined relative to the Pt(II) tetraphenyltetrabenzoporpyhrin (Pt[TPTBP]),[21] are about 1.0–1.5% (Table 1), ranging from 1.07 for X = Me and MeO to 1.52 for X = CF$_3$. These quantum yields are 2–3 times those of osmium(VI)-nitrido[15] corroles and 5–6 times those of platinum(IV)-aryl[18] corroles, which have been measured under identical conditions (Table 1). The moderate quantum yields notwithstanding, the ReO corroles examined here appear to be the most strongly phosphorescent metallocorrole emitters reported to date. The photostability of the dyes was found to be excellent (Fig. S15–S19†) with no detectable photobleaching after 1 h irradiation with a high power 590 nm LED array (irradiance 1600 W m^{-2}).

Oxygen sensing

Although a large number of oxygen indicators that are excitable in the UV, blue, and green parts of the electromagnetic spectrum are available,[2,3,6] there are relatively few indicators that can be excited with orange-red light and emit in the NIR part of the spectrum. To demonstrate the potential use of ReO corroles for optical oxygen sensing, we embedded one of them – Re[T*p*CF$_3$PC](O) – into polystyrene, which we chose as a model polymer matrix. The oxygen-dependent phosphorescence of the corrole was read out with a compact fiber-optic fluorometer (Firesting-mini, PyroScience) modified with a 590 nm LED to enable excitation within the Q-band. As shown in Fig. 2, the embedded corrole behaves much like other oxygen indicators embedded into polystyrene. The Stern–Volmer plots are not-linear and can be fit from an equation

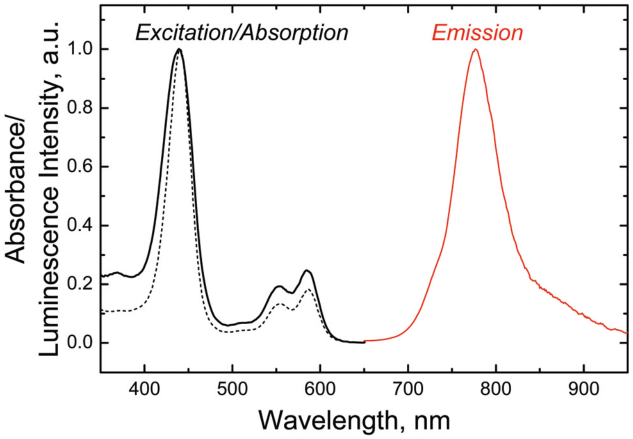

Fig. 1 Absorption (black dashed line), phosphorescence excitation (black solid line; λ_{em} 775 nm) and emission (red line; λ_{exc} 590 nm) spectra of Re[T*p*CF$_3$PC](O) in toluene. Phosphorescence spectra were measured in anoxic conditions.

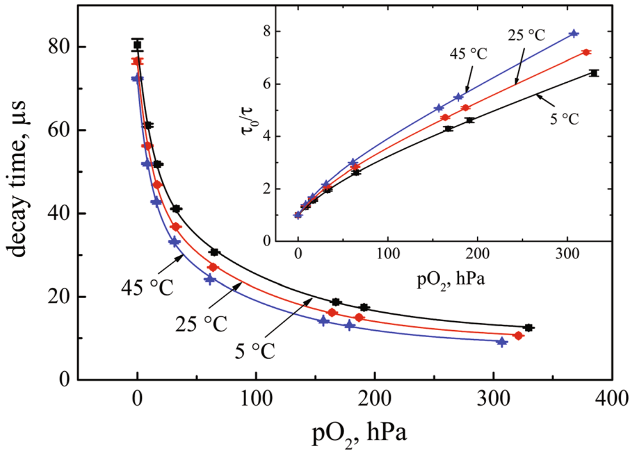

Fig. 2 Decay time and Stern–Volmer plots (inset) for the oxygen sensor based on Re[T*p*CF$_3$PC](O) embedded into polystyrene.

derived from a so-called "two-site model" that assumes localization of the dye in two different environments:[22]

$$\frac{I}{I_0} = \frac{\tau}{\tau_0} = \frac{f}{1 + K_{\mathrm{SV}}^1 [\mathrm{O_2}]} + \frac{1-f}{1 + K_{\mathrm{SV}}^2 [\mathrm{O_2}]}, \tag{1}$$

where f is the fraction of the total emission for the first microenvironment, and K_{SV}^1 and K_{SV}^2 are the Stern–Volmer constants for each component. Although the equation is not physically meaningful for the decay time plots, it fits them almost ideally (Fig. 2, inset). The fit parameters for different temperatures are reported in the ESI (Table S1,† where K_{SV}^2 has been expressed as $K_{\mathrm{SV}}^1 \cdot m$, m being a constant).

Both the decay time in the absence of oxygen (τ_0) and the Stern–Volmer constant (K_{SV}^1, *i.e.* the sensitivity of the material) were found to be temperature-dependent and to slightly decrease and increase, respectively, with temperature (Table S1 and Fig. S22†). The dynamic range of the sensor is from 0.4 to 400 hPa O_2, consistent with the τ_0 value of the indicator and the permeability of the matrix. Measurements up to oxygen-saturated conditions are possible (Fig. S20 and S21†) but the signal-to-noise ratio decreases due to strong quenching of the luminescence intensity (>10 fold) at high pO_2. Although the new dyes are inferior to the benchmark NIR indicators based on benzoporphyrins in respect to the luminescence brightness,[21] they may still be useful for some applications where some flexibility of spectral properties is of primary importance (*e.g.* multi-parameter optical sensors). Particularly, excitation between 520 and 600 nm combined with NIR emission may be beneficial for these applications.

Triplet–triplet annihilation upconversion

The efficient population of the triplet state in many porphyrinoid systems allows for their use as TTAU sensitizers. The mechanism of TTAU involves the excitation of a sensitizer with the light of lower energy, triplet–triplet energy transfer to an annihilator and subsequent TTA resulting in the annihilator's higher energy fluorescence (Fig. S23†). The NIR phosphorescence of ReO corroles suggests that the intersystem crossing is very efficient in these complexes. Additionally, relatively long phosphorescence decay times (>50 μs) enable efficient quenching of the triplet state by annihilator molecules. The suitability of ReO corroles as TTAU sensitizers was investigated with Re[T*p*CF$_3$PC](O) as a model compound; the results are expected to be similar for the other ReO corroles. For an acceptor, we used Solvent green 5,[23] which is a perylene dye with suitable spectral properties (emission in the green part of the spectrum (Fig. S24†) and high fluorescence quantum yields) and triplet state energy. The evaluation of ReO corroles as sensitizers is complicated owing to the absence of laser diodes covering the spectral region corresponding to the lowest-energy Q band. Accordingly, we used the Xe lamp of a fluorometer as the excitation source, setting the excitation wavelength to 590 ± 7 nm. Although the irradiance was only about 22.3 W m^{-2}, which is about 50 times lower than the maximum solar irradiance on the Earth's surface, the upconverted emission from the perylene dye was clearly visible in the emission spectrum (Fig. 3). Comparison with Pt[TPTBP], a benchmark sensitizer for the upconversion,[24–30] revealed a slightly lower upconversion efficiency for the ReO corrole, the upconversion quantum yields being 0.16 and 0.24% for Re[T*p*CF$_3$PC](O) and Pt[TPTBP], respectively. We may thus conclude that the ReO corrole is a viable sensitizer for TTAU covering the orange part of the electromagnetic spectrum.

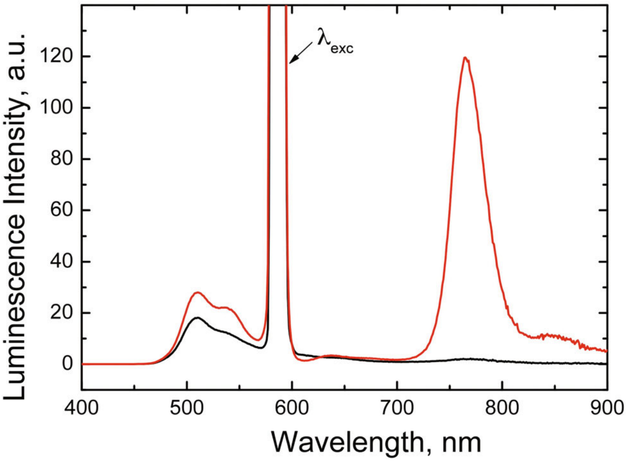

Fig. 3 Luminescence spectra (λ_{exc} 590 ± 7 nm) of solutions containing 1 × 10^{-4} M of the sensitizer, Re[T*p*CF$_3$PC](O) (black) or Pt[TPTBP] (red), and 5 × 10^{-4} M of the annihilator (Solvent green 5) in anoxic toluene.

Conclusion

An investigation of the photophysical properties of a series of ReO corroles has revealed fairly efficient NIR phosphorescence of these dyes at room temperature. The phosphorescence decay times in anoxic toluene solution vary between 56 and 74 μs and become longer upon immobilization in polystyrene. Although the emission quantum yields are not unusually high in absolute terms (1.07–1.52%), they are the highest reported to date for phosphorescent corrole derivatives. We also demonstrated application of one of the complexes as an indicator in an optical oxygen sensor and as a sensitizer in triplet–triplet annihilation-based upconversion, where the ReO corroles are able to efficiently collect light in the yellow-orange part of the spectrum. Although the present dyes are not superior to the benchmark benzoporphyrin complexes currently used for these applications, they are likely to prove useful in certain applications such as optical multianalyte sensors on account of their excellent photostability. Finally, like their gold analogues,[19] amphiphilic ReO corroles are likely to prove useful as sensitizers in photodynamic therapy, an area we hope to address in the near future.

Experimental section

Photophysical measurements

All compounds were prepared as previously described.[11] Absorption spectra were acquired on a Cary 50 UV-vis spectrophotometer (Varian) and emission spectra on a Fluorolog 3 fluorescence spectrometer from Horiba (Japan) equipped with a NIR-sensitive photomultiplier R2658 from Hamamatsu (Japan). All spectra were corrected for the sensitivity of the photomultiplier. Relative luminescence quantum yields were measured using platinum(II) tetraphenyltetrabenzoporphyrin (Pt[TPTBP]) as a standard, for which a quantum yield of 21% has been determined in anoxic toluene.[21] This value is different from that reported earlier (51%)[31] and used for calculating the quantum yields of OsN corroles.[15] A corrected value for an OsN corrole has accordingly been included in Table 1 for comparison with the present results. The solutions in a sealable quartz cell (Hellma Analytics, Mülheim, Germany) were deoxygenated by bubbling high purity nitrogen or argon (6.0 and 5.0, respectively, Linde gas, Austria) for at least 15 min. Luminescence decay times in solution were measured on the Fluorolog 3 spectrometer equipped with a DeltaHub module (Horiba Scientific) controlling a SpectraLED-456 (λ = 456 nm) and using DAS-6 Analysis software for data analysis.

The photostability of the dyes was evaluated *via* their UV-Vis spectra following irradiation of air-saturated toluene solutions with a high power 590 nm LED array (12 high power LEDs, OSRAM Oslon, http://www.led-tech.de) equipped with a lens condenser to achieve maximum light intensity. Photon flux was measured with a Li-250A light meter from Li-COR (http://www.licor.com).

Preparation and characterization of oxygen sensors

The metallocorrole (Re[T*p*CF$_3$PC](O), 1 mg), polystyrene (MW 250 000, Acros, 100 mg), and lipophilic titanium dioxide (Kemira, 100 mg) were dissolved and/or dispersed in chloroform (1.2 g). The resulting slurry was knife-coated onto a polyethylene terephthalate support (wet film thickness 75 µm), which was then dried in an oven at 60 °C for 3 h. Phosphorescence decay times were measured with a compact phase Firesting-mini fluorometer from PyroScience, modified with a yellow 590 nm LED for excitation into the corrole Q band. The modulation frequency was 3 kHz. A 4 mm piece of the sensor foil was glued to the distal end of the plastic fiber connected to the Firesting-mini. The gas composition was adjusted with mass flow-through controllers from MKS Instruments by mixing nitrogen (99.999%), oxygen (99.999%), and compressed air. The gas mixtures were bubbled through a water-filled glass flask containing the sensor as well as a reference oxygen sensor acquired from PyroScience used to determine the actual oxygen partial pressure produced by the gas-mixing device. The temperature was controlled with a ThermoHaake K10 cryostat.

Triplet–triplet annihilation upconversion

Triplet–triplet annihilation upconversion was studied on the Fluorolog 3 fluorometer. Anoxic toluene solutions containing 1×10^{-4} M of the sensitizer and 5×10^{-4} M of the annihilator Solvent Green 5 were excited at 590 nm (14 nm slits) with spectral acquisition in the front face mode. Photon flux was measured with a Li-250A light meter.

Conflicts of interest

The authors declare no competing financial interests.

Acknowledgements

This work was supported by NANO2021 grant no. 262229 of the Research Council of Norway (AG).

References

1 L. Xiao, Z. Chen, B. Qu, J. Luo, S. Kong, Q. Gong and J. Kido, *Adv. Mater.*, 2011, **23**, 926–952.

2 X. Wang and O. S. Wolfbeis, *Chem. Soc. Rev.*, 2014, **43**, 3666–3761.

3 M. Quaranta, S. M. Borisov and I. Klimant, *Bioanal. Rev.*, 2012, **4**, 115–157.

4 J. Zhao, W. Wu, J. Sun and S. Guo, *Chem. Soc. Rev.*, 2013, **42**, 5323–5351.

5 J. Zhou, Q. Liu, W. Feng, Y. Sun and F. Li, *Chem. Rev.*, 2015, **115**, 395–465.

6 E. Roussakis, Z. Li, A. J. Nichols and C. L. Evans, *Angew. Chem., Int. Ed.*, 2015, **54**, 8340–8362.

7 A. B. Alemayehu and A. Ghosh, *J. Porphyrins Phthalocyanines*, 2011, **15**, 106–110.

8 K. E. Thomas, A. B. Alemayehu, J. Conradie, C. Beavers and A. Ghosh, *Inorg. Chem.*, 2011, **50**, 12844–12851.

9 A. B. Alemayehu, H. Vazquez-Lima, C. M. Beavers, K. J. Gagnon, J. Bendix and A. Ghosh, *Chem. Commun.*, 2014, **50**, 11093–11096.

10 A. B. Alemayehu, K. J. Gagnon, J. Terner and A. Ghosh, *Angew. Chem., Int. Ed.*, 2014, **53**, 14411–14414.

11 R. F. Einrem, K. J. Gagnon, A. B. Alemayehu and A. Ghosh, *Chem. – Eur. J.*, 2016, **22**, 517–520.

12 J. H. Palmer, M. W. Day, A. D. Wilson, L. M. Henling, Z. Gross and H. B. Gray, *J. Am. Chem. Soc.*, 2008, **130**, 7786–7787.

13 E. Rabinovitch, I. Goldberg and Z. Gross, *Chem. – Eur. J.*, 2011, **17**, 12294–12301.

14 A. Ghosh, *Chem. Rev.*, 2017, **117**, 3798–3881.

15 S. M. Borisov, A. Alemayehu and A. Ghosh, *J. Mater. Chem. C*, 2016, **4**, 5822–5828.

16 J. H. Palmer, A. C. Durrell, Z. Gross, J. R. Winkler and H. B. Gray, *J. Am. Chem. Soc.*, 2010, **132**, 9230–9231.

17 W. Sinha, L. Ravotto, P. Ceroni and S. Kar, *Dalton Trans.*, 2015, **44**, 17767–17773.

18 A. B. Alemayehu, L. J. McCormick, K. J. Gagnon, S. M. Borisov and A. Ghosh, *ACS Omega*, 2018, **3**, 9360–9368.

19 A. B. Alemayehu, N. U. Day, T. Mani, A. B. Rudine, K. E. Thomas, O. A. Gederaas, S. A. Vinogradov, C. C. Wamser and A. Ghosh, *ACS Appl. Mater. Interfaces*, 2016, **8**, 18935–18942.

20 C. M. Lemon, D. C. Powers, P. J. Brothers and D. G. Nocera, *Inorg. Chem.*, 2017, **56**, 10991–10997.

21 P. W. Zach, S. A. Freunberger, I. Klimant and S. M. Borisov, *ACS Appl. Mater. Interfaces*, 2017, **9**, 38008–38023.

22 E. R. Carraway, J. N. Demas, B. A. DeGraff and J. R. Bacon, *Anal. Chem.*, 1991, **63**, 337–342.

23 G. Seybold and G. Wagenblast, *Dyes Pigm.*, 1989, **11**, 303–317.

24 T. N. Singh-Rachford and F. N. Castellano, Supra-Nanosecond Dynamics of a Red-to-Blue Photon Upconversion System, *Inorg. Chem.*, 2009, **48**, 2541–2548.

25 T. N. Singh-Rachford and F. N. Castellano, *J. Phys. Chem. Lett.*, 2010, **1**, 195–200.

26 S. T. Roberts, C. W. Schlenker, V. Barlier, R. E. McAnally, Y. Zhang, J. N. Mastron, M. E. Thompson and S. E. Bradforth, *J. Phys. Chem. Lett.*, 2011, **2**, 48–54.

27 Z. Jiang, M. Xu, F. Li and Y. Yu, *J. Am. Chem. Soc.*, 2013, **135**, 16446–16453.

28 J.-H. Kim, F. Deng, F. N. Castellano and J.-H. Kim, *ACS Photonics*, 2014, **1**, 382–388.

29 C. Mongin, J. H. Golden and F. N. Castellano, *ACS Appl. Mater. Interfaces*, 2016, **8**, 24038–24048.

30 B. Tian, Q. Wang, Q. Su, W. Feng and F. Li, *Biomaterials*, 2017, **112**, 10–19.

31 S. M. Borisov, G. Nuss, W. Haas, R. Saf, M. Schmuck and I. Klimant, *J. Photochem. Photobiol., A*, 2009, **201**, 128–135.

Ambient-temperature near-IR phosphorescence and potential applications of rhenium-oxo corroles[1]

Sergey M. Borisov,*[,a] Rune F. Einrem,[b] Abraham B. Alemayehu,[b] and Abhik Ghosh*[,b]

[a]Institute of Analytical Chemistry and Food Chemistry, Graz University of Technology,
Stremayrgasse 9, 8010 Graz, Austria; Email: sergey.borisov@tugraz.at.
[b]Department of Chemistry, UiT – The Arctic University of Norway, N-9037 Tromsø,
Norway; Email: abhik.ghosh@uit.no.

---

[1] Electronic supplementary information (ESI) available

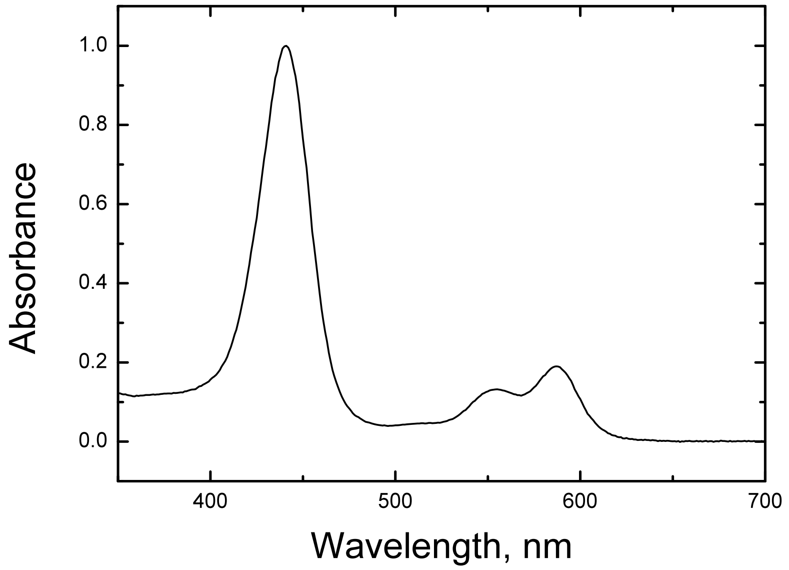

Figure S1. Absorption spectrum of Re[TPC](O) in toluene.

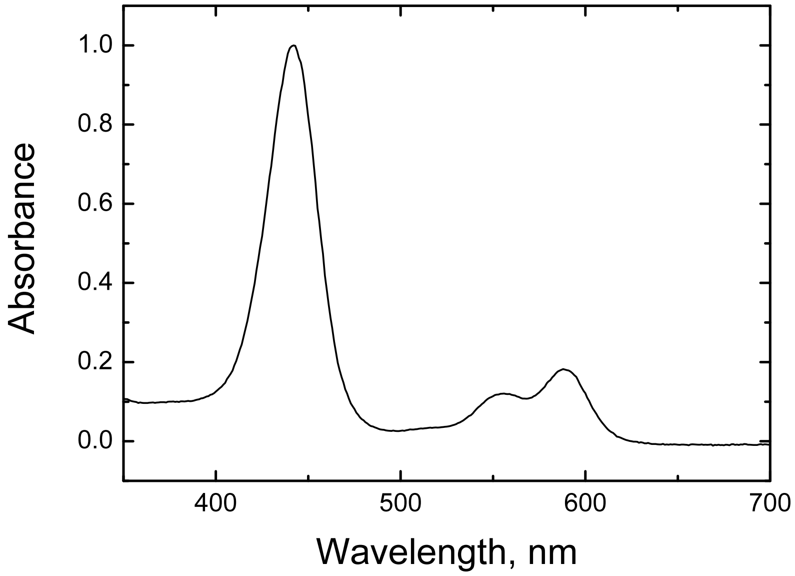

Figure S2. Absorption spectrum of Re[T*p*MePC](O) in toluene.

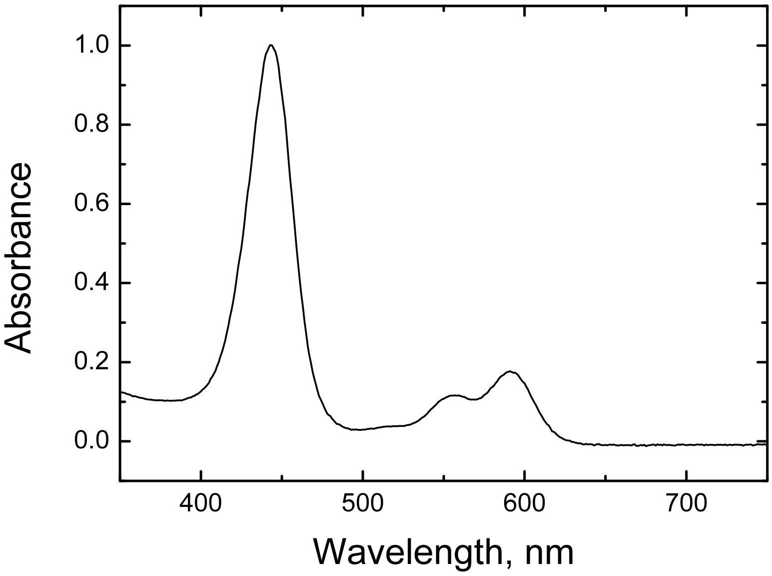

Figure S3. Absorption spectrum of Re[T*p*OMePC](O) in toluene.

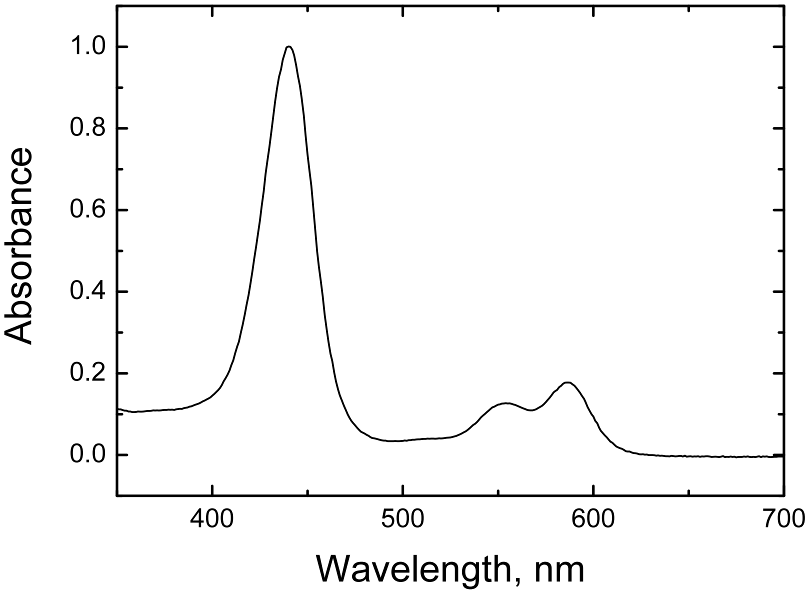

Figure S4. Absorption spectrum of Re[T*p*FPC](O) in toluene.

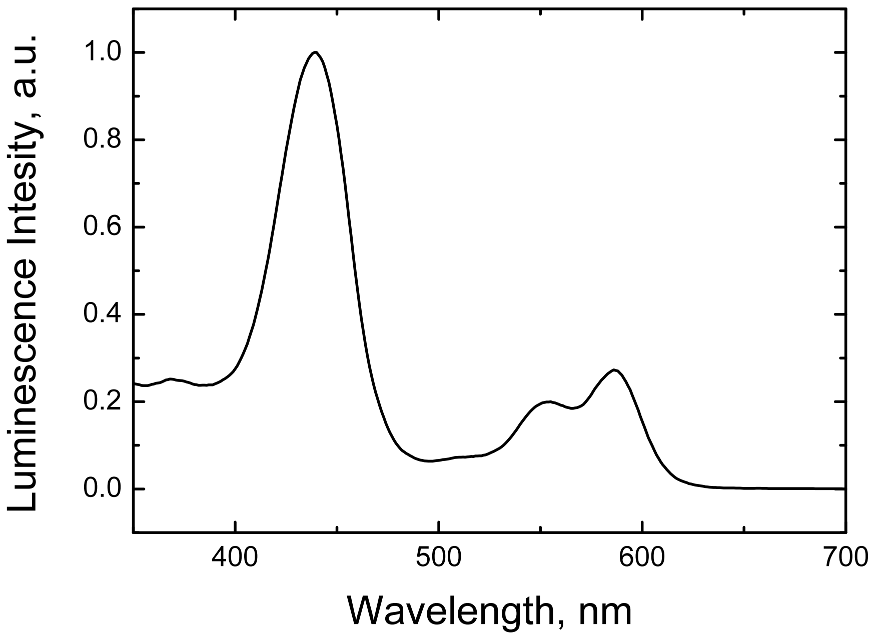

Figure S5. Excitation spectrum of Re[TPC](O) in anoxic toluene (λ_{em} = 770 nm).

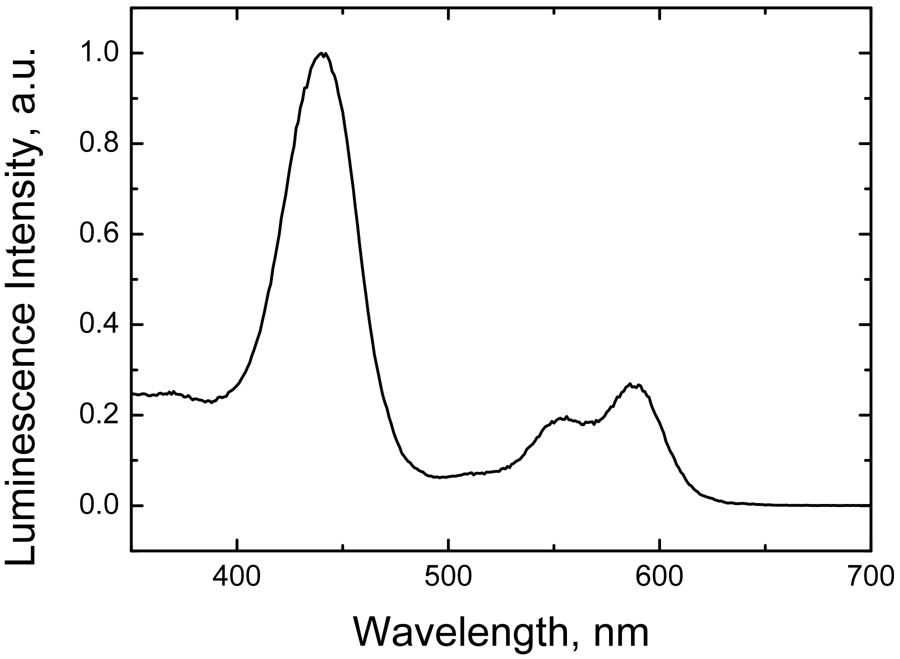

Figure S6. Excitation spectrum of Re[T*p*MePC](O) in anoxic toluene (λ_{em} = 770 nm).

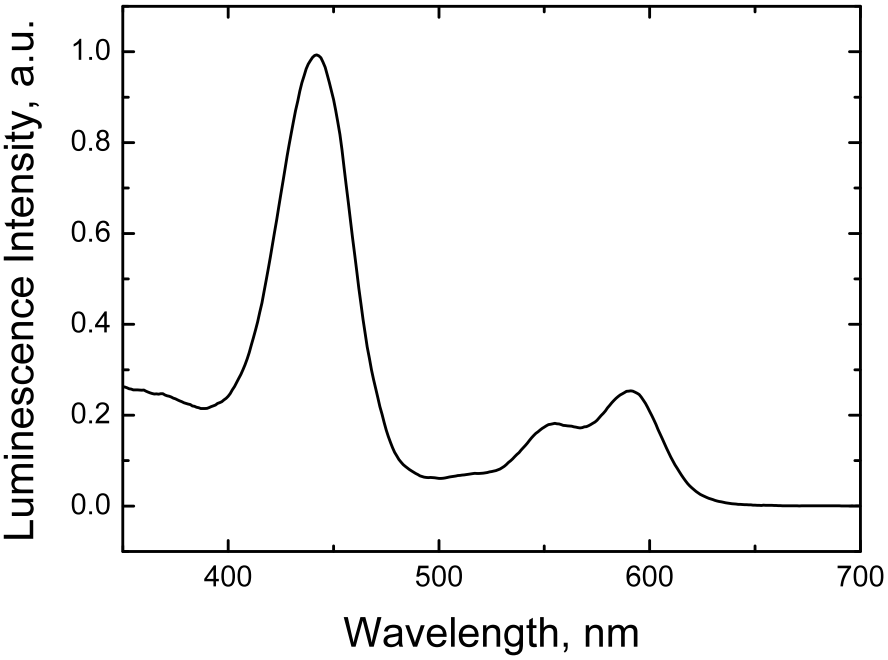

Figure S7. Excitation spectrum of Re[T*p*OMePC](O) in anoxic toluene (λ_{em} = 770 nm).

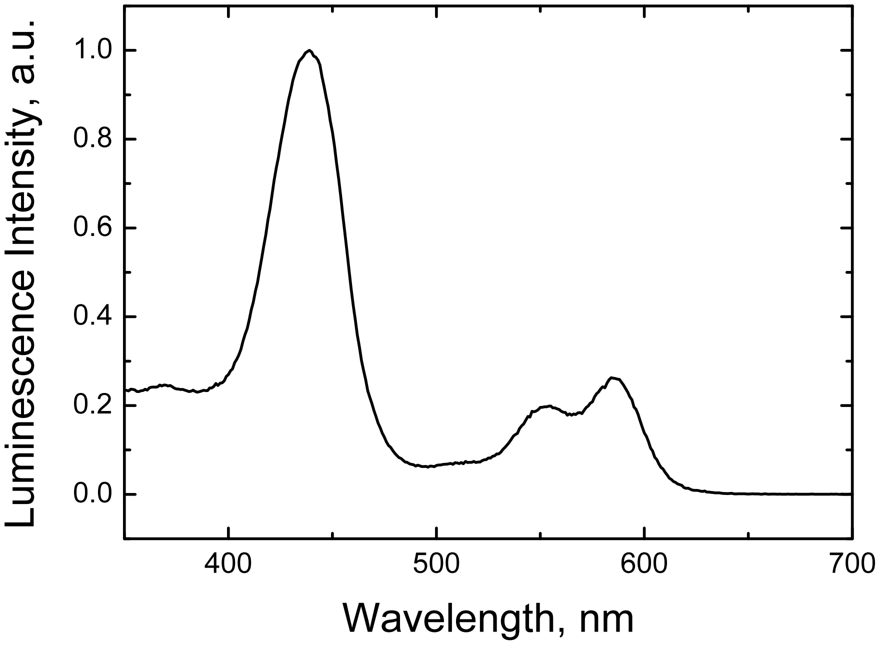

Figure S8. Excitation spectrum of Re[T*p*FPC](O) in anoxic toluene (λ_{em} = 770 nm).

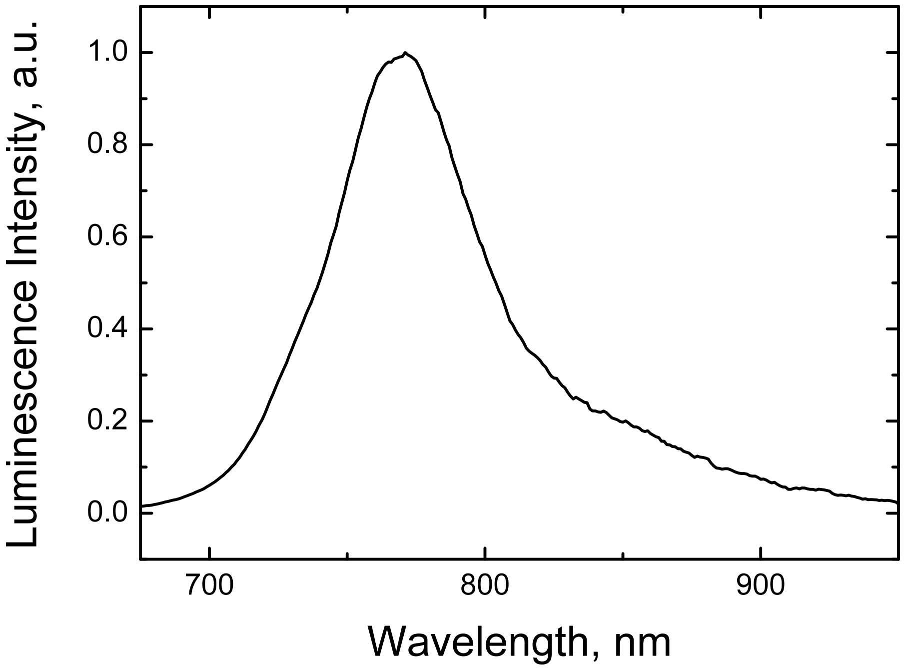

Figure S9. Emission spectrum of Re[TPC](O) in anoxic toluene (λ_{exc} = 590 nm).

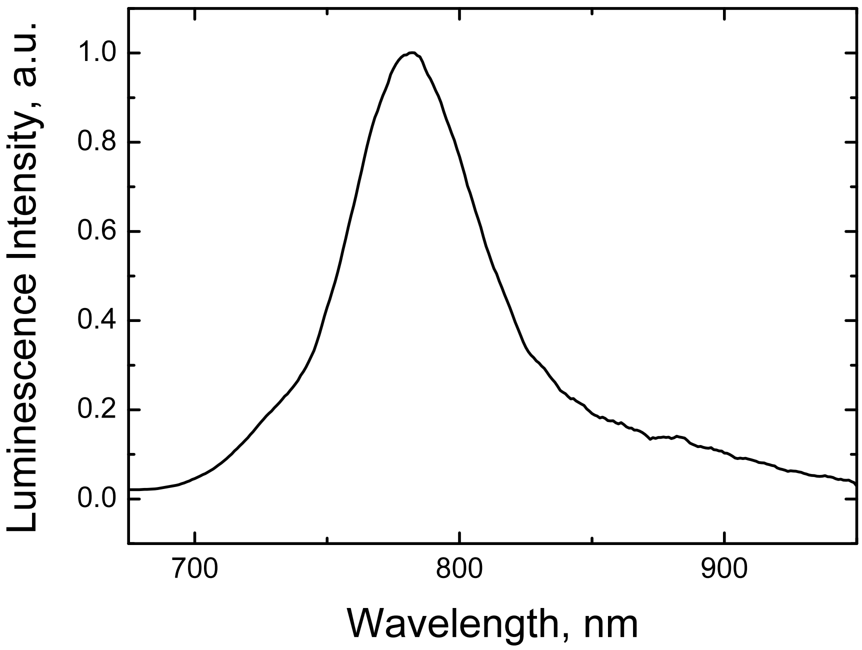

Figure S10. Emission spectrum of Re[T*p*MePC](O) in anoxic toluene (λ_{exc} = 590 nm).

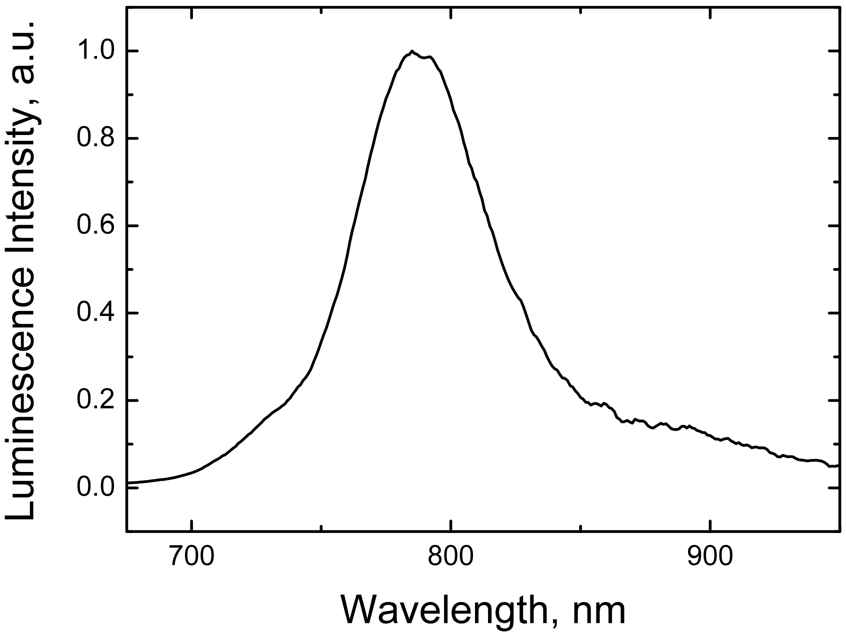

Figure S11. Emission spectrum of Re[T*p*OMePC](O) in anoxic toluene (λ_{exc} = 590 nm).

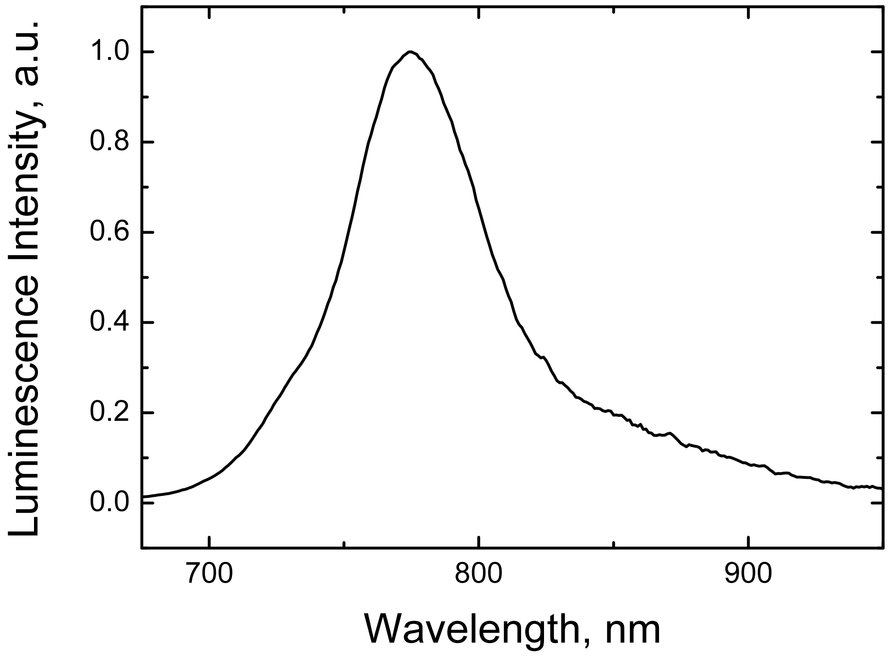

Figure S12. Emission spectrum of Re[T*p*FPC](O) in anoxic toluene (λ_{exc} = 590 nm).

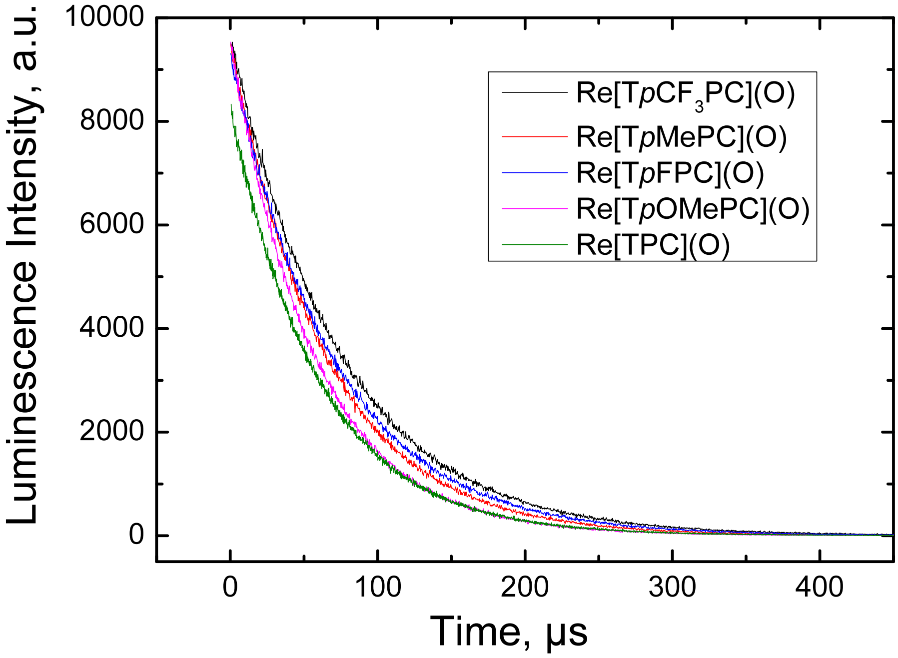

Figure S13. Phosphorescence decay of Rhenium-Oxo Corroles in anoxic toluene (λ_{exc} = 455 nm).

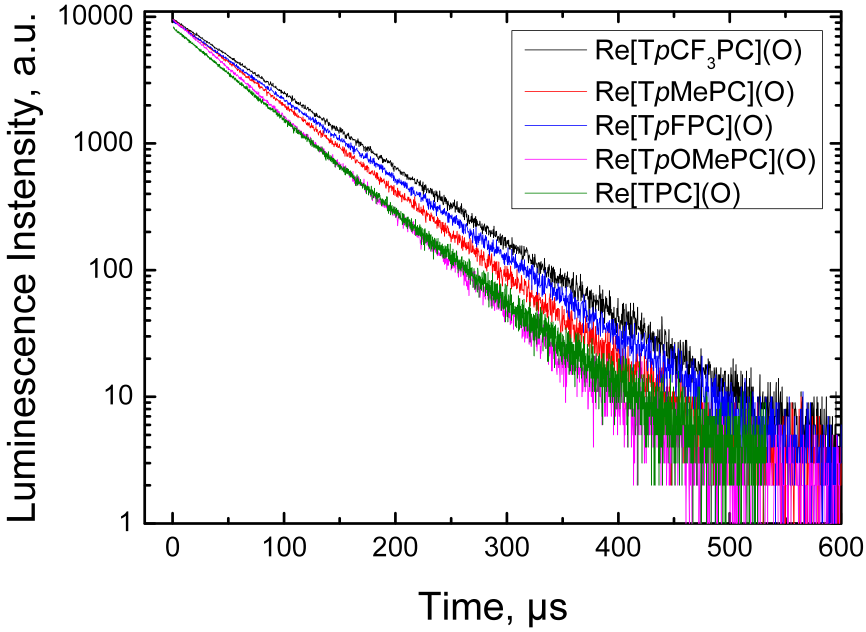

Figure S14. Phosphorescence decay of Rhenium-Oxo Corroles in anoxic toluene (λ_{exc} = 455 nm).

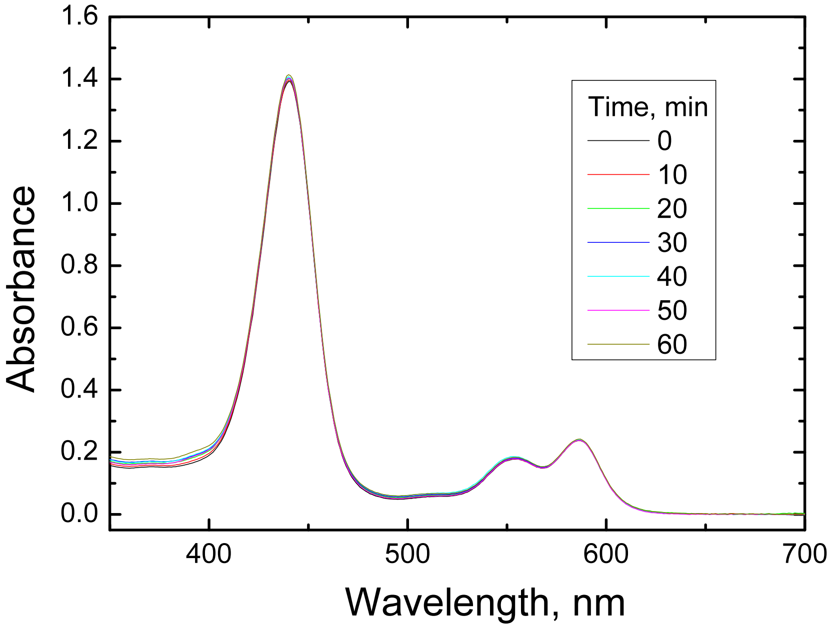

Figure S15. Absorption spectra of Re[T*p*CF_3PC](O) in air-saturated toluene solution during irradiation with a high power 590-nm LED array.

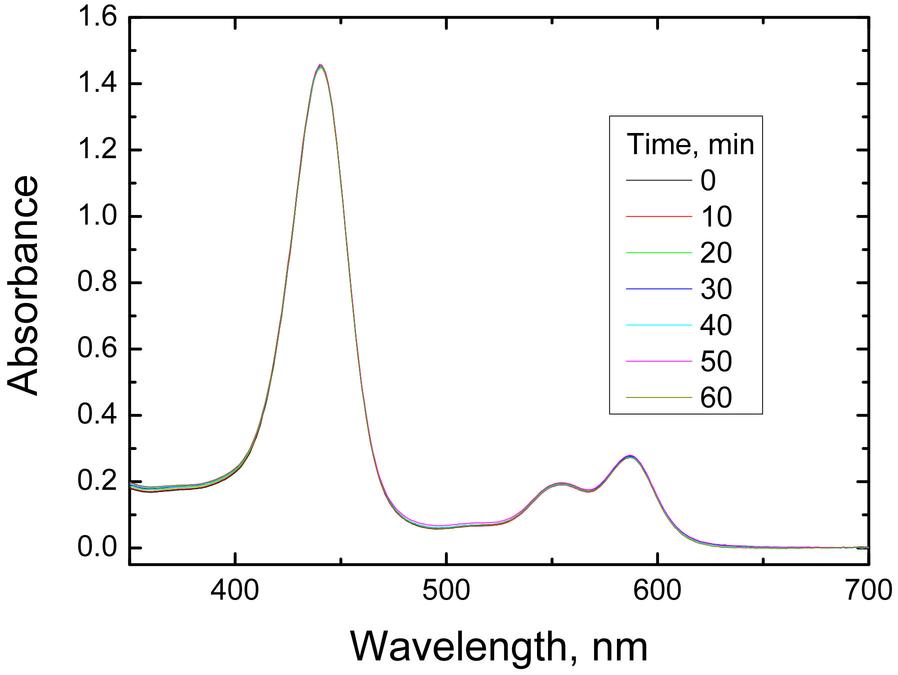

Figure S16. Absorption spectra of Re[TPC](O) in air-saturated toluene solution during irradiation with a high power 590-nm LED array.

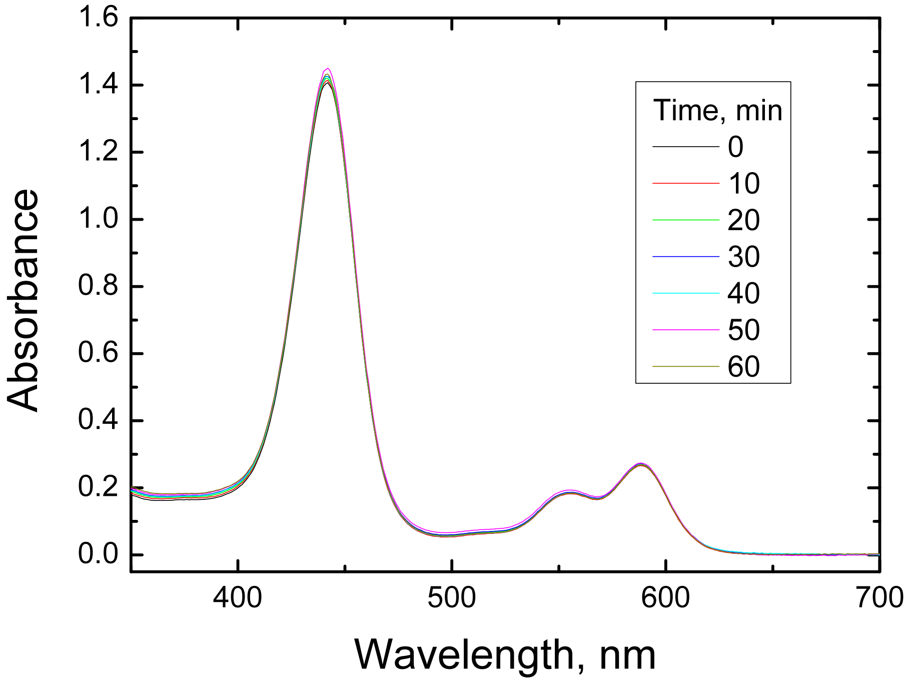

Figure S17. Absorption spectra of Re[T*p*MePC](O) in air-saturated toluene solution during irradiation with a high power 590-nm LED array.

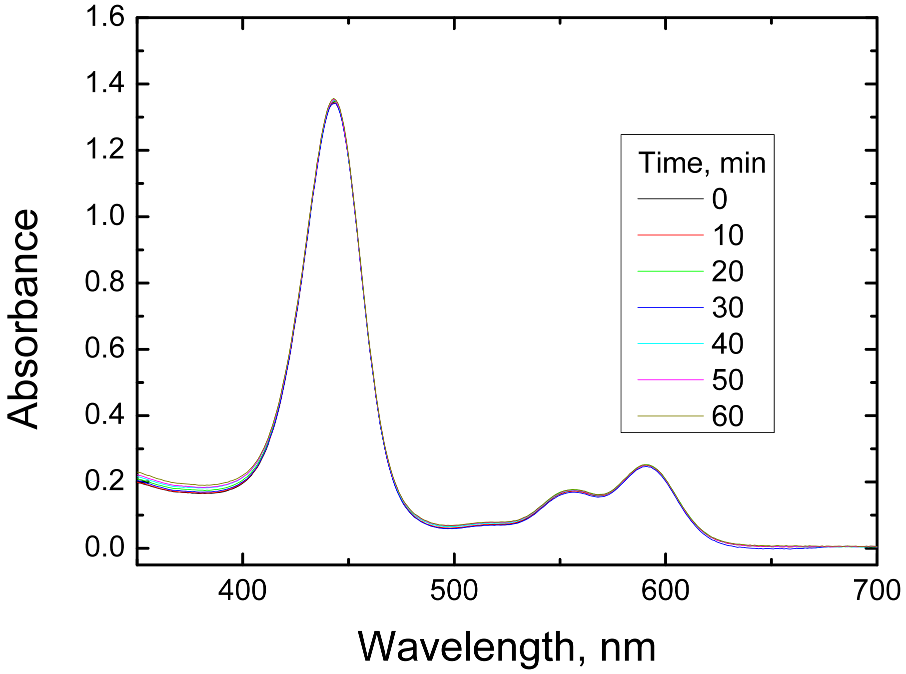

Figure S18. Absorption spectra of Re[T*p*OMePC](O) in air-saturated toluene solution during irradiation with a high power 590-nm LED array.

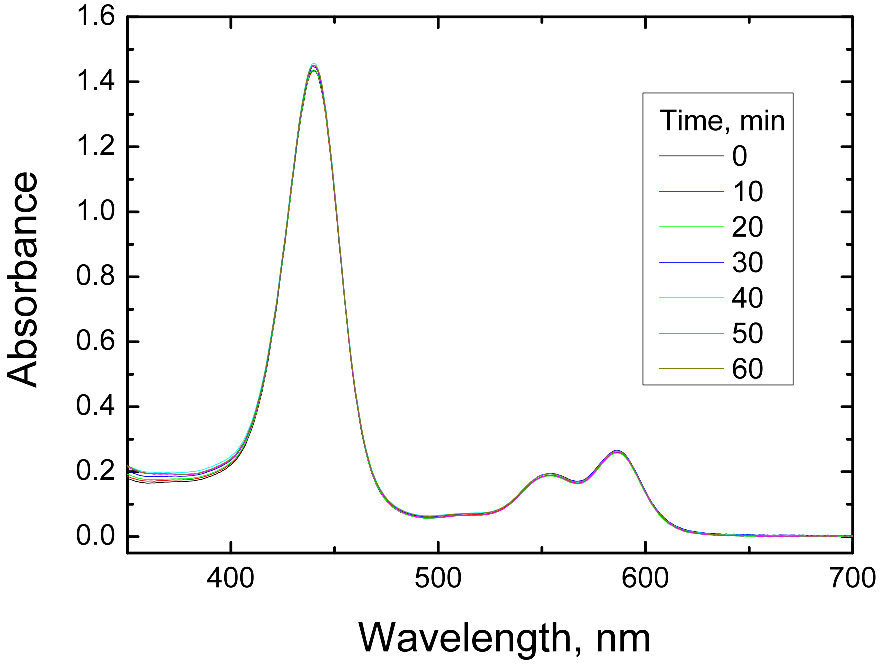

Figure S19. Absorption spectra of Re[T*p*FPC](O) in air-saturated toluene solution during irradiation with a high power 590-nm LED array.

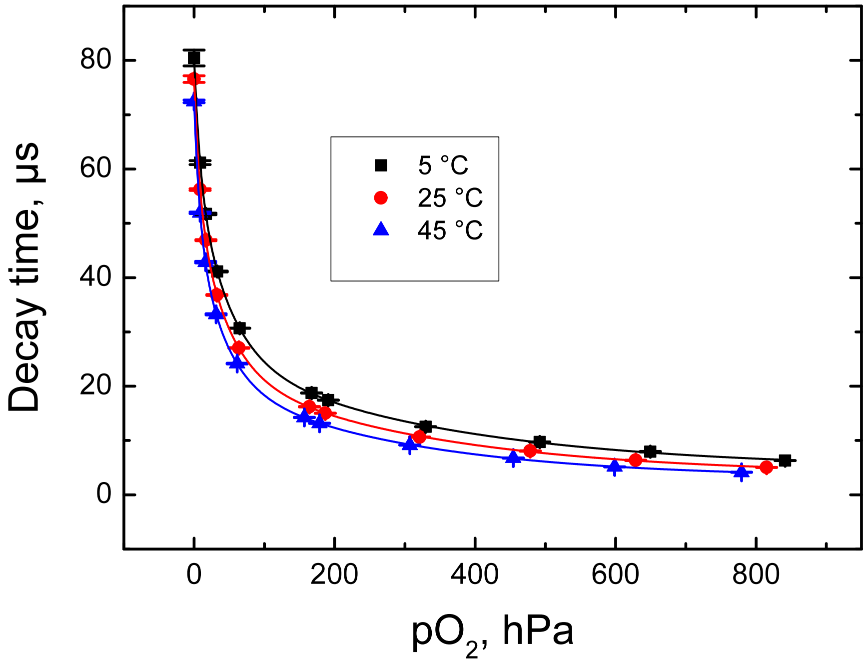

Figure S20. Decay time plots for the oxygen sensor based on Re[T*p*CF_3PC](O) embedded into polystyrene.

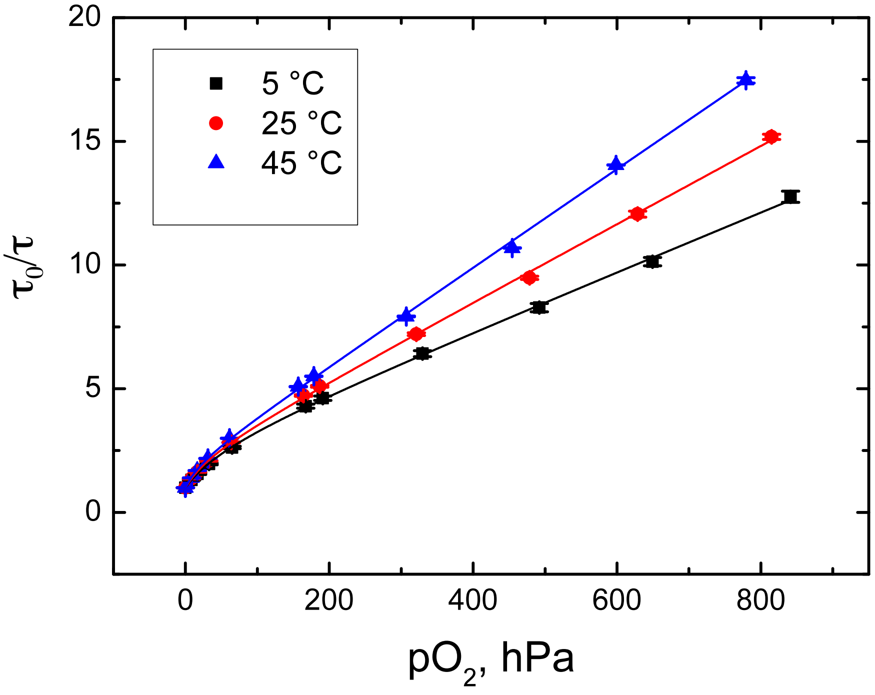

Figure S21. Stern-Volmer plots for the oxygen sensor based on Re[T*p*CF_3PC](O) embedded into polystyrene.

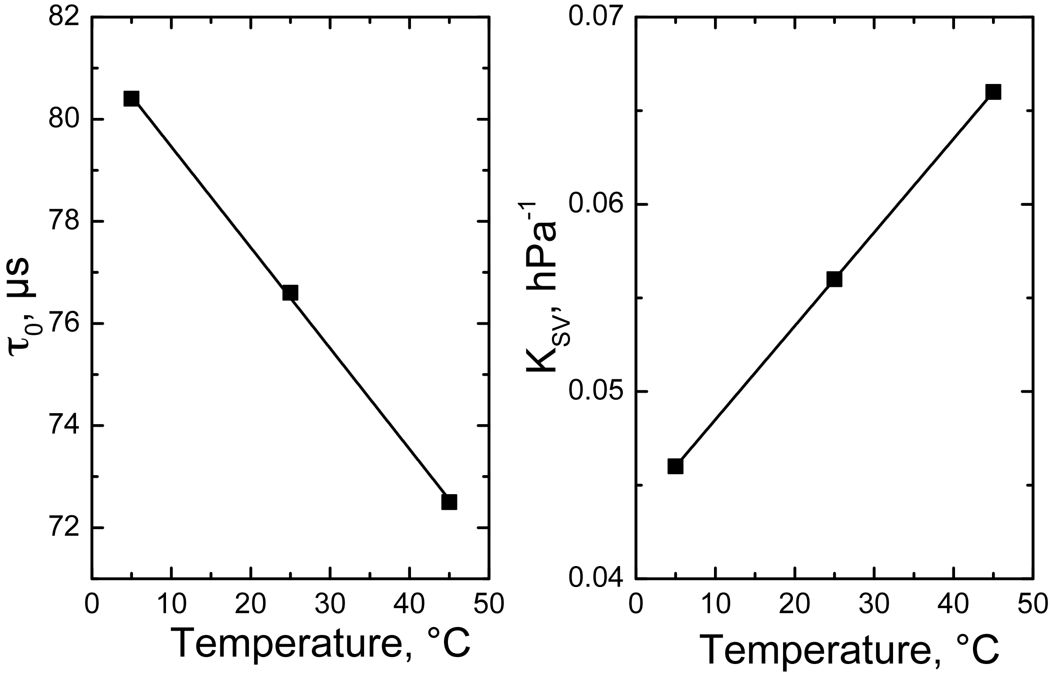

Figure S22. Temperature dependence of the phosphorescence decay time in the absence of oxygen τ_0 (left) and Stern-Volmer constant K_{SV} (right). The lines represent linear fit.

Table S1. Oxygen sensing properties of the sensor based on Re[T*p*CF$_3$PC](O) embedded into polystyrene.$^{(a)}$

τ_0 at 5 °C, µs	τ_0 at 25 °C, µs	τ_0 at 45 °C, µs	dτ_0/dT at 25 °C, %/K	K_{SV}^1 at 5 °C, hPa^{-1}	K_{SV}^1 at 25 °C, hPa^{-1}	K_{SV}^1 at 45 °C hPa^{-1}	dK_{SV}^1/dT at 25 °C, %/K
80.4	76.6	72.5	-0.26	0.046	0.056	0.066	0.89

(a) Non-linear fit according to two site model, eq. 1. Constant fit parameters: m = 0.076; f = 0.77 for all temperatures.

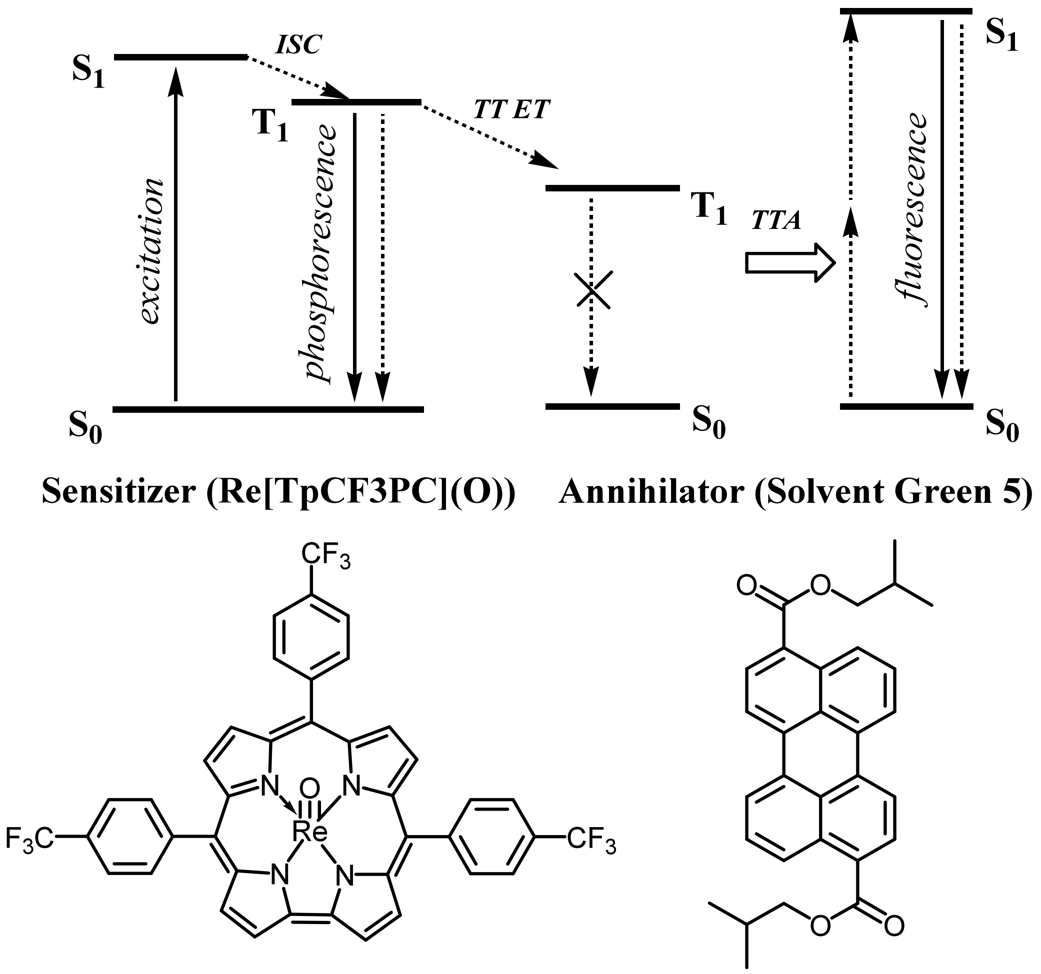

Figure S23. Schematic representation of the mechanism of upconversion based on triplet-triplet annihilation.

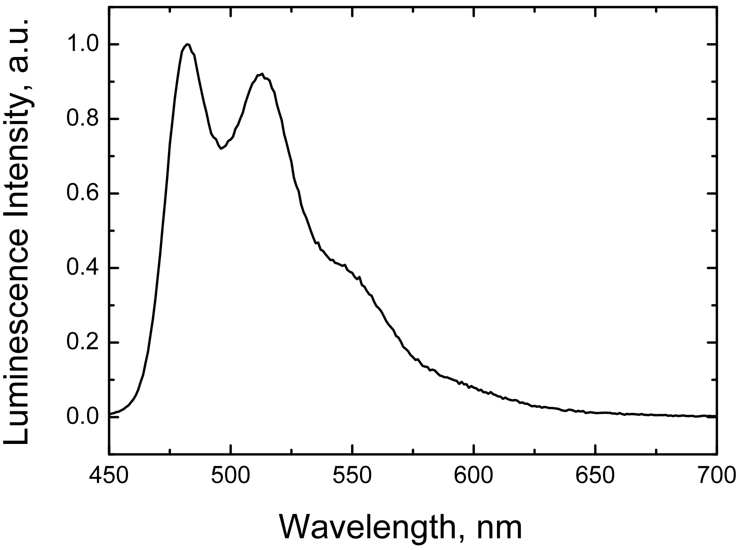

Figure S24. Emission spectrum of Solvent green 5 in toluene (λ_{exc} = 400 nm).

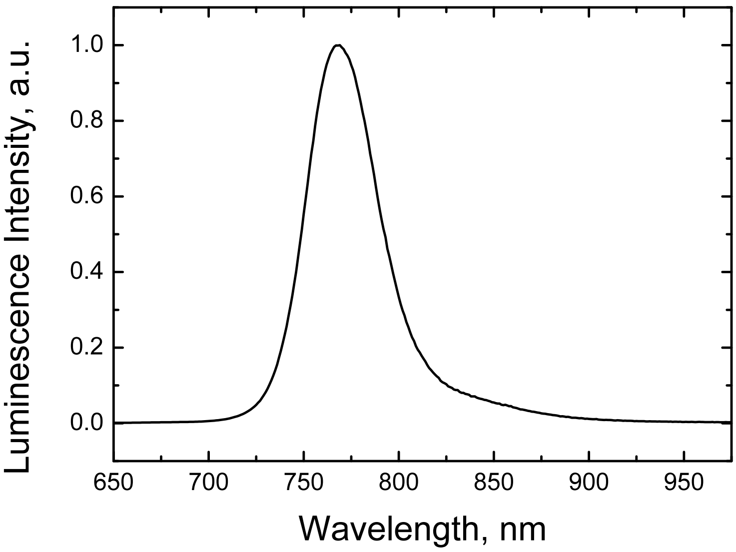

Figure S25. Emission spectrum of Pt[TPTBP] in anoxic toluene (λ_{exc} = 585 nm).

Paper B

ACS OMEGA

http://pubs.acs.org/journal/acsodf

Article

Amphiphilic Rhenium-Oxo Corroles as a New Class of Sensitizers for Photodynamic Therapy

Rune F. Einrem, Abraham B. Alemayehu, Sergey M. Borisov,* Abhik Ghosh,* and Odrun A. Gederaas*

Cite This: *ACS Omega* 2020, 5, 10596−10601

Read Online

ACCESS | Metrics & More | Article Recommendations | Supporting Information

ABSTRACT: A set of rhenium(V)-oxo *meso*-triarylcorroles bearing ester and carboxylic acid functionalities were synthesized with a view to determining their potential for photodynamic therapy. Toward this end, we measured their near-IR phosphorescence and their ability to sensitize singlet oxygen formation. The two esters studied, Re^VO 5,10,15-tris(*meta*-carbomethoxyphenyl)corrole and Re^VO 5,10,15-tris(*para*-carbomethoxyphenyl)corrole, were found to exhibit phosphorescence quantum yields of around 1% and fairly long phosphorescence lifetimes of about 60 μs in toluene. The corresponding carboxylic acids, which were examined in ethanolic/aqueous media, in contrast, showed much lower phosphorescence quantum yields on the order of 0.01% and somewhat shorter phosphorescent lifetimes. The quantum yields for singlet oxygen formation, on the other hand, turned out to be equally high (0.72 ± 0.02) for the esters and corresponding carboxylic acids. For the two carboxylic acids, we also carried out photocytotoxicity measurements on rat bladder cancer cells (AY27) and human colon carcinoma cells (WiDr). Cell viability measurements (MTT assays) indicated 50% cell death (LD_{50}) for AY27 cells upon 5 min of blue light exposure with the meta carboxylic acid and upon 7 min of exposure with the para carboxylic acid; complete cell death resulted after 20 min for both compounds. The WiDr cells proved less sensitive, and LD_{50} values were reached after 8 and 12 min illumination with the meta and para carboxylic acids, respectively.

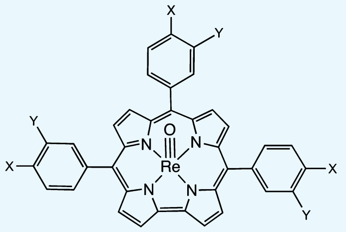

	X	Y
Re[T*p*CO$_2$CH$_3$PC](O)	CO$_2$CH$_3$	H
Re[T*m*CO$_2$CH$_3$PC](O)	H	CO$_2$CH$_3$
Re[*p*TCPC](O)	CO$_2$H	H
Re[*m*TCPC](O)	H	CO$_2$H

INTRODUCTION

Photodynamic therapy (PDT) relies on the combined action of a photosensitizer, light, and molecular oxygen to treat a variety of medical conditions, notably cancer and various skin conditions and increasingly also bacterial, viral, and fungal infections.[1,2] A common, but far from exclusive, mechanism involves photoexcitation of the sensitizer to a short-lived singlet excited state (S_1), intersystem crossing to a longer lived triplet state (T_1), and energy transfer to ground-state triplet oxygen ($^3\Sigma_g$), leading to highly reactive singlet oxygen ($^1\Delta_g$) as the primary cytotoxic species. From the very earliest days of PDT,[3] porphyrins have been a cornerstone of the method because of their preferential uptake and accumulation in tumors and other rapidly dividing cells, relative to normal tissues.[4−8] The recent efflorescence of the field of porphyrin analogues, particularly corroles,[9−12] now promises a plethora of new photosensitizers. Thus, gold triarylcorroles, which exhibit near-infrared (NIR) phosphorescence at room temperature, have been found to exhibit strong photocytotoxicity against cancer cells.[13−15] Other 5d metallocorroles, such as rhenium(V)-oxo[16] [but not rhenium(V)-imido[17]], osmium(VI)-nitrido,[18] iridium(III),[19] and platinum(IV)[20] corroles, have also been found to exhibit room-temperature NIR phosphorescence,[21−25] but their photocytotoxic behavior remains unexplored. Within this growing class of complexes, Re^VO corroles are particularly attractive on account of easy accessibility and their impressive thermal, chemical, and photochemical stability. Presented herein, accordingly, are a set of Re^VO *meso*-triarylcorroles bearing ester and carboxylic acid functionalities (Chart 1) and measurements of their NIR phosphorescence, sensitization of singlet oxygen formation,

Chart 1. Compounds Studied in This Work.

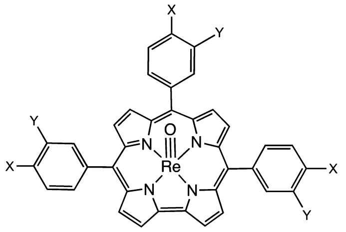

	X	Y
Re[T*p*CO$_2$CH$_3$PC](O)	CO$_2$CH$_3$	H
Re[T*m*CO$_2$CH$_3$PC](O)	H	CO$_2$CH$_3$
Re[*p*TCPC](O)	CO$_2$H	H
Re[*m*TCPC](O)	H	CO$_2$H

Received: March 11, 2020
Accepted: April 15, 2020
Published: April 27, 2020

https://dx.doi.org/10.1021/acsomega.0c01090
ACS Omega 2020, 5, 10596−10601

and photocytotoxicity vis-à-vis rat bladder cancer cells (AY27)[26−28] and human colon carcinoma cells (WiDr).[29] The results are promising and argue for more in-depth studies of the biomedical potential of $\mathrm{Re^{V}O}$ corroles.

■ RESULTS AND DISCUSSION

Photophysical Properties. The compounds depicted in Chart 1 were synthesized via standard methods,[16] as described in the Experimental Section. The UV−vis spectra of the new complexes (Figures S1−S4) are also very similar to those of other $\mathrm{Re^{V}O}$ corroles reported previously.[16] The new complexes were all found to exhibit NIR phosphorescence at room temperature, albeit with considerable differences between the lipophilic esters Re[T*m*$\mathrm{CO_2CH_3}$PC](O) and Re[T*p*$\mathrm{CO_2CH_3}$PC](O) (Figure 1A) and the corresponding free acids Re[*m*TCPC](O) and Re[*p*TCPC](O) (Figure 1B). The two esters showed $\lambda_{\mathrm{max,em}}$ values around 775 ± 2 nm, quantum yields of around 1% [relative to the Pt(II) tetraphenyltetrabenzoporpyrin (Pt[TPTBP])],[30] and phosphorescence lifetimes of about 60 μs (Table 1). The phosphorescence decay was found to be monoexponential (Figures S5 and S6).

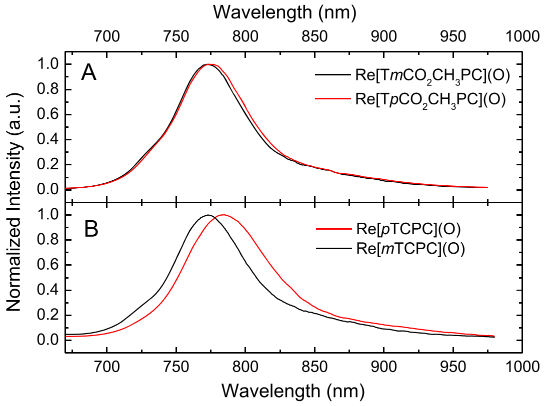

Figure 1. Phosphorescence spectra of $\mathrm{Re^{V}O}$ corroles. (A) Carboxylic acid methyl esters (in anoxic toluene, λ_{ex} 440 nm, and 23 °C); (B) carboxylic acids (in anoxic EtOH with 3×10^{-3} M NaOH, λ_{ex} 432 nm, and 25 °C).

The $\mathrm{Re^{V}O}$ corrole free acids exhibit much weaker NIR phosphorescence, with quantum yields below 0.1%, more than an order of magnitude below those measured for analogous lipophilic $\mathrm{Re^{V}O}$ corroles. However, because ethanol was used as the solvent in these measurements to ensure solubility of the more hydrophilic free acids, efficient radiation-less deactivation via O−H vibrations might be an important factor behind the low quantum yields.[31,32] Addition of small amounts of NaOH to the ethanolic solutions led to slight enhancements of the quantum yields as well as to small hypsochromic shifts (~6 nm) of the emission maxima (Table 2). The enhancement of the phosphorescence quantum yields may be a result of deaggregation of the dyes upon deprotonation of the COOH groups. The phosphorescence decay times are not monoexponential (Figures S7−S10), which might reflect the existence of several species (monomers/dimers). Interestingly, in the basic solutions, the contribution of the shorter- lifetime component appears to increase. The dyes are also soluble in water at basic pH values, but the phosphorescence turned out to be even weaker, with quantum yields below 0.001%. Evidently, radiationless deactivation of the excited states is even stronger than in ethanol. The overall conclusion from the data is that Re[*m*TCPC](O) is a weaker emitter than Re[*p*TCPC](O), with the former exhibiting quantum yields about half that of the latter, a finding consistent with the shorter phosphorescence decay times of the former complex.

Table 2. Photophysical Properties of Amphiphilic ReO Corroles at 25 °C in Anoxic solutions

complex	Solvent	$\lambda_{\mathrm{max,em}}$ (nm)	ϕ (%)	τ (μs)
Re[*p*TCPC](O)	EtOH	783	~0.03	38 (91%), 1.2 (9%)
Re[*p*TCPC](O)	EtOH + 3×10^{-3} M NaOH	777	~0.05	27 (73%), 1.0 (27%)
Re[*m*TCPC](O)	EtOH	773	~0.01	5.9 (44%), 1.3 (56%)
Re[*m*TCPC](O)	EtOH + 3×10^{-3} M NaOH	766	~0.02	13 (23%), 1.7 (77%)

Sensitization of Singlet Oxygen Formation. The efficiency of singlet oxygen formation was evaluated with an assay using 9,10-dimethylanthracene (DMA) as a singlet oxygen acceptor[33] and methylene blue as a sensitizer with a known quantum yield for singlet oxygen formation (Φ_{Δ} = 0.48).[21] Figure 2 shows the kinetics of decomposition of DMA

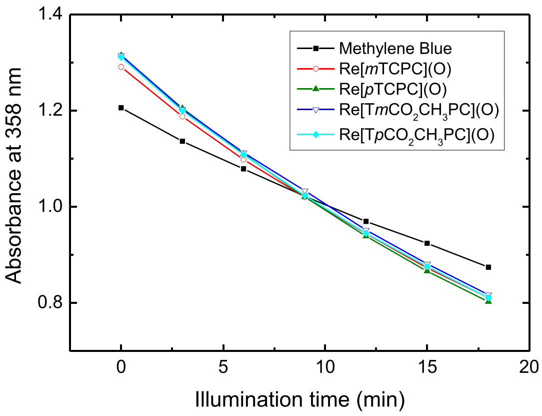

Figure 2. Kinetics of degradation of DMA (0.2 mM) of an air-saturated solution in EtOH/THF (9:1 v/v) upon irradiation with 595 ± 5 nm light in the presence of a sensitizer. Note that the absorbance at 358 nm reflects the contribution of the sensitizer and of the acceptor.

Table 1. Photophysical Properties of Lipophilic $\mathrm{Re^{V}O}$ Corroles in Anoxic Toluene at 23 °C: Maxima of the Absorption and Emission Spectra ($\lambda_{\mathrm{max,abs}}$ and $\lambda_{\mathrm{max,em}}$, Respectively), Molar Absorption Coefficients (ε), Emission Quantum Yields (ϕ), and Decay Times (τ)

compound	$\lambda_{\mathrm{max,abs}}$ [nm, $\varepsilon \times 10^{-4}$ ($\mathrm{M^{-1}cm^{-1}}$)]	$\lambda_{\mathrm{max,em}}$ (nm)	ϕ (%)	τ (μs)
Re[T*p*$\mathrm{CO_2CH_3}$PC](O)	441 (11.17), 555 (1.61), 587 (2.05)	776	1.2	66
Re[T*m*$\mathrm{CO_2CH_3}$PC](O)	439 (8.37), 553 (1.20), 586 (1.57)	773	1.1	57
Pt[TPTBP]	430, 564, 614	770	21	47

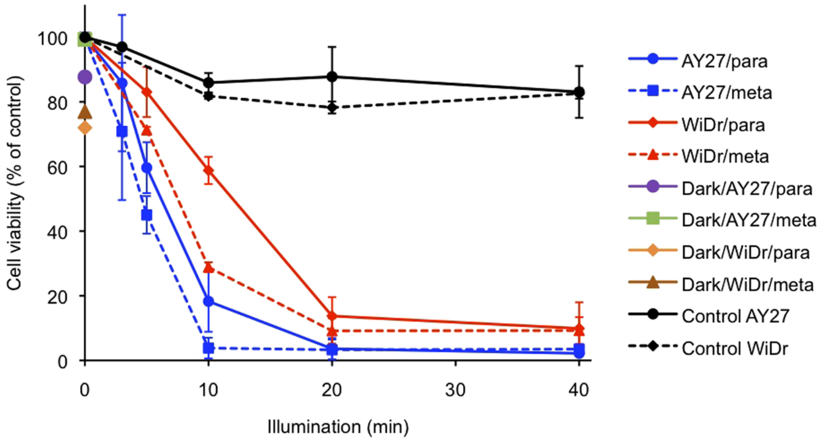

Figure 3. Viability of AY27 and WiDr cells upon incubation with Re[*m*TCPC](O) and Re[*p*TCPC](O) (10 μM, 24 h) as a function of blue light exposure (435 nm, 0−40 min). The black lines refer to control cells, which were exposed to light but not to a photosensitizer. Dark toxicity refers to the cell viability at 0 min of illumination on the *y* axis. Each data point is the average from three experiments ± SD relative to untreated cells.

under irradiation of solutions of sensitizers in ethanol with 595 ± 5 nm light, and the corresponding UV−vis spectra are summarized in Figure S11. The kinetics was virtually identical for the ester and carboxylic acid substituents and was also independent of the position of the substituent. It should be noted that the solutions contained 10% v/v of tetrahydrofuran (THF) to ensure solubility of the more lipophilic ester complexes. The Φ_Δ values obtained for all four corroles in EtOH/THF mixture are extremely similar (0.72 ± 0.02). We may conclude that all four compounds are powerful photosensitizers of singlet oxygen in spite of the very weak phosphorescence of the free acids.

PDT Experiments. The phototoxic/cytotoxic effects of the $Re^{V}O$ corrole free acids, Re[*m*TCPC](O) and Re[*p*TCPC](O), were evaluated for rat bladder cancer cells (AY27)[26,27] and human colon carcinoma cells (WiDr),[29] indicating that these compounds trigger cell changes leading to cell death (Figure 3). Cell viability was determined in both cell lines after incubation with the meta- and para-isomeric complexes (10 μM, 24 h). The concentration of the compounds was chosen on the basis of earlier PDT studies on AY27 cells with the analogous gold complexes (Au[*m*/*p*TCPC]) on the AY27 cell line with the analogous gold complexes (Au[*m*/*p*TCPC]) and the same light source.[14]

For both cell lines, the experiments described above showed a clear dependence of cell viability on the period of blue light exposure in the presence of the photosensitizer. For the AY27 cell line, both isomeric complexes were found to exhibit similar activity, resulting in 50% cell death after about 5 min of blue light exposure and essentially complete extermination after 10 min. For the WiDr cell line, the meta-isomer proved somewhat more active, effecting approximately 50% cell death in about 8 min of illumination and 95% in 20 min. During the same periods, the para-isomer achieved about 40 and 90% cell death. For comparison, illumination in the absence of a photosensitizer resulted in no more than 10% cell death after 40 min.

The effects of the photosensitizers on AY27 and WiDr cells were also investigated in the absence of light (dark toxicity). Incubation with the photosensitizers in the absence of light resulted in modest cell death rates for the WiDr cell line, about 23 and 28% after incubation (24 h, 37 °C) with the meta and para isomers of the photosensitizer, respectively (Figure 3, green and pink violet points, respectively). Much weaker dark toxicity was observed for the AY27 cells, with death rates around 1 and 12% after incubation with the meta and para isomers, respectively.

CONCLUSIONS

Along with our earlier work on gold corroles,[14] the present study underscores the growing importance of 5d metallocorroles as a new class of anticancer compounds, especially as photosensitizers in PDT. Within this family, the $Re^{V}O$ corroles have been of particular interest, by virtue of their ease of accessibility and superior thermal, chemical, and photochemical stability.[16] The new complexes reported here have delivered on that promise. The two esters studied, $Re^{V}O$ 5,10,15-tris(*meta*-carbomethoxyphenyl)corrole and $Re^{V}O$ 5,10,15-tris(*para*-carbomethoxyphenyl)corrole, exhibit phosphorescence quantum yields of approximately 1% and reasonably long phosphorescence lifetimes of about 60 μs in anoxic toluene. Much lower phosphorescence quantum yields on the order of 0.01% and somewhat shorter phosphorescent lifetimes were found for the $Re^{V}O$ carboxylic acids derived from the esters, probably because of efficient radiationless deactivation in aqueous/ethanolic media, in which these amphiphilic compounds were examined. The quantum yields for singlet oxygen formation, on the other hand, turned out to be equally high (0.72 ± 0.02) for both the esters and carboxylic acids. Gratifyingly, the $Re^{V}O$ carboxylic acids were found to exhibit high photocytotoxicity against rat bladder cancer cells (AY27) and human colon carcinoma cells (WiDr), achieving 50% cell death within 5−7 min of blue light exposure. Ongoing research in our laboratories accordingly focuses both on improved $Re^{V}O$ corrole-based phototherapeutics and on a wider evaluation of the expanding class of 5d metallocorroles.

EXPERIMENTAL SECTION

Chemical Syntheses and Characterization. *Materials and Instrumentation.* Except for solvents, all chemicals were obtained from Sigma-Aldrich and used as purchased. CHROMASOLV HPLC-grade *n*-hexane, dichloromethane, ethyl acetate, and toluene were used for column chromatography. Silica gel 60 (0.04−0.063 mm particle size; 230−400 mesh, Sigma) was used for column chromatography, and the columns used were generally about 12 cm in height and 3 cm in diameter. UV−vis spectra were recorded on an HP 8454 spectrophotometer at room temperature. High-resolution electrospray ionization (ESI) mass spectra were recorded on an LTQ Orbitrap XL spectrometer. ^{1}H NMR spectra were recorded on a Bruker Advance III HD 400 MHz spectrometer.

General Procedure for the Synthesis of Re^{V}O meso-(m/p-Carbomethoxyphenyl)corrole. To a 50 mL round-bottom flask equipped with a magnetic stirrer and reflux condenser, were added the free-base corrole H_3[T*p*/*m*CO_2CH_3PC] (100 mg, 0.142 mmol, 1 equiv), $Re_2(CO)_{10}$ (185 mg, 0.283 mmol, 2 equiv), potassium carbonate (100 mg), and 1,2,4-trichlorobenzene (8 mL). The contents were deoxygenated with argon and then heated to ∼180 °C overnight with constant stirring under argon. Upon cooling, the reaction mixture was loaded directly onto a silica gel column and chromatographed with *n*-hexane as the mobile phase, whereupon 1,2,4-trichlorobenzene eluted first. The desired complex eluted upon changing the eluent to dichloromethane and was further purified by preparative thin-layer chromatography with dichloromethane as the eluent.

Re[TpCO$_2$CH$_3$PC](O). Yield 68 mg (53.17%). UV−vis (CH_2Cl_2) λ_{max} [nm, $\varepsilon \times 10^{-4}$ (M^{-1} cm^{-1})]: 441 (11.17), 555 (1.61), 587 (2.05). ^{1}H NMR (400 MHz, −20 °C): δ 9.67 (d, 2H, $^3J_{HH}$ = 4.40 Hz, β-H); 9.32 (d, 4H, $^3J_{HH}$ = 4.48 Hz, β-H); 9.12 (d, 2H, $^3J_{HH}$ = 5.20 Hz, β-H); 8.66 (d, 2H, $^3J_{HH}$ = 7.52 Hz, 5,15-*o*1-Ph); 8.58 (d, 1H, $^3J_{HH}$ = 7.96 Hz, 10-*o*1-Ph); 8.52 (d, 2H, $^3J_{HH}$ = 8.20 Hz, 5,15-*o*2-Ph); 8.49 (d, 1H, $^3J_{HH}$ = 7.88 Hz, 10-*o*2-Ph); 8.41 (d, 2H, $^3J_{HH}$ = 7.84 Hz, 5,15-*m*2-Ph); 8.35 (d, 1H, $^3J_{HH}$ = 7.94 Hz, 10-*m*2-Ph); 8.16 (d, 2H, $^3J_{HH}$ = 7.60 Hz, 5,15-*m*1-Ph); 7.99 (d, 1H, $^3J_{HH}$ = 7.96 Hz, 10-*m*1-Ph); 4.03 (s, 6H, 5,15-*p*-CH_3); 4.01 (s, 3H, 10-*p*-CH_3). MS (ESI): M^+ 900.16 (expt), 900.15 (calcd for $C_{43}H_{29}N_4O_7Re$); elemental Anal. Calcd for $C_{43}H_{29}N_4O_7Re$: C, 57.39; H, 3.25; N, 6.23. Found: C, 57.89; H, 3.88; N, 5.78. IR ν_{ReO}: 989 cm^{-1}.

Re[TmCO$_2$CH$_3$PC](O). Yield 49 mg (39.27%). UV−vis (CH_2Cl_2) λ_{max} [nm, $\varepsilon \times 10^{-4}$ (M^{-1} cm^{-1})]: 439 (8.37), 553 (1.20), 586 (1.57). ^{1}H NMR (400 MHz, −20 °C): δ 9.72 (d, 2H, $^3J_{HH}$ = 4.04 Hz, β-H); 9.34 (d overlapping, 4H, $^3J_{HH}$ = 4.28 Hz, β-H); 9.25 (s, 1H, 5,15-*o*1m-Ph); 9.17 (s, 0.5H, 10-*o*1m-Ph); 9.13 (d, 2H, $^3J_{HH}$ = 4.68 Hz, β(−H); 8.82 (d, 1H, $^3J_{HH}$ = 7.60 Hz, 5,15-o1-Ph); 8.74 (1.5H, 5,15-o2m-Ph overlapping with 10-o1-Ph); 8.58 (s, 0.5H, 10-o2m-Ph); 8.48 (overlapping d, 3H, $^3J_{HH}$ = 6.88 Hz, 5,10,15-p-Ph); 8.32 (d, 1H, $^3J_{HH}$ = 7.20 Hz, 5,15-*o*2-Ph); 8.16 (d, 0.5H, $^3J_{HH}$ = 7.92 Hz, 10-*o*2-Ph); 8.04 (t, 1H, $^3J_{HH}$ = 7.72 Hz 5,15-*m*1-Ph); 7.99 (t, 0.5H, $^3J_{HH}$ = 7.56 Hz 10-*m*1-Ph); 7.92 (t, 1H, $^3J_{HH}$ = 8.00 Hz 5,15-*m*2-Ph); 7.86 (t, 0.5H, $^3J_{HH}$ = 7.72 Hz, 10-*m*2-Ph); 4.01 (s, 3H, 5,15-*m*1-CO_2CH_3); 3.98 (s, 1.5H, 10-*m*1-CO_2CH_3); 3.92 (s, 3H, 5,15-*m*2-CO_2CH_3); 3.88 (s, 1.5H, 10-*m*2-CO_2CH_3) note: The suffix m denotes the chemical shift in an atropisomeric species. MS (ESI): M^+ 900.16 (expt), 900.16 (calcd for $C_{43}H_{29}N_4O_7Re$); elemental Anal. Calcd for $C_{43}H_{29}N_4O_7Re$: C, 57.39; H, 3.25; N, 6.23. Found: C, 57.60; H, 3.12; N, 5.93. IR ν_{ReO}: 985 cm^{-1}.

Hydrolysis of Re^{V}O meso-(m/p-Carbomethoxyphenyl)-corrole. The Re^{V}O *meso*-(*m*/*p*-carbomethoxyphenyl)corrole (32 mg, 0.036 mmol) was dissolved in THF (50 mL) in a 250 mL round-bottom flask equipped with a magnetic stirrer and a reflux condenser. Aqueous NaOH (0.07 M, 20 mL) was added, and the mixture was heated at reflux (∼100 °C) for 24 h. Upon cooling to room temperature, the mixture was transferred to a separatory funnel containing ethyl acetate (150 mL) and washed with 0.5 M HCl. The organic phase was collected and washed three times with water, dried over anhydrous sodium sulfate, and filtered, and the filtrate was rotary evaporated to dryness. The residue was sonicated with a minimum volume of dichloromethane, and the resulting suspension was filtered. The residue on the filter paper was washed further with dichloromethane and collected as the pure Re[TCPC](O) product.

Re[pTCPC](O). Yield 19.7 mg (64.5%). UV−vis (THF) λ_{max} (nm), [$\varepsilon \times 10^{-4}$ (M^{-1} cm^{-1})]: 439 (11.06), 553 (1.34), 585 (1.87). MS (ESI): M^+ 858.11 (expt), 858.11 (calcd for $C_{40}H_{23}N_4O_7Re$); elemental Anal. Calcd for $C_{40}H_{23}N_4O_7Re \cdot H_2O$: C, 54.85; H, 2.88; N, 6.40. Found: C, 55.22; H, 3.25; N, 6.18. IR ν_{ReO}: 990 cm^{-1}.

Re[mTCPC](O). Yield 17.3 mg (56.6%). UV−vis (THF) λ_{max} (nm), [$\varepsilon \times 10^{-4}$ (M^{-1} cm^{-1})]: 438 (10.03), 553 (1.37), 586 (1.81). MS (ESI): M^+ 858.11 (expt), 857.10 (calcd for $C_{40}H_{23}N_4O_7Re$); elemental Analy. Calcd for $C_{40}H_{23}N_4O_7Re \cdot H_2O$: C, 54.85; H, 2.88; N, 6.40. Found: C, 54.44; H, 3.13; N, 6.23. IR ν_{ReO}: 992 cm^{-1}.

Photophysical Measurements. UV−vis absorption spectra were acquired on a Cary 50 UV−vis spectrophotometer (Varian), and emission spectra were acquired on a Fluorolog 3 fluorescence spectrometer (Horiba, Japan) equipped with NIR-sensitive photomultiplier R2658 (Hamamatsu, Japan). All spectra were corrected for the sensitivity of the photomultiplier. Relative luminescence quantum yields were determined, according to Crosby and Demas using the following equation:[34]

$$\phi_x = \phi_r \frac{S_x}{S_r} \frac{1 - 10^{-A_r}}{1 - 10^{-A_x}} \frac{{n_x}^2}{{n_r}^2}$$

where S_x and S_r are integrated areas under corrected emission spectra, A is the absorbance of the dye at the excitation wavelength, and n is the refractive index of the media, while x and r refer to analyzed dye and reference, respectively. Platinum(II) tetraphenyltetrabenzoporphyrin (Pt[TPTBP]) was used as the standard, for which a quantum yield of 21% had been determined in anoxic toluene.[30] Sample solutions in sealable quartz cells (Hellma Analytics, Mülheim, Germany) were deoxygenated by bubbling high purity nitrogen or argon (99.9999 and 99.999% purity, respectively, Linde gas, Austria) for at least 15 min. Luminescence decay times in solution were measured on the Fluorolog 3 spectrometer equipped with a DeltaHub module (Horiba) controlling a SpectraLED-456 lamp (λ = 456 nm) and using DAS-6 analysis software (Horiba) for data analysis.

Singlet oxygen quantum yields (Φ_Δ) were determined according to the literature procedure.[33] DMA was used as a singlet oxygen acceptor (c = 0.20 mM). A solution of DMA along with a sensitizer (concentration adjusted to identical absorbance at 595 nm) in EtOH/THF (9:1 v/v) was irradiated in a screw-cap quartz cuvette with the Xe lamp of the fluorometer (λ_{max} 595 nm, slit width 10 nm). Degradation of DMA was assessed via absorption measurements at 358 nm. The solution was magnetically stirred during irradiation and shaken after each irradiation period to ensure air-saturated conditions. Singlet oxygen quantum yields were determined relative to methylene blue, Φ_Δ = 0.48, which is the average of two values reported by Gross et al.[33] and Usui et al.[35]

PDT Experiments. *Materials and Instrumentation.* RPMI-1640 medium, L-glutamine, fetal bovine serum (FBS), sodium pyruvate, nonessential amino acids, trypsin, and phosphate buffered saline (PBS) were obtained from Gibco BRL, Life Technologies (Inchinnan, Scotland). Gentamicin sulfate was purchased from Schering Corp (Kenilworth, NJ), absolute ethanol from Arcus A/S (Oslo, Norway), and MTT [3-(4,5 dimethylthiazol-2-yl)-2,5-diphenyltetrazolium bromide] solution from Sigma-Aldrich (St. Louis, MO). Other chemicals were of the highest quality and commercially available.

The syngeneic rat bladder cancer cell line AY27 was kindly provided by Professor S. Selman, University of Ohio, USA, while the WiDr cell line was derived from a human primary adenocarcinoma of the rectosigmoid colon (P. Noguchi, 1979). Both cell lines were cultured in Corning/Sarstedt, 60 mm × 15 mm dishes, Nunc Denmark, and grown in RPMI-1640 medium, containing 10% v/v FBS, L-glutamine (80 mg/L), penicillin (100 U/mL), streptomycin (100 U/mL), and fungizone (0.25 mg/mL). The cell lines were grown in an atmosphere of 95% air and 5% CO_2 at 37 °C and were subcultured approximately twice a week.

In the phototoxicity measurements, cells at room temperature were illuminated from below by a LumiSource (PCI Biotech AS, Oslo) lamp. The lamp is designed to provide homogenous illumination of living cells in an in vitro setting across an area of 45 × 17 cm. The lamp consists of four tubes (4 × 18 W Osram L 18/67) that emit light at a peak wavelength of 435 nm, resulting in 13 mW/cm^2 light intensity at the cells, that is, near the bottom of cell dishes. Both light-sensitive solutions and cells were covered with aluminum foil during the entire experiments. All dishes were covered with aluminium foil and incubated for 24 h (37 °C, 5% CO_2).

Viability Assays on AY27 and WiDr Cancer Cell Lines. Day 1. The cells were washed with PBS, harvested from the cultivation flasks, and loosened with trypsin (2%, 3 mL). After 3−5 min, growth medium (10 mL) was added, and the cell suspension was transferred to a 50-mL tube and centrifuged (5 min, 1500 rpm, 4 °C), followed by removal of dead cells. The cell pellet was carefully resuspended in the growth medium (0.5 mL), prior to further dilution with growth medium to a total volume of 10 mL. The cell suspension (20 μL) was then added to a Bürker chamber. The cell numbers in four 1 mm^2 squares were manually counted, which provided the cell concentration in the stock solution. After dilution with growth medium, the cells were seeded in 6 cm Petri dishes containing 3 mL of cell suspension (0.25−0.35 × 10^6 cells/dish). The dishes were incubated for ∼24 h at 37 °C, with each experiment including 20−30 dishes.

Day 2. Growth medium was removed, and new medium was added (3 mL, 37 °C) to the control dishes (without the photosensitizer). For PDT experiments, growth medium was removed, and photosensitizer-containing medium (10 μM, 3 mL, 37 °C) was added to the remaining dishes in the dark. Cells with only photosensitizer-containing medium were used for dark toxicity assessments while samples without any treatment (with either light or photosensitizer) were used as controls. After a postincubation period (24 h, 37 °C, 5% CO_2) after illumination, the MTT cell proliferation assay[36,37] was performed as follows: Growth medium was removed, and the cells were incubated in MTT solution (0.5 mg/mL, 1 h, 37 °C, 5% CO_2, Sigma-Aldrich, St. Louis, MO). The MTT solution was then decanted off and replaced by isopropanol (2 mL). The dishes were then placed on a plate shaker for (200 rpm) 30 min. Dead cells were then removed by centrifuging the cell suspensions (5 min, 1500 rpm), as previously described for the AY27 cell line.[26] The absorbance of the supernatant was measured at 595 nm with a Shimadzu UV-1700 spectrophotometer. The data so obtained were processed and compared with those for cells without any treatment (with either light or photosensitizer).

Day 3. The control dishes (which did not undergo either light nor photosensitizer) were washed twice with PBS (3 mL, 37 °C), followed by addition of growth medium (3 mL, 37 °C), and placed in an incubator (37 °C, 5% CO_2). Additional PBS was added (3 mL, 37 °C) to all the other dishes before illumination with blue light. After illumination over different time intervals, the PBS was removed, and growth medium was added (3 mL, 37 °C). All dishes were then placed under further incubation (24 h, 37 °C).

Day 4. Twenty-four hours after illumination, MTT assays were performed to measure the indirect activity of living cells. MTT working solutions (0.5 mg/mL) were freshly made using a 1:9 mixture of MTT stock solution (5 mg/mL, 37 °C) and growth medium (37 °C). All the dishes were carefully washed with PBS (2 mL) before the MTT working solution (2 mL, 1 h, 37 °C) was added. After incubation, the MTT working solution was removed, and isopropanol (2 mL, room temperature) was added before the Petri dishes were placed on an orbital shaker (30 min, 70 rpm). The shaken suspensions were transferred to 15 mL tubes and centrifuged (5 min, 1500 rpm, 4 °C). The supernatants were transferred into cuvettes and diluted 10-fold with isopropanol. The absorbance at λ_{ex} = 595 nm was measured on a double-beam UV−vis spectrophotometer (UV-1700 Shimadzu, Japan) using isopropanol as reference.

■ ASSOCIATED CONTENT

Supporting Information

The Supporting Information is available free of charge at https://pubs.acs.org/doi/10.1021/acsomega.0c01090.

UV−vis spectra, phosphorescence decays, NMR, mass, and IR spectra (PDF)

■ AUTHOR INFORMATION

Corresponding Authors

Sergey M. Borisov − *Institute of Analytical Chemistry and Food Chemistry, Graz University of Technology, 8010 Graz, Austria;* orcid.org/0000-0001-9318-8273; Email: sergey.borisov@tugraz.at

Abhik Ghosh − *Department of Chemistry, UiT—The Arctic University of Norway, N-9037 Tromsø, Norway;* orcid.org/0000-0003-1161-6364; Email: abhik.ghosh@uit.no

Odrun A. Gederaas − *Department of Clinical and Molecular Medicine and Department of Physics, Norwegian University of Science and Technology, NTNU, N-7491 Trondheim, Norway;* Email: odrun.gederaas@ntnu.no

Authors

Rune F. Einrem − *Department of Chemistry, UiT—The Arctic University of Norway, N-9037 Tromsø, Norway*

Abraham B. Alemayehu − *Department of Chemistry, UiT—The Arctic University of Norway, N-9037 Tromsø, Norway;* orcid.org/0000-0003-0166-8937

Complete contact information is available at: https://pubs.acs.org/10.1021/acsomega.0c01090

Notes

The authors declare no competing financial interest.

■ ACKNOWLEDGMENTS

This work was supported by the Research Council of Norway (grant no. 262229 to A.G.), with supplementary funding from the Cancer Research Foundation of St. Olav's University Hospital, Trondheim. We thank Matthias Schwar (TU Graz) for the singlet oxygen assays.

■ REFERENCES

(1) Bonnett, R. *Chemical Aspects of Photodynamic Therapy*; CRC: Boca Raton, FL, 2000; p 324.

(2) *Handbook of photodynamic therapy : updates on recent applications of porphyrin-based compounds*; Pandey, R. K., Kessel, D., Dougherty, T. J., Eds.; World Scientific: New Jersey, 2016; p 564.

(3) Patrice, T.; Moan, J.; Peng, Q. An outline of the history of PDT. *Photodynamic Therapy*; Royal Society of Chemistry: London, 2003, pp 1−18.

(4) Spikes, J. D. Porphyrins and related compounds as photodynamic sensitizers. *Ann. N.Y. Acad. Sci.* **1975**, *244*, 496−508.

(5) Bonnett, R. Photosensitizers of the porphyrin and phthalocyanine series for photodynamic therapy. *Chem. Soc. Rev.* **1995**, *24*, 19−33.

(6) Sternberg, E. D.; Dolphin, D.; Brückner, C. Porphyrin-based photosensitizers for use in photodynamic therapy. *Tetrahedron* **1998**, *54*, 4151−4202.

(7) Abrahamse, H.; Hamblin, M. R. New photosensitizers for photodynamic therapy. *Biochem. J.* **2016**, *473*, 347−364.

(8) Ethirajan, M.; Chen, Y.; Joshi, P.; Pandey, R. K. The Role of Porphyrin Chemistry in Tumor Imaging and Photodynamic Therapy. *Chem. Soc. Rev.* **2011**, *40*, 340−362.

(9) Ghosh, A. Electronic Structure of Corrole Derivatives: Insights from Molecular Structures, Spectroscopy, Electrochemistry, and Quantum Chemical Calculations. *Chem. Rev.* **2017**, *117*, 3798−3881.

(10) Nardis, S.; Mandoj, F.; Stefanelli, M.; Paolesse, R. Metal complexes of corrole. *Coord. Chem. Rev.* **2019**, *388*, 360−405.

(11) Teo, R. D.; Hwang, J. Y.; Termini, J.; Gross, Z.; Gray, H. B. Fighting Cancer with Corroles. *Chem. Rev.* **2017**, *117*, 2711−2729.

(12) Jiang, X.; Liu, R. X.; Liu, H. Y.; Chang, C. K. Corrole-based photodynamic antitumor therapy. *J. Chin. Chem. Soc.* **2019**, *66*, 1090−1099.

(13) Teo, R. D.; Gray, H. B.; Lim, P.; Termini, J.; Domeshek, E.; Gross, Z. A Cytotoxic and Cytostatic Gold(III) Corrole. *Chem. Commun.* **2014**, *50*, 13789−13792.

(14) Alemayehu, A. B.; Day, N. U.; Mani, T.; Rudine, A. B.; Thomas, K. E.; Gederaas, O. A.; Vinogradov, S. A.; Wamser, C. C.; Ghosh, A. Gold Tris(carboxyphenyl)corroles as Multifunctional Materials: Room Temperature Near-IR Phosphorescence and Applications to Photodynamic Therapy and Dye-Sensitized Solar Cells. *ACS Appl. Mater. Interfaces* **2016**, *8*, 18935−18942.

(15) Lemon, C. M.; Powers, D. C.; Brothers, J.; Nocera, D. G. Gold Corroles as Near-IR Phosphors for Oxygen Sensing. *Inorg. Chem.* **2017**, *56*, 10991−10997.

(16) Einrem, R. F.; Gagnon, K. J.; Alemayehu, A. B.; Ghosh, A. Metal-Ligand Misfits: Facile Access to Rhenium-Oxo Corroles by Oxidative Metalation. *Chem.—Eur. J.* **2016**, *22*, 517−520.

(17) Alemayehu, A. B.; Teat, S. J.; Borisov, S. M.; Ghosh, A. Rhenium-Imido Corroles. *Inorg. Chem.* **2020**, *59*, 6382−6389.

(18) Alemayehu, A. B.; Gagnon, K. J.; Terner, J.; Ghosh, A. Oxidative Metalation as a Route to Size-Mismatched Macrocyclic Complexes: Osmium Corroles. *Angew. Chem., Int. Ed.* **2014**, *53*, 14411−14414.

(19) Palmer, J. H.; Day, M. W.; Wilson, A. D.; Henling, L. M.; Gross, Z.; Gray, H. B. Iridium Corroles. *J. Am. Chem. Soc.* **2008**, *130*, 7786−7787.

(20) Alemayehu, A. B.; Vazquez-Lima, H.; Beavers, C. M.; Gagnon, K. J.; Bendix, J.; Ghosh, A. Platinum corroles. *Chem. Commun.* **2014**, *50*, 11093−11096.

(21) Borisov, S. M.; Einrem, R. F.; Alemayehu, A. B.; Ghosh, A. Ambient-temperature near-IR phosphorescence and potential applications of rhenium-oxo corroles. *Photochem. Photobiol. Sci.* **2019**, *18*, 1166−1170.

(22) Borisov, S. M.; Alemayehu, A.; Ghosh, A. Osmium-Nitrido Corroles as NIR Indicators for Oxygen Sensors and Triplet Sensitizers for Organic Upconversion and Singlet Oxygen Generation. *J. Mater. Chem. C* **2016**, *4*, 5822−5828.

(23) Palmer, J. H.; Durrell, A. C.; Gross, Z.; Winkler, J. R.; Gray, H. B. Near-IR Phosphorescence of Iridium(III) Corroles at Ambient Temperature. *J. Am. Chem. Soc.* **2010**, *132*, 9230−9231.

(24) Sinha, W.; Ravotto, L.; Ceroni, P.; Kar, S. NIR-Emissive Iridium(III) Corrole Complexes as Efficient Singlet Oxygen Sensitizers. *Dalton Trans.* **2015**, *44*, 17767−17773.

(25) Alemayehu, A. B.; MCormick, L. J.; Gagnon, K. J.; Borisov, S. M.; Ghosh, A. Stable Platinum(IV) Corroles: Synthesis, Molecular Structure, and Room-Temperature Near-IR Phosphorescence. *ACS Omega* **2018**, *3*, 9360−9368.

(26) Gederaas, O. A.; Johnsson, A.; Berg, K.; Manandhar, R.; Shrestha, C.; Skåre, D.; Ekroll, I. K.; Høgset, A.; Hjelde, A. Photochemical internalization in bladder cancer - development of an orthotopic in vivo model. *J. Photochem. Photobiol. Sci.* **2017**, *16*, 1664−1676.

(27) Larsen, E. L.; Randeberg, L. L.; Gederaas, O. A.; Arum, C. J.; Hjelde, A.; Zhao, C. M.; Chen, D.; Krokan, H. E.; Svaasand, L. O. Monitoring of hexyl 5-aminolevulinate-induced photodynamic therapy in rat bladder cancer by optical spectroscopy. *J. Biomed. Opt.* **2008**, *13*, 044031.

(28) Lindgren, M.; Gederaas, O. A.; Siksjø, M.; Hansen, T. A.; Chen, L.; Mettra, B.; Andraud, C.; Monnereau, C. Influence of Polymer Charge on the Localization and Dark- and Photo-Induced Toxicity of a Potential Type I Photosensitizer in Cancer Cell Models. *Molecules* **2020**, *25*, 1127.

(29) Noguchi, P.; Wallace, R.; Johnson, J.; Earley, E. M.; O'Brien, S.; Ferrone, S.; Pellegrino, M. A.; Milstien, J.; Needy, C.; Browne, W.; Petricciani, J. Characterization of WiDr: A human colon carcinoma cell line. *In Vitro* **1979**, *15*, 401−408.

(30) Zach, P. W.; Freunberger, S. A.; Klimant, I.; Borisov, S. M. Electron-Deficient Near-Infrared Pt(II) and Pd(II) Benzoporphyrins with Dual Phosphorescence and Unusually Efficient Thermally Activated Delayed Fluorescence: First Demonstration of Simultaneous Oxygen and Temperature Sensing with a Single Emitter. *ACS Appl. Mater. Interfaces* **2017**, *9*, 38008−38023.

(31) *Hydrogen Bonding and Transfer in the Excited State, I & II*; Han, K.-L., Zhao, G.-J., Eds.; Wiley: Hoboken, NJ, 2011.

(32) *Fluorescence Spectroscopy in Biology: Advanced Methods and their Applications to Membranes, Proteins, DNA, and Cells*; Hof, M., Hutterer, R., Fidler, V., Eds.; Springer: Heidelberg, 2005.

(33) Gross, E.; Ehrenberg, B.; Johnson, F. M. Singlet Oxygen Generation by Porphyrins and the Kinetics of 9,10-Dimethylanthracene Photosensitization in Liposomes. *Photochem. Photobiol.* **1993**, *57*, 808−813.

(34) Crosby, G. A.; Demas, J. N. Measurement of photoluminescence quantum yields. Review. *J. Phys. Chem.* **1971**, *75*, 991−1024.

(35) Usui, Y.; Koike, H.; Kurimura, Y. An Efficient Regeneration of Singlet Oxygen from 2,5-Diphenylfuran Endoperoxide Produced by a Dye-Sensitized Oxygenation. *Bull. Chem. Soc. Jpn.* **1987**, *60*, 3373−3378.

(36) Mosmann, T. Rapid Colorimetric Assay for Cellular Growth and Survival: Application to Proliferation and Cytotoxicity Assays. *J. Immunol. Methods* **1983**, *65*, 55−63.

(37) Carmichael, J.; DeGraff, W. G.; Gazdar, A. F.; Minna, J. D.; Mitchell, J. B. Evaluation of a tetrazolium-based semiautomated colorimetric assay: assessment of radiosensitivity. *Cancer Res.* **1987**, *47*, 943−946.

Supporting Information

Amphiphilic Rhenium-Oxo Corroles as a New Class of Sensitizers for Photodynamic Therapy

Rune F. Einrem,[a] Abraham B. Alemayehu,[a] Sergey M. Borisov,*[b]
Abhik Ghosh*[a] and Odrun A. Gederaas*[c]

[a] Department of Chemistry, UiT – The Arctic University of Norway, N-9037 Tromsø, Norway
[b] Institute of Analytical Chemistry and Food Chemistry, Graz University of Technology, Stremayrgasse 9, 8010 Graz, Austria
[c] Department of Clinical and Molecular Medicine and Department of Physics, Norwegian University of Science and Technology, NTNU, N-7491 Trondheim, Norway

* Correspondence: sergey.borisov@tugraz.at (SMB), abhik.ghosh@uit.no (AG), odrun.gederaas@ntnu.no (OAG)

Content Page

A. UV-vis spectra

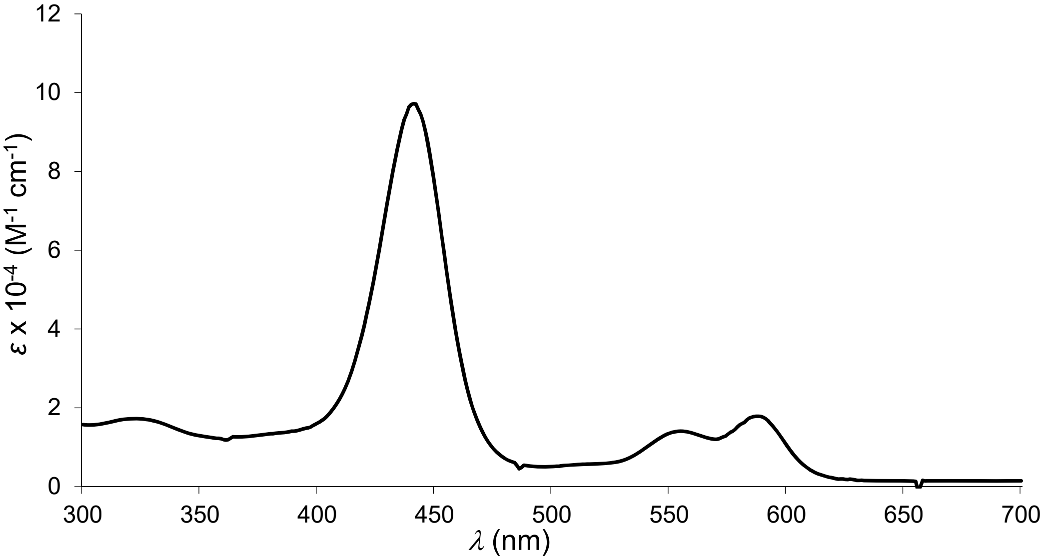

Figure S1. UV-vis spectrum in DCM of Re[T*p*CO_2CH_3PC](O).

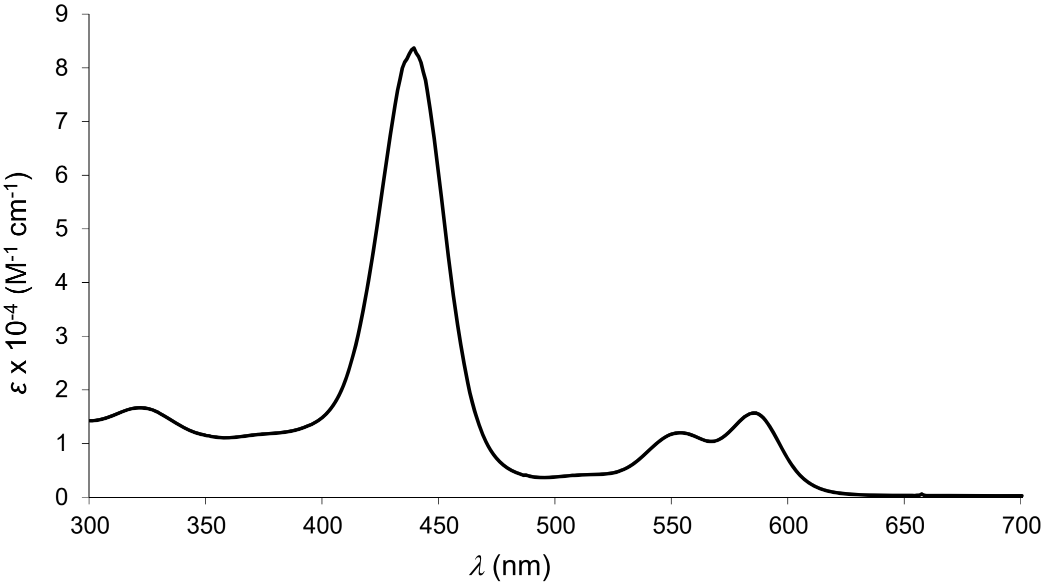

Figure S2. UV-vis spectrum in DCM of Re[T*m*CO_2CH_3PC](O).

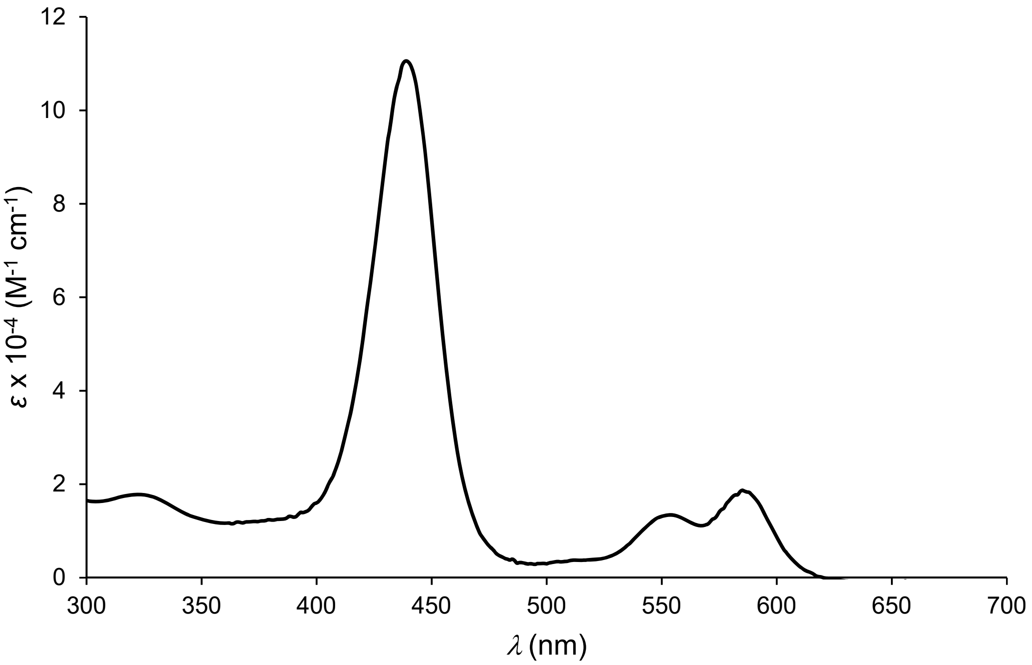

Figure S3. UV-vis spectrum in DCM of Re[*p*TCPC](O).

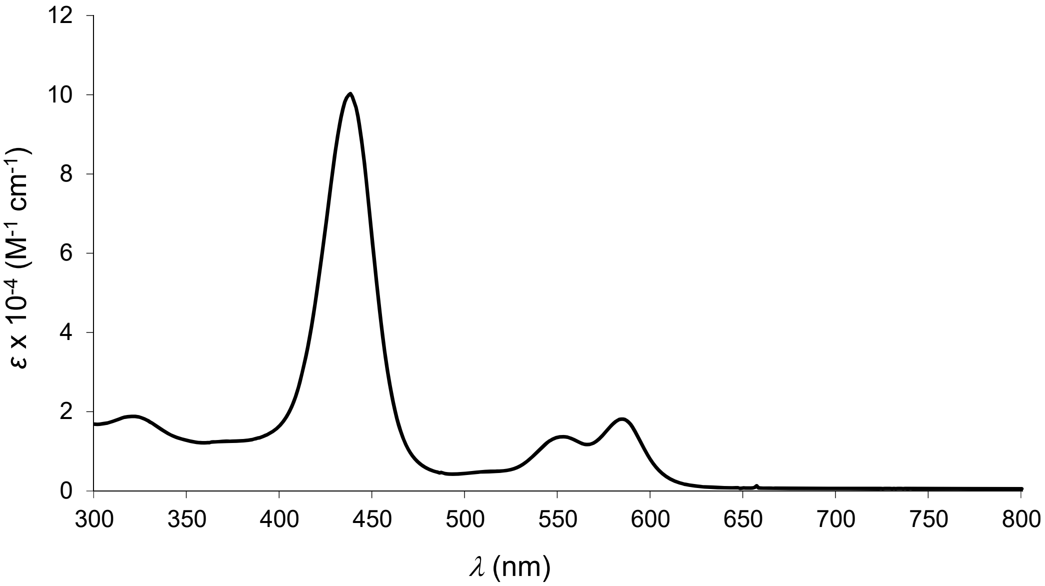

Figure S4. UV-vis spectrum in DCM of Re[*m*TCPC](O).

B. Phosphorescence decays

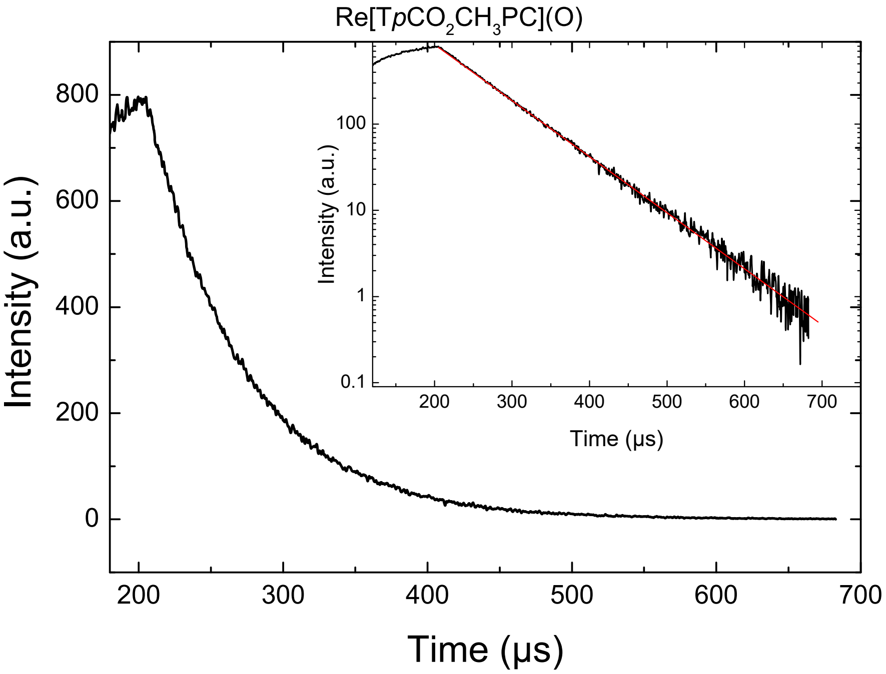

Figure S5. Phosphorescence decay of Re[T*p*CO$_2$CH$_3$PC](O) in anoxic toluene. The inset shows the logarithmic plot.

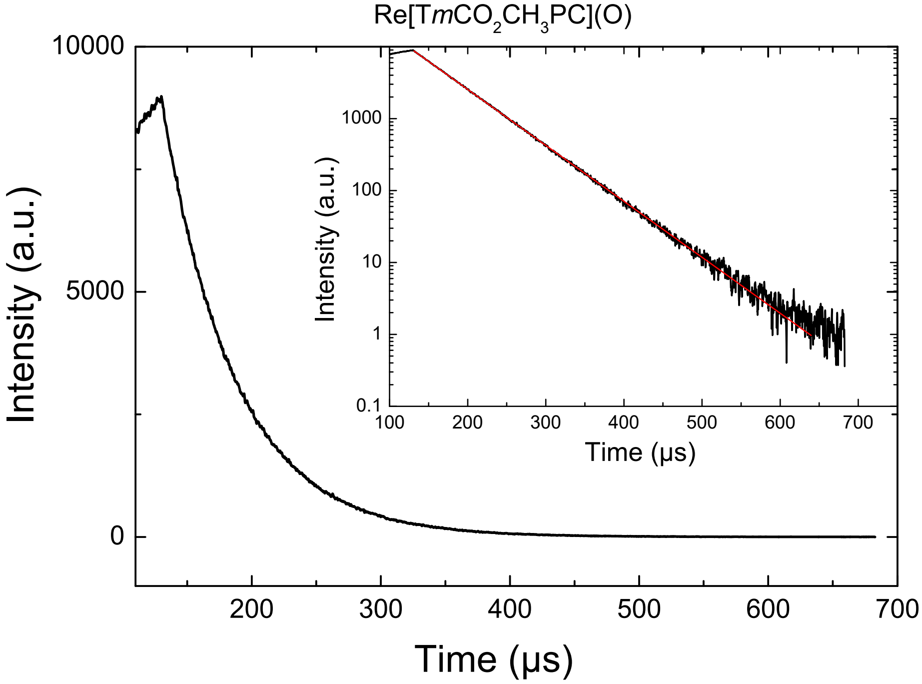

Figure S6. Phosphorescence decay of Re[T*m*CO$_2$CH$_3$PC](O) in anoxic toluene. The inset shows the logarithmic plot.

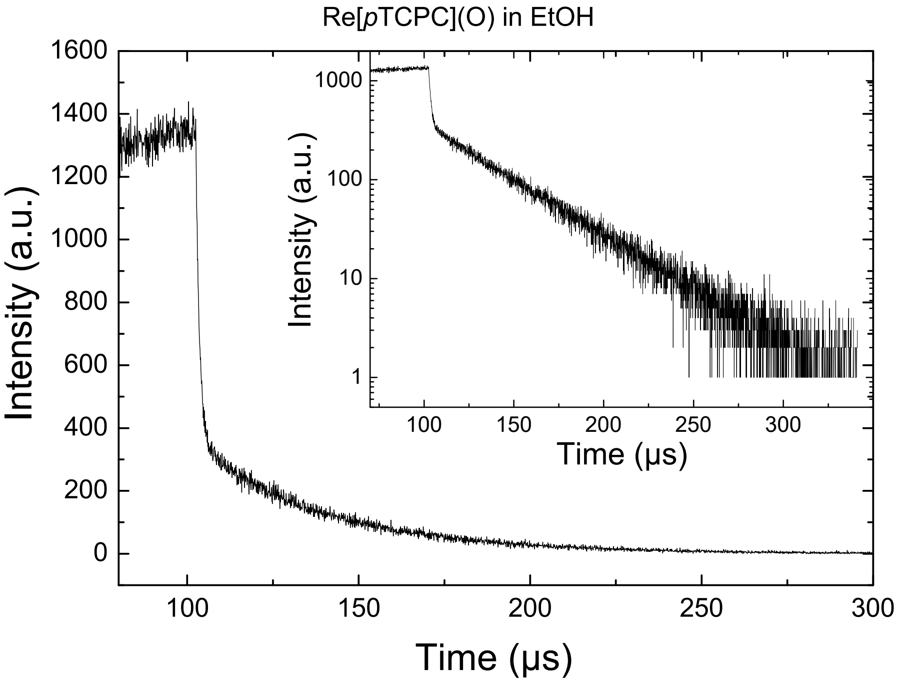

Figure S7. Phosphorescence decay of Re[*p*TCPC](O) in anoxic ethanol. The inset shows the logarithmic plot.

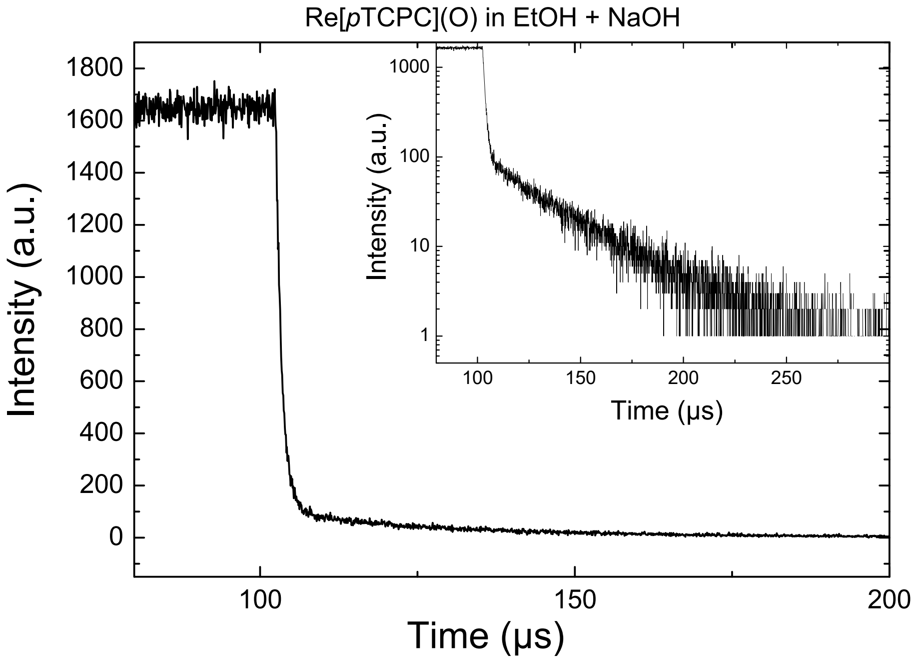

Figure S8. Phosphorescence decay of Re[*p*TCPC](O) in anoxic ethanol with added NaOH ($3 \cdot 10^{-3}$ M). The inset shows the logarithmic plot.

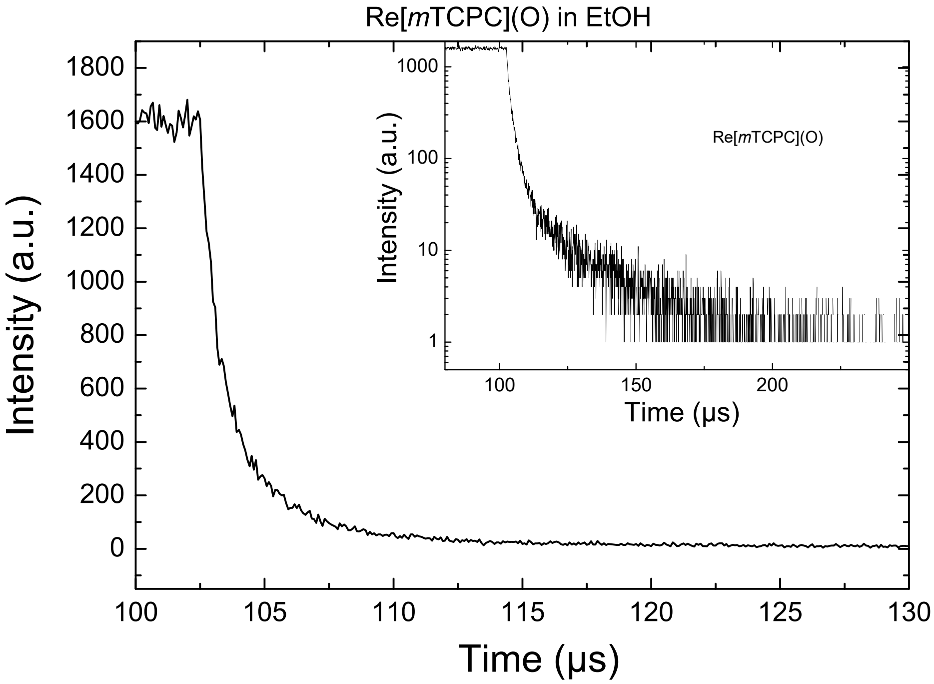

Figure S9. Phosphorescence decay of Re[*m*TCPC](O) in anoxic ethanol. The inset shows the logarithmic plot.

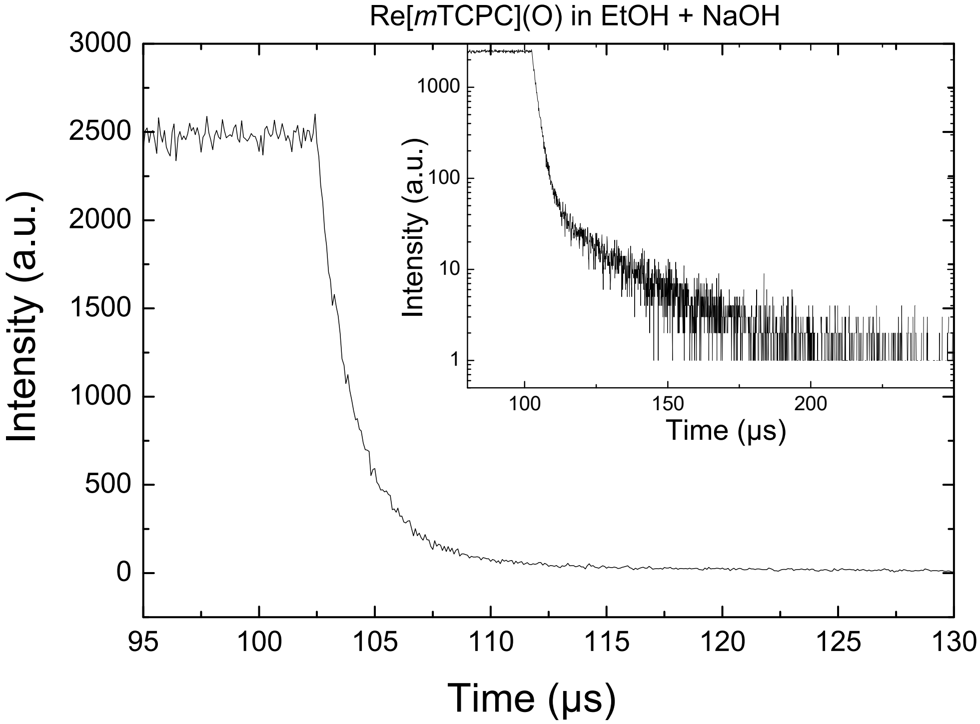

Figure S10. Phosphorescence decay of Re[*m*TCPC](O) in anoxic ethanol with added NaOH ($3 \cdot 10^{-3}$ M). The inset shows the logarithmic plot.

C. Singlet oxygen assay

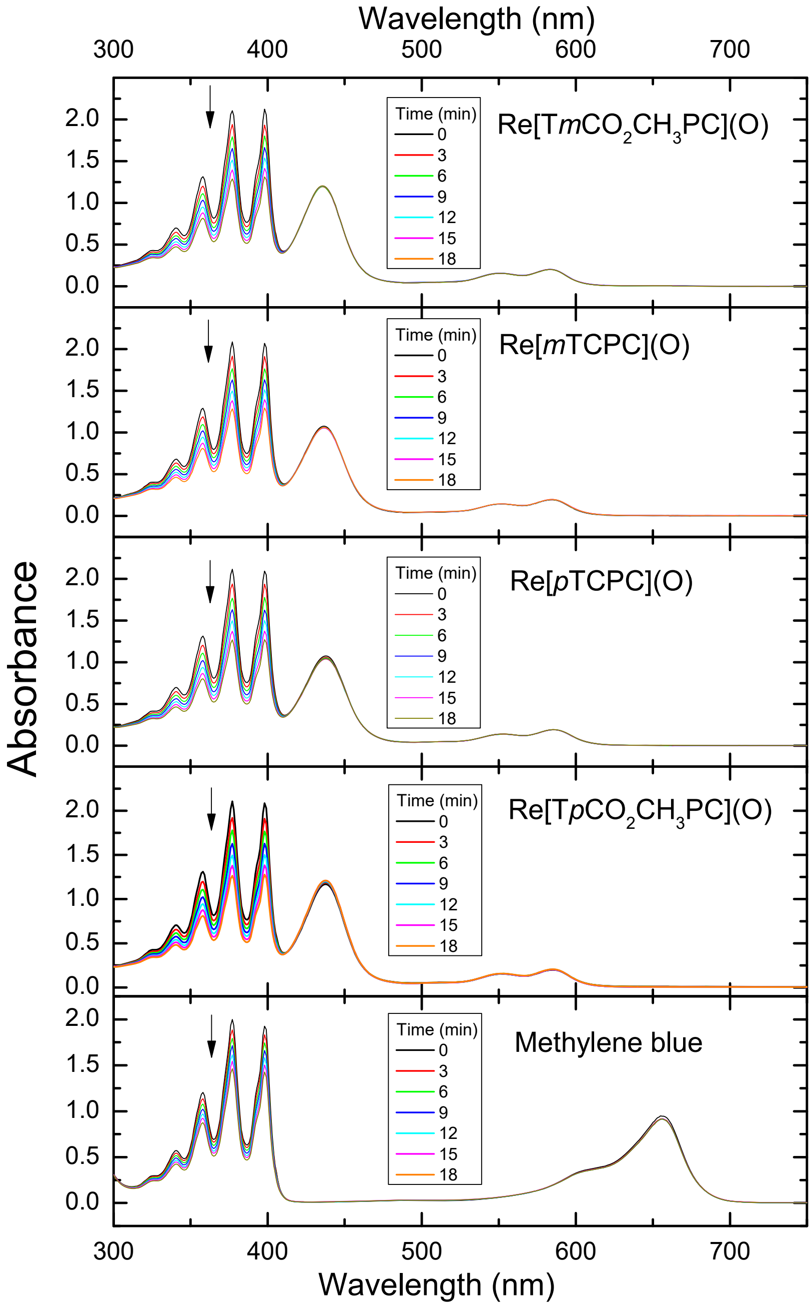

Figure S11. UV-vis spectra of air-saturated solutions containing 9,10-dimethylanthracene and a sensitizer upon irradiation with 595±5 nm light.

D. ^{1}H NMR spectra

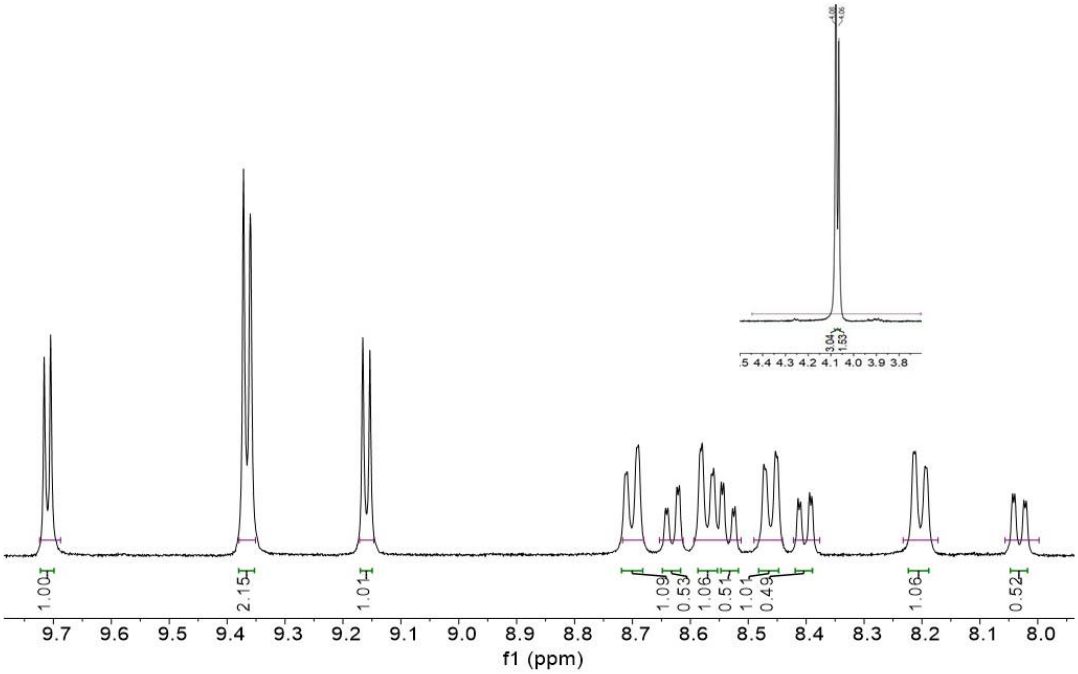

Figure S12. ^{1}H NMR (400 Hz, CD_2Cl_2, -20°C) spectrum of Re[T*p*CO_2CH_3PC](O).

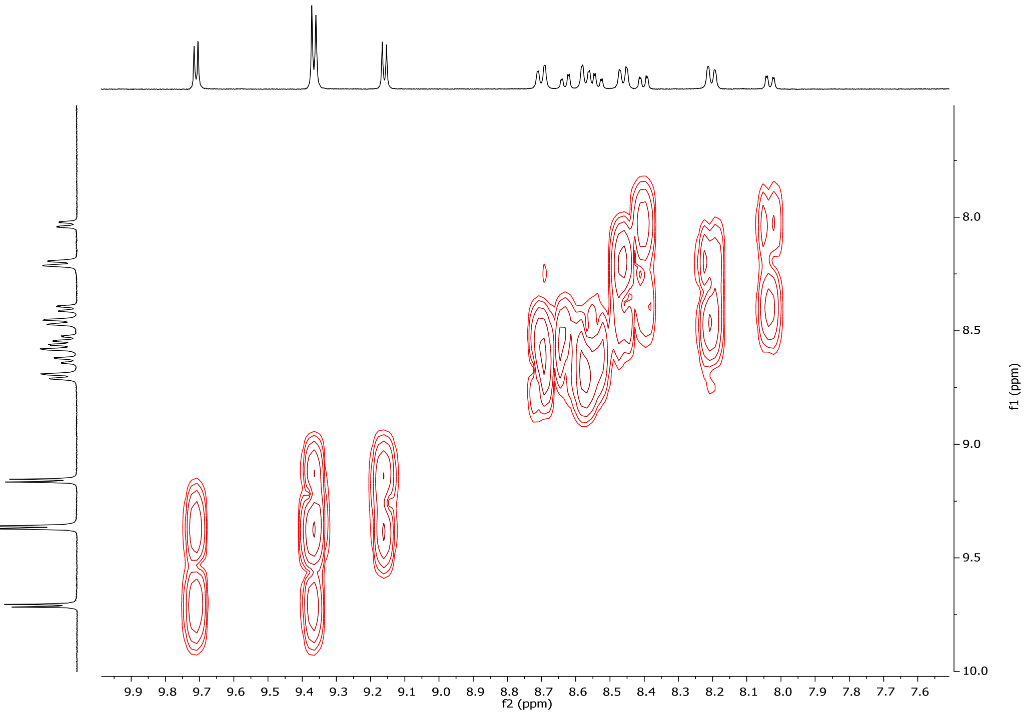

Figure S13. COSY (400Hz CD_2Cl_2, -20°C) of Re[T*p*CO_2CH_3PC](O).

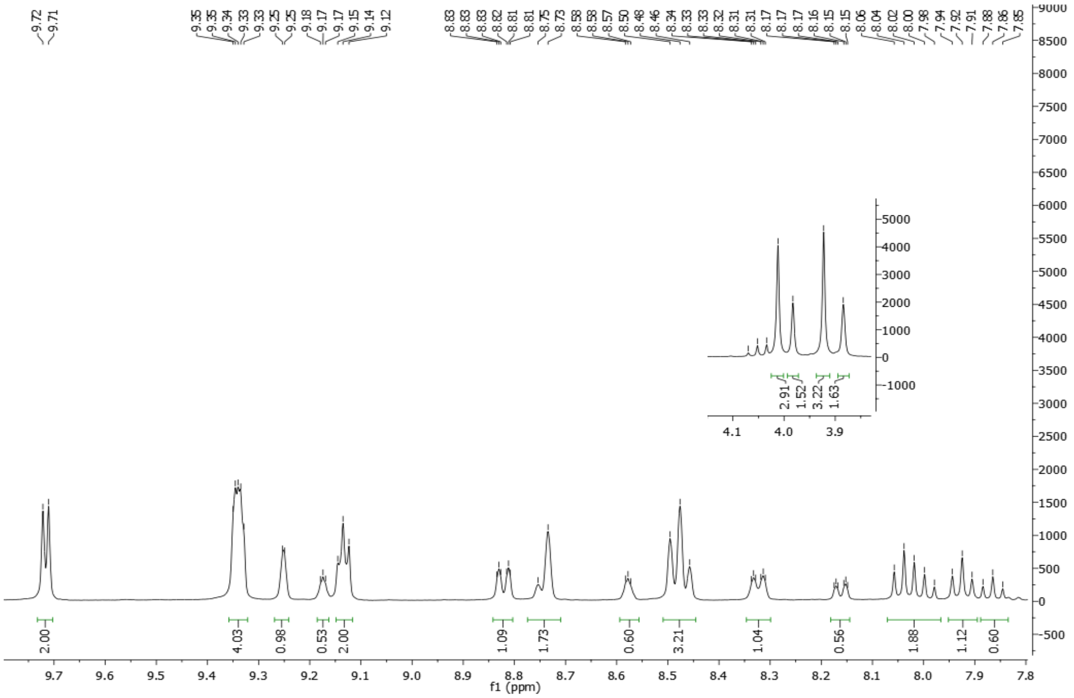

Figure S14. ^{1}H NMR (400 Hz, CD_2Cl_2, -20°C) spectrum of Re[T*m*CO_2CH_3PC](O).

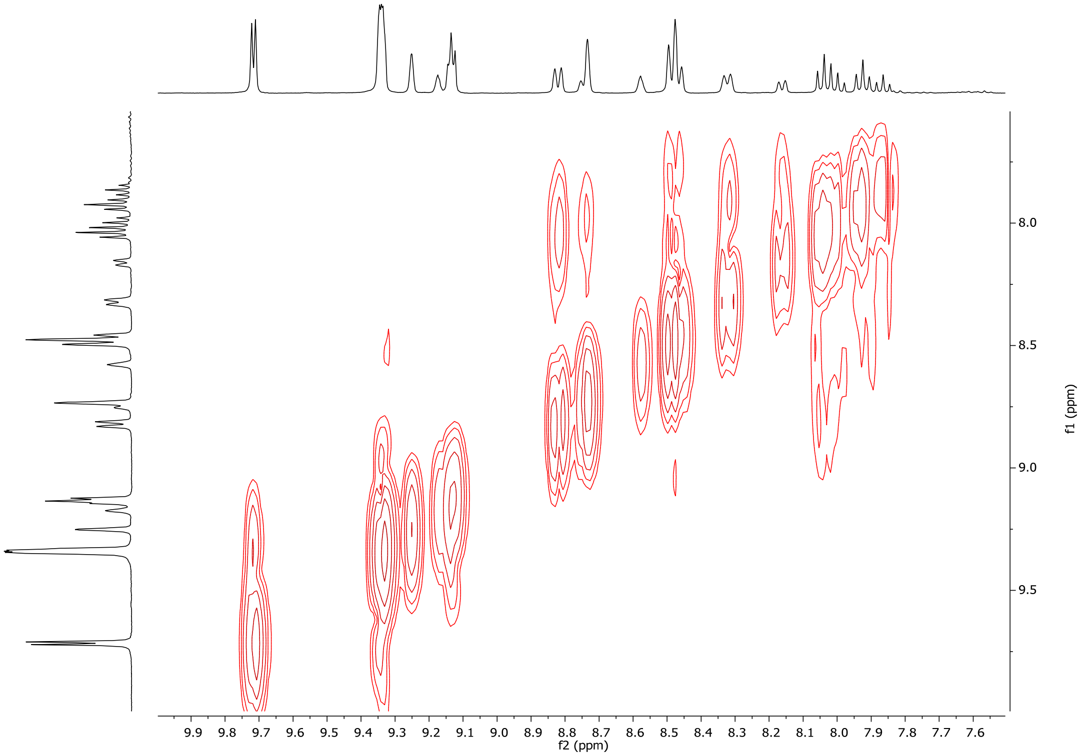

Figure S15. COSY (400Hz, CD_2Cl_2, -20°C) of Re[T*m*CO_2CH_3PC](O).

E. ESI mass spectra

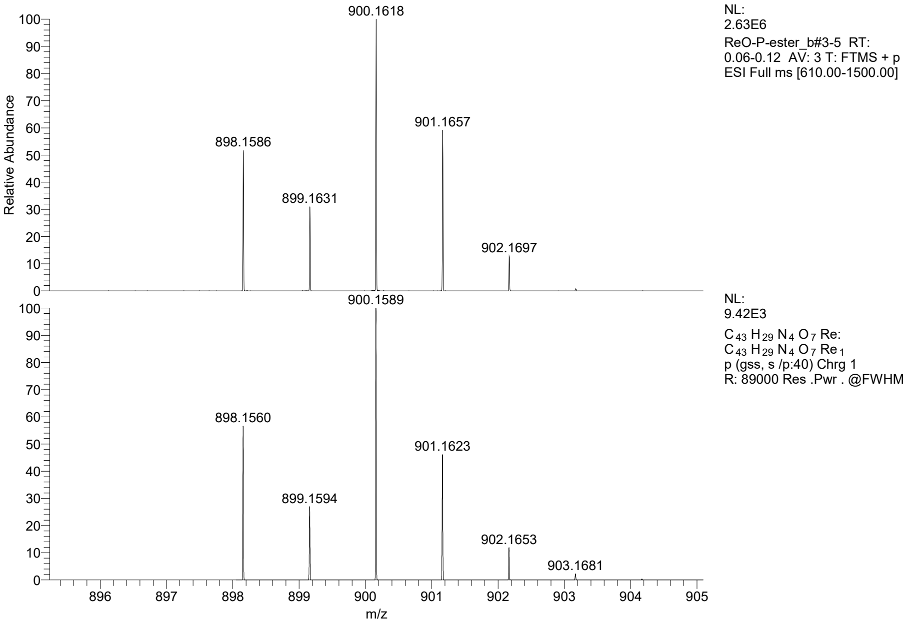

Figure S16. ESI-MS of Re[T*p*CO_2CH_3PC](O).

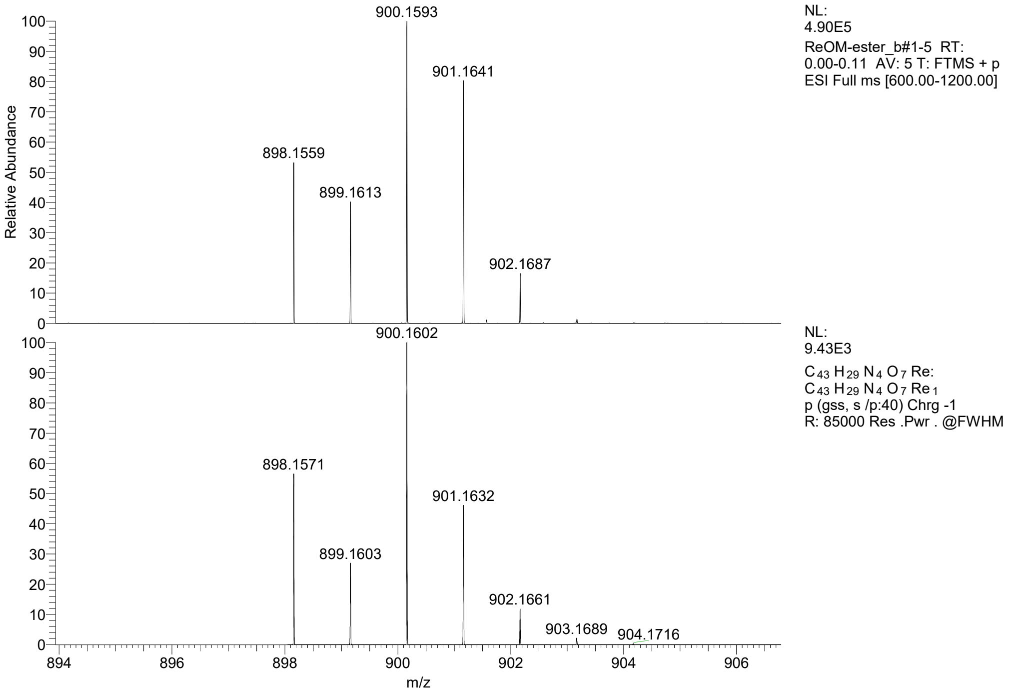

Figure 17. ESI-MS of Re[T*m*CO_2CH_3PC](O).

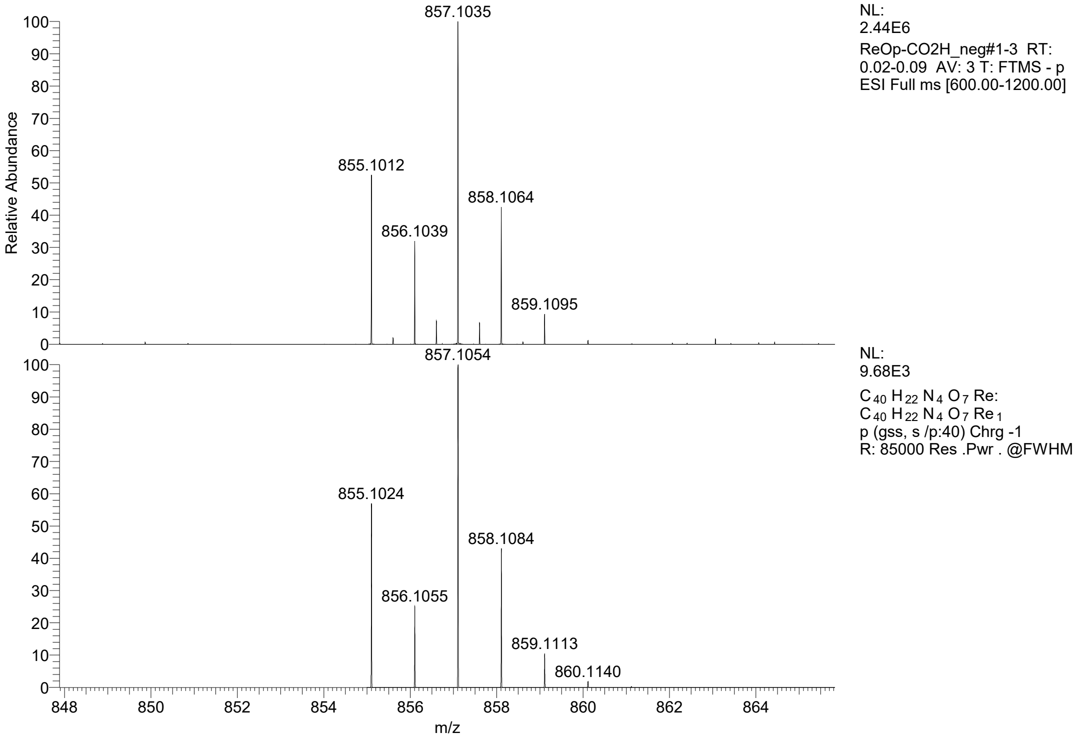

Figure S18. ESI-MS of Re[*p*TCPC](O).

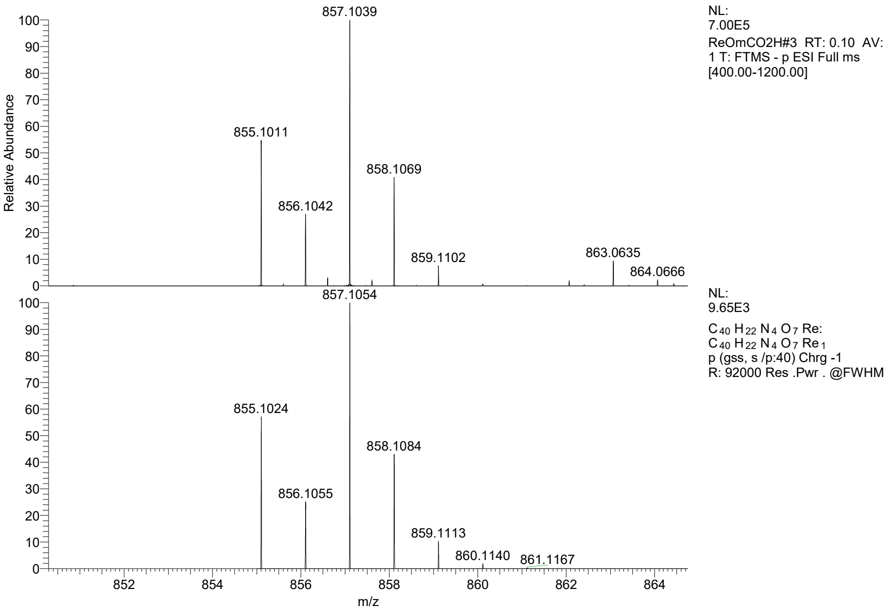

Figure S19. ESI-MS of Re[*m*TCPC](O).

F. FT-IR spectra

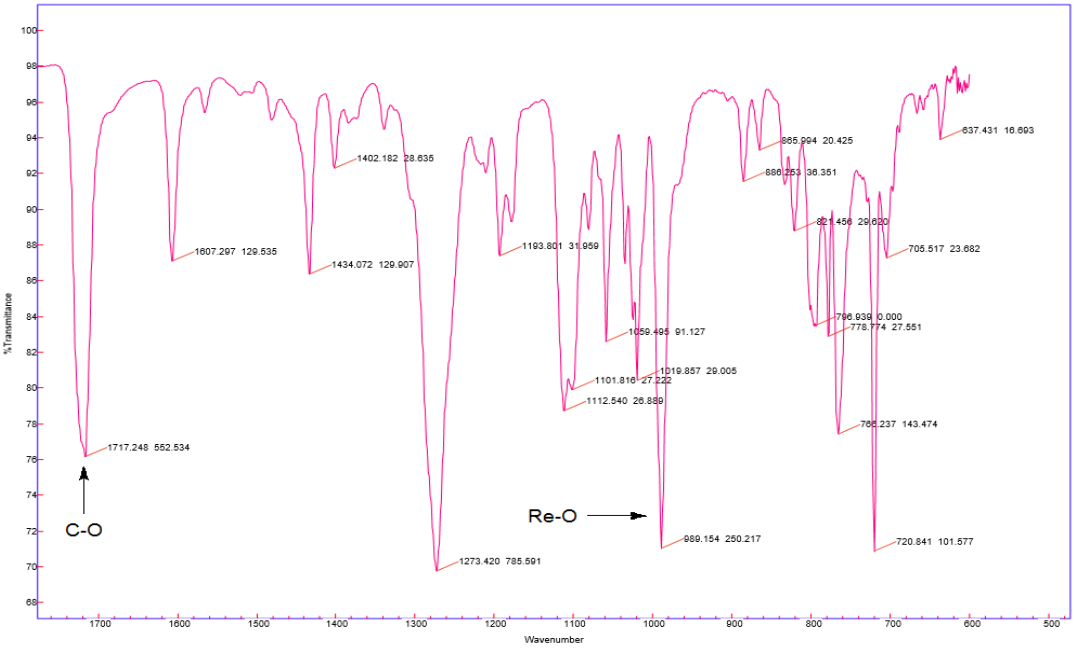

Figure S20. IR spectrum of Re[T*p*CO_2CH_3PC](O).

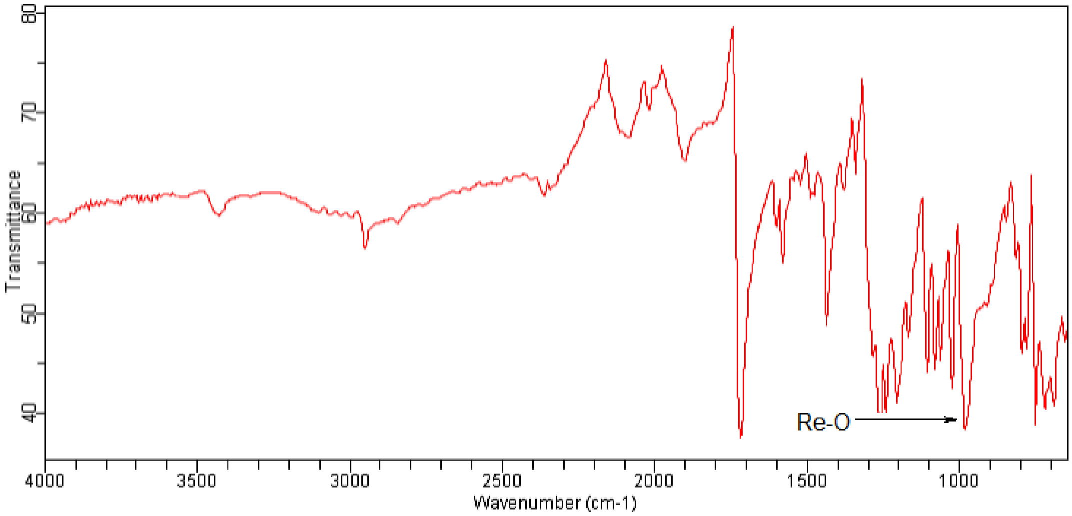

Figure S21. IR spectrum of Re[T*m*CO_2CH_3PC](O).

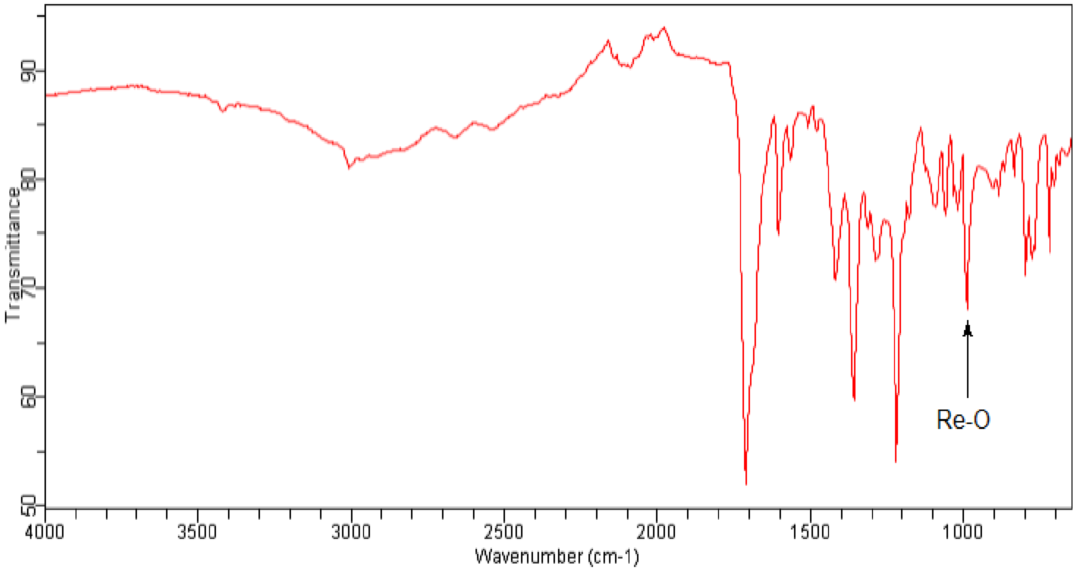

Figure S22. IR spectrum of Re[*p*TCPC](O).

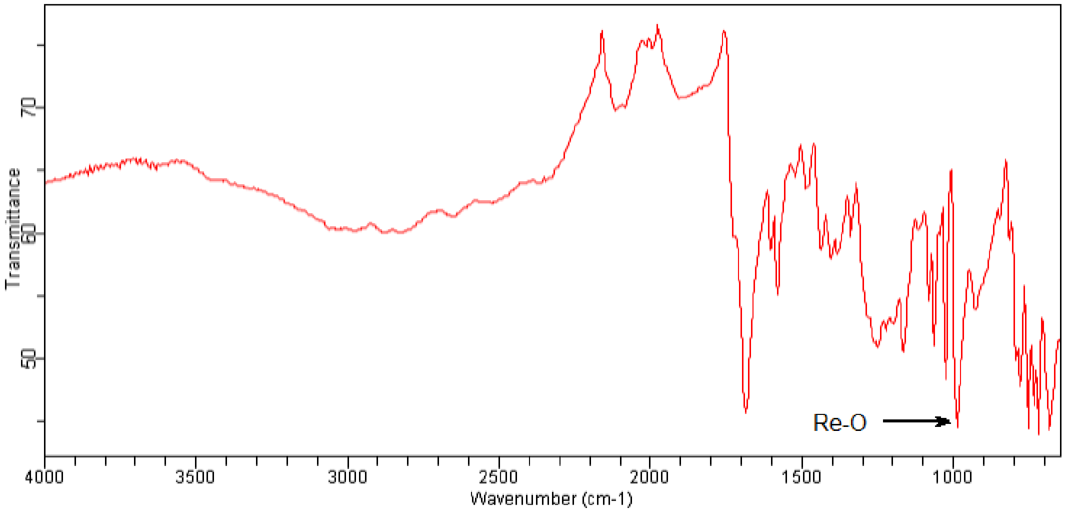

Figure S23. IR spectrum of Re[*m*TCPC](O).

Paper C

scientific reports

OPEN

Synthesis and molecular structure of perhalogenated rhenium-oxo corroles

Abraham B. Alemayehu[1], Rune F. Einrem[1], Laura J. McCormick-McPherson[2], Nicholas S. Settineri[2,3] & Abhik Ghosh[1]✉

As part of our efforts to develop rhenium-oxo corroles as photosensitizers for oxygen sensing and photodynamic therapy, we investigated the potential β-perhalogenation of five ReO *meso*-tris(*para*-X-phenyl)corroles, Re[T*p*XPC](O) (X = CF_3, H, F, CH_3, and OCH_3), with elemental chlorine and bromine. With Cl_2, β-octachlorinated products Re[Cl_8T*p*XPC](O) were rapidly obtained for X = CF_3, H, and CH_3, but X = OCH_3 resulted in overchlorination on the *meso*-aryl groups. Full β-octabromination proved slower relative to Cu and Ir corroles, but the desired Re[Br_8T*p*XPC](O) products were finally obtained for X = H and F after a week at room temperature. For X = CH_3 and OCH_3, these conditions led to undecabrominated products Re[Br_{11}T*p*XPC](O). Compared to the β-unsubstituted starting materials, the β-octahalogenated products were found to exhibit sharp ^1H NMR signals at room temperature, indicating that the aryl groups are locked in place by the β-halogens, and substantially redshifted Soret and Q bands. Single-crystal X-ray structures of Re[Cl_8T*p*CF_3PC](O), Re[Cl_8T*p*CH_3PC](O), and Re[Br_8T*p*FPC](O) revealed mild saddling for one Cl_8 structure and the Br_8 structure. These structural variations, however, appear too insignificant to explain the slowness of the β-octabromination protocols, which seems best attributed to the deactivating influence of the high-valent Re center.

The remarkable β-octachlorination and β-octabromination of metallotetraarylporphyrins was first reported by the Traylor, Dolphin and their research groups in the 1980s[1,2]. During the 1990s, iron and manganese complexes of β-octahalogenoporphyrins were intensively investigated as rugged, synthetic models of cytochrome P450[3–6]. β-Octahalogeno-*meso*-tetraarylporphyrin derivatives also provided textbook examples of saddling, a nonplanar distortion in which the pyrrole rings are alternately tilted up and down relative to the mean porphyrin plane[7–11]. The compounds became the subject of a battery of spectroscopic, electrochemical, and structural studies, which yielded a rich body of insights on substituent effects in porphyrin derivatives[10,12–15].

With the advent of simple, one-pot syntheses[16–19] of corroles[20,21], β-octabromination was also found to work for certain corrole derivatives[22,23]. In our laboratory, we prepared some of the first β-octabromo-*meso*-triarylcorroles, initially the copper complexes[24,25] and subsequently also the free bases[26–28]. Remarkably, a number of crystal structures of β-octabrominated metallocorroles revealed planar corrole rings, underscoring the rigidity of the corrole ring system relative to porphyrins[23,29–31]. Today we know that saddling in corroles is largely limited to copper[32–37] corroles (and in part to silver[38] corroles but not gold[39–42] corroles), where it is thought to be a manifestation of ligand noninnocence, i.e., a distortion mode that facilitates $Cu^{II}(d_{x2-y2})$-corrole$^{\cdot 2-}$ antiferromagnetic coupling[43–46].

The present study is part of our ongoing efforts to functionalize and derivatize 5d metallocorroles[38–42,47–54]. These complexes provide unusual examples of a large transition metal ion coordinated to a sterically constrained macrocyclic ligand. Despite the steric mismatch inherent in their structures, a good fraction of these complexes exhibit remarkable thermal, chemical, and photochemical stability. Many also exhibit near-IR phosphorescence and also efficiently sensitize singlet oxygen formation, which has led to applications in oxygen sensing, photodynamic therapy, and dye-sensitized solar cells[55–63]. The chemical reactivity of these complexes, by and large, remains poorly explored, with only a handful of reports on the subject. β-Octachlorination has been reported for an OsN corrole[64], while gold corroles have been polyiodinated, with 4–5 iodines attached to the β-positions[65,66]. A couple of examples of metal-centered reactivity have also been documented; thus, MoO[67] and ReO[50] corroles have been transformed to the MX_2 (X = Cl, Ph) derivatives, so-called Viking helmet corroles[68], while OsN corroles

[1]Department of Chemistry, UiT – The Arctic University of Norway, 9037 Tromsø, Norway. [2]Advanced Light Source, Lawrence Berkeley National Laboratory, Berkeley, CA 94720-8229, USA. [3]Department of Chemistry, University of California, Berkeley, Berkeley, CA 94720, USA. ✉email: abhik.ghosh@uit.no

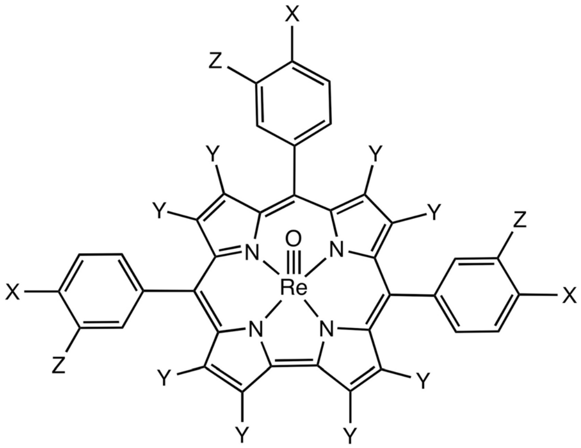

Compound	X	Y	Z
Re[T*p*XPC](O)	CF_3, H, F, CH_3, OCH_3	H	H
Re[Cl_8T*p*XPC](O)	CF_3, H, CH_3	Cl	H
Re[Br_8T*p*XPC](O)	H, F	Br	H
Re[Br_{11}T*p*XPC](O)	CH_3, OCH_3	Br	Br

Figure 1. ReO corroles synthesized in this work.

have been found to act as unusual π-acceptor metallaligands toward Pt(II)[64]. Herein we document our efforts to halogenate rhenium(V)-oxo triarylcorroles with elemental chlorine and bromine (Fig. 1).

The main contributions of this work may be described as threefold. First and foremost are the products themselves, which should serve as starting materials in a variety of cross-coupling reactions, affording, for example, ReO undecaarylcorroles via the Suzuki–Miyaura reaction. The products thus obtained are likely to further extend the growing range of applications of ReO corroles[60,61]. Second, three of the *β*-octahalogenated products have yielded single-crystal X-ray structures, shedding light on potential distortion modes available to these sterically congested species. Third, although the "messy" reaction conditions did not allow us to devise kinetic studies, qualitative observations indicate major differences in the times required for *β*-octabromination as a function of the coordinated metal, which appear to be ascribable to the electronic effects of the coordinated metal, as described below.

Results and discussion

Synthetic method development. Optimizing the conditions for *β*-octachlorination proved relatively straightforward[69]. In the final, optimized protocol, a saturated, greenish-yellow solution of chlorine (Cl_2) in chloroform was added dropwise, over a period of 20 min, to a benzene solution of *β*-unsubstituted ReO corroles, Re[T*p*XPC](O), maintained at 0 °C in an ice bath. The ice bath was removed after 1 h and the reaction was allowed to continue at room temperature for 24 h. After work-up, HR-ESI mass spectrometry and ^{1}H NMR spectroscopy showed that all eight *β*-hydrogens had been fully replaced by chlorine atoms for $X = CF_3$, H and CH_3. For $X = OCH_3$, the most electron-donating substituent, however, overchlorination was observed, with Cl_8, Cl_9 and Cl_{10} products appearing in a ratio of approximately 15:100:80 (see Figure S11 in the Supplementary Material).

Finding the optimum conditions for *β*-octabromination, in contrast, involved a fair amount of trial and error. Initial experiments with up to 100 equiv liquid bromine (Br_2) in chloroform led after 4 h to a mixture of Br_4, Br_5, Br_6, and Br_7 products, with only traces of Br_8. Increasing the reaction time to 16 h also led to the same complex mixtures. Increasing the reaction time to 48 h, however, led to the selective formation of Br_6 and Br_7 derivatives as the major products, with the Br_8 appearing as a minor product. We surmised that increasing the concentration of elemental bromine and lengthening the reaction time even further might result in full *β*-octabromination. Accordingly, we increased the amount of elemental bromine threefold and extended the reaction time to 7 days. As before, we began with 100 equiv of Br_2 added dropwise over a 20-min period. On the 2nd day, we added another 100 equiv of Br_2 dropwise over 20 min. We did the same on the 3rd day and let the reaction run for an additional 4 days, i.e., a total of 7 days. After work up, HR-MS and ^{1}H NMR showed that octabrominated complexes Re[Br_8T*p*XPC](O) had cleanly formed for X = H and F. For $X = CH_3$ and OCH_3, on the other hand, over-bromination had occurred, resulting in the undecabrominated complexes Re[Br_{11}T*p*XPC](O).

The long times needed for *β*-octabromination of ReO corroles, and presumably also for OsN corroles, may be contrasted with the rapid reactions observed for Cu[24] and Ir[23] corroles. The difference is most simply ascribed to the higher oxidation state of the central metal in the case of the ReO and OsN complexes, which presumably

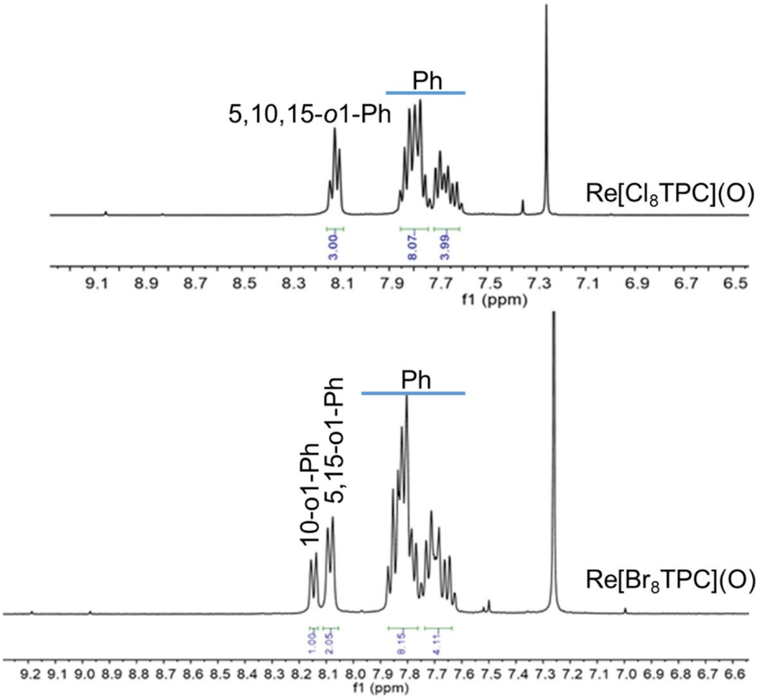

Figure 2. ^{1}H NMR spectra of Re[Cl_8TPC](O) (top) and Re[Br_8TPC](O) (bottom) in $CDCl_3$ at 298 K.

deactivates the corrole toward electrophilic substitution. Such a rationale is in line with the redox potentials of the metallocorroles; the oxidation potentials of ReO[50] and OsN[52] corroles are substantially higher than those of analogous Cu[24,38] and Ir[23] corroles.

^{1}H NMR and UV–Vis spectroscopy. Both types of spectra clearly reflect the effect of β-octahalogenation. The most obvious change in the ^{1}H NMR spectra is associated with the disappearance of the β-proton signals between 8.5 and 10 ppm (Fig. 2). Another highly characteristic change is that unlike the room-temperature ^{1}H NMR spectra of starting complexes[50], the spectra of the β-perhalogenated products are already sharp at room temperature. The broad ^{1}H NMR spectra of Re[T*p*XPC](O) at room temperature reflect partially restricted rotation of the *meso*-aryl groups and only around − 20 °C or so do the aryl *ortho* and *meta* signals split into distinguishable *o*,*o*′and *m*,*m*′signals. In β-perhalogenated products, the aryls are effectively locked in place even at room temperature.

Like a number of other classes of 5d metallocorroles[40,51,52,54], ReO triarylcorroles exhibit sharp, intense Soret bands and characteristic, double-humped Q bands[50]. The qualitative shapes of these features persist relatively unaltered upon β-octahalogenation. β-Octahalogenation does, however, engender significant redshifts for each of these features. Thus, for β-octachlorination, the Soret and Q bands redshift by around 9 and 13–16 nm, respectively, while for β-octabomination, the corresponding shifts are 17–19 and 21–22 nm, respectively (Table 1 and Fig. 3).

X-ray crystallography and molecular structure. The molecular structures of β-perhalogenated ReO corroles were expected to be of unusual interest as a window into potential deformation pathways of the corrole macrocycle in response to extreme peripheral crowding[70]. In general, β-octahalogenation does not result in significant nonplanar deformations for metallocorroles, reflecting the rigidity of the direct pyrrole–pyrrole linkage[23,28–31]. Coinage metal corroles, especially Cu[32–37] corroles but also Ag[38] corroles, constitute the major exceptions to this generalization. These metallocorroles are intrinsically saddled, as a result of a specific metal(d)-corrole(π) orbital interaction, which results in a noninnocent, partial M^{II}-corrole$^{\cdot 2-}$ character of the complexes. Importantly, the degree of saddling in Cu corroles, while substantial even in β-unsubstituted triarylcorrole derivatives, can be greatly enhanced by β-octasubstitution. The same orbital interaction, however, is energetically unfavorable for Au corroles[40]. Accordingly, even undecasubstituted Au corroles are fairly rigorously planar[29,30,38,40–42]. So, as a matter of fact, are six-coordinate Ir corroles, including Ir β-octabrominated derivatives[23,56,62]. Diboron corroles provide another example of a dramatic structural influence of β-octasubstitution. Thus, while simple corroles yield strongly domed complexes with *cisoid* FBOBF groups[71], β-octabromo-*meso*-triarylcorroles yield unbridged bis-BF_2 complexes, with the BF_2 groups on opposite sides of corrole macrocycle[72].

Three of the products obtained here, including one octabrominated and two octachlorinated products, yielded single-crystal X-ray structures (Table 2). The Re–O and Re–N bond distances, as well as the displacement of the Re atom above the mean N_4 plane, all turned out to be essentially identical to those observed for β-unsubstituted ReO corroles (Fig. 4)[50]. Interestingly, modest variations were observed for the conformations of the corrole

Compound	N	Soret	Q_1	Q_2	Ref
Re[T*p*CF_3PC](O)	320 (1.77)	438 (10.74)	552 (1.63)	585 (1.99)	[50]
Re[TPC](O)	320 (1.64)	439 (10.09)	552 (1.99)	585 (2.34)	[50]
Re[T*p*FPC](O)	319 (1.57)	438 (10.16)	553 (1.53)	585 (1.93)	[50]
Re[T*p*CH_3PC](O)	318 (2.92)	440 (11.18)	555 (1.86)	587 (2.37)	[50]
Re[Cl_8T*p*CF_3PC](O)	349 (2.17)	447 (11.04)	565 (1.58)	599 (2.24)	This work
Re[Cl_8TPC](O)	349 (2.04)	448 (9.93)	567 (1.41)	599 (2.11)	This work
Re[Cl_8T*p*CH_3PC](O)	350 (2.54)	449 (11.00)	568 (1.70)	601 (2.47)	This work
Re[Br_8T*p*FPC](O)	357 (2.08)	456 (9.77)	574 (1.43)	607 (2.12)	This work
Re[Br_8TPC](O)	357 (2.28)	456 (10.45)	575 (1.59)	607 (2.40)	This work
Re[Br_{11}T*p*CH_3PC](O)	359 (2.07)	458 (9.70)	574 (1.44)	608 (2.10)	This work
Re[Br_{11}T*p*OCH_3PC](O)	356 (1.15)	459 (8.59)	574 (1.15)	608 (1.72)	This work

Table 1. UV–Vis spectral data in dichloromethane, λ_{max} and $\varepsilon \times 10^{-4}$ (M^{-1} cm^{-1}), for the compounds studied.

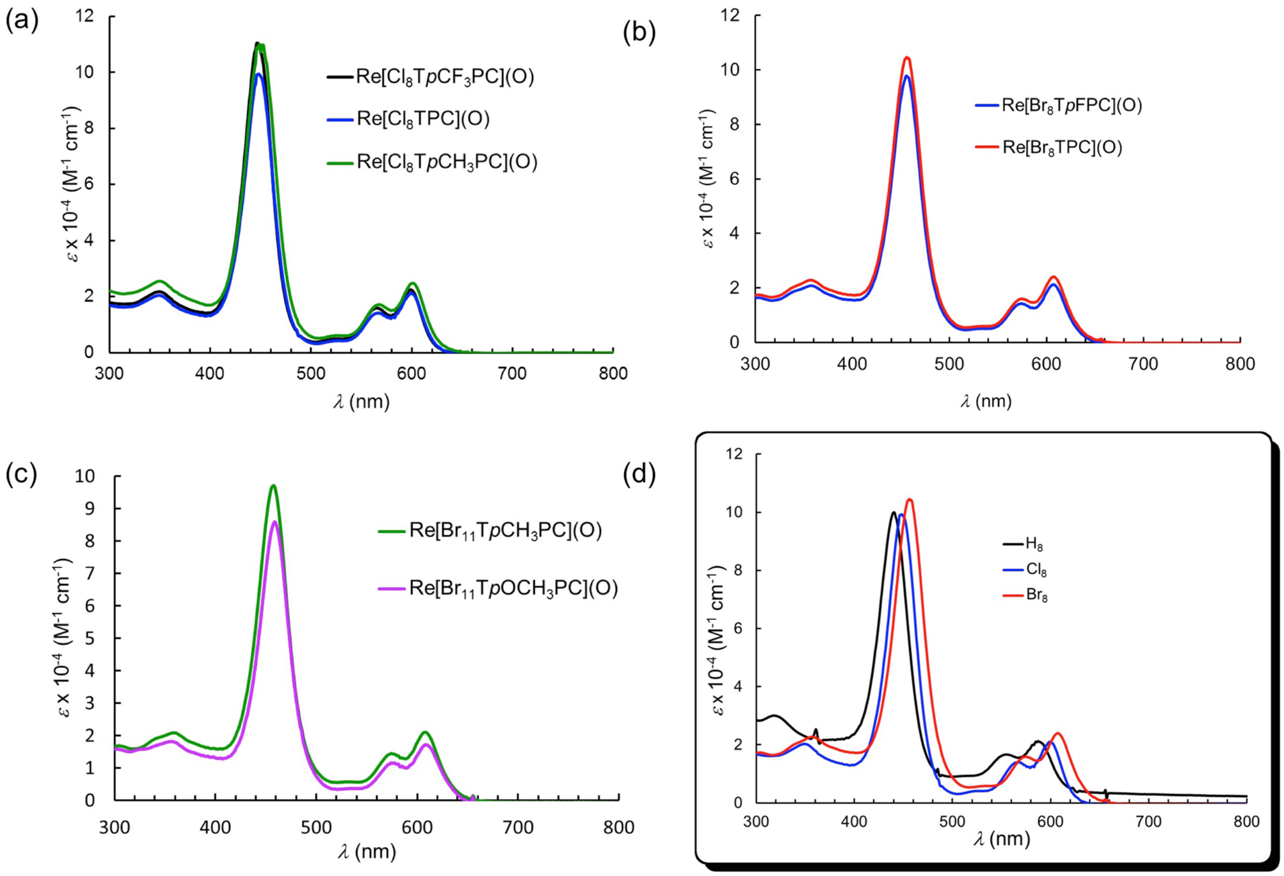

Figure 3. UV–Vis spectra in dichloromethane for (**a**) Re[Cl_8T*p*XPC](O) (X = CF_3, H and CH_3), (**b**) Re[Br_8T*p*XPC](O) (X = F and H) and (**c**) Re[Br_{11}T*p*XPC](O) (X = CH_3 and OCH_3). (**d**) Comparative UV–Vis spectra for Re[TPC](O) (black), Re[Cl_8TPC](O) (blue), and Re[Br_8TPC](O) (red).

macrocycles. Aligning the mean N_4 planes of β-H_8, β-Cl_8, and β-Br_8 structures showed that the corrole macrocycles in these systems might be described as slightly domed, planar, and slightly, if somewhat irregularly, saddled, respectively (Fig. 5 and Table 3). The β-Br_8 crystal structure reported here thus represents a rare example of a saddled corrole, aside from the coinage metal corroles.

Might the above structural differences play a role in explaining the slow rates of β-octabromination of ReO triarylcorroles relative to Cu and Ir triarylcorroles? Given that the above differences are rather minor (Table 3), we believe that the answer is essentially 'no'; as stated above, the high oxidation state of the Re center provides the most plausible explanation for the slowness of the octabromination.

Sample	Re[Cl_8T*p*CF_3PC](O)	Re[Cl_8T*p*CH_3PC](O)	Re[Br_8T*p*FPC](O)
Chemical formula	C_{40} H_{12} Cl_8 F_9 N_4 O Re	C_{40} H_{21} Cl_8 N_4 O Re	C_{37} H_{12} Br_8 F_3 N_4 O Re
Formula mass	1203.78	1041.87	1411.38
Crystal system	Triclinic	Triclinic	Triclinic
Crystal size (mm^3)	0.200 × 0.170 × 0.150	0.050 × 0.030 × 0.010	0.080 × 0.080 × 0.030
Space group	*P*-1	*P*-1	*P-1*
λ (Å)	0.7288	0.7288	0.7288
a (Å)	16.0327(12)	12.5075(5)	11.7273(4)
b (Å)	17.3203(13)	12.9074(6)	14.1820(5)
c (Å)	17.8739(13)	13.7640(5)	14.6880(5)
α (deg)	116.0080(10)	74.8780(10)	100.8390(10)
β (deg)	90.679(2)	85.9610(10)	106.6030(10)
γ (deg)	102.117(2)	82.5010(10)	90.7700(10)
Z	2	2	2
V (Å^3)	4330.8(6)	2125.22(15)	2293.38(14)
Temperature (K)	100(2)	100(2)	100(2)
Density (g/cm^3)	1.998	1.765	2.269
Measured reflections	108,021	59,434	151,248
Unique reflections	25,785	8713	11,449
Parameters	1231	567	602
Restraints	59	9	6
R_{int}	0.0685	0.0511	0.0405
θ range (deg.)	1.341–31.393	1.573–27.142	2.027–29.131
R_1, wR_2 all data	0.0780, 0.1432	0.0332, 0.0794	0.0259, 0.0526
S (GooF) all data	1.112	1.075	1.039
Max/min res. dens. (e/Å^3)	2.370/ – 2.057	2.163/ – 1.534	1.714/ – 1.377

Table 2. Crystallographic data for the complexes analyzed.

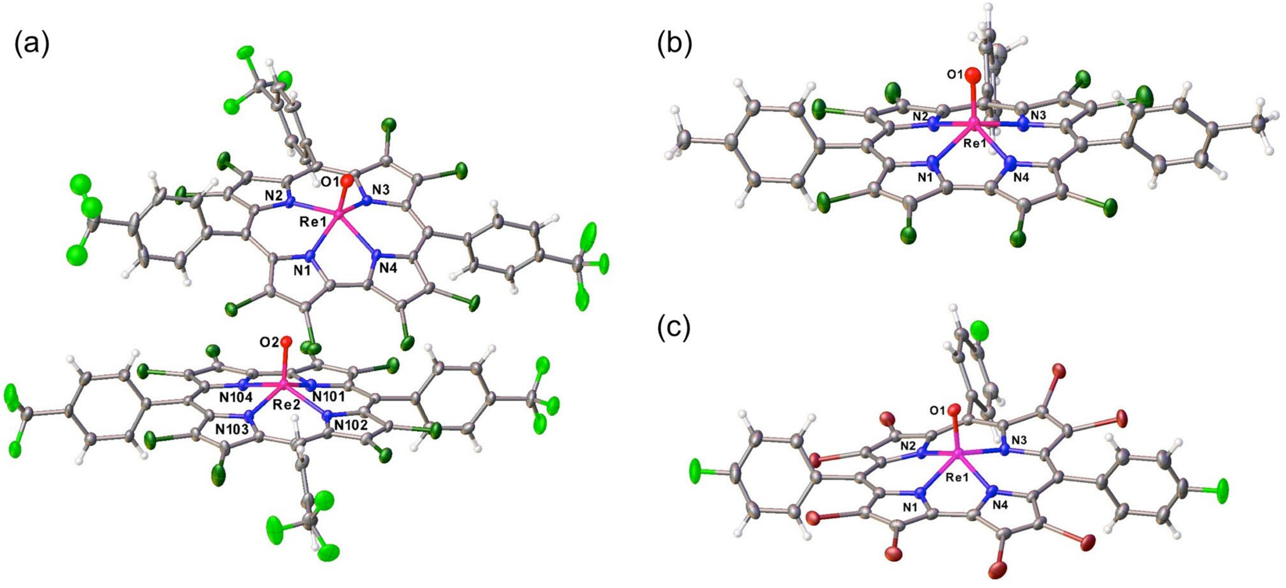

Figure 4. Thermal ellipsoid plots (50%) for (**a**) Re[Cl_8T*p*CF_3PC](O), (**b**) Re[Cl_8T*p*CH_3PC](O), and (**c**) Re[Br_8T*p*FPC](O). Selected distances (Å) for (**a**) Re[Cl_8T*p*CF_3PC](O): Re1-N1 1.997(5), Re1-N2 2.015(4), Re1-N3 2.025(4), Re1-N4 1.995(4), and Re1-O1 1.670(4); Re2-N101 1.989(4), Re2-N102 2.014(4), Re2-N103 2.019(4), Re2-N104 1.980(4), Re2-O2 1.672. Selected distances (Å) for Re[Cl_8T*p*CH_3PC](O): Re1-N1 1.995(3), Re1-N2 2.019(3), Re1-N3 2.017(3), Re1-N4 1.992(3), and Re1-O1 1.677(3). Selected distances (Å) for Re[Br_8T*p*FPC](O): Re1-N1 1.996(2), Re1-N2 2.019(2), Re1-N3 2.011(2), Re1-N4 1.997(2), and Re1-O1 1.673(2).

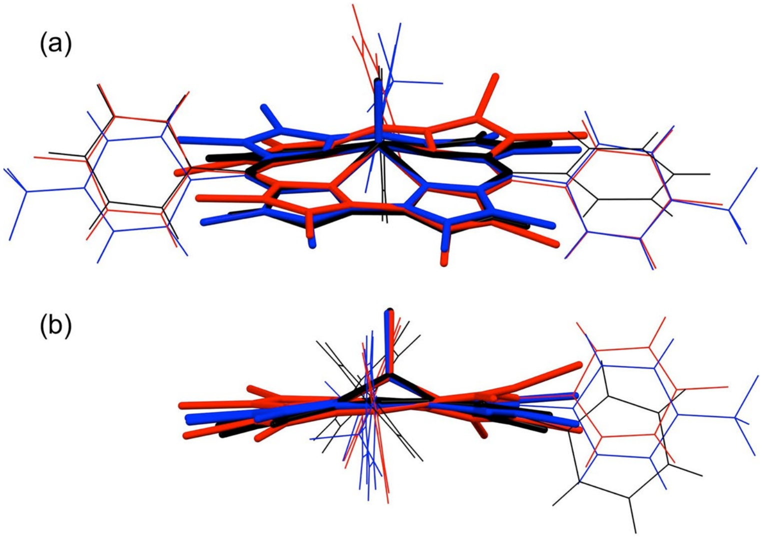

Figure 5. *Mercury* overlay of the nitrogen atoms of Re[TPC](O) (black), molecule 1 of Re[Cl_8T*p*CF_3PC](O) (blue) and Re[Br_8T*p*FPC](O). (**a**) View from above C1–C19 toward C10. (**b**) View along C5–C15.

Molecule	Re–N_4 (Å)	$\chi_{C8-C9-C11-C12}$ (°)	$\phi_{C5-Re-C15}$ (°)
Re[TPC](O)	0.704	7.2	155.1
Re[Cl_8T*p*CF_3PC](O); molecule 1	0.671	15.4	155.1
Re[Cl_8T*p*CF_3PC](O); molecule 2	0.659	6.7	154.0
Re[Cl_8T*p*CH_3PC](O)	0.671	8.5	157.4
Re[Br_8T*p*FPC](O)	0.668	11.9	152.5

Table 3. Measures of nonplanarity for Re corroles: the Re–N4 displacement (Å), the C8–C9–C11–C12 saddling dihedral (°), and the C5–Re–C15 angle (°).

Conclusion

In summary, we have optimized reaction conditions leading to β-perhalogenation of ReO triarylcorroles with elemental chlorine and bromine. β-Perhalogenation is accompanied by highly characteristic changes in the ^{1}H NMR and UV–Vis spectra of the compounds. Three of the β-octahalogenated products, including two of the octachlorinated complexes and one octabrominated complex, yielded single-crystal X-ray structures. On the whole, the structures were remarkably similar to those of β-unsubstituted ReO corroles. Minor variations were observed in regard to macrocycle conformation. Thus, whereas β-unsubstituted ReO corroles are generally slightly domed, one octachlorinated complex and the octabrominated complex were found to exhibit slightly saddled macrocycles. These structural differences, however, appear to be too minor to explain the comparative slowness of β-octabromination of ReO triarylcorroles, relative to their Cu and Ir counterparts. The slowness is more plausibly attributed to the high oxidation state of the Re center, which leads to a higher oxidation potential for the corrole macrocycle and, in turn, a lower susceptibility to electrophilic attack. It is hoped that the β-perhalogenated complexes reported herein will act as substrates in Suzuki–Miyaura and other palladium-catalyzed transformations, thereby affording additional avenues for the elaboration of ReO corroles.

Experimental section

Materials. Rhenium-oxo *meso*-triarylcorroles, Re[T*p*XPC](O), were synthesized as previously reported[50]. Chlorine gas (Cl_2), liquid bromine (Br_2), benzene, and chloroform were purchased from Sigma-Aldrich. Silica gel 60 (0.04–0.063 mm particle size, 230–400 mesh, Merck) was used for flash chromatography and silica gel 60 preparative thin-layer chromatography (PTLC) plates (20 cm × 20 cm, 0.5 mm thick; Merck) were used for final purification of all complexes.

Instrumental methods. UV–visible spectra were recorded on an HP 8453 spectrophotometer. ^{1}H NMR spectra (298 K, $CDCl_3$) were recorded on a 400 MHz Bruker Avance III HD spectrometer equipped with a 5-mm BB/1H SmartProbe and referenced to residual $CHCl_3$ at 7.26 ppm. High-resolution electrospray-ionization (HR-ESI) mass spectra were recorded from methanolic solution on an LTQ Orbitrap XL spectrometer.

General procedure for the synthesis of Re[Cl_8T*p*XPC](O). To a 10-mL benzene solution of Re[T*p*XPC](O) (X = CF_3: 15 mg, 0.016 mmol; X = H: 25 mg, 0.034 mmol; X = CH_3: 20 mg, 0.026 mmol) chilled to 0 °C in an ice-bath, was added a greenish-yellow, saturated solution of chlorine (Cl_2, 10 mL) in chloroform over a period of 20 min. After an hour at 0 °C, the ice-bath was removed and the reaction was allowed to continue under stirring at room temperature for a total of 24 h. The reaction mixture was then quenched by washing twice with 20% aqueous sodium metabisulfite solution (20 mL × 2). The organic phase was thoroughly washed with distilled water, dried with sodium sulfate, and rotary-evaporated to dryness. The resulting crude product was dissolved in a minimum amount of dichloromethane and loaded onto a silica gel column prepared with 3:1 hexane/dichloromethane and eluted with the same solvent system. The resulting greenish-red product was collected, evaporated to dryness, and further purified via preparative thin-layer chromatography with the same solvent system. Yields and analytical details of new compounds are given below. X-ray-quality crystals of Re[Cl_8T*p*CF_3PC](O) and Re[Cl_8T*p*CH_3PC](O) were obtained by slow diffusion of methanol vapor into concentrated dichloromethane solutions of the complexes.

Re[Cl_8T*p*CF_3PC](O). Yield 11.5 mg (59.22%). UV–Vis (CH_2Cl_2) λ_{max} [nm, $\varepsilon \times 10^{-4}$ (M^{-1} cm^{-1})]: 349 (2.17), 447 (11.04), 565 (1.58), 599 (2.24). ^1H NMR (400 MHz, 25 °C) δ: 8.29 (d, 3H, $^3J_{HH}$ = 7.92 Hz, 5,10,15-*o*1-Ph); 8.09 (d, 2H, $^3J_{HH}$ = 7.96 Hz, 5,15-*o*2-Ph); 8.05 (d, 1H, $^3J_{HH}$ = 7.60 Hz, 10-*o*2-Ph); 7.98 (d, 4H, $^3J_{HH}$ = 6.40 Hz, 5,15-*m*1& *m*2-Ph); 7.92 (d, 1H, $^3J_{HH}$ = 9.80 Hz, 10-*m*1-Ph); 7.84 (d, 1H, $^3J_{HH}$ = 8.00 Hz, 10-*m*2-Ph). Elemental analysis calcd for $C_{40}H_{12}ON_4F_9Cl_8Re$: C 39.86, H 1.00, N 4.65; found: C 40.27, H 1.21. N 4.24. MS (ESI): M^+ = 1203.7915 (expt), 1203.7880 (calcd for $C_{40}H_{12}ON_4F_9Cl_8Re$).

Re[Cl_8TPC](O). Yield 23 mg (66.71%). UV–Vis (CH_2Cl_2) λ_{max} [nm, $\varepsilon \times 10^{-4}$ (M^{-1} cm^{-1})]: 349 (2.04), 448 (9.93), 567 (1.41), 599 (2.11). ^1H NMR (400 MHz, 25 °C): δ 8.12 (d, 3H, $^3J_{HH}$ = 7.48 Hz, 5,10,15-*o*1-Ph); 7.85–7.73 (m, 8H, Ph); 7.70–7.60 (m, 4H, Ph). Elemental analysis calcd for $C_{37}H_{15}ON_4Cl_8Re$: C 44.38, H 1.51, N 5.60; found; C 44.07, H 1.37, N 5.18. MS (ESI): M^+ = 999.8272 (expt), 999.8258 (calcd for $C_{37}H_{15}ON_4Cl_8Re$).

Re[Cl_8T*p*CH_3PC](O). Yield 15.3 mg (56.39%). UV–Vis (CH_2Cl_2) λ_{max} [nm, $\varepsilon \times 10^{-4}$ (M^{-1} cm^{-1})]: 350 (2.54), 449 (11.00), 568 (1.70), 601 (2.47). ^1H NMR (400 MHz, 25 °C): δ 7.97 (d, 3H, $^3J_{HH}$ = 8.24 Hz, 5,10,15-*o*1-Ph); 7.64 (d, 2H, $^3J_{HH}$ = 7.96 Hz, 5,15-*o*2-Ph); 7.60 (d, 2H, $^3J_{HH}$ = 7.68 Hz, 5,15-*m*1-Ph); 7.55 (d, 1H, $^3J_{HH}$ = 8.92 Hz, 10-*o*2-Ph); 7.49 (d, 3H, $^3J_{HH}$ = 7.72 Hz, 10-*m*1& 5,15-*m*2-Ph); 7.43 (d, 1H, $^3J_{HH}$ = 7.72 Hz, 10-*m*2-Ph); 2.72 (s, 6H, 5,15-*p*-CH_3); 2.69 (s, 3H, 10-*p*-CH_3). MS (ESI): Elemental analysis calcd for $C_{40}H_{21}ON_4Cl_8Re$: C 46.04, H 2.03, N 5.37; found: C 46.11, H 1.67, N 5.60. MS (ESI): M^+ = 1041.8746 (expt), 1041.8728 (calcd for $C_{40}H_{21}ON_4Cl_8Re$).

General procedure for the synthesis of Re[Br_8T*p*XPC](O) and Re[Br_{11}T*p*XPC](O). To a chloroform solution of Re[T*p*XPC](O) (10 mL; X = F: 8 mg, 0.0102 mmol; X = H: 16 mg, 0.022 mmol; X = CH_3: 10 mg, 0.013 mmol, and X = OCH_3: 15 mg, 0.018 mmol) was added a solution of liquid bromine (a total of 300 equiv) solution in chloroform in three 10-mL portions (each containing 100 equiv Br_2 and added over 20 min) at 24-h intervals over 3 days. The reaction was then allowed to proceed under stirring at room temperature for a total of 7 days. The resulting mixture was quenched by washing with 20% aqueous sodium metabisulfite (25 mL × 3). The organic phase was then washed with distilled water (50 mL), dried over sodium sulfate, and rotary evaporated to dryness. The crude reaction mixture was loaded onto a silica gel column prepared with 4:1 hexane/dichloromethane and eluted with the same solvent system. The greenish-red product was rotary evaporated to dryness and further purified via preparative thin-layer chromatography with the same eluent. Detailed analytical and respective yield of the compounds synthesized are given below. X-ray-quality crystals of Re[Br_8T*p*FPC](O) were obtained by slow diffusion of methanol vapor into a concentrated benzene solution of the complex.

Re[Br_8T*p*FPC](O). Yield 9 mg (62.09%). UV–Vis (CH_2Cl_2) λ_{max} [nm, $\varepsilon \times 10^{-4}$ (M^{-1} cm^{-1})]: 357 (2.08), 456 (9.77), 574 (1.43), 607 (2.12). ^1H NMR (400 MHz, 25 °C): δ 8.11 (m, 1H, 10-*o*1-Ph); 8.05 (m, 2H, 5,15-*o*1-Ph); 7.78 (m, 2H, $^3J_{HH}$ = 7.68 Hz, 5,15-*o*2-Ph); 7.65 (m, 1H, 10-*o*2-Ph); 7.55–7.36 (m, 6H, 5,10,15-*m*1 & *m*2-Ph). Elemental analysis calcd for $C_{37}H_{12}F_3ON_4Br_8Re$: C 31.50, H 0.86, N 3.97; found: C 31.78, H 1.24, N 3.68. MS (ESI): M^+ = 1411.3885 (expt), 1411.3889(calcd for $C_{37}H_{12}F_3ON_4Br_8Re$).

Re[Br_8TPC](O). Yield 20 mg (66.76%). UV–Vis (CH_2Cl_2) λ_{max} [nm, $\varepsilon \times 10^{-4}$ (M^{-1} cm^{-1})]: 357 (2.28), 456 (10.45), 575 (1.59), 607 (2.40). ^1H NMR (400 MHz, 25 °C): δ 8.14 (d, 1H, $^3J_{HH}$ = 7.48 Hz, 10-*o*1-Ph); 8.08 (d, 2H, $^3J_{HH}$ = 7.40 Hz, 5,15-*o*1-Ph); 7.86–7.62 (m, 12H, Ph). Elemental analysis calcd for $C_{37}H_{15}ON_4Br_8Re$: C 32.75, H 1.11, N 4.13; found: C 32.49, H 0.95, N 3.88. MS (ESI): M^+ = 1357.4166 (expt), 1357.4174(calcd for $C_{37}H_{15}ON_4Br_8Re$).

Re[Br_{11}T*p*CH_3PC](O). Yield 12 mg (56.36%). UV–Vis (CH_2Cl_2) λ_{max} [nm, $\varepsilon \times 10^{-4}$ (M^{-1} cm^{-1})]: 359 (2.07), 458 (9.70), 574 (1.44), 608 (2.10). ^1H NMR (400 MHz, 25 °C): δ 8.35 (s, 1H, Ph); 8.28 (s, 1H, Ph); 8.02 (s, 1H, Ph); 7.97 (d, 1H, $^3J_{HH}$ = 7.68 Hz, Ph); 7.92 (d, 2H, $^3J_{HH}$ = 8.44 Hz, Ph); 7.68 (d, 3H, $^3J_{HH}$ = 8.08 Hz, Ph); 7.59 (d, 1H, $^3J_{HH}$ = 7.84 Hz, Ph); 7.53 (s, 1H, Ph); 2.78 (s, 6H, 5,15-*p*CH_3); 2.72 (s, 3H, 10-*p*CH_3). MS (ESI): Elemental analysis calcd for $C_{40}H_{18}ON_4Br_{11}Re$: C 29.37, H 1.11, N 3.43; found: C 29.59, H 1.41, N 3.33. M^+ = 1635.1998 (expt), 1635.1936(calcd for $C_{40}H_{18}ON_4Br_{11}Re$).

Re[Br_{11}T*p*OCH_3PC](O). Yield 19 mg (59.81%). UV–Vis (CH_2Cl_2) λ_{max} [nm, $\varepsilon \times 10^{-4}$ (M^{-1} cm^{-1})]: 356 (1.82), 459 (8.59), 574 (1.15), 608 (1.72). ^1H NMR (400 MHz, 25 °C): δ 8.34 (s, 1H, Ph); 8.28 (s, 1H, Ph); 8.01 (s, 1H, Ph); 7.71 (d, 2H, $^3J_{HH} = 8.72$ Hz, Ph); 7.57 (d, 2H, $^3J_{HH} = 8.36$ Hz, Ph); 7.35 (d, 3H, $^3J_{HH} = 9.32$ Hz, Ph); 7.19 (d, 1H, $^3J_{HH} = 8.20$ Hz, Ph); 4.23 (s, 6H, 5,15-*p*OCH$_3$); 4.18 (s, 3H, 10-*p*OCH$_3$). Elemental analysis calcd for $C_{40}H_{18}O_4N_4Br_{11}Re$: C 28.53, H 1.08, N 3.33; found: C 28.17, H 1.35, N 2.98. MS (ESI): M$^+$ =1683.1775 (expt), 1683.1784(calcd for $C_{40}H_{18}O_4N_4Br_{11}Re$).

X-ray structure determinations. All X-ray diffraction data were collected on beamline 12.2.1 at the Advanced Light Source of Lawrence Berkeley National Laboratory, Berkeley, California. The samples were mounted on MiTeGen kapton loops and placed in a 100(2) K nitrogen cold stream provided by an Oxford Cryostream 700 Plus low temperature apparatus on the goniometer head of a Bruker D8 diffractometer equipped with PHOTONII CPAD detector. Diffraction data were collected using synchrotron radiation monochromated with silicon(111) to a wavelength of 0.7288(1) Å. In each case, an approximate full-sphere of data was collected using 1° ϕ and ω scans. Absorption corrections were applied using SADABS[73]. The structure was solved by intrinsic phasing (SHELXT)[74] and refined by full-matrix least squares on F^2 (SHELXL-2014)[75] using the ShelXle GUI[76]. Appropriate scattering factors were applied using the XDISP[77] program within the WinGX suite[78]. All non-hydrogen atoms were refined anisotropically. Hydrogen atoms were geometrically calculated and refined as riding atoms.

Accession codes

The crystal structures described in this paper have been deposited at the Cambridge Crystallographic Data Centre and been assigned the following deposition numbers CCDC 1532043-1532045.

Received: 30 July 2020; Accepted: 27 October 2020

References

1. Traylor, T. G. & Tsuchiya, S. Perhalogenated tetraphenylhemins: stable catalysts of high turnover catalytic hydroxylations. *Inorg. Chem.* **26**, 1338–1339 (1987).
2. Dolphin, D., Traylor, T. G. & Xie, L. Y. Polyhaloporphyrins: unusual ligands for metals and metal-catalyzed oxidations. *Acc. Chem. Res.* **30**, 251–259 (1997).
3. Grinstaff, M. W., Hill, M. G., Labinger, J. A. & Gray, H. B. Mechanism of catalytic oxygenation of alkanes by halogenated iron porphyrins. *Science* **264**, 1311–1313 (1994).
4. Lyons, J. E., Ellis, P. E. & Myers, H. K. Halogenated metalloporphyrin complexes as catalysts for selective reactions of acyclic alkanes with molecular oxygen. *J. Catal.* **155**, 59–73 (1995).
5. Groves, J. T., Shalyaev, K. V., Bonchio, M. & Carofiglio, T. Rapid catalytic oxygenation of hydrocarbons with perhalogenated ruthenium porphyrin complexes. *Stud. Surf. Sci. Catal.* **110**, 865–872 (1997).
6. Costas, M. Selective C–H oxidation catalyzed by metalloporphyrins. *Coord. Chem. Rev.* **255**, 2912–2932 (2011).
7. Mandon, D. *et al.* *β*-Halogenated-pyrrole porphyrins. Molecular structures of 2,3,7,8,12,13,17,18-octabromo-5,10,15,20-tetramesitylporphyrin, nickel(II) 2,3,7,8,12,13,17,18-octabromo-5,10,15,20-tetramesitylporphyrin, and nickel(II) 2,3,7,8,12,13,17,18-octabromo-5,10,15,20-tetrakis(pentafluorophenyl)porphyrin. *Inorg. Chem.* **31**, 2044–2049 (1992).
8. Grinstaff, M. W. *et al.* Structures, electronic properties, and oxidation–reduction reactivity of halogenated iron porphyrins. *Inorg. Chem.* **34**, 4896–4902 (1995).
9. Birnbaum, E. R. *et al.* ^{19}F NMR spectra and structures of halogenated porphyrins. *Inorg. Chem.* **34**, 3625–3632 (1995).
10. Thomassen, I. K., Vazquez-Lima, H., Gagnon, K. J. & Ghosh, A. Octaiodoporphyrin. *Inorg. Chem.* **54**, 11493–11497 (2015).
11. Ochsenbein, P. *et al.* Conformational effects on the redox potentials of tetraarylporphyrins halogenated at the *β*-pyrrole positions. *Angew. Chem. Int. Ed.* **33**, 348–350 (1994).
12. Bhyrappa, P. & Krishnan, V. Octabromotetraphenylporphyrin and its metal derivatives: Electronic structure and electrochemical properties. *Inorg. Chem.* **30**, 239–245 (1991).
13. Ghosh, A. *et al.* Electrochemistry of nickel and copper β-octahalogeno-meso-tetraarylporphyrins. Evidence for important role played by saddling-induced metal(dx2-y2)–porphyrin("a2u") orbital interactions. *J. Phys. Chem. B* **105**, 8120–8124 (2001).
14. Kadish, K. M. & Van Caemelbecke, E. Electrochemistry of metalloporphyrins in nonaqueous media. In *Encyclopedia of Electrochemistry Bioelectrochemistry* Vol. 9 (ed. Wilson, G. S.) 175–228 (Wiley-VCH, Weinheim, 2002).
15. Shao, J., Steene, E., Hoffman, B. M. & Ghosh, A. EPR, ENDOR, and DFT studies on (*β*-Octahalo-meso-tetraarylporphyrin)copper complexes: characterization of the metal(d_{x2-y2})-porphyrin(a_{2u}) orbital interaction. *Eur. J. Inorg. Chem.* **2005**, 1609–1615 (2005).
16. Gross, Z., Galili, N. & Saltsman, I. The first direct synthesis of corroles from pyrrole. *Angew. Chem. Int. Ed.* **38**, 1427–1429 (1999).
17. Paolesse, R. *et al.* 5,10,15-Triphenylcorrole: a product from a modified Rothemund reaction. *Chem. Commun.* **14**, 1307–1308 (1999).
18. Ghosh, A. A perspective of pyrrole–aldehyde condensations as versatile self-assembly processes. *Angew. Chem. Int. Ed.* **43**, 1918–1931 (2004).
19. Orłowski, R., Gryko, D. & Gryko, D. T. Synthesis of corroles and their heteroanalogs. *Chem. Rev.* **117**, 3102–3137 (2017).
20. Ghosh, A. Electronic structure of corrole derivatives: insights from molecular structures, spectroscopy, electrochemistry, and quantum chemical calculations. *Chem. Rev.* **117**, 3798–3881 (2017).
21. Nardis, S., Mandoj, F., Stefanelli, M. & Paolesse, R. Metal complexes of corrole. *Coord. Chem. Rev.* **388**, 360–405 (2019).
22. Golubkov, G. *et al.* High-valent manganese corroles and the first perhalogenated metallocorrole catalyst. *Angew. Chem. Int. Ed.* **40**, 2132–2134 (2001).
23. Palmer, J. H., Durrell, A. C., Gross, Z., Winkler, J. R. & Gray, H. B. Iridium corroles. *J. Am. Chem. Soc.* **130**, 7786–7787 (2008).
24. Wasbotten, I. H., Wondimagegn, T. & Ghosh, A. Electronic absorption, resonance raman, and electrochemical studies of planar and saddled copper(III) meso-triarylcorroles. Highly substituent-sensitive soret bands as a distinctive feature of high-valent transition metal corroles. *J. Am. Chem. Soc.* **124**, 8104–8116 (2002).
25. Alemayehu, A. B., Hansen, L. K. & Ghosh, A. Nonplanar, noninnocent, and chiral: a strongly saddled metallocorrole. *Inorg. Chem.* **49**, 7608–7610 (2010).
26. Capar, C., Thomas, K. E. & Ghosh, A. Reductive demetalation of copper corroles: first simple route to free-base *β*-octabromocorroles. *J. Porphyrins Phthalocyanines* **12**, 964–967 (2008).
27. Capar, C., Hansen, L.-K., Conradie, J. & Ghosh, A. *β*-octabromo-*meso*-tris(pentafluorophenyl)corrole: reductive demetalation-based synthesis of a heretofore inaccessible, perhalogenated free-base corrole. *J. Porphyrins Phthalocyanines* **14**, 509–512 (2010).
28. Capar, J. *et al.* Improved syntheses of *β*-octabromo-*meso*-triarylcorrole derivatives. *J. Inorg. Biochem.* **153**, 162–166 (2015).
29. Rabinovitch, E., Goldberg, I. & Gross, Z. Gold(I) and gold(III) corroles. *Chem. Eur. J.* **17**, 12294–12301 (2011).

30. Thomas, K. E., Gagnon, K. J., McCormick, L. J. & Ghosh, A. Molecular structure of gold 2,3,7,8,12,13,17,18-octabromo-5,10,15-tris(4′′-pentafluorosulfanylphenyl)corrole: Potential insights into the insolubility of gold octabromocorroles. *J. Porphyrins Phthalocyanines* **22**, 596–601 (2018).
31. Norehim, H.-K. *et al.* Ligand noninnocence in FeNO corroles: insights from *β*-octabromocorrole complexes. *Dalton Trans.* **45**, 681–689 (2018).
32. Alemayehu, A. B., Gonzalez, E., Hansen, L. K. & Ghosh, A. Copper corroles are inherently saddled. *Inorg. Chem.* **48**, 7794–7799 (2009).
33. Thomas, K. E., Conradie, J., Hansen, L. K. & Ghosh, A. A metallocorrole with orthogonal pyrrole rings. *Eur. J. Inorg. Chem.* **2011**, 1865–1870 (2011).
34. Berg, S., Thomas, K. E., Beavers, C. M. & Ghosh, A. Undecaphenylcorroles. *Inorg. Chem.* **51**, 9911–9916 (2012).
35. Thomas, K. E. *et al.* Halterman corroles and their use as a probe of the conformational dynamics of the inherently chiral copper corrole chromophore. *Inorg. Chem.* **57**, 4270–4276 (2018).
36. Thomassen, I. K., McCormick, L. J. & Ghosh, A. Synthesis and molecular structure of a copper octaiodocorrole. *ACS Omega* **3**, 5106–5110 (2018).
37. Thomas, K. E., Settineri, N. S., Teat, S. J., Steene, E. & Ghosh, A. Molecular structure of copper and *μ*-oxodiiron octafluorocorrole derivatives: insights into ligand noninnocence. *ACS Omega* **5**, 10176–10182 (2020).
38. Thomas, K. E. *et al.* Ligand noninnocence in coinage metal corroles: a silver knife-edge. *Chem. Eur. J.* **21**, 16839–16847 (2015).
39. Alemayehu, A. B. & Ghosh, A. Gold corroles. *J. Porphyrins Phthalocyanines* **15**, 106–110 (2011).
40. Thomas, K. E., Alemayehu, A. B., Conradie, J., Beavers, C. & Ghosh, A. Synthesis and molecular structure of gold triarylcorroles. *Inorg. Chem.* **50**, 12844–12851 (2011).
41. Thomas, K. E., Beavers, C. M. & Ghosh, A. Molecular structure of a gold *β*-octakis(trifluoromethyl)-*meso*-triarylcorrole: an 85° difference in saddling dihedral relative to copper. *Mol. Phys.* **110**, 2439–2444 (2012).
42. Capar, J. *et al.* Demetalation of Copper undecaarylcorroles: molecular structures of a free-base undecaarylisocorrole and a gold undecaarylcorrole. *J. Inorg. Biochem.* **162**, 146–153 (2016).
43. Brückner, C., Briñas, R. P. & Bauer, J. A. K. X-ray structure and variable temperature nmr spectra of [*meso*-Triarylcorrolato] copper(III). *Inorg. Chem.* **42**, 4495–4497 (2003).
44. Steene, E., Dey, A. & Ghosh, A. *β*-octafluorocorroles. *J. Am. Chem. Soc.* **125**, 16300–16309 (2003).
45. Bröring, M., Brégier, F., Tejero, E. C., Hell, C. & Holthausen, M. C. Revisiting the electronic ground state of copper corroles. *Angew. Chem. Int. Ed.* **46**, 445–448 (2007).
46. Lim, H. *et al.* X-ray absorption spectroscopy as a probe of ligand noninnocence in metallocorroles: the case of copper corroles. *Inorg. Chem.* **58**, 6722–6730 (2019).
47. Buckley, H. L. & Arnold, J. Recent developments in out-of-plane metallocorrole chemistry across the periodic table. *Dalton Trans.* **44**, 30–36 (2015).
48. Ziegler, J. A., Buckley, H. L. & Arnold, J. Synthesis and reactivity of tantalum corrole complexes. *Dalton Trans.* **46**, 780–785 (2017).
49. Alemayehu, A. B., Vazquez-Lima, H., Gagnon, K. J. & Ghosh, A. Tungsten biscorroles: new chiral sandwich compounds. *Chem. Eur. J.* **22**, 6914–6920 (2016).
50. Einrem, R. F., Gagnon, K. J., Alemayehu, A. B. & Ghosh, A. Metal-ligand misfits: facile access to rhenium-oxo corroles by oxidative metalation. *Chem. Eur. J.* **22**, 517–520 (2016).
51. Alemayehu, A. B., Teat, S. J., Borisov, S. M. & Ghosh, A. Rhenium-imido corroles. *Inorg. Chem.* **59**, 6382–6389 (2020).
52. Alemayehu, A. B., Gagnon, K. J., Terner, J. & Ghosh, A. Oxidative metalation as a route to size-mismatched macrocyclic complexes: osmium corroles. *Angew. Chem. Int. Ed.* **53**, 14411–14414 (2014).
53. Alemayehu, A. B. *et al.* Platinum corroles. *Chem. Commun.* **50**, 11093–11096 (2014).
54. Alemayehu, A. B., McCormick, L. J., Gagnon, K. J., Borisov, S. M. & Ghosh, A. Stable platinum(IV) corroles: synthesis, molecular structure, and room-temperature near-IR phosphorescence. *ACS Omega* **3**, 9360–9368 (2018).
55. Palmer, J. H., Durrell, A. C., Gross, Z., Winkler, J. R. & Gray, H. B. Near-IR phosphorescence of iridium(III) corroles at ambient temperature. *J. Am. Chem. Soc.* **132**, 9230–9231 (2010).
56. Sinha, W., Ravotto, L., Ceroni, P. & Kar, S. NIR-emissive iridium(III) corrole complexes as efficient singlet oxygen sensitizers. *Dalton Trans.* **44**, 17767–17773 (2015).
57. Borisov, S. M., Alemayehu, A. & Ghosh, A. Osmium-nitrido corroles as NIR indicators for oxygen sensors and triplet sensitizers for organic upconversion and singlet oxygen generation. *J. Mater. Chem. C* **4**, 5822–5828 (2016).
58. Lemon, C. M., Powers, D. C., Brothers, P. J. & Nocera, D. G. Gold corroles as near-IR phosphors for oxygen sensing. *Inorg. Chem.* **56**, 10991–10997 (2017).
59. Alemayehu, A. B. *et al.* Gold tris(carboxyphenyl)corroles as multifunctional materials: room temperature near-ir phosphorescence and applications to photodynamic therapy and dye-sensitized solar cells. *ACS Appl. Mater. Interfaces* **8**, 18935–18942 (2016).
60. Borisov, S. M., Einrem, R. F., Alemayehu, A. B. & Ghosh, A. Ambient-temperature near-IR phosphorescence and potential applications of rhenium-oxo corroles. *Photochem. Photobiol. Sci.* **18**, 1166–1170 (2019).
61. Einrem, R. F., Alemayehu, A. B., Borisov, S. M., Ghosh, A. & Gederaas, O. A. Amphiphilic rhenium-oxo corroles as a new class of sensitizers for photodynamic therapy. *ACS Omega* **5**, 10596–10601 (2020).
62. Thomassen, I. K., McCormick-McPherson, L. J., Borisov, S. M. & Ghosh, A. Iridium corroles exhibit weak near-infrared phosphorescence but efficiently sensitize singlet oxygen formation. *Sci. Rep.* **10**, 7551 (2020).
63. Teo, R. D., Hwang, J. Y., Termini, J., Gross, Z. & Gray, H. B. Fighting cancer with corroles. *Chem. Rev.* **117**, 2711–2729 (2017).
64. Reinholdt, A., Alemayehu, A. B., Gagnon, K. J., Bendix, J. & Ghosh, A. Electrophilic activation of osmium-nitrido corroles. The OsN triple bond as a π-acceptor metalla-ligand in a heterobimetallic $\mathrm{Os^{VI}N\text{-}Pt^{II}}$ complex. *Inorg. Chem.* **59**, 5276–5280 (2020).
65. Soll, M. *et al.* One-pot conversion of fluorophores to phosphorophores. *Org. Lett.* **18**, 5840–5843 (2016).
66. Sudhakar, K. *et al.* Effect of selective CF_3 substitution on the physical and chemical properties of gold corroles. *Angew. Chem. Int. Ed.* **56**, 9837–9841 (2017).
67. Johansen, I. *et al.* Substituent effects on metallocorrole spectra: insights from chromium-oxo and molybdenum-oxo triarylcorroles. *J. Porphyrins Phthalocyanines* **15**, 1335–1344 (2011).
68. Schweyen, P. *et al.* Viking helmet corroles: activating inert oxidometal corroles. *Chem. Eur. J.* **23**, 13897–13900 (2017).
69. Mahammed, A., Botoshanskya, M. & Gross, Z. Chlorinated corroles. *Dalton Trans.* **41**, 10938–10940 (2012).
70. Thomas, K. E., Alemayehu, A. B., Conradie, J., Beavers, C. M. & Ghosh, A. The structural chemistry of metallocorroles: combined X-ray crystallography and quantum chemistry studies afford unique insights. *Acc. Chem. Res.* **45**, 1203–1214 (2012).
71. Albrett, A. M. *et al.* Corrole as a binucleating ligand: preparation, molecular structure and density functional theory study of diboron corroles. *J. Am. Chem. Soc.* **130**, 2888–2889 (2008).
72. Albrett, A. M. *et al.* Mono- and diboron corroles: factors controlling stoichiometry and hydrolytic reactivity. *Inorg. Chem.* **53**, 5486–5493 (2014).
73. Krause, L., Herbst-Irmer, R., Sheldrick, G. M. & Stalke, D. Comparison of silver and molybdenum microfocus X-ray sources for single-crystal structure determination. *J. Appl. Cryst.* **48**, 3–10 (2015).
74. Sheldrick, G. M. SHELXT—integrated space-group and crystal-structure determination. *Acta Cryst.* **A71**, 3–8 (2015).
75. Sheldrick, G. M. Crystal structure refinement with SHELXL. *Acta Cryst.* **C71**, 3–8 (2015).

76. Hübschle, C. B., Sheldrick, G. M. & Dittrich, B. ShelXle: a Qt graphical user interface for SHELXL. *J. Appl. Cryst.* **44**, 1281–1284 (2011).
77. Kissel, L. & Pratt, R. H. Corrections to tabulated anomalous-scattering factors. *Acta Cryst.* **A46**, 170–175 (1990).
78. Farrugia, L. J. WinGX and ORTEP for windows: an update. *J. Appl. Cryst.* **45**, 849–854 (2012).

Acknowledgements

We acknowledge Grant No. 262229 (to AG) from the Research Council of Norway. This research used resources of the Advanced Light Source, a U.S. DOE Office of Science User Facility under Contract No. DE-AC02-05CH11231.

Author contributions

A.B.A. and R.F.E. carried out the synthetic work; L.J.M.M. and N.S.S. carried out the X-ray structure determinations. A.G. planned and supervised the project. The manuscript was largely composed by A.B.A. and A.G.

Competing interests

The authors declare no competing interests.

Additional information

Supplementary information is available for this paper at https://doi.org/10.1038/s41598-020-76308-7.

Correspondence and requests for materials should be addressed to A.G.

Supplementary Material

Synthesis and Molecular Structure of Perhalogenated Rhenium-Oxo Corroles

Abraham B. Alemayehu,[1] Rune F. Einrem,[1] Laura J. M^{c}Cormick-M^{c}Pherson,[2] Nicholas S. Settineri,[2,3] and Abhik Ghosh*,[1]

[1]Department of Chemistry, UiT – The Arctic University of Norway, N-9037 Tromsø, Norway; Email: abhik.ghosh@uit.no (AG)
[2]Advanced Light Source, Lawrence Berkeley National Laboratory, Berkeley, CA 94720-8229, USA
[3]Department of Chemistry, University of California, Berkeley, Berkeley, California 94720, USA

Table of contents

a) NMR Spectra

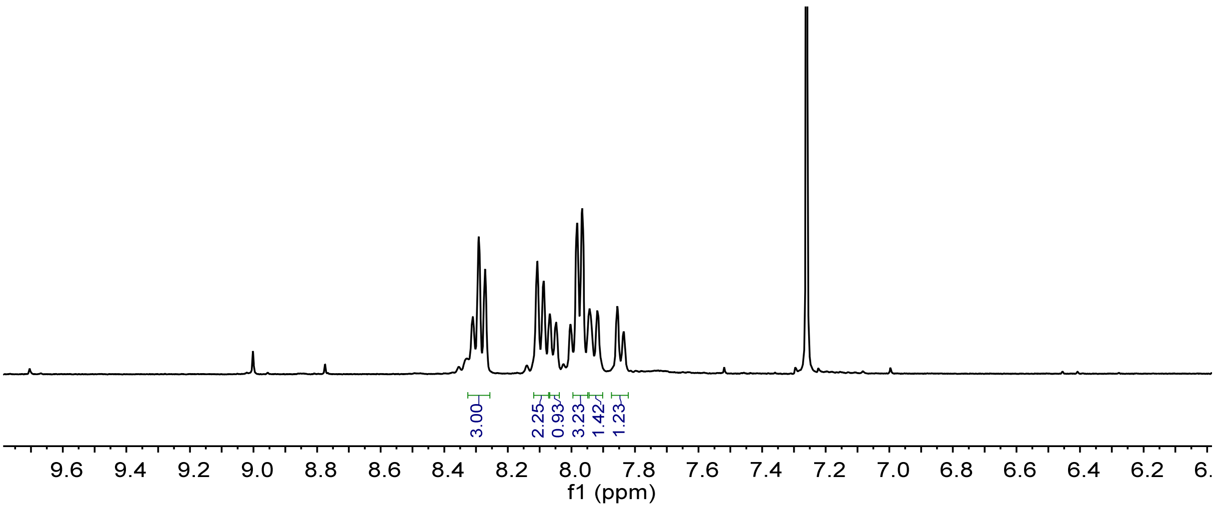

Figure S1. ^{1}H NMR spectrum of Re[Cl$_8$T*p*CF$_3$PC](O) in CDCl$_3$ at 298 K.

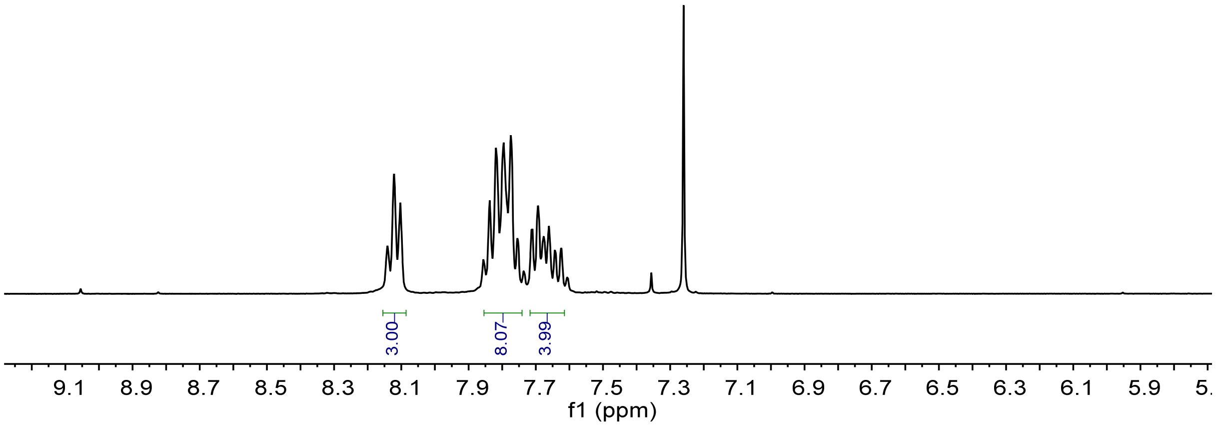

Figure S2. ^{1}H NMR spectrum of Re[Cl$_8$TPC](O) in CDCl$_3$ at 298 K.

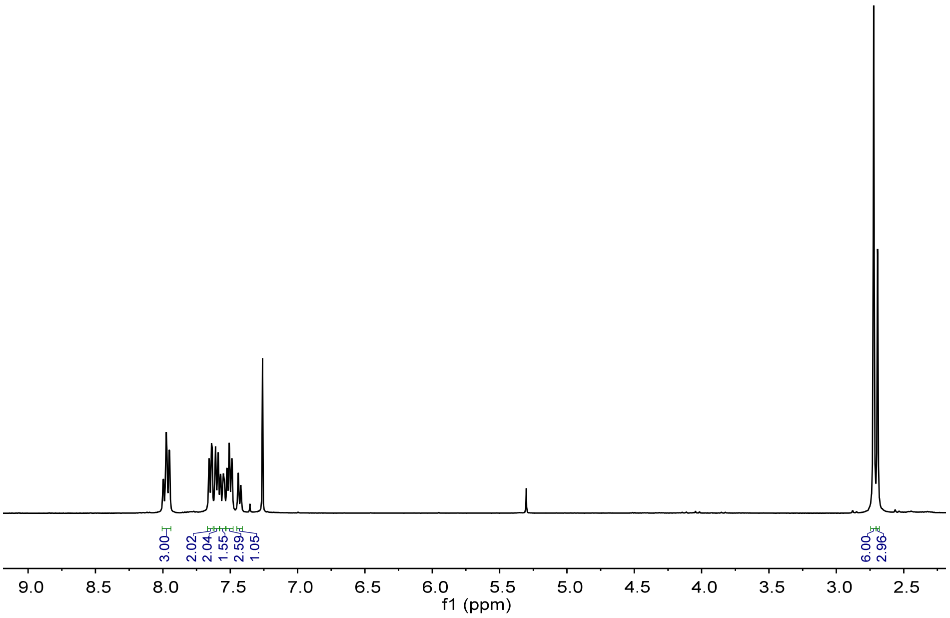

Figure S3. ^{1}H NMR spectrum of Re[Cl$_8$T*p*CH$_3$PC](O) in CDCl$_3$ at 298 K.

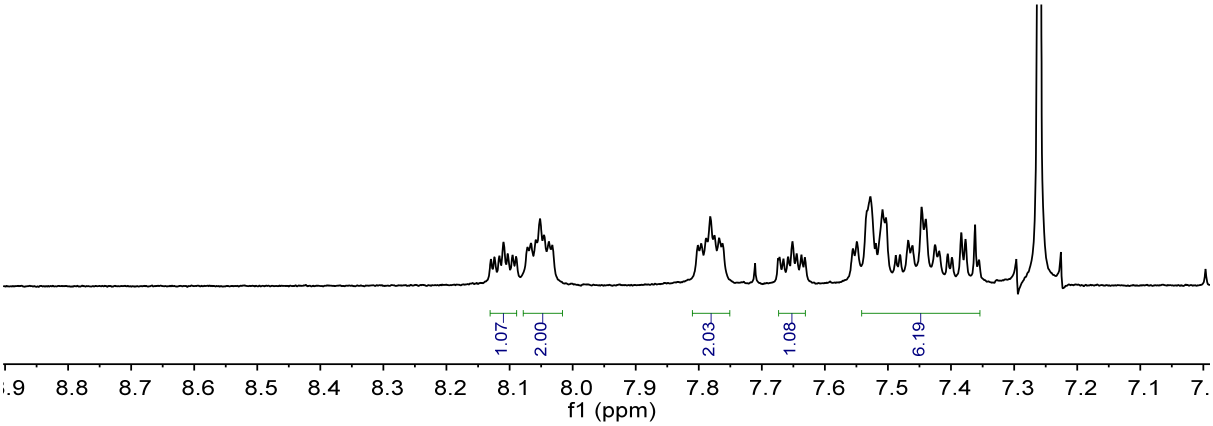

Figure S4. ^{1}H NMR spectrum of Re[Br$_8$T*p*FPC](O) in CDCl$_3$ at 298 K.

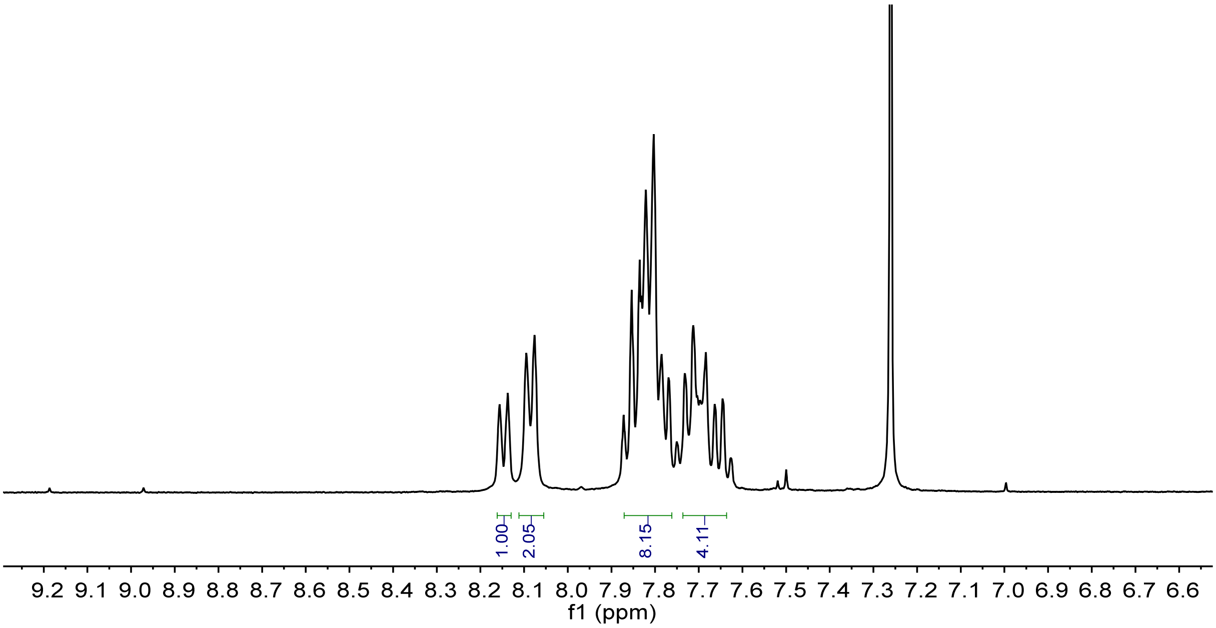

Figure S5. ^{1}H NMR spectrum of Re[Br$_8$TPC](O) in CDCl$_3$ at 298 K.

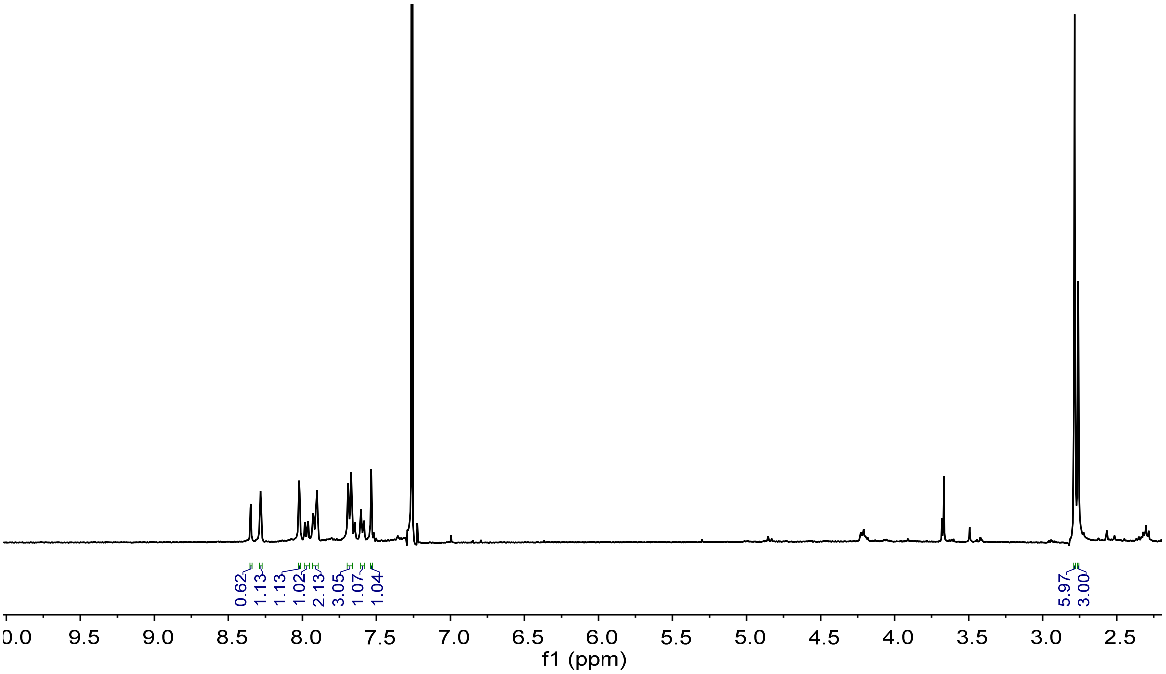

Figure S6. ^{1}H NMR spectrum of Re[Br$_{11}$T*p*CH$_3$PC](O) in CDCl$_3$ at 298 K.

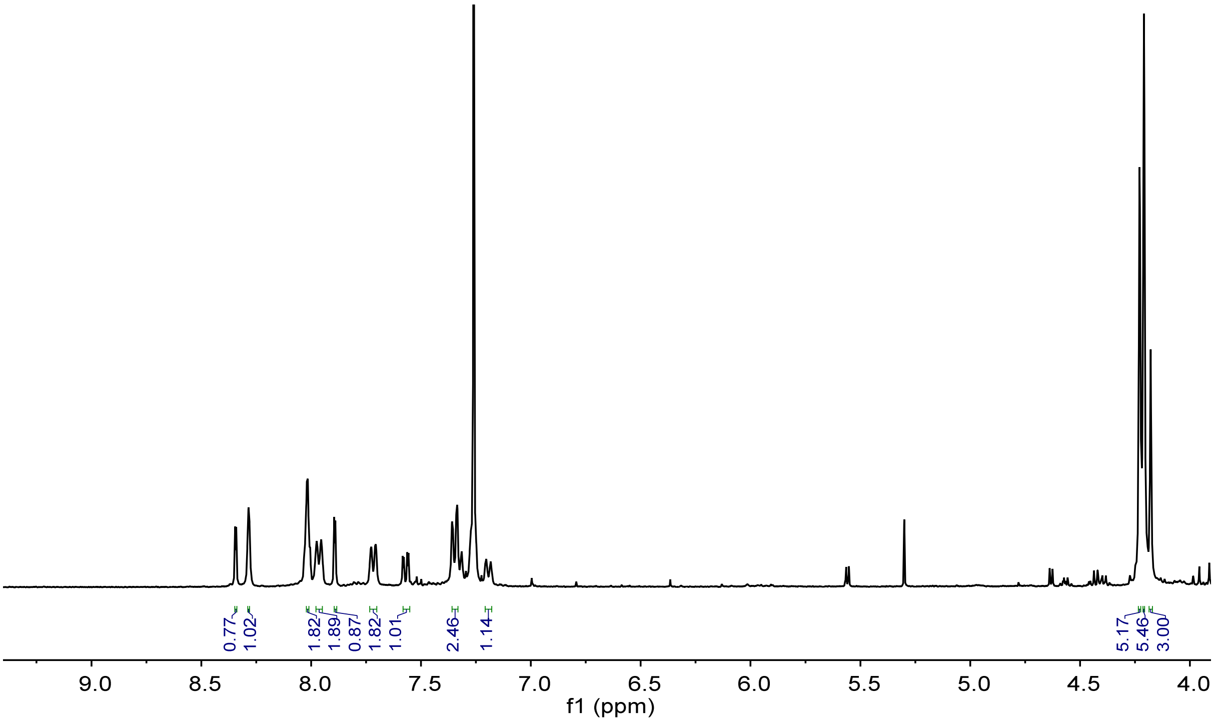

Figure S7. ^{1}H NMR spectrum of Re[Br$_{11}$T*p*CH$_3$PC](O) in CDCl$_3$ at 298 K.

b) ESI mass Spectra

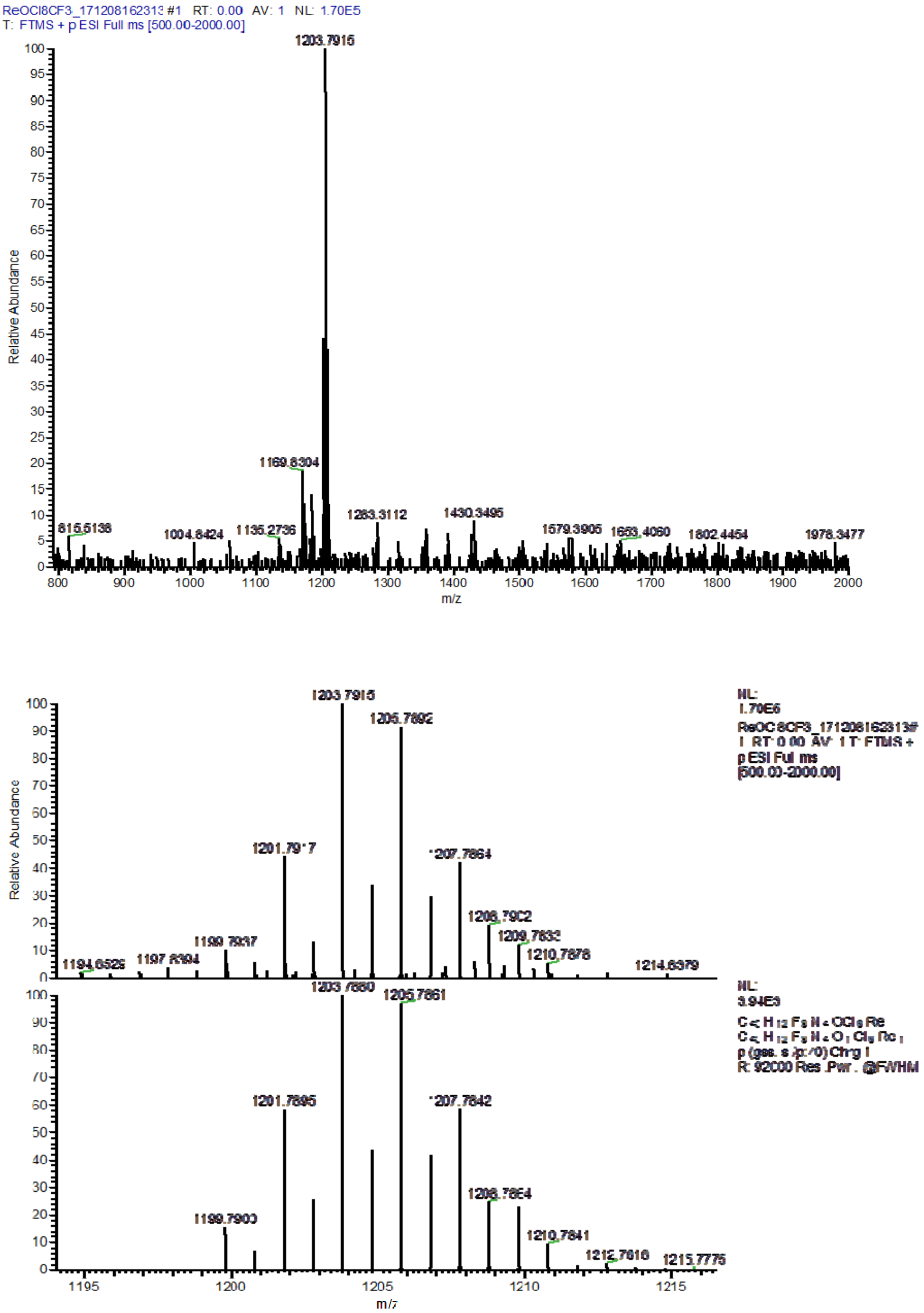

Figure S8. ESI-MS of Re[Cl$_8$T*p*CF$_3$PC](O): experimental (top) and simulation (bottom).

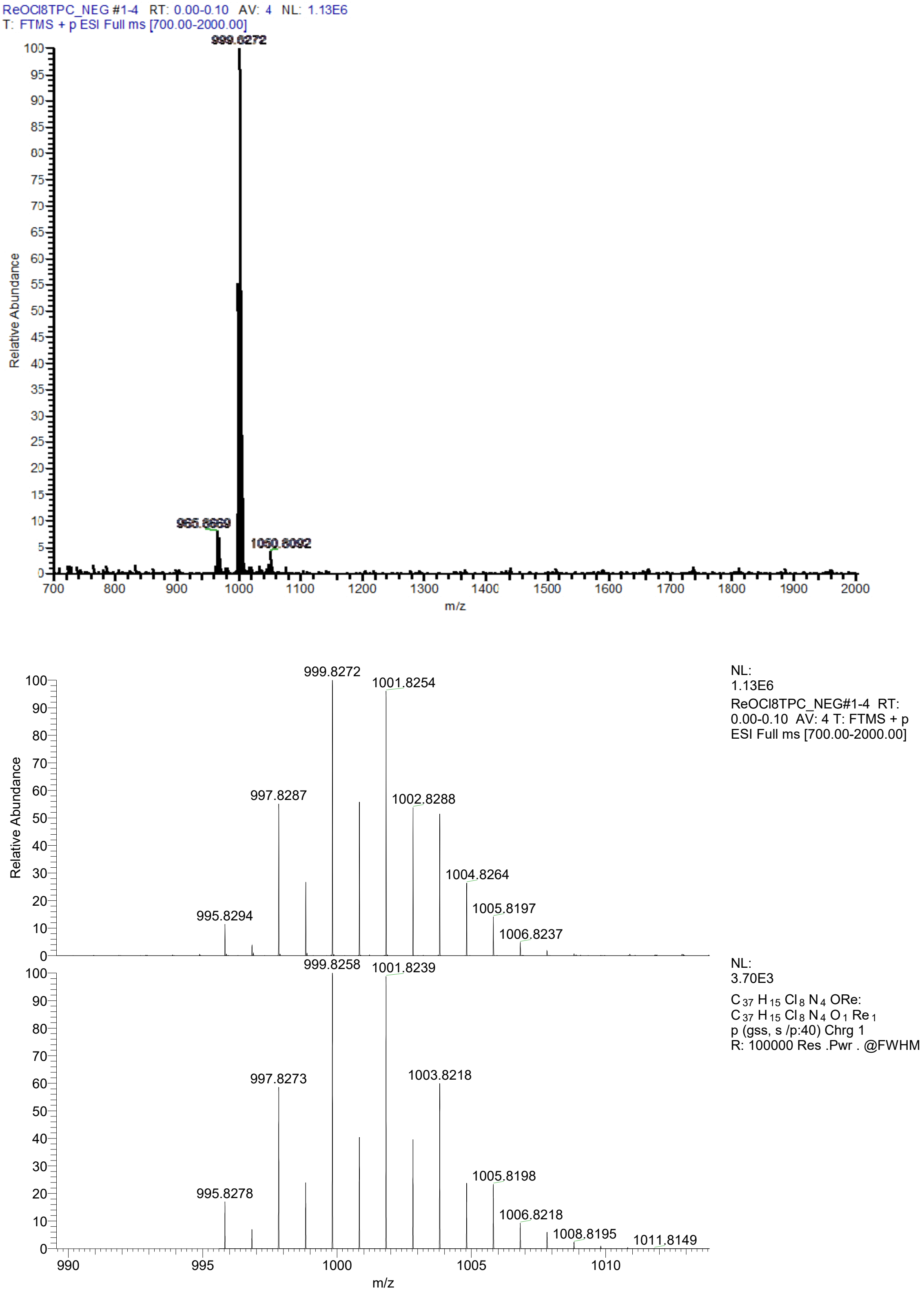

Figure S9. ESI-MS of Re[Cl_8TPC](O): experimental (top) and simulation (bottom).

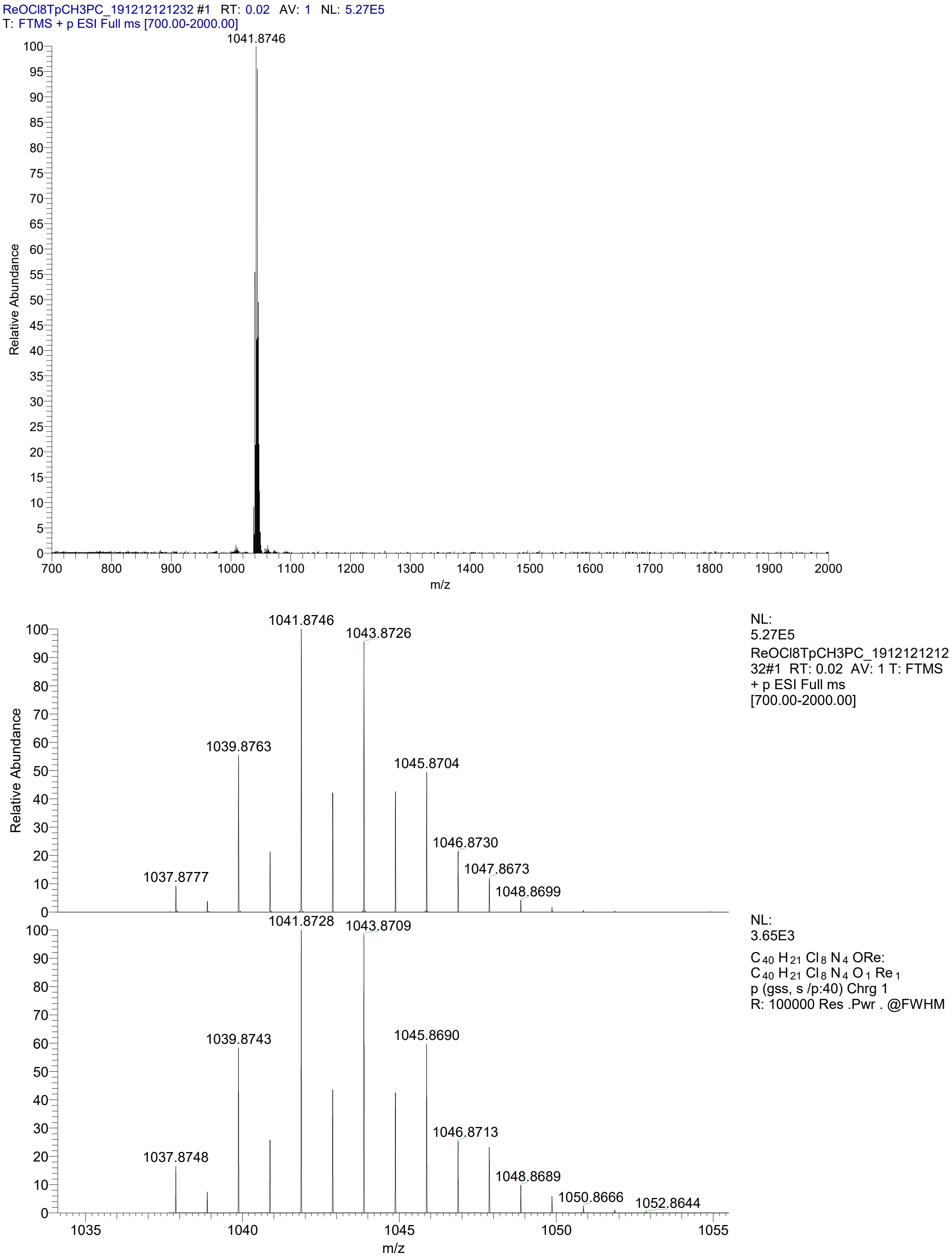

Figure S10. ESI-MS of Re[Cl$_8$T*p*CH$_3$PC](O): experimental (top) and simulation (bottom).

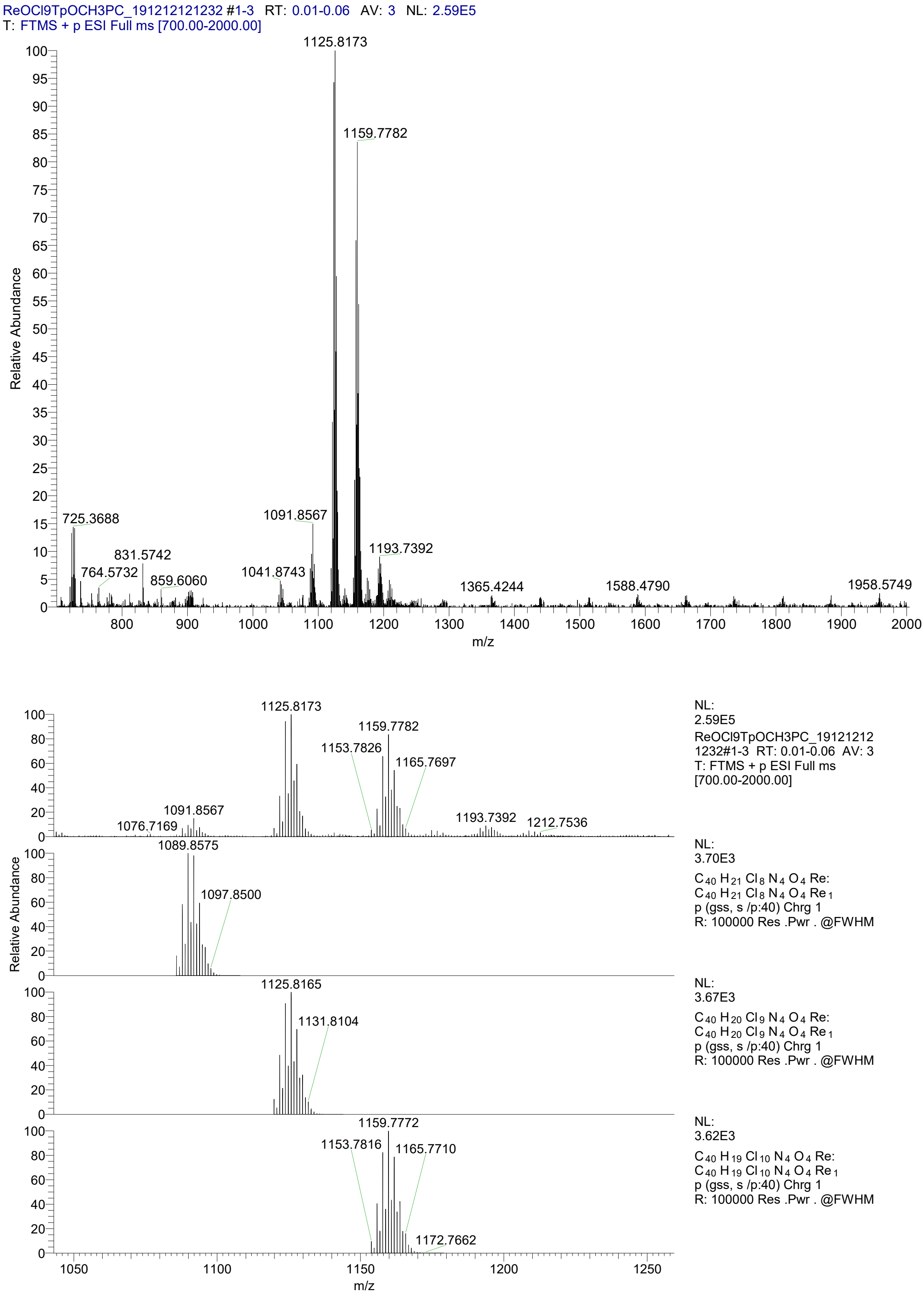

Figure S11. Contd.

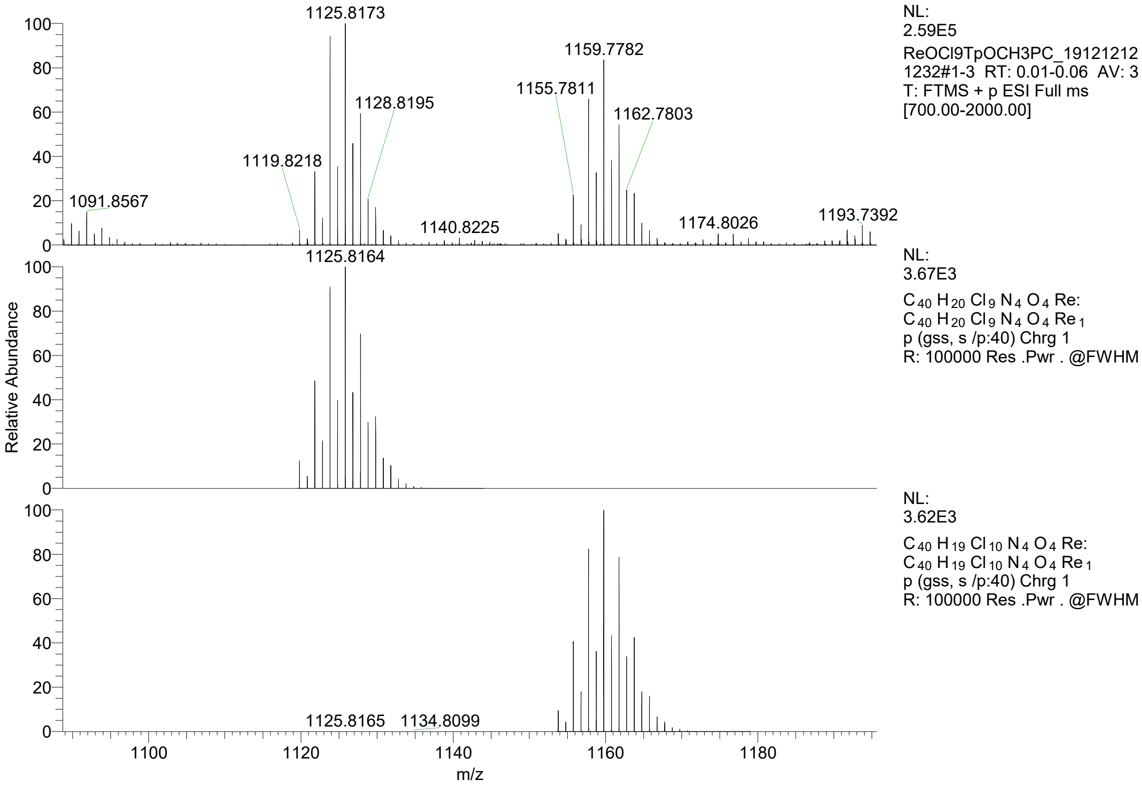

Figure S11. ESI-MS spectrum of Re[Cl$_9$T*p*OCH$_3$PC](O) and Re{Cl$_{10}$T*p*OCH$_3$PC}(O): experimental (top) and two simulations (bottom).

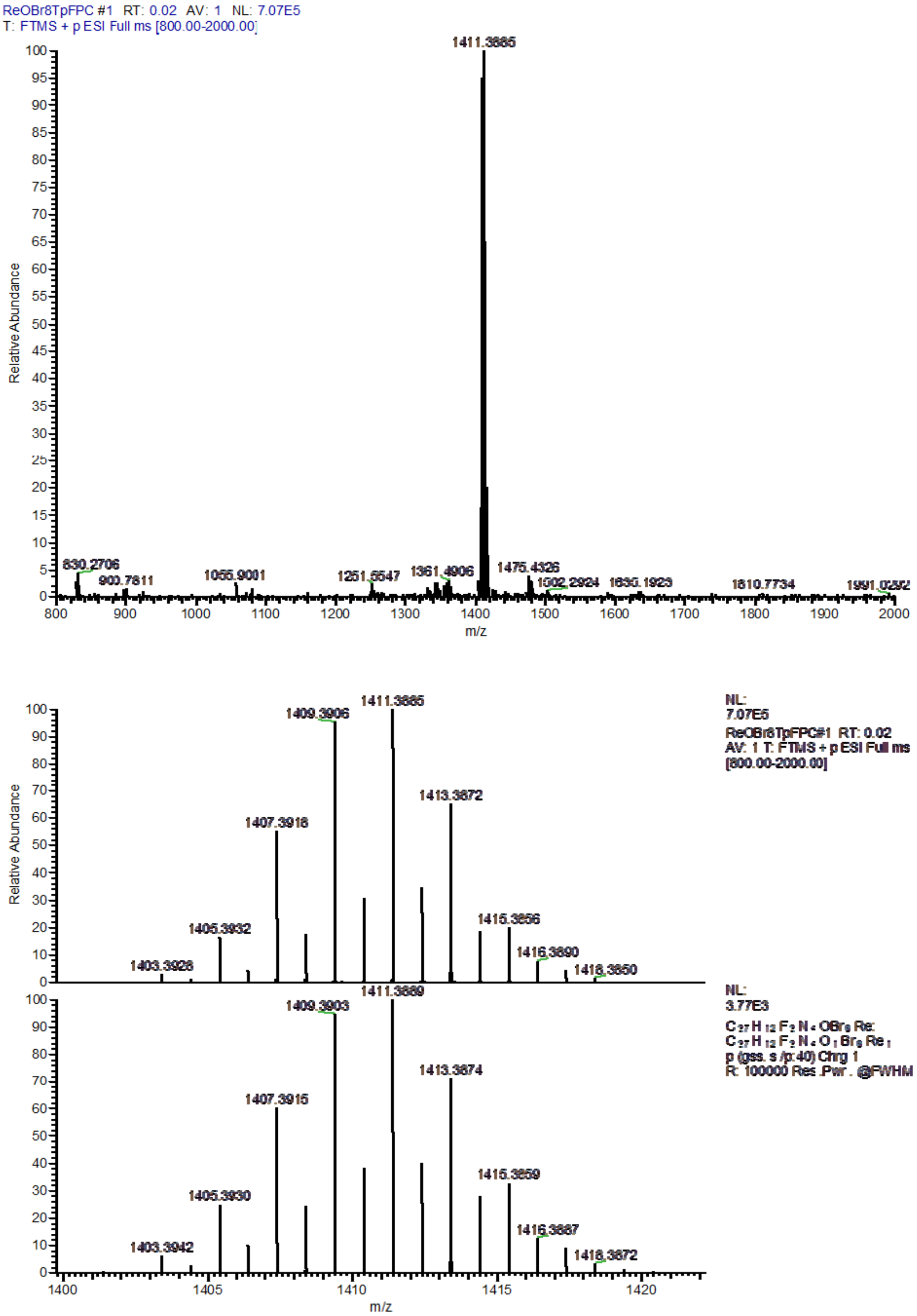

Figure S12. ESI-MS of Re[Br₈T*p*FPC](O): experimental (top) and simulation (bottom).

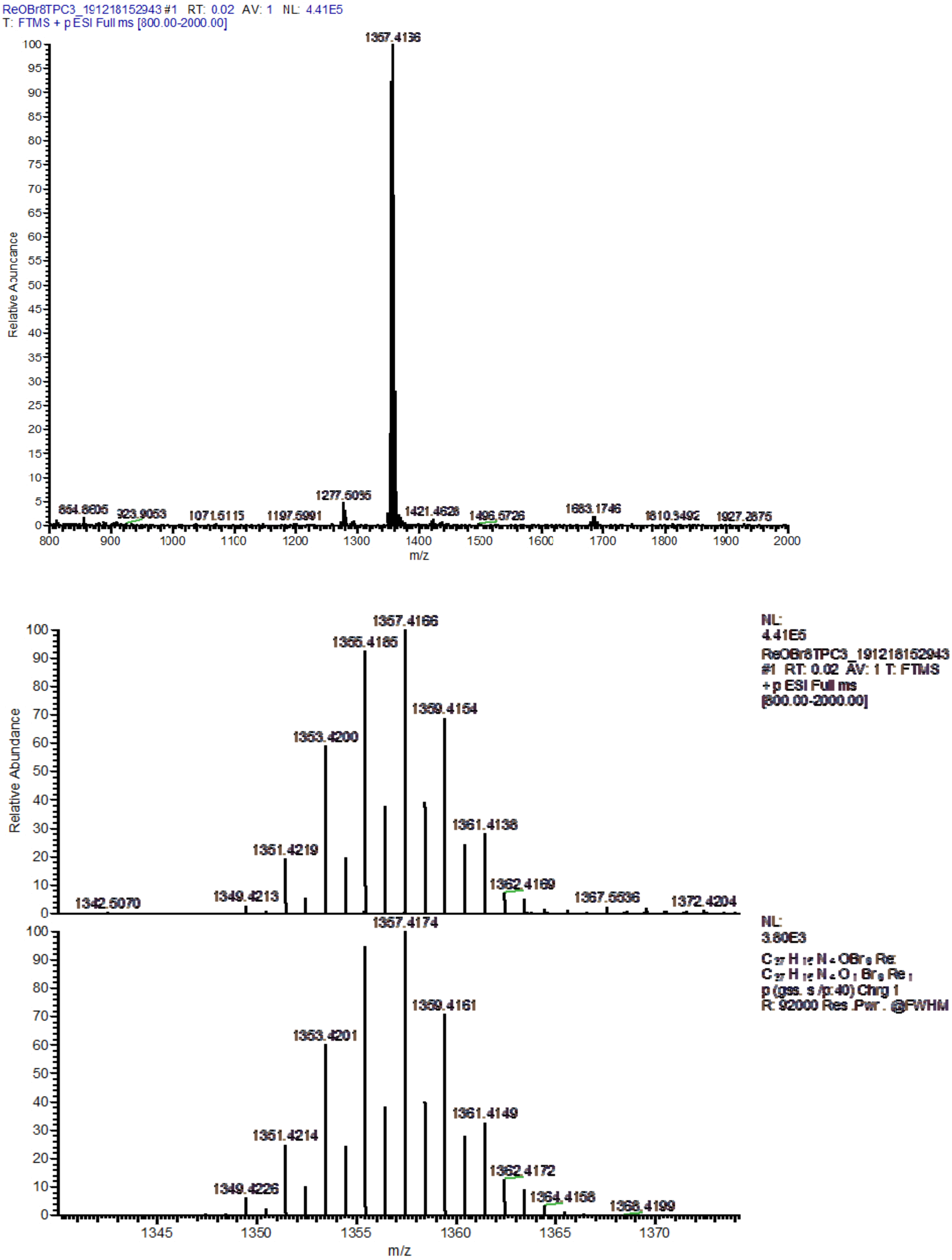

Figure S13. ESI-MS of Re[Br_8TPC](O): experimental (top) and simulation (bottom).

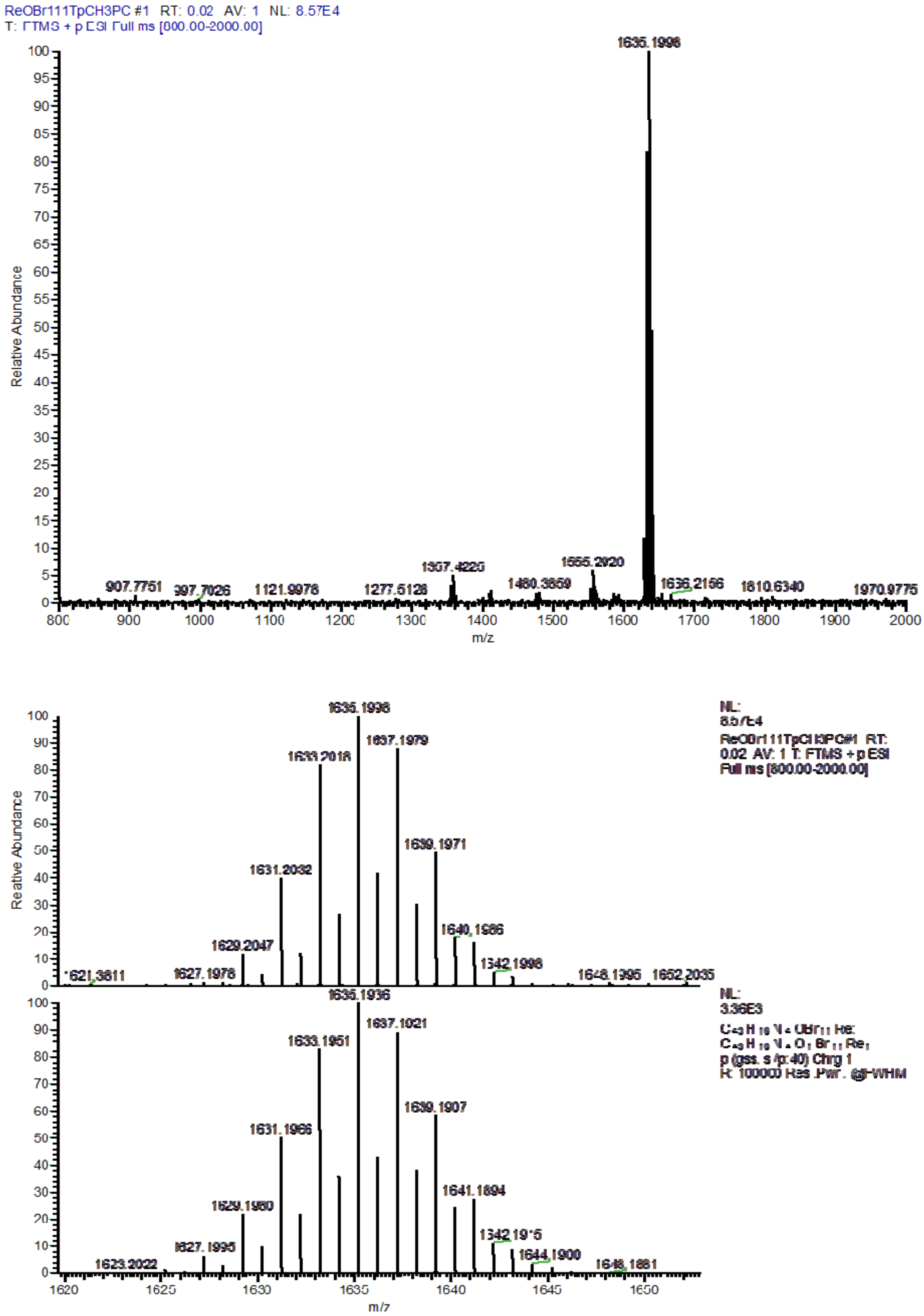

Figure S14. ESI-MS of Re[Br$_{11}$T*p*CH$_3$PC](O): experimental (top) and simulation (bottom).

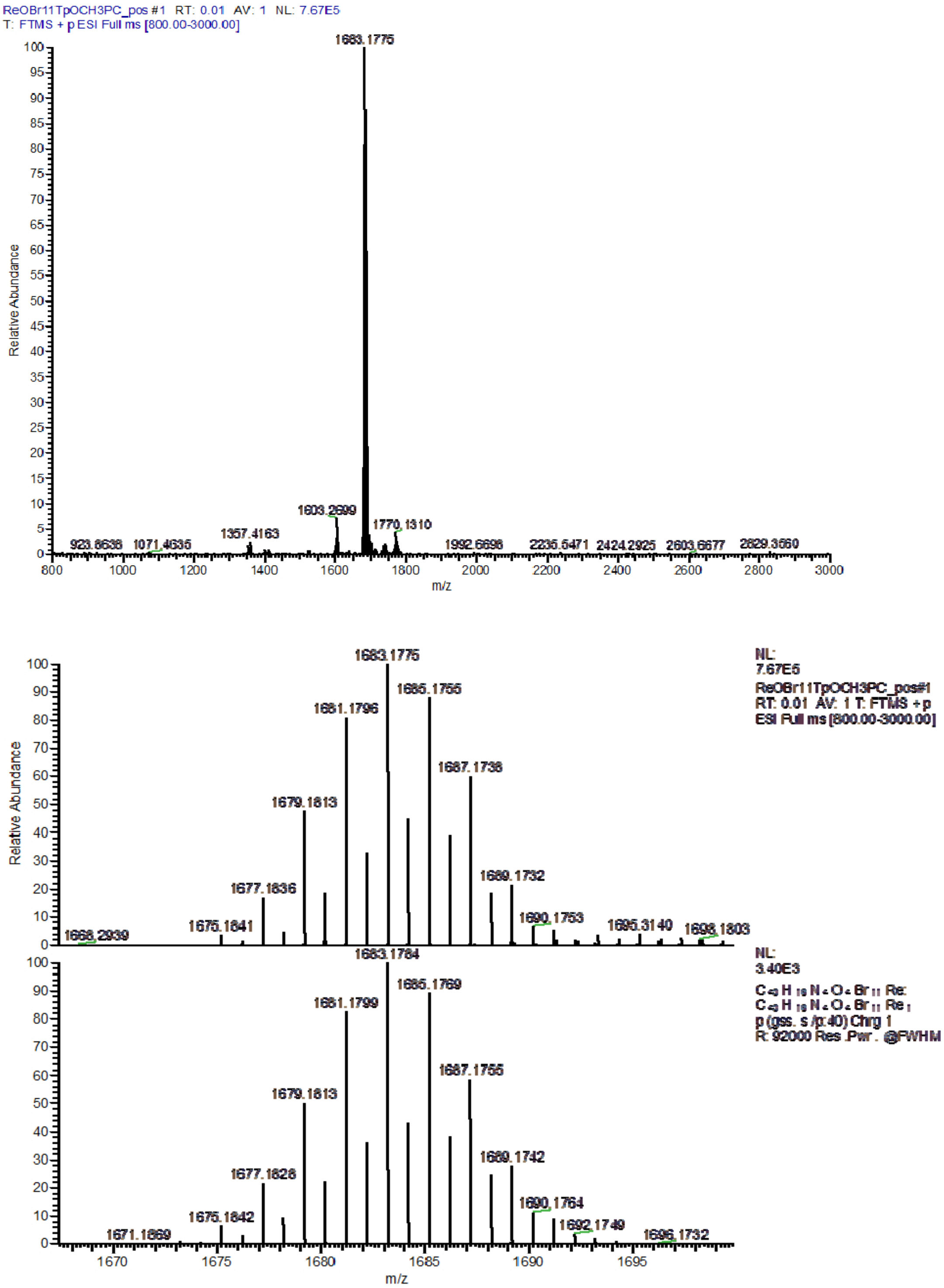

Figure S15. ESI-MS of Re[Br$_{11}$T*p*OCH$_3$PC](O); experimental (top) and simulation (bottom).

Paper D

ACS APPLIED ENERGY MATERIALS

www.acsaem.org Article

Heavy Metal Effects on the Photovoltaic Properties of Metallocorroles in Dye-Sensitized Solar Cells

Tomohiro Higashino, Yuma Kurumisawa, Abraham B. Alemayehu, Rune F. Einrem, Debashis Sahu, Daniel Packwood, Kosaku Kato, Akira Yamakata,* Abhik Ghosh,* and Hiroshi Imahori*

Cite This: *ACS Appl. Energy Mater.* 2020, 3, 12460−12467 Read Online

ABSTRACT: Finding strategies for effective charge separation is a prerequisite for realizing efficient solar energy conversion in photovoltaic and photocatalytic devices. Porphyrinoids, including porphyrins and related macrocycles such as phthalocyanines and corroles, are versatile ligands that can accommodate a single metal atom for most metal ions, and their photophysical and electrochemical properties can be tuned by the metal atom in the cavity. Herein, we evaluated the photovoltaic properties of the dye-sensitized solar cells (DSSCs) based on Au^{III}-, $Re^{V}O$-, and $Os^{VI}N$-corroles with COOH anchoring groups at the *para*- and *meta*-positions of the *meso*-phenyl groups. The DSSCs based on Au^{III}-corroles exhibited a power conversion efficiency (PCE) of 4.2%, which is remarkably higher than those for the $Re^{V}O$- and $Os^{VI}N$-corroles. Femtosecond time-resolved transient absorption measurements have shown that the electron injection from the excited singlet state competes with intersystem crossing, and that intersystem crossing for Au^{III}-corroles is slower than those for $Re^{V}O$- and $Os^{VI}N$-corroles. Consequently, the high incident photon-to-current efficiencies and resultant short-circuit current densities and PCEs for Au^{III}-corroles are attributed to the high electron injection efficiencies owing to the slower intersystem crossing than $Re^{V}O$- and $Os^{VI}N$-corroles. In addition, the higher PCE for a Au^{III}-corrole with a *meta*-COOH group (4.2%) as opposed to a *para*-COOH group (3.4%) is explained by the stronger Au−TiO_2 interactions supported by XPS measurements and theoretical calculations. These results imply that both the substituents and the metal ion have a large influence on the photovoltaic performances. Overall, DSSCs based on the Au^{III}-corroles were found to exhibit the highest photovoltaic performance among corrole-based DSSCs.

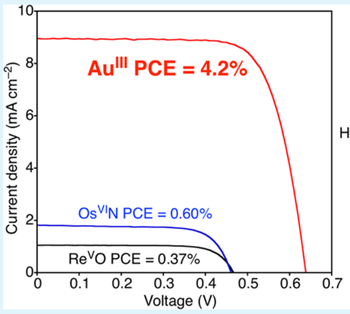

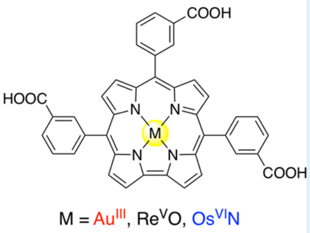

KEYWORDS: *dye-sensitized solar cells, corrole, gold, rhenium, osmium, electron transfer, intersystem crossing*

■ INTRODUCTION

Obtaining a high charge separation efficiency is essential for achieving efficient solar energy conversion in photovoltaic and photocatalytic devices.[1−4] Toward this end, a variety of compounds including organic dyes and metal complexes have been developed as sensitizers.[5−7] Porphyrinoids, including porphyrins and related macrocycles such as phthalocyanines and corroles, are versatile ligands that can accommodate a single metal atom for most metal ions[8−11] and their photophysical and electrochemical properties can be tuned by the metal atom in the cavity. Metalloporphyrinoids have attracted much attention as potential light-harvesting sensitizers for solar energy conversion because of their enhanced absorption bands in the visible region.[12−20] In particular, zinc porphyrins and phthalocyanines with relatively long-lived excited singlet states have been frequently used as sensitizers in dye-sensitized solar cells (DSSCs),[15−20] with power conversion efficiencies (PCEs) in certain cases exceeding 10%.[21−26] However, many other metal complexes suffer from short-lived excited singlet states as a result of fast relaxation to the triplet state and the ground state due to the heavy atom effect. In DSSCs, electron injection from the excited singlet state of sensitizers to TiO_2 usually occurs within hundreds of femtoseconds to tens of picoseconds.[27,28] Electron injection from the excited singlet state of metalloporphyrinoids, accordingly, is competitive with the fast relaxation process. Moreover, because the triplet states are substantially lower in energy than the singlet energy levels, the driving force for electron injection from the excited triplet state to TiO_2 is almost zero or endothermic. Overall, efficient electron injection from the excited states of metalloporphyrinoids to TiO_2 is hampered by the fast relaxation processes, leading to poor photovoltaic performance.

Received: September 30, 2020
Accepted: November 12, 2020
Published: November 25, 2020

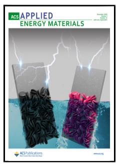

https://dx.doi.org/10.1021/acsaem.0c02427
ACS Appl. Energy Mater. 2020, 3, 12460−12467

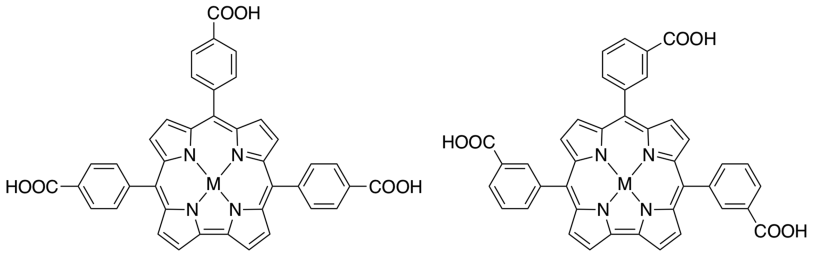

Au-A (M = Au)
Re-A (M = Re≡O)
Os-A (M = Os≡N)

Au-B (M = Au)
Re-B (M = Re≡O)
Os-B (M = Os≡N)

Figure 1. Molecular structures of 5d metallocorroles with *para*-carboxyphenyl groups (**Au-A**, **Re-A**, and **Os-A**) and *meta*-carboxyphenyl groups (**Au-B**, **Re-B**, and **Os-B**).

Meanwhile, Au^{III}-corroles with long-lived excited triplet states have been employed as the sensitizer and donor in bulk heterojunction solar cells.[29] We also reported that PCEs of DSSCs with Au^{III}-corroles (0.17−3.5%) are much larger than those with free-base corroles (0.08−0.14%).[30] This result contradicts the notion that electron injection is possible only from excited singlet states, since the lifetimes of the excited singlet states of Au^{III}-corroles with no fluorescence are supposedly much shorter than those of free-base corroles (∼5 ns).[30] This contradiction tempted us to scrutinize the effects of a heavy metal atom on the photovoltaic properties of metallocorroles in DSSCs. Herein, we report photovoltaic properties of the DSSCs based on Au^{III}-,[31] $Re^{V}O$-,[32] and $Os^{VI}N$[33]-corroles with COOH anchoring groups at the *para*- and *meta*-positions of the *meso*-phenyl groups (Figure 1). We found that the remarkably enhanced performance of DSSCs based on Au^{III}-corroles results from the higher electron injection efficiencies (ϕ_{inj}) due to the slow intersystem crossing relative to $Re^{V}O$- and $Os^{VI}N$-corroles.

RESULTS AND DISCUSSION

Synthesis and Optical and Electrochemical Properties of Metallocorroles. The synthesis and characterization of the metallcorroles studied are described in the Supporting Information (Figures S1 and S2). The UV−vis absorption spectra of the compounds in THF are displayed in Figure 2. The central metal has a significant impact on the optical properties. Consistent with their strongly domed geometries, $Re^{V}O$- and $Os^{VI}N$-corroles exhibit red-shifted Soret and Q-bands relative to those of Au^{III}-corroles. The absorption features for *para*- and *meta*-substituted corroles, on the other hand, are almost the same for a given central metal, showing that the substituents on the *meso*-aryl groups have little influence on the optical properties. The optical HOMO−LUMO gaps of the metallocorroles were estimated from the onset of the lowest-energy Q-bands and found to be 2.08 eV for **Au-A**, 2.10 eV for **Au-B**, 2.03 eV for **Re-A**, 2.04 eV for **Re-B**, 2.00 eV for **Os-A**, and 2.01 eV for **Os-B**.

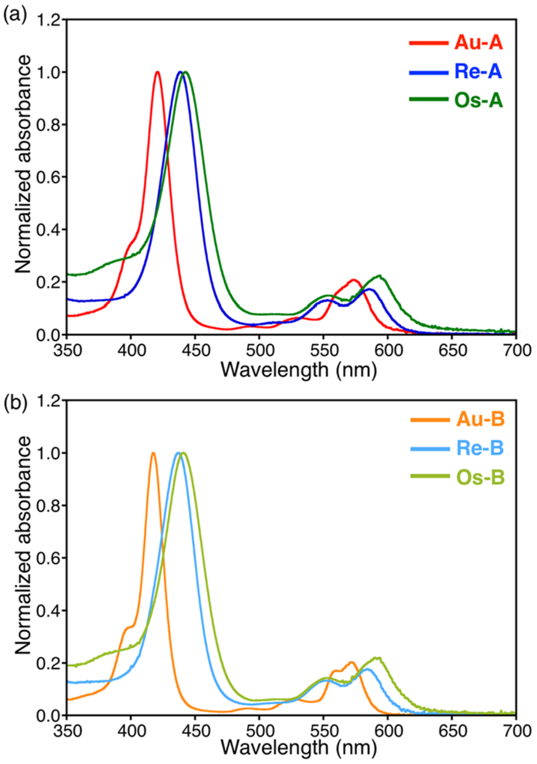

Figure 2. Normalized UV−vis absorption spectra of (a) *para*-substituted metallocorroles **Au-A** (red), **Re-A** (blue), and **Os-A** (green) and (b) *meta*-substituted metallocorroles **Au-B** (orange), **Re-B** (light blue), and **Os-B** (yellow-green) in THF.

The redox potentials of the metallocorroles were determined by differential pulse voltammetry (DPV) in THF versus NHE with tetrabutylammonium hexafluorophosphate (Bu_4NPF_6) as an electrolyte (Table 1 and Figure S3). The first oxidation potentials of **Au-A** and **Au-B** are +1.11 and +1.10 V, respectively. The first oxidation potentials of the $Re^{V}O$- and $Os^{VI}N$-corroles are shifted in the positive direction (+1.26 V for **Re-A**, +1.23 V for **Re-B**, +1.16 V for **Os-A**, and +1.14 V for **Os-B**) relative to those of the Au^{III}-corroles. On the other hand, the first reduction potentials of **Au-A** (−0.83 V), **Re-A** (−0.86 V), and **Os-A** (−0.87 V) are largely independent of the central metal. In contrast, the first reduction potential of **Au-B** (−0.91 V) is upshifted relative to those of **Re-B** (−1.10 V) and **Os-B** (−1.05 V).[10]

The first oxidation potentials and optical HOMO−LUMO gaps allowed the calculation of the oxidation potentials for the excited singlet states of the metallocorroles (Table 1). We also estimated the driving forces for electron injection from the metallocorrole excited singlet state (ΔG_{inj}^{S1}) to the conduction band (CB) of the TiO_2 (−0.5 V vs NHE) and for the reduction of the metallocorrole radical cation by the I^-/I_3^- redox shuttle (+0.4 V vs NHE). All the electron-transfer (ET) processes from the metallocorrole excited singlet state are expected to occur efficiently because these driving forces are more negative than −0.27 eV.[26] On the other hand, the energy levels of the excited triplet states are estimated to be 1.55−1.61 eV, based on the phosphorescence peaks of Au^{III}-, $Re^{V}O$-, and

Table 1. Electrochemical Properties of the Metallocorroles

corroles	E_{ox1} (V)[a]	E_{red1} (V)[a]	E_{0-0} (eV)	E_{ox}^{S1} (V)[b]	E_{ox}^{T1} (V)[c]	ΔG_{inj}^{S1} (eV)[d]	ΔG_{inj}^{T1} (eV)[d]	ΔG_{reg} (eV)[e]
Au-A	1.11	−0.83	2.08	−0.97	−0.45	−0.47	+0.05	−0.71
Au-B	1.10	−0.91	2.10	−1.00	−0.46	−0.50	+0.04	−0.70
Re-A	1.26	−0.86	2.03	−0.77	−0.35	−0.27	+0.15	−0.86
Re-B	1.23	−1.10	2.04	−0.81	−0.38	−0.31	+0.12	−0.83
Os-A	1.16	−0.87	2.00	−0.84	−0.42	−0.34	+0.08	−0.76
Os-B	1.14	−1.05	2.01	−0.87	−0.44	−0.37	+0.06	−0.74

[a]Determined by DPV (vs NHE). [b]Determined by adding E_{0-0} to E_{ox1}. [c]Estimated from the phosphorescence spectra and E_{ox1}. [d]Driving force for electron injection from the excited singlet or triplet states to the CB of the TiO_2 (−0.5 V vs NHE). [e]Driving force for the reduction of the corrole radical cation by the I^-/I_3^- redox shuttle (+0.4 V vs NHE).

Os^{VI}N-corroles in the 770−800 nm range.[30,34−36] As a result, the oxidation potentials of the excited triplet states of the metallocorroles are estimated to be ca. −0.35−−0.45 V versus NHE, which are less negative than the CB of the TiO_2 (−0.5 vs NHE) (Figure S4). Accordingly, ET from the excited triplet state should be inhibited owing to the positive driving forces involved (ΔG_{inj}^{T1}).

Adsorption Behavior. The adsorption properties of the metallocorroles on a TiO_2 film were examined as follows. A TiO_2 electrode was immersed in an ethanol/THF (v/v = 4:1) solution of the metallocorrole to give a metallocorrole-stained TiO_2 electrode for DSSCs. The metallocorrole surface coverage (Γ) on TiO_2 was estimated by measuring the absorbance of the metallocorrole that was dissolved from the metallocorrole-stained TiO_2 electrode into 0.1 M NaOH solution of 1:1 mixture of THF and water. The adsorption profiles revealed faster adsorption of metallocorroles with *meta*-carboxylic acid groups (**Au-B**, **Re-B**, and **Os-B**) than that of metallocorroles with *para*-carboxylic acid groups (**Au-A**, **Re-A**, and **Os-A**) (Figure S5). The metallocorroles with *meta*-carboxylic acid groups reached constant surface coverage on the TiO_2 electrode within 8 h. On the other hand, the metallocorroles with *para*-carboxylic acid groups required 15−24 h to reach saturation coverage. The faster adsorption profiles of **Au-B**, **Re-B**, and **Os-B** may be attributed to cooperative triple anchoring of three *meta*-carboxylic acid groups to TiO_2, which is much less likely with the *para*-carboxylic acid groups. The saturation Γ values of the corrole dyes were found to be as follows: 1.6×10^{-10} mol cm^{-2} for **Au-A**, 1.5×10^{-10} mol cm^{-2} for **Au-B**, 2.1×10^{-10} mol cm^{-2} for **Re-A**, 1.7×10^{-10} mol cm^{-2} for **Re-B**, 1.7×10^{-10} mol cm^{-2} for **Os-A**, and 1.5×10^{-10} mol cm^{-2} for **Os-B**. Interestingly, the saturation Γ values of the metallocorrole dyes with *para*-carboxylic acid were found to be slightly higher than those of the corresponding metallocorrole dyes with *meta*-carboxylic acid.[37]

The FTIR spectra of **Au-A** and **Au-B** powders display characteristic peaks of ν(C═O) and ν(O−H) of the carboxylic acid group at around 1700 and 1400 cm^{-1}, respectively (Figure S6). In contrast, the FTIR spectra of **Au-A** and **Au-B** on TiO_2 exhibit significant changes of the ν(C═O) and ν(O−H) peaks, indicating adsorption of the carboxylic acid groups on the TiO_2 surface.[38,39]

Photovoltaic Performances of the DSSCs Based on the Metallocorroles. The photovoltaic properties of the DSSCs were measured under standard AM1.5 conditions using an electrolyte solution containing the I^-/I_3^- redox shuttle. To maximize the photovoltaic performances, we investigated the effects of immersion time (Figure S7). The PCE increased with increasing immersion time to reach saturation values in 15 h for **Au-A** (2.1%), **Re-A** (0.71%), and **Os-A** (0.35%), 5 h for **Au-B** (3.8%) and **Re-B** (0.30%), and 3 h for **Os-B** (0.54%). By fixing the respective immersion time, we also sensitized each metallocorrole at various concentrations of chenodeoxycholic acid (CDCA), a coadsorbent for the suppression of dye aggregation (Figure S8). Optimal PCEs were attained at different equivalents of CDCA (**Au-A**: 2.7% with 6 equiv of CDCA; **Au-B**: 4.1% with 6 equiv of CDCA; **Re-A**: 0.83% with 6 equiv of CDCA; **Re-B**: 0.37% with 15 equiv of CDCA; **Os-A**: 0.39% with 10 equiv of CDCA; and **Os-B**: 0.60% with 3 equiv of CDCA). The large dependence on the CDCA concentration indicates a strong dye aggregation tendency, which may be attributed to the lack of bulky substituents on the *meso*-aryl groups. Lastly, the DSSCs were stored under dark conditions to enhance their photovoltaic properties via the aging effect[39,40] (Figure S9). The DSSCs based on **Au-A**, **Au-B**, and **Os-A** were found to exhibit the highest PCEs after aging for 1 day, while the DSSCs based on **Re-A**, **Re-B**, and **Os-B** revealed no improvement of the PCEs after aging. The photocurrent−voltage (*J*−*V*) characteristics of the fully optimized DSSCs are shown in Figure 3 and Figure S10 and the detailed photovoltaic parameters are summarized in Table 2.

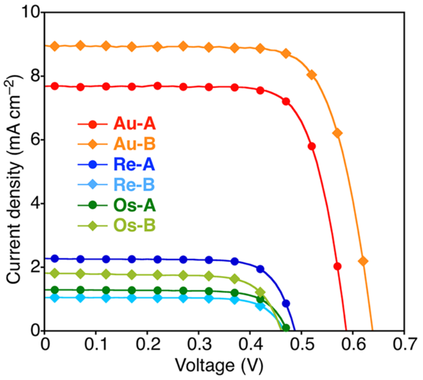

Figure 3. Photocurrent−voltage (*J*−*V*) characteristics of the DSSCs based on **Au-A** (red), **Au-B** (orange), **Re-A** (blue), **Re-B** (light blue), **Os-A** (green), and **Os-B** (yellow-green) under conditions optimized for achieving the highest efficiencies.

The optimized PCEs of the DSSCs based on **Au-A** (3.4%) and **Au-B** (4.2%) are 1 order of magnitude higher than those of the DSSCs based on **Re-A**, **Re-B**, **Os-A**, and **Os-B** (0.37−0.83%). The PCEs of the DSSC are somewhat improved compared to those under previous conditions and as far as we know, the value of 4.2% is the highest reported for DSSCs with corroles.[30] The photocurrent action spectra of the DSSCs and the absorption spectra of the metallocorrole-stained TiO_2

Table 2. Photovoltaic Performance Characteristics of the DSSCs Based on the Metallocorrole Dyes[a]

corrole	J_{SC} (mA cm^{-2})	V_{OC} (V)	ff	PCE (%)
Au-A[b]	7.7 (7.3)	0.59 (0.58)	0.75 (0.75)	3.4 (3.2)
Au-B[c]	9.0 (8.9)	0.64 (0.64)	0.74 (0.73)	4.2 (4.2)
Re-A[d]	2.3 (2.2)	0.49 (0.48)	0.75 (0.75)	0.83 (0.80)
Re-B[e]	1.0 (1.0)	0.47 (0.47)	0.76 (0.75)	0.37 (0.37)
Os-A[f]	1.3 (1.3)	0.47 (0.47)	0.74 (0.74)	0.45 (0.44)
Os-B[g]	1.8 (1.6)	0.46 (0.48)	0.72 (0.75)	0.60 (0.59)

[a] Photovoltaic parameters (J_{SC}: short-circuit current density; V_{OC}: open-circuit voltage; and ff: fill factor) deriving from the highest PCE. The values in parenthesis denote average values from three independent experiments. [b] Immersion time: 15 h; CDCA: 6 equiv; aging: 1 day. [c] Immersion time: 5 h; CDCA: 6 equiv; aging: 1 day. [d] Immersion time: 15 h; CDCA: 6 equiv; aging: none. [e] Immersion time: 5 h; CDCA: 15 equiv; aging: none. [f] Immersion time: 15 h; CDCA: 3 equiv; aging: 1 day. [g] Immersion time: 3 h, CDCA: 10 equiv; aging: none.

electrodes are shown in Figure 4. The integrated short-circuit current densities (J_{SC}) from the photocurrent action spectra were determined to be 7.03, 8.85, 2.02, 0.98, 1.26, and 1.71 mA cm^{-2} for **Au-A**, **Au-B**, **Re-A**, **Re-B**, **Os-A**, and **Os-B**, respectively, which agrees well with the J_{SC} values obtained from the $J-V$ characteristics. The DSSCs based on the Au^{III}-corroles exhibit significantly higher incident photon-to-current efficiency (IPCE) values than those based on Re^{V}O- and Os^{VI}N-corroles (Figure 4a). The IPCE is calculated by the following equation: IPCE = LHE × ϕ_{inj} × η_{col}, where light-harvesting efficiency (LHE) is the number of absorbed photons per incident photons, ϕ_{inj} is the efficiency of the electron injection, and η_{col} is the efficiency of the charge collection. The LHE values for all the metallocorroles are likely to be unity at 380−600 nm considering the high absorbance in the absorption spectra and the effect of the light-scattering layer in the real DSSCs (Figure 4b). The η_{col} values should also be comparable, considering the large driving forces for dye regeneration. Thus, the ϕ_{inj} values are primarily responsible for the large difference in the IPCE values. To generate a photocurrent, electron injection from the excited singlet states to the CB of the TiO_2 must be competitive with the fast relaxation processes of the nonfluorescent, singlet excited state of metallocorroles. Because the driving forces are positive (ΔG_{inj}^{T1} in Table 1), electron injection from the excited triplet states of the metallocorroles is impossible. The high IPCE values of the DSSCs based on **Au-A** and **Au-B** imply that electron injection is competitive with the fast relaxation process, i.e., intersystem crossing.

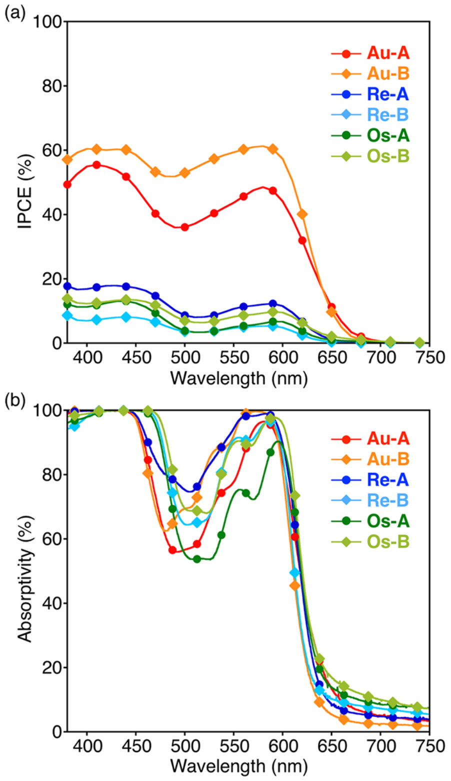

Figure 4. (a) Photocurrent action spectra of the DSSCs based on **Au-A** (red), **Au-B** (orange), **Re-A** (blue), **Re-B** (light blue), **Os-A** (green), and **Os-B** (yellow-green) under conditions optimized for achieving the highest efficiencies. (b) Absorption spectra of the TiO_2 electrodes with metallocorroles. The light-scattering layers were not used to obtain an accurate absorption profile.

Transient Absorption Spectroscopy. To probe the photodynamics of the metallocorroles, time-resolved transient absorption (TA) spectroscopy measurements were performed for **Au-B**, **Re-B**, and **Os-B** with excitation at wavelengths for the Soret band maxima. In THF solution, the obtained picosecond TA spectra exhibit short-lived (<0.1−1 ps) and long-lived (>100 ps) components (Figure S11). Because the microsecond TA spectra for **Au-B** show similar features corresponding to the long-lived component (Figure S12), the short-lived and long-lived components can be assigned to the excited singlet and triplet states, respectively. From the transient absorption profiles at 760 nm, the excited singlet state is transformed into the excited triplet state with τ = 0.98 ps for **Au-B**, τ < 0.1 ps for **Re-B**, and τ = 0.46 ps for **Os-B** (Figure 5a). Thus, the intersystem crossing for **Au-B** is slower than those for **Re-B** and **Os-B**.

Next, we conducted the TA spectroscopy measurements on metallocorrole-adsorbed TiO_2 films on a CaF_2 surface under a N_2 atmosphere (Figure 5b). We monitored the transient absorption profiles of the characteristic absorption at 5000 nm corresponding to the free electron in the CB of the TiO_2.[41] Upon excitation, the transient absorption profiles exhibited the increase in the absorption of free electron in the CB of the TiO_2 (0.1−0.2 ps), suggesting that the electron injection from the excited singlet state competes with the intersystem crossing (<0.1−1 ps). Notably, the intensity of the transient absorption for **Au-B** was found to be significantly larger than those for **Re-B** and **Os-B**. These results imply that the ϕ_{inj} value for **Au-B** is higher than those for **Re-B** and **Os-B**. In addition, the trend of intensities for transient absorption (**Au-B** > **Os-B** > **Re-B**) is in good agreement with that for the intersystem crossing rates. Overall, the higher PCE for **Au-B** can be rationalized in terms of a higher ϕ_{inj} value due to slow intersystem crossing relative to **Re-B** and **Os-B**.

Interactions between Gold Atom and TiO_2. To shed light into the higher IPCE value for **Au-B** than for **Au-A**, we conducted X-ray photoelectron spectroscopy (XPS) measurements (Figure 6). The Au 4f photoelectron spectra of **Au-A** and **Au-B** powder display two peaks at 90.3 and 86.6 eV and 89.6 and 86.0 eV, respectively. After adsorption, the spectra show two peaks at 91.2 and 87.9 eV for **Au-A** and 91.9 and 89.1 eV for **Au-B**. These shifts suggest a direct interaction between the single gold atom of the Au^{III}-corroles and the

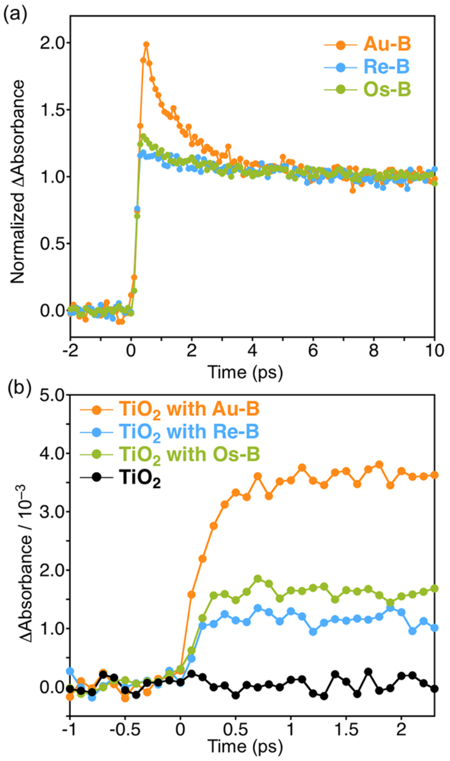

Figure 5. (a) Transient absorption profiles for **Au-B**, **Re-B**, and **Os-B** in THF at 760 nm. (b) Transient absorption profiles for TiO_2 with **Au-B**, **Re-B**, and **Os-B** at 5000 nm. The samples were excited at wavelengths for the Soret band maxima. For measurements of dye-sensitized TiO_2 films, the absorptivity at the excitation wavelength are 100% for **Au-B**, 93% for **Re-B**, and 93% for **Os-B**.

TiO_2 surface. It is noteworthy that the shifts of the peaks for **Au-B** (ca. 3 eV) are larger than those for **Au-A** (ca. 1 eV), implying stronger Au−TiO_2 interaction for **Au-B**. To support this interpretation, we performed theoretical calculations. The calculated structures of the Au^{III}-corroles on TiO_2 revealed that the closest Au−Ti and Au−O distances are 4.0 and 3.5 Å for **Au-A** and 3.7 and 3.3 Å for **Au-B**, respectively (Figure S13). The shorter Au−Ti and Au−O distances for **Au-B** indicate stronger Au−TiO_2 interactions than **Au-A**. These XPS and computational results support that the gold atom of the **Au-B** interacts more strongly with TiO_2 than that of **Au-A**. Taking into account the stronger Au−TiO_2 interaction for **Au-B**, the ϕ_{inj} values for **Au-B** are expected to be higher than those for **Au-A** because of faster electron injection from the excited singlet state. Thus, the stronger Au−TiO_2 interaction for **Au-B** than for **Au-A** agrees well with the higher photovoltaic properties of **Au-B** than **Au-A**.

■ CONCLUSIONS

We synthesized gold, rhenium, and osmium corroles to evaluate the effects of the noble metal on the photovoltaic properties of metallocorrole-based DSSCs. The DSSCs based on **Au-A** and **Au-B** exhibited PCEs of 3.4 and 4.2%, respectively, which are remarkably higher than those for the $Re^{V}O$- and $Os^{VI}N$-corroles. Femtosecond TA measurements showed that electron injection from the excited singlet state competes with intersystem crossing and that intersystem crossing for Au^{III}-corroles is slower than those for $Re^{V}O$- and $Os^{VI}N$-corroles. Consequently, the high IPCE values and resultant J_{SC} and PCEs for Au^{III}-corroles are attributed to the high ϕ_{inj} values as a result of slow intersystem crossing relative to $Re^{V}O$- and $Os^{VI}N$-corroles. The higher PCE for **Au-B**

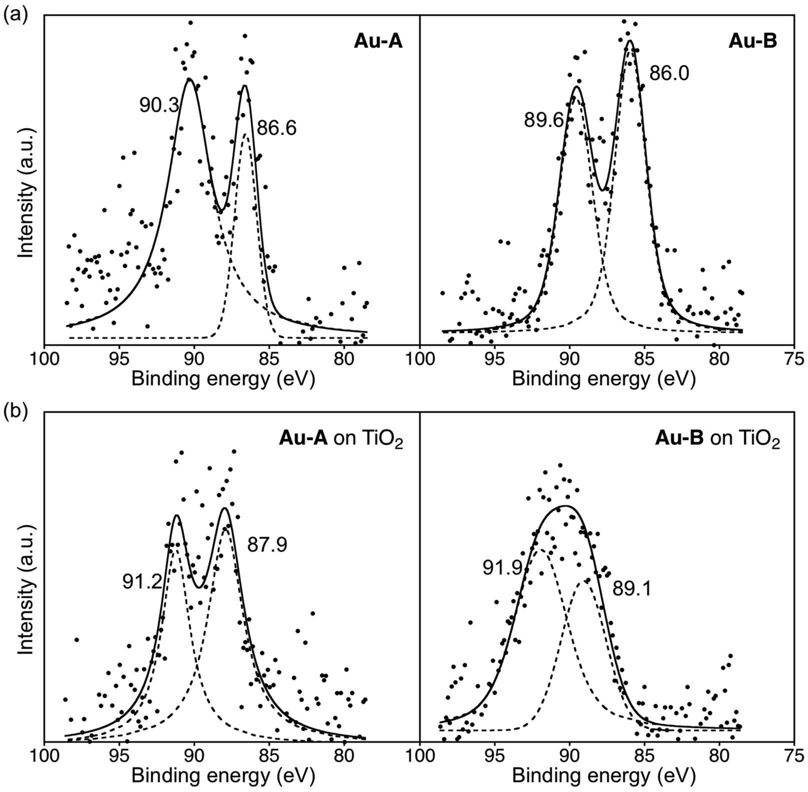

Figure 6. X-ray photoelectron Au 4f spectra of (a) **Au-A** and **Au-B** powder and (b) **Au-A** and **Au-B** on TiO_2.

relative to **Au-A** is explained by the stronger Au−TiO_2 interactions for the former, which is supported by XPS measurements and quantum chemical calculations. These results imply that both peripheral substituents and the metal ion have a large influence on the photovoltaic properties of the metallocorroles. Although the value of 4.2% for **Au-B** is the highest one ever reported for DSSCs with corroles, the PCE is still lower than those reported for other sensitizers such as porphyrins. Considering that many efficient sensitizers possess donor−π−acceptor (push−pull) structures,[6,7] the introduction of donor−π−acceptor (push−pull) structures may improve PCEs of the DSSCs with corroles.

EXPERIMENTAL SECTION

Instruments and Materials. Commercially available solvents and reagents were used without further purification unless otherwise mentioned. The 5d metallocorroles used in this study were prepared as previously reported.[30-36] UV/Vis absorption spectra of the films were measured with a PerkinElmer Lambda 900 UV/vis/NIR spectrometer. Attenuated total reflectance-Fourier transform infrared spectra were taken with the Golden Gate diamond anvil ATR accessory (Nicolet 6700, Thermo Scientific), using typically 64 scans at a resolution of 2 cm^{-1}. All samples were placed in contact with the diamond window using the same mechanical force.

Electrochemical Measurements. Electrochemical measurements were made using an ALS 660A electrochemical analyzer. Redox potentials were determined by DPV in THF containing 0.1 M Bu_4NPF_6. A glassy carbon (3 mm diameter) working electrode, Ag/$AgNO_3$ reference electrode, and Pt wire counter electrode were employed. Ferrocene (+0.642 V vs NHE) was used as an external standard for the DPV measurements.

X-ray Photoelectron Spectroscopy (XPS) Measurements. The XPS data were acquired using an ULVAC-PHI 5500MT system equipped with a Mg Kα X-ray source (1253.6 eV) and a hemispherical energy analyzer. The samples were mounted on indium foil and then transferred to an analyzer chamber. The electron takeoff angle was set at 45°. The S2 pressure of the main XPS chamber was maintained at less than 1×10^{-8} Torr during analysis. The C 1s peak at 285 eV was used as a reference. Peaks of interests were deconvoluted by Gaussian/Lorentzian mixed functions with the PeakFit 4.12 program.

Calculations of the Surface-Binding Structure. Full structural relaxations for all systems were carried out in the Vienna *ab initio* simulation package code.[42] The calculated results are obtained from density functional theory using plane-wave basis sets, PAW-PBE pseudopotentials, and the rev-vdW-DF2 exchange−correlation functional.[43−45] The rev-vdW-DF2 exchange−correlation functional accounts the van der Waals component of the interaction between the molecule and metal oxide surface. We have modeled the TiO_2(101) anatase[46,47] slabs using vacuum gaps of 30.5 Å. Other studies have shown that the (101) plane of the anatase is the most stable surface and is mostly free of vacancies.[48]

We used slabs of around 4.41 Å in thickness. All atoms in the bottom half of the slab were frozen during geometry optimization. This modeled TiO_2 slab contained 75 Ti and 175 O atoms and the unit cell had dimensions of 27.21 Å (*a* axis), 18.88 Å (*b* axis), and 34.97 Å (*c* axis). The structural relaxations were performed using 1 × 1 × 1 Gamma centered *k* point grids and 450 eV basis set cutoffs. All the calculated molecular figures were drawn with the Mercury software.

Preparation of the DSSCs. The TiO_2 electrodes and the sealed cells for photovoltaic measurements were prepared according to literature procedures.[40,49] A nanocrystalline TiO_2 layer of 8 μm (*d* = 20 nm, 18NR-T, Greatcell Solar) was coated on the FTO glass plate via a screen-printing method. A submicrocrystalline TiO_2 layer of 4 μm (*d* = 400 nm, CCIC:PST400C, JGC-C&C) was then formed on top of the FTO. The size of the TiO_2 film was 0.16 cm^2 (4 × 4 mm). The TiO_2 electrode was immersed in an ethanol/THF solution (v/v = 4:1) of the metallocorroles (0.20 mM) either in the presence or absence of CDCA at 25 °C. A sandwich cell was prepared using the dye-anchored TiO_2 film as a working electrode and a counter Pt electrode, which were assembled with a hotmelt-ionomer film Surlyn polymer gasket (DuPont, 50 μm). The electrolyte solution was composed of 1.0 M 1,3-dimethylimidazolium iodide, 0.03 M I_2, 0.05 M LiI, 0.01 M guanidinium thiocyanate, and 0.5 M 4-*tert*-butylpyridine in an 85:15 acetonitrile/valeronitrile mixture.

Photovoltaic Measurements. Incident photon-to-current efficiency (IPCE) and photocurrent−voltage (*I*−*V*) performance were measured under air at room temperature on an action spectrum measurement setup (CEP-2000RR, Bunkoukeiki) and a solar simulator (PEC-L10, Peccell Technologies) with a simulated sunlight of AM 1.5 (100 mW cm^{-2}), respectively: IPCE (%) = $100 \times 1240 \times i/(W_{in} \times \lambda)$, where *i* is the photocurrent density (A cm^{-2}), W_{in} is the incident light intensity (W cm^{-2}), and λ is the excitation wavelength (nm). The light intensity at each wavelength was calibrated with BS-520BK (Bunkoukeiki). During the photovoltaic measurements, a black mask (0.16 cm^2) was used to ensure an accurate measure of the incident light.

Transient Absorption Spectroscopy. The picosecond transient absorption measurements were carried out by the pump−probe method with a Ti:sapphire regenerative amplifier (Spectra Physics, Solstice) and optical parametric amplifiers (OPA; Spectra Physics, TOPAS Prime). The samples were photoexcited by a pulse at wavelengths for the Soret band maxima (2 μJ $pulse^{-1}$) from TOPAS. The transient absorption spectra were measured with a supercontinuum probe generated by focusing a 1250 nm OPA signal into a 5 mm-thick BaF_2 plate. After the sample, the probe was dispersed with a polychromator and detected with a diode array (UNISOKU, PK120-C). For kinetic trace measurements at 760 nm, the second harmonics of the OPA signal were used as probe pulses. The light transmitting through the sample was detected by a photomultiplier tube (Hamamatsu Photonics, H11903-20). For kinetic trace measurements at 5000 nm, the IR pulse from TOPAS was detected by an MCT detector after passing through the sample. The microsecond transient absorption measurements were carried out with the laser system provided by UNISOKU according to the following procedure: A sample was excited by a Panther optical parametric oscillator pumped by a Nd:YAG laser (Continuum, Surelite SLI-10; 4−6 ns FWHM) at λ = 570 nm. The photodynamics was monitored by continuous exposure to a Xe lamp as a probe light and a photomultiplier tube (UNISOKU, NIR-PD1) as a detector. The output from the photodiodes and a photomultiplier tube was recorded with a digitizing oscilloscope (Iwatsu, Digital Oscilloscope DS-5532).

ASSOCIATED CONTENT

Supporting Information

The Supporting Information is available free of charge at https://pubs.acs.org/doi/10.1021/acsaem.0c02427.

Experimental section, synthetic details, high-resolution mass spectra, electrochemical properties, photovoltaic properties, and transient absorption spectra (PDF)

AUTHOR INFORMATION

Corresponding Authors

Akira Yamakata − *Quantum Interface Laboratory, Graduate School of Engineering, Toyota Technological Institute, Nagoya 468-8511, Japan*; orcid.org/0000-0003-3179-7588; Email: yamakata@toyota-ti.ac.jp

Abhik Ghosh − *Department of Chemistry and Arctic Center for Sustainable Energy, UiT − The Arctic University of Norway, 9037 Tromsø, Norway*; orcid.org/0000-0003-1161-6364; Email: abhik.ghosh@uit.no

Hiroshi Imahori − *Department of Molecular Engineering, Graduate School of Engineering and Institute for Integrated*

Cell-Material Sciences (WPI-iCeMS), Kyoto University, Kyoto 615-8510, Japan; orcid.org/0000-0003-3506-5608; Email: imahori@scl.kyoto-u.ac.jp

Authors

Tomohiro Higashino − *Department of Molecular Engineering, Graduate School of Engineering, Kyoto University, Kyoto 615-8510, Japan*

Yuma Kurumisawa − *Department of Molecular Engineering, Graduate School of Engineering, Kyoto University, Kyoto 615-8510, Japan*

Abraham B. Alemayehu − *Department of Chemistry and Arctic Center for Sustainable Energy, UiT* − *The Arctic University of Norway, 9037 Tromsø, Norway*

Rune F. Einrem − *Department of Chemistry and Arctic Center for Sustainable Energy, UiT* − *The Arctic University of Norway, 9037 Tromsø, Norway*

Debashis Sahu − *Institute for Integrated Cell-Material Sciences (WPI-iCeMS), Kyoto University, Kyoto 606-8501, Japan*

Daniel Packwood − *Institute for Integrated Cell-Material Sciences (WPI-iCeMS), Kyoto University, Kyoto 606-8501, Japan*

Kosaku Kato − *Quantum Interface Laboratory, Graduate School of Engineering, Toyota Technological Institute, Nagoya 468-8511, Japan;* orcid.org/0000-0002-9977-7439

Complete contact information is available at: https://pubs.acs.org/10.1021/acsaem.0c02427

Notes

The authors declare no competing financial interest.

ACKNOWLEDGMENTS

This work was supported by the JSPS (KAKENHI grant nos. JP18K14198 (T.H.), JP20H05841(T.H.), JP20H05838 (A.Y.), JP18H03898 (H.I.), and JP20H05832 (H.I.)) and the Research Council of Norway (grant no. 262229 to A.G.).

REFERENCES

(1) Imahori, H.; Kang, S.; Hayashi, H.; Haruta, M.; Kurata, H.; Isoda, S.; Canton, S. E.; Infahsaeng, Y.; Kathiravan, A.; Pascher, T.; Chábera, P.; Yartsev, A. P.; Sundström, V. Photoinduced Charge Carrier Dynamics of Zn-Porphyrin-TiO_2 Electrodes: The Key Role of Charge Recombination for Solar Cell Performance. *J. Phys. Chem. A* **2011**, *115*, 3679−3690.

(2) Rao, A.; Chow, P. C. Y.; Gélinas, S.; Schlenker, C. W.; Li, C.-Z.; Yip, H.-L.; Jen, A. K. Y.; Ginger, D. S.; Friend, R. H. The Role of Spin in the Kinetic Control of Recombination in Organic Photovoltaics. *Nature* **2013**, *500*, 435−439.

(3) Jailaubekov, A. E.; Willard, A. P.; Tritsch, J. R.; Chan, W.-L.; Sai, N.; Gearba, R.; Kaake, L. G.; Williams, K. J.; Leung, K.; Rossky, P. J.; Zhu, X.-Y. Hot Charge-Transfer Excitons Set the Time Limit for Charge Separation at Donor/acceptor Interfaces in Organic Photovoltaics. *Nat. Mater.* **2013**, *12*, 66−73.

(4) Umeyama, T.; Imahori, H. Electron Transfer and Exciplex Chemistry of Functionalized Nanocarbons: Effects of Electronic Coupling and Donor Dimerization. *Nanoscale Horiz.* **2018**, *3*, 352−366.

(5) She, Z.; Cheng, Y.; Zhang, L.; Li, X.; Wu, D.; Guo, Q.; Lan, J.; Wang, R.; You, J. Novel Ruthenium Sensitizers with a Phenothiazine Conjugated Bipyridyl Ligand for High-Efficiency Dye-Sensitized Solar Cells. *ACS Appl. Mater. Interfaces* **2015**, *7*, 27831−27837.

(6) Wang, J.; Liu, K.; Ma, L.; Zhan, X. Triarylamine: Versatile Platform for Organic, Dye-Sensitized, and Perovskite Solar Cells. *Chem. Rev.* **2016**, *116*, 14675−14725.

(7) Brogdon, P.; Cheema, H.; Delcamp, J. H. Near-Infrared-Absorbing Metal-Free Organic, Porphyrin, and Phthalocyanine Sensitizers for Panchromatic Dye-Sensitized Solar Cells. *ChemSusChem* **2018**, *11*, 86−103.

(8) Kadish, K. M.; Smith, K. M.; Guilard, R. *The Porphyrin Handbook*; Elsevier: 2000; Vols. *1*−*20*.

(9) Sorokin, A. B. Phthalocyanine Metal Complexes in Catalysis. *Chem. Rev.* **2013**, *113*, 8152−8191.

(10) Ghosh, A. Electronic Structure of Corrole Derivatives: Insights from Molecular Structures, Spectroscopy, Electrochemistry, and Quantum Chemical Calculations. *Chem. Rev.* **2017**, *117*, 3798−3881.

(11) Fang, Y.; Ou, Z.; Kadish, K. M. Electrochemistry of Corroles in Nonaqueous Media. *Chem. Rev.* **2017**, *117*, 3377−3419.

(12) Gust, D.; Moore, T. A.; Moore, A. L. Mimicking Photosynthetic Solar Energy Transduction. *Acc. Chem. Res.* **2001**, *34*, 40−48.

(13) Imahori, H. Giant Multiporphyrin Arrays as Artificial Light-Harvesting Antennas. *J. Phys. Chem. B* **2004**, *108*, 6130−6143.

(14) Mahmood, A.; Hu, J.-Y.; Xiao, B.; Tang, A.; Wang, X.; Zhou, E. Recent Progress in Porphyrin-Based Materials for Organic Solar Cells. *J. Mater. Chem. A* **2018**, *6*, 16769−16797.

(15) Imahori, H.; Umeyama, T.; Ito, S. Large π-Aromatic Molecules as Potential Sensitizers for Highly Efficient Dye-Sensitized Solar Cells. *Acc. Chem. Res.* **2009**, *42*, 1809−1818.

(16) Li, L.-L.; Diau, E. W.-G. Porphyrin-Sensitized Solar Cells. *Chem. Soc. Rev.* **2013**, *42*, 291−304.

(17) Urbani, M.; Grätzel, M.; Nazeeruddin, M. K.; Torres, T. Meso-Substituted Porphyrins for Dye-Sensitized Solar Cells. *Chem. Rev.* **2014**, *114*, 12330−12396.

(18) Higashino, T.; Imahori, H. Porphyrins as Excellent Dyes for Dye-Sensitized Solar Cells: Recent Developments and Insights. *Dalton Trans.* **2015**, *44*, 448−463.

(19) Song, H.; Liu, Q.; Xie, Y. Porphyrin-Sensitized Solar Cells: Systematic Molecular Optimization, Coadsorption and Cosensitization. *Chem. Commun.* **2018**, *54*, 1811−1824.

(20) Ji, J.-M.; Zhou, H.; Kim, H. K. Rational Design Criteria for D−π−A Structured Organic and Porphyrin Sensitizers for Highly Efficient Dye-Sensitized Solar Cells. *J. Mater. Chem. A* **2018**, *6*, 14518−14545.

(21) Bessho, T.; Zakeeruddin, S. M.; Yeh, C.-Y.; Diau, E. W.-G.; Grätzel, M. Highly Efficient Mesoscopic Dye-Sensitized Solar Cells Based on Donor-Acceptor-Substituted Porphyrins. *Angew. Chem., Int. Ed.* **2010**, *49*, 6646−6649.

(22) Yella, A.; Lee, H.-W.; Tsao, H. N.; Yi, C.; Chandiran, A. K.; Nazeeruddin, M. K.; Diau, E. W.-G.; Yeh, C.-Y.; Zakeeruddin, S. M.; Grätzel, M. Porphyrin-Sensitized Solar Cells with Cobalt (II/III)-Based Redox Electrolyte Exceed 12 Percent Efficiency. *Science* **2011**, *334*, 629−634.

(23) Yella, A.; Mai, C.-L.; Zakeeruddin, S. M.; Chang, S.-N.; Hsieh, C.-H.; Yeh, C.-Y.; Grätzel, M. Molecular Engineering of Push-Pull Porphyrin Dyes for Highly Efficient Dye-Sensitized Solar Cells: The Role of Benzene Spacers. *Angew. Chem., Int. Ed.* **2014**, *53*, 2973−2977.

(24) Mathew, S.; Yella, A.; Gao, P.; Humphry-Baker, R.; Curchod, B. F. E.; Ashari-Astani, N.; Tavernelli, I.; Rothlisberger, U.; Nazeeruddin, M. K.; Grätzel, M. Dye-Sensitized Solar Cells with 13% Efficiency Achieved through the Molecular Engineering of Porphyrin Sensitizers. *Nat. Chem.* **2014**, *6*, 242−247.

(25) Zhou, H.; Ji, J.-M.; Kang, S. H.; Kim, M. S.; Lee, H. S.; Kim, C. H.; Kim, H. K. Molecular Design and Synthesis of D−π−A Structured Porphyrin Dyes with Various Acceptor Units for Dye-Sensitized Solar Cells. *J. Mater. Chem. C* **2019**, *7*, 2843−2852.

(26) Kurumisawa, Y.; Higashino, T.; Nimura, S.; Tsuji, Y.; Iiyama, H.; Imahori, H. Renaissance of Fused Porphyrins: Substituted Methylene-Bridged Thiophene-Fused Strategy for High-Performance Dye-Sensitized Solar Cells. *J. Am. Chem. Soc.* **2019**, *141*, 9910−9919.

(27) Listorti, A.; O'Regan, B.; Durrant, J. R. Electron Transfer Dynamics in Dye-Sensitized Solar Cells. *Chem. Mater.* **2011**, *23*, 3381−3399.

(28) Piatkowski, P.; Martin, C.; di Nunzio, M. R.; Cohen, B.; Pandey, S.; Hayse, S.; Douhal, A. Complete Photodynamics of the Efficient YD2-*o*-C8-Based Solar Cell. *J. Phys. Chem. C* **2014**, *118*, 29674−29687.

(29) Lai, S.-L.; Wang, L.; Yang, C.; Chan, M.-Y.; Guan, X.; Kwok, C.-C.; Che, C.-M. Gold(III) Corroles for High Performance Organic Solar Cells. *Adv. Funct. Mater.* **2014**, *24*, 4655−4665.

(30) Alemayehu, A. B.; Day, N. U.; Mani, T.; Rudine, A. B.; Thomas, K. E.; Gederaas, O. A.; Vinogradov, S. A.; Wamser, C. C.; Ghosh, A. Gold Tris(carboxyphenyl)corroles as Multifunctional Materials: Room Temperature Near-IR Phosphorescence and Applications to Photodynamic Therapy and Dye-Sensitized Solar Cells. *ACS Appl. Mater. Interfaces* **2016**, *8*, 18935−18942.

(31) Thomas, K. E.; Alemayehu, A. B.; Conradie, J.; Beavers, C.; Ghosh, A. Synthesis and Molecular Structure of Gold Triarylcorroles. *Inorg. Chem.* **2011**, *50*, 12844−12851.

(32) Einrem, R. F.; Gagnon, K. J.; Alemayehu, A. B.; Ghosh, A. Metal-Ligand Misfits: Facile Access to Rhenium-Oxo Corroles by Oxidative Metalation. *Chem. − Eur. J.* **2016**, *22*, 517−520.

(33) Alemayehu, A. B.; Gagnon, K. J.; Terner, J.; Ghosh, A. Oxidative Metalation as a Route to Size-Mismatched Macrocyclic Complexes: Osmium Corroles. *Angew. Chem., Int. Ed.* **2014**, *53*, 14411−14414.

(34) Borisov, S. M.; Alemayehu, A.; Ghosh, A. Osmium-Nitrido Corroles as NIR Indicators for Oxygen Sensors and Triplet Sensitizers for Organic Upconversion and Singlet Oxygen Generation. *J. Mater. Chem. C* **2016**, *4*, 5822−5828.

(35) Borisov, S. M.; Einrem, R. F.; Alemayehu, A. B.; Ghosh, A. Ambient-Temperature near-IR Phosphorescence and Potential Applications of Rhenium-Oxo Corroles. *Photochem. Photobiol. Sci.* **2019**, *18*, 1166−1170.

(36) Einrem, R. F.; Alemayehu, A. B.; Borisov, S. M.; Ghosh, A.; Gederaas, O. A. Amphiphilic Rhenium-Oxo Corroles as a New Class of Sensitizers for Photodynamic Therapy. *ACS Omega* **2020**, *5*, 10596−10601.

(37) Rochford, J.; Chu, D.; Hagfeldt, A.; Galoppini, E. Tetrachelate Porphyrin Chromophores for Metal Oxide Semiconductor Sensitization: Effect of the Spacer Length and Anchoring Group Position. *J. Am. Chem. Soc.* **2007**, *129*, 4655−4665.

(38) Wang, Q.; Campbell, W. M.; Bonfantani, E. E.; Jolley, K. W.; Officer, D. L.; Walsh, P. J.; Gordon, K.; Humphry-Baker, R.; Nazeeruddin, M. K.; Grätzel, M. Efficient Light Harvesting by Using Green Zn-Porphyrin-Sensitized Nanocrystalline TiO_2 Films. *J. Phys. Chem. B* **2005**, *109*, 15397−15409.

(39) Kurotobi, K.; Toude, Y.; Kawamoto, K.; Fujimori, Y.; Ito, S.; Chabera, P.; Sundström, V.; Imahori, H. Highly Asymmetrical Porphyrins with Enhanced Push-Pull Character for Dye-Sensitized Solar Cells. *Chem. − Eur. J.* **2013**, *19*, 17075−17081.

(40) Higashino, T.; Fujimori, Y.; Sugiura, K.; Tsuji, Y.; Ito, S.; Imahori, H. Tropolone as a High-Performance Robust Anchoring Group for Dye-Sensitized Solar Cells. *Angew. Chem., Int. Ed.* **2015**, *54*, 9052−9056.

(41) Yamakata, A.; Vequizo, J. J. M.; Matsunaga, H. Distinctive Behavior of Photogenerated Electrons and Holes in Anatase and Rutile TiO_2 Powders. *J. Phys. Chem. C* **2015**, *119*, 24538−24545.

(42) Kresse, G.; Furthmüller, J. Efficient Iterative Schemes for *ab initio* Total-Energy Calculations Using a Plane-Wave Basis Set. *Phys. Rev. B* **1996**, *54*, 11169−11186.

(43) Klimeš, J.; Bowler, D. R.; Michaelides, A. Chemical Accuracy for the van Der Waals Density Functional. *J. Phys.: Condens. Matter* **2010**, *22*, No. 022201.

(44) Klimeš, J.; Bowler, D. R.; Michaelides, A. Van der Waals Density Functionals Applied to Solids. *Phys. Rev. B* **2011**, *83*, 195131.

(45) Hamada, I. Van Der Waals Density Functional Made Accurate. *Phys. Rev. B* **2014**, *89*, 121103.

(46) Li, H.; Guo, Y.; Robertson, J. Calculation of TiO_2 Surface and Subsurface Oxygen Vacancy by the Screened Exchange Functional. *J. Phys. Chem. C* **2015**, *119*, 18160−18166.

(47) Treacy, J. P. W.; Hussain, H.; Torrelles, X.; Grinter, D. C.; Cabailh, G.; Bikondoa, O.; Nicklin, C.; Selcuk, S.; Selloni, A.; Lindsay, R.; Thornton, G. Geometric Structure of Anatase TiO_2(101). *Phys. Rev. B* **2017**, *95*, No. 075416.

(48) Wanbayor, R.; Deák, P.; Frauenheim, T.; Ruangpornvisuti, V. First Principles Theoretical Study of the Hole-Assisted Conversion of CO to CO_2 on the Anatase TiO_2(101) Surface. *J. Chem. Phys.* **2011**, *134*, 104701.

(49) Ito, S.; Murakami, T. N.; Comte, P.; Liska, P.; Grätzel, C.; Nazeeruddin, M. K.; Grätzel, M. Fabrication of Thin Film Dye Sensitized Solar Cells with Solar to Electric Power Conversion Efficiency over 10%. *Thin Solid Films* **2008**, *516*, 4613−4619.

Paper E

RSC Advances

ROYAL SOCIETY OF CHEMISTRY

PAPER

View Article Online
View Journal | View Issue

Check for updates

Cite this: *RSC Adv.*, 2021, **11**, 34086

Regioselective formylation of rhenium-oxo and gold corroles: substituent effects on optical spectra and redox potentials †

Rune F. Einrem,[a] Einar Torfi Jonsson,[a] Simon J. Teat,[b] Nicholas S. Settineri,[bc] Abraham B. Alemayehu*[a] and Abhik Ghosh*[a]

Received 19th July 2021
Accepted 29th September 2021

DOI: 10.1039/d1ra05525a

rsc.li/rsc-advances

Vilsmeier–Haack formylation of ReO and Au *meso*-triarylcorroles over 16–18 hours affords moderate to good yields (47–65%) of the ReO-3-formyl and Au-3,17-diformyl derivatives in a highly regioselective manner. Formylation was found to effect substantial upshifts for redox potentials (especially the reduction potentials) as well as significant to dramatic redshifts for both the Soret and Q bands.

Introduction

Our research on 5d metallocorroles[1–4] began a decade ago, with two publications documenting the first examples of gold corroles. The first of these reported gold insertion into β-octabromo-*meso*-triarylcorroles,[5] which was also accomplished at about the same time by Gross and coworkers.[6] The second paper described Au insertion into simple *meso*-triarylcorroles with Au(III) acetate[7] – a significant breakthrough, considering the steric mismatch between the large ionic radii of 5d transition metals and the relatively constricted central cavity of corroles. The 'acetate method' has since become the method of choice for the synthesis of Au corroles. Understandably, we were intrigued by the possibility of inserting other heavier transition metals into corroles and, to our satisfaction, the first ^{99}TcO,[8] ReO,[9] ReNAr,[10] RuN,[11] OsN,[12] and Pt[13,14] triarylcorroles (as well as Mo and W biscorroles[15–17] and quadruple-bonded Re corrole dimers[18]) were synthesized in our Tromsø laboratory. Several of the 5d metallocorroles[19–24] were found to exhibit room-temperature NIR phosphorescence, leading to applications as oxygen sensors and as photosensitizers in photodynamic therapy and dye-sensitized solar cells.[25–27] In contrast (compared to 3d metallocorroles,[28,29] especially Cu corroles[30–34]), the chemical reactivity of the 5d complexes remains poorly explored. Peripheral functionalizations accomplished so far include β-perchlorination[35] and perbromination,[36,37] as well as polyiodinations.[38,39] Metal-centered transformations include the generation of Mo and Re Viking-helmet dichlorido derivatives from the corresponding oxido precursors.[40,41] In an alternative approach, the use of water-soluble, axial phosphine ligands has led to water-soluble iridium corroles.[42] A final, more esoteric example consists of the use of an OsN corrole as a π-acceptor ligand in formation of an Os^{VI}N–Pt^{II} heterobimetallic complex.[35] Here we document our efforts to formylate ReO and Au corroles *via* the Vilsmeier–Haack method,[43] which has previously been used for free-base, aluminum and gallium corroles.[44–47] As before, the reaction was found to proceed in a highly regioselective manner, with ReO and Au corroles affording mono- and diformyl derivatives, respectively (Fig. 1). Optical and electrochemical characterization of the products permitted a moderately detailed, experimental picture of the substantial electronic effects of β-formyl groups, as recounted below.

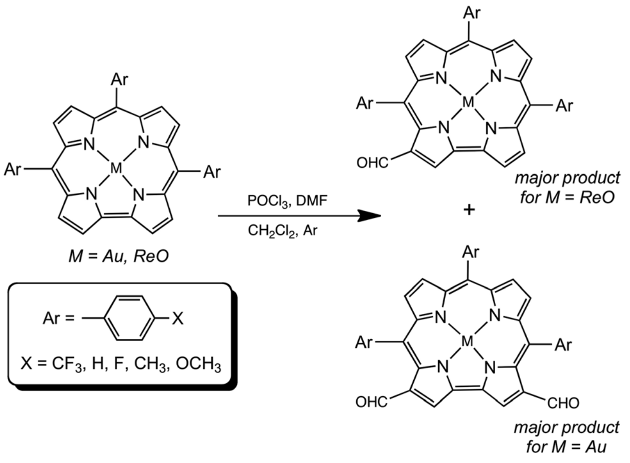

Fig. 1 Formylation of Au and ReO corroles.

---

[a] *Department of Chemistry, UiT – The Arctic University of Norway, N-9037 Tromsø, Norway. E-mail: abraham.alemayehu@uit.no; abhik.ghosh@uit.no*

[b] *Advanced Light Source, Lawrence Berkeley National Laboratory, Berkeley, CA 94720-8229, USA*

[c] *Department of Chemistry, University of California, Berkeley, Berkeley, California 94720, USA*

† Electronic supplementary information (ESI) available. CCDC 2091847 and 2091848. For ESI and crystallographic data in CIF or other electronic format see DOI: 10.1039/d1ra05525a

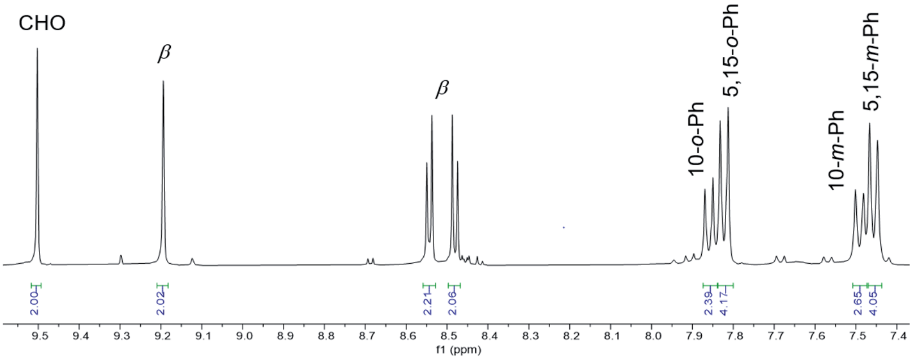

Fig. 2 Aromatic region of the ^{1}H NMR spectrum (400 MHz, $CDCl_3$, 293 K) of Au[T*p*FPC-3,17-$(CHO)_2$].

Results and discussion

(a) Synthesis and proof of composition

Vilsmeier–Haack formylation, carried out over 16–18 h at 0 °C to room temperature, proceeded smoothly for both ReO and Au *meso*-tris(*para*-X-phenyl)corroles, M[T*p*XPC] (M = ReO, Au), regioselectively affording good yields of the 3-monoformyl (~50%) and 3,17-diformyl (~60%) derivatives for the two metals, respectively. The major products, hereafter denoted as Re[T*p*XPC-3-CHO](O) and Au[T*p*XPC-3,17-$(CHO)_2$], were fully characterized and the regiochemistry of formylation was established largely *via* ^{1}H NMR spectroscopy. In particular, the simplicity of the ^{1}H NMR of the Au-diformyl derivatives (relative to the ReO-monoformyl derivatives) immediately suggested a regiochemistry consistent with time-averaged C_{2v} symmetry (Fig. 2 and 3). The minor products – the ReO-diformyl and Au-monoformyl derivatives – generally could not be fully characterized. Surprisingly, two minor products – Re[T*p*CH_3PC-3,17-$(CHO)_2$](O) and Au[T*p*CH_3PC-3-CHO] – proved amenable to single-crystal X-ray structure determination (Table 1 and Fig. 4 and 5). The structures established that the formyl groups are essentially coplanar with the mean plane of the pyrrole rings they are attached to, but aside from that, they proved largely unremarkable. Finally, in a brief examination of their reactivity, ReO 3-formylcorroles were found to undergo facile Knoevenagel condensation with active methylene compounds (Fig. 6). While

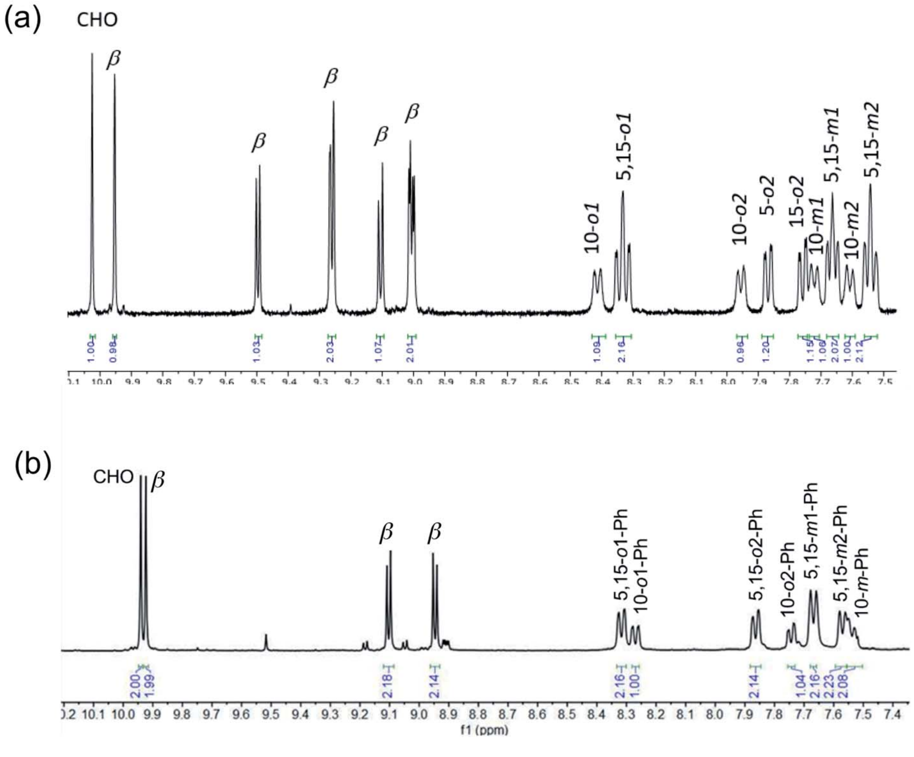

Fig. 3 Aromatic region of the ^{1}H NMR spectra (400 MHz, $CDCl_3$, 273 K) of (a) Re[T*p*CH_3PC-3-CHO](O) and (b) Re[T*p*CH_3PC-3-17-$(CHO)_2$](O). Note the different numbers of β protons in the two complexes. Note also that the most downfield singlet has been tacitly assigned as the formyl proton.

Table 1 Selected crystallographic data for the complexes analyzed

	Re[T*p*CH$_3$PC-3,17-(CHO)$_2$](O)	Au[T*p*FPC-3-CHO]
Chemical formula	$C_{45}H_{36}N_4O_3Re$	$C_{38}H_{20}F_3N_4OAu$
Formula mass	866.98	802.55
Crystal system	Triclinic	Monoclinic
Crystal size (mm^3)	0.230 × 0.080 × 0.020	0.100 × 0.020 × 0.010
Space group	$P\bar{1}$	$C2/c$
λ (Å)	0.7288	0.7288
a (Å)	9.5807(4)	20.9037(12)
b (Å)	12.6649(6)	19.7169(12)
c (Å)	29.1467(13)	15.8376(10)
α (deg)	95.279(2)	90
β (deg)	91.627(2)	91.467(3)
γ (deg)	90.341(2)	90
Z	4	8
V (Å^3)	3520.1(3)	6525.4(7)
Temperature (K)	100(2)	100(2)
Density (g cm^{-3})	1.636	1.634
Measured reflections	131 064	84 580
Unique reflections	21 566	10 078
Parameters	975	424
Restraints	40	0
R_{int}	0.0354	0.0697
θ Range (deg.)	1.744–31.439	2.913–31.600
R_1, wR_2 all data	0.0361, 0.0667	0.0453, 0.1001
S (GooF) all data	1.092	1.070
Max/min res. dens. (e Å^{-3})	2.379/−2.218	1.925/−1.512

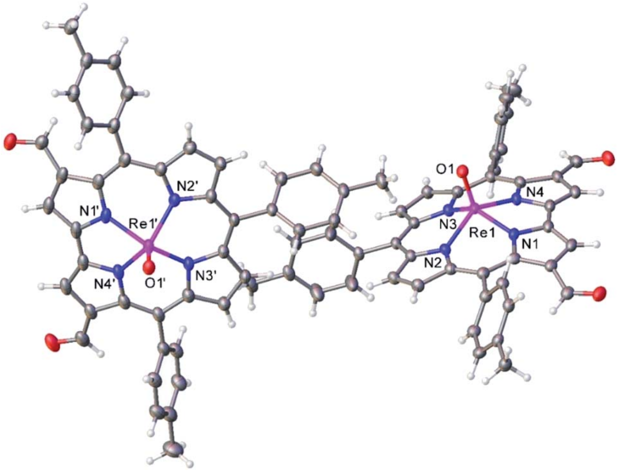

Fig. 4 Thermal ellipsoid plot for Re[T*p*CH$_3$PC-3,17-(CHO)$_2$](O). Selected distances (Å): Re1–N1 2.007(2), Re1–N2 2.012(2), Re1–N3 2.013(2), Re1–N4 1.999(2), and Re1–O1 1.681(2), Re1′–N1′ 1.999(2), Re1′–N2′ 2.016(2), Re1′–N3′ 2.013(2), Re1′–N4′ 2.000(2), Re1′–O1′ 1.685.

a full exposition of reactivity studies is outside the scope of the present study, a few examples of protocols involving cyanoacetic acid are given in the experimental section.

(b) Electronic absorption spectra and redox potentials

Formylation engenders significant redshifts for both the Soret bands and double-humped Q bands of the ReO and Au corroles (Table 2, Fig. 7 and 8). Thus, 3-monoformylation redshifts the Soret maxima by about 8 nm (for either metal), while diformylation brings about redshifts about one-and-a-half (for ReO) to twice (for Au) that magnitude. For the lowest-energy Q bands (for either metal), mono- and diformylation result in redshifts of 20–25 and 37–41 nm, respectively. Interestingly, formylation appears to weaken the intensity of the Soret band, suggesting a certain weakening of macrocyclic aromaticity, while strengthening the Q band, potentially indicating corrole to formyl charge transfer character for the latter feature.

Formylation has a substantial impact on the redox potentials of both ReO and Au corroles (which all correspond to ligand-centered processes[1,3,7,9,48]), the impact on reduction potentials being particularly dramatic (Table 2). Thus, 3-formylation upshifts oxidation potentials of ReO triarylcorroles by 100–170 mV and the reduction potentials by ~300 mV (Fig. 9). Likewise, 3,17-diformylation upshifts oxidation potentials of Au triarylcorroles by ~260 mV and the reduction potentials by 500–650 mV (Fig. 10). The larger shifts for the reduction potentials may be qualitatively understood in terms of the ability of the strongly electron-withdrawing formyl substituents to stabilize a negative charge. The effect also translates to smaller electrochemical HOMO–LUMO gaps (*i.e.*, the algebraic difference between the first oxidation and reduction potentials) for the formylated metallocorroles relative to their β-unsubstituted counterparts. For one of the Au corroles, Au[T*p*FPC], we were able to determine the effect of both mono- and diformylation. For both oxidation and reduction potentials, the second formyl group was found to have a distinctly smaller effect relative to the first one – *i.e.*, a nonadditive effect (Fig. 11).

The redox potentials of the compounds studied also provide a potential explanation for the observed tendency toward

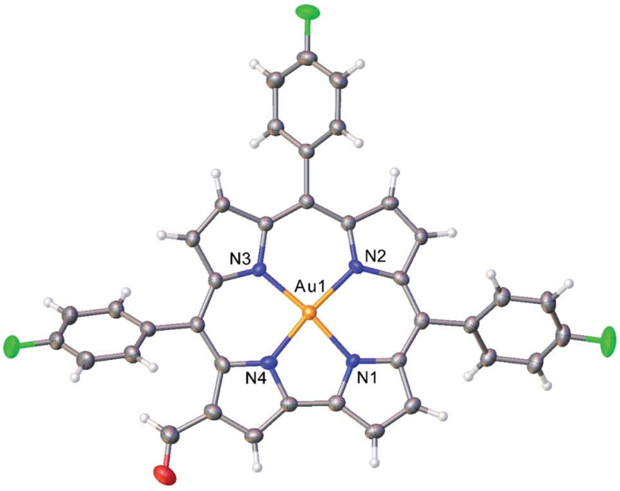

Fig. 5 Thermal ellipsoid plot for Au[T*p*FPC-3-CHO]. Selected distances (Å): Au1–N1 1.939, Au1–N2 1.973, Au1–N3 1.958, Au1–N4 1.950.

monoformylation for ReO corroles and toward diformylation for Au corroles. The oxidation potentials of β-unsubstituted Au triarylcorroles are about 200 mV lower than those of analogous ReO complexes, suggesting that the former are more nucleophilic. (It may be noted that the higher oxidation potentials in the Re case correlates with the higher oxidation state of the Re center, +V, compared to +III for Au. A similar metal oxidation state dependence has long been known for metalloporphyrins.[49]) Moreover, the oxidation potentials of the ReO–monoformyl complexes are about the same as those of analogous Au-diformyl complexes, potentially explaining why formylation stops at the monoformyl stage for ReO triarylcorroles.

Conclusion

Vilsmeier–Haack formylation has been found to proceed in a highly regioselective manner for ReO and Au triarylcorroles, affording 3-formyl and 3,17-diformyl derivatives, respectively, as the major products. The difference in reactivity between the two metals appears at least partially attributable to a difference in oxidation potential, and hence nucleophilicity, between the two families of 5d metallocorroles. The formyl groups engender significant to dramatic redshifts of the Soret and Q bands and large upshifts for the redox potentials for both series of metallocorroles. A preliminary study demonstrating successful Knoevenagel condensations suggests that the formylated products should serve as versatile starting materials for a wide range of functionalized, potentially water-soluble 5d metallocorroles.

Experimental section

Materials and instruments

Except for solvents, all chemicals were obtained from Sigma-Aldrich and used as such. Dichloromethane used in syntheses was dried over 3 Å molecular sieves. CHROMASOLV HPLC-grade *n*-hexane and dichloromethane were used for column chromatography. Silica gel 60 (0.04–0.063 mm particle size; 230–400 mesh, Sigma) was used for column chromatography, with columns about 8 cm in height and 3 cm in diameter. UV-vis spectra were recorded on an HP 8454 spectrophotometer at room temperature. High-resolution electrospray ionization (ESI) mass spectra were recorded on an LTQ Orbitrap XL spectrometer. ^{1}H NMR spectra were recorded on a Bruker Avance III HD 400 MHz spectrometer. Cyclic voltammetry analyses were carried out in dry dichloromethane containing 0.1 M TBAP as a supporting electrolyte. An EG&G 263A potentiostat with a standard three-electrode set-up, consisting of a glassy carbon working electrode (3 mm i.d.), a platinum wire counter electrode, and saturated calomel reference electrode (SCE), was used for cyclic voltammetry.

General procedure for formylation of Re^{V}O triarylcorroles

To a 50 mL round-bottom flask equipped with a magnetic stir-bar, a rubber septum, and an argon in/outlet, and placed in an ice/water bath, were added dichloromethane (5.0 mL), $POCl_3$ (20 mmol, 1.8 mL), and DMF (23 mmol, 1.8 mL) were added. The metallocorrole[7,9] starting material (0.075 mmol, ~55 mg) was dissolved in dichloromethane (10 mL) and added *via* syringe to the chilled solution. The mixture was left to stir under a constant flow of argon at 0 °C for 15 minutes, whereupon it was allowed to warm to room temperature and left to stir overnight. The following morning, the reaction was quenched with water (3 × 100 mL). The organic phase was dried and subjected to column chromatography on silica gel with 3 : 1 *n*-

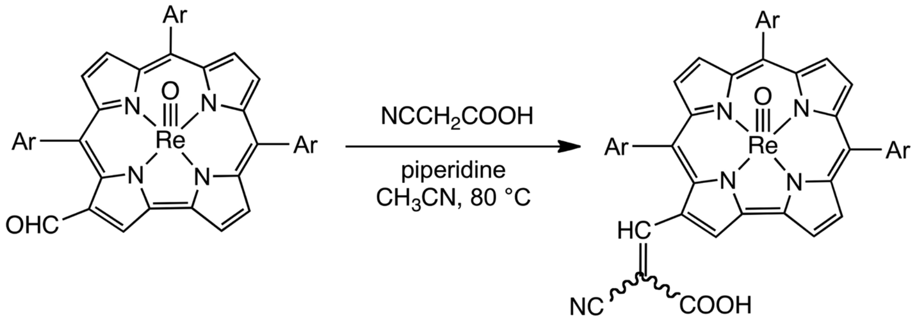

Fig. 6 Knoevenagel condensation of ReO 3-formylcorroles with cyanoacetic acid.

Table 2 UV-vis absorption maxima (nm), redox potentials (V) and electrochemical HOMO–LUMO gaps (Δ*E*, V) for selected compounds

Compound	Soret	Q	$E_{1/2-\mathrm{ox2}}$	$E_{1/2-\mathrm{ox1}}$	$E_{1/2-\mathrm{red1}}$	$E_{1/2-\mathrm{red2}}$	Δ*E*	Ref.
Au[T*p*OCH$_3$PC]	420	560, **580**	1.32	0.76	−1.57	—	2.33	6
Au[T*p*CH$_3$PC]	420	560, **576**	1.35	0.78	−1.42	—	2.20	6
Au[TPC]	418	560, **575**	1.35	0.80	−1.38	—	2.18	6
Au[T*p*FPC]	419	559, **573**	1.38	0.85	−1.37	—	2.22	6
Au[T*p*CH$_3$PC-3-CHO]	428	581, 602	—	—	—	—	—	tw
Au[T*p*FPC-3-CHO]	427	580, 597	—	1.03	−1.02	−1.46	2.05	tw
Au[T*p*OCH$_3$PC-3,17-(CHO)$_2$]	439	597, 618	1.36	1.03	−0.92	−1.42	1.95	tw
Au[T*p*CH$_3$PC-3,17-(CHO)$_2$]	439	596, 615	—	1.07	−0.92	−1.43	1.99	tw
Au[TPC-3,17-(CHO)$_2$]	437	596, 611	—	1.14	−0.87	−1.39	2.01	tw
Au[T*p*FPC-3,17-(CHO)$_2$]	436	597, 609	—	1.20	−0.81	−1.34	2.01	tw
Re[T*p*OCH$_3$PC](O)	441	556, **592**	—	0.93	−1.29	—	2.22	8
Re[T*p*CH$_3$PC](O)	440	555, **587**	—	0.94	−1.29	—	2.23	8
Re[TPC](O)	439	552, **585**	—	0.98	−1.26	—	2.24	8
Re[T*p*FPC](O)	438	553, **585**	—	1.01	−1.23	—	2.24	8
Re[T*p*CF$_3$PC](O)	438	552, **585**	—	1.10	−1.16	—	2.26	8
Re[T*p*OCH$_3$PC-3-CHO](O)	449	609	1.30	1.03	−1.00	−1.40	2.03	tw
Re[T*p*CH$_3$PC-3-CHO](O)	449	611	1.41	1.08	−0.96	−1.36	2.04	tw
Re[TPC-3-CHO](O)	452	613	—	1.15	−0.89	−1.29	2.04	tw
Re[T*p*FPC-3-CHO](O)	448	608	—	1.17	−0.90	−1,30	2.07	tw
Re[T*p*CF$_3$PC-3-CHO](O)	448	607	—	1.23	−0.84	−1,25	2.07	tw

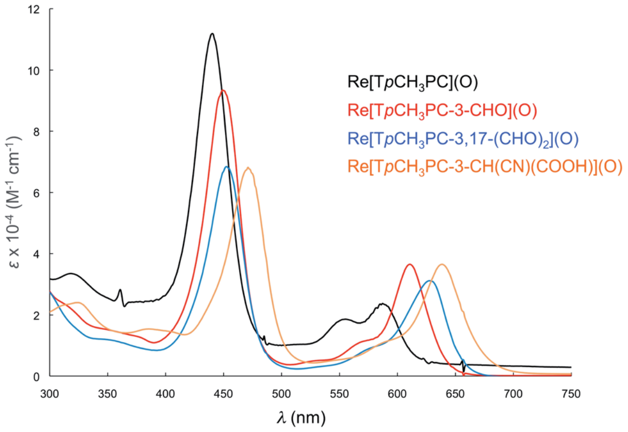

Fig. 7 Comparative UV-vis spectra in dichloromethane for Re[T*p*CH$_3$PC](O) (black), Re[T*p*CH$_3$PC-3-CHO](O) (red), (c) Re[T*p*CH$_3$-PC-3,17-(CHO)$_2$](O) (blue), (d) Re[T*p*CH$_3$PC-3-CH(CN)(COOH)](O) (saffron).

hexane/dichloromethane as eluent. Further elution with dichloromethane with up to 0–5% methanol led to product isolation.

Re[TPC-3-CHO](O). Yield 34.5 mg (62.8%). UV-vis (CH$_2$Cl$_2$) $\lambda_{\max}$ [nm, $\varepsilon \times 10^{-4}$ (M^{-1} cm^{-1})]: 449 (8.47), 609 (3.19). ^{1}H NMR (400 MHz, 20 °C) δ: 10.06 (s, 1H, CHO); 9.96 (s, 1H, β-H); 9.52 (d, 1H, $^3J_{\mathrm{HH}}$ = 4.4 Hz, β-H); 9.25 (d overlapping, 2H, $^3J_{\mathrm{HH}}$ = 4.3 Hz, β-H); 9.09 (d, 1H, $^3J_{\mathrm{HH}}$ = 5.0 Hz, β-H); 9.00 (d overlapping, 2H, $^3J_{\mathrm{HH}}$ = 4.9 Hz, β-H); 8.55 (d, 1H, $^3J_{\mathrm{HH}}$ = 7.6 Hz, 10-*o*1-Ph); 8.45 (d overlapping, 2H, $^3J_{\mathrm{HH}}$ = 8.2 Hz, 5,15-*o*1-Ph); 8.07 (d, 1H, $^3J_{\mathrm{HH}}$ = 6.6 Hz, 10-*o*2-Ph); 7.99 (d, 2H, $^3J_{\mathrm{HH}}$ = 7.6 Hz, 5/15-*o*2-Ph); 7.82 (m, 10H, 5/15-*o*2-Ph + 5,10,15-*m*-Ph + 5,10,15-*p*-Ph). MS (ESI): M$^+$ = 754.1383 (expt), 754.1375 (calcd for $C_{38}H_{23}N_4O_2Re$). Elemental analysis (%) calcd for $C_{38}H_{23}N_4O_2Re$: C 60.55, H 3.08, N 7.43, found C 60.93, H 3.36, N 7.59. IR ν_{ReO}: 992 cm^{-1}, ν_{CHO}: 1659 cm^{-1}

Re[T*p*CH$_3$PC-3-CHO](O). Yield 31.1 mg (56.6%). UV-vis (CH$_2$Cl$_2$) $\lambda_{\max}$ [nm, $\varepsilon \times 10^{-4}$ (M^{-1} cm^{-1})]: 449 (9.34), 611 (3.65). ^{1}H NMR (400 MHz, 0 °C) δ: 10.03 (s, 1H, CHO); 9.95 (s, 1H, β-H); 9.50 (d, 1H, $^3J_{\mathrm{HH}}$ = 4.4 Hz, β-H); 9.26 (d, 2H, $^3J_{\mathrm{HH}}$ = 4.5 Hz, β-H); 9.11 (d, 1H, $^3J_{\mathrm{HH}}$ = 5.1 Hz, β-H); 9.01 (dd, 2H, $^3J_{\mathrm{HH}}$ = 4.9, 1.9 Hz, β-H); 8.41 (d, 1H, $^3J_{\mathrm{HH}}$ = 7.5 Hz, 10-*o*1-Ph); 8.33 (t, 2H, $^3J_{\mathrm{HH}}$ = 9.3 Hz, 5,15-*o*1-Ph); 7.96 (d, 1H, $^3J_{\mathrm{HH}}$ = 7.5 Hz, 10-*o*2-Ph); 7.87 (d, 1H, $^3J_{\mathrm{HH}}$ = 7.6 Hz, 5/15-*o*2-Ph); 7.76 (d, 1H, $^3J_{\mathrm{HH}}$ = 6.7 Hz, 5/15-*o*1-Ph); 7.72 (d, 1H, $^3J_{\mathrm{HH}}$ = 7.7 Hz, 10-*m*1-Ph); 7.66 (t, 2H, $^3J_{\mathrm{HH}}$ = 6.7 Hz, 5,15-*m*1-Ph); 7.61 (d, 1H, $^3J_{\mathrm{HH}}$ = 7.7 Hz, 10-*m*2-Ph); 7.54 (t, 2H, $^3J_{\mathrm{HH}}$ = 7.5 Hz, 5,15-*m*2-Ph); 2.72 (s, 3H, 10-*p*-CH$_3$); 2.70 (s, 6H, 5,15-*p*-CH$_3$). MS (ESI): M$^+$ = 796.1853 (expt), 796.1845 (calcd for $C_{41}H_{29}N_4O_2Re$). Elemental analysis (%) calcd for $C_{41}H_{29}N_4O_2Re$: C 61.87, H 3.67, N 7.04; found C 61.63, H 3.62, N 7.34. IR (cm^{-1}): ν_{ReO} 992, ν_{CHO} 1659.

Re[T*p*OCH$_3$PC-3-CHO](O). Yield 36 mg (65.4%). UV-vis (CH$_2$Cl$_2$) $\lambda_{\max}$ [nm, $\varepsilon \times 10^{-4}$ (M^{-1} cm^{-1})]: 452 (11.06), 613 (4.14). ^{1}H NMR (400 MHz, −20 °C, dichloromethane-d2) δ: 9.97 (s, 1H, CHO); 9.93 (s, 1H, β-H); 9.50 (d, 1H, $^3J_{\mathrm{HH}}$ = 4.4 Hz, β-H); 9.32 (d, 1H, $^3J_{\mathrm{HH}}$ = 4.9 Hz, β-H); 9.25 (d, 1H, $^3J_{\mathrm{HH}}$ = 4.4 Hz, β-H); 9.15 (d, 1H, $^3J_{\mathrm{HH}}$ = 5.0 Hz, β-H); 9.06 (t, 2H, $^3J_{\mathrm{HH}}$ = 4.3 Hz, β-H); 8.44 (d, 1H, $^3J_{\mathrm{HH}}$ = 6.5 Hz, 10-*o*1-Ph); 8.34 (d, 2H, $^3J_{\mathrm{HH}}$ = 8.3 Hz, 5,15-*o*1-Ph); 8.02 (d, 1H, $^3J_{\mathrm{HH}}$ = 6.6 Hz, 10-*o*2-Ph); 7.89 (d, 1H, $^3J_{\mathrm{HH}}$ = 6.2 Hz, 5/15-*o*2-Ph); 7.82 (d, 1H, $^3J_{\mathrm{HH}}$ = 6.2 Hz, 5/15-*o*2-Ph); 7.43 (d, 1H, $^3J_{\mathrm{HH}}$ = 5.9 Hz, 10-*m*1-Ph); 7.39–7.31 (m, 3H, 10-*m*2-Ph & 5,15-*m*1-Ph); 7.27–7.23 (m, 2H, 5,15-*m*2-Ph); 4.06 (s, 6H, 5,15-*p*-OCH$_3$); 4.04 (s, 3H, 10-*p*-OCH$_3$). MS (ESI): M$^+$ = 844.1695 (expt), 844.1692 (calcd for $C_{41}H_{29}N_4O_5Re$). Elemental analysis (%) calcd for $C_{41}H_{29}N_4O_5Re$: C 58.35, H 3.46, N 6.64; found C 58.13, H 3.62, N 6.54. IR (cm^{-1}): ν_{ReO} 992, ν_{CHO} 1655.

Re[T*p*FPC-3-CHO](O). Yield 35 mg (63.8%). UV-vis (CH$_2$Cl$_2$) $\lambda_{\max}$ [nm, $\varepsilon \times 10^{-4}$ (M^{-1} cm^{-1})]: 448 (8.87), 608 (2.93). ^{1}H NMR

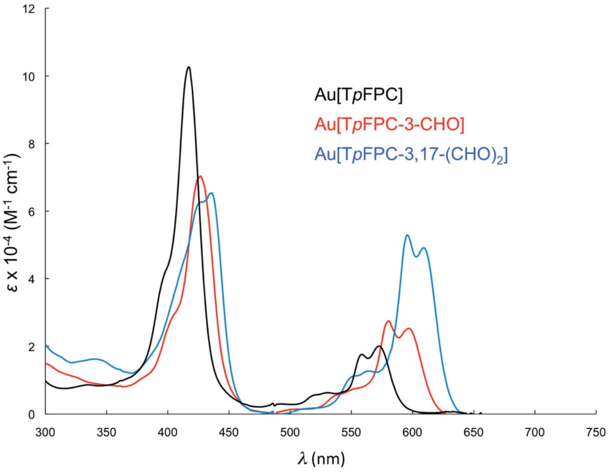

Fig. 8 Comparative UV-vis spectra in dichloromethane for Au[T*p*FPC] (black), Au[T*p*FPC-3-CHO] (red), (c) Au[T*p*FPC-3,17-(CHO)$_2$] (blue).

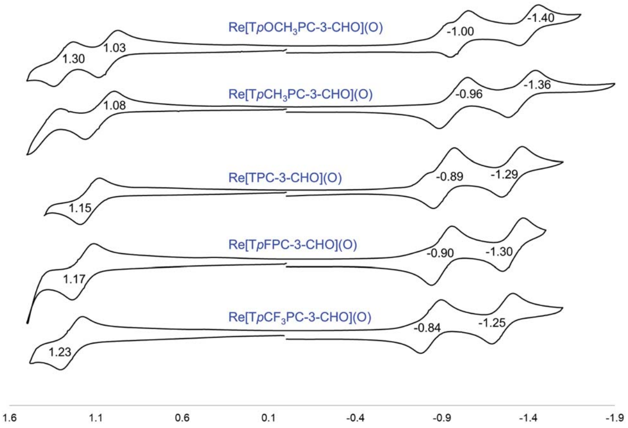

Fig. 9 Cyclic voltammograms (V *vs.* SCE) for Re[T*p*XPC-3-CHO](O) derivatives in dichloromethane containing 0.1 M TBAP.

(400 MHz, CDCl$_3$, 20 °C) δ: 10.07 (s, 1H, CHO); 10.05 (s, 1H, β-H); 9.52 (d, 1H, $^3J_{HH} = 4.4$ Hz, β-H); 9.22 (d, 1H, $^3J_{HH} = 4.4$ Hz, β-H); 9.21 (d, 1H, $^3J_{HH} = 4.9$ Hz, β-H); 9.06 (d, 1H, $^3J_{HH} = 5.0$ Hz, β-H); 8.975 (d, 1H, $^3J_{HH} = 4.9$ Hz, β-H); 8.972 (d, 1H, $^3J_{HH} = 5.1$ Hz, β-H); 8.46–8.38 (m, 3H, Ph-H); 7.93 (m, 2H, Ph-H); 7.81 (m, 2H, Ph-H); 7.54–7.59 (m, 3H, Ph-H); 7.42–7.59 (m, 2H, Ph-H). MS (ESI): M$^+$ = 808.1107 (expt), 808.1103 (calcd for $C_{38}H_{20}F_3N_4O_2$-Re). Elemental analysis (%) calcd for $C_{38}H_{20}F_3N_4O_2Re$: C 56.50, H 2.50, N 6.94; found C 56.23, H 2.62, N 6.63 IR ν_{ReO}: 1007 cm^{-1}, ν_{CHO}: 1730, 1666 cm^{-1}.

Re[T*p*CF$_3$PC-3-CHO](O). Yield 25 mg (47.6%). UV-vis (CH$_2$Cl$_2$) λ_{max} [nm, $\varepsilon \times 10^{-4}$ (M^{-1} cm^{-1})]: 448 (9.21), 607 (3.17). ^{1}H NMR (400 MHz, −20 °C, CDCl$_3$) δ: 10.14 (s, 1H, CHO); 9.99 (s, 1H, β-H); 9.61 (d, 1H, $^3J_{HH} = 4.4$ Hz, β-H); 9.27 (dd, 2H, $^3J_{HH} = 9.4$, 4.7 Hz, β-H); 9.06 (d, 1H, $^3J_{HH} = 5.1$ Hz, β-H); 9.01 (dd overlapping, 2H, $^3J_{HH} = 4.9$, 3.4 Hz, β-H); 8.68 (d, 1H, $^3J_{HH} = 8.0$ Hz, 10-*m*1-Ph); 8.63 (dd overlapping, 2H, $^3J_{HH} = 12.0$, 8.1 Hz, 5,15-*m*1-Ph); 8.22–8.14 (m, 5H, 10-*m*2-Ph & 5,15-*m*2-Ph & 10-*o*-Ph); 8.10–8.00 (m, 4H, 5,15-*o*-Ph). MS (ESI): M$^-$ = 958.1015 (expt), 958.1008 (calcd for $C_{41}H_{20}F_9N_4O_2Re$). Elemental analysis (%) calcd for $C_{41}H_{20}F_9N_4O_2Re$: C 51.41, H 2.10, N 5.85; found C 51.13, H 2.32, N 5.54. IR ν_{ReO}: 992 cm^{-1}, ν_{CHO}: 1663 cm^{-1}.

Re[T*p*CH$_3$PC-3,17-(CHO)$_2$](O). Small quantities of this minor product were combined from multiple syntheses to derive the following spectroscopic data. UV-vis (CH$_2$Cl$_2$) λ_{max} [nm, $\varepsilon \times 10^{-4}$ (M^{-1} cm^{-1})]: 452 (6.84), 628 (3.12). ^{1}H NMR (400 MHz, −20 °C, CDCl$_3$) δ: 9.94 (s, 2H, CHO); 9.92 (s, 2H, β-H); 9.10 (d, 2H, $^3J_{HH} = 5.0$ Hz, β-H); 8.95 (d, 2H, $^3J_{HH} = 5.0$ Hz, β-H); 8.32 (d, 2H, $^3J_{HH} = 8.6$ Hz, 5,15-*o*1-Ph); 8.27 (d, 1H, $^3J_{HH} = 7.7$ Hz, 10-*o*1-Ph); 7.86 (d, 2H, $^3J_{HH} = 8.8$ Hz, 5,15-*o*2-Ph); 7.74 (d, 1H, $^3J_{HH} = 7.6$ Hz, 10-*o*2-Ph); 7.67 (d, 2H, $^3J_{HH} = 7.7$ Hz, 5,15-*m*1-Ph); 7.57 (d, 2H, $^3J_{HH} = 7.6$ Hz, 5,15-*m*2-Ph); 7.99 (d, 2H, $^3J_{HH} = 8.0$ Hz, 10-*m*-Ph); 2.71 (s, 6H, 5,15-*p*-CH$_3$); 2.70 (s, 3H, 10-*p*-CH$_3$). MS (ESI): M$^+$ = 824.1807 (expt), 824.1792 (calcd for $C_{42}H_{29}N_4O_3Re$).

General synthesis of cyanoacetic-acid (Knoevenagel) adducts

To a two-necked 50 mL round-bottom flask equipped with a rubber septum, a reflux condenser, a magnetic stir-bar, and an argon inlet/outlet, was added the desired Re^{V}O-corrole-3-CHO derivative (0.04 mmol, ∼30 mg), dissolved in acetonitrile (10 mL). To this solution, cyanoacetic acid (30 mg, 0.04 mmol) and piperidine (two drops) were added. The reaction mixture was heated to reflux (∼80 °C) and left to stir for ∼1 hour under argon. After cooling, the reaction was quenched by washing with water (3 × 100 mL), prior to purification *via* column chromatography on silica gel using dichloromethane with 5% methanol as mobile phase. Unreacted monoformyl starting material eluted first, followed by the desired product.

Re[TPC-3-CH(CN)(CO$_2$H)](O). Yield 21 mg (64.3%). UV-vis (CH$_2$Cl$_2$) λ_{max} [nm, $\varepsilon \times 10^{-4}$ (M^{-1} cm^{-1})]: 470 (7.32), 637 (3.98). ^{1}H NMR (400 MHz, −20 °C) δ: 10.62 (s, 1H, β-H); 9.54 (d, 1H, $^3J_{HH} = 4.4$ Hz, β-H); 9.25 (d, 1H, $^3J_{HH} = 4.4$ Hz, β-H); 9.22 (d, 1H, $^3J_{HH} = 4.9$ Hz, β-H); 9.00 (d, 1H, $^3J_{HH} = 5.0$ Hz, β-H); 8.96 (d, 2H, $^3J_{HH} = 4.5$ Hz, β-H); 8.75 (s, 1H, C–H); 8.53 (d, 1H, $^3J_{HH} = 7.4$ Hz, 10-*o*1-Ph); 8.42 (t, 2H, $^3J_{HH} = 8.6$ Hz, 5,15-*o*1-Ph); 8.06 (d, 1H, $^3J_{HH} = 6.7$ Hz, 10-*m*1-Ph); 7.86 (m, 10H, 10-*o*2/*m*2/*p*-Ph, 5,15-*o*2/*m*/*p*-Ph). MS (ESI): M$^+$ = 821.1360 (expt), 821.1366 (calcd for $C_{41}H_{24}N_5O_3Re$). Elemental analysis (%) calcd for $C_{41}H_{24}N_5O_3Re$: C 59.99, H 2.95, N 8.53; found C 59.73, H 2.62, N 8.59. IR (cm^{-1}): ν_{ReO} 996, ν_{CHO} 1570 cm^{-1}, ν_{CN}: 1704 cm^{-1}.

Re[T*p*CH$_3$PC-3-CH(CN)(CO$_2$H)](O). Yield 23.9 mg (79.74%). UV-vis (CH$_2$Cl$_2$) λ_{max} [nm, $\varepsilon \times 10^{-4}$ (M^{-1} cm^{-1})]: 471 (6.82), 638 (3.65). ^{1}H NMR (400 MHz, 0 °C) δ: 10.58 (s, 1H, β-H); 9.52 (d, 1H, $^3J_{HH} = 4.6$ Hz, β-H); 9.23 (dd, 2H, $^3J_{HH} = 6.8$, 4.6 Hz, β-H); 9.03 (d, 1H, $^3J_{HH} = 4.8$ Hz, β-H); 8.96 (d, 2H, $^3J_{HH} = 5.1$ Hz, β-H); 8.73 (s, 1H, CH); 8.40 (d, 1H, $^3J_{HH} = 7.6$ Hz, 10-*o*1-Ph); 8.30 (d, 1H, $^3J_{HH} = 7.8$ Hz, 5/15-*o*1-Ph); 8.26 (d, 1H, $^3J_{HH} = 7.8$ Hz, 5/15-*o*1-Ph); 7.96 (d, 1H, $^3J_{HH} = 7.4$ Hz, 10-*o*2-Ph); 7.83 (d, 1H, $^3J_{HH} = 8.1$ Hz, 10-*m*1-Ph); 7.74 (t, 3H, $^3J_{HH} = 8.7$ Hz, 10-*m*2-Ph & 5,15-*o*2-Ph); 7.69–7.59 (m, 3H, 5,15-*m*1-Ph & 5/15-*m*2-Ph); 7.55 (d, 1H, $^3J_{HH} = 7.7$ Hz, 5/15-*m*2-Ph); 2.80 (s, 3H, 10-*p*-CH$_3$); 2.71 (s, 6H, 5,15-*p*-CH$_3$). MS (ESI): M$^+$ = 863.1831 (expt), 863.1836 (calcd for $C_{44}H_{30}N_5O_3Re$). Elemental analysis (%) calcd for $C_{44}H_{30}N_5O_3Re$: C 61.24, H 3.50, N 8.12; found C 61.13, H 3.62, N 8.54.

Re[T*p*FPC-CH(CN)(CO$_2$H)](O). Yield 19.7 mg (66.2%). UV-vis (CH$_2$Cl$_2$) λ_{max} [nm, $\varepsilon \times 10^{-4}$ (M^{-1} cm^{-1})]: 470 (4.31), 637 (2.19).

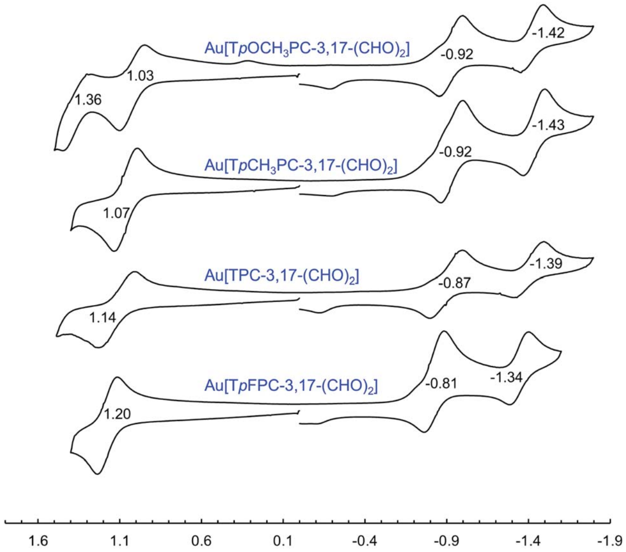

Fig. 10 Cyclic voltammograms (V *vs.* SCE) for Au[T*p*XPC-3,17-(CHO)$_2$] derivatives in dichloromethane containing 0.1 M TBAP.

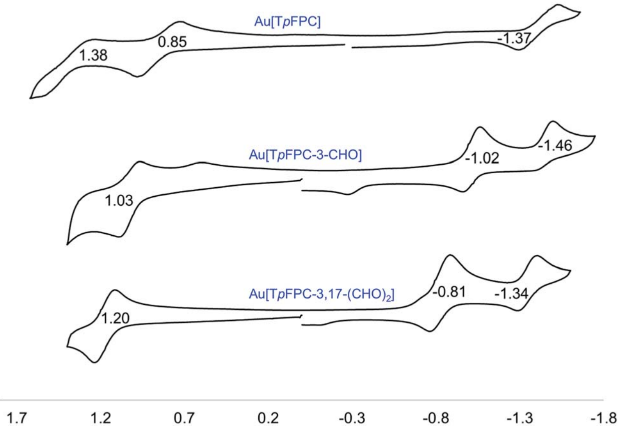

Fig. 11 Cyclic voltammograms (V *vs.* SCE) for Au[T*p*XPC-(CHO)$_n$] (n = 0, 1, 2) derivatives in dichloromethane containing 0.1 M TBAP.

^{1}H NMR (400 MHz, THF, 20 °C) δ: 10.63 (s, 1H, β-H); 9.79 (d, 1H, $^3J_{HH} = 4.4$ Hz, β-H); 9.29 (dd, 2H, $^3J_{HH} = 4.68$, 2.4 Hz, β-H); 9.09 (d, 1H, $^3J_{HH} = 5.0$ Hz, β-H); 9.03 (dd, 2H, $^3J_{HH} = 7.0$, 5.0 Hz, β-H); 8.66 (s, 1H, CH); 8.50 (ddd, 1H, $^3J_{HH} = 8.1$, 5.4, 2.3 Hz, 10-*m*1-Ph); 8.43 (ddd, 1H, $^3J_{HH} = 8.1$, 5.4, 2.3 Hz, 5/15-*m*1-Ph); 7.97–7.86 (m, 3H, 5/15-*m*1-Ph, 10-*m*2, *o*1-Ph); 7.74–7.48 (m, 7H, Ph-H). MS (ESI): M$^+$ 875.1163 (expt), 875.1163 (calcd for $C_{41}H_{21}F_3N_5O_3Re$). Elemental analysis (%) calcd for $C_{41}H_{21}F_3N_5O_3Re$: C 56.29, H 2.42, N 8.01; found C 56.13, H 2.62, N 8.34. IR ν_{ReO}: 996 cm^{-1}, ν_{CHO}: 1328 cm^{-1}.

Re[TpCF$_3$PC-CH(CN)(CO$_2$H)](O). Yield 11 mg (46.7%). UV-vis (CH$_2$Cl$_2$) λ_{max} [nm, $\varepsilon \times 10^{-4}$ (M^{-1} cm^{-1})]: 466 (8.45), 631 (4.36). ^{1}H NMR (400 MHz, CDCl$_3$, 20 °C) δ: 10.58 (s, 1H, β-H); 9.55 (d, 1H, $^3J_{HH} = 4.6$ Hz, β-H); 9.18 (d, 1H, $^3J_{HH} = 4.7$ Hz, β-H); 9.13 (d, 1H, $^3J_{HH} = 4.7$ Hz, β-H); 8.93 (d, 1H, $^3J_{HH} = 5.0$, β-H); 8.90–8.86 (m, 2H, β-H); 8.52–8.46 (m, 4H, *m*1-Ph + CH); 8.11 (dd, 4H, $^3J_{HH} = 12.4$, 8.8 Hz, 5,10,15-*m*2-Ph/10-*o*1-Ph); 8.02 (s broad, 3H, 10-*o*2-Ph/5,15-*o*1-Ph); 7.95 (d, 2H, $^3J_{HH} = 3.8$ Hz, 5,15-*o*2-Ph). MS (ESI): M$^-$ 1025.1069 (expt), 1025.1064 (calcd for $C_{44}H_{21}F_9N_5O_3Re$). Elemental analysis (%) calcd for $C_{44}H_{21}F_9N_5O_3Re$: C 51.57, H 2.07, N 6.83; found C 51.33, H 2.32, N 6.54. IR ν_{ReO}: 996 cm^{-1}, ν_{CHO}: 1328 cm^{-1}.

General procedure for formylation of Au triarylcorroles

To a 50 mL round-bottom flask equipped with a magnetic stirbar, a rubber septum, and an argon inlet/outlet and placed in an ice/water bath, were added dichloromethane (5 mL), POCl$_3$ (20 mmol, 1.8 mL), and DMF (23 mmol, 1.8 mL). Metallocorrole (0.025 mmol, ~20 mg) was dissolved in DCM (10 mL) and added *via* syringe to the cold solution. The mixture was left to stir under a constant flow of argon at 0 °C for 15 minutes upon heating to room temperature. The reaction was left to stir overnight. The following morning the reaction was quenched *via* washing with water (3 × 100 mL) before purification through silica gel column chromatography using a mixture of *n*-hexane/dichloromethane (3 : 1) as eluent to isolate any unreacted starting material. The desired product was isolated by further elution with dichloromethane or a mixture with dichloromethane and methanol (5%).

Au[TPC-3,17-(CHO)$_2$]. Yield 20 mg (61.17%). UV-vis (CH$_2$Cl$_2$) λ_{max} [nm, $\varepsilon \times 10^{-4}$ (M^{-1} cm^{-1})]: 426 (7.53), 437 (8.33), 596 (6.78), 611 (6.66). ^{1}H NMR (400 MHz, 20 °C) δ: 9.65 (s, 2H, CHO); 9.53 (s, 2H, β-H); 8.66 (d, 2H, $^3J_{HH} = 5.1$ Hz, β-H); 8.58 (d, 2H, $^3J_{HH} = 5.1$ Hz, β-H); 8.10 (m, 5H, 5,15-*o*-Ph + 10-*p*-Ph); 7.77 (m, 10H, 5,10,15-*m*-Ph + 10-*o*-Ph + 5,15-*p*-Ph). MS (ESI): M$^+$ = 776.1583 (expt), 776.1579 (calcd for $C_{39}H_{23}N_4O_2Au$). Elemental analysis (%) calcd for $C_{39}H_{23}N_4O_2Au$: C 60.32, H 2.99, N 7.21; found C 60.13, H 3.12, N 7.54.

Au[T*p*CH$_3$PC-3-CHO]. Yield 2.3 mg (11.3%). UV-vis (CH$_2$Cl$_2$) λ_{max} [nm, $\varepsilon \times 10^{-4}$ (M^{-1} cm^{-1})]: 428 (9.84), 581 (4.02), 602 (4.21). ^{1}H NMR (400 MHz, 20 °C) δ: 9.76 (s, 1H, CHO); 9.54 (s, 1H, β-H); 8.97 (d, 1H, $^3J_{HH} = 4.2$ Hz, β-H); 8.90 (d, 1H, $^3J_{HH} = 4.9$ Hz, β-H); 8.70 (d overlapping, 2H, $^3J_{HH} = 8.0$ Hz, β-H); 8.64 (d overlapping, 2H, $^3J_{HH} = 4.8$ Hz, β-H); 8.10 (d, 2H, $^3J_{HH} = 7.8$ Hz, 10-*o*-Ph); 7.99 (d, 4H, $^3J_{HH} = 7.7$ Hz, 5,15-*o*-Ph); 7.62 (d, 2H, $^3J_{HH} = 7.8$ Hz, 10-*m*-Ph); 7.54 (dd, 4H, $^3J_{HH} = 12.6$, 7.7 Hz, 5,15-*m*-Ph); 2.70 (s, 3H, *p*-CH$_3$), 2.68 (s, 6H, *p*-CH$_3$). MS (ESI): M$^+$ = 791.2080 (expt), 791.2079 (calcd for $C_{41}H_{29}N_4OAu$). Elemental analysis (%) calcd for $C_{41}H_{29}N_4OAu$: C 62.28, H 3.70, N 7.09; found C 62.53, H 3.62, N 7.43. IR ν_{CHO}: 1655 cm^{-1}.

Au[T*p*CH$_3$PC-3,17-(CHO)$_2$]. Yield 10.7 mg (53.5%). UV-vis (CH$_2$Cl$_2$) λ_{max} [nm, $\varepsilon \times 10^{-4}$ (M^{-1} cm^{-1})]: 425 (4.35), 439 (4.77), 596 (3.53), 615 (3.73). ^{1}H NMR (400 MHz, 20 °C) δ: 9.58 (s, 2H, CHO); 9.27 (s, 2H, β-H); 8.62 (d, 2H, $^3J_{HH} = 5.0$ Hz, β-H); 8.56 (d, 2H, $^3J_{HH} = 5.1$ Hz, β-H); 7.94 (d overlapping, 2H, $^3J_{HH} = 8.0$ Hz, 10-*o*-Ph); 7.91 (d overlapping, 4H, $^3J_{HH} = 7.8$ Hz, 5,15-*o*-Ph); 7.57 (d, 2H, $^3J_{HH} = 7.8$ Hz, 10-*m*-Ph); 7.53 (d, 4H, $^3J_{HH} = 7.7$ Hz, 5,15-*m*-Ph); 2.68 (s, 9H, *p*-CH$_3$). MS (ESI): M$^+$ = 819.2029 (expt), 818.2029 (calcd for $C_{42}H_{29}N_4O_2Au$). Elemental analysis (%) calcd for $C_{42}H_{29}N_4O_2Au$: C 61.62, H 3.57, N 6.84; found C 61.23, H 3.62, N 6.56. IR ν_{CHO}: 1663 cm^{-1}.

Au[T*p*OCH$_3$PC-3,17-(CHO)$_2$]. Yield 10.2 mg (51.1%). UV-vis (CH$_2$Cl$_2$) λ_{max} [nm, $\varepsilon \times 10^{-4}$ (M^{-1} cm^{-1})]: 426 (5.63), 439 (5.70), 597 (4.29), 618 (4.44). ^{1}H NMR (400 MHz, 20 °C, CD$_2$Cl$_2$)

δ: 9.70 (s, 2H, CHO); 9.35 (s, 2H, β-H); 8.67 (d, 2H, $^3J_{HH} = 5.0$ Hz, β-H); 8.60 (d, 2H, $^3J_{HH} = 5.0$ Hz, β-H); 7.99 (d broad, 6H, $^3J_{HH} = 8.0$ Hz, *m*-Ph); 7.32–7.27 (m, 6H, *o*-Ph); 4.08 (s, 6H, 5,15-*p*-OCH_3); 4.06 (s, 3H, 10-*p*-OCH_3). MS (ESI): $M^+ = 866.1806$ (expt), 866.1807 (calcd for $C_{42}H_{29}N_4O_5Au$). Elemental analysis (%) calcd for $C_{42}H_{29}N_4O_5Au$: C 58.21, H 3.37, N 6.46; found C 58.43, H 3.82, N 6.01.

Au[T*p*FPC-3-CHO]. Yield 4.1 mg (20.5%). UV-vis (CH_2Cl_2) λ_{max} [nm, $\varepsilon \times 10^{-4}$ (M^{-1} cm^{-1})]: 427 (7.02), 580 (2.75), 597 (2.53). ^1H NMR (20 °C, 400 MHz) δ: 9.68 (s, 1H, CHO); δ 9.42 (S, 1H, β-H); 8.86 (d, 1H, $^3J_{HH} = 4.5$ Hz, β-H); 8.80 (d, 1H, $^3J_{HH} = 4.9$ Hz, β-H); 8.59–8.55 (m, 4H, β-H); 8.11–8.07 (m, 2H, Ph-H); 8.00–7.94 (m, 4H, Ph-H); 7.47–7.34 (m, 6H, Ph-H). MS (ESI): $M^+ = 802.1257$ (expt), 802.1260 (calcd for $C_{38}H_{20}F_3N_4OAu$). Elemental analysis was not performed.

Au[T*p*FPC-3,17-(CHO)₂]. Yield 10 mg (52.8%). UV-vis (CH_2Cl_2): λ_{max} (nm), [$\varepsilon \times 10^{-4}$ (M^{-1} cm^{-1})]: 436 (6.53), 597 (4.29), 609 (4.91). ^1H NMR (400 MHz, $CDCl_3$, 20 °C) δ: 9.52 (s, 2H, CHO); 9.16 (s, 2H, β-H); 8-53-8.54 (d, 2H, $^3J_{HH} = 5.0$ Hz, β-H); 8.49 (d, 2H, $^3J_{HH} = 5.1$ Hz, β-H); 7.97–7.94 (m, 2H, Ph-H); 7.92–7.88 (m, 4H, Ph-H); 7.35–7.45 (m, 6H, Ph-H). MS (ESI): $M^+ = 830.1207$ (expt), 830.1209 (calcd for $C_{39}H_{20}F_3N_4O_2Au$). Elemental analysis (%) calcd for $C_{39}H_{29}F_3N_4O_2Au$: C 56.40, H 2.43, N 6.75; found: C 56.76, H 2.62, N 7.11.

X-ray crystallography

X-ray quality crystals were obtained *via* slow diffusion of methanol vapor into concentrated dichloromethane solutions of the compounds in question. X-ray data were collected (as previously described[37]) on beamline 12.2.1 at the Advanced Light Source, Lawrence Berkeley National Laboratory. Samples were mounted on MiTeGen Kapton loops and placed in a 100(2)-K nitrogen cold stream provided by an Oxford Cryostream 800 Plus low-temperature apparatus on the goniometer head of a Bruker D8 diffractometer equipped with a PHOTON II CPAD detector operating in shutterless mode. Diffraction data were collected using synchrotron radiation monochromated using silicon(111) to a wavelength of 0.7288(1)Å. An approximate full-sphere of data was collected using a combination of φ and ω scans with scan speeds of one second per degree for the φ scans and one and three seconds per degree for the ω scans at $2\theta = 0$ and $-20°$, respectively. The structures were solved by intrinsic phasing (SHELXT[50]) and refined by full-matrix least-squares on F^2 (SHELXL-2014 (ref. 51)). All non-hydrogen atoms were refined anisotropically. Hydrogen atoms were geometrically calculated and refined as riding atoms. Additional crystallographic information has been summarized in Table 1.

Conflicts of interest

There are no conflicts to declare.

Acknowledgements

This work was supported by the Research Council of Norway (grant no. 262229 and 324139 to AG) and the Arctic Center for Sustainable Energy at UiT – The Arctic University of Norway. The work also used resources of the Advanced Light Source, which is a DOE Office of Science User Facility under contract no. DE-AC02-05CH11231.

References

1 A. Ghosh, *Chem. Rev.*, 2017, **117**, 3798–3881.
2 S. Nardis, F. Mandoj, M. Stefanelli and R. Paolesse, *Coord. Chem. Rev.*, 2019, **388**, 360–405.
3 Y. Fang, Z. Ou and K. M. Kadish, *Chem. Rev.*, 2017, **117**, 3377–3419.
4 A. B. Alemayehu, K. E. Thomas and R. F. Einrem, *Acc. Chem. Res.*, 2021, **54**, 3095–3107.
5 A. B. Alemayehu and A. Ghosh, *J. Porphyrins Phthalocyanines*, 2011, **15**, 106–110.
6 E. Rabinovitch, I. Goldberg and Z. Gross, *Chem.–Eur. J*, 2011, **17**, 12294–12301.
7 K. E. Thomas, A. B. Alemayehu, J. Conradie, C. Beavers and A. Ghosh, *Inorg. Chem.*, 2011, **50**, 12844–12851.
8 R. F. Einrem, H. Braband, T. Fox, H. Vazquez-Lima, R. Alberto and A. Ghosh, *Chem.–Eur. J*, 2016, **22**, 18747–18751.
9 R. F. Einrem, K. J. Gagnon, A. B. Alemayehu and A. Ghosh, *Chem.–Eur. J*, 2016, **22**, 517–520.
10 A. B. Alemayehu, S. J. Teat, S. M. Borisov and A. Ghosh, *Inorg. Chem.*, 2020, **59**, 6382–6389.
11 A. B. Alemayehu, H. Vazquez-Lima, K. J. Gagnon and A. Ghosh, *Inorg. Chem.*, 2017, **56**, 5285–5294.
12 A. B. Alemayehu, K. J. Gagnon, J. Terner and A. Ghosh, *Angew. Chem., Int. Ed.*, 2014, **53**, 14411–14414.
13 A. B. Alemayehu, H. Vazquez-Lima, C. M. Beavers, K. J. Gagnon, J. Bendix and A. Ghosh, *Chem. Commun.*, 2014, **50**, 11093–11096.
14 A. B. Alemayehu, L. J. McCormick, K. J. Gagnon, S. M. Borisov and A. Ghosh, *ACS Omega*, 2018, **3**, 9360–9368.
15 A. B. Alemayehu, H. Vazquez-Lima, K. J. Gagnon and A. Ghosh, *Chem.–Eur. J*, 2016, **22**, 6914–6920.
16 A. B. Alemayehu, H. Vazquez-Lima, L. J. McCormick and A. Ghosh, *Chem. Commun.*, 2017, **53**, 5830–5833.
17 C. Schies, A. B. Alemayehu, H. Vazquez-Lima, K. E. Thomas, T. Bruhn, G. Bringmann and A. Ghosh, *Chem. Commun.*, 2017, **53**, 6121–6124.
18 A. B. Alemayehu, L. J. McCormick-McPherson, J. Conradie and A. Ghosh, *Inorg. Chem.*, 2021, **60**, 8315–8321.
19 J. H. Palmer, A. C. Durrell, Z. Gross, J. R. Winkler and H. B. Gray, *J. Am. Chem. Soc.*, 2010, **132**, 9230–9231.
20 W. Sinha, L. Ravotto, P. Ceroni and S. Kar, *Dalton Trans.*, 2015, **44**, 17767–17773.
21 S. M. Borisov, A. B. Alemayehu and A. Ghosh, *J. Mater. Chem. C*, 2016, **4**, 5822–5828.
22 C. M. Lemon, D. C. Powers, P. J. Brothers and D. G. Nocera, *Inorg. Chem.*, 2017, **56**, 10991–10997.
23 A. B. Alemayehu, N. U. Jae Day, T. Mani, A. B. Rudine, K. E. Thomas, O. A. Gederaas, S. A. Vinogradov, C. C. Wamser and A. Ghosh, *ACS Appl. Mater. Interfaces*, 2016, **8**, 18935–18942.

24 S. M. Borisov, R. F. Einrem, A. B. Alemayehu and A. Ghosh, *Photochem. Photobiol. Sci.*, 2019, **18**, 1166–1170.

25 R. D. Teo, J. Y. Hwang, J. Termini, Z. Gross and H. B. Gray, *Chem. Rev.*, 2017, **117**, 2711–2729.

26 A. Mahammed and Z. Gross, *Coord. Chem. Rev.*, 2019, **379**, 121–132.

27 C. M. Lemon, *Pure Appl. Chem.*, 2020, **92**, 1901–1919.

28 G. Golubkov, *et al.*, *Angew. Chem., Int. Ed.*, 2001, **40**, 2132–2134.

29 J. F. B. Barata, M. G. P. M. S. Neves, M. A. F. Fautino, A. C. Tomé and J. A. Cavaleiro, *Chem. Rev.*, 2017, **117**, 3192–3253.

30 J. H. Palmer, A. C. Durrell, Z. Gross, J. R. Winkler and H. B. Gray, *J. Am. Chem. Soc.*, 2008, **130**, 7786–7787.

31 K. E. Thomas, J. Conradie, L. K. Hansen and A. Ghosh, *Eur. J. Inorg. Chem.*, 2011, 1865–1870.

32 S. Berg, K. E. Thomas, C. M. Beavers and A. Ghosh, *Inorg. Chem.*, 2012, **51**, 9911–9916.

33 K. E. Thomas, L. J. McCormick, D. Carrié, H. Vazquez-Lima, G. Simmoneaux and A. Ghosh, *Inorg. Chem.*, 2018, **57**, 4270–4276.

34 I. K. Thomassen, L. J. McCormick and A. Ghosh, *ACS Omega*, 2018, **3**, 5106–5110.

35 A. Reinholdt, A. B. Alemayehu, K. J. Gagnon, J. Bendix and A. Ghosh, *Inorg. Chem.*, 2020, **59**, 5276–5280.

36 J. H. Palmer, A. C. Durrell, Z. Gross, J. R. Winkler and H. B. Gray, *J. Am. Chem. Soc.*, 2008, **130**, 7786–7787.

37 A. B. Alemayehu, R. F. Einrem, L. J. McCormick-McPherson, N. S. Settineri and A. Ghosh, *Sci. Rep.*, 2020, **10**, 19727.

38 M. Soll, *et al.*, *Org. Lett.*, 2016, **18**, 5840–5843.

39 K. Sudhakar, *et al.*, *Angew. Chem., Int. Ed.*, 2017, **56**, 9837–9841.

40 P. Schweyen, K. Brandhorst, M. Hoffmann, B. Wolfram, M.-K. Zaretzke and M. Bröring, *Chem.–Eur. J*, 2017, **23**, 13897–13900.

41 H. Vazquez-Lima, J. Conradie, M. A. L. Johansen, S. R. Martinsen, A. B. Alemayehu and A. Ghosh, *Dalton Trans.*, 2021, **50**, 12843–12849.

42 I. K. Thomassen, D. Rasmussen, R. F. Einrem and A. Ghosh, *ACS Omega*, 2021, **6**, 16683–16687.

43 A. Vilsmeier and A. Haack, *Ber. Dtsch. Chem. Ges.*, 1927, **27**, 119–122, DOI: 10.1002/cber.19270600118.

44 R. Paolesse, L. Jaquinod, M. O. Senge and K. M. Smith, *J. Org. Chem.*, 1997, **62**, 6193–6198.

45 I. Saltsman, A. Mahammed, I. Goldberg, E. Tkachenko, M. Botoshansky and Z. Gross, *J. Am. Chem. Soc.*, 2002, **124**, 7411–7420.

46 R. Paolesse, S. Nardis, M. Venanzi, M. Mastroianni, M. Russo, F. Fronczek and M. G. H. Vicente, *Chem.–Eur. J*, 2003, **9**, 1192–1197.

47 K. Sorasaenee, P. Taqavi, L. M. Henling, H. B. Gray, E. Tkachenko, A. Mahammed and Z. Gross, *J. Porphyrins Phthalocyanines*, 2007, **11**, 189–197.

48 S. Ganguly and A. Ghosh, *Acc. Chem. Res.*, 2019, **52**, 2003–2014.

49 J.-H. Fuhrhop, K. M. Kadish and D. G. Davis, *J. Am. Chem. Soc.*, 1973, **95**, 5140–5147.

50 G. M. Sheldrick, *Acta Crystallogr., Sect. A: Found. Crystallogr.*, 2015, **71**, 3–8.

51 G. M. Sheldrick, *Acta Crystallogr., Sect. C: Struct. Chem.*, 2015, **71**, 3–8.

Electronic Supplementary Material (ESI) for RSC Advances.

Supplementary Information

Regioselective Formylation of Rhenium-Oxo and Gold Corroles: Substituent Effects on Optical Spectra and Redox Potentials

Rune F. Einrem,[a] Einar Torfi Jonsson,[a] Simon J. Teat,[b] Nicholas S. Settineri,[b,c]
Abraham B. Alemayehu,*[,a] and Abhik Ghosh*[,b]

[1]Department of Chemistry, UiT – The Arctic University of Norway, N-9037 Tromsø, Norway; Email: abraham.alemayehu@uit.no (ABA), abhik.ghosh@uit.no (AG)
[2]Advanced Light Source, Lawrence Berkeley National Laboratory,
Berkeley, CA 94720-8229, USA
[3]Department of Chemistry, University of California, Berkeley, Berkeley, California 94720, USA

A. UV-vis spectra

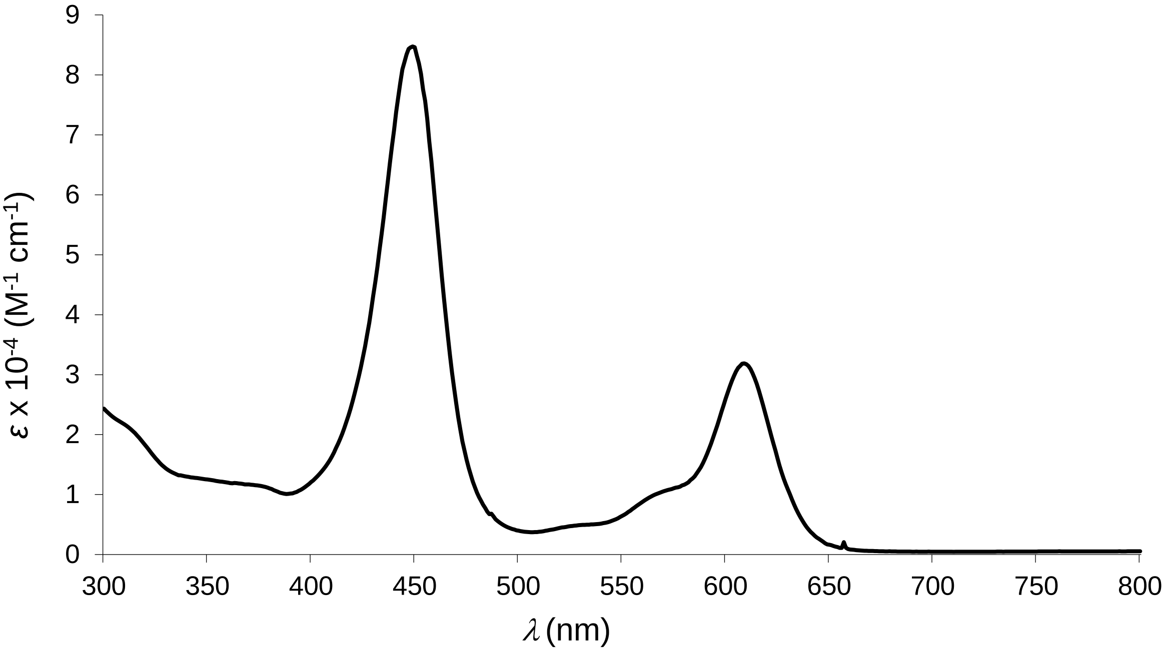

Figure S1. UV-vis spectrum of Re[TPC-3-CHO](O) in dichloromethane.

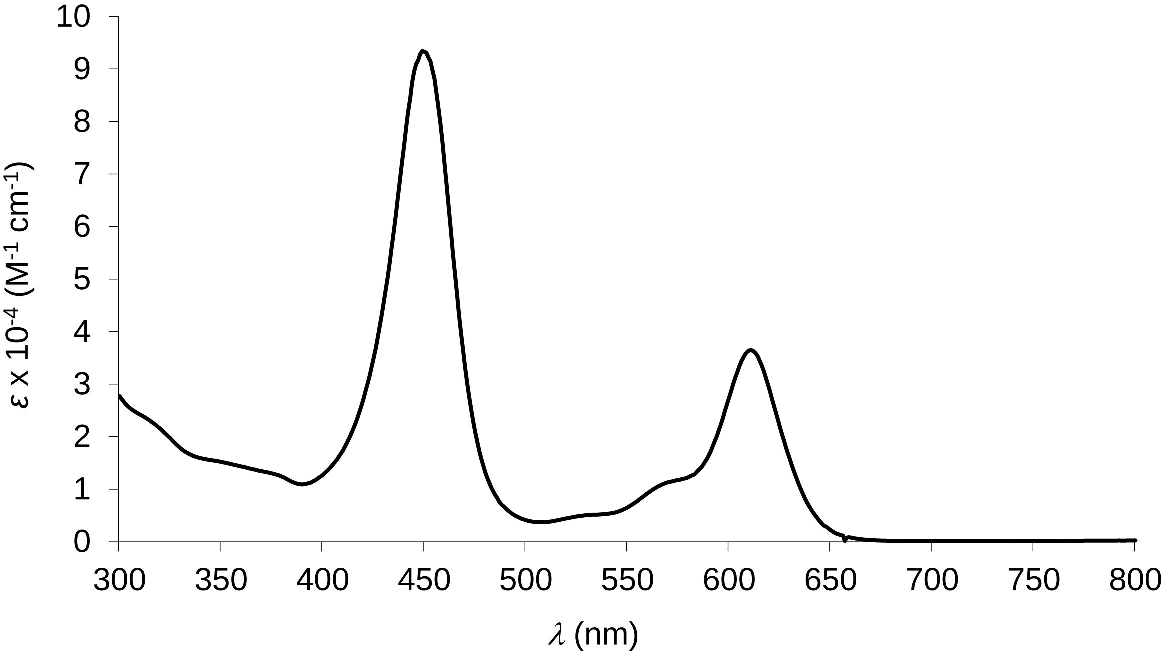

Figure S2. UV-vis spectrum of Re[T*p*CH_3PC-3-CHO](O) in dichloromethane.

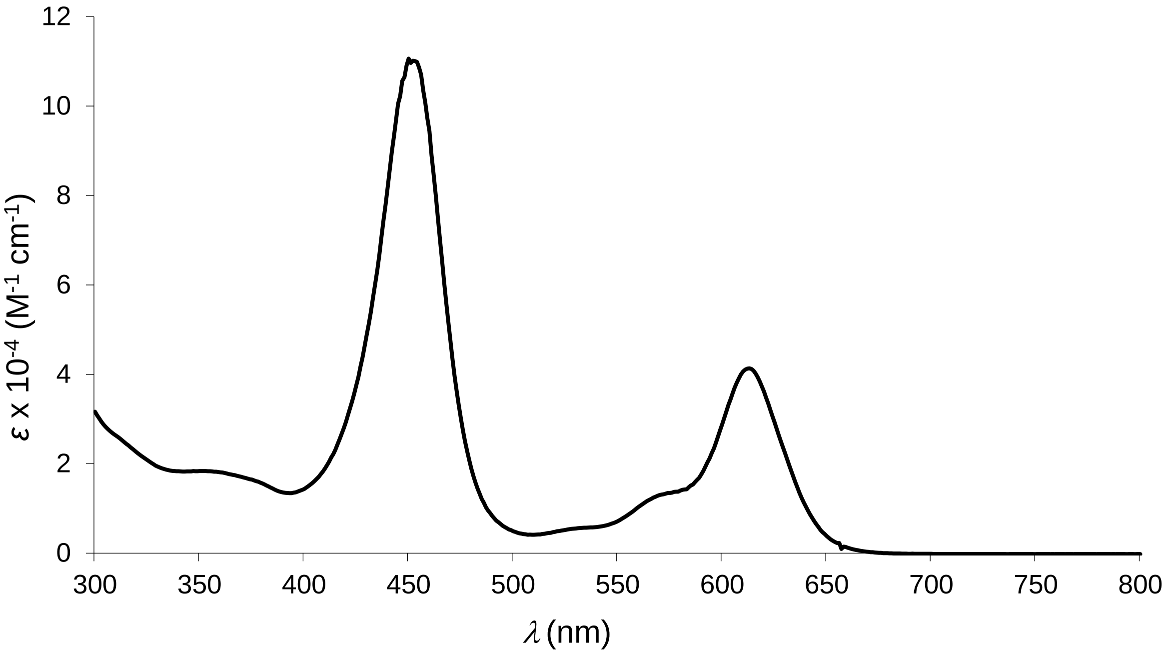

Figure S3. UV-vis spectrum of Re[T*p*OCH3PC-3-CHO](O) in dichloromethane.

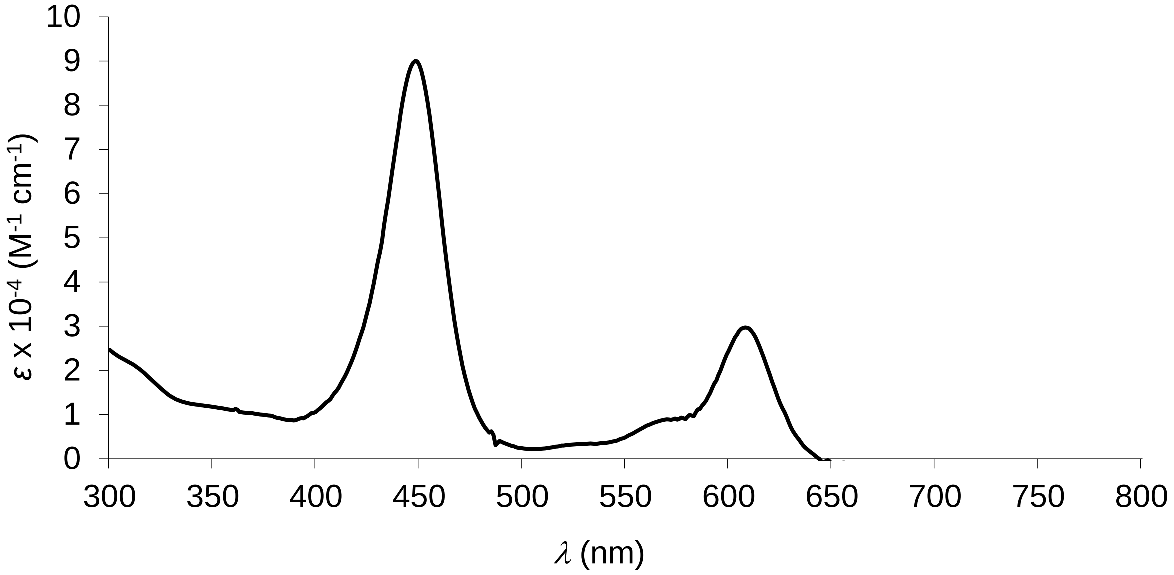

Figure S4. UV-vis spectrum of Re[T*p*FPC-3-CHO](O) in dichloromethane.

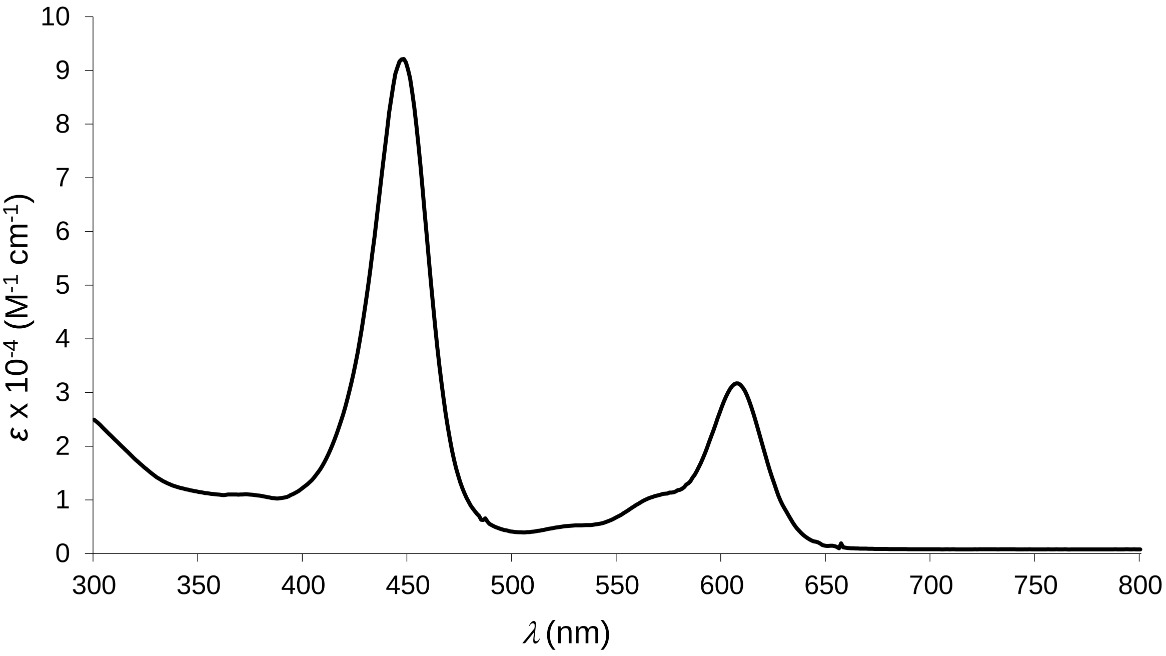

Figure S5. UV-vis spectrum of Re[T*p*CF_3PC-3-CHO](O) in dichloromethane.

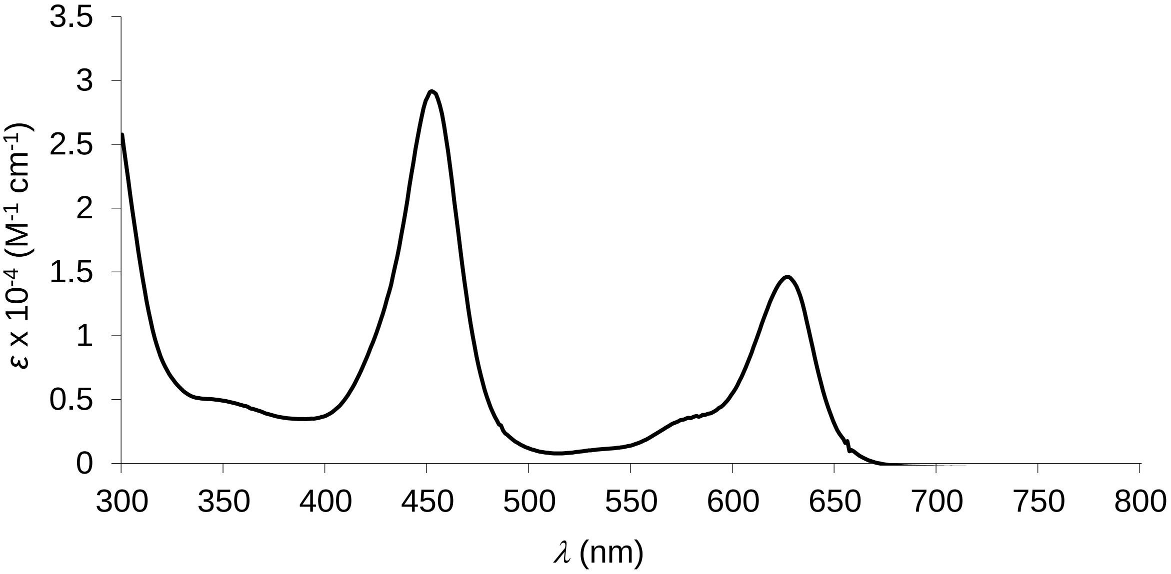

Figure S6. UV-vis spectrum of Re[T*p*FPC-3,17-$(CHO)_2$](O) in dichloromethane.

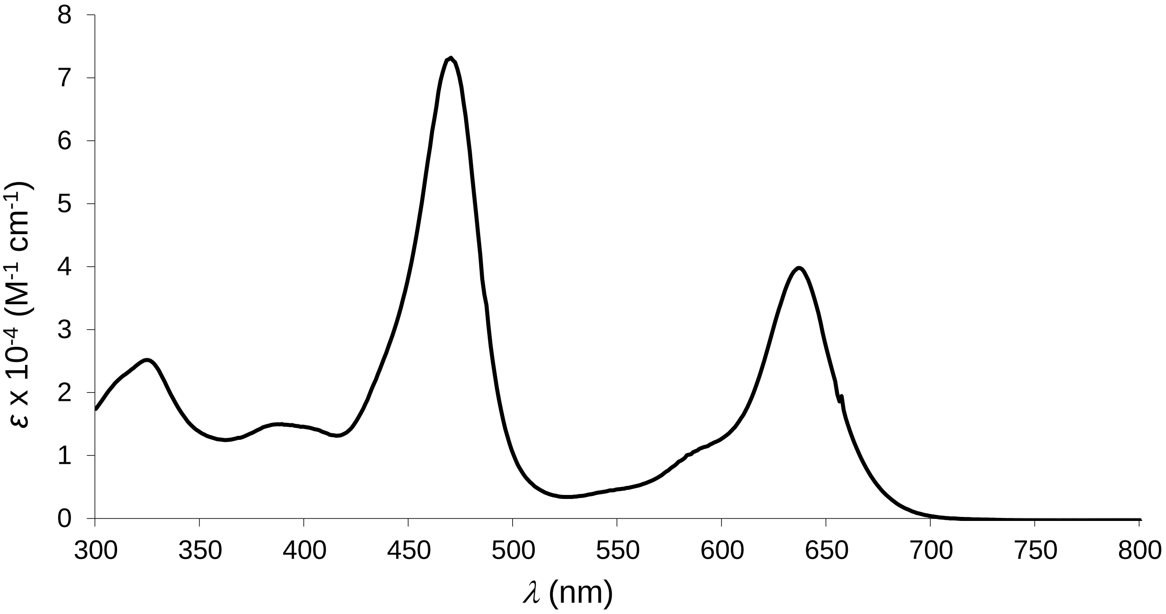

Figure S7. UV-vis spectrum of Re[TPC-3-CH(CN)COOH](O) in dichloromethane.

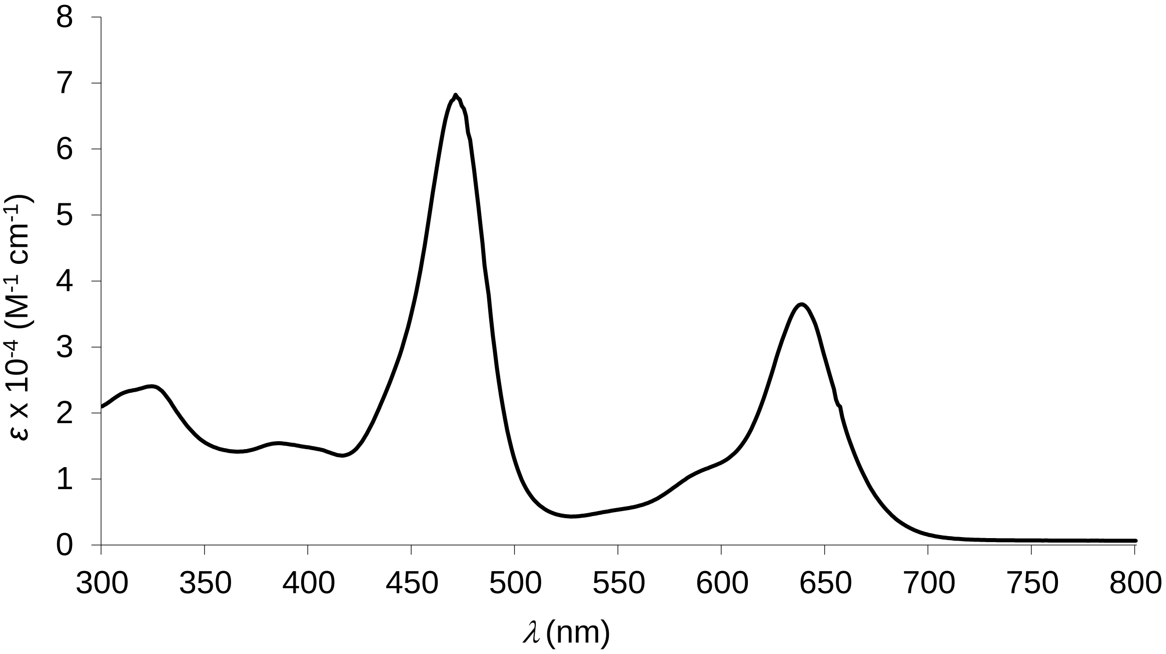

Figure S8. UV-vis spectrum of Re[T*p*CH_3PC-3-CH(CN)COOH](O) in dichloromethane.

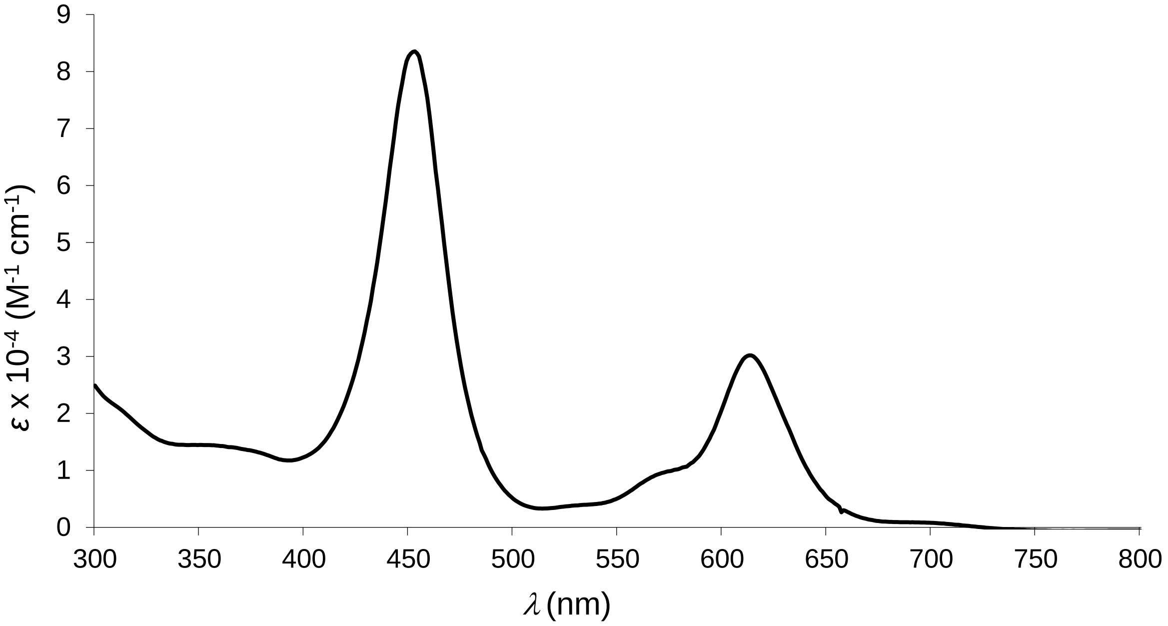

Figure S9. UV-vis spectrum of Re[T*p*OCH$_3$PC-3-CH(CN)COOH](O) in dichloromethane.

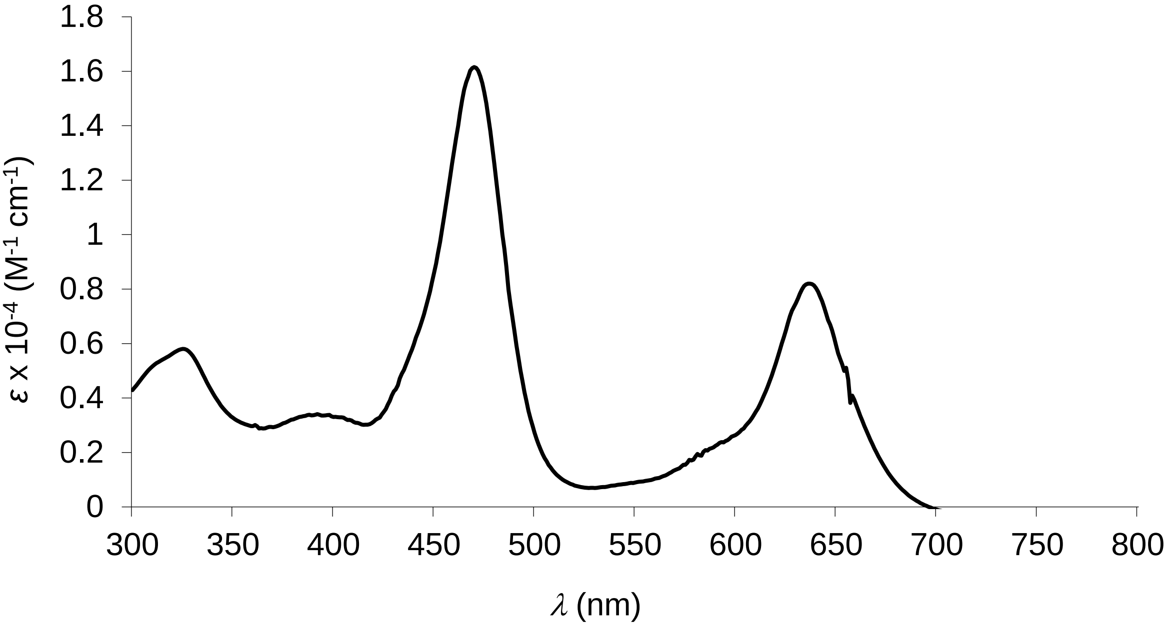

Figure S10. UV-vis spectrum of Re[T*p*FPC-3-CH(CN)COOH](O) in dichloromethane.

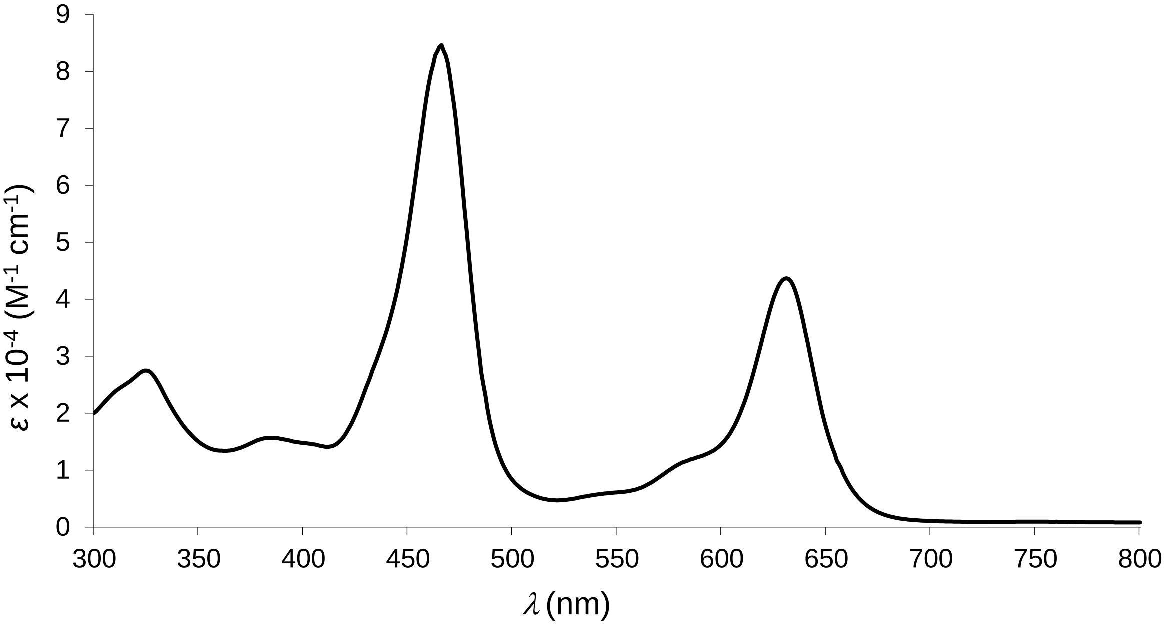

Figure S11. UV-vis spectrum of Re[T*p*CF_3PC-3-CH(CN)COOH](O) in dichloromethane.

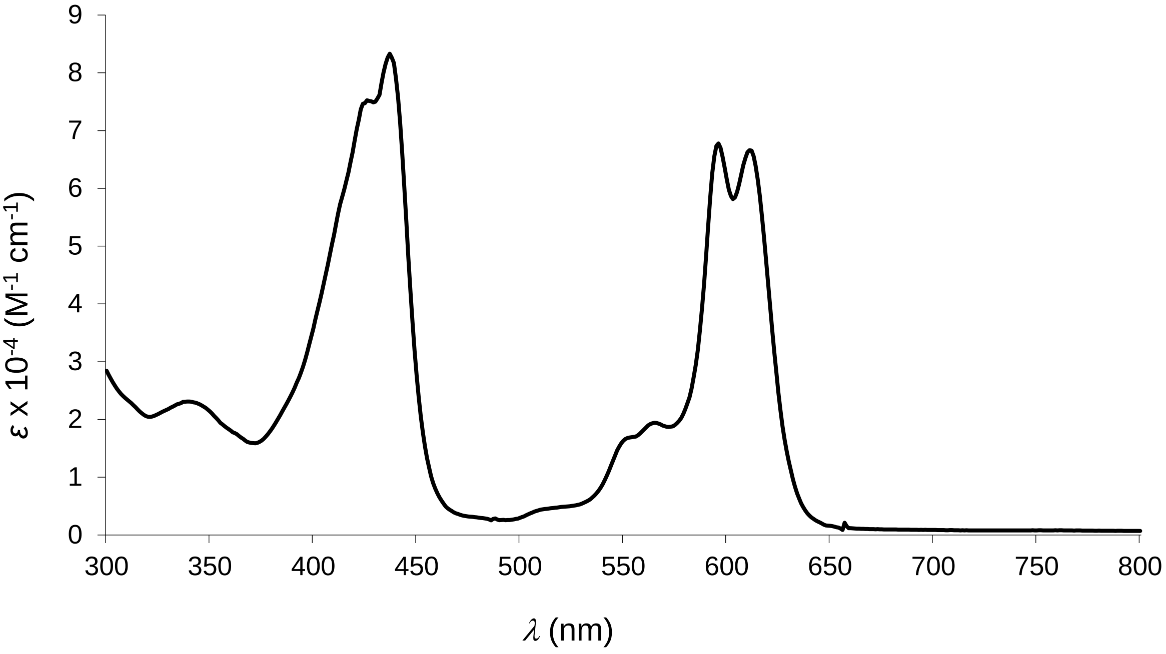

Figure S12. UV-vis spectrum of Au[TPC-3,17-$(CHO)_2$] in dichloromethane.

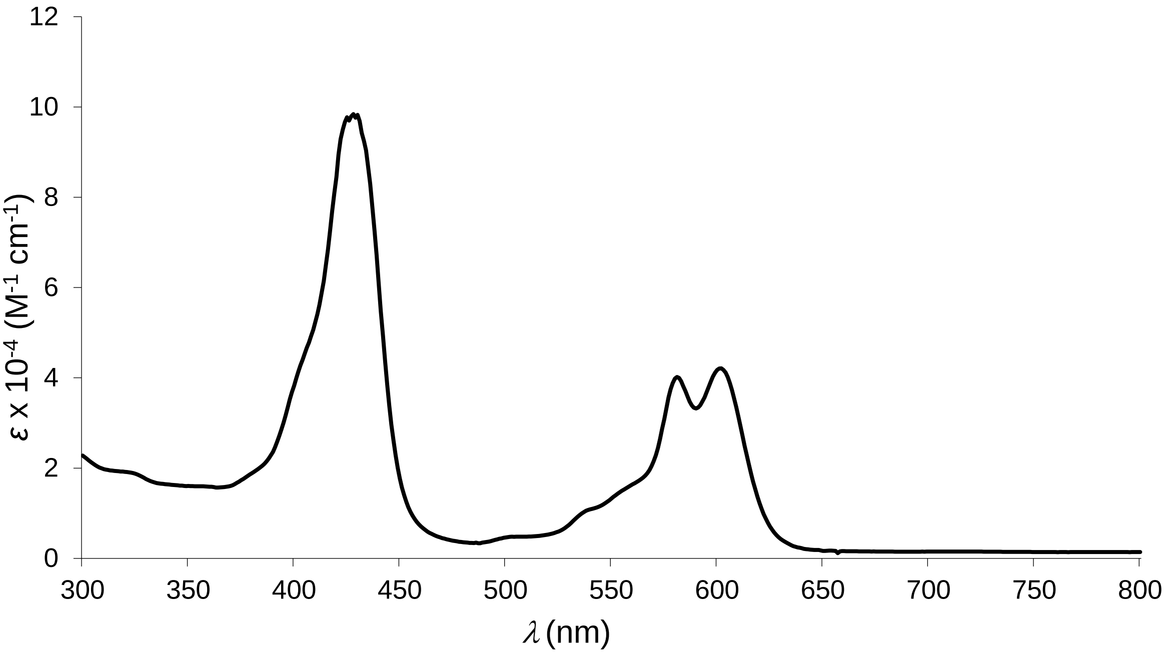

Figure S13. UV-vis spectrum of Au[T*p*CH_3PC-3-CHO] in dichloromethane.

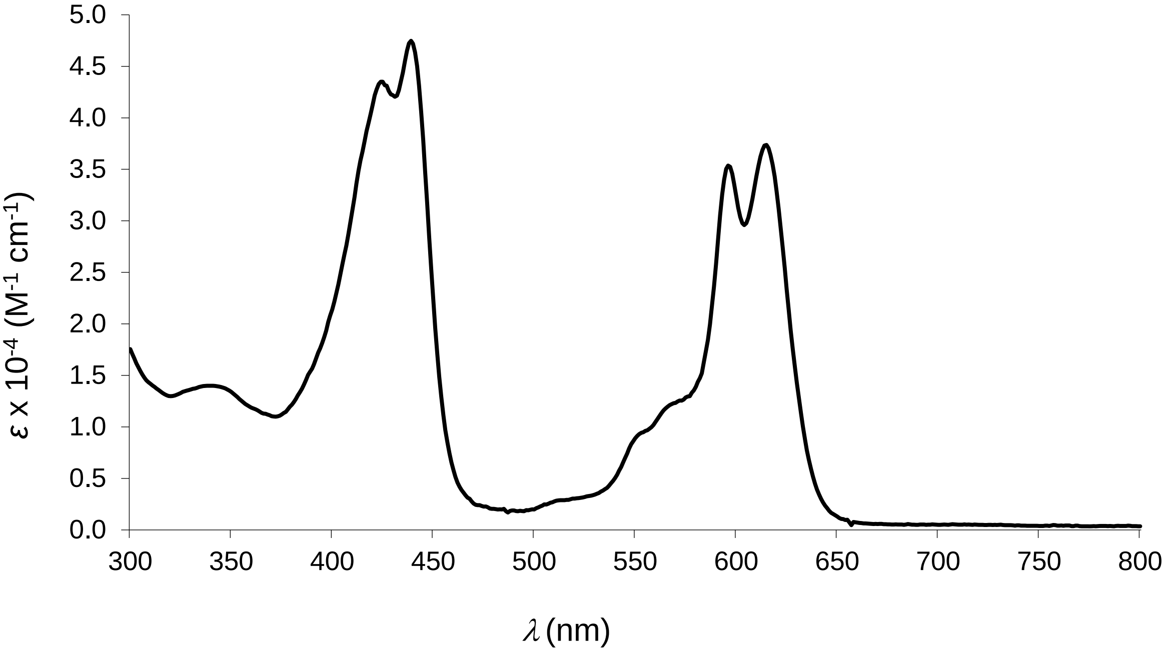

Figure S14. UV-vis spectrum of Au[T*p*CH_3PC-3,17-$(CHO)_2$] in dichloromethane.

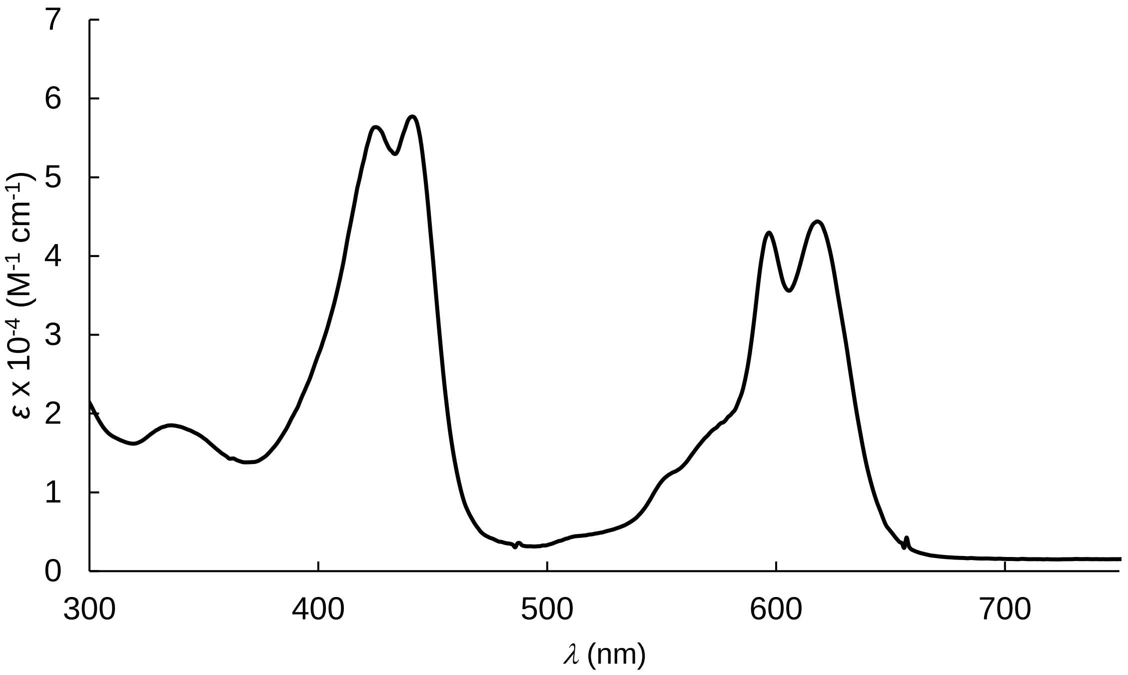

Figure S15. UV-vis spectrum of Au[T*p*OCH$_3$PC-3,17-(CHO)$_2$] in dichloromethane.

B. HRMS-ESI mass spectra

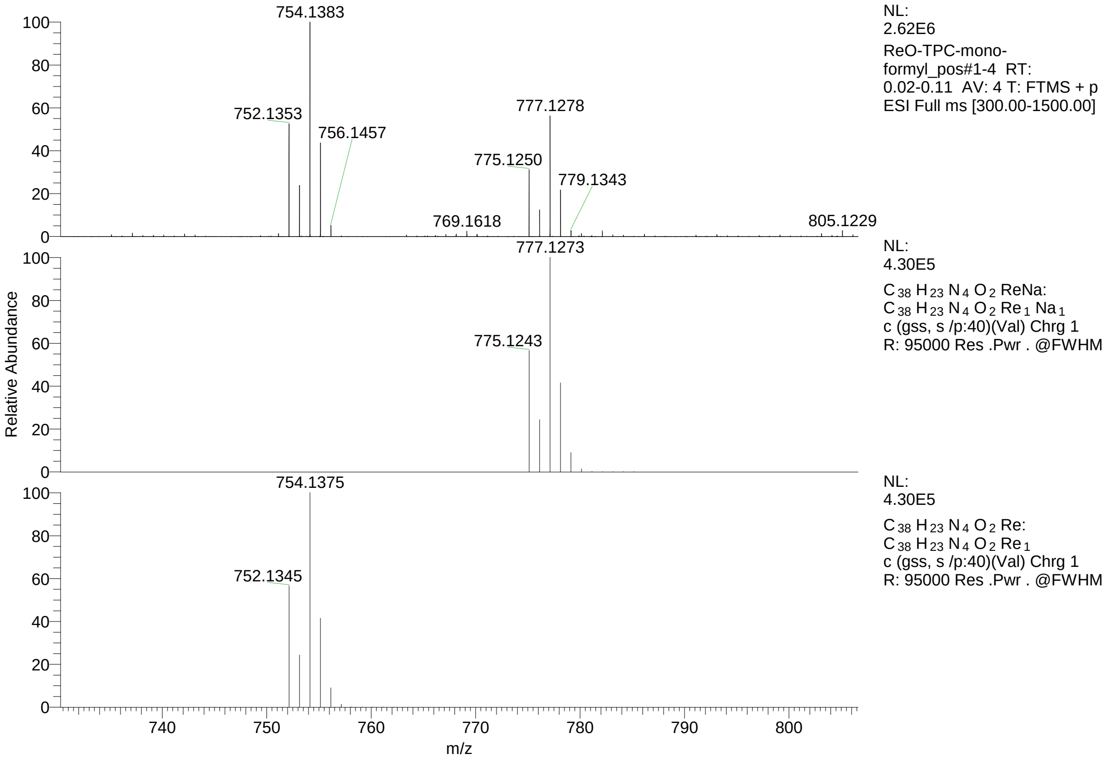

Figure S16. HRMS-ESI mass spectrum of Re[TPC-3-CHO](O).

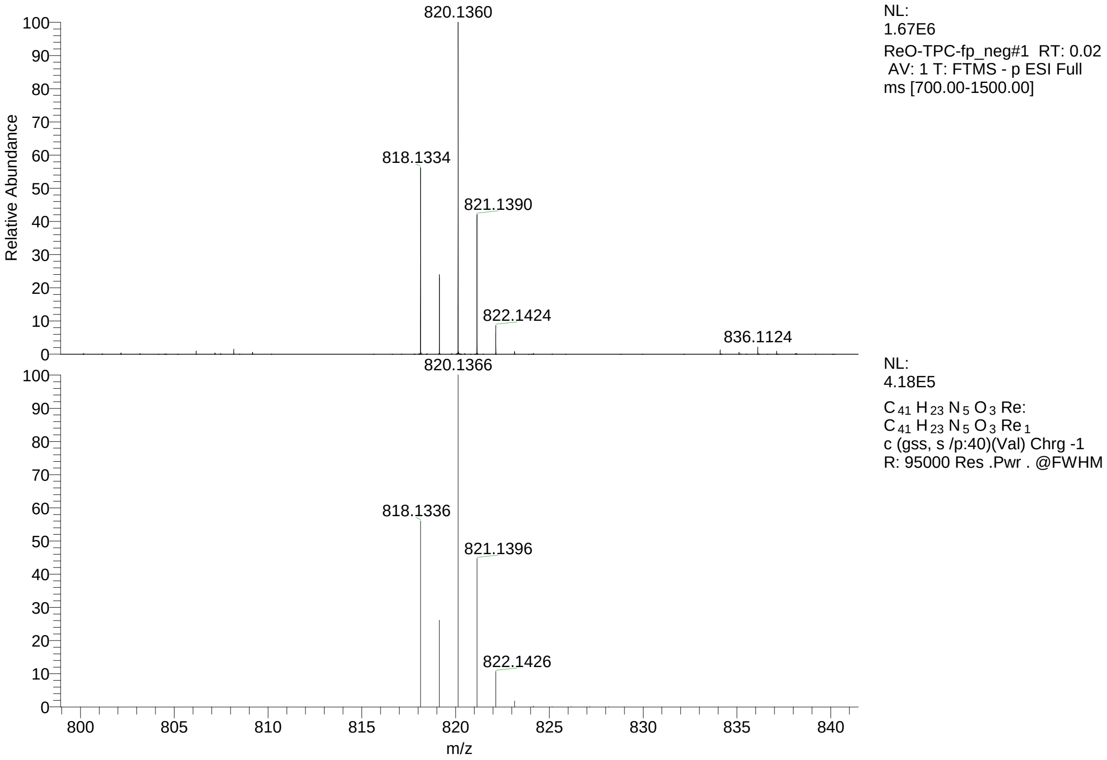

Figure S17. HRMS-ESI mass spectrum of Re[TPC-3-CH(CN)COOH](O).

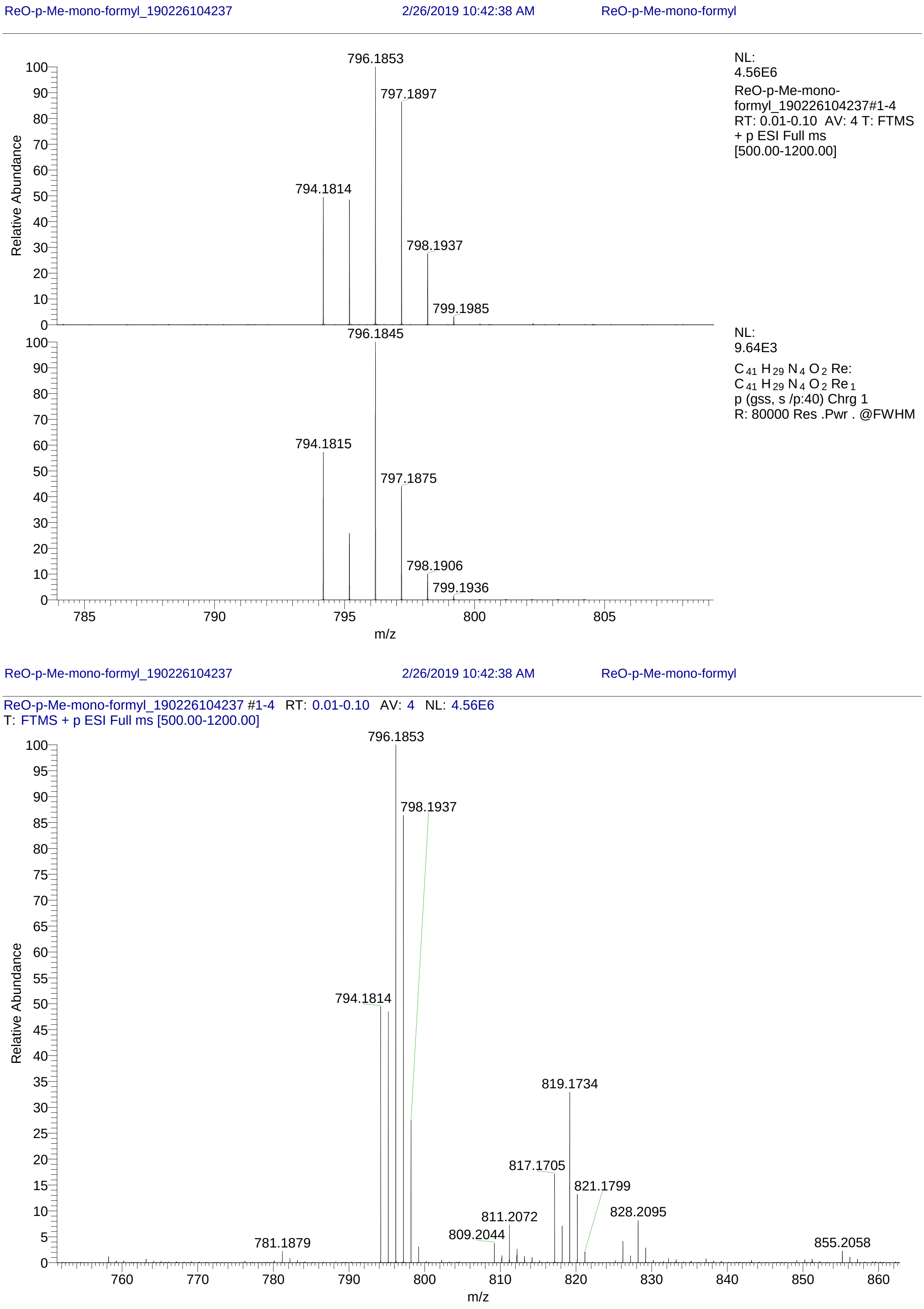

Figure S18. HRMS-ESI mass spectra of Re[T*p*CH$_3$PC-3-CHO](O).

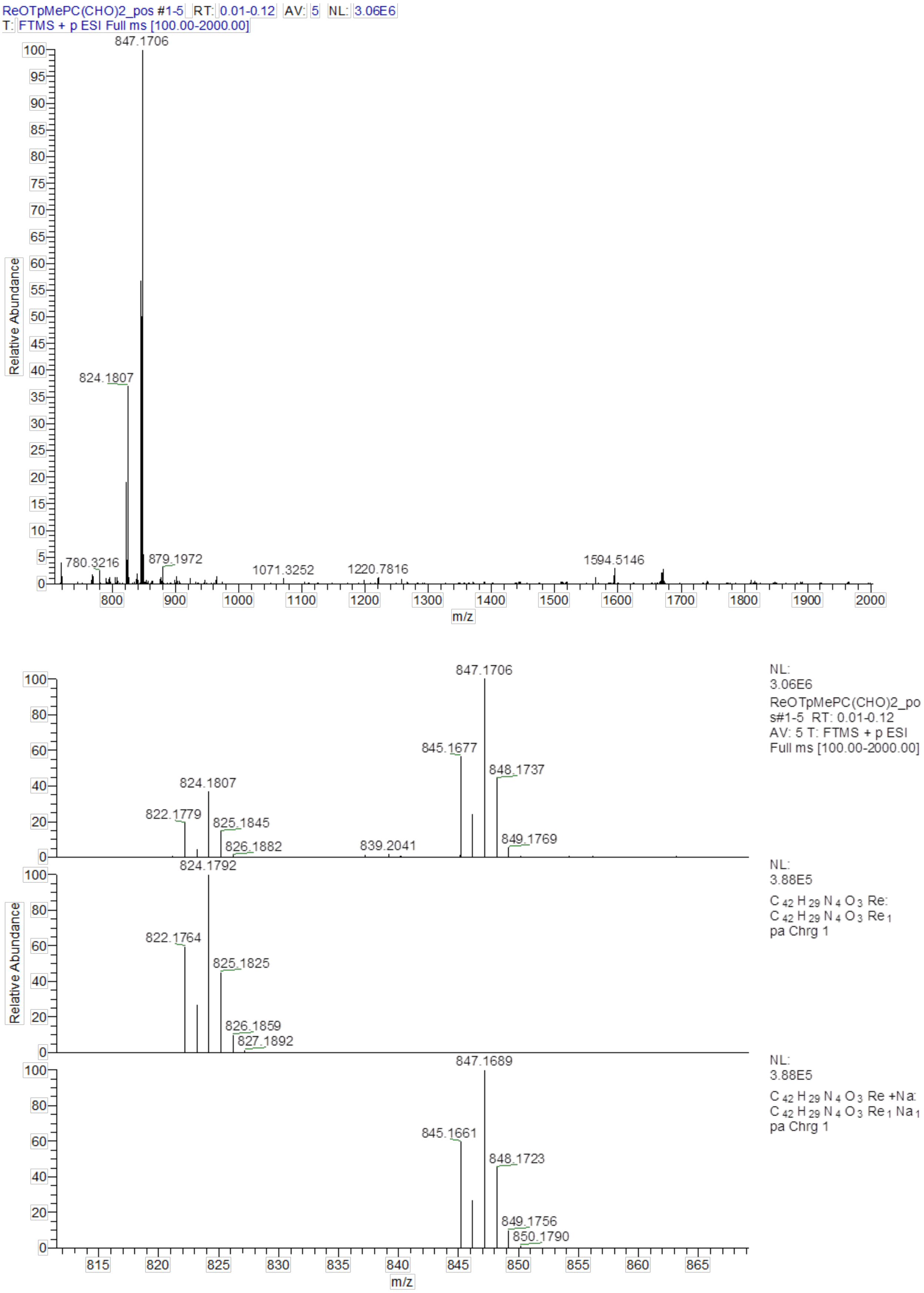

Figure S19. HRMS-ESI mass spectra of Re[T*p*CH$_3$PC-3,17-(CHO)$_2$](O).

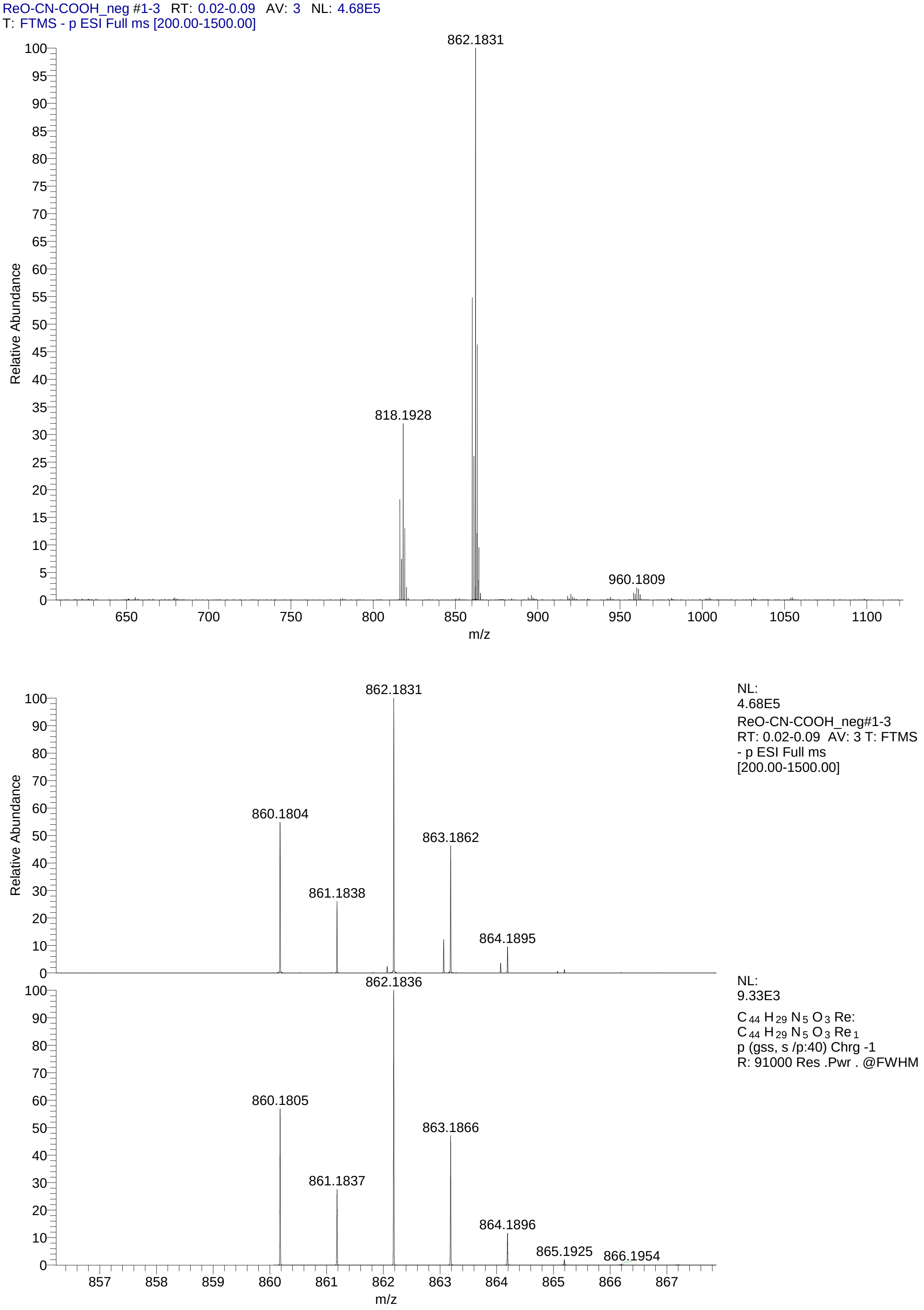

Figure S20. HRMS-ESI mass spectra of Re[T*p*CH$_3$PC-3-CH(CN)COOH](O).

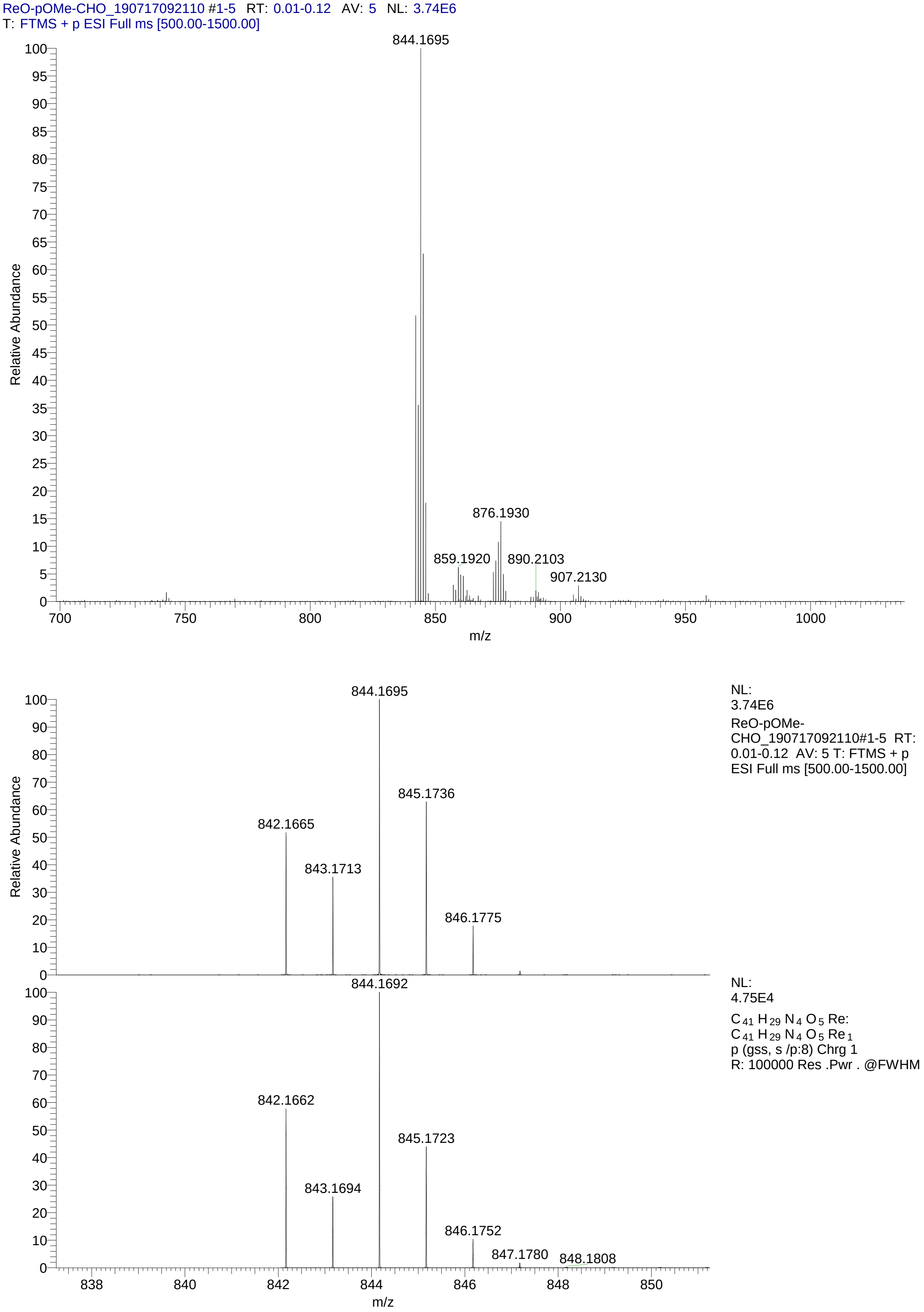

Figure S21. HRMS-ESI mass spectra of Re[T*p*OCH$_3$PC-3-CHO](O).

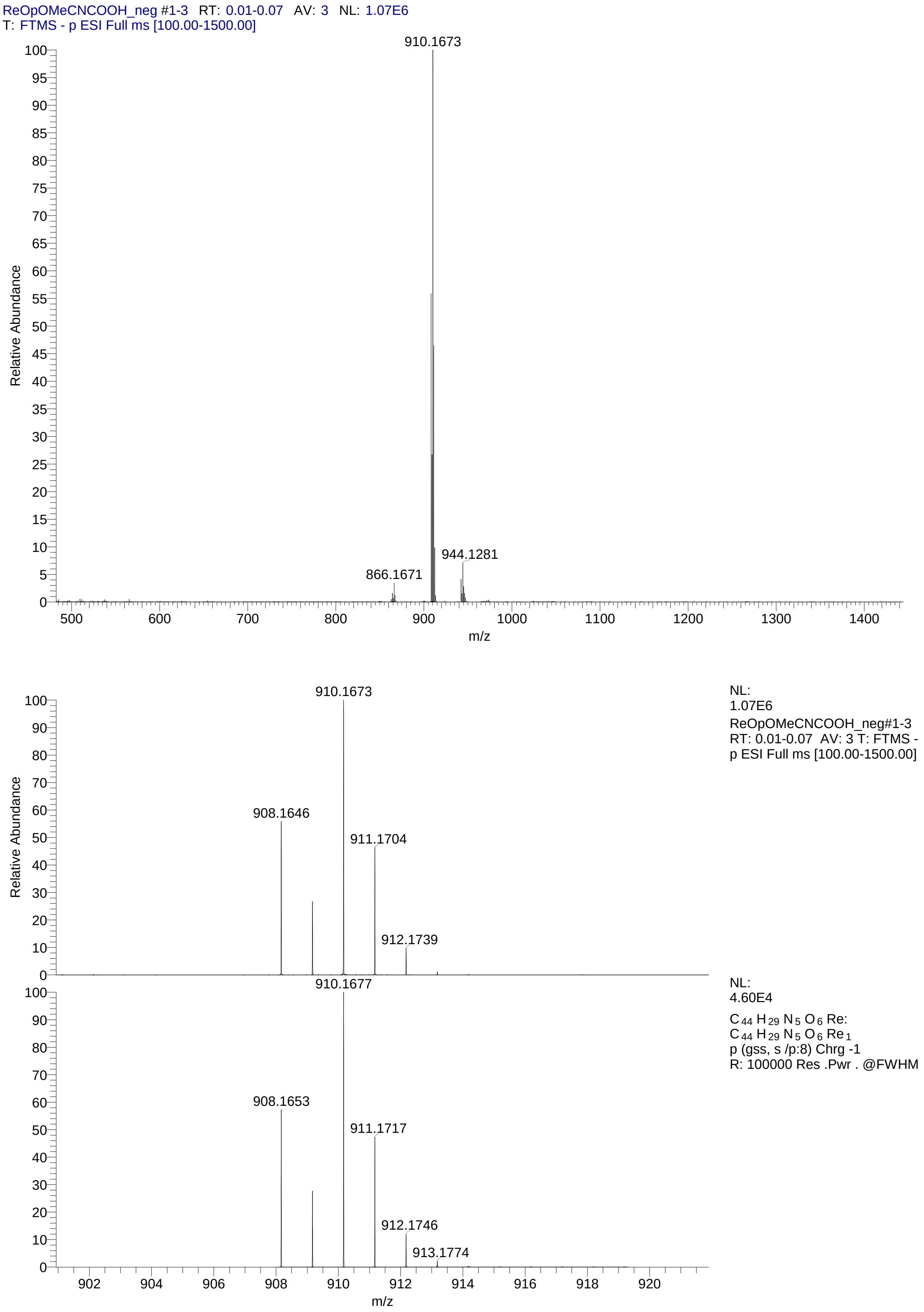

Figure S22. HRMS-ESI mass spectra of Re[T*p*OCH$_3$PC-3-CH(CN)COOH](O).

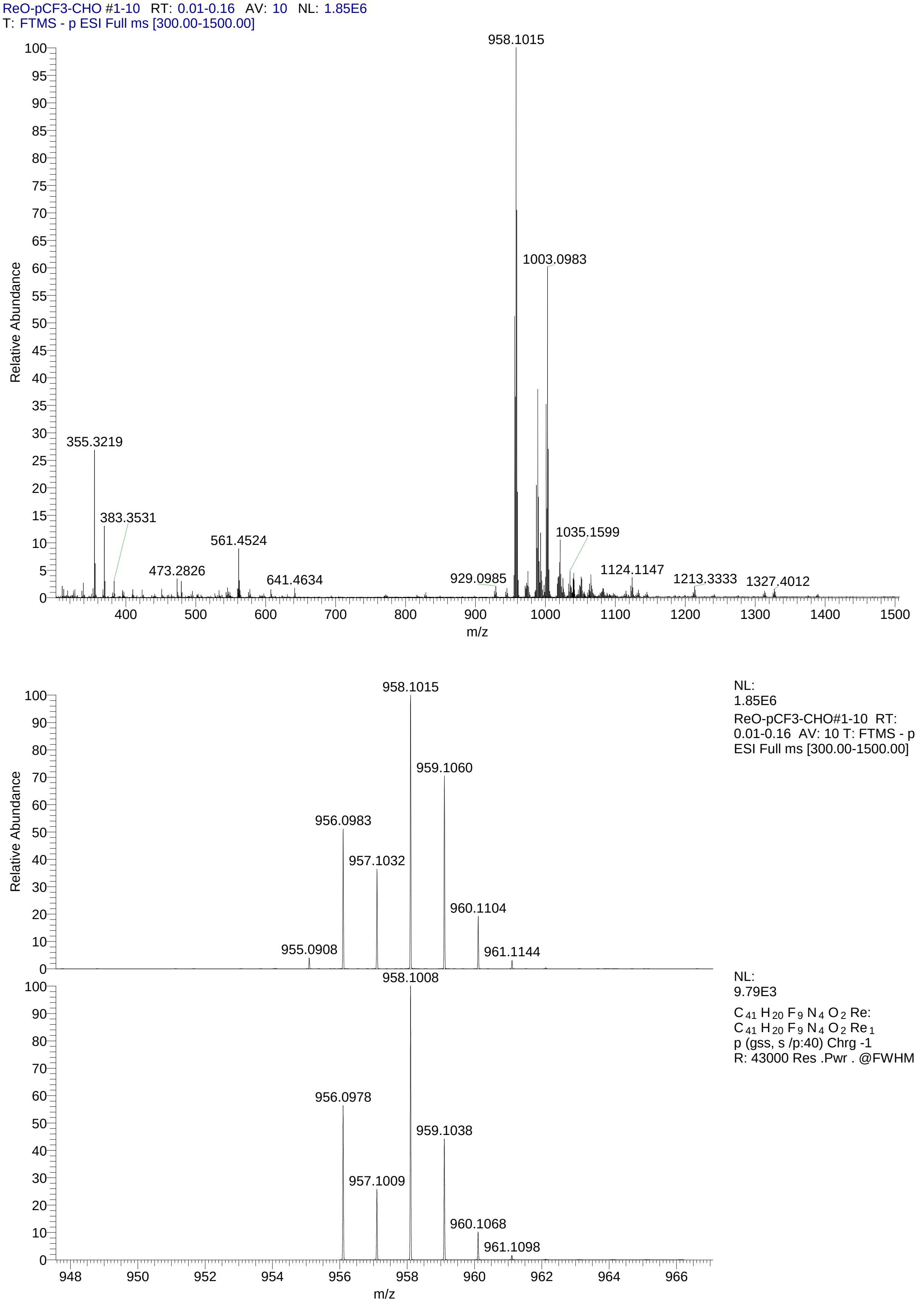

Figure S23. HRMS-ESI mass spectra of Re[T*p*CF$_3$PC-3-CHO](O).

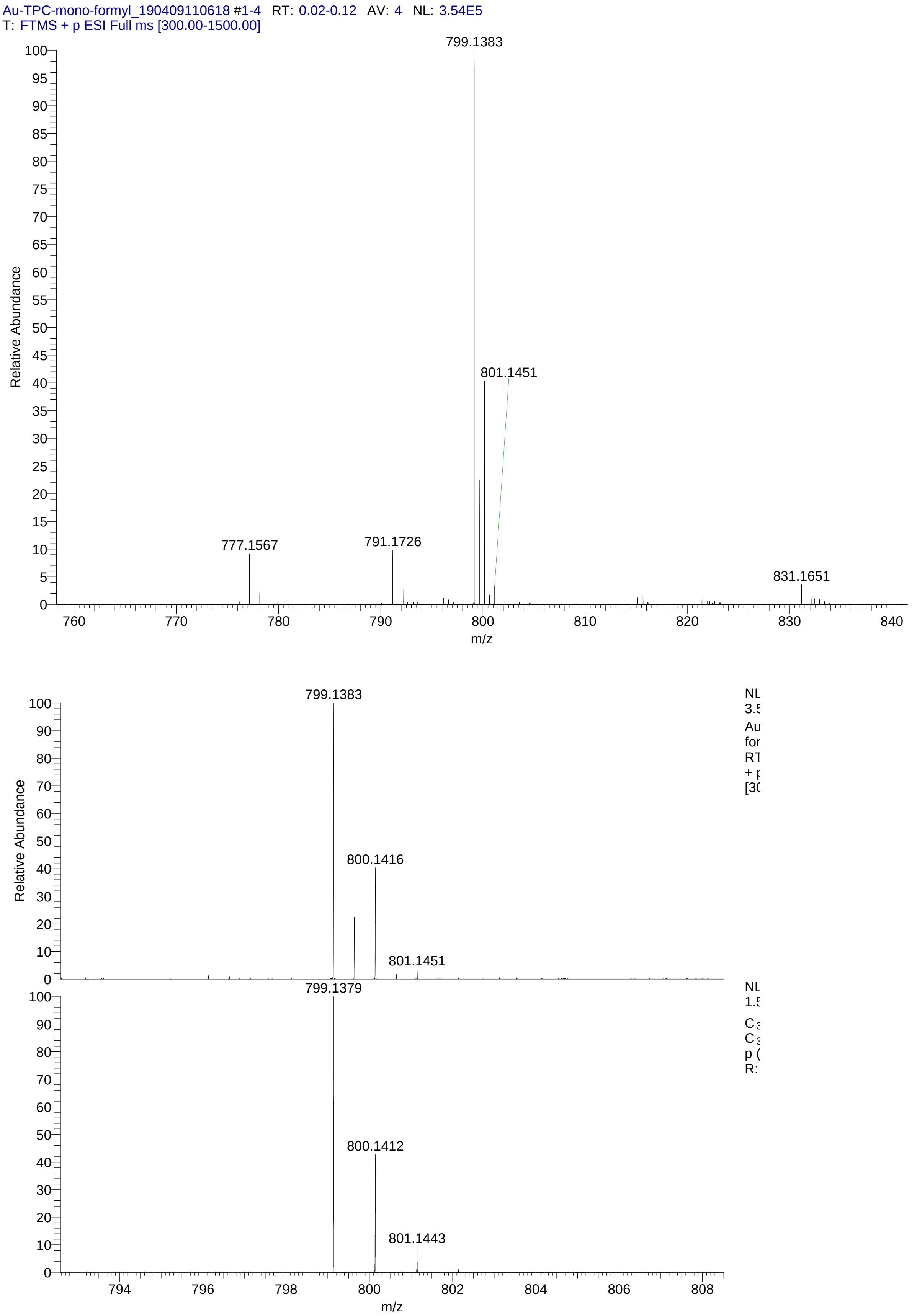

Figure S24. HRMS-ESI mass spectrum of Au[TPC-3,17-(CHO)$_2$].

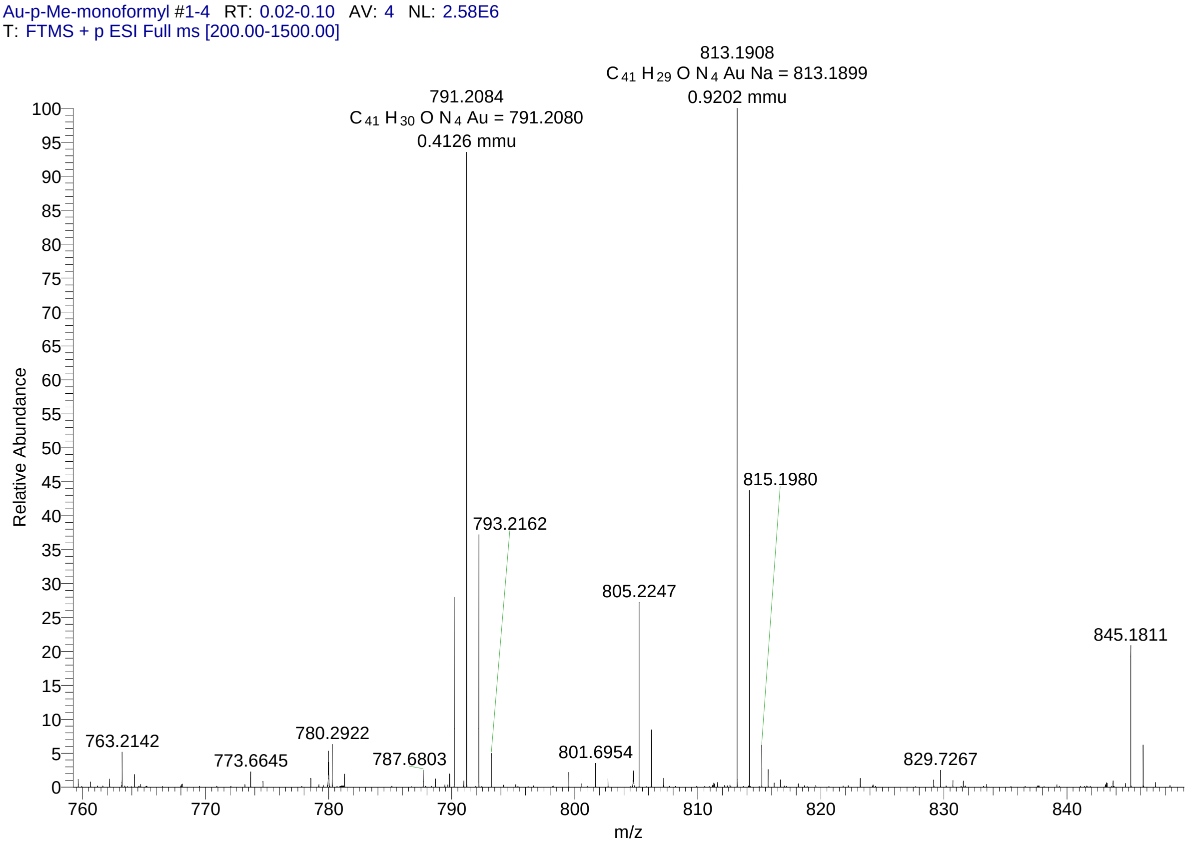

Figure S25. HRMS-ESI mass spectrum of Au[T*p*CH$_3$PC-3-CHO].

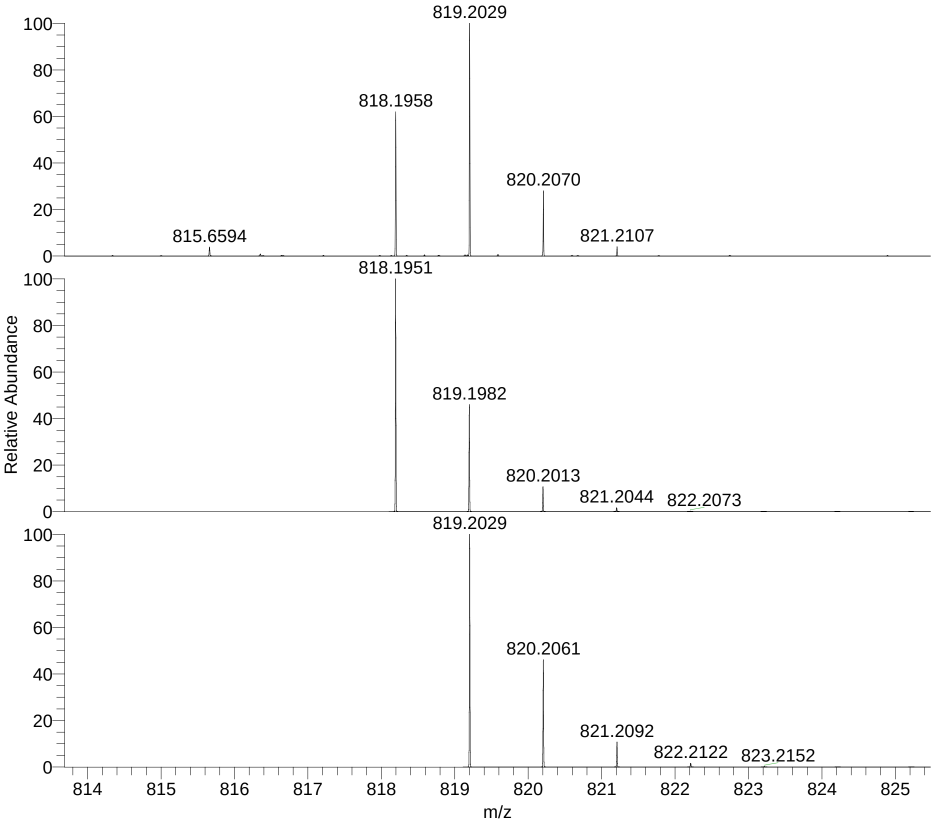

Figure S26. HRMS-ESI mass spectrum of Au[T*p*CH$_3$PC-3,17-(CHO)$_2$].

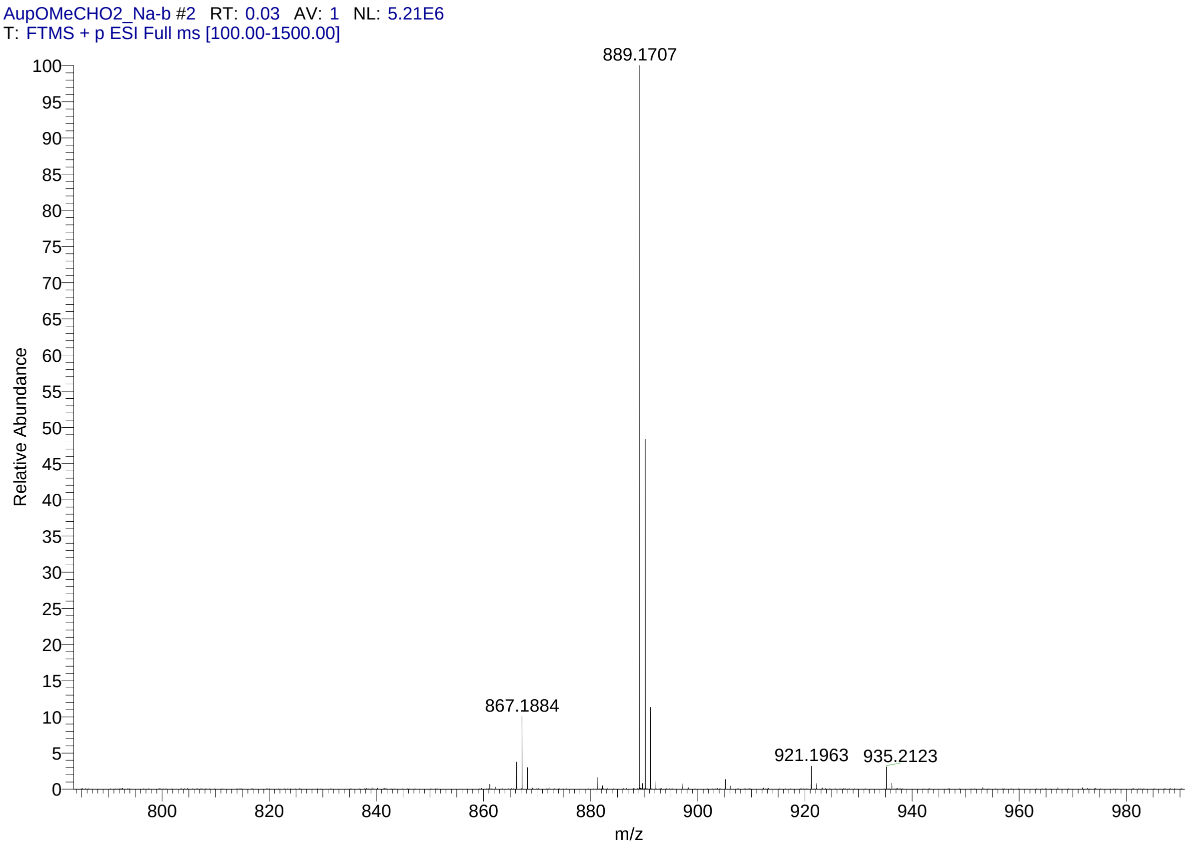

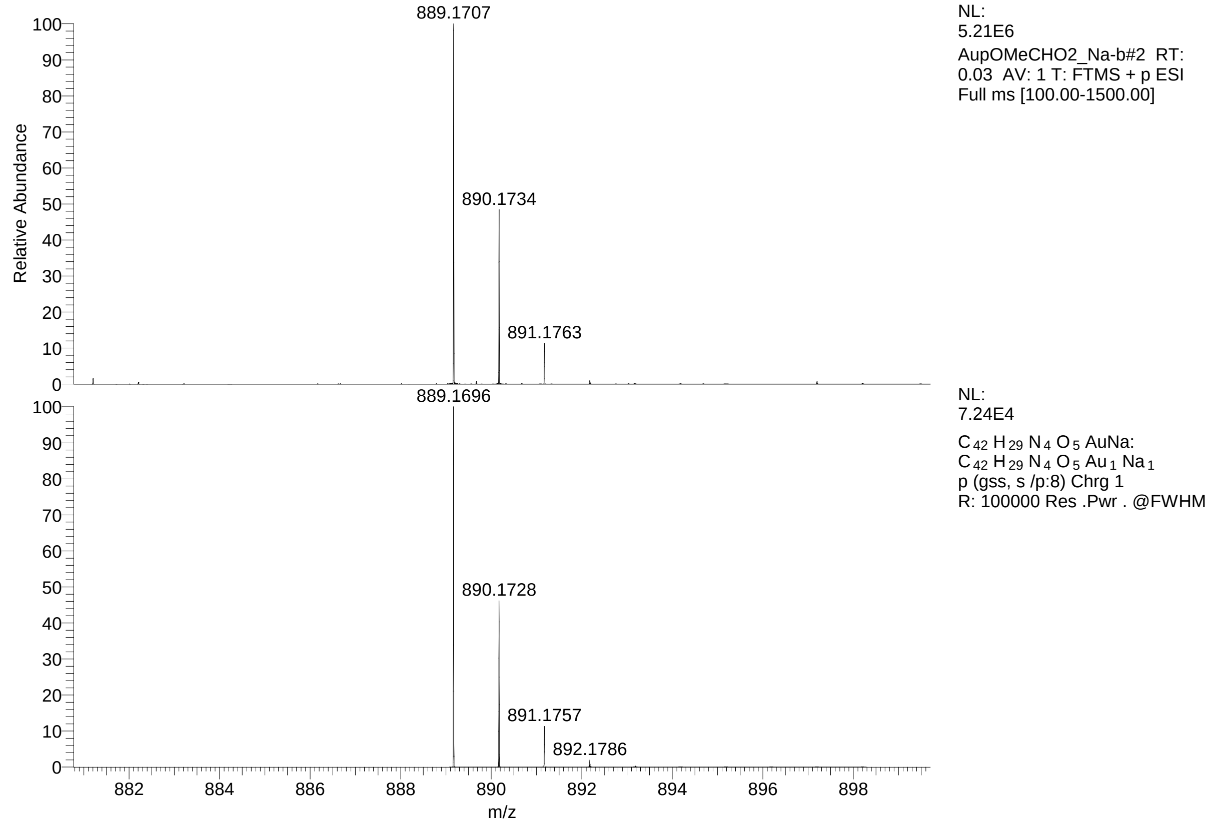

Figure S27. HRMS-ESI mass spectrum of Au[T*p*OCH$_3$PC-3,17-(CHO)$_2$].

C. ^{1}H NMR spectra

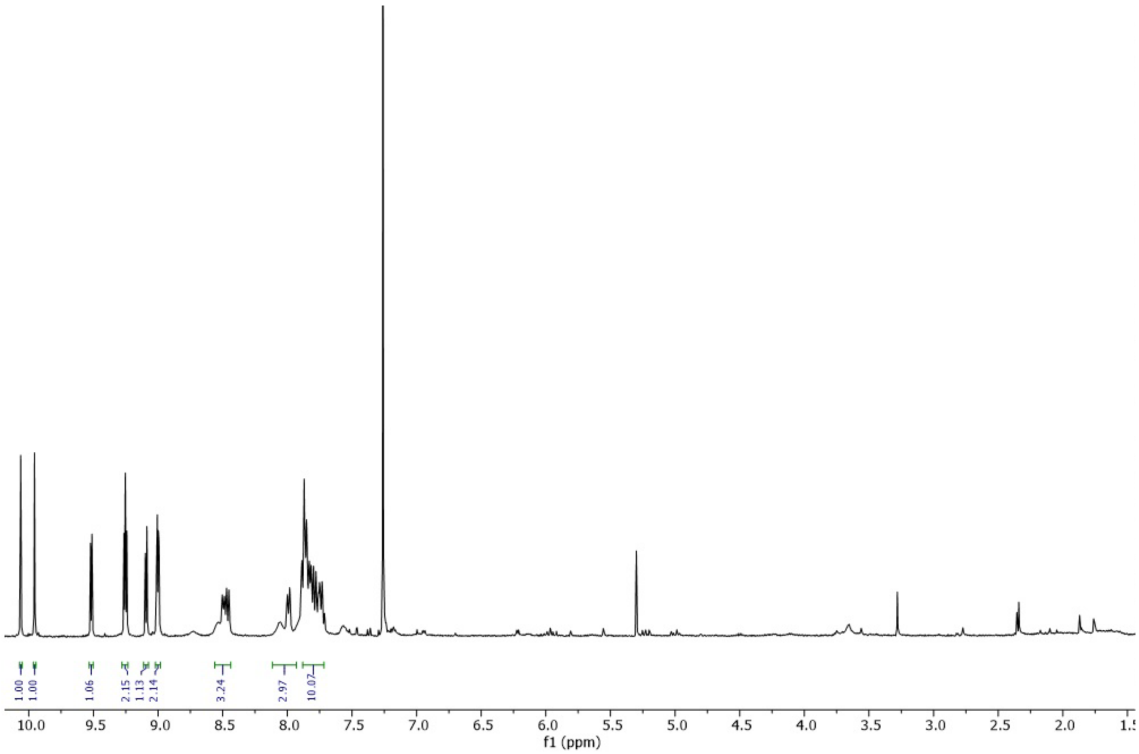

Figure S28. ^{1}H NMR spectrum of Re[TPC-3-CHO](O) at -20°C.

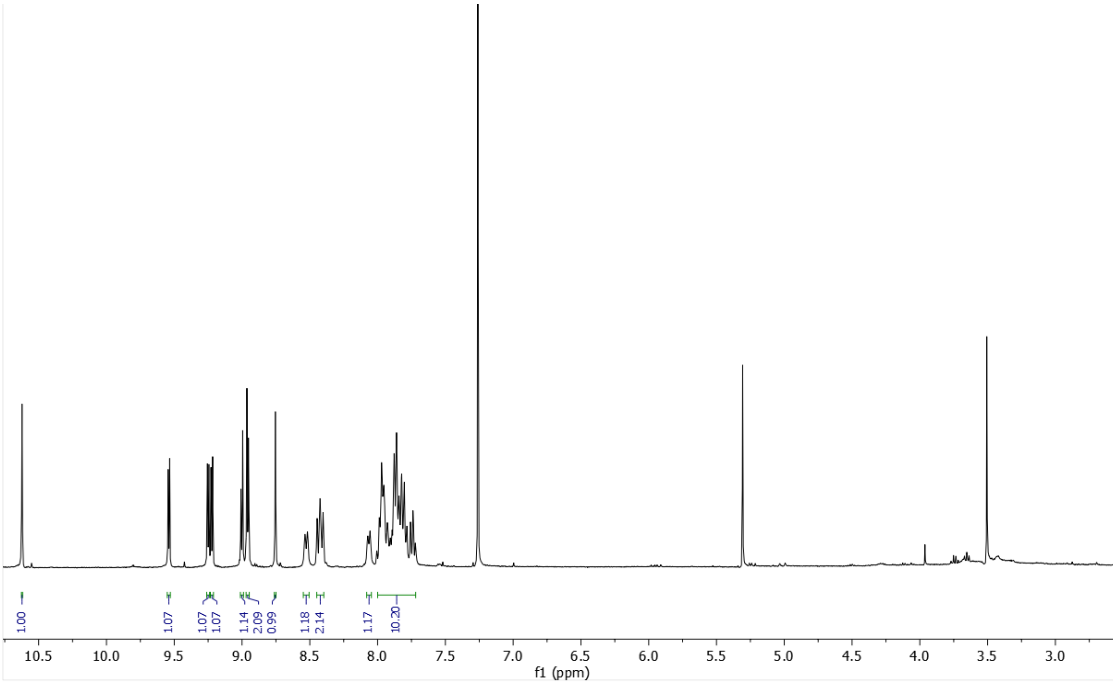

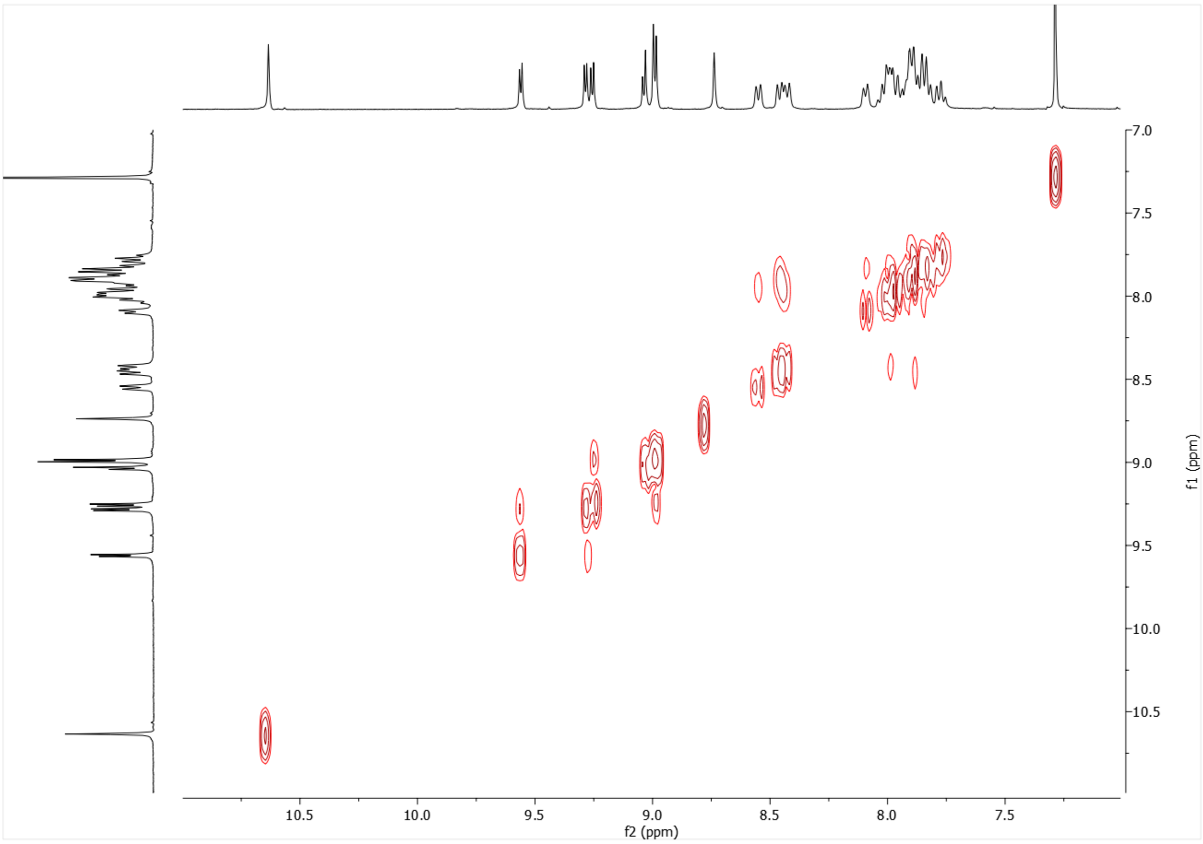

Figure S29. ^{1}H NMR and ^{1}H—^{1}H COSY spectra of Re[TPC-3-CH(CN)COOH](O) at -20°C.

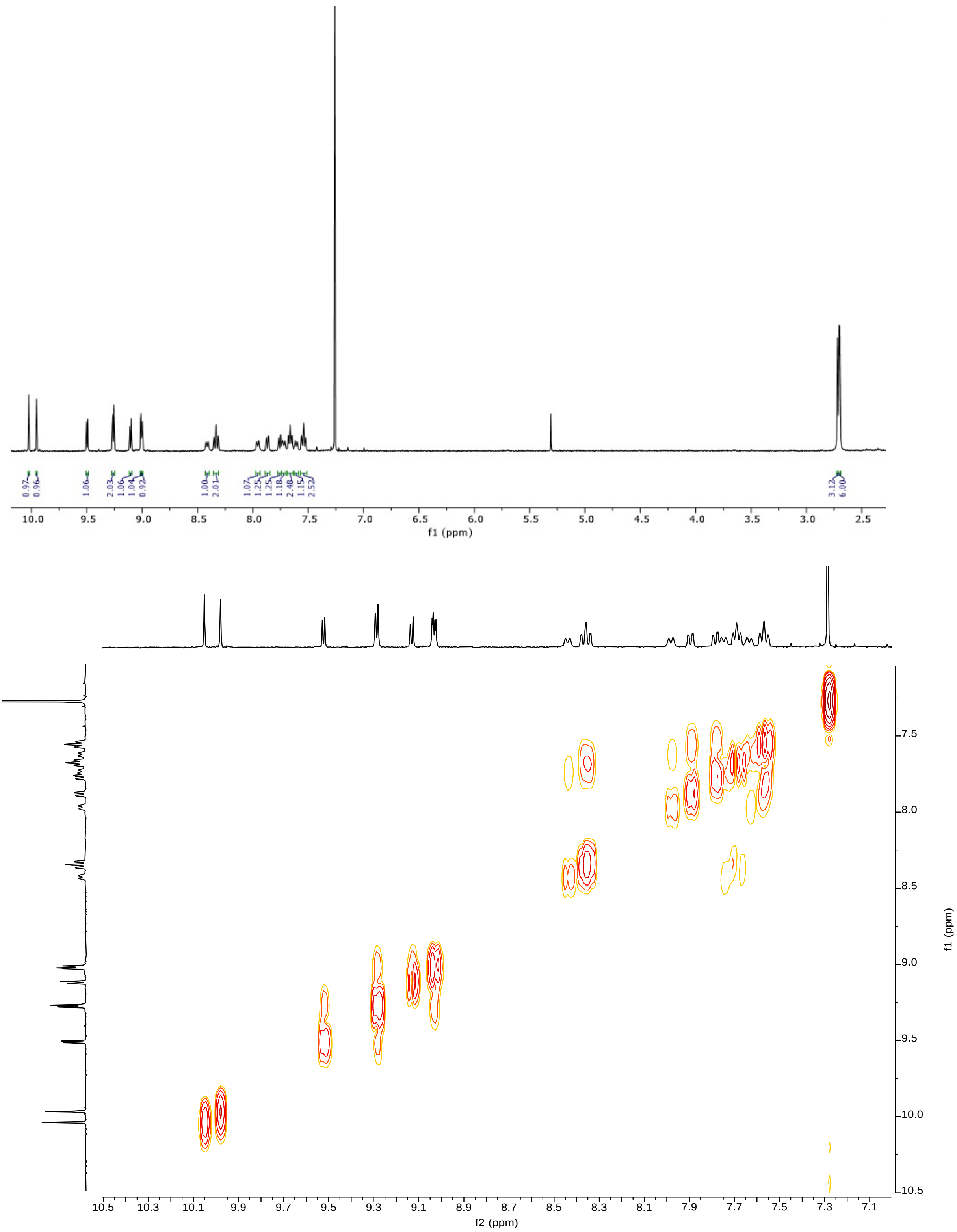

Figure S30. ^{1}H NMR and ^{1}H—^{1}H COSY spectrum of Re[T*p*CH$_3$PC-3-CHO](O) at -20°C.

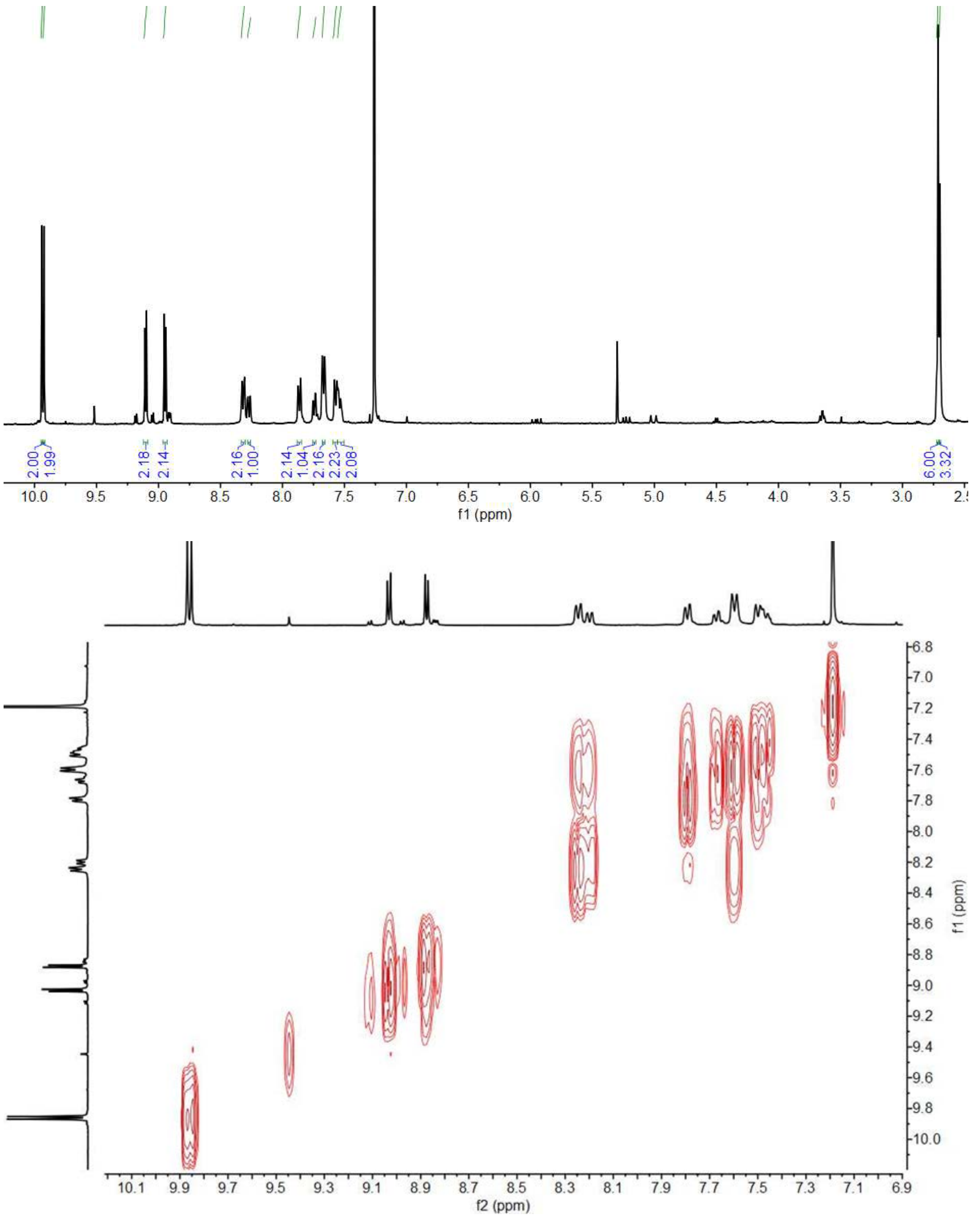

Figure S31. ^{1}H NMR and ^{1}H—^{1}H COSY spectra of Re[T*p*CH$_3$PC-3,17-(CHO)$_2$](O) at -20°C.

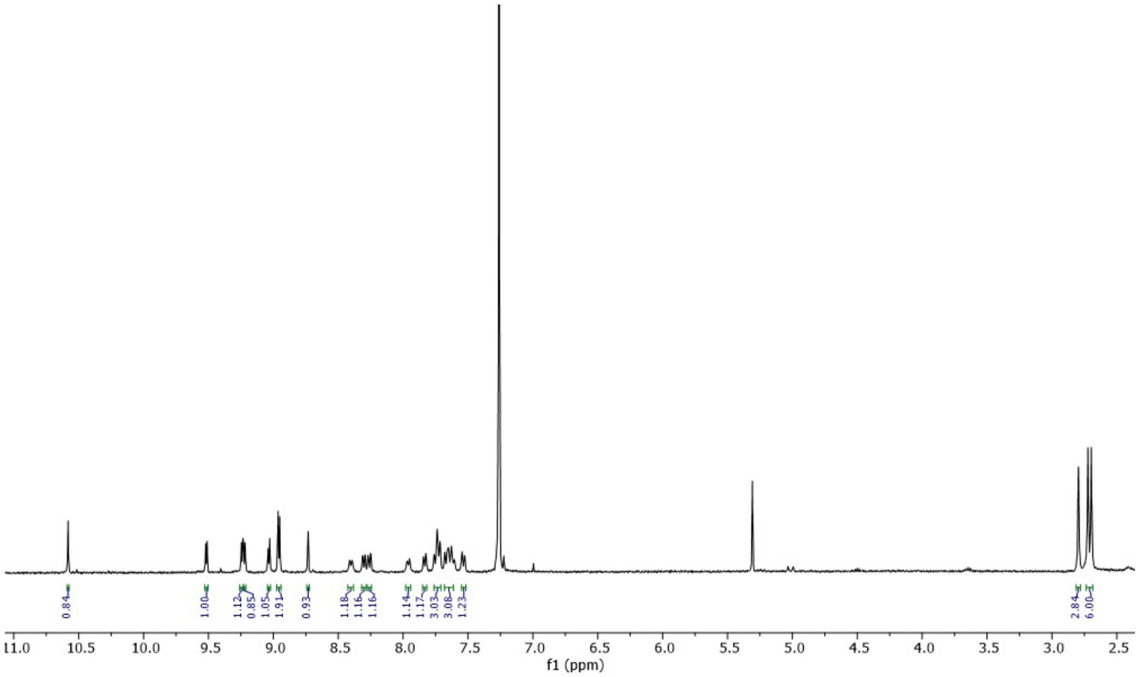

Figure S32. ^{1}H NMR spectrum of Re[T*p*CH_3PC-3-CH(CN)COOH](O) in $CDCl_3$ at -20°C.

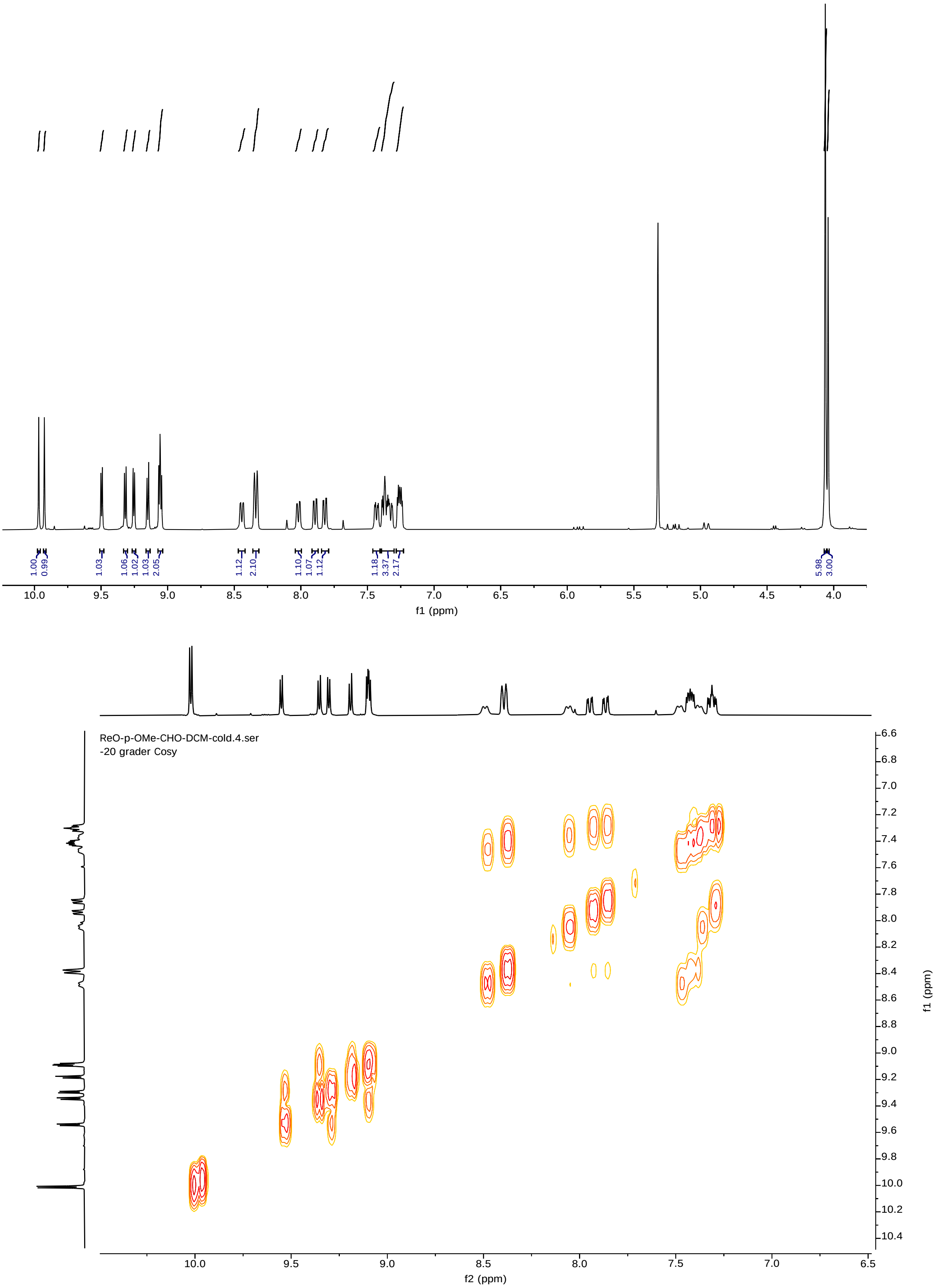

Figure S33. ^{1}H NMR and ^{1}H—^{1}H COSY spectra of Re[T*p*OCH$_3$PC-3-CHO](O) in CDCl$_3$ at -20°C.

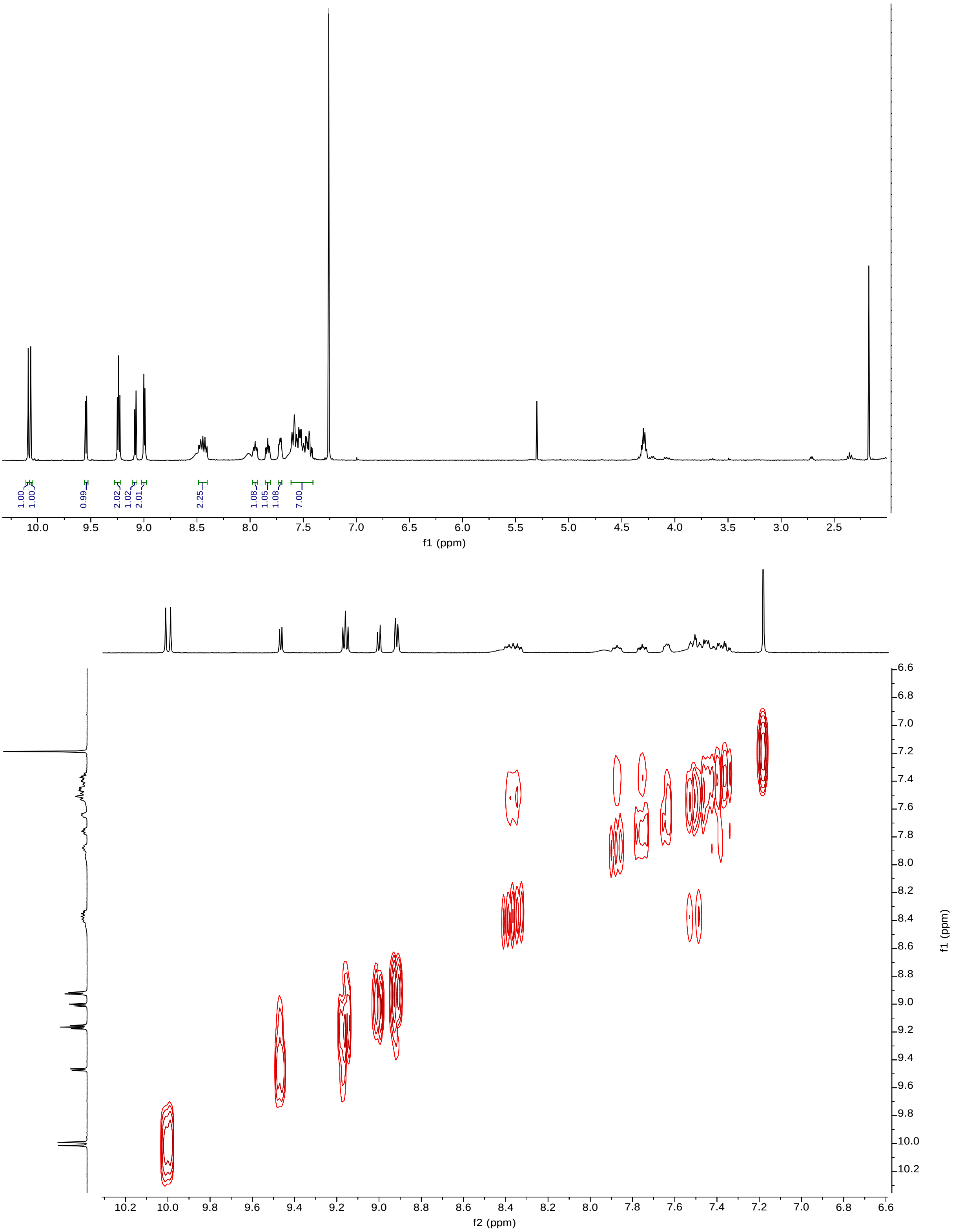

Figure S34. ^{1}H NMR and ^{1}H—^{1}H COSY spectra of Re[T*p*FPC-3-CHO]O in CDCl$_3$ at 20°C.

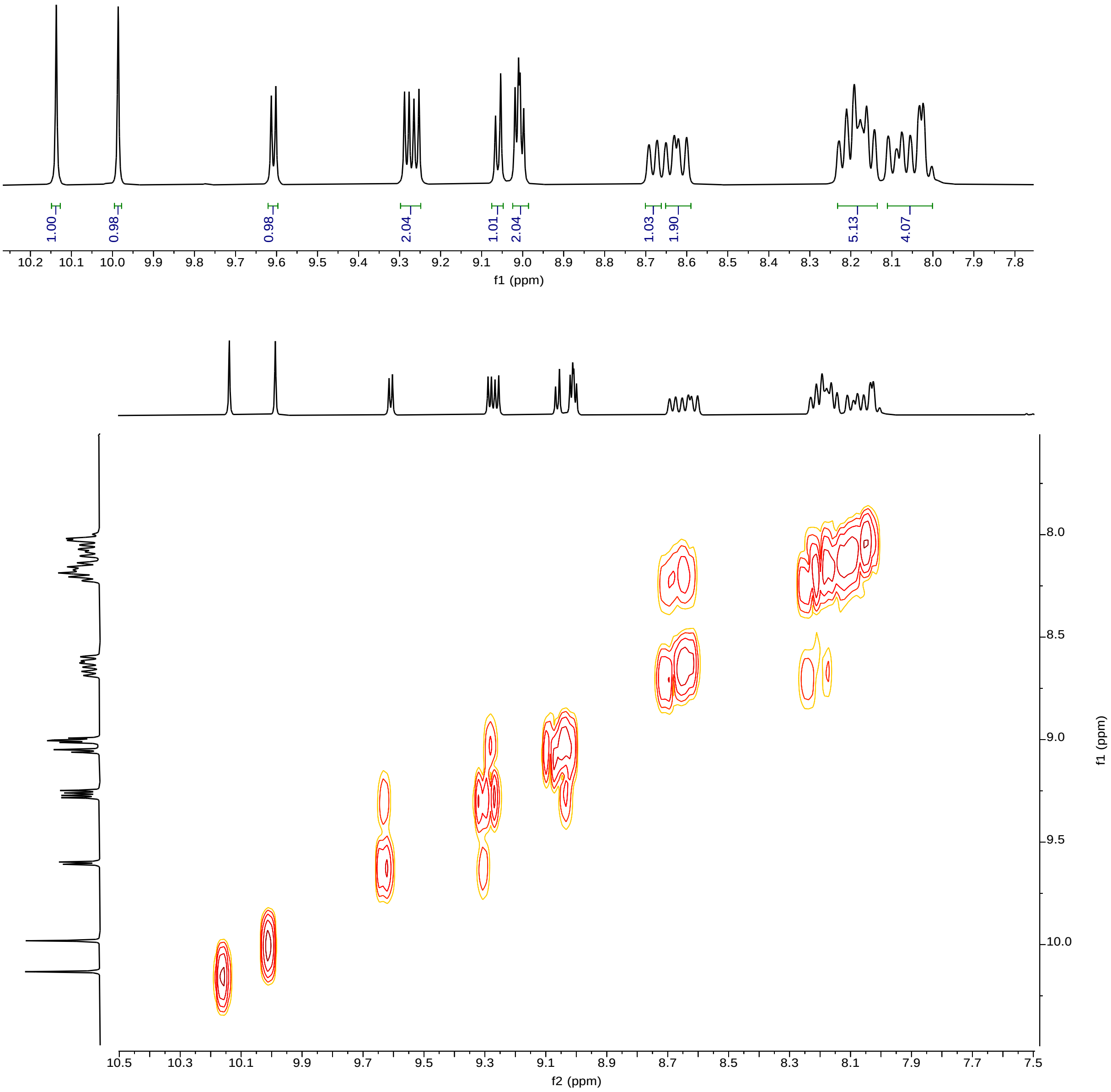

Figure S35. ^{1}H NMR and ^{1}H—^{1}H COSY spectra of Re[T*p*CF$_3$PC-3-CHO]O in CDCl$_3$ at -20°C.

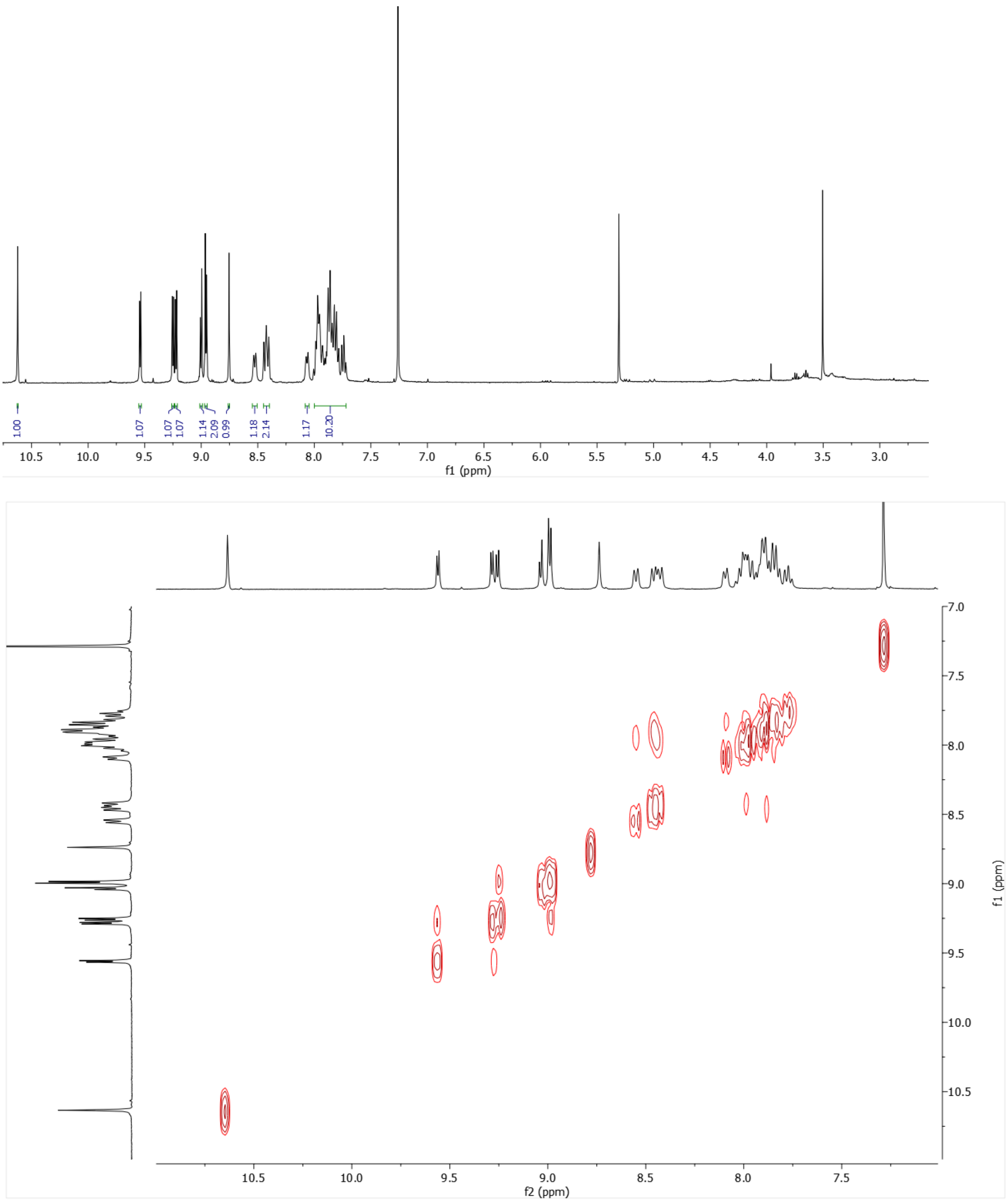

Figure S36. ^{1}H NMR and ^{1}H—^{1}H COSY spectra of Re[TPC-3-CH(CN)COOH](O) in $CDCl_3$ at -20°C.

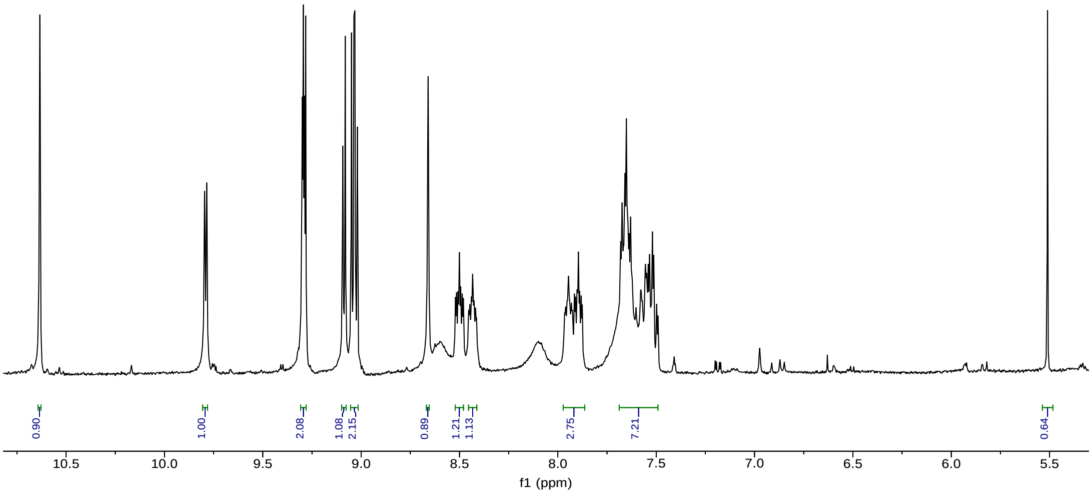

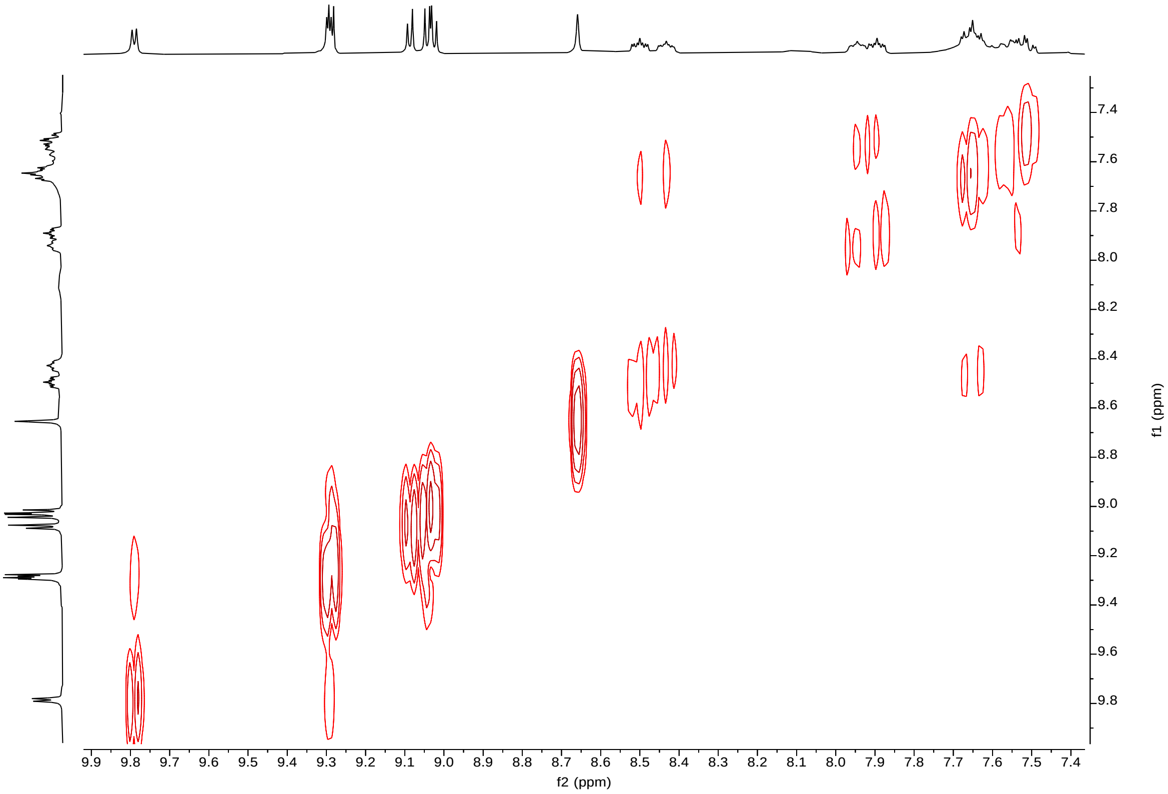

Figure S37. ^{1}H NMR and ^{1}H—^{1}H COSY spectra of Re[T*p*FPC-3-(CN)COOH](O) in tetrahydrofuran-d_8 at 20°C.

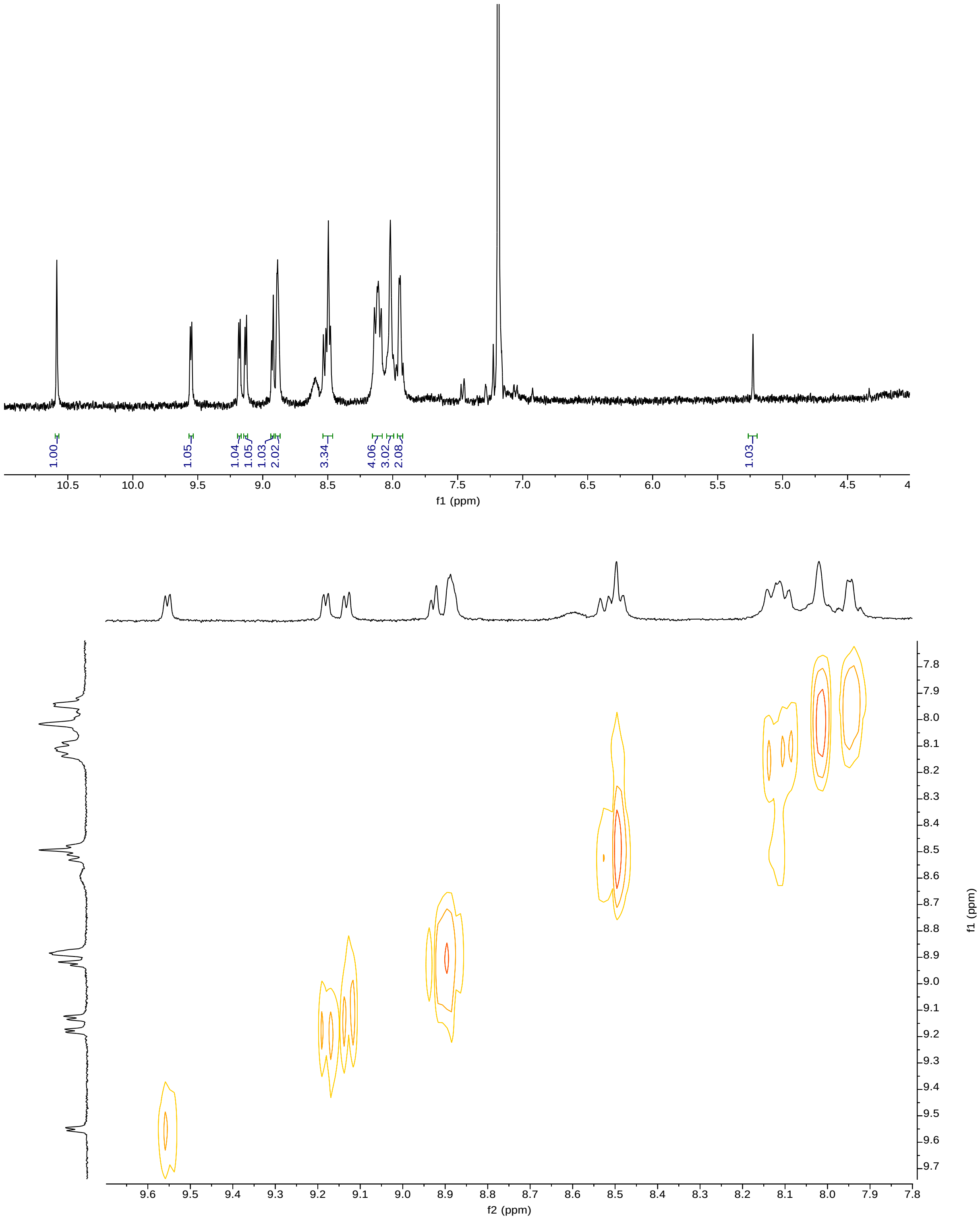

Figure S38. ^{1}H NMR and ^{1}H—^{1}H COSY spectra of Re[T*p*CF$_3$PC-3-(CN)COOH](O) in CDCl$_3$ at 20°C.

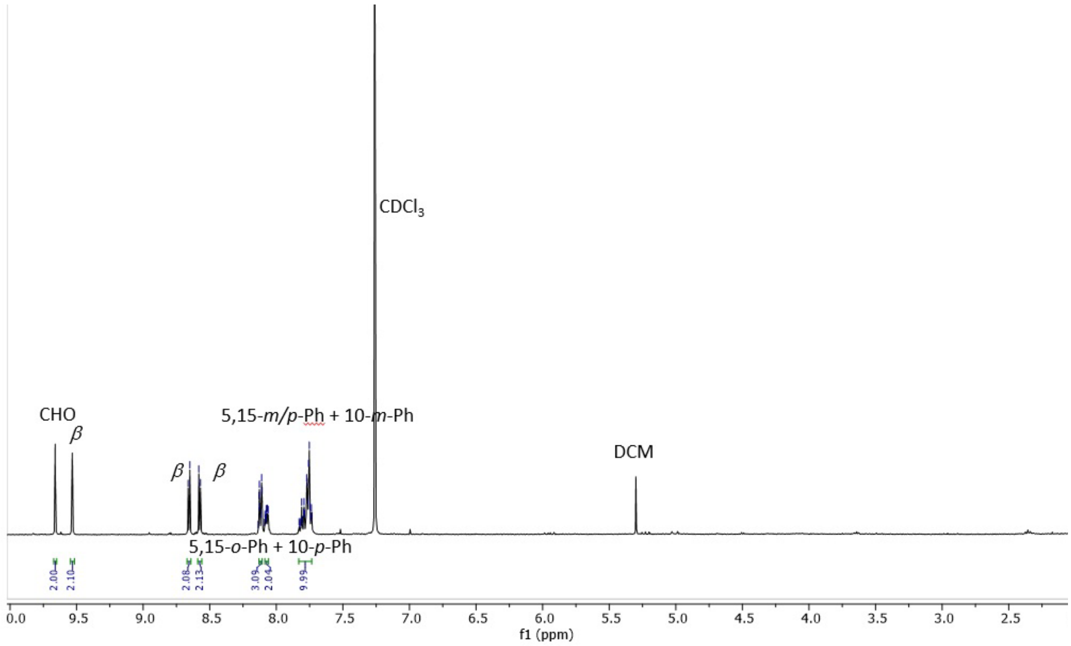

Figure S39. ^{1}H NMR spectrum of Au[TPC-3,17-(CHO)$_2$] in CDCl$_3$ at -20°C.

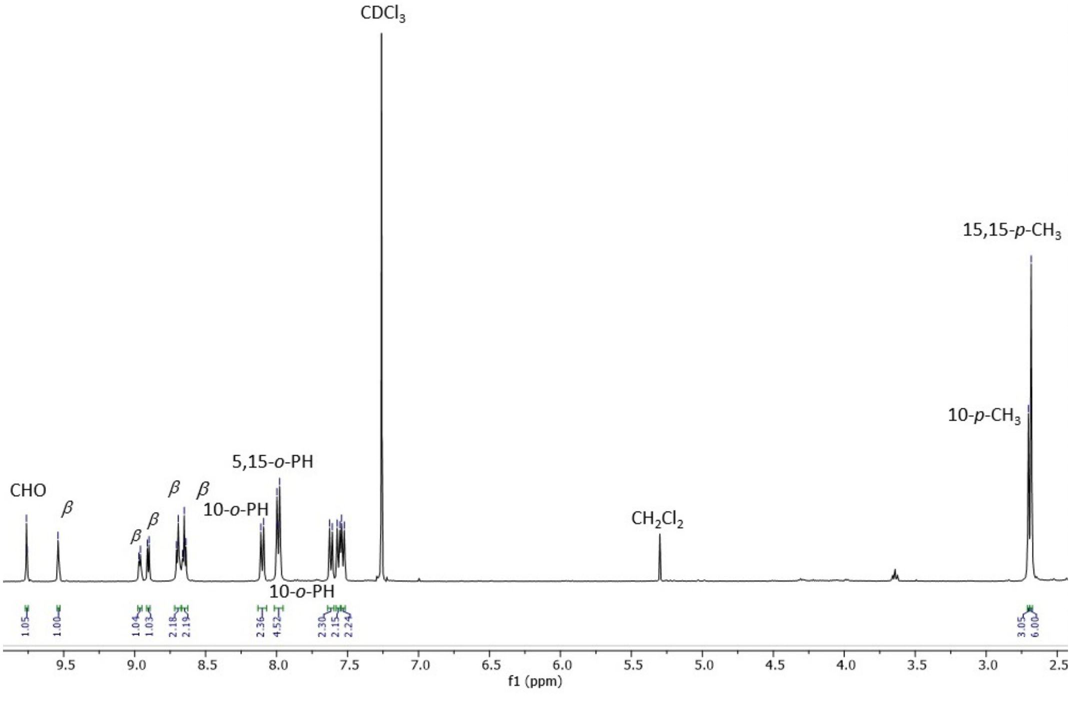

Figure S40. ^{1}H NMR spectrum of Au[T*p*CH$_3$PC-3-CHO] in CDCl$_3$ at -20°C.

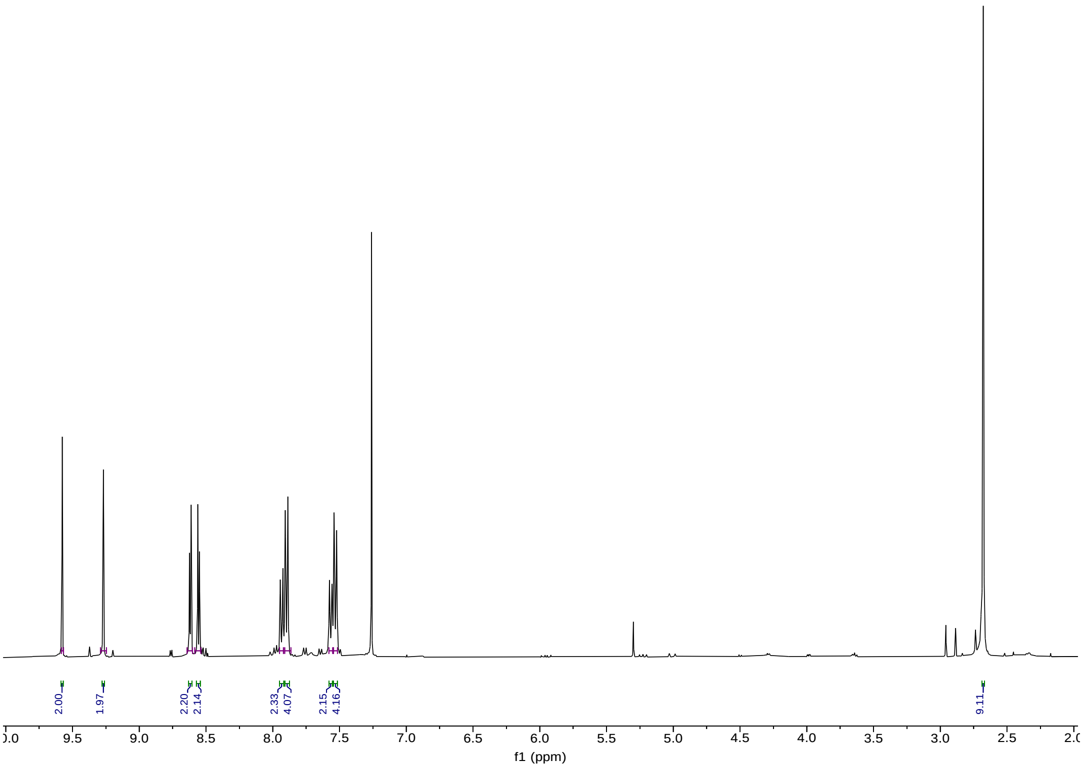

Figure S41. ^{1}H NMR spectrum of Au[T*p*CH_3PC-3,17-$(CHO)_2$] in $CDCl_3$ at -20°C.

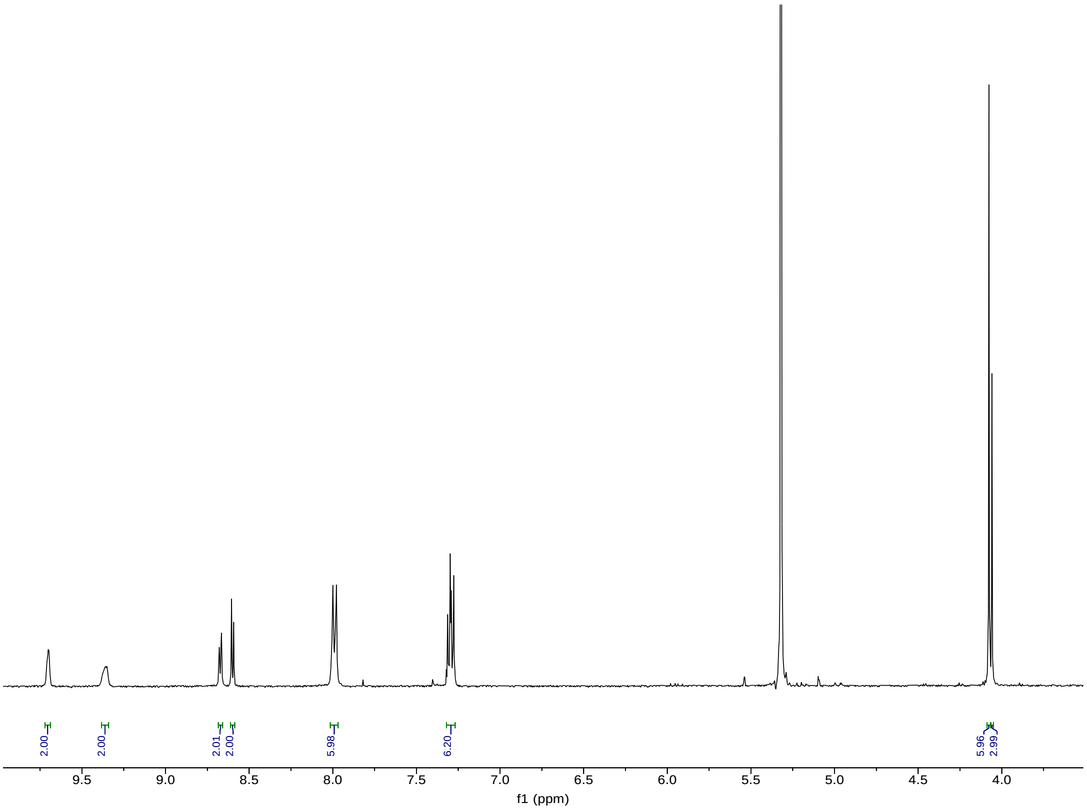

Figure S42. ^{1}H NMR spectrum of Au[T*p*OCH_3PC-3,17-$(CHO)_2$] in $CDCl_3$ at -20°C.

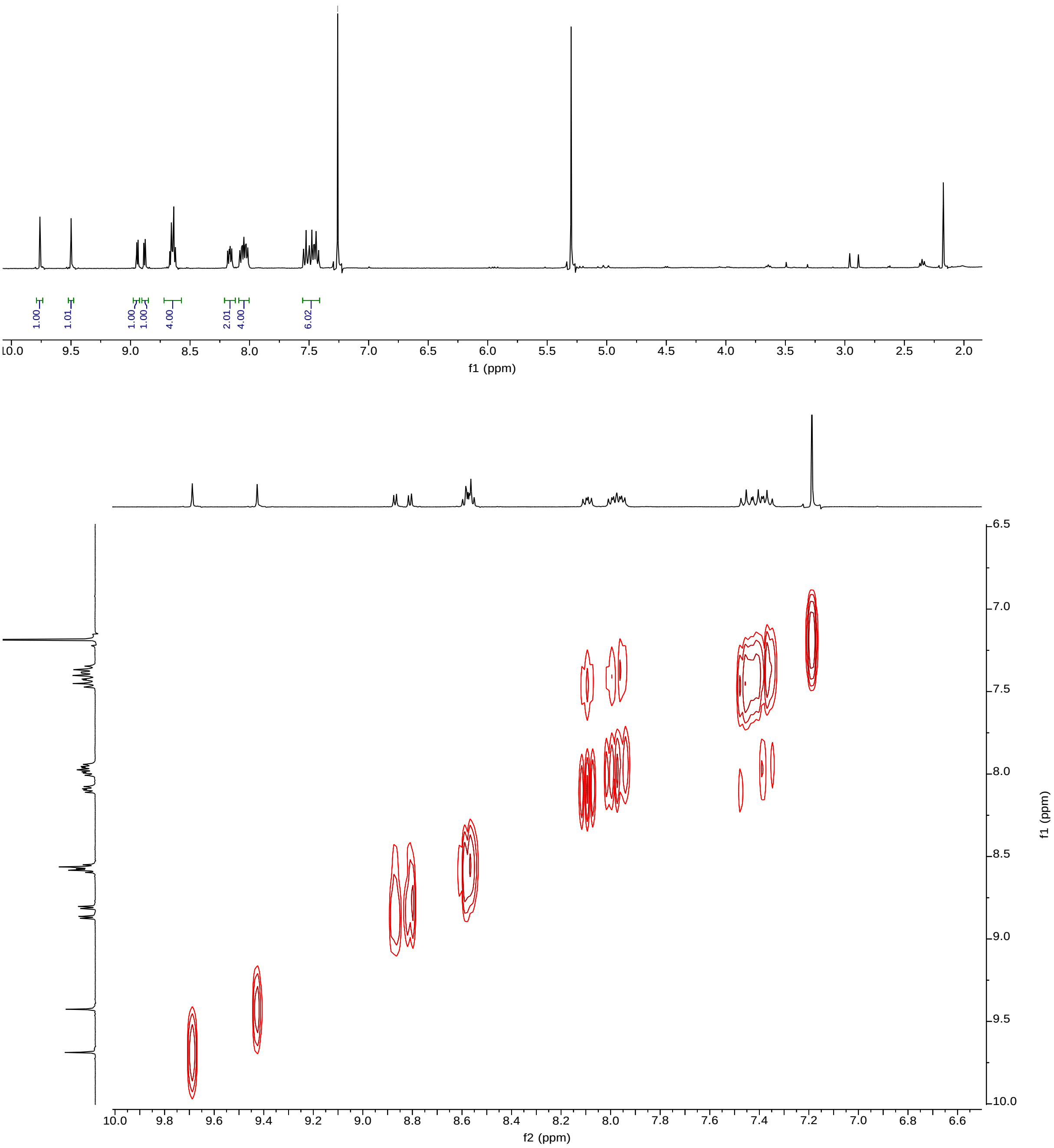

Figure S193. ^{1}H NMR and ^{1}H—^{1}H COSY spectra of Au[T*p*FPC-3-CHO] in $CDCl_3$ at 20°C.

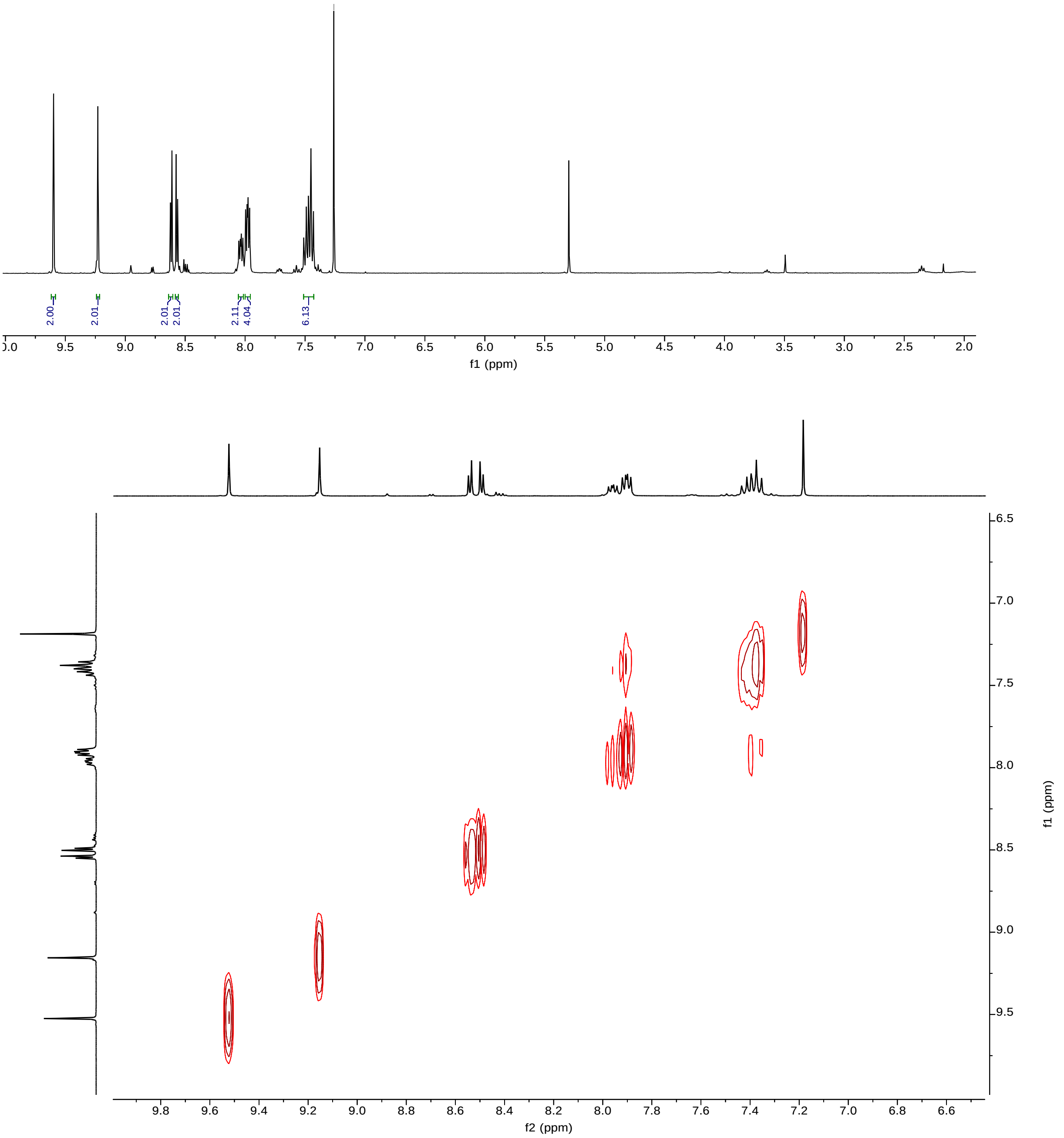

Figure S44. ^{1}H NMR and ^{1}H—^{1}H COSY spectra of Au[T*p*FPC-3,17-(CHO)$_2$] in CDCl$_3$ at 20°C.

D. Partial characterization of minor products

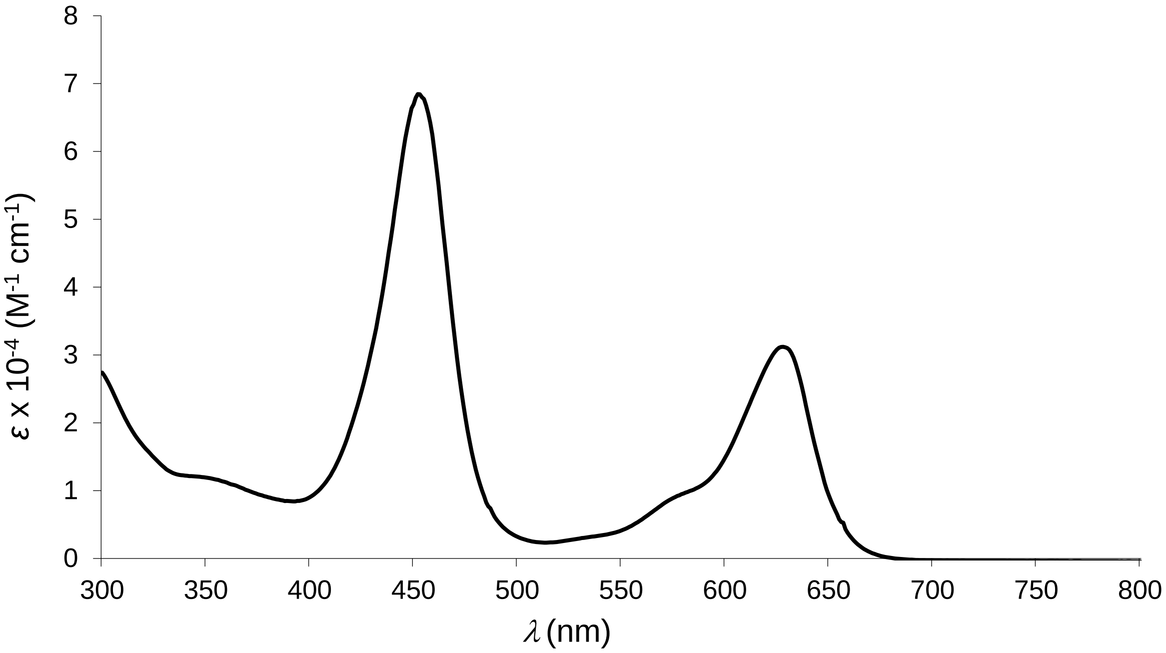

Figure S45. UV-vis spectrum of Re[T*p*CH_3PC-3,17-$(CHO)_2$] in dichloromethane.

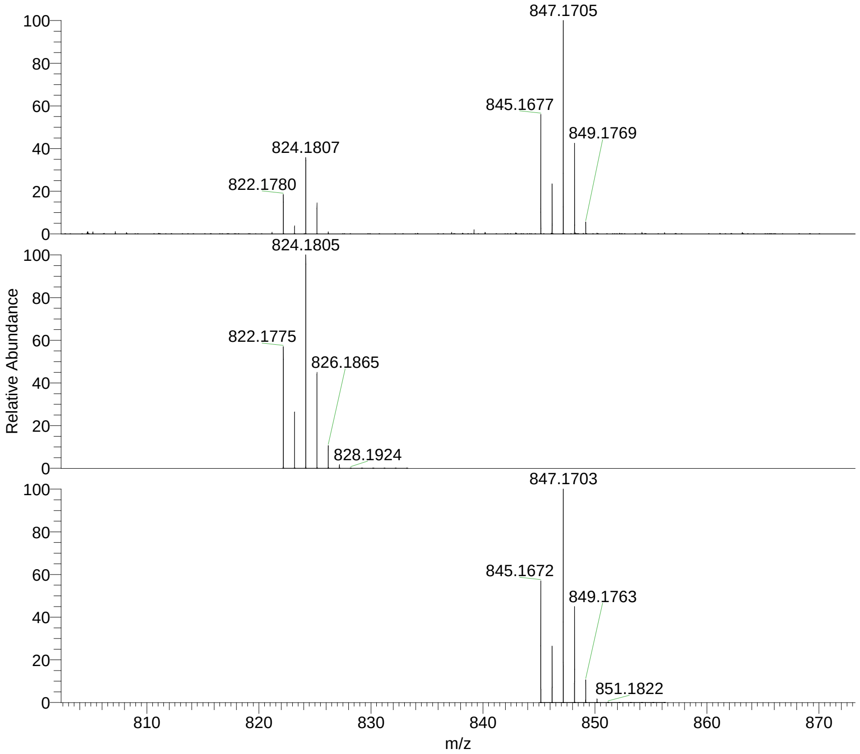

Figure S46. ESI mass spectrum of Re[T*p*CH_3PC-3,17-$(CHO)_2$](O).

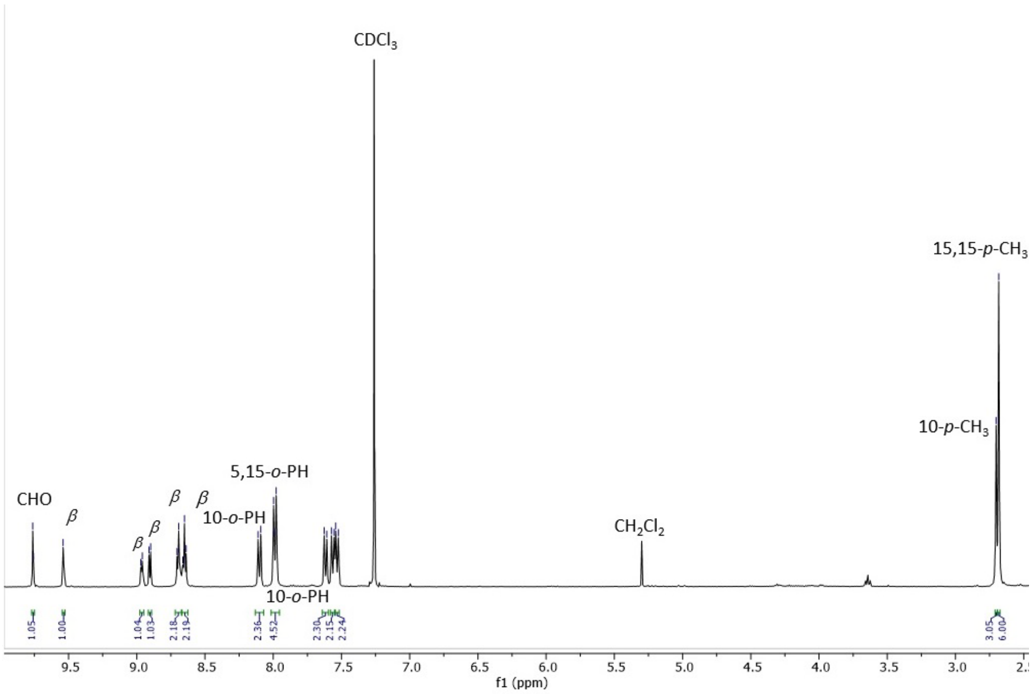

Figure S47. ^{1}H NMR spectrum of Au[T*p*CH_3PC-3-CHO] in $CDCl_3$ at -20°C.

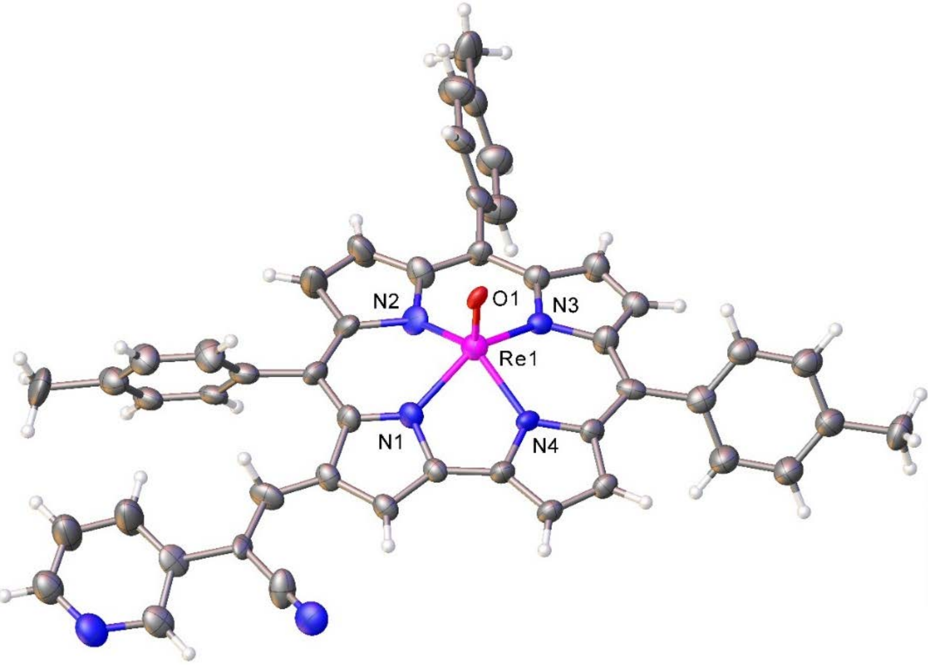

Figure S48. Thermal ellipsoid plot for the Knoevenagel condensate of Re[T*p*CH_3PC-3-CHO] with pyridin-3-ylacetonitrile. Selected distances (Å): Re1-N1 2.003(18), Re1-N2 1.87(2), Re1-N3 1.973(18), Re1-N4 1.956(16). Re(1)-N(3) 1.973(18) Re(1)-N(4) 1.956(16). The relatively poor quality of the structure implies that it should be only as proof of connectivity.

Paper F

ACS OMEGA

http://pubs.acs.org/journal/acsodf

Article

Simple, Axial Ligand-Mediated Route to Water-Soluble Iridium Corroles

Ivar K. Thomassen, Daniel Rasmussen, Rune F. Einrem, and Abhik Ghosh*

Cite This: *ACS Omega* 2021, 6, 16683−16687

Read Online

ABSTRACT: The synthesis and purification of water-soluble porphyrin-type compounds for photodynamic therapy and other medical applications is often a tedious exercise. Here, we have investigated the simple stratagem of adding a water-soluble axial ligand to the standard protocol for iridium insertion into simple *meso*-triarylcorroles. Early results showed that six-coordinate Ir[T*p*XPC](dna)$_2$ derivatives, in which T*p*XPC = tris(*para*-X-phenyl)corrole (X = CF_3, CN, H, and OMe) and dna = dinicotinic acid, are highly water-soluble. In the end, however, all axially nitrogen-ligated complexes proved unstable with respect to chromatographic purification and storage. Five-coordinate water-soluble phosphine adducts, fortunately, proved a great improvement. From the point of view of ease of purification and storage, the best products proved to be Ir[T*p*XPC](L), where X = CF_3 and OMe and L = tris(2-carboxyethyl)phosphine (tcep) and trisodium tris(3-sulfonatophenyl)phosphine (tppts); carefully optimized synthetic protocols are presented for these four compounds.

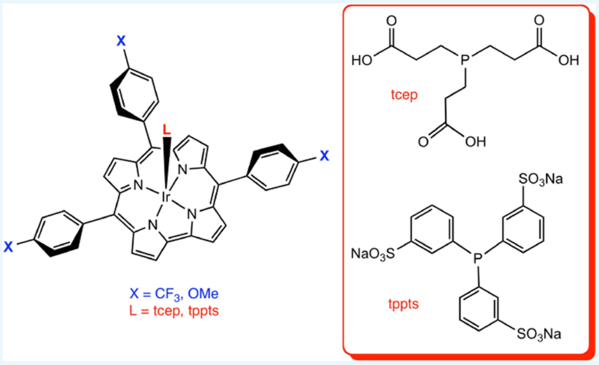

INTRODUCTION

Porphyrin-type compounds have long been a cornerstone of photodynamic therapy.[1−5] Recently, porphyrin analogues such as corroles[6,7] have also proved promising as anticancer compounds.[8,9] Several families of 5d metallocorroles (including ReO,[10] OsN,[11] Ir,[12] Pt,[13] and Au[14−17] corroles) that we and others have studied in recent years are relevant in this connection. Although they were originally of interest primarily as curious, size-mismatched metal−ligand assemblies, their photophysical properties, especially near-infrared (NIR) phosphorescence under ambient conditions, now promise a wide range of practical applications,[18,19] such as in oxygen sensors, photodynamic therapy, and dye-sensitized solar cells and for triplet−triplet annihilation upconversion.[20−28] A number of these applications, especially in the biomedical sphere, require water-soluble derivatives of the complexes, which are typically accessible via cumbersome synthetic and purification steps.[2,29,30] A recent reinvestigation of iridium corroles (in which 4-picolinic acid derivatives were found to be partially water-soluble) suggested that the use of water-soluble axial ligands might afford a simple, one-pot route to water-soluble Ir corroles as a new class of singlet oxygen photosensitizers.[31] The beguilingly simple exercise, however, threw up unexpected challenges. Many of the compounds synthesized proved unstable, decomposing upon chromatographic purification or storage. Here, we detail carefully optimized synthetic protocols for four complexes (Scheme 1) that could be readily purified and stored and are therefore suitable for further investigations of potential applications.

RESULTS AND DISCUSSION

Six different *meso*-tris(*para*-X-phenyl)corrole ligands, H_3[T*p*XPC] (X = NO_2, CF_3, CN, H, Me, and OMe),[32−34] as well as *meso*-tris(pentafluorophenyl)corrole, H_3[TPFPC],[35] were examined throughout as equatorial ligands. For axial ligands, we initially examined five nitrogen ligands—4-picolinic acid (4pa; Figure 1), 3,5-pyridinedicarboxylic acid (also known as dinicotinic acid, dna), nitrilotriacetic acid (nta), 5-hydroxypyridine-3-carboxylic acid, and 4-pyridylboronic acid. Four different stationary phases were used for chromatographic purification of the complexes—silica gel, basic and neutral alumina, Florisil, and fully endcapped C_{18} reversed-phase silica gel. Although iridium insertion could be accomplished for all of the corroles except X = NO_2, the great majority of the complexes proved unstable; bright green solutions of the freshly prepared complexes frequently turned brown, often with the decomposition product sticking to the glass walls of the reaction vessel. The most promising of the lot proved to be the dna complexes Ir[T*p*XPC](dna)$_2$ (X = CF_3, CN, H, and OMe; Figure 2), exhibiting high water solubility, but these too proved unstable upon chromatographic workup and/or

Received: May 7, 2021
Accepted: June 7, 2021
Published: June 15, 2021

https://doi.org/10.1021/acsomega.1c02399
ACS Omega 2021, 6, 16683−16687

Scheme 1. Synthesis of Four Stable, Water-Soluble Iridium Corroles

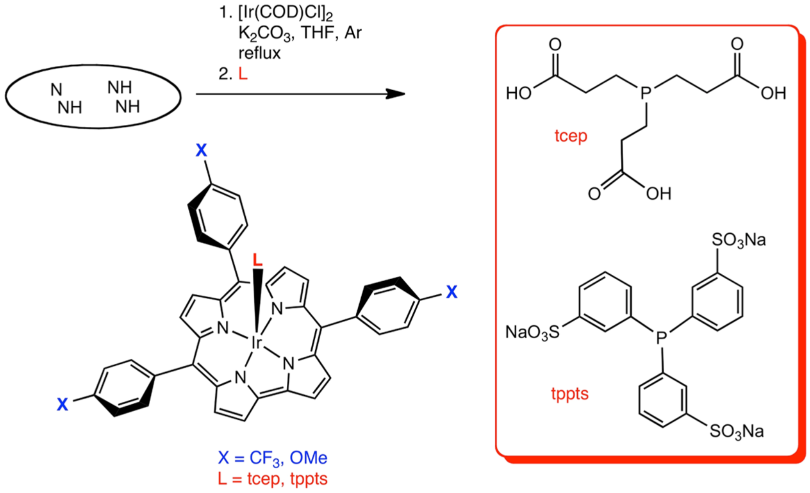

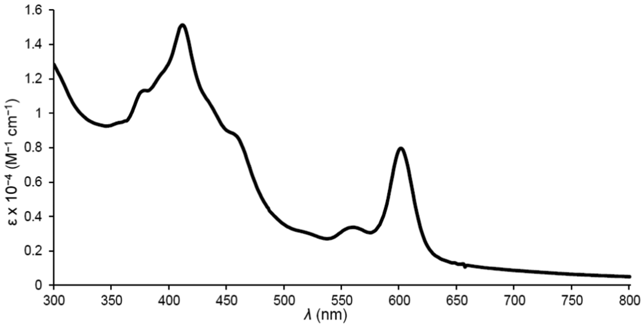

Figure 1. UV−vis spectrum of Ir[T*p*OMePC](4pa)$_2$ in methanol.

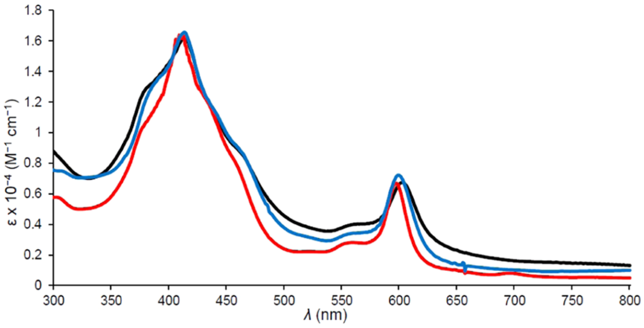

Figure 2. UV−vis comparison of freshly prepared Ir[T*p*OMePC](dna)$_2$ (black), Ir[TPC](dna)$_2$ (red), and Ir[T*p*CF$_3$PC](dna)$_2$ (blue) in methanol.

storage, as indicated by the disappearance of the highly characteristic optical spectra. Attempts to avoid chromatography by resorting to solvent extraction and vacuum filtration ultimately also proved unsuccessful.

Mass spectrometric analyses of the decomposed complexes generally revealed large quantities of free axial ligands, suggesting that they tend to fall off during chromatographic purification. This observation led us to switch to water-soluble phosphine ligands,[36] of which we examined three—tris(2-carboxyethyl)phosphine (tcep), trisodium tris(3-sulfonatophenyl)phosphine (tppts), and tris(hydroxymethyl)phosphine (thp). Like triphenylphosphine,[37] these phosphine ligands also led to five-coordinate complexes, which fortunately also proved distinctly more stable than the nitrogen-ligated complexes described above. Of the phosphine complexes, the thp derivatives proved poorly soluble in water (presumably reflecting the lower hydrophilicity of the alcohol functionality relative to carboxylate and sulfonate) and were accordingly excluded from further examination in our study. Fortunately, the tcep and tppts complexes proved fully soluble in distilled water (see Figures 3−5 and Table 1 for representative optical spectra and spectral data). A number of tcep complexes (especially for X = CN, H, and Me), however, proved somewhat hygroscopic, and the optical spectra exhibited broadening upon prolonged standing in water. In contrast, Ir[T*p*CF$_3$PC](tcep) proved unusually rugged, remaining unchanged in air and both aqueous and nonaqueous solutions for days. Finally, the tppts complexes proved highly stable (albeit slightly hygroscopic, thereby thwarting our attempts at

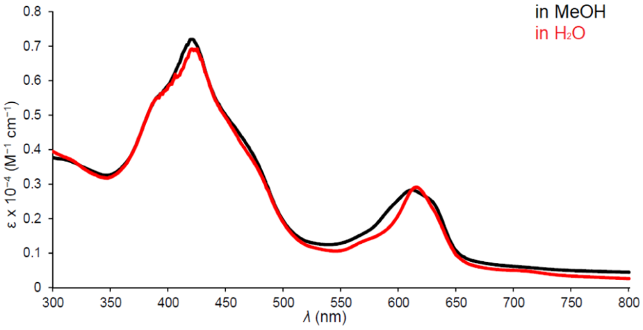

Figure 3. UV−vis spectrum of Ir[T*p*CF$_3$PC](tcep) in methanol and water.

Table 1. Absorption Maxima (*λ*, nm) for Ir Corroles[a]

complex	solvent	*B*	*Q*
Ir[T*p*OMePC](tcep)	MeOH	389, 411*	609*
Ir[T*p*OMePC](tppts)	MeOH	391, 413*	559, 594*
Ir[T*p*CF$_3$PC](tcep)	MeOH	420*	610*
Ir[T*p*CF$_3$PC](tppts)	MeOH	413*, 427	556, 594*
Ir[T*p*OMePC](tcep)	H_2O	416*	615*
Ir[T*p*CF$_3$PC](tcep)	H_2O	425*	615*
Ir[T*p*CF$_3$PC](tppts)	H_2O	413*	557, 595*

[a] The numbers marked with an asterisk indicate the wavelengths with the most intense absorption.

obtaining accurate elemental analyses) as well as readily purifiable via column chromatography on regular silica gel without any problems.

A brief word on the optical spectra of the new compounds may be of interest. The spectra (Figures 1−5) clearly show highly distinctive absorption profiles, including a complex Soret manifold and a Q manifold, whose shape also varies considerably. Thus, the sharp and intense Q band of Ir[TpCF$_3$PC](tppts) (Figure 4) may be distinguished from those of the tcep complexes (Figures 3 and 5). These distinctive spectra provided simple “spectroscopic handles” for assessing the integrity and purity of the compounds studied. A discussion of the electronic origin of the diverse absorption profiles, while of significant theoretical interest, is outside the scope of this study.

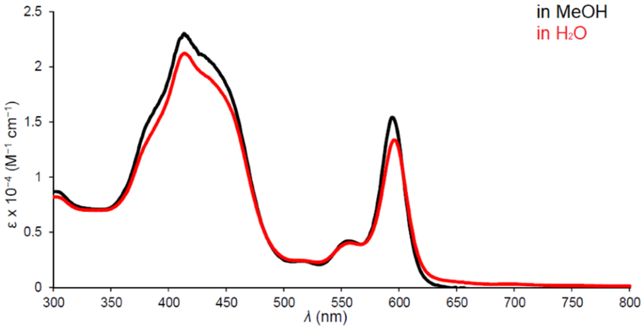

Figure 4. UV−vis spectrum of Ir[TpCF$_3$PC](tppts) in methanol and water.

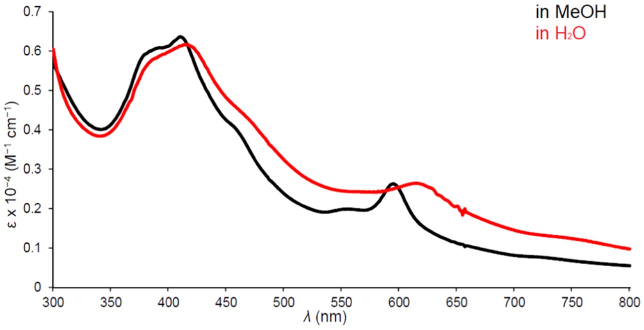

Figure 5. UV−vis spectrum of Ir[TpOMePC](tcep) in methanol and water.

A couple of phosphine complexes exhibited a small quantity of impurity in their NMR spectra (see Figures S9−S16 in the Supporting Information); we have not identified this species as of yet but view a six-coordinate water or solvent adduct as a plausible candidate.

CONCLUSIONS

The present study was motivated by a desire to synthesize water-soluble iridium corroles for photodynamic therapy and other biomedical applications via the simple stratagem of employing a water-soluble axial ligand. Although ultimately successful, the exercise entailed unexpected challenges. Thus, the complexes with axial amine ligands such as 4-picolinic acid and dinicotinic acid proved unstable, decomposing over hours to days upon standing in water. Five-coordinate phosphine complexes, in contrast, proved much more stable and readily purifiable with reversed-phase column chromatography, with tcep and tppts emerging as the most promising axial ligands. Of the various complexes synthesized, Ir[TpCF$_3$PC](tppts) is arguably the most attractive, considering its high water solubility, long-term stability in solution, and distinctive optical signature. The performance of the new compounds in photocytotoxicity measurements is currently under evaluation and will be reported in due course.

EXPERIMENTAL SECTION

Materials. Tris(2-carboxyethyl)phosphine hydrochloride (99%), trisodium tris(3-sulfonatophenyl)phosphine (<10% phosphine oxide), and tris(hydroxymethyl)phosphine (95%) were purchased from Strem Chemicals, Inc. Free-base corroles were prepared as previously reported.[33−35] Unless otherwise mentioned, all other chemicals were obtained from Sigma-Millipore (Merck).

Instrumental Methods. UV−visible spectra were recorded on an HP 8453 spectrophotometer. ^{1}H NMR, ^{19}F NMR, and ^{31}P NMR spectra were recorded on a 400 MHz Bruker Avance III HD spectrometer equipped with a 5 mm BB/1H SmartProbe in CD$_3$OD or (CD$_3$)$_2$SO. ^{1}H NMR spectra were referenced to residual CH$_3$OH (3.31 ppm) or to (CH$_3$)$_2$SO (2.50 ppm). High-resolution electrospray-ionization (HR-ESI) mass spectra were recorded from methanolic solution on an LTQ Orbitrap XL spectrometer.

General Procedure for the Synthesis of Ir[T*p*XPC](L) (X = OMe, CF$_3$; L = tcep, tppts). The iridium complexes were prepared according to a modified version of a previously reported procedure.[12] Bis(1,5-cyclooctadiene)diiridium(I) dichloride (1.5 equiv) and potassium carbonate (10 equiv) were dissolved in an anhydrous tetrahydrofuran (THF) solution (20 mL) of a free-base corrole (∼0.025−0.1 mmol, 1 equiv). After degassing with argon for a few minutes, the solution was brought to reflux under an inert atmosphere. Heating was discontinued after 90 min, and the phosphine (1 equiv) was added as a solution of anhydrous methanol (10 mL); the reaction mixture was then left to stir for 30 min. As alluded to above, four products were purified and fully characterized, as described below. Because of the hygroscopic nature of the compounds, satisfactory elemental analyses, in general, could not be obtained; the yields accordingly should be regarded as upper limits.

Ir[TpOMePC](tcep). The reaction mixture was rotary-evaporated to dryness. The dark solid residue was suspended in dichloromethane and thoroughly shaken; the solvent was decanted off to remove unreacted free-base corrole and other nonpolar impurities. This step was repeated with ethyl acetate and acetonitrile, finally leaving behind a dark green solid, which was dissolved in methanol. The solution was filtered to remove any remaining salts, and the filtrate was evaporated to dryness. The resulting solid was dissolved in a minimum amount of methanol and chromatographed on a fully C$_{18}$-endcapped reversed-phase silica gel column with different MeCN/MeOH mixed solvents as the mobile phase (as detailed below), yielding the expected product along with some silica particles as a light green solid. The silica particles were removed by suspending the solid in pentane, sonicating the suspension briefly, and filtering off the pentane solution containing the dissolved/micro-suspended silica. The dark green solid residue was dissolved in methanol and transferred to a new vessel; upon removal of the solvent under vacuum, the product was obtained as a deep green, hygroscopic solid. Yield 98 mg (85%). UV−vis (CH_3OH) λ_{max} (nm) [$\epsilon \times 10^{-4}$ (M^{-1} cm^{-1})]: 389 (sh, 0.56), 411 (0.62), 609 (0.25). ^{1}H NMR (400 MHz, methanol-d_4) δ 8.63 (d, J = 4.0 Hz, 2H), 8.48 (d, J = 4.0 Hz, 2H), 8.29 (d, J = 4.7 Hz, 2H), 8.09 (t, J = 4.8 Hz, 2H), 7.91−7.80 (m, 4H), 7.32−7.14 (m, 8H), 4.00 (d, J = 4.6 Hz, 9H), −0.19 (t, J = 8.2 Hz, 6H), −1.58 (t, J = 8.2 Hz, 6H). ^{31}P NMR (162 MHz, composite pulse-decoupled, methanol-d_4) δ −22.43. MS (ESI): [M$^-$] = 1055.2415 (expt), 1055.2406 (calcd for $IrC_{49}H_{43}N_4O_9P$).

Ir[TpOMePC](tppts). The reaction mixture was rotary-evaporated to dryness, yielding a dark green solid. The residue was dissolved in a minimum amount of methanol and subjected to column chromatography (regular silica gel, 10:1 MeCN/MeOH, then 4:1 MeCN/MeOH) to obtain the title compound as a dichroic brown-green solid. Yield 16.6 mg (22.5%). UV−vis (CH_3OH) λ_{max} (nm) [$\epsilon \times 10^{-4}$ (M^{-1} cm^{-1})]: 391 (sh, 1.82), 413 (2.02), 559 (sh, 0.72), 594 (0.84). ^{1}H NMR (400 MHz, DMSO-d_6) δ 7.94 (d, J = 1.8 Hz, 4H), 7.83 (dt, J = 7.6, 1.5 Hz, 4H), 7.52 (t, J = 7.6 Hz, 6H), 7.48−7.43 (m, 6H), 4.19−3.93 (m, 9H), 3.38 (t, J = 6.4 Hz, 3H), 2.23 (t, J = 7.4 Hz, 3H), 1.63 (p, J = 6.9 Hz, 3H), 1.29−1.17 (m, 3H). ^{31}P NMR (162 MHz, composite pulse-decoupled, DMSO-d_6) δ 26.36. MS (ESI): [M$^-$] = 1328.1142 (expt), 1328.1154 (calcd for $IrC_{58}H_{44}N_4O_{12}S_3PNa$).

Ir[TpCF$_3$PC](tcep). The purification was carried out as for Ir[T*p*OMePC](tcep) to afford the title compound as a deep green, hygroscopic solid. Yield 26 mg (90%). UV−vis (CH_3OH) λ_{max} (nm) [$\epsilon \times 10^{-4}$ (M^{-1} cm^{-1})]: 420 (0.70), 610 (0.26). ^{1}H NMR (400 MHz, methanol-d_4) δ 8.73 (t, J = 3.8 Hz, 2H), 8.62 (d, J = 7.9 Hz, 4H), 8.55 (d, J = 7.9 Hz, 2H), 8.48 (d, J = 4.8 Hz, 2H), 8.33 (dd, J = 4.8, 1.5 Hz, 2H), 8.13−8.11 (m, 2H), 7.98 (d, J = 8.0 Hz, 4H), 7.94 (d, J = 8.0 Hz, 2H), −0.28 to −0.33 (m, 6H), −2.13 (s, 6H). ^{19}F NMR (377 MHz, methanol-d_4) δ −63.27. ^{31}P NMR (162 MHz, composite pulse-decoupled, methanol-d_4) δ −22.66. MS (ESI): [M$^-$] = 1169.1697 (expt), 1169.1710 (calcd for $IrC_{49}H_{34}N_4F_9O_6P$).

Ir[TpCF$_3$PC](tppts). The reaction mixture was rotary-evaporated to dryness, yielding a dark green solid. The residue was suspended in dichloromethane and shaken thoroughly, and the solvent was decanted off to remove unreacted free-base corrole and other less polar impurities. The solid residue was dissolved in a minimum amount of methanol and subjected to column chromatography (regular silica gel, 5:1 CH_2Cl_2/MeOH, then 1:1 CH_2Cl_2/MeOH), affording the product as a dichroic red-green solid. Yield 26 mg (52%). UV−vis (CH_3OH) λ_{max} (nm) [$\epsilon \times 10^{-4}$ (M^{-1} cm^{-1})]: 413 (2.68), 427 (sh, 2.47), 556 (sh, 0.49), 594 (1.79). ^{1}H NMR (400 MHz, methanol-d_4) δ 8.64 (d, J = 4.3 Hz, 2H), 8.43 (d, J = 4.8 Hz, 2H), 8.16 (d, J = 4.8 Hz, 2H), 8.03−7.95 (m, 4H), 7.90 (d, J = 4.3 Hz, 2H), 7.88−7.51 (m, 8H), 7.39−7.34 (m, 3H), 6.76 (t, J = 7.8 Hz, 3H), 5.33 (d, J = 1.8 Hz, 3H), 3.89 (dd, J = 7.9, 1.6 Hz, 3H). ^{19}F NMR (377 MHz, methanol-d_4) δ −63.30. ^{31}P NMR (162 MHz, composite pulse-decoupled, methanol-d_4) δ −25.59. MS (ESI): [M$^-$] = 1421.0710 (expt), 1421.0716 (calcd for $IrC_{58}H_{34}N_4F_9O_9S_3P$).

ASSOCIATED CONTENT

Supporting Information

The Supporting Information is available free of charge at https://pubs.acs.org/doi/10.1021/acsomega.1c02399.

UV−vis, HR-ESI mass, and ^{1}H NMR spectra (PDF)

AUTHOR INFORMATION

Corresponding Author

Abhik Ghosh − *Department of Chemistry, UiT—The Arctic University of Norway, N-9037 Tromsø, Norway;* orcid.org/0000-0003-1161-6364; Email: abhik.ghosh@uit.no

Authors

Ivar K. Thomassen − *Department of Chemistry, UiT—The Arctic University of Norway, N-9037 Tromsø, Norway;* orcid.org/0000-0001-7592-6260
Daniel Rasmussen − *Department of Chemistry, UiT—The Arctic University of Norway, N-9037 Tromsø, Norway*
Rune F. Einrem − *Department of Chemistry, UiT—The Arctic University of Norway, N-9037 Tromsø, Norway*

Complete contact information is available at: https://pubs.acs.org/10.1021/acsomega.1c02399

Author Contributions

I.K.T. carried out the majority of the experimental work; D.R. and R.F.E. provided significant assistance. A.G. planned and coordinated the research. I.K.T. and A.G. together wrote the manuscript.

Notes

The authors declare no competing financial interest.

ACKNOWLEDGMENTS

This work was supported by the Research Council of Norway (grant no. 262229 to A.G.) and the Arctic Center for Sustainable Energy at UiT—The Arctic University of Norway.

REFERENCES

(1) Bonnett, R. *Chemical Aspects of Photodynamic Therapy*; CRC Press, 2000.

(2) Pandey, R. K.; Kessel, D.; Dougherty, T. J. *Handbook of Photodynamic Therapy: Updates on Recent Applications of Porphyrin-Based Compounds*; World Scientific, 2016.

(3) Amos-Tautua, B. M.; Songca, S. P.; Oluwafemi, O. S. Application of porphyrins in antibacterial photodynamic therapy. *Molecules* **2019**, *24*, No. 2456.

(4) Lin, Y.; Zhou, T.; Bai, R.; Xie, Y. Chemical approaches for the enhancement of porphyrin skeleton-based photodynamic therapy. *J. Enzyme Inhib. Med. Chem.* **2020**, *35*, 1080−1099.

(5) Tian, J.; Huang, B.; Nawaz, M. H.; Zhang, W. Recent advances of multi-dimensional porphyrin-based functional materials in photodynamic therapy. *Coord. Chem. Rev.* **2020**, *420*, No. 213410.

(6) Ghosh, A. Electronic Structure of Corrole Derivatives: Insights from Molecular Structures, Spectroscopy, Electrochemistry, and Quantum Chemical Calculations. *Chem. Rev.* **2017**, *117*, 3798−3881.

(7) Nardis, S.; Mandoj, F.; Stefanelli, M.; Paolesse, R. Metal complexes of corrole. *Coord. Chem. Rev.* **2019**, *388*, 360−405.

(8) Teo, R. D.; Hwang, J. Y.; Termini, J.; Gross, Z.; Gray, H. B. Fighting Cancer with Corroles. *Chem. Rev.* **2017**, *117*, 2711−2729.

(9) Jiang, X.; Liu, R.-X.; Hai-Yang, L.; Chang, C. K. Corrole-based photodynamic antitumor therapy. *J. Chin. Chem. Soc.* **2019**, *66*, 1090−1099.

(10) Einrem, R. F.; Gagnon, K. J.; Alemayehu, A. B.; Ghosh, A. Metal-Ligand Misfits: Facile Access to Rhenium-Oxo Corroles by Oxidative Metalation. *Chem. - Eur. J.* **2016**, *22*, 517−520.

(11) Alemayehu, A. B.; Gagnon, K. J.; Terner, J.; Ghosh, A. Oxidative Metalation as a Route to Size-Mismatched Macrocyclic Complexes: Osmium Corroles. *Angew. Chem., Int. Ed.* **2014**, *53*, 14411−14414.

(12) Palmer, J. H.; Durrell, A. C.; Gross, Z.; Winkler, J. R.; Gray, H. B. Iridium Corroles. *J. Am. Chem. Soc.* **2008**, *130*, 7786−7787.

(13) Alemayehu, A. B.; Vazquez-Lima, H.; Beavers, C. M.; Gagnon, K. J.; Bendix, J.; Ghosh, A. Platinum Corroles. *Chem. Commun.* **2014**, *50*, 11093−11096.

(14) Alemayehu, A. B.; Ghosh, A. Gold Corroles. *J. Porphyrins Phthalocyanines* **2011**, *15*, 106−110.

(15) Rabinovich, E.; Goldberg, I.; Gross, Z. Gold(I) and Gold(III) Corroles. *Chem. Eur. J.* **2011**, *17*, 12294−12301.

(16) Thomas, K. E.; Alemayehu, A. B.; Conradie, J.; Beavers, C.; Ghosh, A. Synthesis and Molecular Structure of Gold Triarylcorroles. *Inorg. Chem.* **2011**, *50*, 12844−12851.

(17) Thomas, K. E.; Vazquez-Lima, H.; Fang, Y.; Song, Y.; Gagnon, K. J.; Beavers, C. M.; Kadish, K. M.; Ghosh, A. Ligand Noninnocence in Coinage Metal Corroles: A Silver Knife-Edge. *Chem. - Eur. J.* **2015**, *21*, 16839−16847.

(18) Mahammed, A.; Gross, Z. Corroles as triplet photosensitizers. *Coord. Chem. Rev.* **2019**, *379*, 121−132.

(19) Lemon, C. M. Corrole photochemistry. *Pure Appl. Chem.* **2019**, *92*, 1901−1919.

(20) Palmer, J. H.; Durrell, A. C.; Gross, Z.; Winkler, J. R.; Gray, H. B. Near-IR Phosphorescence of Iridium(III) Corroles at Ambient Temperature. *J. Am. Chem. Soc.* **2010**, *132*, 9230−9231.

(21) Sinha, W.; Ravotto, L.; Ceroni, P.; Kar, S. NIR-Emissive Iridium(III) Corrole Complexes as Efficient Singlet Oxygen Sensitizers. *Dalton Trans.* **2015**, *44*, 17767−17773.

(22) Alemayehu, A. B.; Day, J.; Mani, N. U.; Rudine, T.; Thomas, A. B.; Gederaas, K. E.; Vinogradov, O. A.; Wamser, S. A.; Ghosh, C. C.; Gold, A. Tris(carboxyphenyl)corroles as Multifunctional Materials: Room Temperature Near-IR Phosphorescence and Applications to Photodynamic Therapy and Dye-Sensitized Solar Cells. *ACS Appl. Mater. Interfaces* **2016**, *8*, 18935−18942.

(23) Borisov, S. M.; Alemayehu, A.; Ghosh, A. Osmium-Nitrido Corroles as NIR Indicators for Oxygen Sensors and Triplet Sensitizers for Organic Upconversion and Singlet Oxygen Generation. *J. Mater. Chem. C* **2016**, *4*, 5822−5828.

(24) Lemon, C. M.; Powers, D. C.; Brothers, P. J.; Nocera, D. G. Gold Corroles as Near-IR Phosphors for Oxygen Sensing. *Inorg. Chem.* **2017**, *56*, 10991−10997.

(25) Alemayehu, A. B.; McCormick, L. J.; Gagnon, K. J.; Borisov, S. M.; Ghosh, A. Stable Platinum(IV) Corroles: Synthesis, Molecular Structure, and Room-Temperature Near-IR Phosphorescence. *ACS Omega* **2018**, *3*, 9360−9368.

(26) Borisov, S. M.; Einrem, R. F.; Alemayehu, A. B.; Ghosh, A. Ambient-temperature near-IR phosphorescence and potential applications of rhenium-oxo corroles. *Photochem. Photobiol. Sci.* **2019**, *18*, 1166−1170.

(27) Einrem, R. F.; Alemayehu, A. B.; Borisov, S. M.; Ghosh, A.; Gederaas, O. A. Amphiphilic Rhenium-Oxo Corroles as a New Class of Sensitizers for Photodynamic Therapy. *ACS Omega* **2020**, *5*, 10596−10601.

(28) Higashino, T.; Kurumisawa, Y.; Alemayehu, A. B.; Einrem, R. F.; Sahu, D.; Packwood, D.; Kato, K.; Yamakata, A.; Ghosh, A.; Imahori, H. Heavy Metal Effects on the Photovoltaic Properties of Metallocorroles in Dye-Sensitized Solar Cells. *ACS Appl. Energy Mater.* **2020**, *3*, 12460−12467.

(29) Singh, S.; Aggarwal, A.; Bhupathiraju, N. V. S. D. K.; Arianna, G.; Tiwari, K.; Drain, C. M. Glycosylated Porphyrins, Phthalocyanines, and Other Porphyrinoids for Diagnostics and Therapeutics. *Chem. Rev.* **2015**, *115*, 10261−10306.

(30) Luciano, M.; Brückner, C. Modifications of Porphyrins and Hydroporphyrins for Their Solubilization in Aqueous Media. *Molecules* **2017**, *22*, No. 980.

(31) Thomassen, I. K.; McCormick-McPherson, L. J.; Borisov, S. M.; Ghosh, A. Iridium Corroles Exhibit Weak Near-Infrared Phosphorescence but Efficiently Sensitize Singlet Oxygen Formation. *Sci. Rep.* **2020**, *10*, No. 7551.

(32) Wasbotten, I. H.; Wondimagegn, T.; Ghosh, A. Electronic Absorption, Resonance Raman, and Electrochemical Studies of Planar and Saddled Copper(III) *Meso*-Triarylcorroles. Highly Substituent-Sensitive Soret Bands as a Distinctive Feature of High-Valent Transition Metal Corroles. *J. Am. Chem. Soc.* **2002**, *124*, 8104−8116.

(33) Gryko, D. T.; Koszarna, B. Refined methods for the synthesis of meso-substituted A_3- and *trans*-A_2B-corroles. *Org. Biomol. Chem.* **2003**, *1*, 350−357.

(34) Koszarna, B.; Gryko, D. T. Efficient Synthesis of *meso*-Substituted Corroles in a H_2O−MeOH Mixture. *J. Org. Chem.* **2006**, *71*, 3707−3717.

(35) Gross, Z.; Galili, N.; Saltsman, I. The First Direct Synthesis of Corroles from Pyrrole. *Angew. Chem., Int. Ed.* **1999**, *38*, 1427−1429.

(36) Pinault, N.; Bruce, D. W. Homogeneous catalysts based on water-soluble phosphines. *Coord. Chem. Rev.* **2003**, *241*, 1−25.

(37) Palmer, J. H.; Mahammed, A.; Lancaster, K. M.; Gross, Z.; Gray, H. B. Structures and Reactivity Patterns of Group 9 Metallocorroles. *Inorg. Chem.* **2009**, *48*, 9308−9315.

A Simple, Axial Ligand-Mediated Route to Water-Soluble Iridium Corroles

Ivar K. Thomassen,[a] Daniel Rasmussen,[a] Rune F. Einrem[a] and
Abhik Ghosh*,[a]

Department of Chemistry, UiT – The Arctic University of Norway, N-9037 Tromsø, Norway;
Email: abhik.ghosh@uit.no.

Contents **Page**

A. UV-Vis spectra

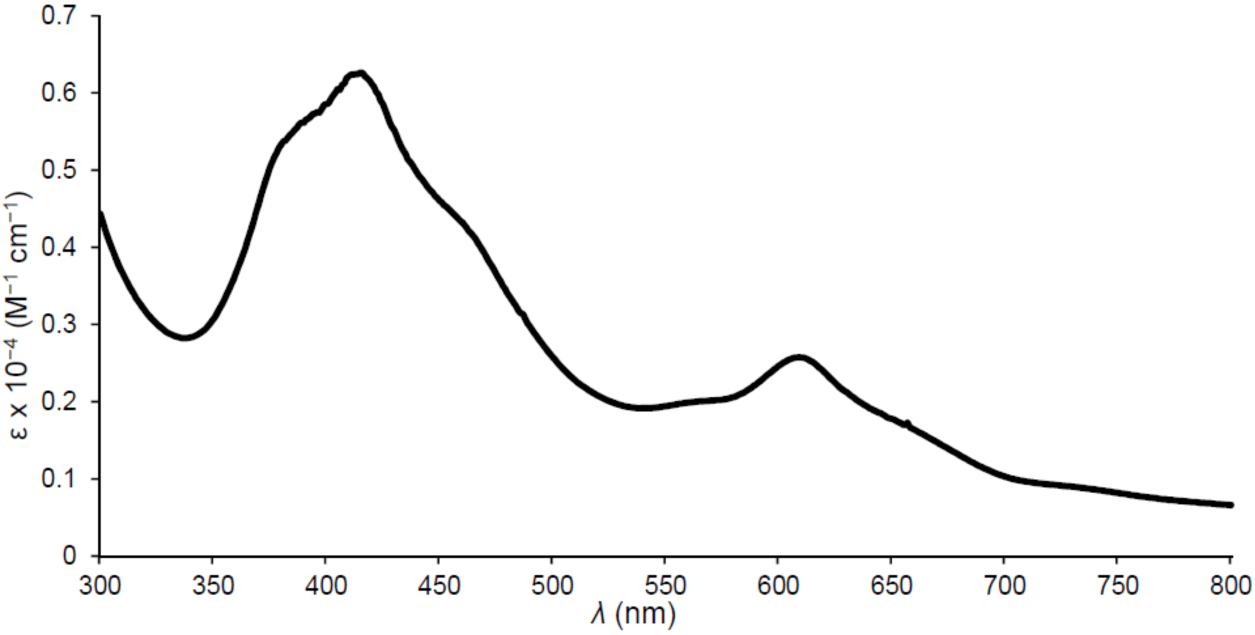

Figure S1. UV-vis spectrum of Ir[(T*p*OMePC)](tcep) in methanol.

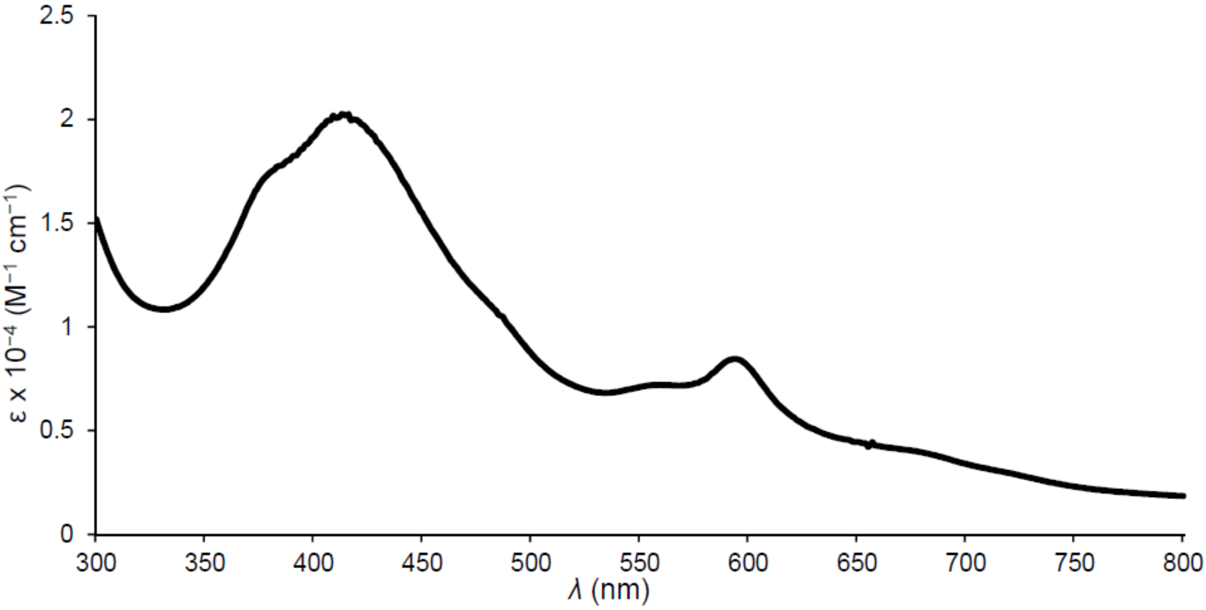

Figure S2. UV-vis spectrum of Ir[T*p*OMePC](tppts) in methanol.

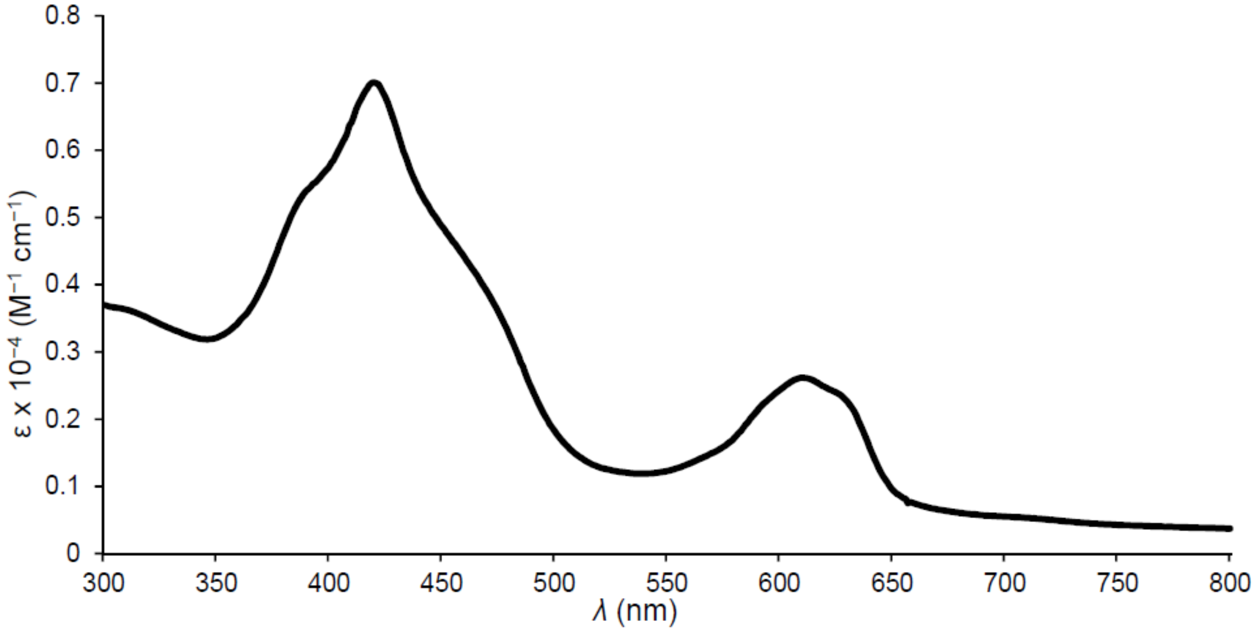

Figure S3. UV-vis spectrum of Ir[T*p*CF$_3$PC](tcep) in methanol.

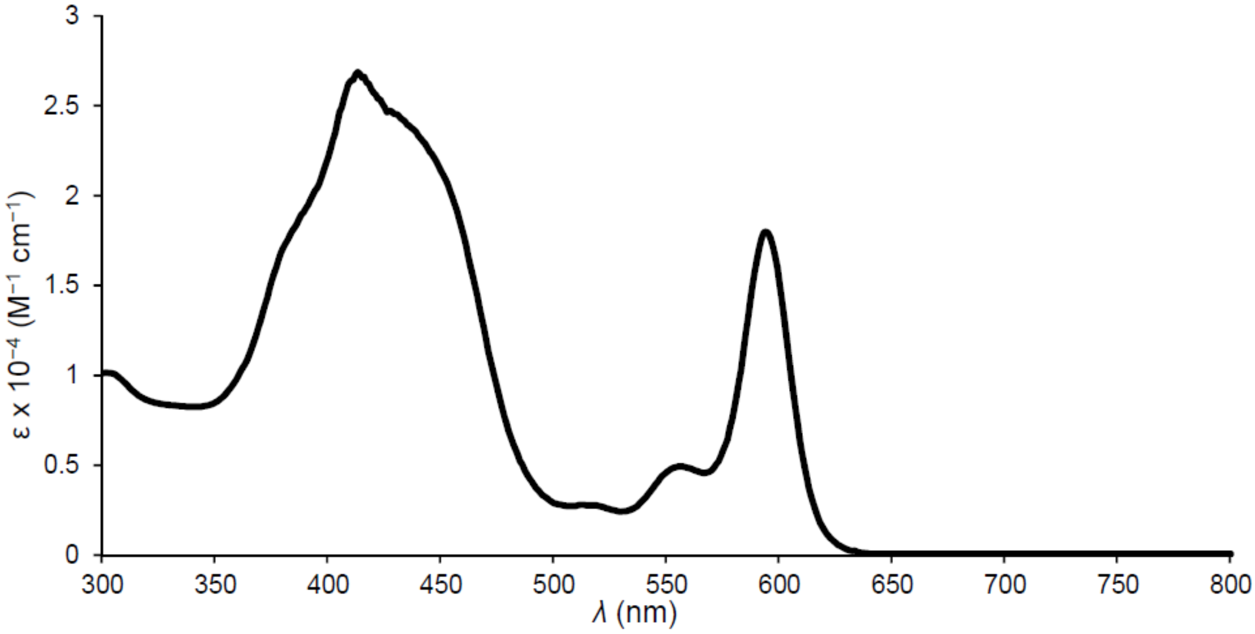

Figure S4. UV-vis spectrum of Ir[T*p*CF$_3$PC](tppts) in methanol.

B. ESI Mass spectra

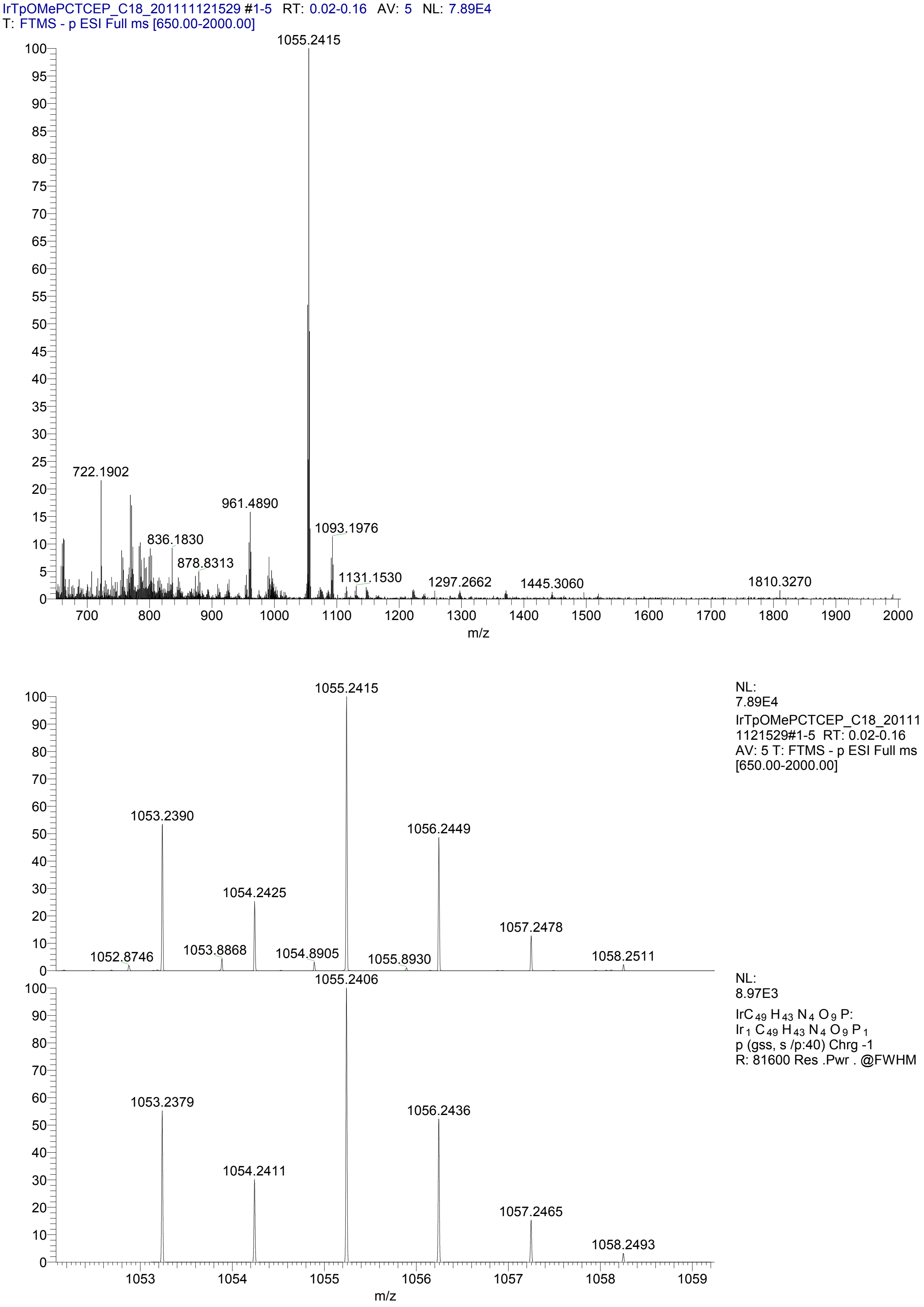

Figure S5. Negative-mode ESI mass spectra of Ir[T*p*OMePC](tcep).

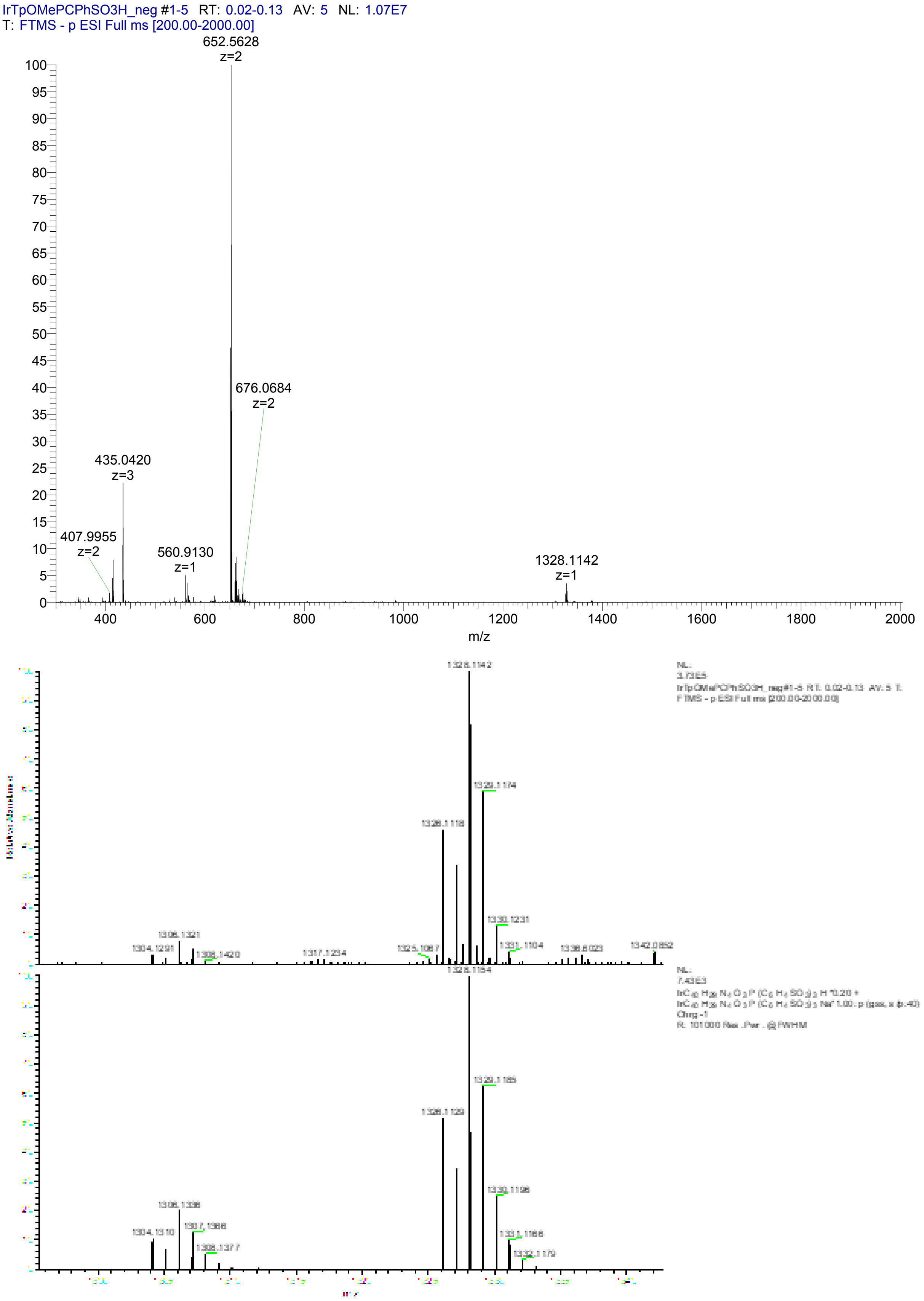

Figure S6. Negative-mode ESI mass spectra of Ir[T*p*OMePC](tppts) (Z=1). *Contd.*

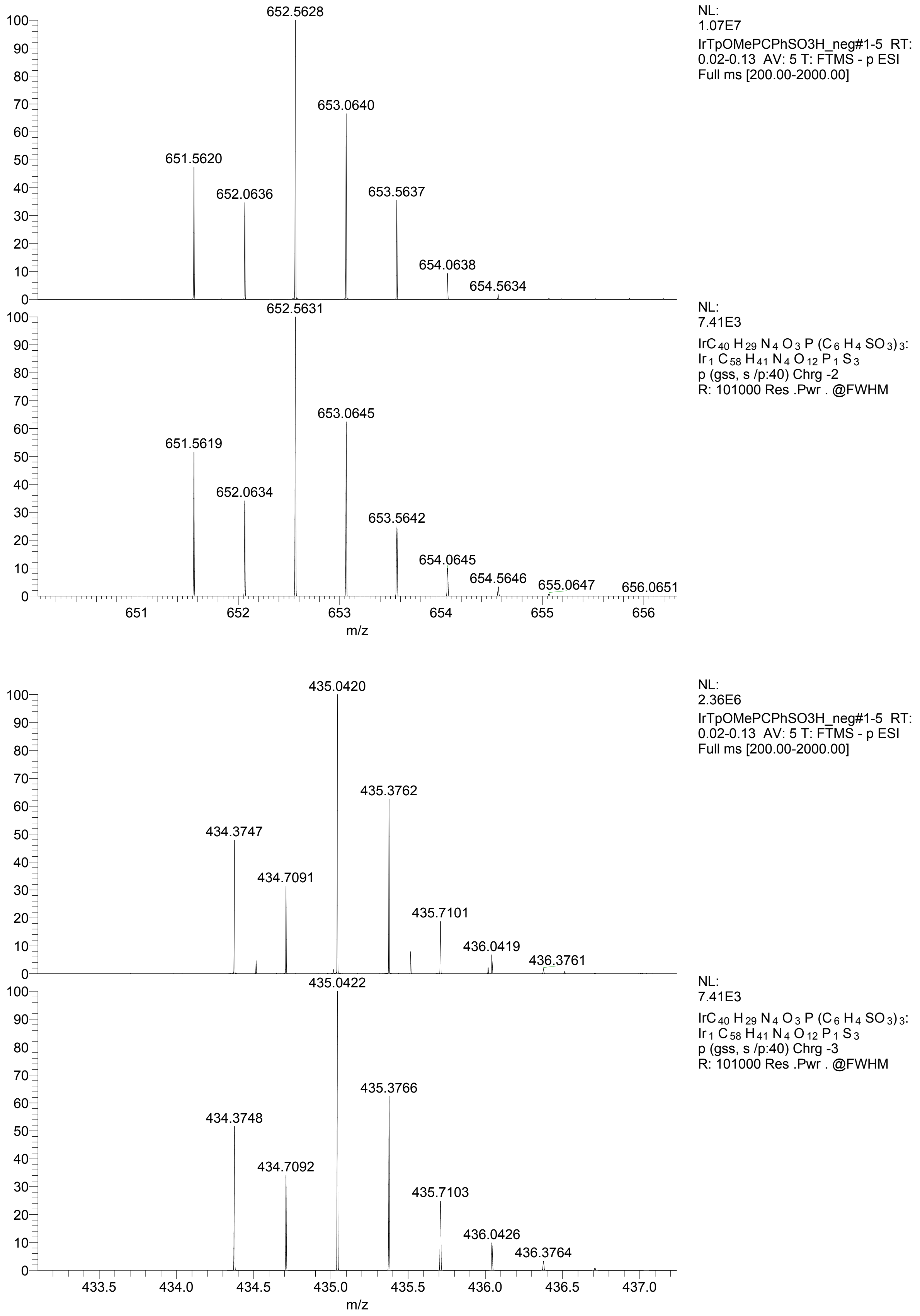

Figure S6 (contd.). Negative-mode ESI mass spectra of Ir[T*p*OMePC](tppts) (Z=2 and 3).

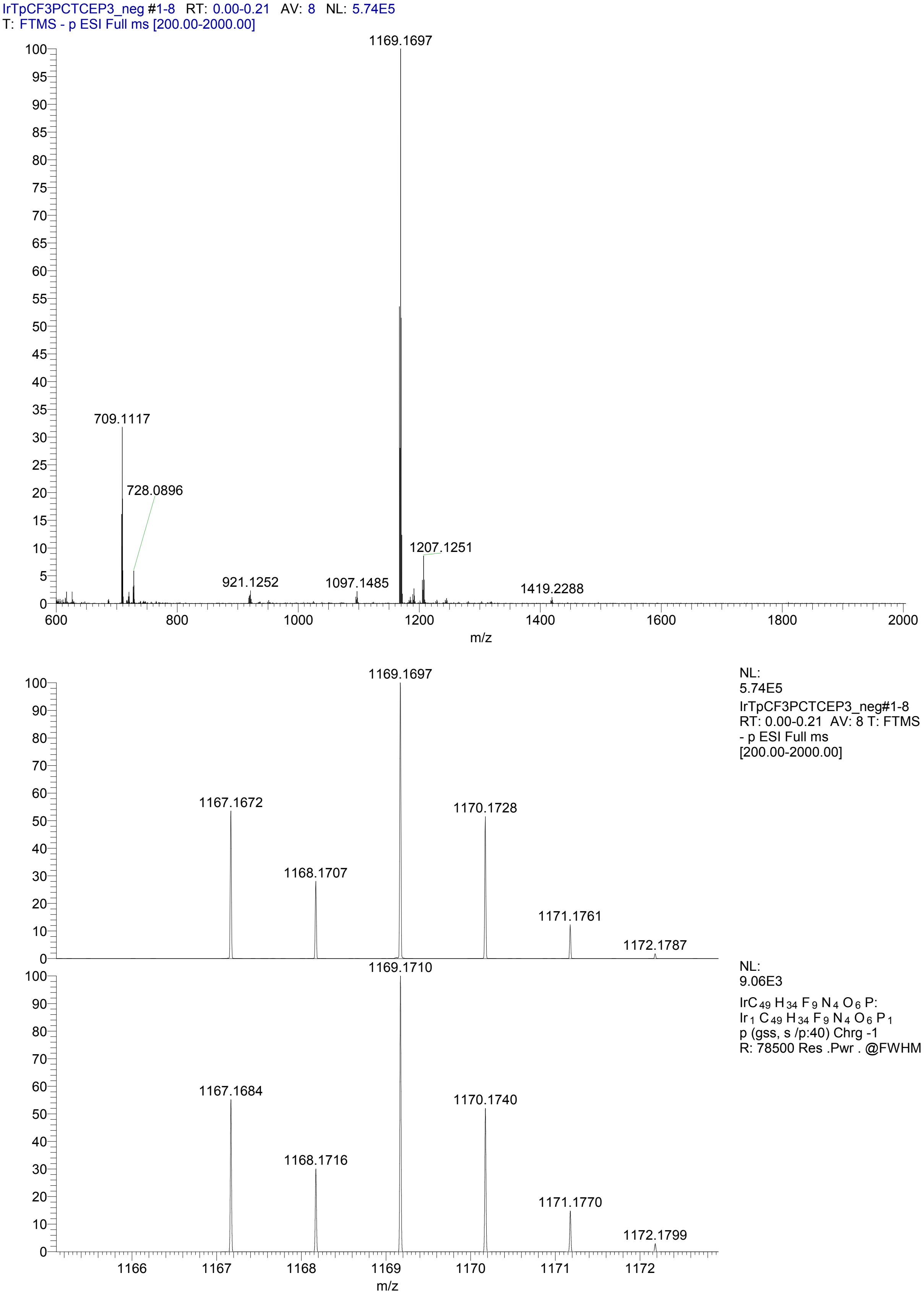

Figure S7. Negative-mode ESI mass spectra of Ir[(T*p*CF$_3$PC)](tcep).

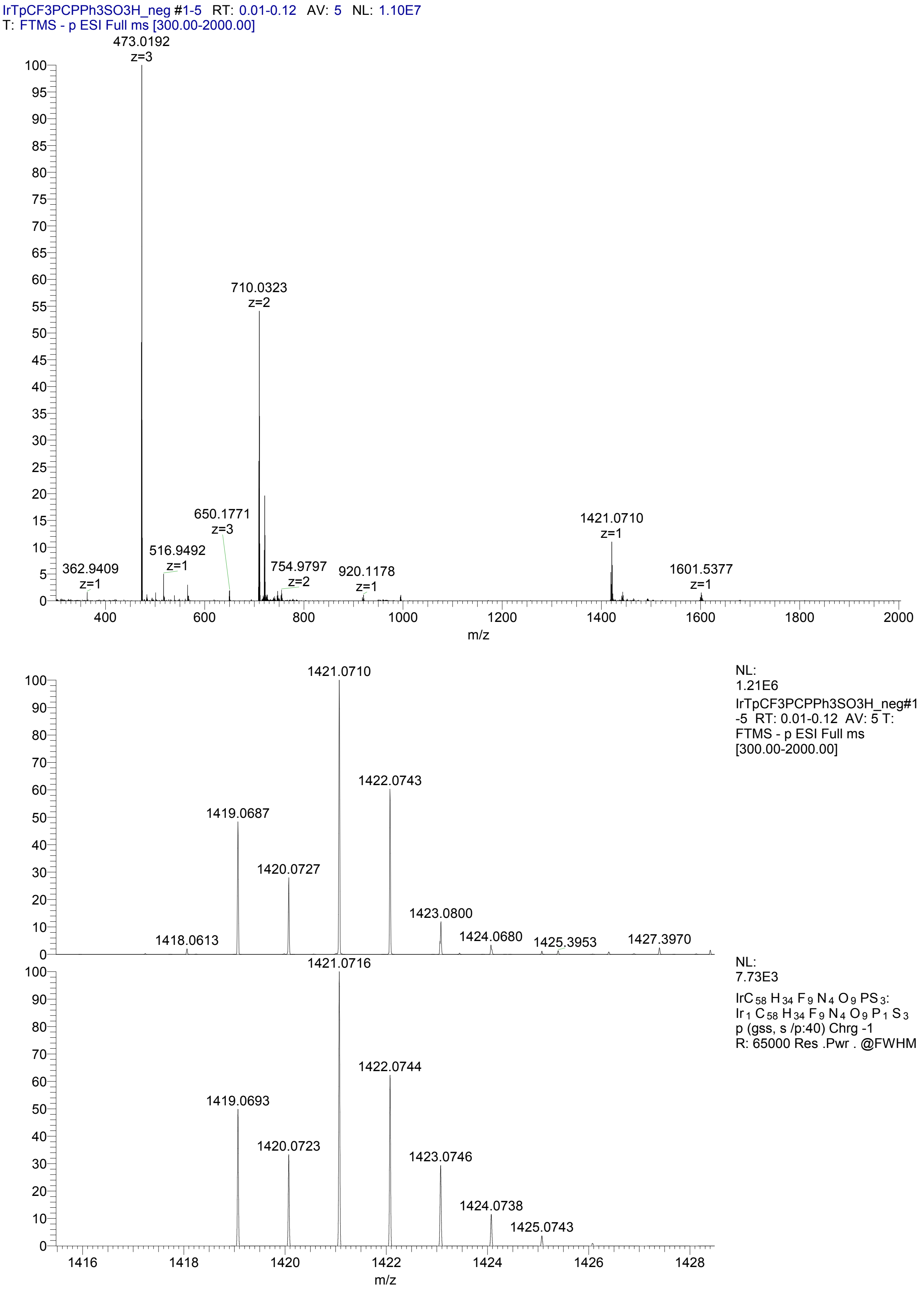

Figure S8. Negative-mode ESI mass spectra of Ir[T*p*CF$_3$PC](tppts) (Z=1). *Contd.*

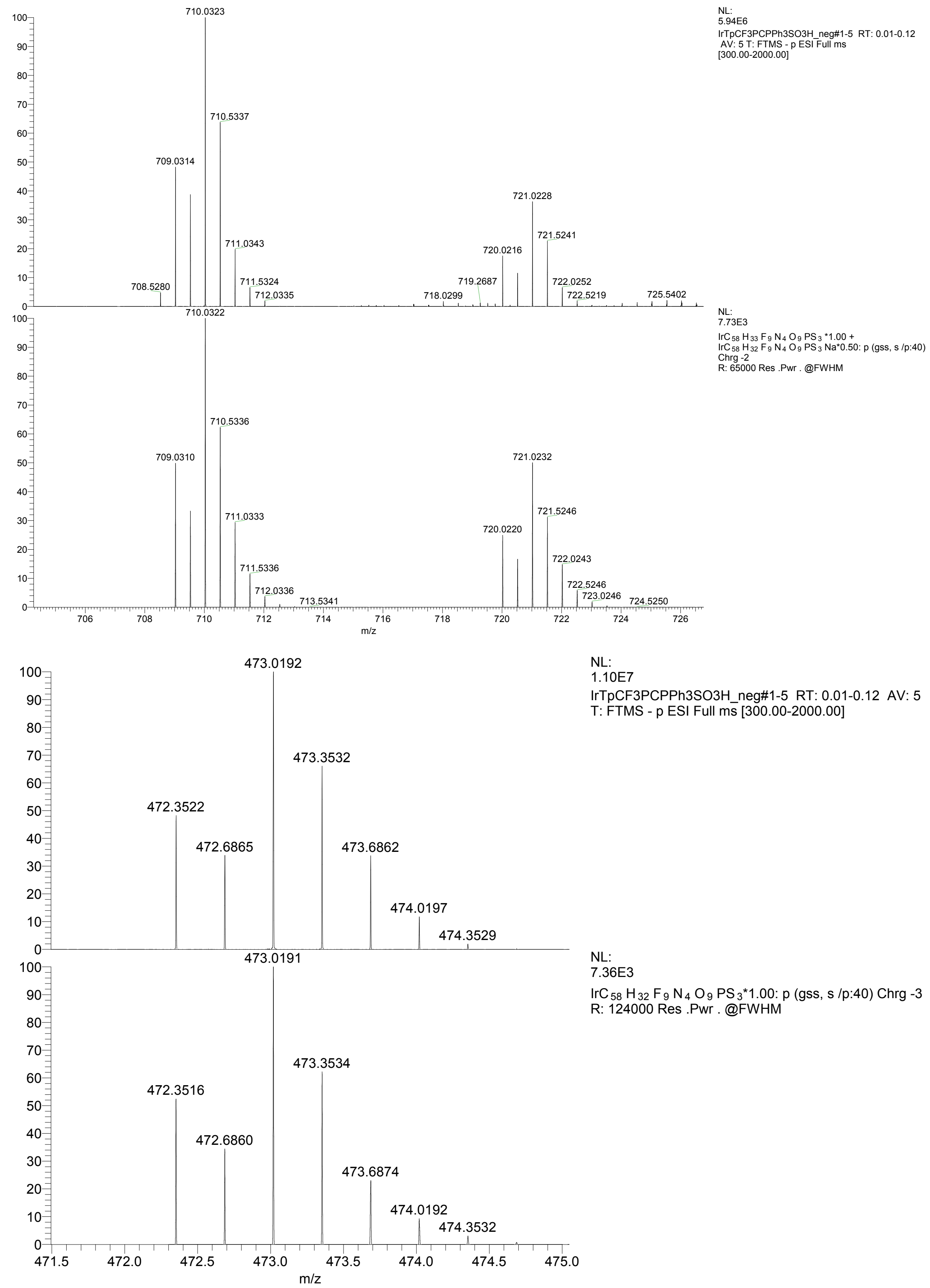

Figure S8 (contd.). Negative-mode ESI mass spectra of Ir[T*p*CF_3PC](tppts) (Z=2 and 3).

C. NMR spectra

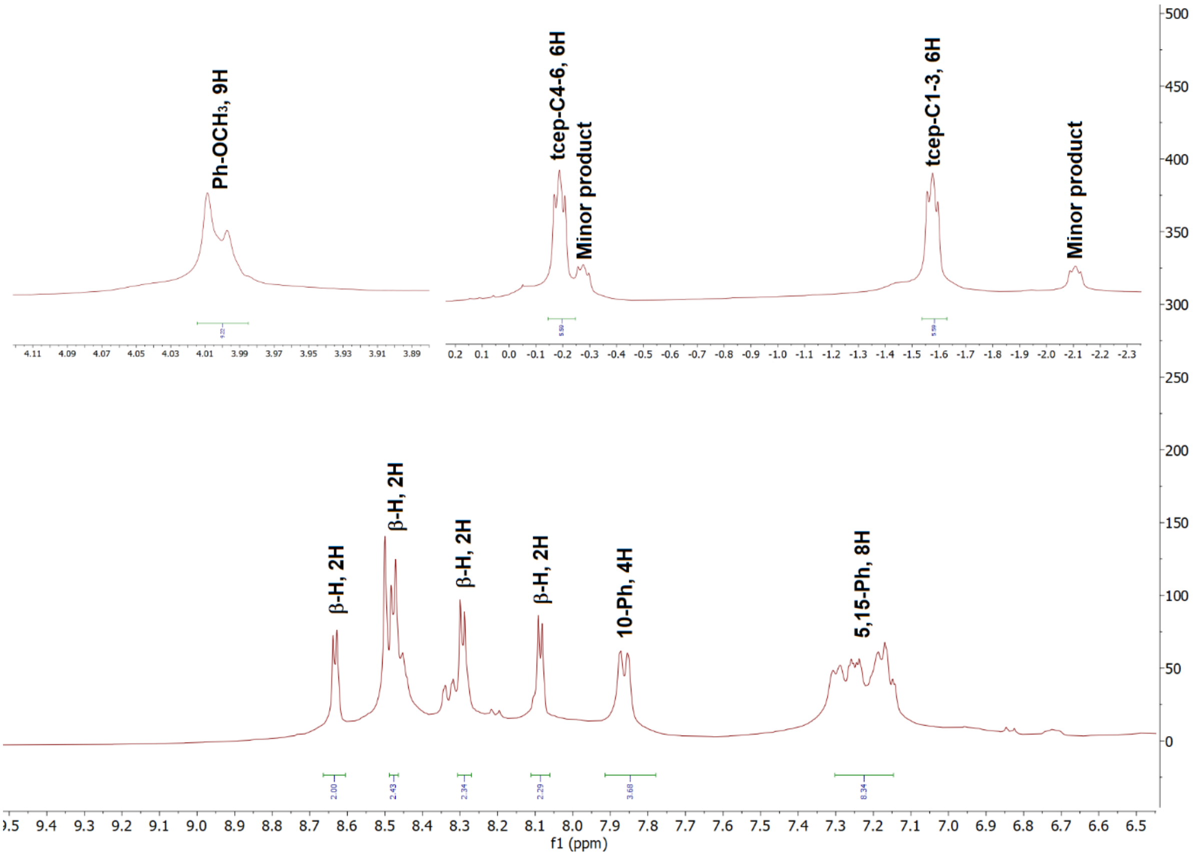

Figure S9. ^{1}H NMR spectrum of Ir[T*p*OMePC](tcep) in methanol-d_4.

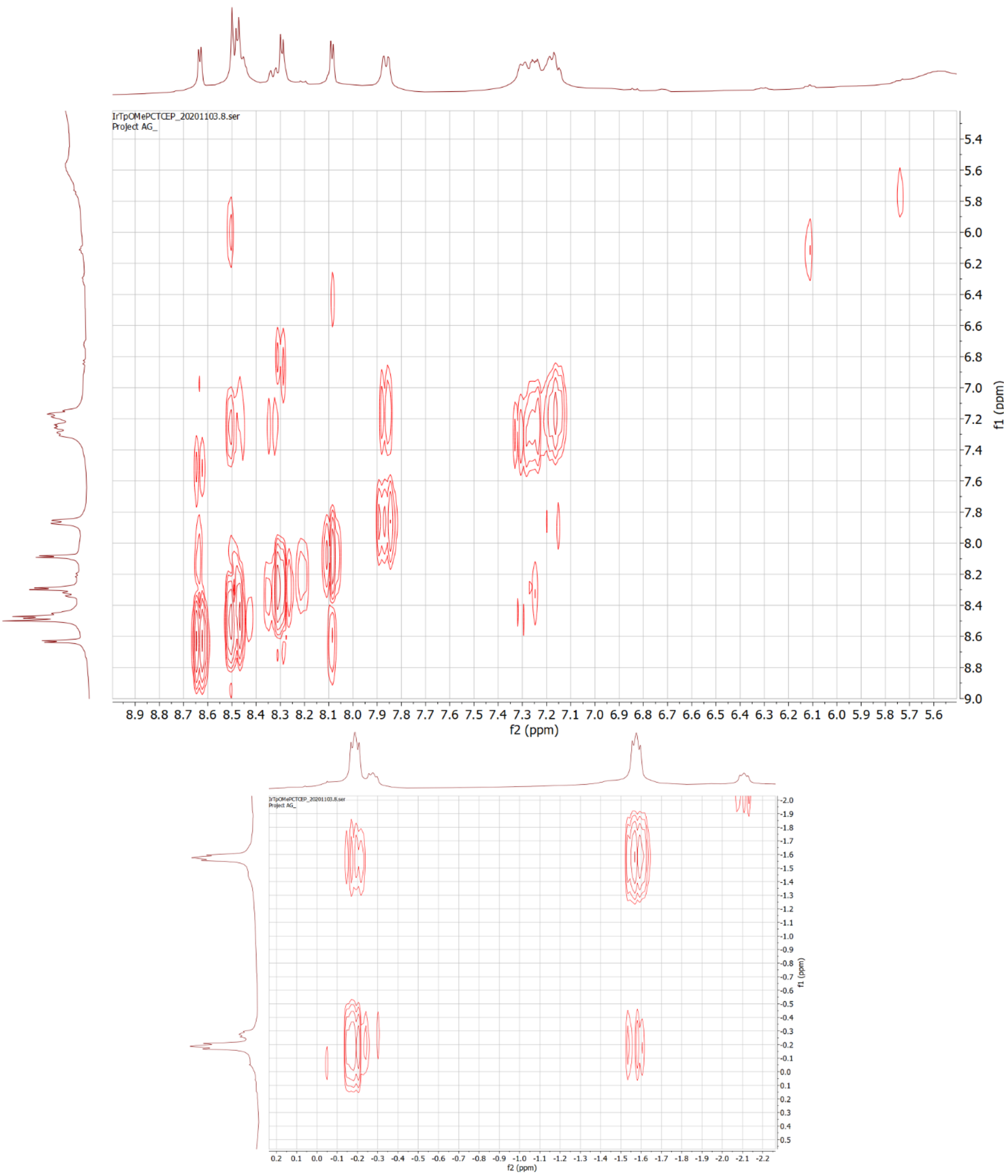

Figure S10. ^1H-^1H COSY of Ir[T*p*OMePC](tcep) in methanol-*d*$_4$. Top: close-up of aromatic area; bottom: close-up of ligand area.

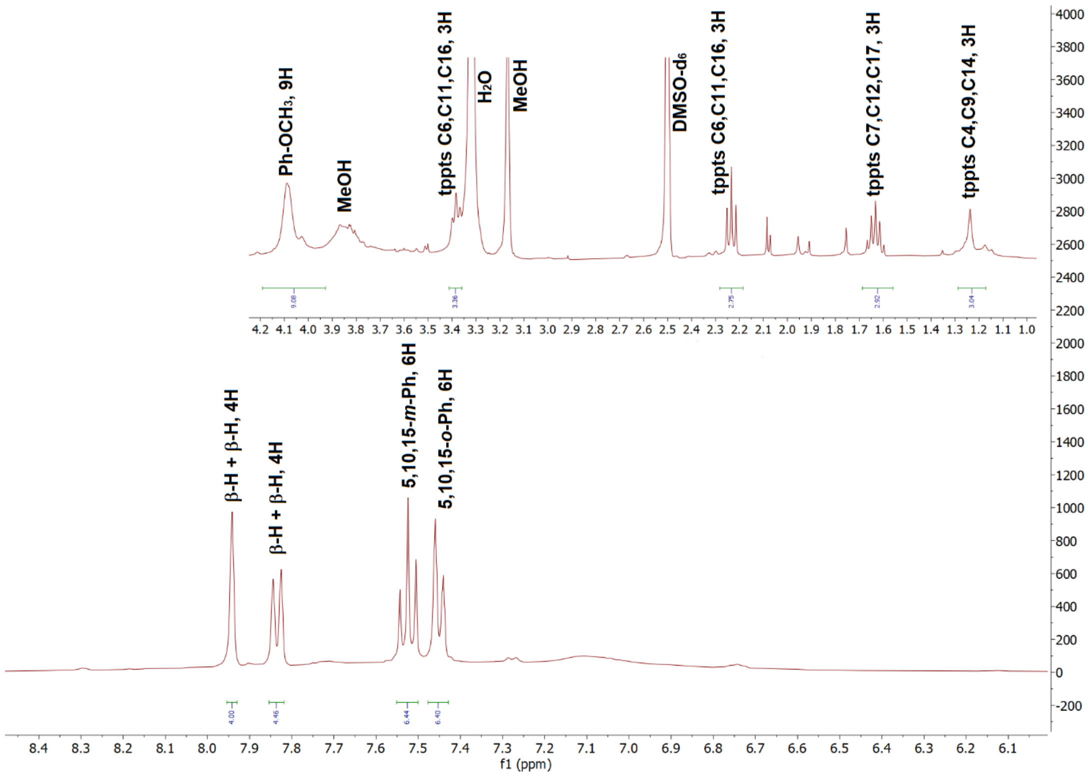

Figure S11. ^{1}H NMR spectrum of Ir[T*p*OMePC](tppts) in DMSO-*d*$_6$.

Figure S12. ^{1}H-^{1}H COSY of Ir[T*p*OMePC](tppts) in DMSO-*d*$_6$.

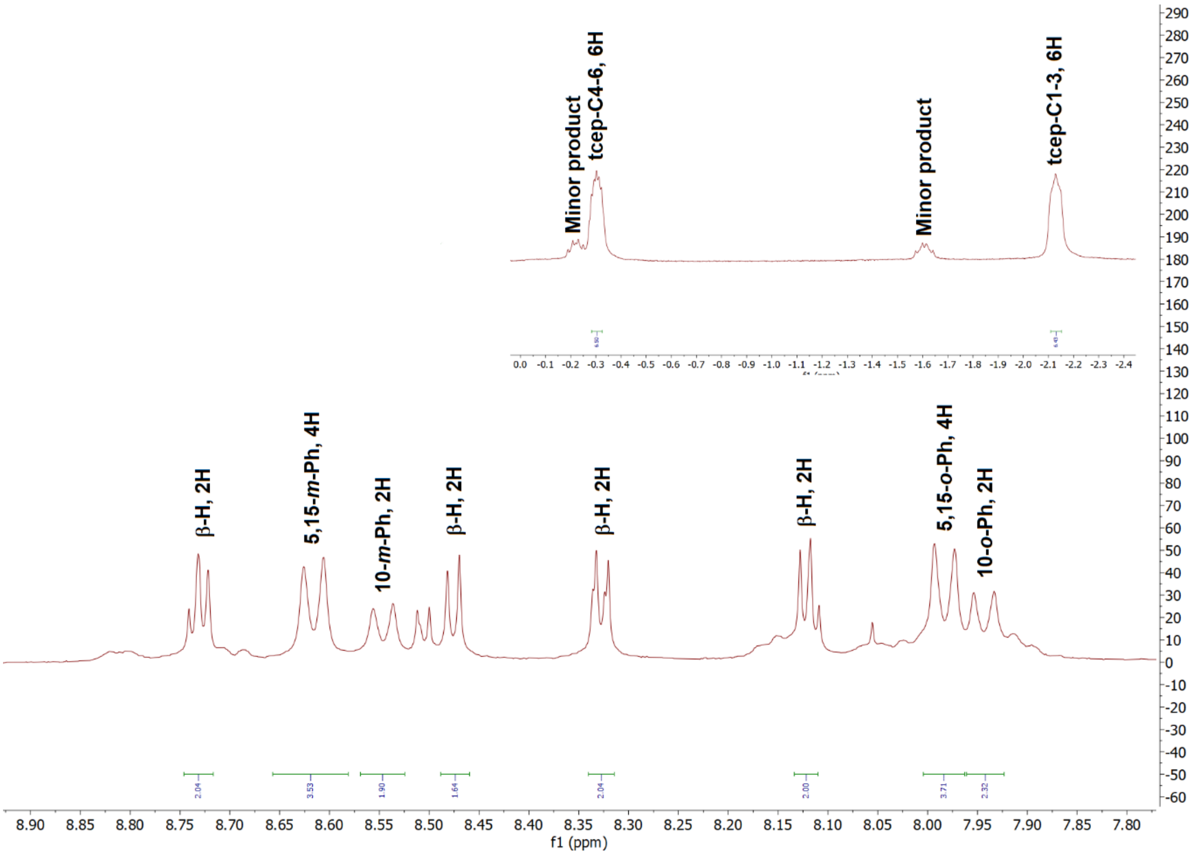

Figure S13. ^{1}H NMR spectrum of Ir[T*p*CF$_3$PC](tcep) in methanol-*d*$_4$.

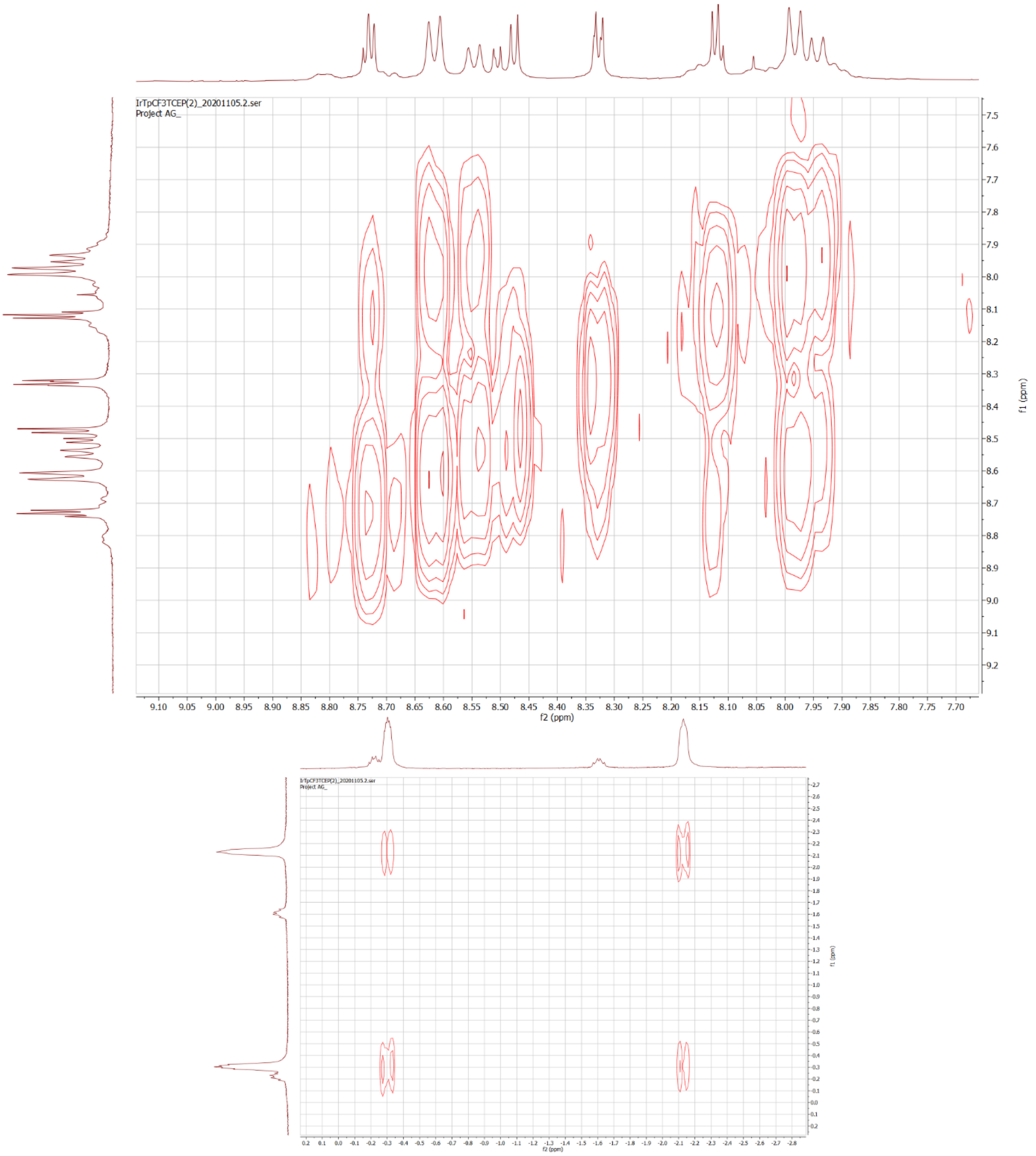

Figure S14. ^{1}H-^{1}H COSY of Ir[T*p*CF$_3$PC](tcep) in methanol-*d*$_4$. Top: close-up of aromatic area; bottom: close-up of ligand area.

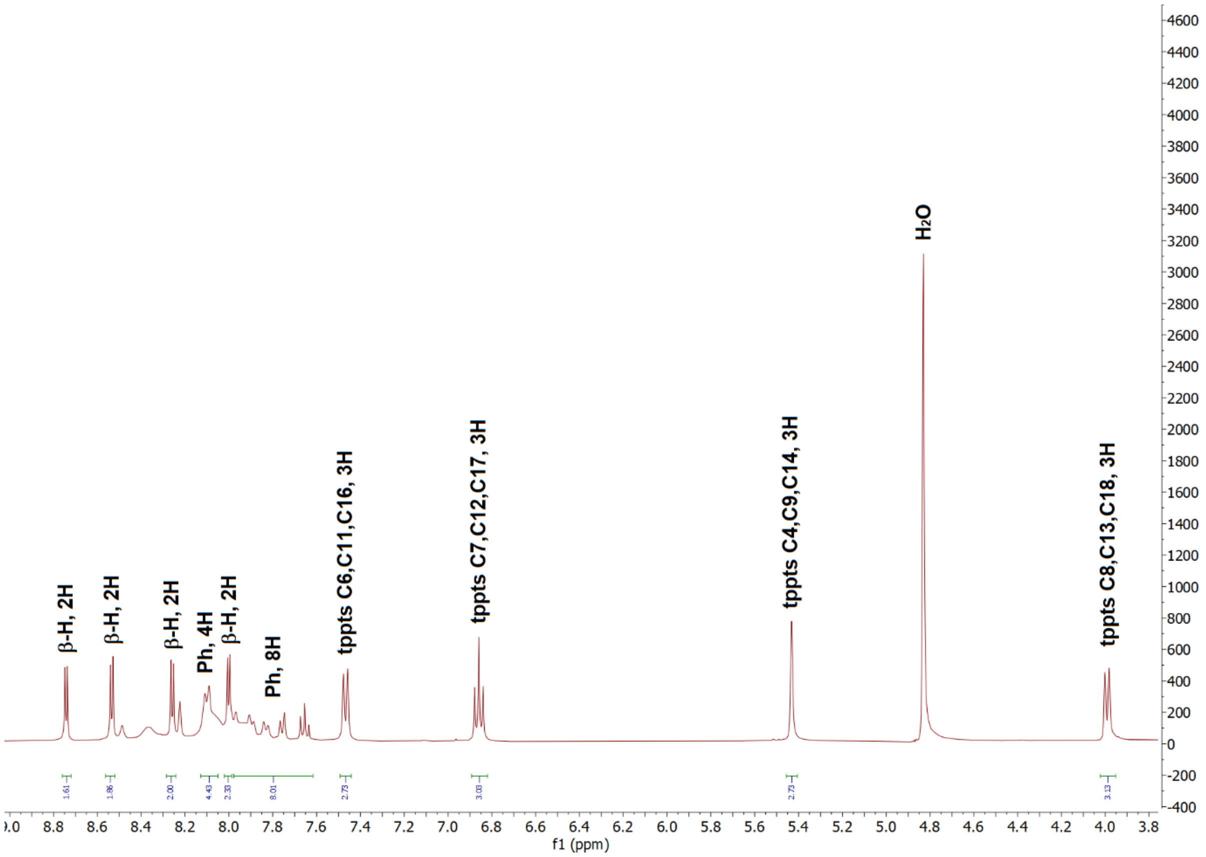

Figure S15. ^{1}H NMR spectrum of Ir[T*p*CF$_3$PC](tppts) in methanol-*d*$_4$.

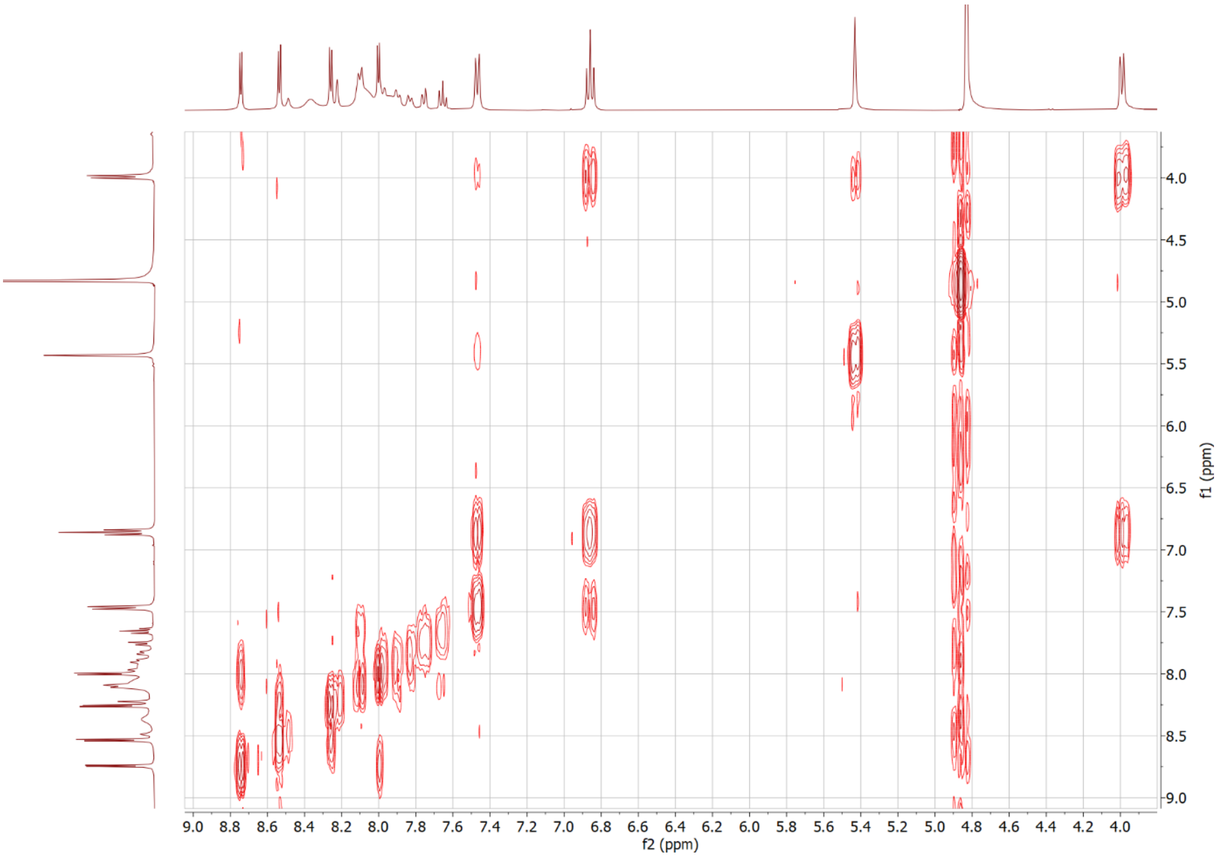

Figure S16. ^{1}H-^{1}H COSY of Ir[T*p*CF$_3$PC](tppts) in methanol-*d*$_4$.

Appendix 1

ACCOUNTS
of chemical research

pubs.acs.org/accounts

Article

The Story of 5d Metallocorroles: From Metal–Ligand Misfits to New Building Blocks for Cancer Phototherapeutics

Abraham B. Alemayehu, Kolle E. Thomas, Rune F. Einrem, and Abhik Ghosh*

Cite This: *Acc. Chem. Res.* 2021, 54, 3095–3107

Read Online

ACCESS | Metrics & More | Article Recommendations

CONSPECTUS: Porphyrin chemistry is Shakespearean: over a century of study has not withered the field's apparently infinite variety. Heme proteins continually astonish us with novel molecular mechanisms, while new porphyrin analogues bowl us over with unprecedented optical, electronic, and metal-binding properties. Within the latter domain, corroles occupy a special place, exhibiting a unique and rich coordination chemistry. The 5d metallocorroles are arguably the icing on that cake.

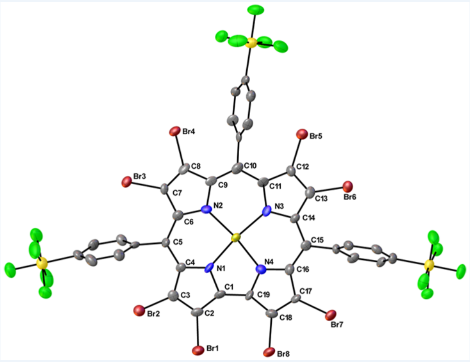

New Zealand chemist Penny Brothers has used the word "misfit" to describe the interactions of boron, a small atom with a predilection for tetrahedral coordination, and porphyrins, classic square-planar ligands. Steve Jobs lionized misfits as those who see things differently and push humanity forward. Both perspectives have inspired us. The 5d metallocorroles are misfits in that they encapsulate a large 5d transition metal ion within the tight cavity of a contracted porphyrin ligand.

Given the steric mismatch inherent in their structures, the syntheses of *some* 5d metallocorroles are understandably capricious, proceeding under highly specific conditions and affording poor yields. Three broad approaches may be distinguished.

(a) In the *metal–alkyl approach*, a free-base corrole is exposed to an alkyllithium and the resulting lithio-corrole is treated with an early transition metal chloride; a variant of the method eschews alkyllithium and deploys a transition metal–alkyl instead, resulting in elimination of the alkyl group as an alkane and insertion of the metal into the corrole. This approach is useful for inserting transition metals from groups 4, 5, and, to some extent, 6, as well as lanthanides and actinides.

(b) In our laboratory, we have often deployed a *low-valent organometallic approach* for the middle transition elements (groups 6, 7, 8, and 9). The reagents are low-valent metal–carbonyl or –olefin complexes, which lose one or more carbon ligands at high temperature, affording coordinatively unsaturated, sticky metal fragments that are trapped by the corrole nitrogens.

(c) Finally, a *metal acetate approach* provides the method of choice for gold and platinum insertion (groups 10 and 11).

This *Account* provides a first-hand perspective of the three approaches, focusing on the last two, which were largely developed in our laboratory. In general, the products were characterized with X-ray crystallography, electrochemistry, and a variety of spectroscopic methods. The physicochemical data, supplemented by relativistic DFT calculations, have provided fascinating insights into periodic trends and relativistic effects.

An unexpected feature of many 5d metallocorroles, given their misfit character, is their remarkable stability under thermal, chemical, and photochemical stimulation. Many of them also exhibit long triplet lifetimes on the order of 100 μs and effectively sensitize singlet oxygen formation. Many exhibit phosphorescence in the near-infrared under ambient conditions. Furthermore, water-soluble ReO and Au corroles exhibit impressive photocytotoxicity against multiple cancer cell lines, promising potential applications as cancer phototherapeutics. We thus envision a bright future for the compounds as rugged building blocks for new generations of therapeutic and diagnostic (theranostic) agents.

■ KEY REFERENCES

- Thomas, K. E.; Alemayehu, A. B.; Conradie, J.; Beavers, C.; Ghosh, A. Synthesis and Molecular Structure of Gold Triarylcorroles. *Inorg. Chem.* **2011**, *50*, 12844–12851.[1] Not the first paper to report gold corroles, but the first to make them readily accessible. The "acetate method" described herein is still the method of choice for Au corroles.
- Alemayehu, A. B.; Vazquez-Lima, H.; Beavers, C. M.; Gagnon, K. J.; Bendix, J.; Ghosh, A. Platinum Corroles.

Received: May 12, 2021
Published: July 23, 2021

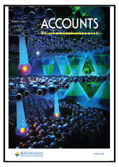

Chart 1. Periodic Table of Corroles[a]

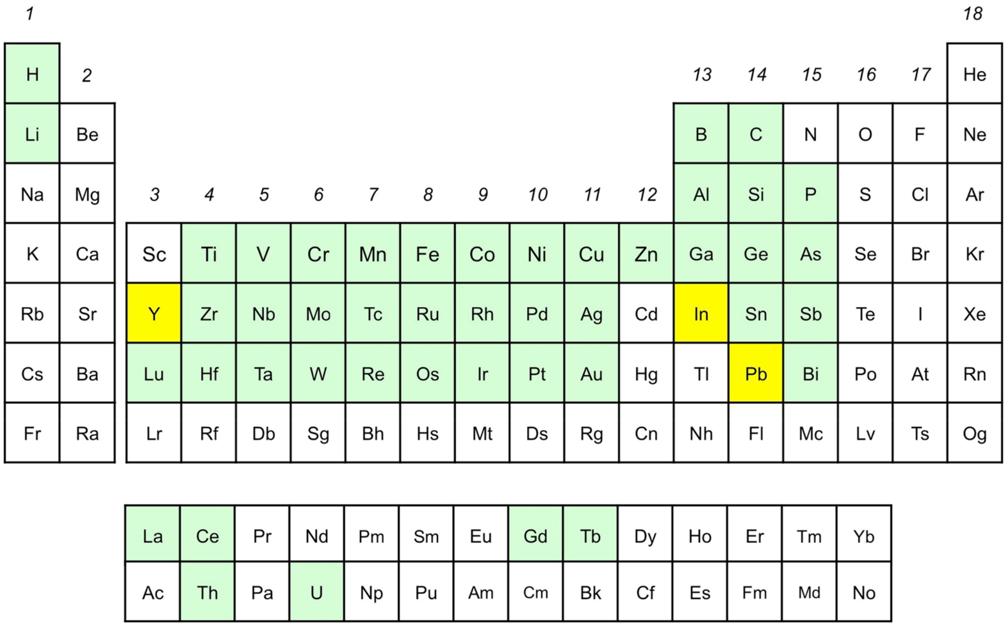

1	2	3	4	5	6	7	8	9	10	11	12	13	14	15	16	17	18
H 🟩																	He
Li 🟩	Be											B 🟩	C 🟩	N	O	F	Ne
Na	Mg											Al 🟩	Si 🟩	P 🟩	S	Cl	Ar
K	Ca	Sc	Ti 🟩	V 🟩	Cr 🟩	Mn 🟩	Fe 🟩	Co 🟩	Ni 🟩	Cu 🟩	Zn 🟩	Ga 🟩	Ge 🟩	As 🟩	Se	Br	Kr
Rb	Sr	Y 🟨	Zr 🟩	Nb 🟩	Mo 🟩	Tc 🟩	Ru 🟩	Rh 🟩	Pd 🟩	Ag 🟩	Cd	In 🟨	Sn 🟩	Sb 🟩	Te	I	Xe
Cs	Ba	Lu 🟩	Hf 🟩	Ta 🟩	W 🟩	Re 🟩	Os 🟩	Ir 🟩	Pt 🟩	Au 🟩	Hg	Tl	Pb 🟨	Bi 🟩	Po	At	Rn
Fr	Ra	Lr	Rf	Db	Sg	Bh	Hs	Mt	Ds	Rg	Cn	Nh	Fl	Mc	Lv	Ts	Og

La 🟩	Ce 🟩	Pr	Nd	Pm	Sm	Eu	Gd 🟩	Tb 🟩	Dy	Ho	Er	Tm	Yb
Ac	Th 🟩	Pa	U 🟩	Np	Pu	Am	Cm	Bk	Cf	Es	Fm	Md	No

[a] Green backgrounds indicate structurally characterized corroles; yellow backgrounds indicate known derivatives that have not been structurally characterized.

Chem. Commun. **2014**, *50*, 11093−11096.[2] Perhaps the best illustration of the sheer capriciousness of 5d metal insertion into corroles and of the ultimate success of the acetate method.

- Alemayehu, A. B.; Gagnon, K. J.; Terner, J.; Ghosh, A. Oxidative Metalation as a Route to Size-Mismatched Macrocyclic Complexes: Osmium Corroles. *Angew. Chem., Int. Ed.* **2014**, *53*, 14411−14414.[3] One of the simpler, higher-yielding syntheses for 5d metallocorroles.
- Einrem, R. F.; Gagnon, K. J.; Alemayehu, A. B.; Ghosh, A. Metal-Ligand Misfits: Facile Access to Rhenium-Oxo Corroles by Oxidative Metalation. *Chem. - Eur. J.* **2016**, *22*, 517−520.[4] Arguably the simplest among all syntheses of 5d metallocorroles.

1. INTRODUCTION

Over the last dozen or so years, an unlikely new chapter has been added to the coordination chemistry of porphyrin-type molecules, namely, the synthesis and characterization of the 5d metallocorroles. Unlikely—because the sterically constrained N_4 cores of corroles are snug even for first-row transition metals, so until a few years ago it was far from clear that 5d transition metals would eventually all yield stable complexes.[5,6] One such complex, $Re^{V}O$ *meso*-tris(trifluoromethyl)corrole, $Re^{V}[TCF_3C](O)$, however, had already been reported in 1998, as the product of an unexpected ring contraction during an attempted rhenium insertion into a porphyrin.[7] A full decade elapsed until the next 5d metallocorroles, six-coordinate iridium(III) corroles, were synthesized by Gray and co-workers.[8] Gold corroles were the next "obvious" target and were synthesized essentially simultaneously by us and by Gross's lab at the Technion.[9,10] Meanwhile, Arnold and co-workers at the University of California, Berkeley, developed the chemistry of early transition metal corroles, focusing on groups 4 and 5.[11] In 2014, the two remaining dominoes, platinum[2] and osmium[3] corroles, fell at our Tromsø laboratory, "completing" the 5d series and indeed an entire rectangle of transition metals from group 4 through 11 in the periodic table of corroles (Chart 1). This Account presents the coordination chemistry of 5d metallocorroles, largely as it unfolded in our laboratory, focusing on synthetic methods, structural chemistry, optical, electrochemical, and photophysical properties, and applications to photomedicine, particularly photodynamic therapy.

The synthetic methods available for 4d and 5d metallocorroles are more limited relative to those available for 3d metallocorroles as well as for metalloporphyrins, reflecting the steric mismatch between the large size of the heavier transition metal ions and the corroles' tight central cavities. (The natural radius of the corroles' central cavity, at ∼1.9 Å, is about 0.1 Å shorter than that of porphyrins, ∼2.0 Å.) Three classes of methods may be broadly distinguished, which we dub the metal−alkyl method,[11] the low-valent organometallic method, and the acetate/carboxylate method. The three approaches appear to be particularly suited for early, middle, and late 4d/5d transition metals, respectively. In this Account, we focus particularly on the latter two approaches, since many of the detailed procedures were worked out in our laboratory.

Understandably, the synthetic procedures for 5d metallocorroles tend to be capricious, with the metal source, solvent, temperature, and added base all playing decisive roles in the formation of the final product. This point may be appreciated from Scheme 1, which summarizes the protocols developed to date with the low-valent organometallic approach. For rhenium, for instance, small differences in reaction conditions favor either ReO corroles or metal−metal-bonded Re corrole dimers. While a high-boiling solvent (such as decalin, 1,2-dichlorobenzene, or 1,2,4-trichlorobenzene), $Re_2(CO)_{10}$, a base, and anaerobic conditions are required for both products, somewhat lower temperatures (160−180 °C) may be used for ReO corroles in contrast to Re corrole dimers, which require temperatures $\gtrsim$180 °C. The key difference appears to lie in the nature of the base: potassium carbonate is the preferred base for ReO corroles and

Scheme 1. Synthetic Methods for 4d and 5d Metallocorroles

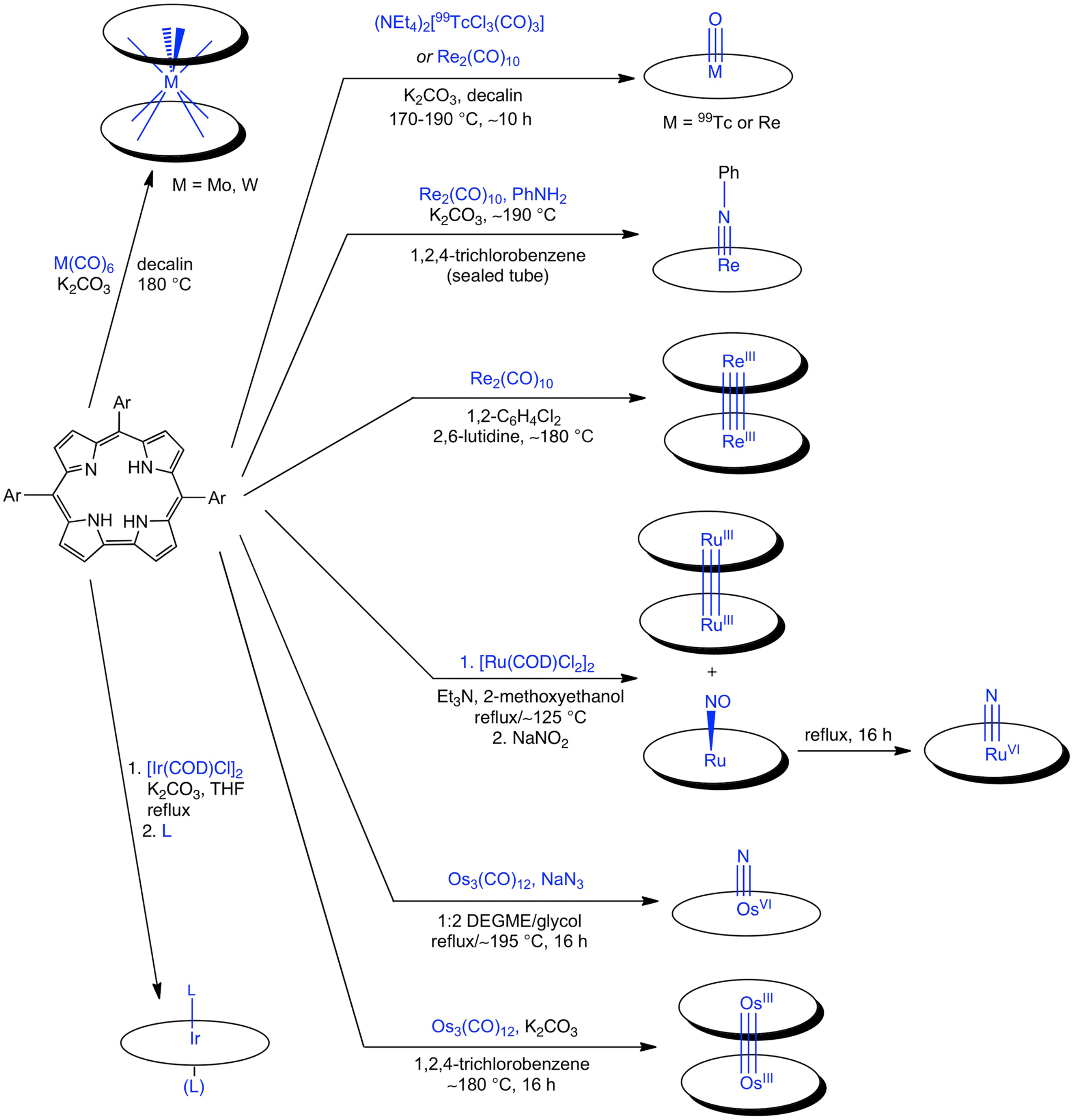

notably fails to afford Re corrole dimers; 2,6-lutidine appears to be the preferred choice for the latter. Thus, it appears that the oxygen atom of ReO corroles derives at least in part from potassium carbonate (as well as adventitious O_2). In the same vein, homologous 4d and 5d elements such as Ru and Os, for all their qualitative similarities, typically require different experimental conditions for insertion into corroles. Overall, the 4d and 5d metallocorroles have given us broad opportunities to practice the coordination chemist's art, opportunities that in our opinion are far from exhausted.

The new compounds emerging out of this endeavor have yielded a treasure trove of structural,[12] spectroscopic, and electrochemical data,[13] allowing for detailed studies of periodic trends and relativistic effects[14] in coordination chemistry. While perusing this Account, the reader is encouraged to examine the data in Table 1 to discern structural trends and resort to the Cambridge Structural Database[15] for additional details using the refcode provided for each structure.

2. EARLY 4d AND 5d METALLOCORROLES (GROUPS 4 AND 5)

The chemistry of group 4 and 5 metallocorroles was largely developed by John Arnold and co-workers and has been reviewed by these authors.[11] In addition, Arnold's former student, Heather Buckley, in her Ph.D. thesis, has provided a lively first-person account of this chemistry.[16] The syntheses

Table 1. Selected Structural Data (Å) from Representative Transition Metal Corroles with Emphasis on 4d and 5d Metallocorroles[a]

complex	M–N$_1$/N$_4$[b]	M–N$_2$/N$_3$[b]	M–N$_{plane}$[c]	M–L[d]	conformation	CSD refcode
Group 4						
Ti[Mes$_2$*p*OCH$_3$PC]Cl	1.993	1.988	0.667	2.220	domed	NIYDUW
{Zr[Mes$_2$*p*OCH$_3$PC](*μ*-Cl)-(THF)}$_2$	2.161–2.166		1.355	2.687	domed	NIYFAE
{Hf[Mes$_2$*p*OCH$_3$PC](*μ*-Cl)}$_2$	2.142–2.157		1.184	2.208	domed	NIYDEG
Group 5						
{Nb[Mes$_2$*p*OCH$_3$PC]}$_2$(*μ*-O)$_3$	2.113	2.121	0.987	2.075	domed	AQUBAS
{Ta[Mes$_2$*p*OCH$_3$PC]}$_2$(*μ*-O)$_3$	2.099	2.111	0.967	2.063	domed	AQOZUE
Ta[Mes$_2$*p*OCH$_3$PC](N^{t}Bu)	2.085	2.046	0.775	1.778	domed	UCIVEK
Ta[Mes$_2$*p*OCH$_3$PC]Cl$_2$	2.065	2.074	0.903	2.374	domed	UCIVAG
Group 6						
Cr[TPFPC](O)	1.928	1.943	0.562	1.570	planar	WIZRUS
Cr[TPFPC](NMes)	1.938	1.948	0.537	4.636	planar	NAQDAL
Mo[TPFPC](O)	2.034	2.0385	0.729	1.684	domed	YEBTIJ
Mo[T*p*OCH$_3$PC]Cl$_2$	2.033	2.0635	0.884	2.3697	domed	NEMMAW
Mo[T*p*CH$_3$PC]$_2$	2.160–2.228		1.179	–	domed	HAPVEC
{W^{VI}[TPFPC]}$_2$(*μ*-O)$_3$	2.058(7)–2.124(7)		0.961	2.0105	domed	CAWVAZ
W[Mes$_2$*p*OCH$_3$PC]Cl$_2$	2.032	2.056	0.867	2.3675	domed	WUNZUC
W[TPC]$_2$	2.150–2.218		1.171		domed	OKIJID
Group 7						
Mn[T*p*CH$_3$PC](Cl)	1.917	1.930	0.374	2.295	planar	VIHNAE
Mn[TPh$_3$PC](O)	1.899	1.920	0.527	1.633	planar	NICFOX
Tc[T*p*OCH$_3$PC](O)	1.981	2.002	0.687	1.660	domed	NATCAP
Re[T*p*FPC](O)	1.991	2.009	0.704	1.668	domed	NAGXEB
Re[T*p*FPC](NPh)	2.000	2.013	0.693	1.721	domed	OJEBAJ
Re[Cl$_8$T*p*CH$_3$PC](O)	1.9935	2.018	0.671	1.677	domed	IPUNUF
Re[Br$_8$T*p*FPC](O)	1.9965	2.015	0.668	1.673	saddled/domed	IPUPAN
{Re[T*p*CH$_3$PC]}$_2$	2.0035	2.0145	0.531	2.236	domed	ISUREW
Group 8						
Fe[TDCPC](NO)	1.900	1.920	0.452	1.641	planar	AGULET
Ru[TPFPC](NO)	1.967	1.998	0.54	1.715	domed	HUQJEI
Ru[TPC](N)	1.969	1.997	0.605	1.613	domed	HAWXIP
{Ru[T*p*CF$_3$PC]}$_2$	1.963	1.982	0.517	2.183	domed	HAWXUB
Os[T*p*CF$_3$PC](N)	1.981	1.999	0.605	1.643	domed	POPTOF
Os[Cl$_8$TPC](N)	1.985	1.995	0.565	1.636	domed	QUFYAU
(AsPh$_4$){Os[T*p*CF$_3$TPC](N)-PtCl$_3$}	1.975	1.983	0.578	1.660	domed	QUFYEY
{Os[T*p*CF$_3$PC]}$_2$	1.979	1.995	0.522	2.240	domed	NODDUI
Group 9						
Co[T*p*MePC](py)$_2$	1.869	1.900		1.991	planar	FIFXEA
Co[TPFPC](PPh$_3$)	1.871	1.885	0.262	2.205	planar	BAQPUF
Rh[TPFPC](py)$_2$	1.942	1.966		2.066	planar	HIQDET
Rh[TPFPC](PPh$_3$)	1.963	1.972	0.227	2.222	domed	MELBUA
Ir[TPFPC](Me$_3$N)$_2$	1.954	1.975		2.186	planar	COHYII
Ir[Br$_8$TPFPC](Me$_3$N)$_2$	1.961	1.988		2.189	planar	COHYOO
Group 10						
(PyMe){Pd[TPFPC]}	1.928	1.947			planar	MUDKOO
Pt^{IV}[TPC$^{\bullet}$](*m*-C$_6$H$_4$CN)(*p*-C$_6$H$_4$CH$_3$)	1.947	1.969		2.1165	planar	FOKQAZ
Pt^{IV}[TPC](*m*-C$_6$H$_4$CN)(py)	1.944	1.9605		2.1245	planar	IQOHII
Group 11						
Cu[TPC]	1.893	1.892			saddled	KAGGIJ
Cu[Br$_8$T*p*MePC]	1.916	1.916			strongly saddled	FUNPIP
Cu[(CF$_3$)$_8$T*p*FPC]	1.926	1.924			exceptionally saddled	OVEVAN
Ag[T*p*FPC]	1.943	1.964			saddled	BAYSUR
Ag[Br$_8$T*p*MePC]	1.983	1.983			strongly saddled	FUNPOV
Au[T*p*FPC]	1.939	1.956			slightly saddled	BAYSOL
Au[Br$_8$TPFPC]	1.937	1.970			slightly saddled	UCEXUX
Au[Br$_8$T*p*SF$_5$PC]	1.937	1.963			planar	AGACAP
Au[(*p*CF$_3$P)$_8$TPC]	1.941	1.964			planar	NISCEA
Au[(CF$_3$)$_8$T*p*FPC]	1.9505	1.935			planar	LUHLUX
Au[I$_4$TPFPC]	1.9145	1.935			almost planar	EBOZAZ
Au[(CF$_3$)$_4$TPFPC]	1.935	1.935			planar	CEBVEN

https://doi.org/10.1021/acs.accounts.1c00290

Table 1. continued

[a]Abbreviations: TDCPP = *meso*-tris(2,6-dichlorophenyl)corrolato; TPFPC = *meso*-tris(pentafluorophenyl)corrolato; TPC = *meso*-triphenylcorrolato; TpXPC = *meso*-tris(*p*-X-phenyl)corrolato. [b]N_1 and N_4 refer to the two nitrogens within the bipyrrole unit of the corrole; N_2 and N_3 refer to the other two nitrogens. [c]$M-N_{plane}$ refers to the displacement of the M atom from the best-fit plane of the four central nitrogens. [d]L refers to the axial ligand(s).

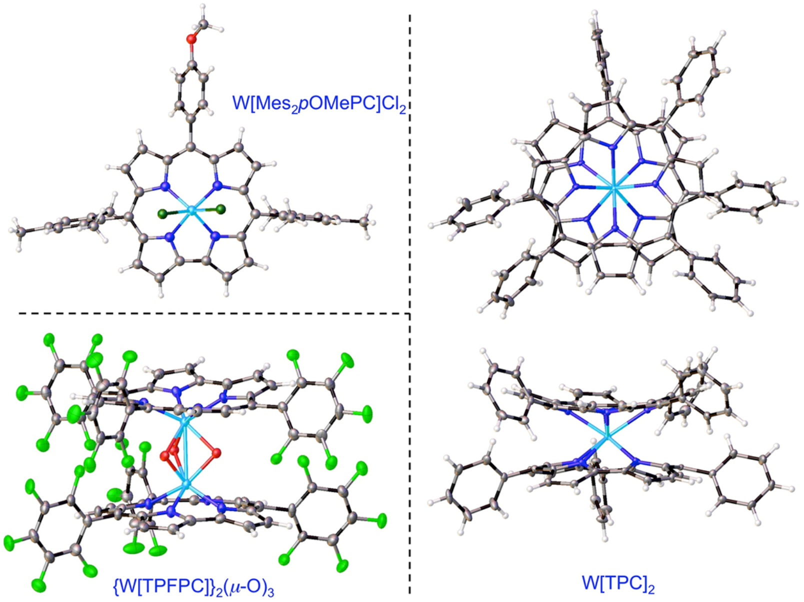

Figure 1. X-ray structures of selected W corroles. See Table 1 for key structural data: CAWVAZ, WUNZUC, and OKIJID.

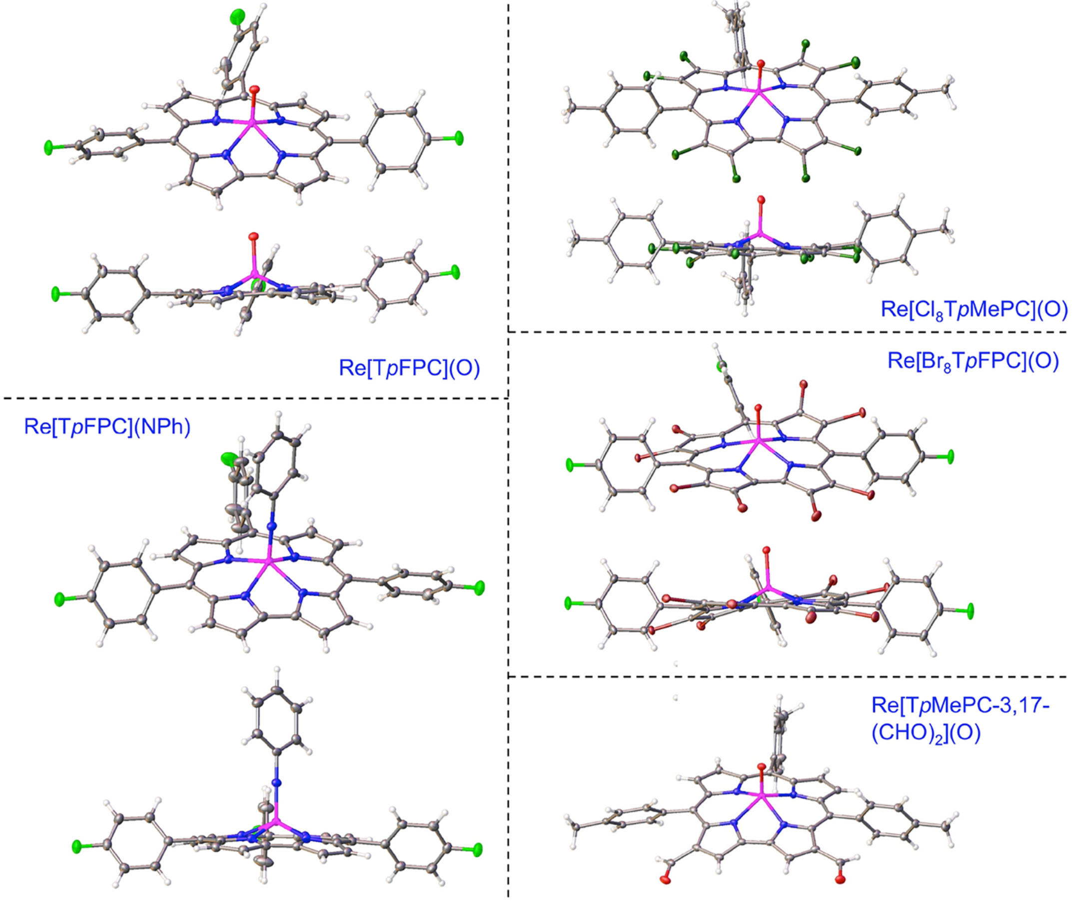

Figure 2. X-ray structures of selected Re corroles. See Table 1 for key structural data, including those for NAGXEB, IPUNUF, IPUPAN, and OJEBAJ.

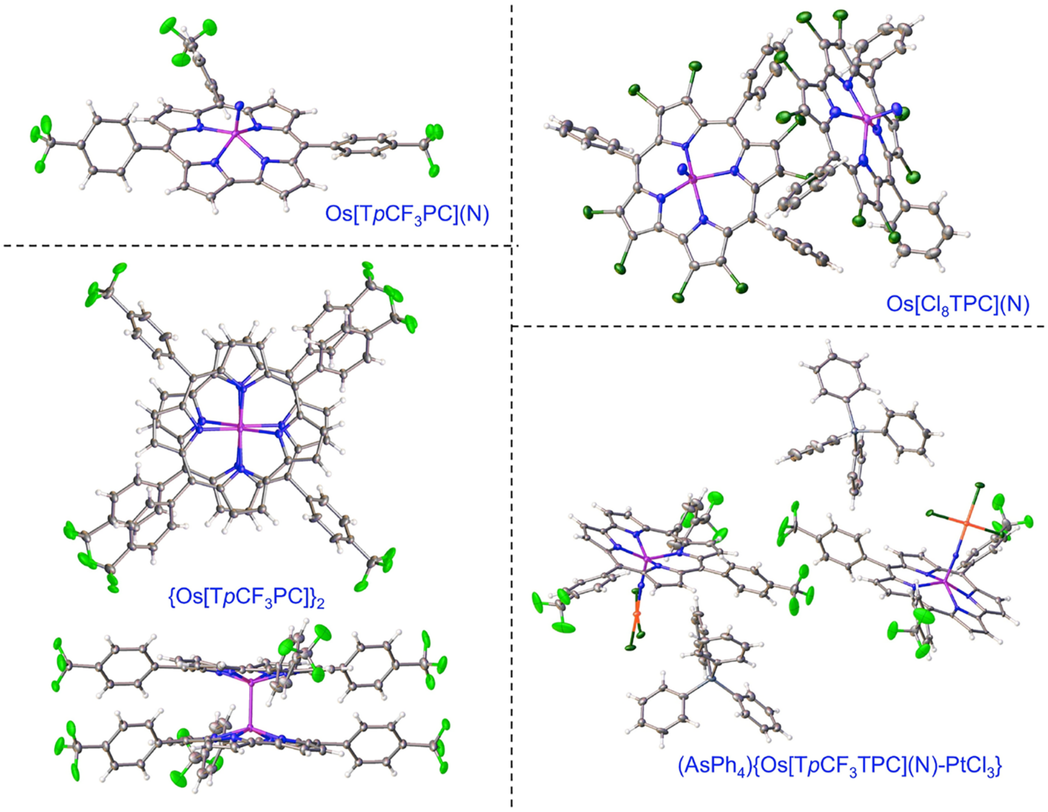

Figure 3. X-ray structures of selected Os corroles. See Table 1 for key structural data: POPTOF, QUFYAU, QUFYEY, and NODDUI.

generally involved some variant of the metal−alkyl method. The lithium salt of the electron-rich ligand 10-(4-methoxyphenyl)-5,15-dimesitylcorrole, Li_3[Mes$_2$*p*OMePhC][17] (Mes = mesityl), proved to be a particularly versatile intermediate in this context. In other cases, the use of a 4d or 5d metal−alkyl precursor allowed the researchers to sidestep the lithium salt and directly access the metallocorrole of interest. Several of the halido and imido complexes proved extraordinarily sensitive to hydrolysis, thwarting attempts at obtaining crystal structures and underscoring the consequences of the highly electropositive and oxophilic nature of these elements. While space does not permit a more detailed discussion, these complexes provide a counterpoint to the far more rugged middle and late 5d metallocorroles that are the main subject of this Account.

3. GROUP 6 METALLOCORROLES (Mo AND W)

Molybdenum-oxo corroles are some of the most rugged among metallocorroles and are readily synthesized by heating a free-base corrole, $Mo(CO)_6$, and a base such as K_2CO_3 in a high-boiling solvent.[18] Oddly, the analogous WO corroles are still unknown. While we do not seriously doubt their existence, attempted insertion of W into H_3[TPFPC] with WCl_6 resulted in the triply bridged binuclear complex $\{W^{VI}[\mathrm{TPFPC}]\}_2(\mu\text{-O})_3$ (Figure 1).[19] Because of relativistic destabilization of the 5d orbitals, WO corroles might be slightly more easily oxidized than MoO corroles. Interestingly, interaction of Li_3[Mes$_2$*p*OMePhC] with WCl_6 in toluene affords a W^VCl_2, as opposed to a $W^{VI}Cl_3$, corrole (Figure 1).[20] An analogous Mo complex, Mo[T*p*OCH$_3$PC]Cl$_2$, has been synthesized by Bröring and coworkers via the interaction of MoO corroles and $SiCl_4$.[21] Careful examination of the published X-ray structure of the latter complex (CSD code NEMMAW) reveals a distinctive skeletal bond length alternation within the bipyrrole part of the molecule, which is often associated with a partial or full corrole radical. Unpublished DFT calculations in our laboratory also suggest a noninnocent corrole for Mo[TPC]Cl$_2$ complexes. Should these conclusions be borne out with additional evidence, $MoCl_2$ corroles would provide unusual examples of ligand noninnocence arising from 4d−π orbital interactions.

In our laboratory, we found that the high-temperature interaction of a free-base corrole with $Mo(CO)_6/W(CO)_6$ under strictly anaerobic conditions results in unique, eight-coordinate metallobiscorroles (Scheme 1 and Figure 1).[22,23] Fascinatingly, the complexes are chiral, thanks to their square antiprismatic coordination, and also conformationally stable and have been successfully resolved via chiral HPLC.[24] Their potential deployment as an inherently chiral structural element remains a fascinating prospect.

4. GROUP 7 METALLOCORROLES (Tc AND Re)

Among all 5d metallocorroles, ReO corroles are arguably the simplest to synthesize (Scheme 1 and Figure 2). Interaction of $Re_2(CO)_{10}$ with free-base corroles in refluxing decalin in the presence of K_2CO_3 affords 50−70% yields of ReO corroles.[4] In a variation of the method, addition of aniline to the reaction mixture resulted in good yields of Re-imido corroles.[25] A collaboration with Roger Alberto of the University of Zurich resulted in the insertion of ^{99}Tc under similar conditions with $(NEt_4)_2[^{99}TcCl_3(CO)_3]$;[26] suitable conditions for ^{99m}Tc insertion, however, have yet to be worked out.

Rhenium-oxo corroles are highly stable and aptly viewed as thermodynamic sinks of Re/corrole chemistry. They do, however, undergo electrophilic substitutions typical of aromatic compounds (see Figure 2 for X-ray structures of selected products). Exposure to elemental bromine over several days affords β-perbrominated derivatives. β-Perchlorination with elemental chlorine is much quicker, occurring over minutes.[27] Vilsmeier–Haack formylation (with DMF/$POCl_3$) also occurs smoothly, affording 3-formyl products in a highly regioselective manner.

5. GROUP 8 METALLOCORROLES (Ru AND Os)

Both metals may be inserted into corroles via the low-valent organometallic approach (Scheme 1).

Ruthenium insertion is most conveniently accomplished with $[Ru(COD)Cl_2]_x$ ($x \geq 2$) in refluxing 2-methoxyethanol with triethylamine as a quencher to neutralize the liberated HCl.[28,29] To effectively intercept the Ru corrole monomer, a trapping agent such as nitrite needs to be added within a minute or two of the beginning of the reaction. Under these conditions, the major product is a $\{RuNO\}^6$ corrole, along with some Ru corrole dimer. Upon prolonged heating, the RuNO corrole transfers its terminal oxygen to an unknown substrate, affording Ru-nitrido corroles.[30] For Os insertion, the reagent of choice is $Os_3(CO)_{12}$ and the reaction is slower and carried out at a higher temperature (~180 °C) in 1:2 DEGME/ethylene glycol [DEGME = 2-(2-methoxyethoxy)ethanol] with NaN_3 as a trapping agent for the initially formed Os corrole monomer.[3] The resulting OsN corroles, like their ReO counterparts,[4] are exceptionally stable, but also amenable to electrophilic aromatic substitution. Thus, β-octachlorination has been accomplished with elemental chlorine, and an OsN octachlorocorrole has been structurally characterized (Table 1 and Figure 3; CSD code QUFYAU). In an attempt to elicit more interesting reactivity, the photochemical interaction of an OsN corrole with Zeise's salt resulted in a binuclear an $Os^{VI}\equiv N-Pt^{II}$ complex. The very short OsN–Pt linkage [1.895(9)–1.917(8) Å] (Table 1 and Figure 3; CSD code QUFYEY) and the downfield ^{195}Pt NMR resonance (−2702 ppm) strongly indicated that the OsN corrole acts as a π-accepting ligand toward the Pt(II) center.[31] The reaction provides a rare example of the successful photochemical activation of a metal–ligand multiple bond that is too kinetically inert to exhibit any significant reactivity under thermal conditions.

6. AN INTERLUDE ON METAL–METAL MULTIPLE BONDING

Ruthenium corrole dimers have for some time been known as dead-end products of Ru insertion into corroles.[28−30] Two new classes of metal–metal multiple-bonded corrole dimers have recently been prepared in our laboratory, the Os[32] and Re[33] corrole dimers (Scheme 1). The Ru and Os corrole dimers are thought to be triple-bonded with a $\sigma^2\pi^4\delta^2\delta^{*2}$ bonding scheme, while the Re corrole dimers are thought to be quadruple-bonded with a $\sigma^2\pi^4\delta^2$ bonding scheme.[34] The metal–metal bond distances are all around 2.23 ± 0.01 Å across the three families of complexes (Table 1 and Figure 3); the UV–vis spectra, to a first approximation, are also rather similar. The redox potentials on the other hand underscore dramatic electronic differences among the three compounds (Figure 4). While the oxidation potentials are similar (suggesting ligand-centered oxidation), the reduction potentials and electrochemical HOMO–LUMO gap vary dramatically as a function of the element. From Ru corrole dimers to Os corrole dimers, the reduction potential downshifts by ~450 mV, reflecting relativistic destabilization of the metal–metal π^*-based LUMO.[32] Indeed, as a result of the high energy of this MO, some of the unpaired electron density in the Os dimer anion is thought to leak onto the corrole. In the case of an Re corrole dimer on the other hand, reduction entails electron addition to a much lower-energy δ^* MO, resulting in a much less negative reduction potential. The electrochemical HOMO–LUMO gaps thus span a range of ~800 mV across the three compounds, with $\{Os[TpMePC]\}_2$ (1.86 V) > $\{Ru[TpMePC]\}_2$ (1.37 V) > $\{Re[TpMePC]\}_2$ (1.06 V) (Figure 4).[33]

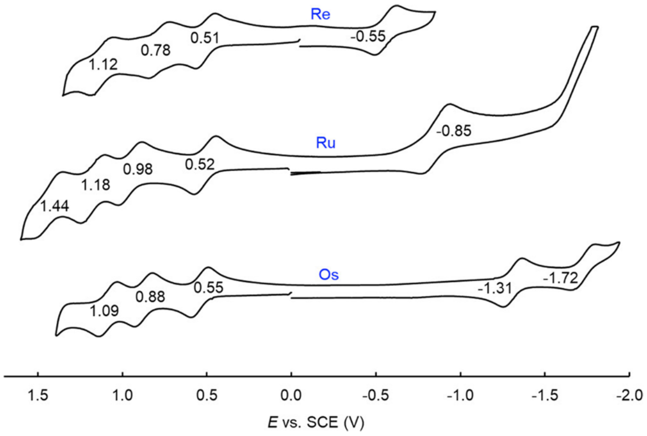

Figure 4. Comparative cyclic voltammograms for $\{M[TpMePC]\}_2$, where M = Re, Ru, and Os. Reproduced with permission from ref 33. Copyright 2021 American Chemical Society.

7. GROUP 9 METALLOCORROLES (Ir)

As mentioned above, Ir was the first 5d transition metal that was deliberately inserted into a corrole. The feat was accomplished by Joshua Palmer, then a Ph.D. student of Harry Gray's at Caltech.[8] The Caltech researchers and Zeev Gross were inspired by a then-recent report of water oxidation by Mes_3Ir^VO and surmised that corrole might stabilize a similar high-valent Ir center.[35] Although Ir was duly inserted (Scheme 1), the desired high-valent chemistry failed to materialize. A large number of six-coordinate 18-electron Ir corrole bis-amine adducts have been synthesized, as well as a smaller number of 16-electron monophosphine adducts (Table 1).[36,37] Very recently, the use of water-soluble phosphines has provided convenient access to water-soluble, five-coordinate Ir corroles.[38]

8. GROUP 10 METALLOCORROLES (Pd AND Pt)

A good way of describing synthetic methods currently available for group 10 corrole derivatives is to say that there is significant scope for improvement. A handful of key breakthroughs have taken place, however. Palladium(II) was inserted in $H_3[TPFPC]$ via interaction with $Pd(OAc)_2$ in pyridine; the $\{Pd[TPFPC]\}^-$ anion was finally isolated in stable form as the *N*-methylpyridinium salt.[39] No Pd(IV) corroles have been reported. Platinum(IV) corroles, on the other hand, have been synthesized in our laboratory; the protocols, however, are quite unsatisfactory.[2] A wide range of Pt sources and a variety of reaction conditions were explored, all without success. Ultimately, through pure serendipity, the interaction of free-base corroles with (*commercially unavailable!*) tetranuclear platinum acetate, $[Pt(OAc)_2]_4 \cdot 2HOAc$, in benzonitrile at 140–150 °C under aerobic conditions and microwave irradiation was found to afford low yields (~6%) of diamagnetic, six-coordinate $Pt^{IV}Ar$ corroles; note that the axial Ar group is

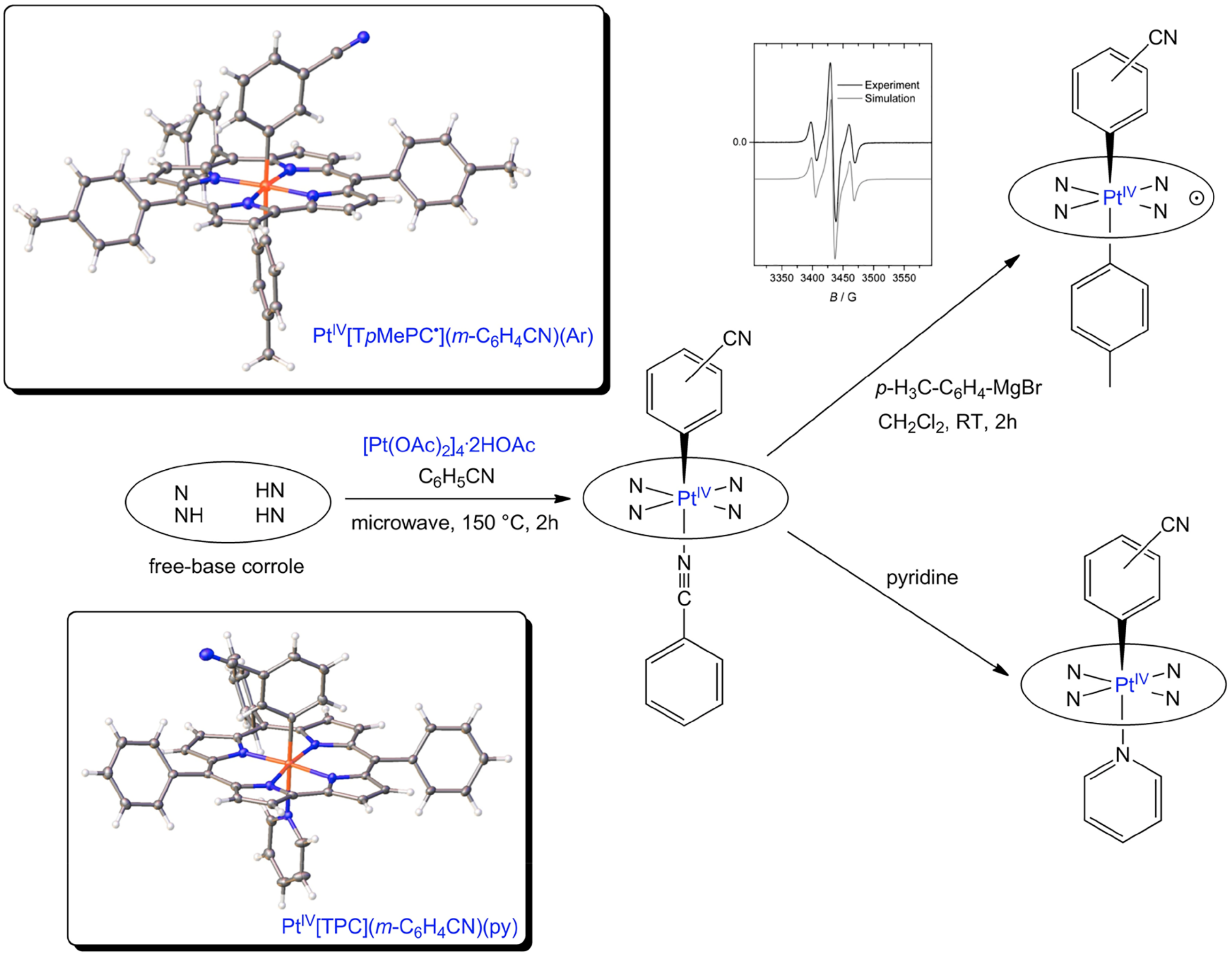

Figure 5. A snapshot of current Pt corrole chemistry: key reaction pathways and X-ray structures. See Table 1 for key structural data: FOKQAZ and IQOHII.

derived via C−H activation of PhCN (Figure 5). These products, however, proved unstable.[2] Attempted displacement of the PhCN-*N* ligand with Ar′MgBr led to neutral, paramagnetic Pt[T*p*XPC](Ar)(Ar′) derivatives, a few of which yielded single-crystal X-ray structures. Several lines of evidence, including EPR spectroscopy, established that these complexes are full-fledged metalloradicals: Pt^{IV}[TpXPC$^{•2-}$](Ar)(Ar′). The unstable PhCN-*N* complexes were also found to react with pyridine, affording stable Pt(IV) complexes with the general formula Pt^{IV}[TpXPC](Ar)(py) (Figure 5).[40] All the structurally characterized products showed strictly planar Pt-corrole cores with short Pt−N distances of 1.957 ± 0.012 Å (Table 1).

9. GROUP 11 METALLOCORROLES

The chemistry of Au corroles had somewhat of a rough start. Attempted Au insertion into simple corroles with $AuCl_3$ or $KAuCl_4$ failed, as the oxidation-prone macrocycles broke apart under the influence of the highly oxidizing Au reagents. With the then-newly available free-base *β*-octabromo-*meso*-triarylcorroles,[41,42] Au insertion finally worked, an important early step in the historical development of the 5d metallocorrole field.[9,10] Unfortunately, the Au octabromocorrole products proved poorly soluble and resistant to yielding X-ray quality crystals.[9,10]

The use of Au(III) acetate finally provided a reliable method for Au insertion into simple *meso*-triarylcorroles, underscoring the power of the "acetate method".[1] The acetate method is still the method of choice today, affording Au corroles for a variety of applications. Even for *β*-octabromocorroles, the acetate method has become the method of choice. The synthesis of Au-[Br_8T$p$$SF_5$PC] (Figure 6)[43] via the acetate method from the corresponding free-base corrole established that fluorinated substituents such as SF_5 help solubilize Au octabromocorroles. In another study, interaction of an undecaarylisocorrole with Au acetate resulted in aromatization, affording a gold undecaarylcorrole (Figure 6).[44] Finally, the Au-acetate method has even worked for azulicorrole, a rare example of a carbacorrole.[45]

Like their ReO counterparts, Au triarylcorroles undergo Vilsmeier−Haack formylation but afford symmetric 3,17-diformyl derivatives. The preference for diformylation appears to be related to the somewhat lower oxidation potentials (and hence greater nucleophilicity) of Au corroles, relative to ReO corroles. Note that Figures 2 and 6 depict as yet unpublished minor products, a ReO 3,17-diformylcorrole and a Au 3-formylcorrole, since these are the compounds that yielded crystal structures.

Gold corroles provide paradigmatic examples of planar (or slightly saddled) four-coordinate metallocorroles.[1,43,44] In so doing, they offer a sharp contrast to Cu corroles, which are *inherently* saddled. Saddling in the Cu case switches on a Cu($d_{x^2-y^2}$)−corrole(π) orbital interaction, allowing some of the

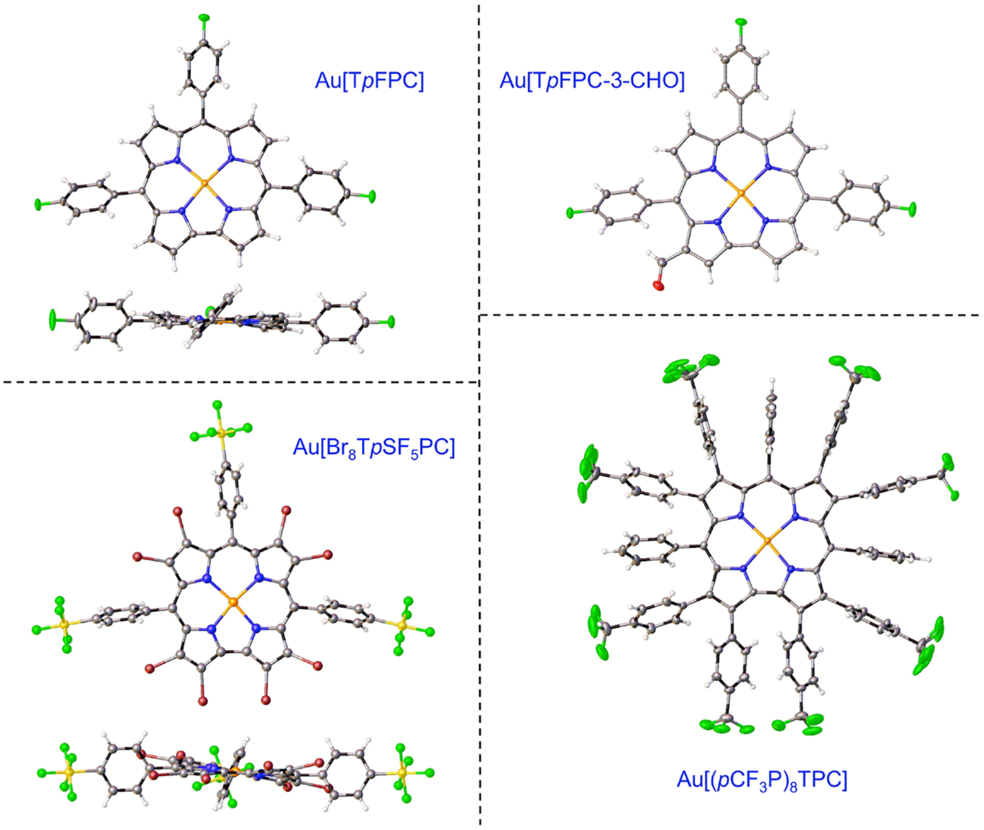

Figure 6. X-ray structures of selected Au corroles. See Table 1 for key structural data, including BAYSOL, AGACAP, and LUHLUX.

corrole π-electron density to flow into the space of the Cu(d$_{x^2-y^2}$) orbital.[46−54] Copper corroles are accordingly rightly viewed as having substantial Cu^{II}-corrole$^{\bullet 2-}$ character. In the case of Au corroles, the relativistically destabilized 5d$_{x^2-y^2}$ orbital is far too high in energy to effectively overlap with the corrole's π-HOMO, which accounts for the planarity of Au corroles. One of the most dramatic illustrations of the difference in conformational preference between Cu and Au corroles is provided by the isoelectronic β-octakis(trifluoromethyl)-*meso*-triarylcorrole complexes, M[(CF$_3$)$_8$T*p*FPC] (M = Cu, Au; Figure 7): while the Cu complex is folded like a taco (CSD code OVEVAN),[55] with adjacent pyrrole rings tilted by as much as 85° relative to each other, the Au complex is flat as a pancake (CSD code LUHLUX).[56]

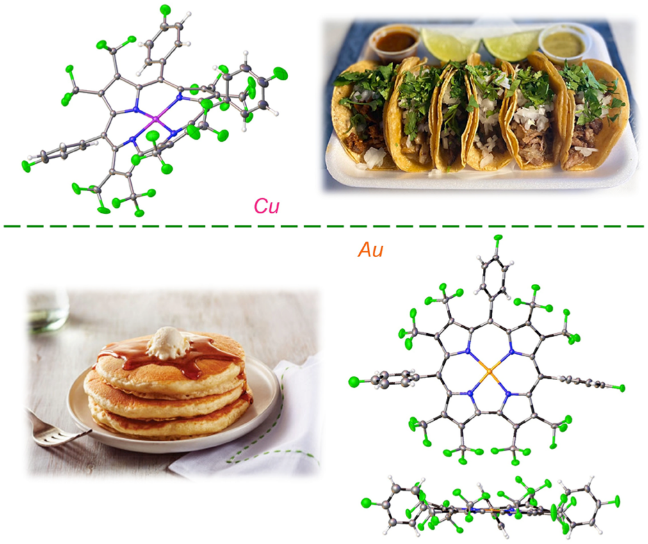

Figure 7. X-ray structures of Cu[(CF$_3$)$_8$T*p*FPC] (the "taco") and Au[(CF$_3$)$_8$T*p*FPC] (the "pancake").

10. PHOTOPHYSICAL PROPERTIES AND APPLICATIONS AS PHOTOTHERAPEUTICS

The middle and late 5d metallocorroles, involving the elements Re−Au, exhibit room-temperature phosphorescence in the near-infrared (Table 2 and Figure 8).[57] Although the phosphorescence quantum yields range from low to moderate (Ir[37,58] < Au[59] < Pt(IV)[40] < OsN[60] < ReO[61]), the complexes in general efficiently sensitize singlet oxygen formation, promising applications as sensitizers in photodynamic therapy. Indeed, amphiphilic Au and ReO triarylcorroles have already exhibited impressive *in vitro* photocytotoxicity against multiple cancer cell lines.[59,62] We remain excited about the possibility of developing nanoconjugated platforms based on 5d metallocorroles, with improved tumor-targeting and imaging (theranostic) capabilities.

Other potential applications have also been briefly examined. Thus, optical sensors based on OsN[60] and ReO[61] corroles exhibit excellent photostability and sensitize singlet oxygen formation with quantum yields >0.75. The complexes have also been found to be promising sensitizers in triplet−triplet annihilation-based upconversion systems. Interestingly, a Au corrole with carboxylic acid anchoring groups has been found to exhibit a surprisingly high power conversion efficiency of 4.2% in dye-sensitized solar cells. The observed photovoltaic activity was initially attributed to triplet-state reactivity of the Au corrole.[59] Subsequently, it became clear that the T$_1$ state is simply not energetic enough to inject an electron into titania. Femtosecond

Table 2. Photophysical Properties of Representative 5d Metallocorroles in Anoxic Toluene at 23 °C[a]

compound	absorbance maxima (nm) Soret	Q	Q	emission maximum (nm)	lifetime (μs)	rel. quantum yield (%)[b]	ref
Re[T*p*CF$_3$PC](O)	440	553	586	777	74	1.52	61
Os[T*p*CF$_3$PC](N)	444	553	593	779	183	0.39	60
Ir[TpCF$_3$PC)]py$_2$	416	602		836	5.6	~0.04	37
Pt^{IV}[T*p*CF$_3$PC](*m*-C$_6$H$_4$CN)(py)	430	569	595	813	23	0.27	40
Au[T*p*CF$_3$PC]	424	564	576	788	98	0.19[c]	59
Pt[TPTBP][b]	430	564	614	770	48	21	63

[a] λ_{ex} = 560−614 nm (at approximately the Q-band maximum). [b] Unless otherwise mentioned, Pt(II) tetraphenyltetrabenzoporpyhrin (Pt[TPTBP]),[63] was used as the reference for quantum yield measurements. [c] This quantum yield is relative to that for fluorescence of rhodamine 6G in ethanol.

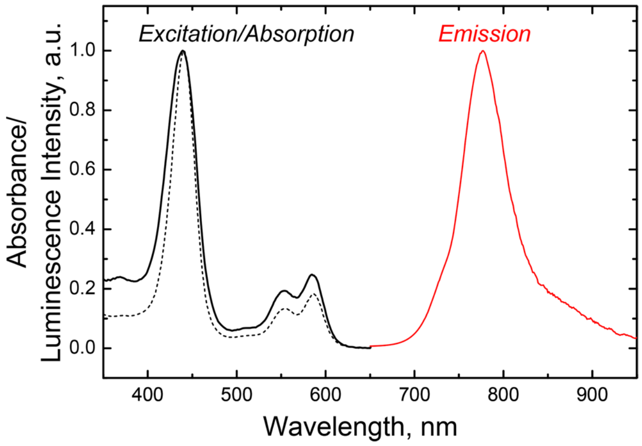

Figure 8. Absorption (black dashed line), phosphorescence excitation (black solid line; λ_{em} 775 nm) and emission (red line; λ_{ex} 590 nm) spectra of Re[T*p*CF$_3$PC](O) in toluene. Phosphorescence spectra were measured under anoxic conditions.

time-resolved transient absorption measurements also strongly indicated that photovoltaic activity reflects electron injection for the S_1 state, which effectively competes with intersystem crossing.[64] Interestingly, ReO and OsN corroles exhibit much poorer photovoltaic activity, possibly as a result of shorter S_1 lifetimes.

11. CONCLUDING REMARKS

What began a few years ago as an amusing exercise to create misfit metal−ligand assemblies has by now yielded a dozen or so families of 5d metallocorroles and a wealth of insights into fundamental questions of structure and bonding and new building blocks for photomedicine.

The low-valent organometallic method has arguably proved the most versatile, affording chiral Mo and W biscorroles, metal−metal-bonded dimers, and a variety of 1:1 metal−corrole derivatives. The acetate method provided a practical route to Au corroles and, less satisfactorily, to platinum(IV) corroles. Gratifyingly, the great majority of middle and late 5d corrole derivatives have proved thermally and photochemically rugged, as well as amenable to selective electrophilic aromatic substitution, foreshadowing a variety of practical applications.

Several of the middle and late 5d corrole derivatives have been found to exhibit NIR phosphorescence under ambient conditions. Although the phosphorescence quantum yields are low (Ir) to moderate (ReO, OsN, Pt, and Au), the complexes have all been found to efficiently sensitize singlet oxygen formation. In addition, amphiphilic Au and ReO corroles have been found to exhibit impressive photocytotoxicity against multiple cancer cell lines *in vitro*. We thus envision a bright future for biomedical applications of the 5d metallocorroles.[65] Bio-, nano-, and radioconjugation promise a wide range of multimodal therapeutic and theranostic agents for cancer. Photothermal therapy, potentially involving metallocorrole nanoconjugates, and combined photodynamic−photothermal therapy, in particular, remain fascinating prospects.

Some of the Au corroles have also proved effective as photosensitizers in dye-sensitized solar cells. Although this photovoltaic activity was originally ascribed to triplet state reactivity, it has become clear that the triplet state is not energetic enough to inject electrons into titania. Instead, femtosecond transient absorption spectroscopy strongly suggests that it is the excited singlet state that does the electron injection, effectively competing with intersystem crossing.

Finally, it is worth emphasizing that opportunities for creative coordination chemistry are far from exhausted. The development of a higher-yielding route to Pt(IV) is an obvious gap in our current knowledge. In the same vein, key aspects of axial coordination chemistry, involving carbene, carbyne, and carbon-atom (carbide) ligands, remain to be uncovered for W, Re, Os, and Ir corroles. Crazier targets include superhigh-valent species such as heptavalent rhenium or iridium or octavalent osmium complexes with nitride, carbide and other, related axial ligands.[66] We remain optimistic that some "misfit" chemist, somewhere, will successfully synthesize one or more of these species.

■ AUTHOR INFORMATION

Corresponding Author

Abhik Ghosh − *Department of Chemistry, UiT—The Arctic University of Norway, N-9037 Tromso, Norway;* orcid.org/0000-0003-1161-6364; Email: abhik.ghosh@uit.no

Authors

Abraham B. Alemayehu − *Department of Chemistry, UiT—The Arctic University of Norway, N-9037 Tromso, Norway;* orcid.org/0000-0003-0166-8937
Kolle E. Thomas − *Department of Chemistry, UiT—The Arctic University of Norway, N-9037 Tromso, Norway;* orcid.org/0000-0002-1616-4902
Rune F. Einrem − *Department of Chemistry, UiT—The Arctic University of Norway, N-9037 Tromso, Norway*

Complete contact information is available at:
https://pubs.acs.org/10.1021/acs.accounts.1c00290

Notes

The authors declare no competing financial interest.

Biographies

Abraham Alemayehu was born in Shambu, Ethiopia. He received his B.Sc. in Chemistry from the University of Addis Ababa in 2000 and his M.Sc. and Ph.D. from UiT—The Arctic University of Norway in 2005 and 2009, respectively. Alemayehu was the first to synthesize several new classes of 4d and 5d metallocorroles. He is currently investigating applications of these materials as cancer phototherapeutics.

Kolle E. Thomas was born in 1977 in Buea, Cameroon. After receiving a B.Sc. in Chemistry from the University of Buea, he obtained his M.Sc. and subsequently a Ph.D. in chemistry from the UiT—The Arctic University of Norway. Subsequently, as a postdoctoral researcher with Prof. Abhik Ghosh, he developed new synthetic methods for a variety of porphyrins, corroles and related ligands, and their metal complexes.

Rune F. Einrem was born in 1993 in Mosjøen, Norway, and has a bachelor's degree in geology and a master's degree in chemistry, both from UiT—The Arctic University of Norway. Einrem has made significant contributions to the chemistry of rhenium corroles and was the first to synthesize ^{99}Tc corroles. He is currently completing his Ph.D. with Prof. Abhik Ghosh in the area of cancer photomedicine.

Abhik Ghosh (b. 1964) is an Indian national and a professor of chemistry at UiT—The Arctic University of Norway. He obtained his B.Sc. (Hons.) at Jadavpur University, Kolkata, and his Ph.D. at the University of Minnesota, the latter under the tutelage of Professor Paul G. Gassman. Over the years, he has been a Senior Fellow at the San Diego Supercomputer Center (1997–2004) and a Visiting Professor at The University of Auckland, New Zealand (2006–2016). His research interests lie at the intersection of bioinorganic, materials, and theoretical chemistry. With former student Steffen Berg, he wrote the textbook *Arrow Pushing in Inorganic Chemistry: A Logical Approach to the Chemistry of the Main Group Elements*, which won the 2014 PROSE Award for Best Textbook in the Physical Sciences and Mathematics. Prof. Ghosh takes a certain pride in being a fluent speaker of Sanskrit and recently with Stanford linguist Paul Kiparsky has written about the possible influence of the periodic Sanskrit alphabet on the emergence of Mendeleev's periodic table (https://www.americanscientist.org/article/the-grammar-of-the-elements).

ACKNOWLEDGMENTS

We acknowledge the Research Council of Norway for long-term support, most recently via grant nos. 262229 and 324139. We would also like to express our deep appreciation for our many collaborators, including but not limited to Prof. Carl Wamser, Prof. Karl Kadish, Prof. Roger Alberto, Prof. Sergey Borisov, Prof. Jeanet Conradie, Dr. Hugo-Vazquez-Lima, Dr. Ivar K. Thomassen, Dr. Sumit Ganguly, Dr. Simon Larsen, Dr. Odrun Gederaas, Dr. Anders Reinholdt, Dr. Henrik Braband, Einar Jonsson, and Dr. Laura M^{c}Cormick-M^{c}Pherson. Likewise, it is a pleasure to acknowledge stimulating discussions with Profs. Jesper Bendix, Penny Brothers, and Heather Buckley and Dr. Joshua Palmer. This research also used resources of the Advanced Light Source, which is a DOE Office of Science User Facility under contract no. DE-AC02-05CH11231.

REFERENCES

(1) Thomas, K. E.; Alemayehu, A. B.; Conradie, J.; Beavers, C.; Ghosh, A. Synthesis and Molecular Structure of Gold Triarylcorroles. *Inorg. Chem.* **2011**, *50*, 12844–12851.

(2) Alemayehu, A. B.; Vazquez-Lima, H.; Beavers, C. M.; Gagnon, K. J.; Bendix, J.; Ghosh, A. Platinum Corroles. *Chem. Commun.* **2014**, *50*, 11093–11096.

(3) Alemayehu, A. B.; Gagnon, K. J.; Terner, J.; Ghosh, A. Oxidative Metalation as a Route to Size-Mismatched Macrocyclic Complexes: Osmium Corroles. *Angew. Chem., Int. Ed.* **2014**, *53*, 14411–14414.

(4) Einrem, R. F.; Gagnon, K. J.; Alemayehu, A. B.; Ghosh, A. Metal-Ligand Misfits: Facile Access to Rhenium-Oxo Corroles by Oxidative Metalation. *Chem. - Eur. J.* **2016**, *22*, 517–520.

(5) Nardis, S.; Mandoj, F.; Stefanelli, M.; Paolesse, R. Metal complexes of corrole. *Coord. Chem. Rev.* **2019**, *388*, 360–405.

(6) Ghosh, A. Electronic Structure of Corrole Derivatives: Insights from Molecular Structures, Spectroscopy, Electrochemistry, and Quantum Chemical Calculations. *Chem. Rev.* **2017**, *117*, 3798–3881.

(7) Tse, M. K.; Zhang, Z. Y.; Chan, K. Synthesis of an Oxorhenium(V) Corrolate from Porphyrin with Detrifluoromethylation and Ring Contraction. *Chem. Commun.* **1998**, 1199–1200.

(8) Palmer, J. H.; Gross, Z.; Gray, H. B.; et al. Iridium Corroles. *J. Am. Chem. Soc.* **2008**, *130*, 7786–7787.

(9) Alemayehu, A. B.; Ghosh, A. Gold Corroles. *J. Porphyrins Phthalocyanines* **2011**, *15*, 106–110.

(10) Rabinovich, E.; Goldberg, I.; Gross, Z. Gold(I) and Gold(III) Corroles. *Chem. - Eur. J.* **2011**, *17*, 12294–12301.

(11) Buckley, H. L.; Arnold, J. Recent Developments in Out-of-Plane Metallocorrole Chemistry Across the Periodic Table. *Dalton Trans.* **2015**, *44*, 30–36.

(12) Thomas, K. E.; Alemayehu, A. B.; Conradie, J.; Beavers, C. M.; Ghosh, A. The Structural Chemistry of Metallocorroles: Combined X-Ray Crystallography and Quantum Chemistry Studies Afford Unique Insights. *Acc. Chem. Res.* **2012**, *45*, 1203–1214.

(13) Ganguly, S.; Ghosh, A. Seven Clues to Ligand Noninnocence: The Metallocorrole Paradigm. *Acc. Chem. Res.* **2019**, *52*, 2003–2014.

(14) For a recent study of relativistic effects in Tc and Re complexes, see: Braband, H.; Benz, M.; Spingler, B.; Conradie, J.; Alberto, R.; Ghosh, A. Relativity as a Synthesis Design Principle: A Comparative Study of (3 + 2) Cycloaddition of Technetium(VII)- and Rhenium-(VII)-Trioxo Complexes with Olefins. *Inorg. Chem.* **2021**, DOI: 10.1021/acs.inorgchem.1c00995.

(15) Groom, C. R.; Bruno, I. J.; Lightfoot, M. P.; Ward, S. C. The Cambridge Structural Database. *Acta Crystallogr., Sect. B: Struct. Sci., Cryst. Eng. Mater.* **2016**, *B72*, 171–179.

(16) Buckley, H. L. Synthesis and Characterization of Metallocorrole Complexes. Ph.D. thesis, UC Berkeley, 2014; https://escholarship.org/uc/item/7jj519jb.

(17) Buckley, H. L.; Chomitz, W. A.; Koszarna, B.; Tasior, M.; Gryko, D. T.; Brothers, P. J.; Arnold, J. Synthesis of lithium corrole and its use as a reagent for the preparation of cyclopentadienyl zirconium and titanium corrole complexes. *Chem. Commun.* **2012**, *48*, 10766–10768.

(18) Johansen, I.; Norheim, H.-K.; Larsen, S.; Alemayehu, A. B.; Conradie, J.; Ghosh, A. Substituent Effects on Metallocorrole Spectra: Insights from Chromium-Oxo and Molybdenum-Oxo Triarylcorroles. *J. Porphyrins Phthalocyanines* **2011**, *15*, 1335–1344.

(19) Nigel-Etinger, I.; Goldberg, I.; Gross, Z. 5d Early-Transition-Metal Corroles: a Trioxo-Bridged Binuclear Tungsten(VI) Derivative. *Inorg. Chem.* **2012**, *51*, 1983–1985.

(20) Padilla, R.; Buckley, H. L.; Ward, A. L.; Arnold, J. Preparation and Characterization of a Tungsten(V) Corrole Dichloride Complex. *J. Porphyrins Phthalocyanines* **2015**, *19*, 150–153.

(21) Schweyen, P.; Brandhorst, K.; Hoffmann, M.; Wolfram, B.; Zaretzke, M.-K.; Bröring, M. Viking Helmet Corroles: Activating Inert Oxidometal Corroles. *Chem. - Eur. J.* **2017**, *23*, 13897–13900.

(22) Alemayehu, A. B.; Vazquez-Lima, H.; Gagnon, K. J.; Ghosh, A. Tungsten Biscorroles: New Chiral Sandwich Compounds. *Chem. - Eur. J.* **2016**, *22*, 6914–6920.

(23) Alemayehu, A. B.; Vazquez-Lima, H.; McCormick, L. J.; Ghosh, A. Relativistic effects in metallocorroles: comparison of molybdenum and tungsten biscorroles. *Chem. Commun.* **2017**, *53*, 5830–5833.

(24) Schies, C.; Alemayehu, A. B.; Vazquez-Lima, H.; Thomas, K. E.; Bruhn, T.; Bringmann, G.; Ghosh, A. Metallocorroles as inherently

chiral chromophores: resolution and electronic circular dichroism spectroscopy of a tungsten biscorrole. *Chem. Commun.* **2017**, *53*, 6121−6124.

(25) Alemayehu, A. B.; Teat, S. J.; Borisov, S. M.; Ghosh, A. Rhenium-Imido Corroles. *Inorg. Chem.* **2020**, *59*, 6382−6389.

(26) Einrem, R. F.; Braband, H.; Fox, T.; Vazquez-Lima, H.; Alberto, R.; Ghosh, A. Synthesis and molecular structure of ^{99}Tc Corroles. *Chem. - Eur. J.* **2016**, *22*, 18747−18751.

(27) Alemayehu, A. B.; Einrem, R. F.; McCormick-McPherson, L. J.; Settineri, N. S.; Ghosh, A. Synthesis and molecular structure of perhalogenated rhenium-oxo corroles. *Sci. Rep.* **2020**, *10*, 19727.

(28) Kadish, K. M.; Burdet, F.; Jerome, F.; Barbe, J.-M.; Ou, Z.; Shao, J.; Guilard, R. Synthesis, Physicochemical and Electrochemical Properties of Metal-Metal Bonded Ruthenium Corrole Homodimers. *J. Organomet. Chem.* **2002**, *652*, 69−76.

(29) Simkhovich, L.; Luobeznova, I.; Goldberg, I.; Gross, Z. Mono- and Binuclear Ruthenium Corroles: Synthesis, Spectroscopy, Electrochemistry, and Structural Characterization. *Chem. - Eur. J.* **2003**, *9*, 201−208.

(30) Alemayehu, A. B.; Vazquez-Lima, H.; Gagnon, K. J.; Ghosh, A. Stepwise Deoxygenation of Nitrite as a Route to Two Families of Ruthenium Corroles: Group 8 Periodic Trends and Relativistic Effects. *Inorg. Chem.* **2017**, *56*, 5285−5294.

(31) Reinholdt, A.; Alemayehu, A. B.; Gagnon, K. J.; Bendix, J.; Ghosh, A. Electrophilic Activation of Osmium-Nitrido Corroles: The OsN Triple Bond as a π-Acceptor Metallaligand in a Heterobimetallic $\mathrm{Os^{VI}N{-}Pt^{II}}$ Complex. *Inorg. Chem.* **2020**, *59*, 5276−5280.

(32) Alemayehu, A. B.; McCormick, L. J.; Vazquez-Lima, H.; Ghosh, A. Relativistic Effects on a Metal−Metal Bond: Osmium Corrole Dimers. *Inorg. Chem.* **2019**, *58*, 2798−2806.

(33) Alemayehu, A. B.; McCormick-McPherson, L. J.; Conradie, J.; Ghosh, A. Rhenium Corrole Dimers: Electrochemical Insights into the Nature of the Metal-Metal Quadruple Bond. *Inorg. Chem.* **2021**, *60*, 8315−8321.

(34) Collman, J. P.; Arnold, H. J. Multiple Metal-Metal Bonds in 4d and 5d Metal-Porphyrin Dimers. *Acc. Chem. Res.* **1993**, *26*, 586−592.

(35) Jacobi, B. G.; Laitar, D. S.; Pu, L.; Wargocki, M. F.; DiPasquale, A. G.; Fortner, K. C.; Schuck, S. M.; Brown, S. N. Stoichiometric and Catalytic Oxygen Activation by Trimesityliridium(III). *Inorg. Chem.* **2002**, *41*, 4815−4823.

(36) Palmer, J. H.; Lancaster, K. M. Molecular Redox: Revisiting the Electronic Structures of the Group 9 Metallocorroles. *Inorg. Chem.* **2012**, *51*, 12473−12482.

(37) Thomassen, I. K.; McCormick-McPherson, L. J.; Borisov, S. M.; Ghosh, A. Iridium Corroles Exhibit Weak Near-Infrared Phosphorescence but Efficiently Sensitize Singlet Oxygen Formation. *Sci. Rep.* **2020**, *10*, 7551.

(38) Thomassen, I. K.; Rasmussen, D.; Einrem, R. F.; Ghosh, A. Simple, Axial Ligand-Mediated Route to Water-Soluble Iridium Corroles. *ACS Omega* **2021**, *6*, 16683.

(39) Chen, Q.-Y.; Fridman, N.; Diskin-Posner, Y.; Gross, Z. Palladium Complexes of Corroles and Sapphyrins. *Chem. - Eur. J.* **2020**, *26*, 9481−9485.

(40) For a series of innocent Pt(IV) corroles, see: Alemayehu, A. B.; McCormick, L. J.; Gagnon, K. J.; Borisov, S. M.; Ghosh, A. Stable Platinum(IV) Corroles: Synthesis, Molecular Structure, and Room-Temperature Near-IR Phosphorescence. *ACS Omega* **2018**, *3*, 9360−9368.

(41) Capar, C.; Thomas, K. E.; Ghosh, A. Reductive Demetalation of Copper Corroles: First Simple Route to Free-Base β-Octabromocorroles. *J. Porphyrins Phthalocyanines* **2008**, *12*, 964−967.

(42) Capar, C.; Hansen, L.-K.; Conradie, J.; Ghosh, A. β-Octabromo-*meso*-tris(pentafluorophenyl)corrole: Reductive Demetalation-Based Synthesis of a Heretofore Inaccessible, Perhalogenated Free-Base Corrole. *J. Porphyrins Phthalocyanines* **2010**, *14*, 509−512.

(43) Thomas, K. E.; Gagnon, K. J.; McCormick, L. J.; Ghosh, A. Molecular structure of gold 2,3,7,8,12,13,17,18-octabromo-5,10,15-tris(4′-pentafluorosulfanylphenyl)corrole: Potential insights into the insolubility of gold octabromocorroles. *J. Porphyrins Phthalocyanines* **2018**, *22*, 596−601.

(44) Capar, J.; Zonneveld, J.; Berg, S.; Isaksson, J.; Gagnon, K. J.; Thomas, K. E.; Ghosh, A. Demetalation of Copper Undecaarylcorroles: Molecular Structures of a Free-Base Undecaarylisocorrole and a Gold undecaarylcorrole. *J. Inorg. Biochem.* **2016**, *162*, 146−153.

(45) Larsen, S.; McCormick-McPherson, L. J.; Teat, S. J.; Ghosh, A. Azulicorrole. *ACS Omega* **2019**, *4*, 6737−6745.

(46) Wasbotten, I. H.; Wondimagegn, T.; Ghosh, A. Electronic Absorption, Resonance Raman, and Electrochemical Studies of Planar and Saddled Copper(III) *Meso*-Triarylcorroles. Highly Substituent-Sensitive Soret Bands as a Distinctive Feature of High-Valent Transition Metal Corroles. *J. Am. Chem. Soc.* **2002**, *124*, 8104−8116.

(47) Bröring, M.; Bregier, F.; Tejero, E. C.; Hell, C.; Holthausen, M. C. Revisiting the Electronic Ground State of Copper Corroles. *Angew. Chem., Int. Ed.* **2007**, *46*, 445−448.

(48) Alemayehu, A. B.; Gonzalez, E.; Hansen, L. K.; Ghosh, A. Copper Corroles Are Inherently Saddled. *Inorg. Chem.* **2009**, *48*, 7794−7799.

(49) Alemayehu, A. B.; Hansen, L. K.; Ghosh, A. Nonplanar, Noninnocent, and Chiral: A Strongly Saddled Metallocorrole. *Inorg. Chem.* **2010**, *49*, 7608−7610.

(50) Berg, S.; Thomas, K. E.; Beavers, C. M.; Ghosh, A. Undecaphenylcorroles. *Inorg. Chem.* **2012**, *51*, 9911−9916.

(51) Thomas, K. E.; Vazquez-Lima, H.; Fang, Y.; Song, Y.; Gagnon, K. J.; Beavers, C. M.; Kadish, K. M.; Ghosh, A. Ligand Noninnocence in Coinage Metal Corroles: A Silver Knife-Edge. *Chem. - Eur. J.* **2015**, *21*, 16839−16847.

(52) Thomassen, I. K.; McCormick, L. J.; Ghosh, A. Synthesis and Molecular Structure of a Copper Octaiodocorrole. *ACS Omega* **2018**, *3*, 5106−5110.

(53) Thomas, K. E.; Settineri, N. S.; Teat, S. J.; Steene, E.; Ghosh, A. Molecular Structure of Copper and μ-Oxodiiron Octafluorocorrole Derivatives: Insights into Ligand Noninnocence. *ACS Omega* **2020**, *5*, 10176−10182.

(54) Lim, H.; Thomas, K. E.; Hedman, B.; Hodgson, K. O.; Ghosh, A.; Solomon, E. I. X-ray Absorption Spectroscopy as a Probe of Ligand Noninnocence in Metallocorroles: The Case of Copper Corroles. *Inorg. Chem.* **2019**, *58*, 6722−6730.

(55) Thomas, K. E.; Conradie, J.; Hansen, L. K.; Ghosh, A. A Metallocorrole with Orthogonal Pyrrole Rings. *Eur. J. Inorg. Chem.* **2011**, *2011*, 1865−1870.

(56) Thomas, K. E.; Beavers, C. M.; Ghosh, A. Molecular Structure of a Gold β-Octakis(trifluoromethyl)-*meso*-triarylcorrole: An 85° Difference in Saddling Dihedral Relative to Copper. *Mol. Phys.* **2012**, *110*, 2439−2444.

(57) Lemon, C. M. Corrole photochemistry. *Pure Appl. Chem.* **2020**, *92*, 1901−1919.

(58) Palmer, J. H.; Durrell, A. C.; Gross, Z.; Winkler, J. R.; Gray, H. B. Near-IR Phosphorescence of Iridium(III) Corroles at Ambient Temperature. *J. Am. Chem. Soc.* **2010**, *132*, 9230−9231.

(59) Alemayehu, A. B.; Day, N. U.; Mani, T.; Rudine, A. B.; Thomas, K. E.; Gederaas, O. A.; Vinogradov, S. A.; Wamser, C. C.; Ghosh, A. Gold Tris(carboxyphenyl)corroles as Multifunctional Materials: Room Temperature Near-IR Phosphorescence and Applications to Photodynamic Therapy and Dye-Sensitized Solar Cells. *ACS Appl. Mater. Interfaces* **2016**, *8*, 18935−18942.

(60) Borisov, S. M.; Alemayehu, A.; Ghosh, A. Osmium-Nitrido Corroles as NIR Indicators for Oxygen Sensors and Triplet Sensitizers for Organic Upconversion and Singlet Oxygen Generation. *J. Mater. Chem. C* **2016**, *4*, 5822−5828.

(61) Borisov, S. M.; Einrem, R. F.; Alemayehu, A. B.; Ghosh, A. Ambient-temperature near-IR phosphorescence and potential applications of rhenium-oxo corroles. *Photochem. Photobiol. Sci.* **2019**, *18*, 1166−1170.

(62) Einrem, R. F.; Alemayehu, A. B.; Borisov, S. M.; Ghosh, A.; Gederaas, O. A. Amphiphilic Rhenium-Oxo Corroles as a New Class of Sensitizers for Photodynamic Therapy. *ACS Omega* **2020**, *5*, 10596−10601.

(63) Zach, P. W.; Freunberger, S. A.; Klimant, I.; Borisov, S. M. *ACS Appl. Mater. Interfaces* **2017**, *9*, 38008−38023.

(64) Higashino, T.; Kurumisawa, Y.; Alemayehu, A. B.; Einrem, R. F.; Sahu, D.; Packwood, D.; Kato, K.; Yamakata, A.; Ghosh, A.; Imahori, H. Heavy Metal Effects on the Photovoltaic Properties of Metallocorroles in Dye-Sensitized Solar Cells. *ACS Appl. Energy Mater.* **2020**, *3*, 12460−12467.

(65) Teo, R. D.; Hwang, J. Y.; Termini, J.; Gross, Z.; Gray, H. B. Fighting Cancer with Corroles. *Chem. Rev.* **2017**, *117*, 2711−2729.

(66) Alemayehu, A. B.; Vazquez-Lima, H.; Teat, S. J.; Ghosh, A. Unexpected Molecular Structure of a Putative Rhenium-Dioxo-Benzocarbaporphyrin Complex. Implications for the Highest Transition Metal Valence in a Porphyrin-Type Ligand Environment. *ChemistryOpen* **2019**, *8*, 1298−1302.